ESRF
The European Synchrotron

ESRF HIGHLIGHTS 2019

Contents

DEAR ESRF USER, DEAR READER

Francesco Sette

After 25 years of User Service Mode (USM) operation, 2019 was a special no-USM year. On 10 December 2018, the ESRF X-ray source was shut down for a 20-month upgrade to a brand-new storage ring, the new Extremely Brilliant Source (EBS), with USM resuming in August 2020. The ESRF beam may have been switched off this year, but ESRF-enabled science never stopped, and, once again, this edition of the *ESRF Highlights* reflects the excellence and diversity of the discoveries made by ESRF users.

Research continues to reach impressive levels

In fact, during 2019, the scientific outcome based on previous years' beamtime at the ESRF reached levels by all means comparable in terms of quantity (for example, number of refereed publications) and quality (for example, number of publications in high-impact journals) – very similar to those of previous USM years. These *Highlights* report on selected examples and underline the long-term impact of research carried out at the ESRF. Meanwhile, excitement for the new opportunities to be unveiled by the EBS drives the preparation for a dynamic and efficient restart of the ESRF public and CRG beamline portfolio, which will begin in March 2020, with the objective to provide a maximum number of operational beamlines on the date of USM restart, on 25 August, 2020.

> “*This edition of the ESRF Highlights reflects the excellence and diversity of the discoveries made by ESRF users. I hope that it will inspire you for your next experiment at the ESRF.*”

During the past year, enthusiasm for EBS has driven the conception and development of new beamlines to be deployed in the coming years, and it has also been demonstrated by impressive activity in terms of workshops, conferences and schools (about 20 since the 2018 User Meeting) to discuss and prepare future EBS science with the user community. These activities not only allowed us to keep contact with ESRF users, but also to attract and interest the next generation of scientists, who will be the main actors for the best use of the new, extremely bright synchrotron source, and who will explore new research fields for the coming decades. We are looking forward to your proposals, starting from the next beamtime proposal submission deadline of 2 March 2020!

First beam for EBS

On 2 December 2019, we celebrated the first injection of electrons in the new EBS storage ring and, on 6 December, the first stored beam. Seeing the first electrons circulating, in perfect accordance with the schedule established in 2015, was an intensely rewarding moment for all the teams who have been working tirelessly on the EBS conception and implementation since its launch in 2015. It marked the successful completion of the engineering and installation of the EBS storage ring within the existing ESRF infrastructure, and the start of the commissioning phase of a brand-new generation of high-energy synchrotrons.

It was also a day of pride for the whole synchrotron community, as this innovative project, based on the principle of international cooperation, aims to serve the world's synchrotron scientists and users. This was possible thanks to the dedication and expertise of the ESRF staff, the collaboration with international partner institutes and industry, and the invaluable strong, constant support and trust of our 22 partner countries, all joining forces for the same goals: pioneering synchrotron science and tackling global challenges that are too complex to be solved by one country alone.

Ready for the challenges ahead

2020 will be equally intense. In parallel to optimising the operation of the new machine, we will also be working assiduously to restart the ESRF experimental programme. In particular, the objective of USM restart by August 2020 with a maximum number of public and CRG beamlines is ESRF's top priority for 2020. In addition, we will continue to advance according to plan on the complex work that will address the completion of the EBS programme and the return of the ESRF to full user operation in the years 2023-2024. This work will be carried out on many fronts, from the launch of EBS flagship beamlines and the new High-Power Laser Platform, to the refurbishment of existing beamlines, the development of key instrumentation and detectors, the development and implementation of the ESRF data-management programme, and the recruitment of new beamline scientists and staff. All ESRF teams are mobilised to provide the synchrotron community with the best tools to push the limits of science.

EBS will provide new tools for the investigation of materials and living matter from the macroscopic world down to the nanometre scale, and hopefully to the direct imaging of conglomerates of a few hundred atoms. It will thus allow scientists to probe complex materials in greater detail, with higher quality, and much faster, sparking new research opportunities in fields such as health, energy, the environment, new sustainable and innovative materials, and also cultural heritage and paleontology. By investigating the complexity of condensed and living matter, EBS will help address global challenges and contribute to their solution for the benefit of our society.

A new page in X-ray science

And what better way, in 2020, to open a new page in X-ray science, than to dedicate it to the women and men who pioneered the field of X-ray science, perhaps already imagining all the wonderful discoveries that would follow thanks to their work. In particular, it is with immense pleasure that I wish to dedicate the ignition of EBS science to Wilhelm Conrad Röntgen, on the 125th anniversary of his discovery of X-rays, and to Rosalind Elsie Franklin, in what would have been her 100th year, for her X-ray crystallography work that is so central to the understanding of the molecular structures of DNA, RNA, viruses, and graphite.

Thanks to everyone's combined hard work, 2019 was an intense but exciting year full of developments and important achievements. Thank you to all the scientists who contributed to this 2019 edition of the *ESRF Highlights*. I hope you enjoy it and that it will inspire you for your next experiment at the ESRF.

FRANCESCO SETTE
Director General,
ESRF

2019
AT THE ESRF

January

H2020 project BEATS launched

The European Horizon2020 project, BEAmline for Tomography at SESAME (BEATS), was launched with the objective to design and construct a beamline for hard-X-ray, full-field tomography at the SESAME synchrotron in Jordan, in collaboration with the ESRF.

© SESAME

H2020 project PaNOSC launched

A Horizon2020 project coordinated by the ESRF to promote open access to data, the Photon and Neutron Open Science Cloud (PaNOSC) brings together six strategic European research infrastructures to help construct the European Open Science Cloud, an ecosystem for universal and cross-disciplinary open access to data through a single access point.

© S. Candé

5 February

Elisa Borfecchia, Young Scientist 2019

Elisa Borfecchia, from the University of Turin in Italy, was awarded the title of Young Scientist 2019 by the ESRF User Organisation for the impressive results on selective catalysis that she obtained with extensive use of X-ray spectroscopy at ID26 and BM23.

© C. Argoud

28 February

Dismantling of third-generation source complete

The dismantling of the ESRF's third-generation storage ring was completed in 11 weeks. Teams removed over 1720 tonnes of equipment, including girders, magnets, vacuum chambers and associated instrumentation, from the storage ring tunnel.

© S. Candé

6 March

ESRF installs first components of EBS

ESRF teams installed the first components for the EBS in the storage ring tunnel: a key milestone in the 150M€ pioneering upgrade programme to replace the third-generation source with a brand-new machine, boosting the performance of its generated X-ray beams by 100.

© S. Candé

21 March

ESRF user wins L'Oréal UNESCO award

Kirsten Marie Ørnsbjerg Jensen, an assistant professor at the University of Copenhagen and a longtime user of the ESRF, was awarded the 2019 L'Oréal-UNESCO international Women in Science Rising Talents award for her work on structural analysis of nanomaterials.

© C. Argoud

22 May

ESRF projects ATTRACT funding

Four ESRF projects were among 170 schemes awarded funding by ATTRACT, a Horizon2020 project funded by the European Union and backed by a consortium of research organisations, including the ESRF, to develop breakthrough detection and imaging technologies for science and society.

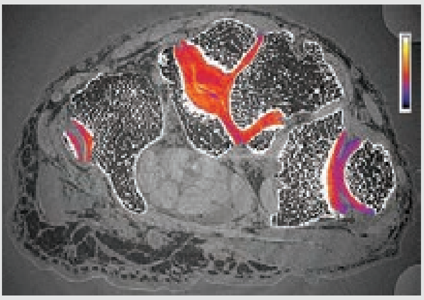

© E. Brun

24 May

EBS girder installation complete

ESRF teams installed the final EBS girder in the storage ring tunnel, marking the successful completion of the girder installation phase of the project. Teams had three months to install 129 new girders supporting over 10 000 components precision-aligned to within 50 microns.

© S. Candé

14 June

ESRF inspires at Street Art Festival

The ESRF inspired Canadian street artist Aaron Li Hill to include a design of the synchrotron as a key part of his monumental fresco for Grenoble Street Art Fest 2019, named 'Process of Acceleration'.

© A. Berlese

14 June

ESRF-India workshop

A symposium on multidisciplinary research at the ESRF was organised by the Regional Centre for Biotechnology in Faridabad, India, as a great opportunity to promote and strengthen the longstanding research collaboration between the ESRF and India.

© C. Argoud

2019
AT THE ESRF

June

ESRF welcomes European Young Scientist winner

The ESRF welcomed Emily Xu, a young British student and laureate of the 2019 European Contest for Young Scientists (EUCYS). The competition was set up in 1989 by the European Commission to promote the ideals of cooperation and exchange between young scientists.

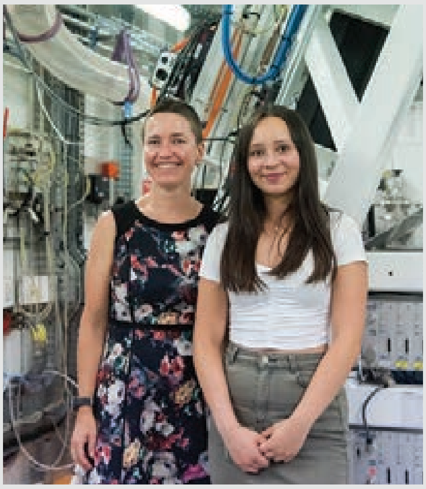
© C. Argoud

September

ESRF/ILL host joint Student Summer Programme

The ESRF/ILL International Student Summer Programme on X-Ray and Neutron Science was held from 1 – 28 September. Twenty international undergraduate students took part in a four-week experimental project, embedded in a research group at the ESRF or ILL, together with a series of introductory lectures on the principles and applications of X-ray and neutron science.


© S. Claisse

10 – 12 October

French Science Festival

The ESRF welcomed the public at the annual French Science Festival. As well as leading 18 sessions with primary school classes from the region, the EPN Campus held a stand showcasing the research carried out at the four institutes, centred around one of the main themes of this year's Science Festival, the Periodic Table.

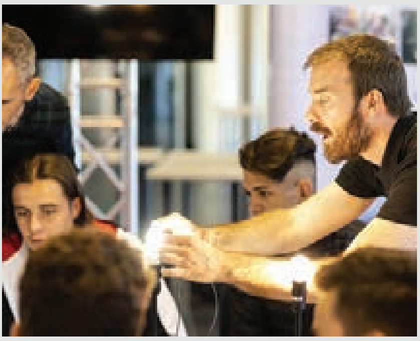
© GIANT Campus: Utopik PHOTOS

October

EU project InnovaXN launched

October saw the launch of InnovaXN, a five-year EU-funded doctoral training programme bringing together the expertise of large-scale research infrastructures, such as the ESRF, with the R&D needs of European industry.

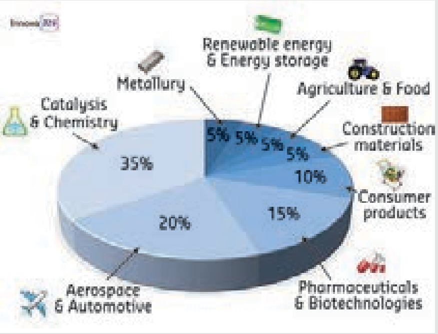

© InnovaXN

11 – 13 November

South Africa–ESRF Light Sources conference

A South Africa–ESRF Light Sources conference was held in Johannesburg to exchange on the scientific collaboration with South Africa, and further collaboration, especially in light of the EBS, in fields such as heritage sciences and palaeontology, medical, geo- and environmental sciences, energy, nano- and material sciences, and competitive industry.

© saip.org.za

15 November

H2020 project STREAMLINE launched

STREAMLINE is a Horizon2020-funded five-year project that will complement the ESRF-EBS upgrade by enhancing user operation through new procedures and systems. STREAMLINE will train existing users in the new EBS opportunities as well as reaching out to new scientific communities in academia and industry.

© h2020-streamline-project.eu

12 – 14 November

Artificial Intelligence workshop

The ESRF hosted an artificial intelligence (AI) workshop, broadcast live from the ESRF's Youtube channel. X-ray and neutron facilities are facing growing challenges in producing, handling, treating and fully exploiting data of increasing volume and complexity. The workshop explored the potential applications of AI in treating data at large-scale facilities.

© C. Argoud

2 December

EBS commissioning started

The first electrons were injected in the new EBS storage ring according to schedule, marking the successful completion of the engineering and installation of EBS within the existing ESRF infrastructure, and the start of the commissioning phase.

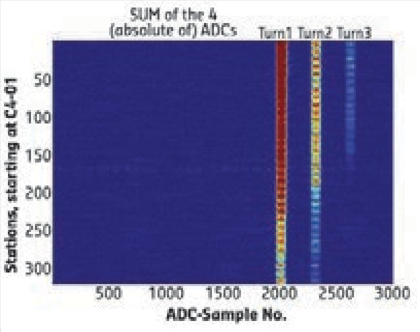

© J.-L. Revol

6 December

First stored beam for EBS

Electrons were stored for the first time in the EBS storage ring, only five days after the start of the commissioning.

© F. Ewald

15 December

Record emittance for EBS

Only 13 days after the start of commissioning, teams were able to accumulate electrons in the storage ring at the world-record horizontal emittance value of 308 pm. The achievement was an important milestone on the way to opening a brand-new generation of high-energy synchrotron to scientific users in August 2020.

© D. Chenevier

STATUS OF THE EBS

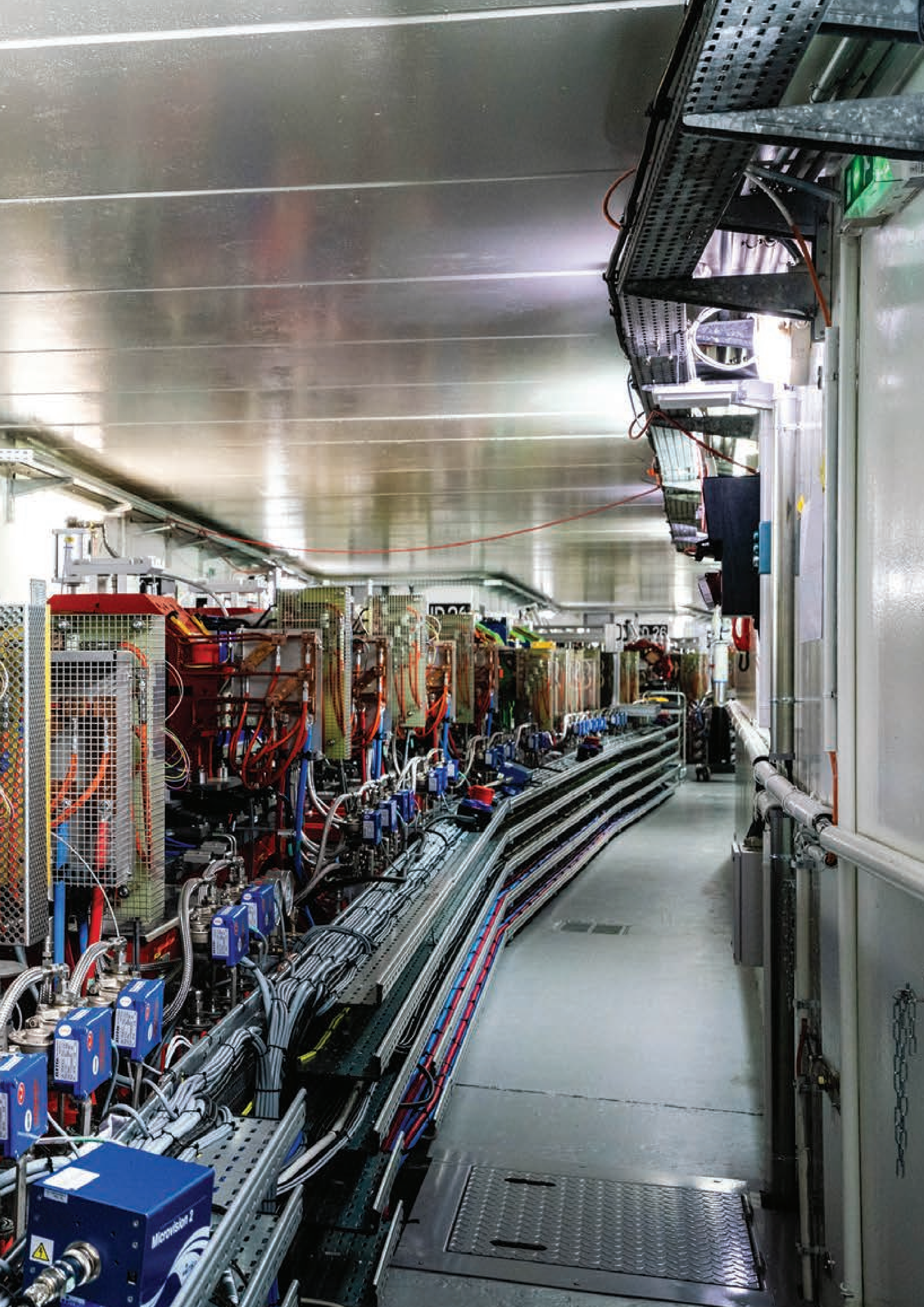
Microvision 2

STATUS OF THE EBS

The past year witnessed the achievement of momentous milestones in the Extremely Brilliant Source (EBS) programme, including the completion of the dismantling and installation phases and the start of commissioning of the EBS storage ring. Work is progressing well on the new flagship EBS beamlines and further beamline upgrades are also underway.

PROJECT OVERVIEW

2019 marked the fifth year of the ESRF's EBS project to implement a new, fourth-generation lattice for the storage ring. This will reduce the equilibrium horizontal emittance from 4 nm to about 134 pm, thus greatly increasing the brilliance and coherence of the X-rays generated and opening up new perspectives for experiments that are not conceivable today. Much of the work of the project in 2019 focused on the dismantling of the previous, third-generation storage ring, which began with the start of the shutdown on 10 December 2018, and on the installation and alignment of the 129 pre-assembled girders that comprise the new lattice. The installation phase was completed successfully by the end of November 2019, with storage ring commissioning commencing on schedule on 2 December.

Fig. 1: Dismantling of the third-generation source began in December 2018. By March, nearly 1800 tonnes of material had been removed from the storage ring tunnel.

The eighth and ninth Machine Advisory Committee (MAC) meetings were held at the ESRF in May and November 2019. Committee members from leading institutes around the world came together to discuss the progress of the EBS project and to make recommendations for the six months ahead. In November, the MAC was impressed with the level of progress made over the year and congratulated the ESRF staff on the timely achievement of key milestones ready for the start of machine commissioning in December.

DISMANTLING PHASE COMPLETED

The dismantling of the previous storage ring took place over 11 weeks, which saw more than 1720 tonnes of material removed, including 160 girders, 200 km of cables and 6000 m of piping. Some components, such as the insertion devices and beam-loss detectors, were recovered to be re-used in the new machine. Work started to individually dismantle and test each piece of equipment removed from the tunnel. Pipes and cables were also disconnected and removed. Cell by cell, the concrete roof was removed, and each girder, insertion device and radiofrequency (RF) cavity lifted out with the three overhead cranes in the Experimental Hall (**Figure 1**).

Following the dismantling, civil works in the tunnel began in February, and included removing concrete pillars and girder support plates from the tunnel floor. Some of the existing trenches in the tunnel floor were then filled with concrete and the tunnel was cleaned and repainted. Finally, 258 new girder support plates were installed on the tunnel floor (**Figure 2**). The civil works phase ended in March.

Fig. 2: Civil works were carried out to prepare the tunnel for the new lattice, including painting and installing new girder support plates.

COMPLETION OF THE INSTALLATION PHASE

The first EBS girder was put into place in March (**Figure 3**), marking the start of the installation, connection and alignment of 129 pre-assembled girders as well as equipment such as the RF cavities and the straight sections. The girder installation was successfully completed in May, marking a major milestone in the project. Thirteen new HOM-damped RF cavities were also installed in the storage ring by the end of May, fully equipped with all ancillaries and connected through the waveguide distribution network to the RF power transmitters. All 32 cells of the storage ring were connected to the cooling system by July, while the installation of 13 000 cables connecting equipment to the control room was completed in September. The equipment tests started progressively as soon as the cabling in each zone was finished.

The installation of the insertion devices in the EBS storage ring started in July and was finished in November (**Figure 4**). All the in-vacuum undulators, including cryogenic permanent magnet undulators, were adapted to the EBS lattice, which required the engineering modification of the cooling layout and the integration of new flexible transitions. The devices were then reinstalled in the storage ring according to schedule. The different sources for the bending magnet beamlines were magnetically characterised and tuned, including eight short bending magnets, eight two-pole wigglers and one high-field, three-pole wiggler.

In July, the EBS magnets were tested for the first time as the principal electromagnets and corrector magnets in four cells were powered up then ramped up to operation settings for three hours. A big change for EBS is that each magnet in the storage ring is powered individually, rather than by family of 32 or 64 magnets as in the previous ring: this gives improved control over the magnets, but it also means there are nearly a thousand separate power supplies to oversee. For this, the concept of 'hot-swapping' was implemented, which means that in the case of a failure on one of the units, it can be changed quickly without losing the beam, ensuring the high reliability of the magnet power supplies.

The injection zone was upgraded as planned, with the reduction of the booster circumference and the installation of magnets and supports in the injection zone taking place in late August. The four ceramic chambers for the injection kickers were delivered and installed in September, followed by vacuum connections and alignment.

Fig. 3: The impressive installation of 129 pre-assembled girders in the storage ring tunnel started in March 2019.

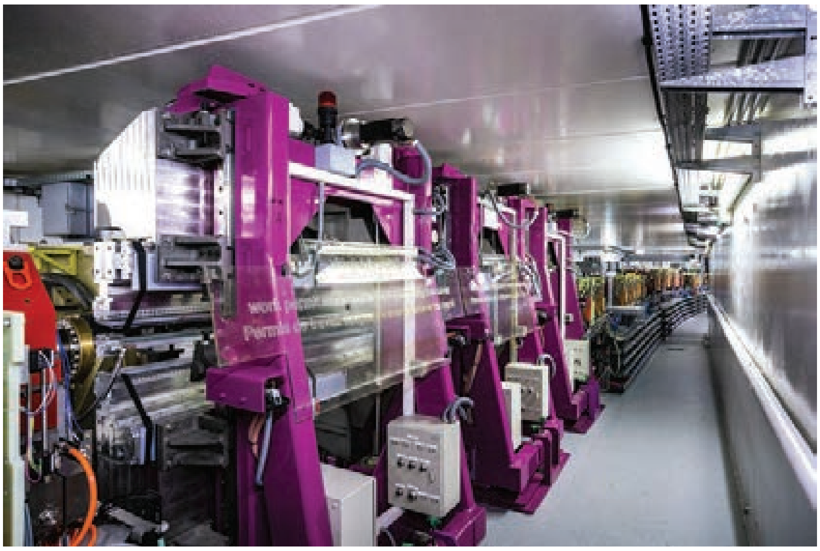

Fig. 4: Following the completion of the girder installation in May, the insertion devices were installed in the storage ring tunnel from July to November.

Concerning the vacuum, the adaptation of the previous in-vacuum insertion devices for EBS was accomplished and the devices were ready for installation by the end of September. The straight sections were installed, connected and baked out by October. The sector valves and bellows were replaced and all girders re-connected and under vacuum by November.

Regarding diagnostic equipment, all of the five stripline chambers, scrapers, pick-up chambers and the beam stop were successfully installed, and the two collimators were installed and aligned between August and November. All other equipment was tested and calibrated by November.

The installation of a new liquid nitrogen loop took place in October and November. On top of the loops and connections, a complete refurbishment of the liquid nitrogen tanks was undertaken, with a new tank added in October to cope with the higher levels of consumption.

A major task in the installation phase was the precision-alignment of the 129 girders and other equipment. Following the installation and alignment of the girder feet and the girders themselves in May, preliminary alignment and then fine alignment was carried out. Next, the DQ2 magnets were installed across girders 2 and 3, and aligned to within less than 100 µm. In addition to the girder alignment, the front ends, straight sections and insertion devices were installed and aligned, with the final alignment of the storage ring to less than 50 µm finished in mid-November (**Figure 5**).

Regarding the EBS control system, which is based on the ESRF-developed Tango Controls framework, a new archive database was developed to allow more data to be stored at higher frequencies while speeding up the extraction time significantly. Significant effort was invested in developing the control software for the power supply hot-swap system, integrating the new beam position monitors with the existing ones, and replacing the hardware to interface the personnel safety system. A complete new set of graphical applications was developed for operating the EBS. The control system was ready on time with all features required to commission the EBS.

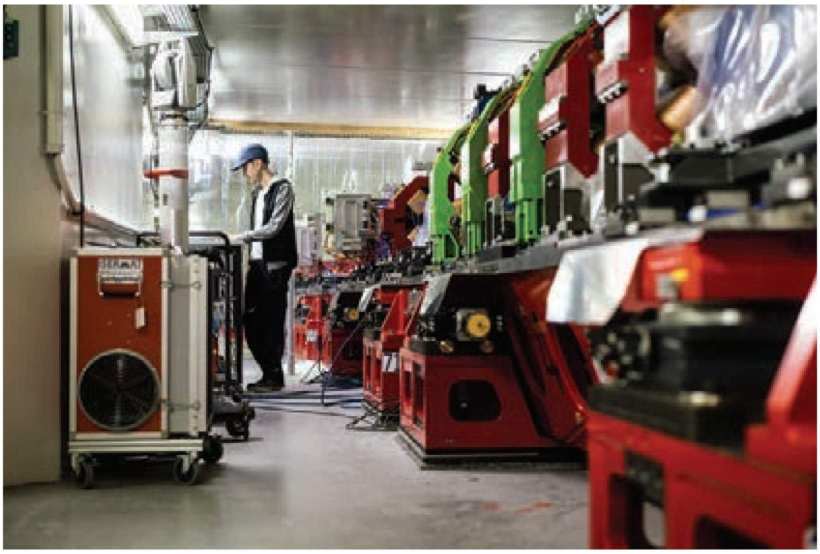

Fig. 5: The precision-alignment of the storage ring components to less than 50 microns was completed in November.

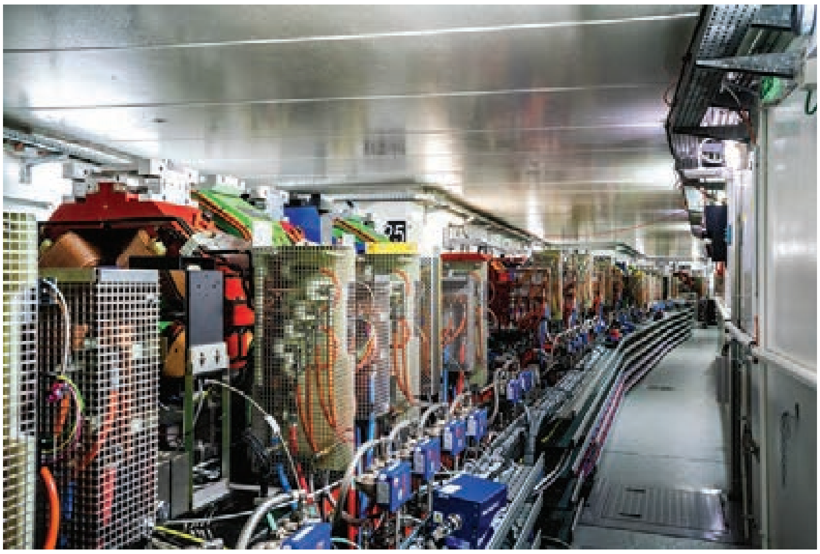

Fig. 6: The installation phase of the EBS was completed on schedule and the machine was ready to commission by the end of November 2019.

The completion of all these tasks is the result of the skill and dedication of ESRF staff, whose contributions have ensured the EBS installation phase has been accomplished successfully and on schedule (**Figure 6**).

STORAGE RING COMMISSIONING STARTED

In mid-November, the storage ring tunnel was closed. Following global power supply tests and the start-up of the injector system, the first electrons were injected into the LINAC and booster, up to TL2. On 2 December, the commissioning phase began with the injection of the first electrons into the EBS storage ring (**Figure 7**). Less than two weeks later, teams were able to accumulate up to 6.5 mA beam current with a world record horizontal emittance of 230 pm. The machine commissioning will run until the end of February 2020. Over the following months, teams will continue to fully characterise all aspects of the machine in terms of hardware performances (vacuum system, RF, power supplies, etc.), identify potential weaknesses, and adopt mitigation solutions. All resources will be used to improve the reliability and the uptime of the new machine up to User Service Mode (USM) standards, with debugging of hardware and software continuing during this time. Diagnostic tools and continuously evolving mathematical algorithms will be utilised to identify potential problems and errors, while simultaneously tuning the machine in order to improve its overall performances, in particular, to bring the machine optics as close as possible to design specifications.

The storage ring commissioning will be followed by six months of beamline commissioning, commencing in March 2020.

PUBLIC BEAMLINE UPGRADE

Of the four selected EBSL beamline projects:

- EBSL1 – ID18: Beamline for coherence applications;
- EBSL2 – ID03: Beamline for hard X-ray diffraction microscopy;

- EBSL3 – BM18: High-throughput, large-field, phase-contrast tomography beamline;
- EBSL8 – ID29: Serial crystallography beamline,

EBSL3 and EBSL8 entered the implementation phase in 2019. The construction of the satellite building for EBSL3 – BM18 progressed according to schedule and the contract for the construction of the experimental hutch in the satellite building was established. The design of the beamline instrumentation was finished and most of the parts have been ordered for assembly and installation.

Following the successful review of the technical design report (TDR) for EBSL8 – ID29, approximately 40% of the contracts for the construction of the infrastructure and the scientific instrumentation were placed. The scientific instrumentation of the old ID29 beamline was removed and construction started in November 2019, as planned.

The TDR for the implementation of EBSL2 – ID03 was started in autumn 2019, as well as an update of the conceptual design report (CDR) for the EBSL1 – ID18 project, following the appointment of a lead scientist and a one-week exchange with the user community in September. The regular beamline refurbishment programme also progressed as part of the EBS beamline-readiness plan.

In addition to the EBSL beamline projects, several existing beamlines are being rebuilt or deeply refurbished. This includes:

- ID27: High-pressure beamline;
- ID24: X-ray absorption beamline with two branches;
- ID21: X-ray microscopy beamline;
- ID14: Nuclear resonance beamline;
- BM23: EXAFS beamline,
- BM29: BioSAXS beamline.

The TDR for the complete reconstruction of ID27 as a long beamline in the Chartreuse Hall has been finalised and reviewed. The detailed design is progressing well and all the long-lead items for the beamline optics have been ordered. The TDRs for the reconstruction of the two branches of ID24 (ED-XAS branch for the HPLF – high power laser facility; DCM branch for high-flux microbeam XAS) have been finalised and the construction phase started. The TDR for the third phase of the upgrade of ID21 has been finalised and approved for the complete reconstruction of the microscope in the experimental hutch. The TDR for the relocation of the nuclear resonance beamline ID18 to port ID14 as a new beamline has been started. The design of the core elements of the new beamline has been finished and the construction of those elements has been initiated for installation on beamline ID18 for testing and first user experiments before relocation to port ID14. The two operating bending magnet beamlines in the public beamline portfolio, BM23 and BM29, are currently being deeply refurbished for EBS-readiness and enhanced performance on their new two-pole wiggler sources.

Fig. 7: Commissioning of the EBS started on 2 December with the first injection of electrons into the new storage ring.

CRG BEAMLINE UPGRADE

In 2019, infrastructure works on beamlines exclusively focused on the Collaborating Research Group (CRG) beamlines. The split of the double-branch beamlines BM26A/B and BM30A/B continued as planned. The Dutch-Belgian CRG, DUBBLE, took over the reactivated beamline BM14 to replace beamline BM26A after the long shutdown.

The construction of the infrastructure for the new French CRG beamline BM07 was finished and the installation of the scientific equipment is underway. Work on deep modifications of the infrastructure of the CRG beamlines BM20 and BM28 continued in preparation for the new source. All CRG beamlines were re-aligned along the new EBS beam trajectory as defined by their choice of source (single-bend, two-pole wiggler A, or two-pole wiggler B). Corresponding works on the lead shielding were started and continued until the start of the EBS commissioning in December. Overall, the works for the EBS-readiness of the CRG beamlines are progressing well and will be finished in time for the restart of the beamlines in the beamline commissioning phase, from March 2 to August 24, 2020.

INSTRUMENTATION AND DATA MANAGEMENT

The EBS project comprises an ambitious instrumentation and technology programme, which is required to gain the greatest benefit from the new source properties.

DETECTOR PROCUREMENT AND DEVELOPMENT STRATEGY

In 2019, several activities were initiated to prepare the reception and installation of the high-performance pixel array detectors for scattering/diffraction beamlines, which will be delivered until 2021. The R&D activities of the EBS detector development plan (DDP) continued to progress, with all technology programmes developing satisfactorily, in particular, the definition and implementation of the upgraded version of the software framework for 2D detectors, LIMA, which will enable scalable systems, able to cope with the high-throughput data streams produced by advanced detectors. The development, in collaboration with the University of Heidelberg, of a new, very-high-dynamic-range and fast detector codenamed XIDER, received a grant from the H2020 ATTRACT initiative (**page 5**). The first test readout ASIC in 65 nm microelectronics technology for this project was received and is under evaluation. The firmware and software required for the SMARTPIX detector reached milestones necessary to build a 1-megapixel prototype ready for first evaluations at the beamline restart in 2020. The DDP went through its first full internal review in May – June 2019. The review looked in detail at the progress, achievements and issues found in the various programmes and R&D projects of the plan.

The collaboration with PSI for the usage and evaluation of the JUNGFRAU detector was extended to include the study of new types of pixelated sensors and the exchange of technical information and cooperation on the implementation of the high-performance computing platforms required to use JUNGFRAU detectors efficiently at storage rings. This aspect is crucial for the integration of the main detector at the new beamline for serial macromolecular crystallography, EBSL8 – ID29.

X-RAY OPTICS AND MECHATRONICS

In X-ray optics, considerable progress was made in the modelling of the propagation of partially coherent X-rays through imperfect optics (lenses, mirrors, etc.). Capabilities in the pressing of aluminium compound refractive lenses were improved and extended to smaller radii, and the surface figure error of a hard X-ray mirror was improved by combining differential deposition and offline metrology tools. Simultaneously, efforts continued to enhance the quality of 2D-surface topography measurements necessary for the correction of such mirror optics. The detailed design of a new thin-film deposition system optimised for multilayer coating of nanofocusing and high-resolution monochromators was completed and is scheduled for delivery in autumn 2020. The EBS beamline shutdown also presented the opportunity to upgrade some of the core tools in the ESRF crystal laboratory. The laboratory X-ray facilities and diamond saws essential for the manufacturing procedures will thus benefit from fundamental upgrades.

In the area of mechatronics, the major on-going development was the spectroscopy double-crystal monochromator prototype (**Figure 8**), where the positions and angles of the crystals are ensured by fast actuators controlled in real time in closed loop with 15 interferometric sensors. After the first tests in November 2018, offline tests with a laser beam, associated with dynamics modelling, resulted in improvements in system performance. For the nanopositioning and active stabilisation stage end-station (ID31), lab tests progressed to validate the concept of a multi-axis online metrology system with the required nanometric performances over a range of several millimetres. In parallel, development of a mechatronics control approach was started through a collaboration with experts from the University of Liège, Brussels.

DATA INFRASTRUCTURE

With experimental data rates expected to increase an estimated 10 to 100 times, dealing with data remains one of the major challenges of the EBS project and beyond. Conceptual work on the IT infrastructure was done to make sure that the new generation of high-resolution detectors on the ESRF beamlines can write data at maximum speed to buffer storage areas. It is from those buffer storage systems that on-line data reduction can take place before sending the data to central storage systems for further processing and finally archiving. Two new sets of computer clusters, based on the latest generation of graphics processing units and central processing units, respectively, have been purchased to increase batch-processing capacity during and after the experiments. In the context of data analysis software, a new version of *silx* (http://www.silx.org), the Scientific Library for eXperimentalists, was released. This library of common algorithms and graphical tools for building data analysis applications will facilitate the long-term maintenance of applications, resulting in an increasing number of applications based on *silx*.

Collaborative efforts continued on the Photon and Neutron Open Science Cloud (PaNOSC – coordinated by the ESRF) project for data

Fig. 8: The double-crystal monochromator prototype was further developed in 2019.

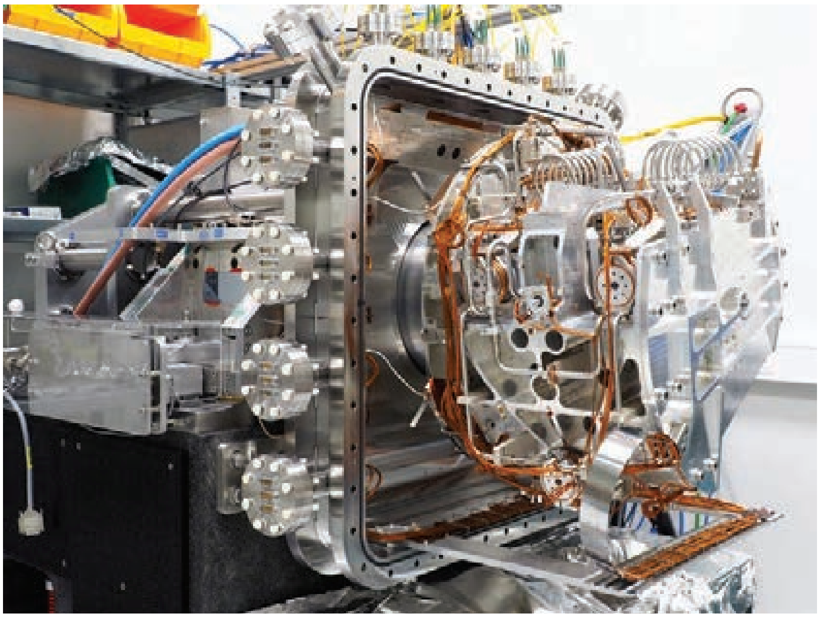
© R. Baker.

analysis software, following acceptance of the proposal by the European Commission and the project launch on 1 December 2018 (**page 178**). PaNOSC will boost and harmonise data management and data services across the ESFRI Photon and Neutron Sources over the next three years. Topics being addressed include data policies, FAIR data principles, rich metadata, data stewardship, data analysis notebooks, remote services for data analysis, long-term archiving, trusted data repositories, and training for users in the context of the European Open Science Cloud (EOSC) to connect data to computation in the most efficient way.

The ESRF Open Data Policy (http://www.esrf.fr/datapolicy) progressed to the implementation phase, with metadata being systematically collected on 18 beamlines, including the Cryo-EM, and raw data being archived for 10 years. Current plans foresee full implementation for all beamlines by the end of 2020. The first version of an electronic notebook was released to some beamlines for testing before the long shutdown. Feedback was very positive, with the e-logbook being considered a big step forward (**page 179**). Development continued during the long shutdown with the addition of new features requested by beamlines and in preparation for the first release of the e-logbook as open data. For this, a new data portal was developed and released. The new data portal enhances the user experience and will provide support for online data analysis. The CalipsoPLUS JRA2 project (led by ESRF and PSI) developed a prototype of data analysis as a service for local and remote users. Much effort was made to set up a generic Jupyter notebook service and a production-ready service for internal users.

Increased effort was invested in developing optimised data analysis algorithms using parallel hardware to handle the increase in data due to new detectors and the new source. A number of experiments will produce such large data sets that the time to process them will by far exceed the acquisition time. The main domains concerned are the imaging beamlines (starting with tomography and coherent diffraction), but also new techniques, such as serial macromolecular crystallography. New areas of research and development will include data compression and machine learning, and in this context, a workshop on Artificial Intelligence Applied to Photon and Neutron Science was organised jointly with the ILL and STFC.

As part of the conversion of scientific data to HDF5, the ESRF organised a workshop with the HDF group on HDF5 in Science and Industry in Europe. The workshop helped address questions around HDF5 and using this data format on the ESRF beamlines.

**J.-C. BIASCI, R. DIMPER, C. NEVO,
P. RAIMONDI, H. REICHERT and J. SUSINI**

SCIENTIFIC HIGHLIGHTS

MATTER AT EXTREMES

During the last decade, an unprecedented surge in high-pressure, high- and low-temperature research has greatly improved our fundamental understanding of materials under extreme conditions. Many scientific breakthroughs have been achieved across fields ranging from Earth and planetary science to physics, chemistry and materials research, and extending into biophysics/biochemistry. In this context, 'matter at extreme pressures and temperatures' was one of the science drivers for the construction of the Extremely Brilliant Source (EBS). In particular, detailed structural, electronic and vibrational studies on much smaller sample volumes and much shorter time scales will become possible with EBS. Higher pressure and temperature states that can be generated only in smaller volumes will be finely characterised. Submicron sample heterogeneities will also become accessible, down to 100 picoseconds, with a deeper understanding of processes such as phase transitions and transport under extreme conditions.

To tackle this challenging scientific programme, an ambitious refurbishment plan is underway at the Matter at Extremes (MEX) beamlines. State-of-the-art CdTe pixel detectors will be installed at the three X-ray diffraction instruments **ID06LVP**, **ID15B** and **ID27** to fully exploit the enhanced photon flux and perform fast shutterless data collection of high-quality powder and single-crystal data under extreme conditions.

Prior to its full reconstruction, the nuclear resonance beamline **ID18** will host two unique instruments: the nanoscope and spectrograph, resulting in an order-of-magnitude improvement of the spatial and energy resolution without compromise on the photon flux. These developments will lead to a reduction of the beam spot from 10 down to 0.2 micron, enabling nuclear resonance scattering experiments in the terapascal pressure regime. In parallel, as featured in this chapter (**page 26**), the new spectrograph developed by A. I. Chumakov *et al.* will improve the energy resolution from 0.5 meV to 0.1 meV, allowing density-of-phonon-states measurements of significantly higher quality.

Several important changes are also foreseen at the two X-ray absorption beamlines, BM23 and ID24. **BM23** will be re-aligned to a new, two-pole wiggler X-ray source and opened to users in January 2021. At this time, the high-energy-resolution micro-XAS station equipped with a five-crystal analyser spectrometer and an optimised XAS-DRIFTS-MS device will be fully operational.

In parallel, **ID24** will be entirely refurbished. The historical EDXAS-S branch will be converted into a high-brilliance XAS beamline equipped with an in-house scanning double-crystal monochromator with outstanding angular resolution. The new branch will provide a variable spot size from 1 μm to 1 mm and a variable flux up to 10^{14} photons/s, which will enable full EXAFS data-collection in ~1 s. This new instrument will be open to users in January 2022. The EDXAS-L branch (ID24-ED) will still be devoted to time-resolved (down to 100 picoseconds) experiments, including dynamic compression and pulsed magnetic field studies. The ID24-ED branch that will host the High Power Laser Facility will be delivered in September 2020 and resume user operation in July 2021.

Finally, a major refurbishment of the high-pressure XRD beamline **ID27** is currently in progress. The new instrument, which will re-open in September 2021, will nicely complement ID15B and ID06LVP, the two high-pressure diffraction beamlines, by providing nano-focusing monochromatic and 'pink' beam capabilities. An expected increase in photon flux by three orders of magnitude will enable microsecond time-resolved studies to bridge the gap between static and picosecond laser-driven dynamic compression experiments available at ID24. This instrument will also provide X-ray emission spectroscopy and X-ray imaging capabilities to widen the panel of techniques offered to ID27 users.

The selection of works presented in this chapter can be seen as a tribute to the former storage ring, which excellently served the user community for more than 25 years. It contains high-quality, in-house and user contributions from diverse research fields, including physics, chemistry and geosciences, illustrating the multidisciplinary nature of the MEX group.

By combining ultrasonic and XRD measurements at ID06LVP, A. R. Thomson *et al.* demonstrate that anomalous continent-sized regions sitting on the Earth's core–mantle boundary could be made from subducted oceanic crust (**page 20**). I. Kupenko *et al.* carried out challenging SMS spectroscopy on ID18 of hematite at Earth's lower mantle conditions, showing that this magnetic material could be a source of magnetic anomalies in specific interior locations of the

Earth (**page 21**). From high-quality single-crystal data collected ID15B, E. Bykova *et al.* determined two new forms of silica that are drastically different from any other known silica phases (**page 23**). In another detailed structural study conducted at ID15B**,** W. Baek *et al.* determined the outstanding mechanical properties of lonsdaleite; a hexagonal lattice modification of diamond (**page 24**). From a combined XRD, SMS and XAS study conducted at three MEX beamlines (ID27, ID18 and BM23), Sans *et al.* probed the stability field and nature of the volume collapse of ε-Fe_2O_3 (**page 27**). At ID24, D. I. Gorbunov *et al.* microscopically observed the magnetisation of the ferrimagnet $HoFe_5Al_7$ in a strong magnetic field (**page 29**). Using the laser-heating system at ID27, D. Laniel *et al.* discovered a layered form of single-bonded nitrogen that is solid at ultrahigh pressure (**page 31**), while D. V. Semenok *et al.* synthesised and characterised *in situ* two new forms of thorium hydrides, ThH_9 and ThH_{10}, which exhibit very high superconducting critical temperatures (146 K and 160 K, respectively) (**page 32**).

In addition to extreme conditions activity, the two XAS beamlines, BM23 and ID24, run an important chemistry programme. Two examples are highlighted in this chapter. The oxidation reactions of organic substrates by non-heme iron activated species were investigated and the kinetics constants determined by G. Capocasa *et al.* using time-resolved XAS and UV-Vis spectroscopies with millisecond resolution (**page 34**). The stoichiometry of cornerstones in bimetallic CeZr-UiO-66 MOFs were revealed by EXAFS spectroscopy by K. A. Lomachenko (**page 36**).

This selection of highlights shows that science under extreme conditions is a vibrant field of research and gives a flavour of what could be achieved in the future. The MEX group and user community are certainly eager to discover the immense possibilities offered by EBS.

M. MEZOUAR

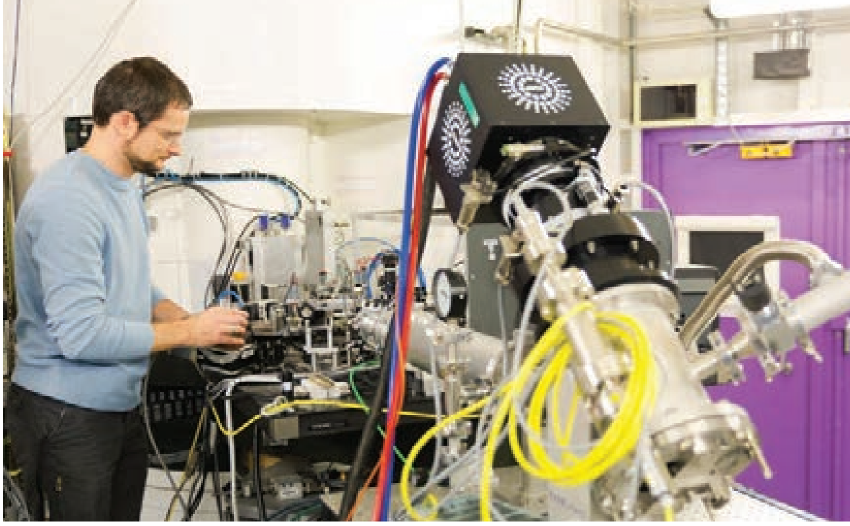

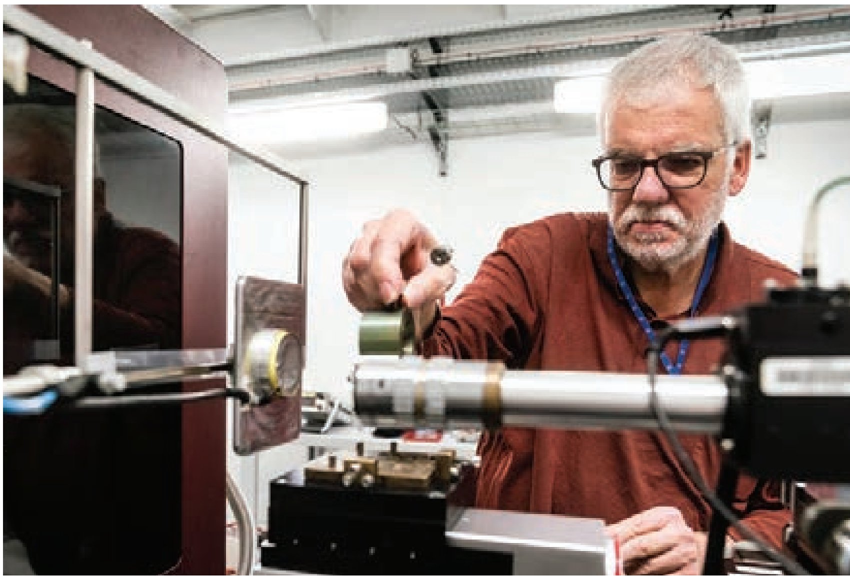

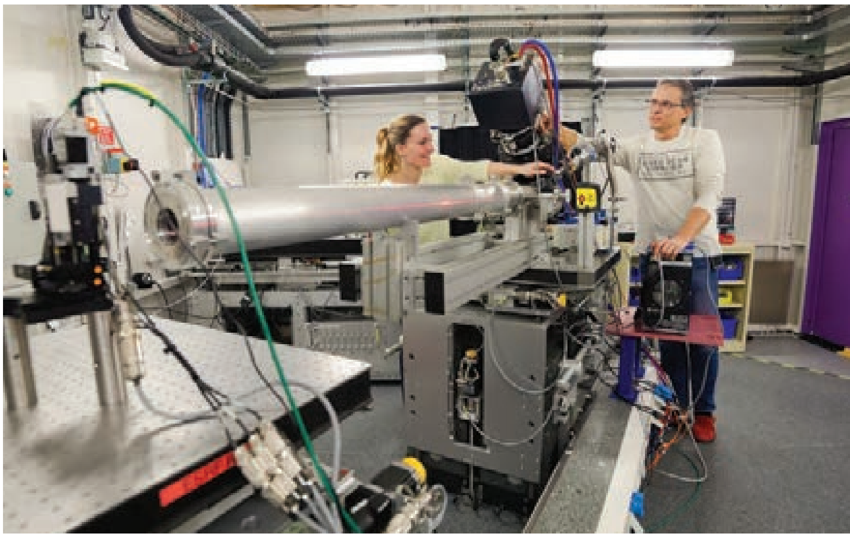

PHASE TRANSITIONS AND ACOUSTIC VELOCITIES OF CALCIUM SILICATE PEROVSKITE

Calcium perovskite is the third most abundant mineral in Earth's lower mantle but its seismic properties are relatively poorly constrained. High-pressure experiments have simultaneously measured the crystallographic and seismic properties of calcium perovskite. This has revealed that anomalous continent-sized regions sitting on the core–mantle boundary could be made from subducted oceanic crust.

The Earth's lower mantle is vast. It extends from 660 km to 2891 km depth below the surface of the planet and contains approximately two-thirds of all the silicate rocks on Earth. Despite the dearth of direct samples from the lower mantle available for study, recent geophysical observations have provided many insights into this remote reservoir of the Earth. Seismic anomalies ranging from widespread scatterers of 10-20 km throughout the uppermost lower mantle to the two antipodal continent-sized large low velocity provinces (LLVPs) that reside on the core–mantle boundary hint that the lower mantle is compositionally highly heterogeneous. However, to provide meaningful insights into the nature of the deep Earth the cause(s) of these seismic observations must be identified. The most likely route to success involves careful comparison of observations of seismic velocities with those predicted using mineralogical models of materials at the conditions of Earth's deep interior, but unfortunately the available mineralogical models are simply not yet up to the task.

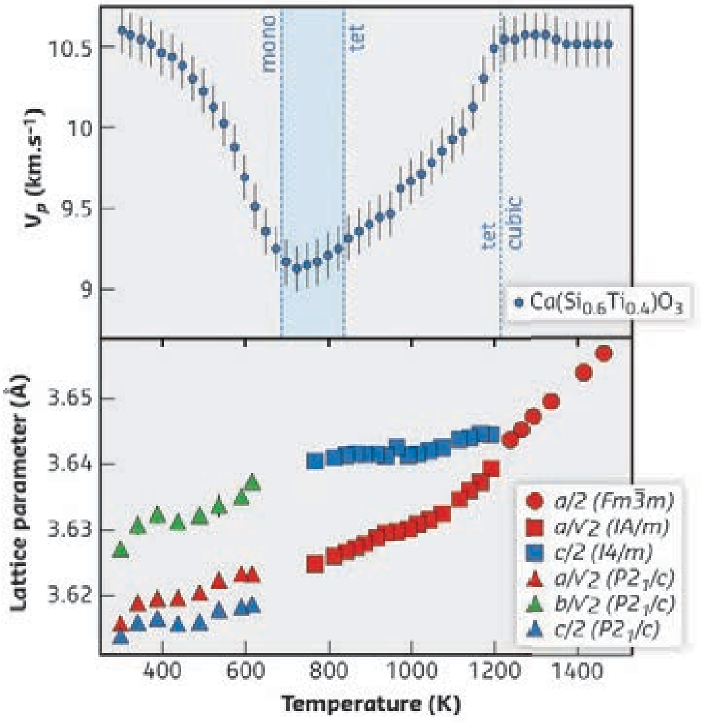

Fig. 9: Compressional wave velocity measurements of Ca[$Si_{0.6}Ti_{0.4}$]O_3 perovskite at ~ 13 GPa (top) and Rietveld refined lattice parameters of the same sample (bottom), both as a function of temperature. Both datasets reveal phase transitions from cubic–tetragonal–monoclinic structures.

Some of the most significant omissions from current mineralogical models **[1]** are well-constrained seismic properties of calcium silicate perovskite (Ca-Pv), which is the lower mantle's third most abundant phase, comprising 5-30 vol.% of common rock assemblages. The main reason for the lack of data on Ca-Pv stems from the unrecoverable nature of perovskite-structured $CaSiO_3$, which undergoes spontaneous amorphisation during room-temperature decompression **[2]**. This behaviour has not only prevented almost all elasticity measurements of Ca-Pv, but also hampered conclusive identification of its crystallographic structure at mantle conditions. Working in the large volume press at beamline **ID06-LVP**, an experimental strategy was developed to simultaneously measure the crystal structure and acoustic velocities of endmember, and Ti-bearing, Ca-Pv samples. Measurements were performed at pressure-temperature (PT) conditions up to 15 GPa and 1800 K, and provide new insights into the nature of the deep Earth.

High-resolution diffraction patterns collected from $CaSiO_3$ and Ca[$Si_{0.6}Ti_{0.4}$]O_3 perovskite confirmed previous expectations that Ca-Pv is cubic at high PT conditions. However, upon cooling to room temperature Ca-Pv samples were observed to undergo one, or two, symmetry-reducing phase transitions that had not been observed before. Concurrent velocity measurements (**Figure 9**), collected using pulse-echo ultrasonic interferometry, revealed these phase transitions are associated with large anomalies in the samples' elasticity, large enough to create observable velocity anomalies if they were to occur in natural Ca-Pv. The observed distortions are completely analogous to similar transitions known to occur in almost all other perovskite materials, *e.g.* $CaTiO_3$, $BaTiO_3$ and/or $SrTiO_3$ but, until now, these phenomena had mostly been ignored in Earth Science.

By combining new experimental measurements with literature high PT-volume measurements, an equation-of-state describing cubic-structured Ca-Pv at high temperature and pressure was constrained. The formalism predicts Ca-Pv's density, compressional and shear sound-wave velocities at almost any mantle conditions, allowing Ca-Pv to be robustly incorporated into mineralogical models (**Figure 10**). This procedure highlighted the inadequacy of previous models for Ca-Pv, which were based on calculations and predict velocities 8-25% higher than the new experimentally constrained model **[1]**.

This is a huge difference, and adoption of the new parameterisation completely alters the interpretation of seismic anomalies from the deep lower mantle, especially the possible explanations of the LLVPs. It is predicted that the seismic signature of recycled oceanic crust, which is enriched in Ca-Pv, should have slower-than-average velocities (the opposite of predictions using previous models) in the lower mantle – allowing the LLVPs to be formed from piles of dense recycled material that has sunk to the core–mantle boundary.

Ultimately, this reconciles the results of geodynamics calculations **[3]** and geochemical studies **[4]**, which both prefer the LLVPs to be long-lived piles of crustal material, because the slow observed seismic velocities from these regions matches those predicted for subducted oceanic crustal rocks.

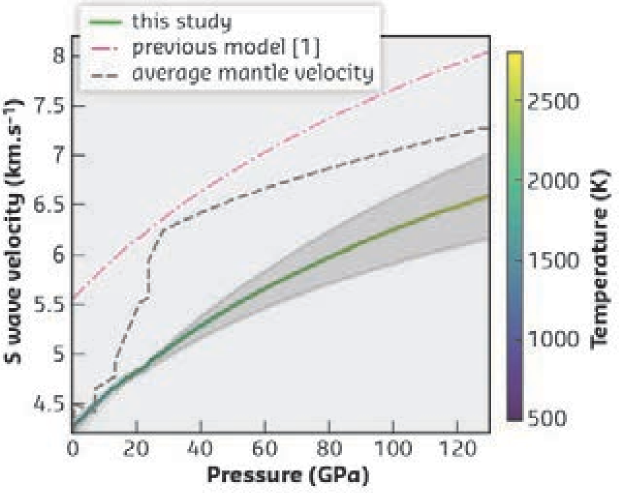

Fig. 10: Velocity of cubic Ca-Pv along a mantle adiabatic temperature profile based on the thermodynamic model from this study (coloured curve with 95% confidence intervals), compared with the average 1D velocity profile of the Earth's mantle (dashed grey curve) and the previous estimates of Ca-Pv's velocity along the same temperature profile from **[1]** (pink curve).

PRINCIPAL PUBLICATION AND AUTHORS

Seismic velocities of $CaSiO_3$ perovskite can explain LLSVPs in Earth's lower mantle, A. R. Thomson (a,b), W. A. Crichton (b), J. P. Brodholt (a,c), I. G. Wood (a), N. C. Siersch (d), J. M. Muir (e), D. P. Dobson (a) and S. A. Hunt (a), *Nature* **572**(7771), 643-647 (2019); doi: 10.1038/s41586-019-1483-x.

(a) Department of Earth Sciences, University College London (UK)
(b) ESRF
(c) Centre for Earth Evolution and Dynamics, University of Oslo (Norway)
(d) Bayeriches Geoinstitut, University of Bayreuth (Germany)
(e) School of Earth and Environment, University of Leeds (UK)

REFERENCES

[1] L. Stixrude, *et al., Geophys. J. Int.* **184**, 1180–1213 (2011).
[2] L. G. Liu *et al., Earth Planet. Sci. Lett.* **28**, 209–211 (1975).
[3] M. Ballmer *et al., Sci. Adv.* **1**, e1500815 (2015).
[4] A. W. Hofmann, *Nature* **385**, 219–229 (1997).

MAGNETISM AT MANTLE TRANSITION ZONE DEPTHS

Hematite (Fe_2O_3), a strongly magnetic mineral, was studied with SMS spectroscopy at temperatures and pressures found down to the Earth's lower mantle. The data show that hematite retains magnetic properties at the depth of the transition zone in certain regions and could therefore be a source of magnetic anomalies there.

The Earth's crust–mantle boundary, the Mohorovičić discontinuity, has been traditionally considered the interface between the magnetic crust and the non-magnetic mantle **[1]**, with elevated temperatures in the mantle thought to be too high to retain any magnetism in the constituting minerals. However, satellite and aeromagnetic data provide evidence for magnetic anomalies in the mantle **[2,3]**, particularly around cooler areas such as subduction zones. The source of the anomalies remains largely unknown, but iron oxides are considered a likely source due to their high critical temperatures **[4]**. Of these, hematite (Fe_2O_3) is the dominant iron oxide at depths of around 300-600 km below the Earth's surface – a transition zone between the upper and the lower mantle **[5]**.

To investigate whether hematite retained magnetism under lower mantle conditions,

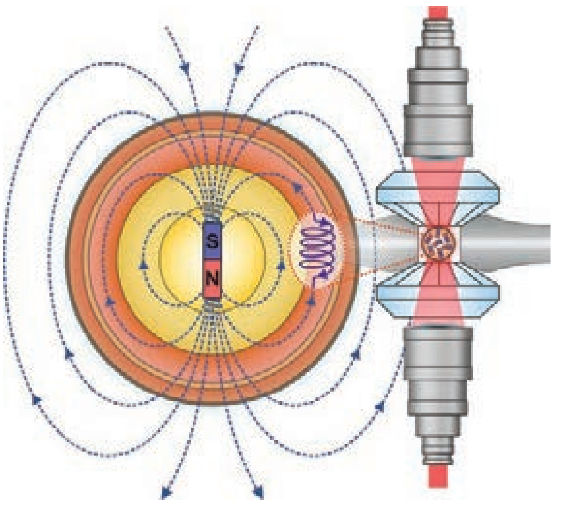

Fig. 11: The interior of the Earth and the experiment graphically illustrated. The blue dotted lines depict the magnetic field surrounding the Earth. Heated samples of the iron oxide hematite were pressed between two opposed diamond anvils and laser-heated (right) to simulate the extreme conditions in the Earth's mantle. It was observed that the iron oxide is magnetic under these conditions in certain regions of the Earth's transition zone.
© Timofey Fedotenko.

samples of synthetic hematite in single crystal and powdered form were compressed in diamond anvil cells and laser-heated to the extreme pressures and temperatures found in the depths of the planet – up to 90 GPa and 1300 K, respectively (**Figure 11**). Synchrotron Mössbauer Source (SMS) spectroscopy was then carried out at beamline **ID18** to investigate the magnetic transitions and critical temperatures of the hematite and its high-pressure phases (**Figure 12**). SMS allows the investigation of magnetism *in situ* at high pressures and high temperatures. One of the advantages of using SMS spectroscopy on laser-heated materials is that the temperature of the sample can be calculated from any collected Mössbauer spectra, acting as an 'internal thermometer' to provide a valuable back-up to temperature measurements taken at the sample surface.

It was found that hematite retains magnetism at pressures corresponding to the Earth's transition zone at relatively cold temperatures, such as those found at subduction zones, and may cause deep magnetic anomalies. The temperature profiles of cross-sections of the Earth's subduction zones were calculated and a band of zones in the West Pacific region was discovered to have plate temperatures low enough for hematite to remain ferromagnetic.

This suggests that the Earth's mantle might not be as magnetically inactive as previously considered, and could also have implications for paleomagnetism. Magnetic anomalies in the band of deep magnetised rock in the West Pacific region correlate with one of the preferred paths of the geomagnetic poles during reversals. Thus, this path could appear in rock records due to the presence of magnetic sources such as hematite in the transition zone, rather than reflect the real geometry of the magnetic field during reversals. The potential deep magnetic sources can contribute to the signal observed on the surface and this should be taken into account when analysing Earth's satellite geomagnetic data, and especially in studies of planetary bodies with only an ancient dynamo, such as Mars.

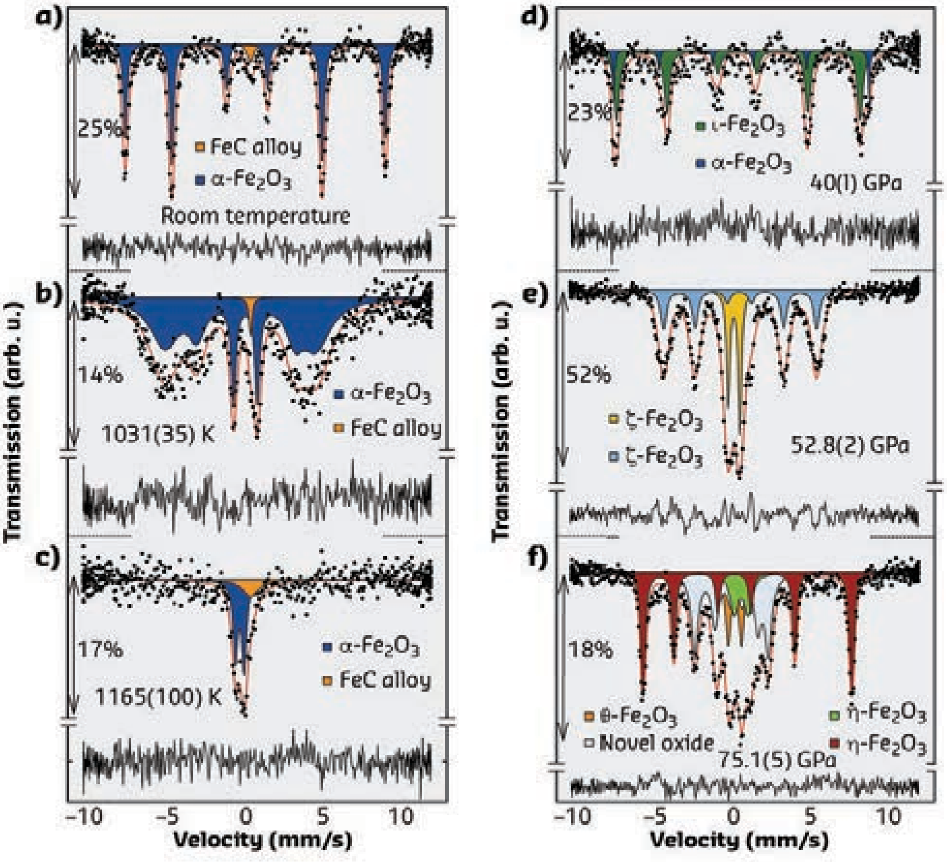

Fig. 12: Evolution of SMS spectra of Fe_2O_3 polymorphs with pressure and temperature. **a–c)** SMS spectra of α-Fe_2O_3 (hematite) at 19.4(4) GPa and at temperatures indicated. **d–f)** Characteristic SMS spectra of Fe_2O_3 high-pressure phases at room temperature and at pressures indicated. The room-temperature SMS spectrum of the Rd_2O_3(II)-structure ι-Fe_2O_3 consists of a single magnetic component, while both the distorted perovskite-structure ζ-Fe_2O_3 and the post-perovskite-structure η-Fe_2O_3 display two Mössbauer components – one magnetically ordered (cyan in **(e)** and dark red in **(f)**) and one non-magnetic (yellow in **(e)** and light green in **(f)**).

PRINCIPAL PUBLICATION AND AUTHORS

Magnetism in cold subducting slabs at mantle transition zone depths, I. Kupenko (a), G. Aprilis (b,c), D. M. Vasiukov (b,c,d), C. McCammon (b), S. Chariton (b), V. Cerantola (b,e), I. Kantor (f), A. I. Chumakov (e), R. Rüffer (e), L. Dubrovinsky (b) and C. Sanchez-Valle (a), *Nature* **570**, 102–106 (2019); doi: 10.1038/s41586-019-1254-8.

(a) Institut für Mineralogie, University of Münster (Germany)
(b) Bayerisches Geoinstitut, University of Bayreuth (Germany)
(c) Material Physics and Technology at Extreme Conditions, Laboratory of Crystallography, University of Bayreuth (Germany)
(d) Department of Physics and Astronomy, Rutgers University (USA)
(e) ESRF
(f) Technical University of Denmark, Kongens Lyngby (Denmark)

REFERENCES

[1] P. J. Wasilewski *et al.*, *Geophys. Res. Lett.* **6**, 541–544 (1979).
[2] R. J. Blakely *et al.*, *Geology* **33**, 445–448 (2005).
[3] P. Chiozzi *et al.*, *Phys. Earth Planet. Inter.* **152**, 267–276 (2005).
[4] D. J. Dunlop & G. Kletetschka, *Geophys. Res. Lett.* **28**, 3345–3348 (2001).
[5] A. B. Woodland *et al.*, *Am. Mineral.* **97**, 1808–1811 (2012).

HIGH-PRESSURE POLYMORPHS OF COESITE BRING A NEW INSIGHT INTO THE COMPLEXITY OF SILICATE MELTS IN EARTH'S INTERIOR

Two new modifications of silica called coesite-IV and coesite-V were observed under compression of coesite above 30 GPa. Their crystal structures, which are drastically different from any other known silica phases, help to understand the properties of silicate liquids and glasses at high pressures.

Modelling of processes involving deep-Earth liquids requires information on their structures and compression mechanisms. However, knowledge of the local structures of silicates and silica (SiO_2) melts at deep-mantle conditions, and of their densification mechanisms, is still limited. A convincing method to obtain a structural model of non-crystalline silica material is to compare (or fit) experimental total scattering data with the pair distribution function of known crystalline phase(s). So far, no crystalline phases that could describe features of the total scattering data of silica and/or silicate glass (acting as proxies of melt) at high pressure are known.

Single-crystal X-ray diffraction in diamond anvil cells was applied in order to study SiO_2 phases, which appear on compression of coesite, and their high-pressure behaviour up to pressures over 70 GPa. The experiments were performed at beamline **ID09A** (now **ID15B**). At pressures above 20 and 25 GPa, the structural transformations to coesite-II and coesite-III, respectively, were observed **[1]**. On compression beyond ca. 30 GPa, a new set of reflections manifests the presence of a new triclinic (space group *P*-1) phase, which was called coesite-IV. Upon further compression, the reflections of coesite-IV split and a new triclinic (space group *P*-1) phase, coesite-V, emerged. Above ~50 GPa, only coesite-V was found. The structure of coesite-IV possesses *tetra*-, *penta*- and *hexa*-coordinated silicon; the structure of coesite-V maintains only *penta*- and *hexa*-coordinated silicon (**Figure 13**). The structures of coesite-IV and coesite-V may be considered as a three-dimensional framework of face- and edge-sharing octahedra with the empty space, filled by SiO_5 and SiO_4 (in coesite-IV), or only SiO_5 (in coesite-V) polyhedra (**Figure 13**). The presence of face-sharing octahedra, the structural element never observed or even expected in silica, silicates or glasses, breaks Pauling's Third rule. The results

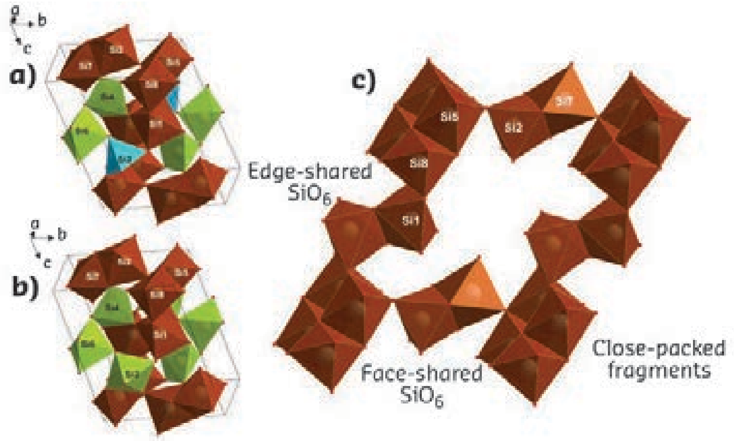

Fig. 13: Crystal structures of coesite-IV and coesite-V. Polyhedral models of the structures of coesite-IV **(a)** and coesite-V **(b)** (SiO_6 octahedra are brown, SiO_5 polyhedra are green; SiO_4 tetrahedra are blue). **c)** A fragment of the structures, similar for both coesite-IV and coesite V, showing a 3D framework of SiO_6 octahedra.

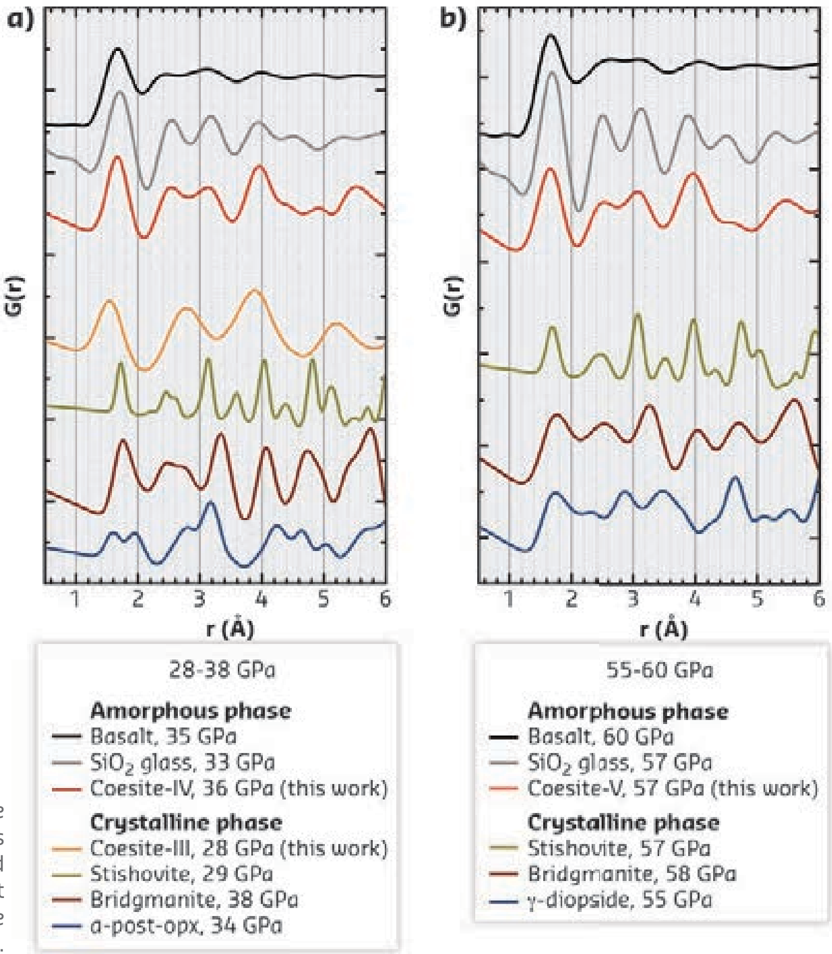

Fig. 14: Pair distribution functions of silica and silicate phases. Solid curves represent pair distribution functions calculated for silica polymorphs and silicates compared with those for basalt and silica glass measured at different pressures: **(a)** in the range from 28 to 38 GPa; **(b)** in the range from 55 to 60 GPa.

suggest that possible silicate liquids in Earth's lower mantle may have complex structures, making them more compressible compared to previously considered models.

It was found that pair distribution functions calculated for coesite-IV and coesite-V indeed closely reproduce experimental data reported recently for compressed silica glass and molten basalt **[2,3]** (**Figure 14**). Moreover, above 45 GPa the densities of coesite-IV and -V within the uncertainty of measurements coincide with the density of silica glass. These observations are strong arguments in support of analogous atomic arrangements in compressed silica glass (and molten basalt) and in coesite-IV or coesite-V. The presence of 'unconventional' structural elements like SiO_5 polyhedra and face-sharing octahedra in the silicate melts would have decreased their density and, even more importantly, caused the drop in their bulk sound velocity (by about 10% in a 100-GPa pressure range). If silicate liquids with such properties are present in the lower mantle, they should be seismically detectable.

PRINCIPAL PUBLICATION AND AUTHORS

Metastable silica high pressure polymorphs as structural proxies of deep Earth silicate melts E. Bykova (a,b), M. Bykov (a,c), A. Černok (a), J. Tidholm (d), S. I. Simak (d), O. Hellman (d,e), M. P. Belov (c), I. A. Abrikosov (c,d), H.-P. Liermann (b), M. Hanfland (f), V. B. Prakapenka (g), C. Prescher (g), N. Dubrovinskaia (h) and L. Dubrovinsky (a), *Nat. Commun.* **9**, 4789 (2018); doi: 10.1038/s41467-018-07265-z.
(a) Bayerisches Geoinstitut, University of Bayreuth (Germany)
(b) Photon Science, DESY, Hamburg (Germany)
(c) Materials Modeling and Development Laboratory, National University of Science and Technology 'MISIS', Moscow (Russia)
(d) Department of Physics, Chemistry and Biology, Linköping University (Sweden)
(e) Department of Applied Physics and Materials Science, California Institute of Technology (USA)
(f) ESRF
(g) Center for Advanced Radiation Sources, University of Chicago, Argonne (USA)
(h) Material Physics and Technology at Extreme Conditions, Laboratory of Crystallography, University of Bayreuth (Germany)

REFERENCES

[1] A. Černok *et al.*, *Zeitschrift für Krist. - Cryst. Mater.* **229,** 761–773 (2014).
[2] C. Prescher *et al.*, *PNAS* **114,** 10041–10046 (2017).
[3] C. Sanloup *et al.*, *Nature* **503,** 104–107 (2013).

BULK MODULUS OF LONSDALEITE UNDER HIGH-PRESSURE EXPERIMENTALLY CONFIRMED

The first experimental study of small lonsdaleite-rich diamond crystals from the Popigai meteoritic impact crater has been performed under compression in a diamond anvil cell using X-ray diffraction (XRD). The bulk modulus of lonsdaleite was found to be lower than that of diamond but may be higher in a possible lonsdaleite/diamond biphase.

Natural and synthetic diamonds show the greatest known hardness and lowest compressibility, with a presence of various structural defects such as stacking faults and inter-growths. These can strongly affect the mechanical and optical properties of diamonds **[1]**. Rare samples obtained under special conditions, such as diamonds formed within meteorites and their impact craters, have exceptional importance for the understanding of diamond properties and can shed light on diamond genesis. Impact diamonds are associated with a lonsdaleite phase (a hexagonal lattice modification), thought to play a fundamental role in the graphite-to-diamond transformation under extreme conditions and an important marker of meteorite impacts **[2]**.

Recent calculations predicted that pure lonsdaleite may have a large bulk modulus and greater hardness than diamond **[3]**, making it a unique object for further theoretical and experimental studies. However, due to the absence of pure lonsdaleite crystals, these properties have never been demonstrated by experimental studies under ambient and/or high-pressure conditions. Lonsdaleite-rich impact diamonds with a record concentration of hexagonal phase were discovered in the Popigai impact crater found in 1946 in Northern Siberia. Samples from this impact crater were the focus of detailed structural investigations.

According to early transmission electron microscopy data, Popigai impact diamonds can be described as a mixture of 5-50 nm domains of graphite, cubic and hexagonal diamonds with a high density of stacking faults (up to five per 10 Å) and micro-twins **[4]**. Individual small diamond crystallites (several µm in length) from Popigai showed good homogeneity and a large amount (up to 30-40 wt. %) of the hexagonal lonsdaleite phase mixed with cubic diamond and graphite sequences **[5,6]**. The samples were compressed in a diamond anvil cell up to 25 GPa and XRD patterns were obtained on beamline ID15B (**Figure 15a**).

In contrast with previous theoretical predictions, it was found that the bulk modulus of lonsdaleite is systematically lower and equal to 93-100% of that of diamond. In absolute values, it equals 406(21) GPa and 431(3) GPa for different samples with different morphologies. **Figure 15b** shows the reference bulk modulus for bulk diamond is 444(3) GPa. The lonsdaleite compressibility is smaller in comparison with that of diamond and depends upon the length of intergrowths and relative orientation of the diamond and lonsdaleite phases.

The XRD experimental data were accompanied by density functional theory simulations, which revealed the possible coexistence of a number of diamond/lonsdaleite and diamond twin biphases with unique nanomechanical properties. As **Figure 16** illustrates, among the different configurations, separate inclusions of one lonsdaleite (001) plane per four diamond (111) demonstrate the lowest energy per carbon atom, suggesting a favourable formation of single-layer lonsdaleite (001) fragments inserted in the diamond matrix. Calculations and powder XRD experiments indicate these biphases could be formed under high-pressure conditions. Following the 2nd-order Birch-Murnaghan equation of state, it was calculated that inclusions of a single (001) lonsdaleite plane between four diamond (111) planes lead to the lowest-energy biphase with the highest bulk modulus – even greater than that of pristine diamond.

The results address important questions about the existence of the pure lonsdaleite phase. It seems that hexagonal lonsdaleite can occur

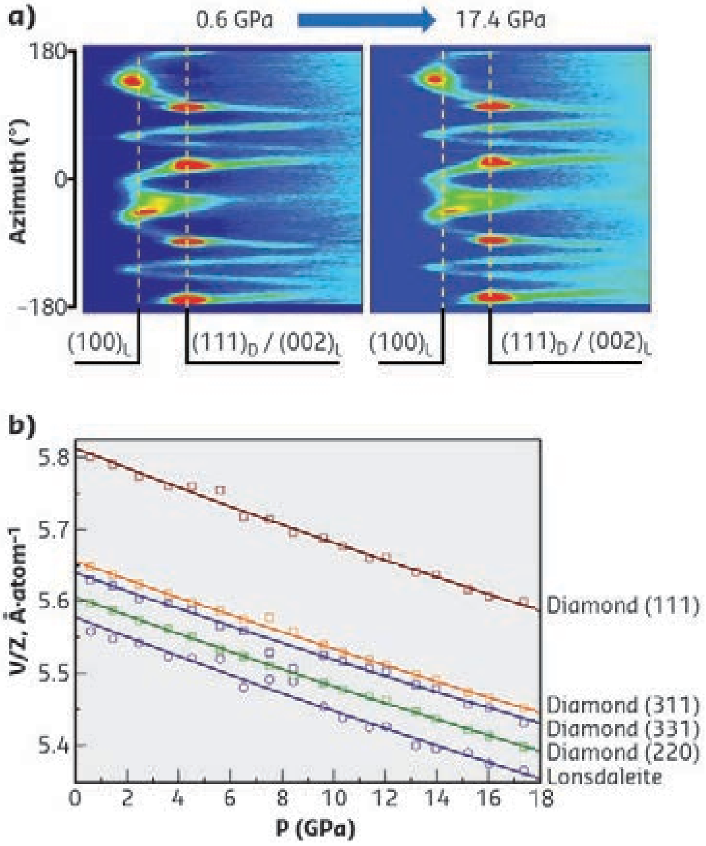

Fig. 15: a) High-pressure background-subtracted X-ray crystal diffraction patterns (radial sweeps of 2D images) of a lonsdaleite-rich sample at 0.6 GPa (left) and 17.4 GPa (right) obtained at ID15B using a diamond anvil cell (λ = 0.41 Å). **b)** Pressure-dependent atomic volumes for a diamond matrix estimated from individual diffraction lines of: (111), (311), (331) and (220); and lonsdaleite intergrowths estimated from (002) diffraction line.

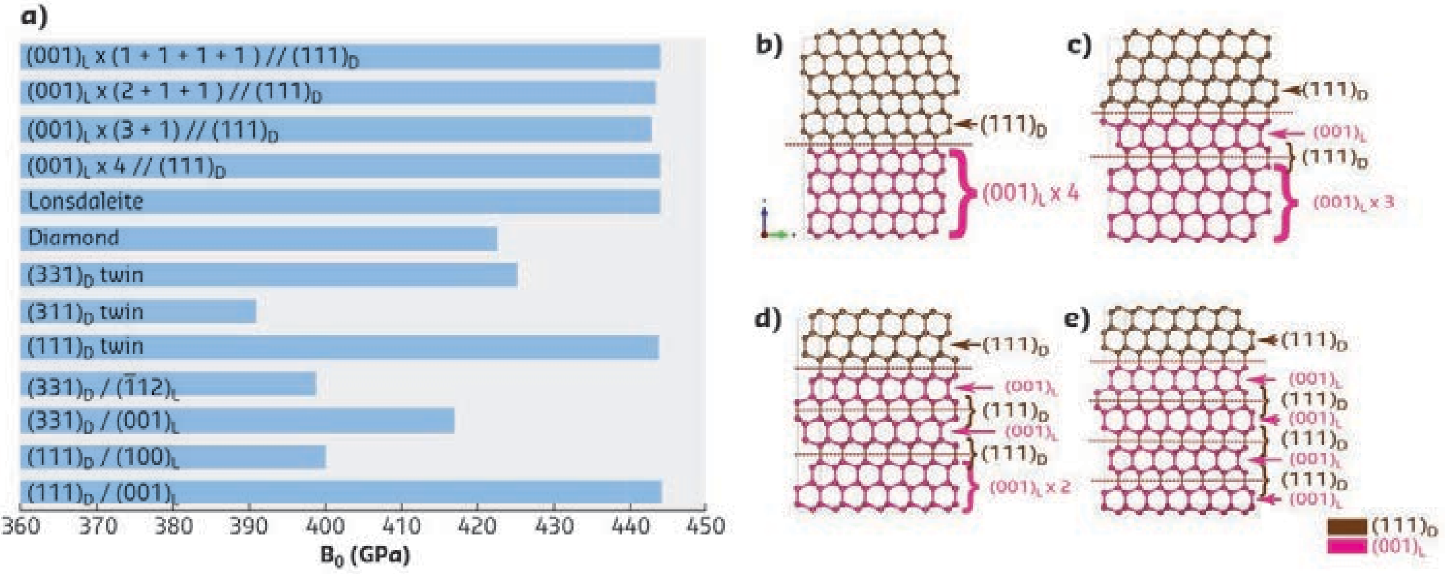

Fig. 16: a) From top to bottom: Theoretical bulk moduli (PBC PBE PW level of theory) of (001)$_L$x(1+1+1+1)//(111)$_D$ (structural model presented in **(e)**), (001)$_L$x(2+1+1)//(111)$_D$ (structural model presented in **(d)**), (001)$_L$x(3+1)//(111)$_D$ (structural model presented in **(c)**), (001)$_L$x4//(111)$_D$ (structural model presented in **(b)**), lonsdaleite, diamond, (311)$_D$ twin, (111)$_D$ twin, (331)$_D$/(-112)$_L$, (311)$_D$/(001)$_L$, (111)$_D$/(100)$_L$, and (111)$_D$/(001)$_L$ biphases.

only as intergrowths with cubic diamond and is not found as an individual crystal. Further experimental and theoretical studies of the graphite-to-diamond transition should take into account only such intergrowths and not individual lonsdaleite phases.

PRINCIPAL PUBLICATION AND AUTHORS

Unique Nanomechanical Properties of Diamond-Lonsdaleite Biphases: Combined Experimental and Theoretical Consideration of Popigai Impact Diamonds, W. Baek (a), S. A. Gromilov (b), A. V. Kuklin (a,c), E. A. Kovaleva (c), A. S. Fedorov (c), A. S. Sukhikh (b), M. Hanfland (d), V. A. Pomogaev (a, e), I. A. Melchakova (a,c), P. V. Avramov (a) and K. V. Yusenko (f), *Nano Lett.* **19(3)** 1570–1576 (2019); doi: 10.1021/acs.nanolett.8b04421.

(a) Kyungpook National University (South Korea)
(b) Novosibirsk State University and Nikolaev Institute of Inorganic Chemistry (Russia)
(c) Siberian Federal University, Krasnoyarsk (Russia)
(d) ESRF
(e) Tomsk State University (Russia)
(f) BAM Federal Institute for Materials Research and Testing, Berlin (Germany)

REFERENCES

[1] A. Bosak *et al., Acta Crystallogr., Sect. B: Struct. Sci.* **B66**, 493–496 (2010).
[2] P. Nemeth *et al., Nat. Commun.* **5**, 5447 (2014).
[3] Q. Zhu *et al., Phys. Rev. B: Condens. Matter Mater. Phys.* **83**, 193410 (2011).
[4] F. Langenhorst, *Mitt. Österr. Miner. Ges.* **148**, 401–412 (2003).
[5] A. P. Yelisseyev *et al., Diam. Relat. Mater.* **58**, 69-77 (2015).
[6] A. P. Yelisseyev *et al., Diam. Relat. Mater.* **89**, 10-17 (2018).

HARD X-RAY SPECTROSCOPY WITH ‘NEWTON’S PRISM’

Spectrographic imaging with visible light has been known since the invention of Newton’s prism. In the hard X-ray domain, this approach is hampered by the constraints of X-ray optics. Here, the principles of spectrographic imaging have been applied to hard X-ray spectroscopy, improving the energy resolution by an order of magnitude without significant loss in intensity.

In hard X-ray spectroscopy, the monochromators and analysers work as narrow-band filters, eliminating photons of all energies other than the desired ones. Within this approach, any attempt to narrow the energy bandwidths to improve the energy resolution inevitably reduces the intensity. A breakthrough solution to this problem would be to complement hard X-ray spectroscopy with the principles of spectrographic imaging, widely used in a vast spectral range from infrared radiation to soft X-rays. A spectrograph keeps radiation components of all energies, dispersing the ‘colours’ spatially. Consequently, the energy resolution is provided by selecting distinct components in space, whereas the availability of all these components keeps the entire intensity.

For visible light, the concept of spectrographic imaging – dispersion of radiation components with various energies in space – has been known since Newton’s time. But for hard X-rays, optical prisms and conventional diffraction gratings are not efficient. Nevertheless, the principles of the angular dispersion of hard X-rays are known **[1]**. They rely on the angular dispersion of X-rays in Bragg diffraction by asymmetrically cut crystals. Combined with focusing optics, this results in dispersing X-rays of different energies in space, and using the entire beam in all spatial coordinates in parallel, which preserves the total intensity. Such a scheme has now been applied to hard X-ray spectroscopy in recent experiments at the ESRF.

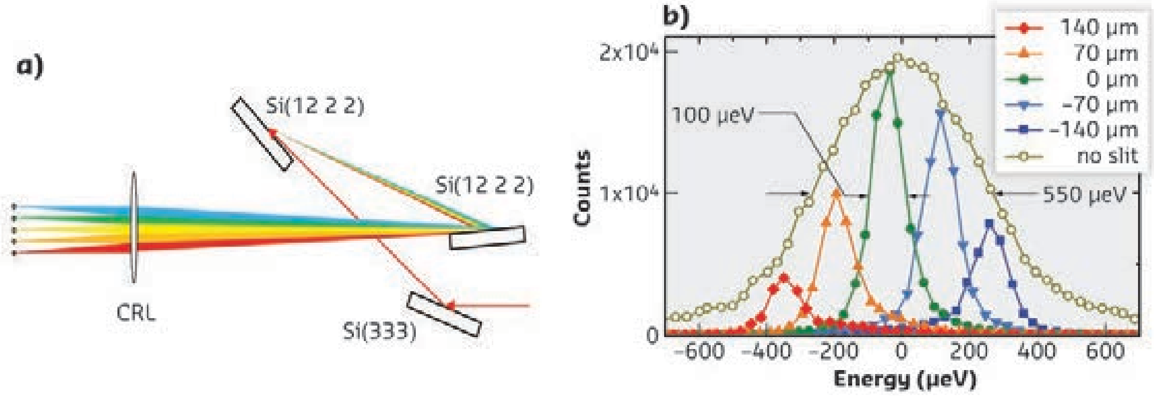

Fig. 17: Principles of a hard X-ray spectrograph. **a)** The main elements of the spectrograph, comprising three silicon crystals that provide angular dispersion of X-rays with various energies, and a focusing compound refractive lens (CRL). **b)** The energy distributions of X-ray components selected by a 20 μm-wide slit at five indicated vertical positions, and the energy distribution of an entire beam measured without the slit (the spectral window of the spectrograph).

Spectrographic hard X-ray imaging was demonstrated at beamline **ID18** in measurements of the density of phonon states by nuclear inelastic scattering using 14.4125 keV photons corresponding to the energy of the nuclear resonance of the ^{57}Fe isotope. The key elements of the hard X-ray spectrograph are shown in **Figure 17a**. The dispersion is provided by the second and the third silicon crystals in the highly asymmetric (12 2 2) reflections. The first silicon crystal is used to maintain the exit beam in the horizontal direction approximately, and the downstream multilayer mirror (not shown) assures this precisely. The compound refractive lens focuses radiation components with different energies to different vertical coordinates, providing the spatial dispersion. Since the radiation components of various energies are separated in space, the scheme allows for measurements of the density of states with several identical (or different) samples in parallel, benefiting from the improved energy resolution and conserved intensity.

Figure 17b shows the energy distributions of X-ray components selected by a 20 µm-wide slit at five indicated vertical positions, and the energy distribution of an entire beam measured without the slit. The measurement without the slit defines the spectral window of the spectrograph. With a sufficiently small slit (in this case – 20 µm), the measurements give the energy resolution of the spectrograph. **Figure 17b** shows that the spectral window of the spectrograph is 550 µeV, and the energy resolution is about 100 µeV. This compares well with the best resolution of Raman spectroscopy. Furthermore, it is about an order of magnitude better than the typical resolution of presently employed hard X-ray inelastic scattering spectrometers. For nuclear inelastic scattering, however, improving the energy resolution is easier as the method does not require energy analysers and momentum resolution.

Figure 18 demonstrates spectrographic imaging in the measurement of the density of phonon states in α-iron. The improved energy resolution reveals anomalous soft modes (**Figure 18**), a previously unknown phenomenon of this already extensively studied system. Additional data show that this phenomenon is intrinsic to an ideal lattice of α-iron, and cannot be attributed to possible imperfections such as impurities, grain boundaries, dislocations, texture, and magnetic domain walls. Plausibly, the observed anomalous dynamics is related to anharmonic effects and/or magneto-elastic waves.

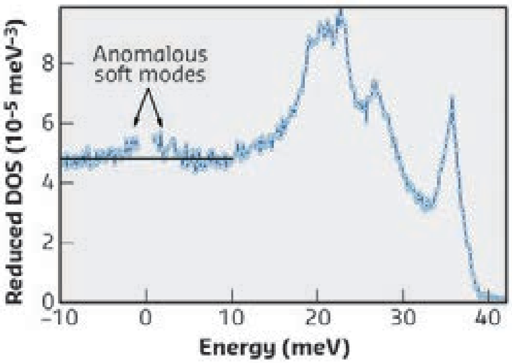

Fig. 18: Anomalous soft dynamics of α-iron. The reduced density of phonon states (reduced DOS) $g(E)/E^2$. Only those points are shown where the systematic uncertainty related to the subtraction of the elastic peak is less than the symbol size. The error bars indicate the statistical uncertainty. The data at positive and negative energies are derived from the corresponding parts of the inelastic spectrum. The black horizontal line shows the Debye level — the expected contribution to the reduced DOS from the acoustic modes. The elevation of the reduced DOS above this line reveals an anomalous soft dynamics of α-iron.

PRINCIPAL PUBLICATION AND AUTHORS

Hard-X-ray spectroscopy with a spectrographic approach, A. I. Chumakov (a), Y. Shvyd'ko (b), I. Sergueev (c), D. Bessas (a) and R. Rüffer (a), *Phys. Rev. Lett.* **123**(9), 097402 (2019); doi: 10.1103/PhysRevLett.123.097402.

(a) ESRF
(d) Advanced Photon Source, Argonne National Laboratory (USA)
(c) DESY, Hamburg (Germany)

REFERENCES

[1] Y. Shvyd'ko in *X-ray Optics – High-Energy-Resolution Applications*, *Springer Series in Optical Sciences* **98**, Springer-Verlag Berlin Heidelberg (2004).

UNVEILING THE BEHAVIOUR OF EPSILON-Fe_2O_3 UNDER EXTREME CONDITIONS

This work presents a joint experimental and theoretical characterisation of the structural, electronic and magnetic behaviour of ε-Fe_2O_3 under extreme conditions. This study showed a volume collapse at 27 GPa, which is associated with a spin-crossover and an increase of coordination of the initial tetrahedrally coordinated iron, leading to a new ε'-phase.

Iron sesquioxides (Fe_2O_3) have attracted great attention with their five different polymorphs found at ambient conditions, each of them revealing different and exciting properties **[1]**. The epsilon phase, in particular, has exhibited paramount magnetic properties (giant coercivity) and has recently been found in basaltic rocks as a nanomineral **[2]**. The latter discovery may reveal that the presence of this material in the Earth's interior is underestimated; however, this

Fig. 19: Scheme of the different experimental and theoretical proofs provided. **a)** SMS of ε'-Fe_2O_3 collected above (36.5 GPa) the critical pressure, (*i.e.*, after the volume collapse). **b)** X-ray diffraction pattern of ε-Fe_2O_3 at 1.6 GPa. **c)** Theoretically simulated phonon dispersion curve of ε-Fe_2O_3 at 25 GPa and 1800K. **d)** EXAFS signals and its Fourier transform before and after the critical pressure. **Centre**: Structure of the ε-Fe_2O_3 compound.

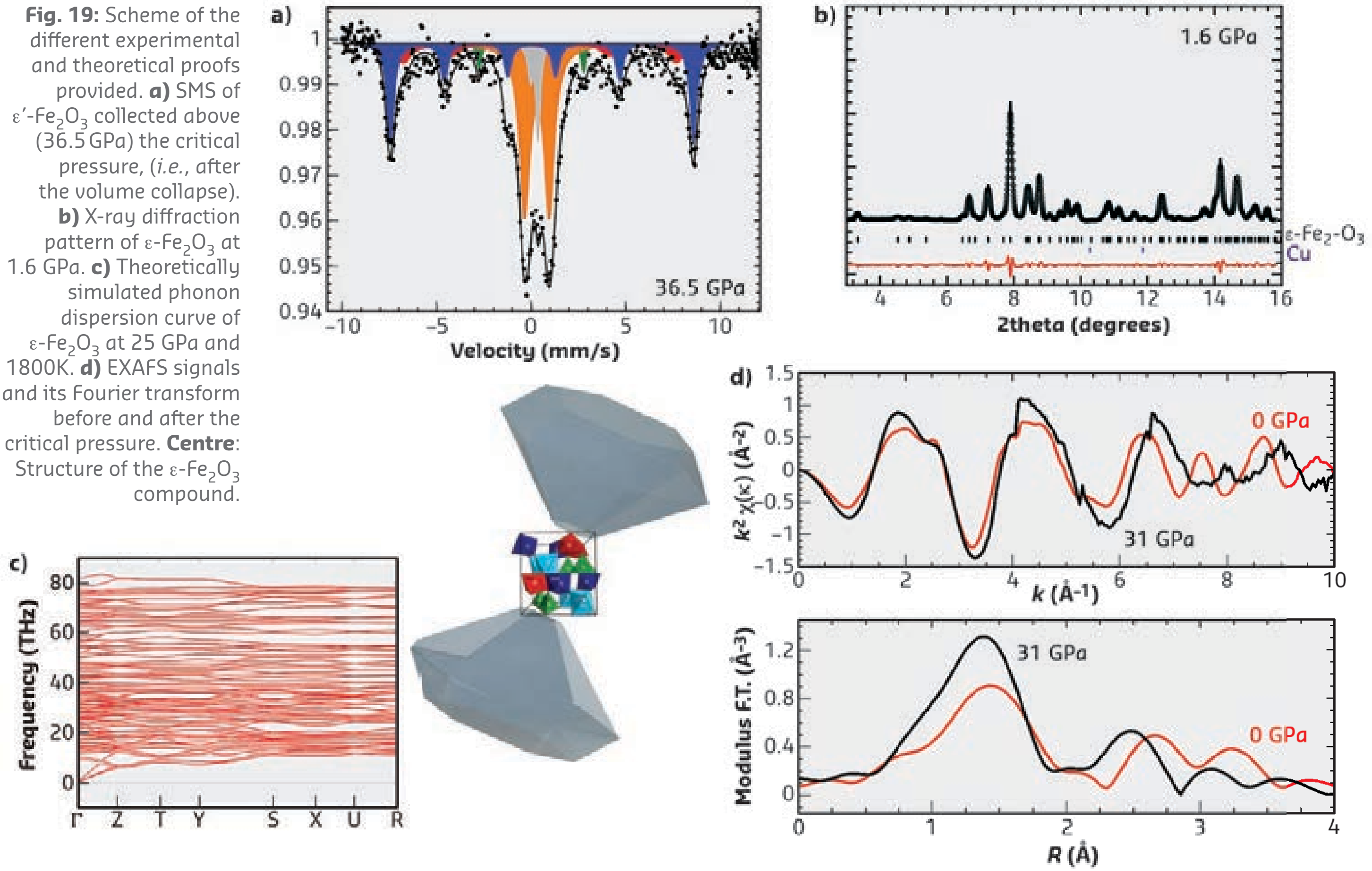

material should be stable at extreme conditions of pressure and temperature. This phase was previously considered as an intermediate product of the transformation between the metastable beta and gamma phases and the thermodynamically stable alpha phase, which led to think that its stability range was poor. The ε-Fe_2O_3 is considered unique because it crystallises in an orthorhombic structure formed by four polyhedral units: a regular octahedron, two distorted octahedral units and a regular tetrahedron (**Figure 19**, centre), and also because it is the only ordered iron sesquioxide polymorph that contains crystallographic iron in tetrahedral coordination in absence of oxygen vacancies.

X-ray diffraction (XRD) at beamline **ID27** (**Figure 19b**) and extended X-ray absorption fine structure (EXAFS) spectroscopy at beamline **BM23** (**Figure 19d**) were carried out under pressure using a diamond anvil cell, in order to describe the local structure around Fe atoms of the ε-Fe_2O_3 phase. The first result was the large structural stability range observed (up to 27 GPa), contradicting the previous assumptions about this compound. A deep analysis of the structural compressibility of this phase shows a pressure-induced volume collapse above 27 GPa, mainly associated to a spin-crossover. Combining experimental and theoretical results, this volume collapse can be explained by the increase of coordination of the initial tetrahedrally coordinated independent iron towards a strongly distorted octahedron (or 5+1 coordination). This distortion is described by the *ab initio* theoretical simulations and reflected in the increase of the Debye-Waller factor associated with the previously tetrahedral iron. Synchrotron Mössbauer spectroscopy (SMS) carried out at beamline **ID18** corroborates the increase of coordination of the previously tetrahedral iron and shows that this new arrangement is coherent with a high-spin-to-intermediate-spin transition (**Figure 19a**), not observed previously in any binary iron oxide counterparts but reported in pentacoordinated iron in complex compounds **[3]**. Thus, the spin-crossover transition responsible for the volume collapse and the structural mechanism driving it have been identified (**Figure 20**). This transition allowed the high-pressure phase to be assigned to a new polymorph of the iron sesquioxide, named ε'-Fe_2O_3. Furthermore, ε-Fe_2O_3 was also found to be dynamically stable at 25 GPa and 1800 K by *ab initio* theoretical simulations (**Figure 19c**) by the absence of imaginary or soft modes, which might indicate that this compound is stable at the Earth's interior conditions.

In conclusion, the structural, electronic and magnetic behaviour of ε-Fe_2O_3 was probed under compression for the first time. Using three different experimental techniques carried out at three different beamlines, combined with *ab initio* theoretical calculations, it was observed that ε-Fe_2O_3 is stable under extreme conditions of pressure and temperature, and therefore the presence of this material in the Earth's interior could be underestimated.

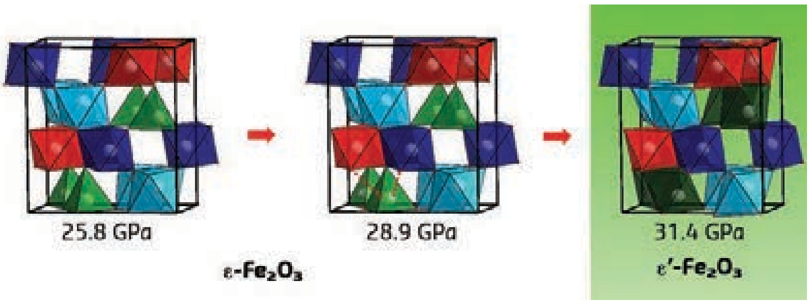

Fig. 20: Sketch of the structural changes induced in the spin-crossover transition.

PRINCIPAL PUBLICATION AND AUTHORS

Stability and nature of the volume collapse of ε-Fe_2O_3 under extreme conditions, J.A. Sans (a), V. Monteseguro (b,c), G. Garbarino (b), M. Gich (d), V. Cerantola (b), V. Cuartero (b,e), M. Monte (b), T. Irifune (f,g), A. Muñoz (h) and C. Popescu (i), *Nat. Commun.* **9**, 4554 (2018); doi: 10.1038/s41467-018-06966-9.

(a) Instituto de Diseño para la Fabricación y Producción Automatizada, Universitat Politècnica de València (Spain)
(b) ESRF
(c) ICMUV, Universitat de València (Spain)
(d) Institut de Ciència de Materials de Barcelona (ICMAB-CSIC) (Spain)
(e) Centro Universitario de la Defensa de Zaragoza (Spain)
(f) Ehime University, Matsuyama (Japan)
(g) Earth-Life Science Institute, Tokyo Institute of Technology (Japan)
(h) Departamento de Física, Instituto de Materiales y Nanotecnología, Universidad de La Laguna (Spain)
(i) CELLS-ALBA Light Source, Barcelona (Spain)

REFERENCES

[1] V. Urbanova *et al.*, *Chem. Mater.* **26**, 6653 (2014).
[2] S. Lee & H. Xu, *Minerals* **8**, 97 (2018).
[3] A. K. Patra *et al.*, *Inorg. Chem.* **45**, 7877 (2006).

MAGNETISATION OF A FERRIMAGNET SEEN MICROSCOPICALLY IN A STRONG MAGNETIC FIELD

An applied magnetic field can tune the exchange and anisotropy interactions of ferrimagnetic materials and induce phase transitions that provide quantitative information on the strength of these interactions. Studies of the rotations of the individual magnetic moments in the ferrimagnet $HoFe_5Al_7$ find contrasting behaviour below and above the compensation point.

Intermetallic compounds based on rare-earth (*R*) and transition-metal (*T*) elements, especially those from the 3*d* group, are important hard-magnetic materials. They combine large magnetic anisotropies typical of the rare-earth elements with high magnetic ordering temperatures typical of the 3*d* elements. Understanding the intrinsic magnetic properties of the *R*-*T* materials is thus of fundamental and practical importance.

Ferrimagnets can be studied very effectively by macroscopic techniques, such as magnetisation measurements, as external magnetic fields affect the ferrimagnetic structure, providing direct quantitative information on the exchange interactions and magnetocrystalline anisotropy. However, the use of this approach is less

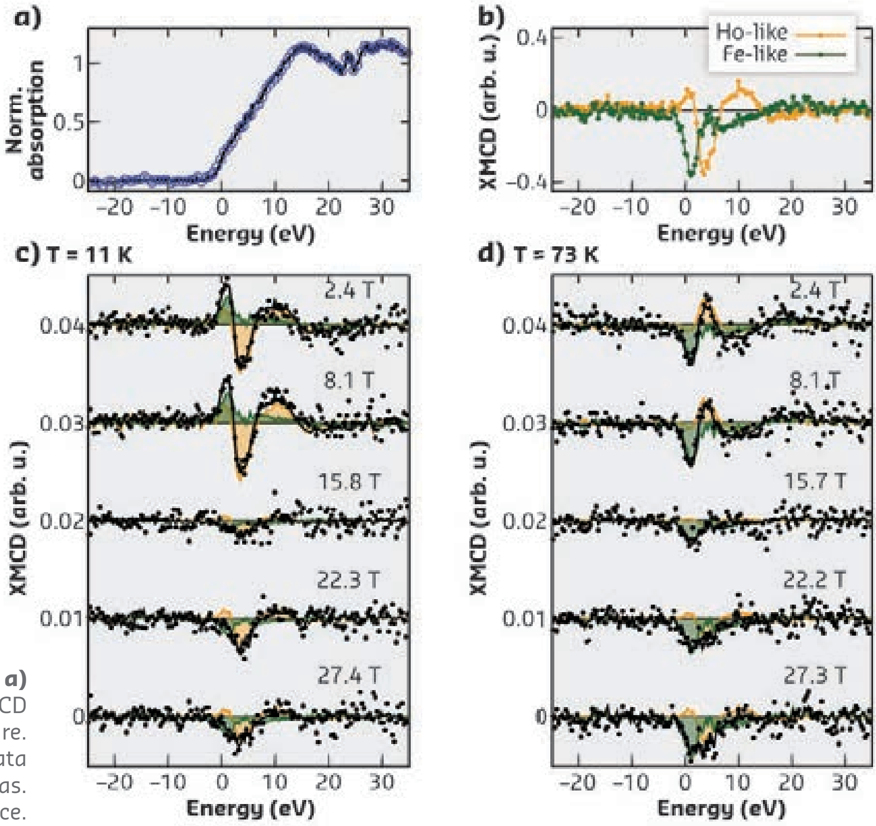

Fig. 21: Fe K-edge absorption and XMCD spectra. **a)** Normalised absorption and **(b)** orthonormal base. XMCD **(c)** below and **(d)** above the compensation temperature. Dots: raw data; black lines: reconstruction of the data using the spectral components shown as shaded areas. Green: Fe sublattice; orange: Ho sublattice.

straightforward for many real systems due to a pronounced field-induced noncollinearity of magnetic moments. This calls for a microscopic technique that follows the evolution of the magnetic structure through field-induced phase transitions. However, the strength of the underlying interactions makes such a microscopic study challenging.

The subject of the present investigation is the strongly anisotropic ferrimagnet $HoFe_5Al_7$ (tetragonal crystal structure) that shows a field-induced phase transition at about 20 T at 2 K for fields applied along the easy magnetisation direction, [110] **[1]**. X-ray magnetic circular dichroism (XMCD) experiments were carried out at **ID24** in transmission in pulsed magnetic fields up to 30 T. For the interpretation of the data, it was noted that the spectral shape is a consequence of a mutually induced signal arising from the other magnetic constituent, *i.e.*, the induced signal at the *T* site is proportional to the magnetisation of the *R* system and vice versa. Singular-value decomposition **[2]** confirmed that the data are indeed described by an orthogonal base of two dominating spectral components representing the *R* and *T* contributions.

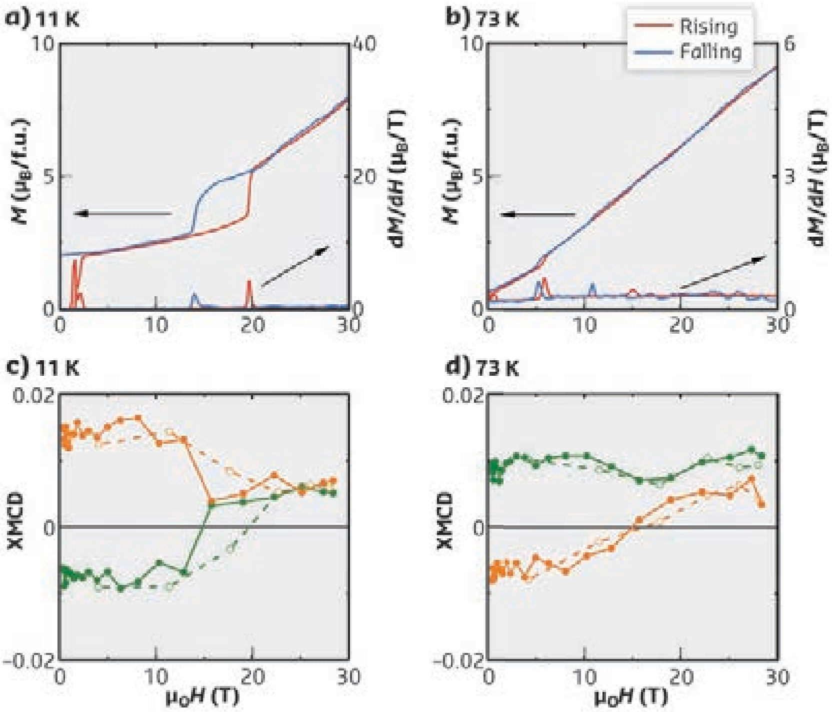

Fig. 22: Bulk magnetisation and field derivative of the **(a)**,**(b)** magnetisation and **(c)**,**(d)** field dependences of the amplitudes of the Fe-like (green) and Ho-like (orange) components below and above the compensation temperature. Open symbols and dashed lines: rising field; full symbols and lines: decreasing field.

Figure 21 shows the normalised Fe K-edge absorption, the orthonormal base to reconstruct the original data, XMCD spectra at selected field values below and above the compensation point, 65 K, and a reconstruction using a linear combination of the Ho and Fe components. The bulk magnetisation of $HoFe_5Al_7$ at 11 K shows a first-order transition between 14 and 19.5 T (**Figure 22**). At 73 K, two transitions can be resolved between 5.5 and 6 T and between 11 and 15 T. The field-dependent Fe- and Ho-sublattice magnetisations inferred from the XMCD data both rotate at the phase transition at 11 K, whereby the Fe magnetisation reverses its sign. Above the compensation temperature, the Ho moment starts to increase continuously above 6 T, reversing sign at about 16 T. For the Fe moment, two small hysteresis loops open at around 10 and 27.5 T, concomitant with the beginning and the end of the reversal of the Ho magnetisation.

The data at 11 K show that the rotation of the Fe and Ho moments proceeds from the easy [110] direction to another easy direction in the basal plane, [1-10], as the projection of the Ho magnetic moment onto the field direction decreases, whereas the projection of the Fe magnetic moment changes sign at the transition. The additional field-induced transition observed above the compensation temperature can be explained by the fact that the Ho-sublattice magnetisation is no longer rigid, as the applied field acts against the Ho-Fe molecular field in this temperature range. Modeling of the individual sublattice magnetisations allowed the determination of the in-plane anisotropy constant, $K \approx 0.5\ \mathrm{MJ/m^3}$, close to the ground state. This study provides the first microscopic insight into the magnetisation process of a strongly anisotropic ferrimagnet in pulsed magnetic fields.

PRINCIPAL PUBLICATION AND AUTHORS

Microscopic Nature of the First-Order Field-Induced Phase Transition in the Strongly Anisotropic Ferrimagnet $HoFe_5Al_7$, D. I. Gorbunov (a), C. Strohm (b), M. S. Henriques (c,d), P. van der Linden (e), B. Pedersen (f), N. V. Mushnikov (g), E. V. Rosenfeld (g), V. Petříček (d), O. Mathon (e), J. Wosnitza (a,h) and A. V. Andreev (d), *Phys. Rev. Lett.* **122**, 127205 (2019); doi: 10.1103/PhysRevLett.122.127205.

(a) Hochfeld-Magnetlabor Dresden (Germany)
(b) Deutsches Elektronen-Synchrotron DESY, Hamburg (Germany)
(c) Institut Laue Langevin, Grenoble (France)
(d) Institute of Physics, Prague (Czech Republic)
(e) ESRF
(f) Heinz Maier-Leibnitz Zentrum, Garching (Germany)
(g) Institute of Metal Physics, Ekaterinburg (Russia)
(h) Institut für Festkörper- und Materialphysik, Dresden (Germany)

REFERENCES

[1] D. I. Gorbunov *et al.*, *J. Phys.: Condens. Matter* **26**, 136001 (2014).
[2] C. Strohm *et al.*, *Phys. Rev. Lett.* **122**, 127204 (2019).

DISCOVERY OF A LAYERED FORM OF SINGLE-BONDED NITROGEN SOLID AT ULTRAHIGH PRESSURE.

Pure molecular nitrogen was investigated to its most extreme conditions yet reached through static compression: 244 GPa and 3300 K. At this pressure and temperature, it was found to transform into a new polymeric single-bonded state comprised of two layers of interconnected N_6 chains, challenging previous experimental and theoretical results.

Over the past 20 years, pure solid nitrogen has been extensively studied to comprehend the pressure-induced transformations in simple molecular systems and to provide insight into achievable polynitrogen arrangements in N-rich compounds, relevant as high energy density materials. The phase diagram of nitrogen displays a remarkable polymorphism, comprising 13 crystalline phases and a single amorphous phase **[1]**. Dominated by diatomic molecular phases (N_2) below 110 GPa, the crystal chemistry of nitrogen radically changes at higher pressures and brings forth a new realm of interatomic interactions where polymeric networks of single-bonded N-N arrangements prevail. As of now, only two single-bonded nitrogen arrangements have been experimentally discovered, namely cubic-gauche polymeric nitrogen (cg-N) and layered polymeric nitrogen (LP-N), with the crystal structure of LP-N still a subject of debate **[2]**. This is at odds with theoretical investigations, which predict a wide array of exotic single-bonded phases. Indeed, between 188 GPa and 263 GPa, six poly-N structures were calculated to have an enthalpy difference of only a few tens of meV in comparison with the most stable phase **[3]**. Remarkably, the dimensionality of these extended single-bonded forms of dense nitrogen should evolve with pressure from 3D, 2D to 3D N_{10} superatoms.

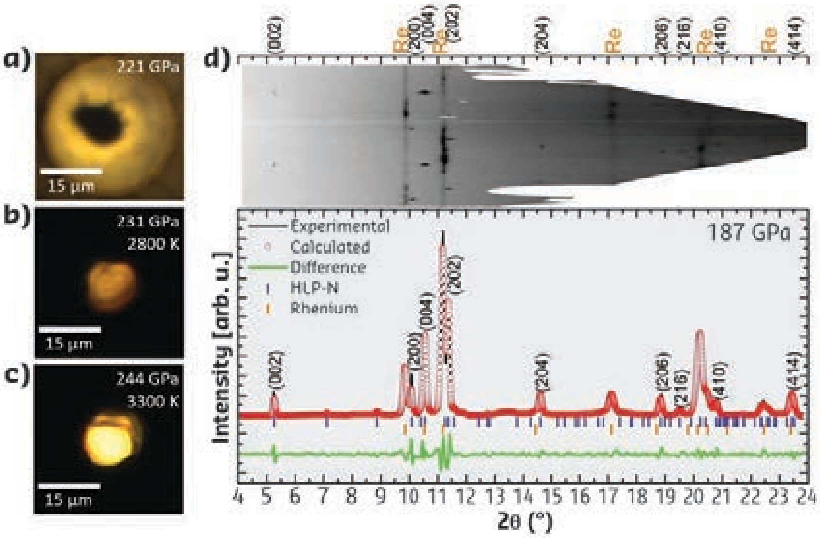

Fig. 23: Microphotographs of the pure nitrogen sample **(a)** under reflection light at 221 GPa before heating, **(b)** under transmission light at 231 GPa after heating to 2800 K and **(c)** under transmission light at 244 GPa after heating to 3300 K. **d)** Le Bail refinement of an integrated X-ray diffraction pattern recorded at 187 GPa following the synthesis of the HLP-N phase at 244 GPa and its decompression. The (hkl) indexes of the experimentally observed diffraction peaks are marked. The raw X-ray diffraction image is shown above and the diffraction spots of the multigrain HLP-N sample can easily be discerned from the Re gasket powder lines.

In the present study, pure nitrogen was progressively compressed and laser-heated to reach previously unattained static pressures of 244 GPa and temperatures of 3300 K. Confirming previous experiments, nitrogen was found to become completely opaque and amorphous above 180 GPa **[4]**. Shown in **Figure 23**, laser-heating the sample to 2800 K at 231 GPa yielded a partial transformation into a transparent phase, a conversion that was completed upon further heating to 3300 K at 244 GPa. The structural characterisation of this phase was achieved by powder X-ray diffraction at the ESRF beamline **ID27** and, combined with Raman spectroscopy measurements and density functional theory (DFT) calculations, a new polymeric nitrogen solid was unveiled. The novel compound's structure was shown to adopt a tetragonal lattice ($P4_2bc$ space group) composed of two distinct layers of interconnected N_6 hexagonal rings – hence coined as the hexagonal layered polymeric nitrogen (HLP-N) phase (**Figure 24**). In this arrangement, each N atom is bonded to three other N atoms with bond lengths varying between 1.30-1.39 Å at 235 GPa, which is typical of N-N single bonds.

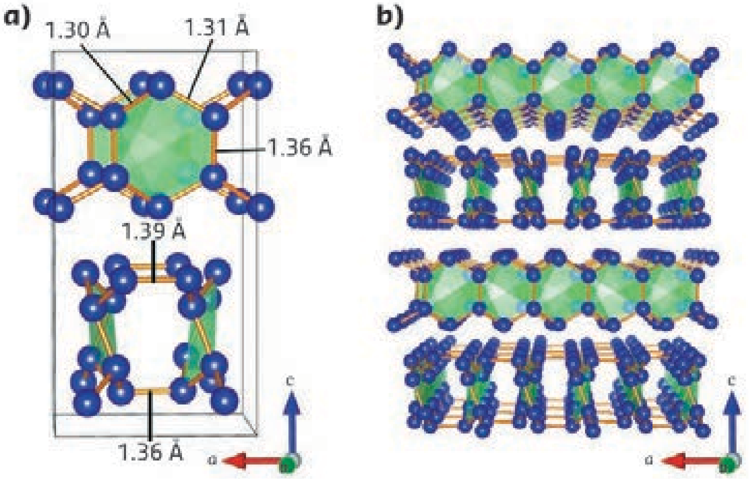

Fig. 24: a) HLP-N tetragonal ($P4_2bc$ space group) crystal structure at 235 GPa, with the five distinct N-N bond lengths marked. For clarity, the inner surface of the N_6 hexagons is filled with a light green plane. **b)** Multiple unit cells of the HLP-N solid, where the infinite and layered nature of the N_6 ring chains is clearly seen.

According to previous DFT calculations performed at 0 K, the LP-N phase is thermodynamically favoured from 188 GPa to 263 GPa, with the HLP-N phase trailing behind by tens of meV/atom **[3]**. As these enthalpy calculations are performed at 0 K, a correction to account for the experimental synthesis at 3300 K was here computed but still yielded the HLP-N phase energetically disadvantageous compared to the LP-N phase by the marginal value of about 12 meV/atom. This result suggests that DFT calculations with a higher degree of precision are needed in order for the theory to match the experiments or that, under these pressure-temperature conditions, a significant activation barrier impedes a transformation towards the LP-N phase and instead promotes the experimental synthesis of the HLP-N solid.

This investigation defies the common assumption of an increasingly simple structural and chemical behaviour concomitantly with pressure, as the complexity of the phase diagram of nitrogen is here unambiguously demonstrated to extend from its molecular state into its polymeric form at high pressure.

PRINCIPAL PUBLICATION AND AUTHORS

Hexagonal layered polymeric nitrogen phase synthesized near 250 GPa,
D. Laniel (a,b), G. Geneste (a),
G. Weck (a), M. Mezouar (c) and
P. Loubeyre (a),
Phys. Rev. Lett. **122**, 066001 (2019);
doi: 10.1103/PhysRevLett.122.066001.
(a) CEA, DAM, DIF, Arpajon (France)
(b) CNES Launcher Directorate, Paris (France)
(c) ESRF

REFERENCES

[1] M. Frost *et al.*, *Phys. Rev. B* **93**, 024113 (2016).
[2] A. A. Adeleke *et al.*, *Phys. Rev. B* **96**, 1–7 (2017).
[3] X. Wang *et al.*, *Phys. Rev. Lett.* X **109**, 175502 (2017).
[4] A. F. Goncharov *et al.*, *Phys. Rev. Lett.* **85**, 1262–1265 (2000).

SUPERCONDUCTIVITY AT 161 K IN THORIUM HYDRIDE ThH_{10}

Synchrotron high-pressure and X-ray diffraction experiments have resulted in the synthesis of a novel high-T_C hydride superconductor, ThH_{10}, with the experimental T_C of 161 K at a pressure of 175 GPa. This is one of the highest critical temperatures that has been achieved experimentally and a step closer to attaining room-temperature superconductivity.

Hydrogen is the first, simplest, and most common chemical element in the Universe. It plays a great role in industrial chemistry, energetics, space technology and environmental projects. The recent dramatic progress of superconductivity to record critical temperatures (T_C, 250-265 K) is due to the properties of atomic hydrogen enclosed in a metal sublattice. The transition of molecular hydrogen to the metallic atomic phase at high pressures was calculated for the first time in 1935 **[1]**. Later, it was proposed that hydrogen-rich compounds with properties similar to pure atomic metallic hydrogen, might form at lower pressures when hydrogen is combined with other elements **[2]**. These chemical compounds, which possess an excess of hydrogen, can only be synthesised at high pressures. They may reach the high-T_C superconductivity previously predicted for a metallic form of pure hydrogen.

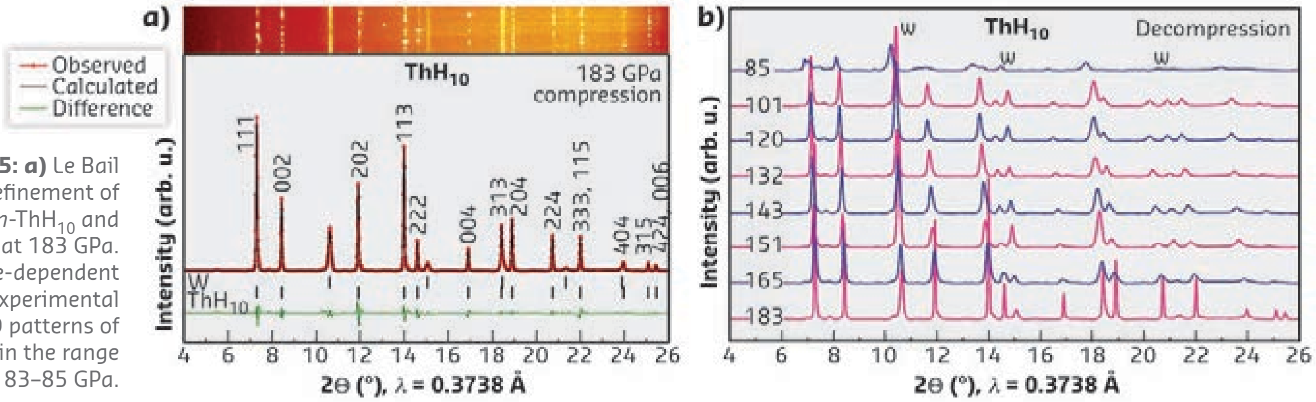

Fig. 25: a) Le Bail refinement of *Fm*$\bar{3}$*m*-ThH_{10} and *bcc*-W at 183 GPa. **b)** Pressure-dependent variation of experimental XRD patterns of *Fm*$\bar{3}$*m*-ThH_{10} in the range of 183–85 GPa.

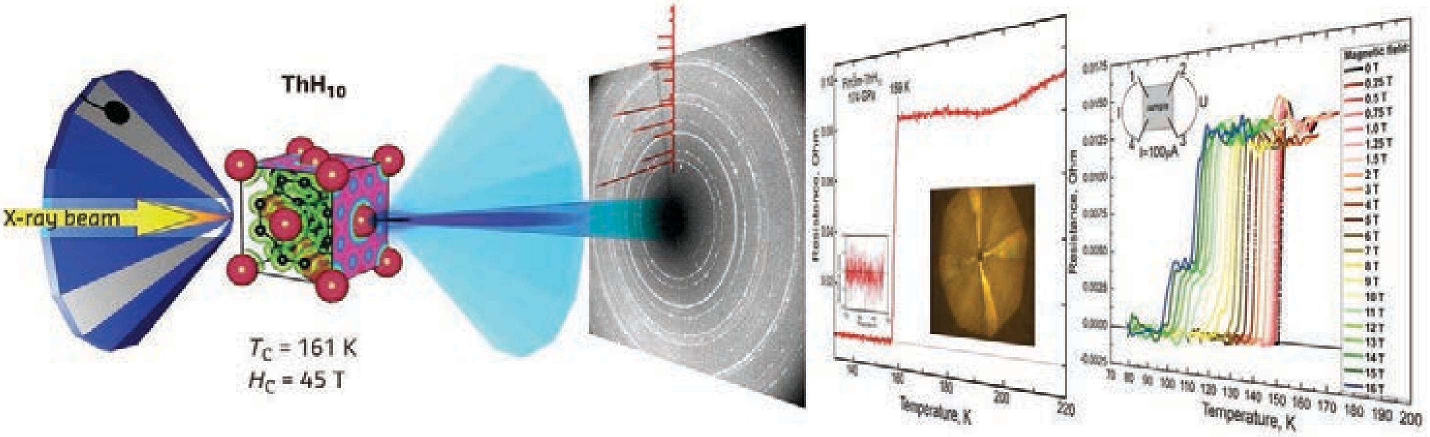

Fig. 26: Synthesis of ThH_{10} in a diamond anvil cell: XRD pattern, dependence of electrical resistance of the sample on temperature and external magnetic field.

Room-temperature superconductivity has been an unattainable dream and subject of speculative discussions for a long time. However, the theoretical prediction of a high-temperature superconductor H_3S **[3]**, followed by experimental confirmation **[4]**, has opened a new chapter in high-pressure physics – the study of superconducting hydrides. Since then, many new hydrides have been predicted and synthesised, *e.g.* LaH_{10} with critical temperature 250–260 K **[5]**, YH_6 and YH_9 with T_C = 226 K and 243 K **[6]**. These results led to an experimental investigation of the Th-H system with a view to synthesising cubic ThH_{10}, which was predicted to be a remarkable high-T_C superconductor **[7]**.

To investigate the possible formation of thorium hydrides, three 50-micron culet diamond-anvil cells were prepared, loaded by a metal piece of thorium in ammonia borane (AB) media, and compressed to 185 GPa. Experimental high-temperature synthesis and X-ray diffraction (XRD) measurements were performed at beamline **ID27**. A short laser heating pulse (200–500 ms) was accompanied by the dissociation of ammonia borane, which leads to the generation of hydrogen with subsequent synthesis of higher hydrides, as was first demonstrated in the synthesis of LaH_{10} **[5a]**. As a result, almost pure cubic ThH_{10} was obtained in the diamond anvil cell (**Figure 25**).

To measure the transport properties of the samples, a special cell with diamond anvils and four Ta/Au electrodes was prepared. A 1-micron-thick thorium sample was sandwiched between the electrodes and AB in the gasket hole. The pressure in the cell was increased to 175 GPa. Heating of the sample led to the emergence of a clear and sharp drop in the electrical resistance to zero at 159–161 K. The superconducting nature of the transition was verified by its dependence on the external magnetic field in the range 0–16 T (**Figure 26**).

During this experiment, two novel high-T_C superconductors, *Fm*$\bar{3}$*m*-ThH_{10} and new *P*6_3*/mmc*-ThH_9 were synthesised, confirming earlier theoretical predictions based on DFT methods **[7]**. ThH_{10} has a unique combination of high superconducting T_C (161 K at 175 GPa), a critical magnetic field of 45 T, and lower bound of stability of 85 GPa, which is far less than that of other high-T_C hydrides. These results will have a strong impact on the understanding of high-pressure chemistry of metal hydrides, aiding attempts to attain room-temperature superconductivity.

PRINCIPAL PUBLICATION AND AUTHORS

Superconductivity at 161 K in thorium hydride ThH_{10}: Synthesis and properties,
D. V. Semenok (a), A. G. Kvashnin (a,b),
A. G. Ivanova (c), V. Svitlyk (d),
V. Y. Fominski (e), A. V. Sadakov (f),
O. A. Sobolevskiy (f), V. M. Pudalov (f),
I. A. Troyan (c) and A. R. Oganov (a,b,g),
Mater. Today in press (2019);
doi: 10.1016/j.mattod.2019.10.005.

(a) Skolkovo Institute of Science and Technology, Skolkovo Innovation Center, Moscow (Russia)
(b) Moscow Institute of Physics and Technology, Dolgoprudny (Russia)
(c) Shubnikov Institute of Crystallography, Federal Scientific Research Center Crystallography and Photonics, Russian Academy of Sciences, Moscow (Russia)
(d) ESRF
(e) National Research Nuclear University MEPhI (Moscow Engineering Physics Institute), Moscow (Russia)
(f) P. N. Lebedev Physical Institute, Russian Academy of Sciences, Moscow (Russia)
(g) International Center for Materials Discovery, Northwestern Polytechnical University, (China)

REFERENCES

[1] E. Wigner & H.B. Huntington, *J. Chem. Phys.* **3**, 764-770 (1935).
[2] N. W. Ashcroft, *Phys. Rev. Lett.* **92**, 187002 (2004).
[3] D. Duan *et al., Sci. Rep.* **4**, 6968 (2014).
[4] (a) A. P. Drozdov *et al., Nature* **525**, 73-76 (2015); (b) I. Troyan *et al., Science* **351**, 1303-1306 (2016).
[5] (a) Z. M. Geballe *et al., Angew. Chem. Int. Ed.* **57**, 688-692 (2017); (b) M. Somayazulu *et al., Phys. Rev. Lett.* **122**, 027001 (2019); (c) A. P. Drozdov *et al., Nature* **569**, 528 (2019).
[6] (a) I. A. Troyan *et al., ArXiv:1908.01534 [Cond-Mat]* (2019); (b) P. P. Kong *et al., ArXiv: 1909.10482 [Cond-Mat]* (2019).
[7] A. G. Kvashnin *et al., ACS Appl. Mater. Interfaces* **10**, 43809-43816 (2018).

DETERMINATION OF THE KINETIC CONSTANTS OF CHEMICAL REACTIONS IN THE MILLISECOND TIMESCALE BY COUPLED XAS AND UV-Vis SPECTROSCOPY

Time-resolved X-ray absorption (XAS) and UV-Vis spectroscopies with millisecond resolution were used simultaneously to investigate oxidation reactions of organic substrates by non-heme iron activated species. It is shown for the first time that the pseudo first-order rate constants of fast bimolecular processes in solution (milliseconds and above) can be determined by the time-resolved XAS technique.

An important challenge in modern chemistry resides in uncovering the structural evolution of species involved in fast chemical reactions, where characteristic time scales range from the seconds to the milliseconds and below, and in developing new experimental strategies to study the reactivity of such intermediates. In this study, time-resolved energy-dispersive X-ray absorption spectroscopy (EDXAS) and UV-Vis spectroscopy were combined to investigate the oxidation reactions of organic substrates by a selected non-heme iron activated species. Pseudo first-order kinetic constants related to fast bimolecular reactions in solution were obtained by the time-resolved XAS technique.

The research was focused on sulfide and alcohol oxidation by the oxo-complex $[N4Py{\bullet}Fe^{IV}O]^{2+}$, deriving from the prototypical non-heme iron complex $[N4Py{\bullet}Fe^{II}]^{2+}$ (N4Py=N,N-bis(2-pyridylmethyl)-N-bis(2-pyridyl)methylamine). The coupled XAS/UV-Vis approach was employed at beamline **ID24** to follow the oxidation of benzyl alcohol to benzaldehyde and the oxidation of a series of thioanisoles, differently substituted in the *para* position of the aromatic ring, to the corresponding methylphenyl sulfoxides. The oxidant $[N4Py{\bullet}Fe^{IV}O]^{2+}$ was prepared *in situ*, under experimental conditions already investigated via the parallel XAS/UV-Vis technique in a pioneering study **[1]**, and all reactions were carried out under pseudo-first-order conditions. In particular, the rate of the iron-oxidation-state evolution during each reaction was determined by following the relative Fe K-edge energy shift in the time-resolved XAS spectra. The values for the kinetic constants obtained by XAS were in very good agreement with those obtained by means of the concomitant UV-Vis detection.

Figure 27a shows the evolution of the Fe K-edge normalised time-resolved EDXAS spectra relative to the oxidation of $PhCH_2OH$ by $[N4Py{\bullet}Fe^{IV}O]^{2+}$ at selected times from reaction start. The XANES spectra show a shift of the Fe K-edge position towards lower energy values, in accordance with the reduction of Fe^{IV} to Fe^{II} throughout the process. **Figure 27b** highlights the variation of ΔE_0 during the reaction, where ΔE_0 is the difference between the K-edge energy position of the XANES spectra at time *t* and the edge position of the first XANES spectrum at t = 0 s, whose experimental decay was fitted with the following equation (blue curve):

$$\Delta E_0(t) = [E_0(i) - E_0(f)]e^{-kt} + E_0(f)$$

where *k* is the reaction kinetic constant, with a value of 0.11 ± 0.05 s^{-1}.

Figure 27c shows the UV-Vis spectrophotometric data recorded simultaneously on the same reaction mixture. The absorbance variation

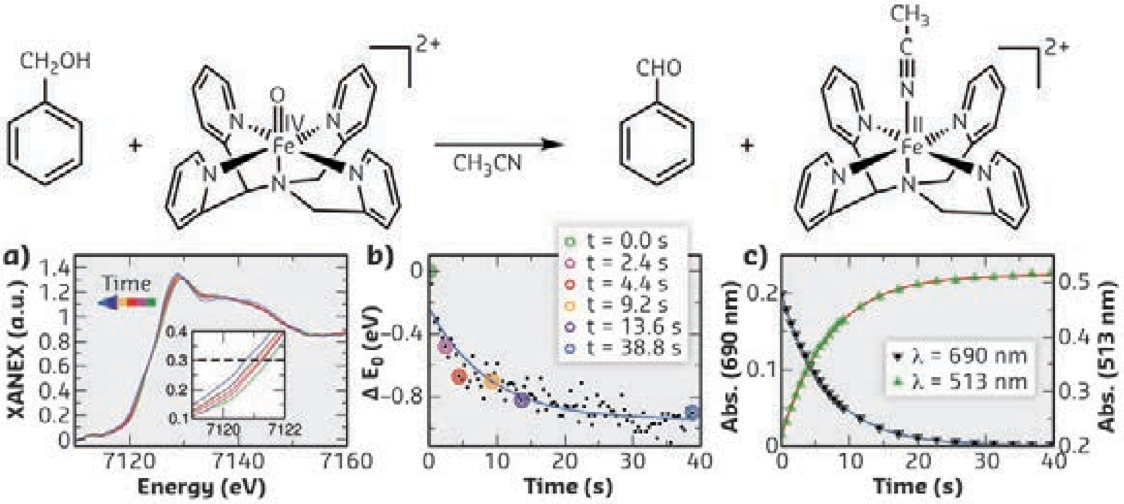

Fig. 27: Oxidation of $PhCH_2OH$ by $[N4Py{\bullet}Fe^{IV}(O)]^{2+}$ followed using the coupled XAS/UV-Vis technique. **a)** Time evolution of the XANES spectra (colours correspond to selected times from the reaction start identified in panel **(b)**. A magnification of Fe K-edge region is shown in the inset. **b)** ΔE_0 *vs* time. The blue curve derives from a first-order kinetic treatment of experimental points. **c)** UV-Vis monitoring of $[N4Py{\bullet}Fe^{IV}(O)]^{2+}$ (downward triangles at λ = 690 nm) and $[N4Py{\bullet}Fe^{II}]^{2+}$(upward triangles at λ = 513 nm) during the reaction. Blue and red curves derive from a first-order kinetic treatment of experimental points.

at 690 nm is due to the decrease in concentration of [N4Py•$Fe^{IV}O]^{2+}$, while the concentration increase of the [N4Py•$Fe^{II}]^{2+}$ species determines the contemporary absorbance increase at 513 nm. The first-order kinetic plots (red and blue curves) provided kinetic constants identical to those determined from the EDXAS spectra (**Figure 28**).

The XAS technique provided quantitative values of the kinetic constants of fast (in the millisecond to second timescales) bimolecular chemical reactions in solution. These results reveal XAS spectroscopy as an innovative tool for the investigation of fast complex chemical processes involving the oxidation of a metal centre, where the use of other experimental techniques would be impossible.

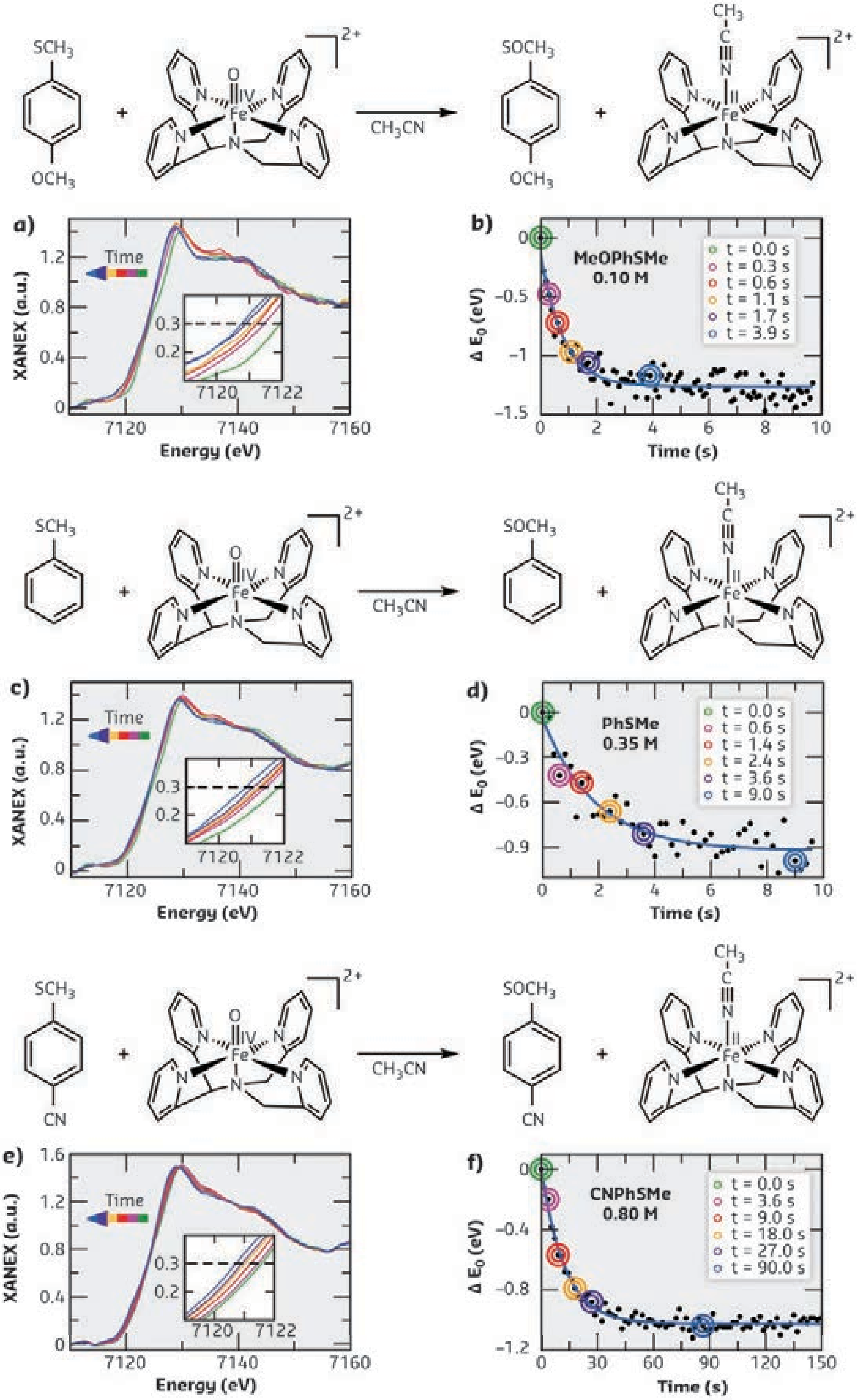

Fig. 28: Time evolution of the Fe K-edge EDXAS spectra of the reactions between **(a)** MeOPhSMe, **(b)** PhSMe and **(c)** CNPhSMe with [N4Py•$Fe^{IV}(O)]^{2+}$. In all cases, the kinetic constants determined via EDXAS were in good agreement with the *k* values measured through UV-Vis and with literature data. Left: Magnifications of Fe K-edge regions are shown in the insets (colours correspond to selected times from the reaction start identified in right panel). Right: ΔE_0 *vs* time. Blue curves were derived from a first-order kinetic treatment of EDXAS experimental points.

PRINCIPAL PUBLICATION AND AUTHORS

Coupled X-ray absorption/UV–vis monitoring of fast oxidation reactions Involving a non-heme iron–oxo complex, G. Capocasa (a), F. Sessa (a), F. Tavani (a), M. Monte (b), G. Olivo (a), S. Pascarelli (b), O. Lanzalunga (a), S. Di Stefano (a) and P. D'Angelo (a), *J. Am. Chem. Soc.* **141**, 2299-2304 (2019);

doi: 10.1021/jacs.8b08687.

(a) Department of Chemistry, University La Sapienza, Rome (Italy).
(b) ESRF

REFERENCES

[1] G. Olivo *et al.*, *J. Phys. Chem. Lett.* **8**, 2958-2963 (2017).

STOICHIOMETRY OF CORNERSTONES IN BIMETALLIC CeZr-UiO-66 MOFS REVEALED BY EXAFS SPECTROSCOPY

In memory of Prof. Carlo Lamberti

Bimetallic metal-organic frameworks (MOFs) constitute a next generation of MOF materials, adding one more degree of freedom to materials design. Advanced extended X-ray absorption fine structure (EXAFS) analysis helped to determine the exact stoichiometry of Ce_xZr_{6-x} cornerstones in UiO-66 MOFs at different overall Ce contents, leading to an explanation of the physical properties of the material.

Bimetallic Ce/Zr-UiO-66 MOFs prove to be promising materials for various catalytic redox applications, representing, together with other multimetallic MOFs, a new generation of porous structures (**Figure 29a**). Although metal substitution in different MOFs is widely discussed in the literature, no direct proof for the existence of mixed-metal cornerstones in UiO-family MOFs has been presented so far. The cornerstones in mixed-metal compounds are usually assumed to be either pure or truly bimetallic (**Figures 29b-c**). However, these chemically different cases have never been investigated, although this point is crucial for rationalising the properties and potential applications of the material.

To address this problem, X-ray absorption spectroscopy (XAS) data at the Zr K-, Ce K- and Ce L_3-absorption edges were collected at beamlines **BM23** and **BM31** for a series of bimetallic Ce_xZr_{6-x}-UiO-66 MOFs. Ce L_3-edge X-ray absorption near-edge structure (XANES) data confirmed the 4+ oxidation state of Ce centres in all the studied Zr/Ce-UiO-66 MOFs. However, XANES spectra of all the compounds were almost identical at all studied edges, which made it difficult to draw any structural conclusion from them. At the same time, Ce and Zr K-edge EXAFS data showed very pronounced differences between the Ce/Zr-UiO-66 MOFs with different Ce content (**Figures 29d-e**). The observed dependence of the EXAFS spectra on Ce content may be qualitatively explained by the preferential formation of $CeZr_5$ clusters, accompanied by pure Zr_6 or Ce_6 cornerstones in the proportion dictated by the total stoichiometry of the sample (**Figure 30a**). This implies a coexistence of $CeZr_5$ and Zr_6 clusters for Ce contents lower than 17% (that is, 1/6) and a mixture of $CeZr_5$ and Ce_6 for higher Ce loadings.

A hypothesis about the preferential formation of $CeZr_5$ cornerstones, put forward after qualitative analysis of the EXAFS data, was tested by quantitative EXAFS fitting at the Zr and Ce K-edges. All 10 EXAFS data sets (five at each edge) were fitted together, leading to the calculation of a global R-factor. The fit was done respecting the physical constraints for interatomic distances and Debye-Waller factors and resulted in excellent agreement with the experimental data (**Figure 30b**), thus confirming the proposed structural model.

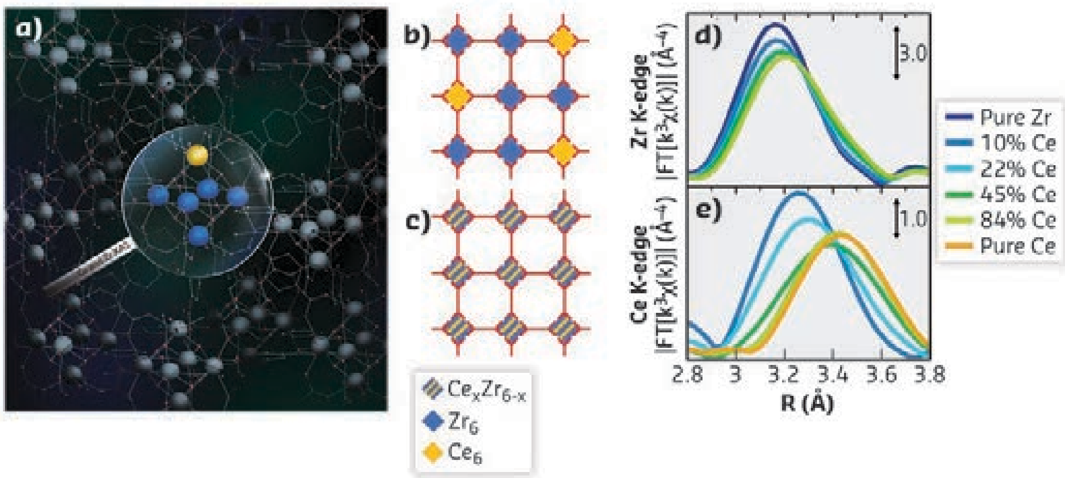

Fig. 29: a) Artistic view of CeZr-UiO-66 MOF structure highlighting the possibility of XAS to distinguish between the Ce (yellow) and Zr (blue) atoms in the cornerstones. **b-c)** Representation of possible mixed-metal Ce_xZr_{6-x}-UiO-66 structures with pure **(b)** and bimetallic **(c)** cornerstones. **d-e)** Close-up of the metal–metal scattering peak in the modulus of not-phase-corrected Fourier transform of k^3-weighted EXAFS data collected at Zr and Ce K-edges for the pure and mixed-metal UiO-66 MOFs. Panel **(a)** courtesy of Y. Lomachenko. Panels **(b-e)** are adapted from the principal publication.

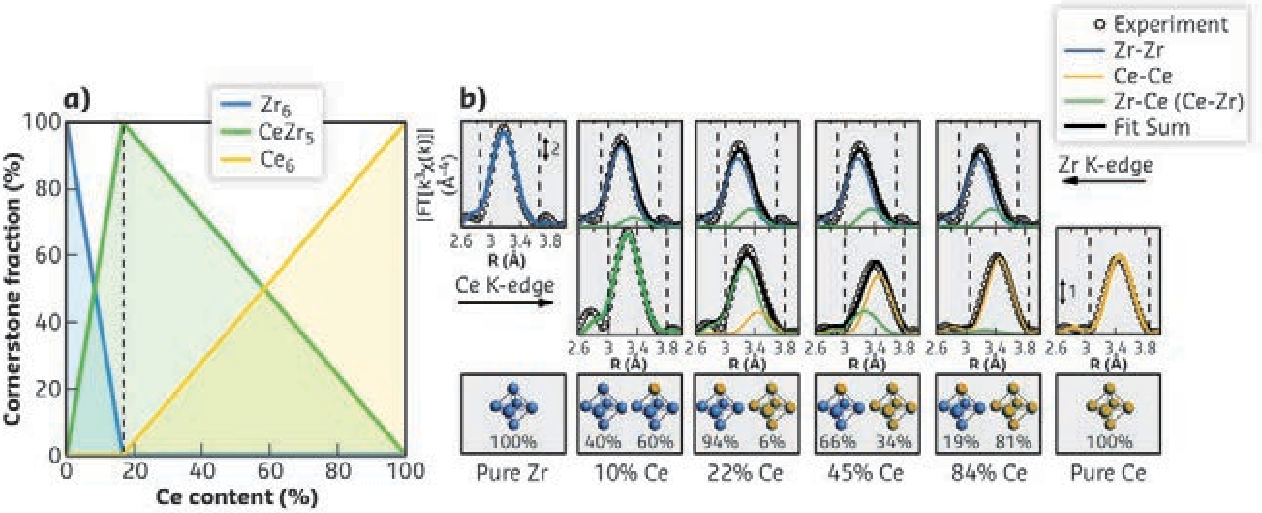

Fig. 30: a) Dependence of the abundance of Zr_6, $CeZr_5$ and Ce_6 cornerstones on Ce content. **b)** Results of the EXAFS fitting based on the model from panel **(a)**. Experimental data are shown as white circles, fitted curves are presented as full lines. Zr–Zr contribution, blue; Ce–Ce contribution, yellow; Zr–Ce and Ce–Zr contribution, green. For mixed-metal MOFs, the sum of the two contributions is shown in black. Bottom panels summarise the cornerstone composition employed for fitting the spectra of each sample. Panel **(b)** is adapted from the principal publication.

The preferential formation of $CeZr_5$ cornerstones explains the trends in the stability of bimetallic UiO-66 MOFs with different Ce content reported previously **[1]**. Indeed, while at low Ce loadings stability decreases linearly with the increase of Ce content, at around 20% it stabilises at the value observed for pure Ce-UiO-66 MOF. According to current EXAFS analysis, this coincides with the disappearance of pure Zr_6 cornerstones, which, due to lower disorder and higher stability compared to Ce_6 and $CeZr_5$ cornerstones, increases the decomposition temperature of the material.

PRINCIPAL PUBLICATION AND AUTHORS

Exact Stoichiometry of Ce_xZr_{6-x} Cornerstones in Mixed-Metal UiO-66 Metal–Organic Frameworks Revealed by Extended X-ray Absorption Fine Structure Spectroscopy, K. A. Lomachenko (a), J. Jacobsen (b), A. L. Bugaev (c), C. Atzori (d), F. Bonino (d), S. Bordiga (d), N. Stock (b) and C. Lamberti (c,e), *J. Am. Chem. Soc.* **140**, 17379-17383 (2018); doi: 10.1021/jacs.8b10343.

(a) ESRF
(b) Institut für Anorganische Chemie, Christian-Albrechts-Universität, Kiel (Germany)
(c) The Smart Materials Research Institute, Southern Federal University, Rostov-on-Don (Russia)
(d) Department of Chemistry, NIS interdepartmental Center and INSTM Reference Center, University of Turin (Italy)
(e) Department of Physics, INSTM Reference Center and CrisDi Interdepartmental Centre for Crystallography, University of Turin (Italy)

REFERENCES

[1] M. Lammert *et al., Dalton Trans.* **46**, 2425-2429 (2017).

STRUCTURAL BIOLOGY

As will no doubt be described – and rightfully celebrated – elsewhere in this edition of the *ESRF Highlights*, the 6 December 2019 saw first stored beam in the ESRF's Extremely Brilliant Source (EBS) storage ring. As well as being a key milestone on the road to the full commissioning of the world's first high-energy, fourth-generation synchrotron source, this achievement has also increased the pulse-rates of the ESRF's beamline scientists. There is now, literally, light at the end of the tunnel, and we can start looking forward to the recommissioning of our facilities and, in August 2020, to welcoming back our external user community.

As with the construction and commissioning of EBS, the recommissioning of the beamlines in order that they make best advantage of post-EBS X-ray beams has taken careful planning. However, 2019 has not been spent 'sitting with our feet up' as, in reality, the opposite has been the case. The major reason for this is that many of the ESRF's Structural Biology facilities are being refurbished/rebuilt and much effort has been, and continues to be, expended to ensure that new functionality will be available as soon as possible after the restart of user operation. Examples of the activity currently taking place include an almost entire rebuild of the BioSAXS beamline **BM29**, a major refurbishment – carried out in collaboration with the EMBL Grenoble outstation – of the completely automatic **MASSIF-1** beamline, and incremental upgrades to the **MASSIF-3**, **ID30B** and **ID23-1** end-stations. As part of these rebuilds/refurbishments, new detectors for BM29 and ID23-1 have been ordered and will be installed in 2020. Moreover, a brand-new facility for time-resolved synchrotron serial crystallography (**EBSL8**) is now being constructed on the **ID29** port. Here, progress has been excellent – at time of writing, the experimental hutches for the new beamline were being assembled in the Chartreuse extension of the Experimental Hall and the project is well on track to welcome its first users in late 2021. These refurbishment/renewal activities have been supplemented by continuing progress in the software development associated with our beamlines: MxCuBE3 and its BioSAXS equivalent BsxCuBE3, the latest, web-based, incarnations of our beamline control user interfaces, will be ready for deployment and intensive testing during the beamline recommissioning period, as will Exi2, the new interface to the ISPyB experiment tracking database. Both activities are being carried out as part of the European-wide MXCuBE and ISPyB collaborations, in which the ESRF continues to play a very active role.

Despite the unavailability of its X-ray-based beamlines, in 2019, Structural Biology at the ESRF has been far from a 'user-less' zone. The **CM01** cryo-electron microscope (cryo-EM) facility has operated at full tilt during the EBS shutdown, while the *in crystallo* optical spectroscopy (icOS) laboratory, the replacement of the Cryobench facility, relocated and upgraded as part of the EBSL8 project, was recommissioned in early 2019 and has welcomed many user experiments throughout the year. While access to CM01 is currently limited to projects for which a suitable sample preparation can be demonstrated, we hope soon to be able to offer 'full service' protocols, including mail-in access to the sample screening and optimisation microscopes of the **Partnership for Structural Biology** (**PSB**) cryo-EM platform located at the Institute de Biologie Structurale. As well as providing an entry point to electron microscopy for scientists with no, or very limited, access to EM facilities, we believe that this endeavour will provide a new paradigm that will eventually allow the wider ESRF user community access to other instruments making up the array of technical platforms available in the PSB.

External user research based on data collected at our facilities before the EBS shutdown continues to feed through to publication. Here, we present a snapshot chosen from many potential high-impact examples. A number of articles presented here describe the results of studies where cryo-EM, often combined with X-ray crystallography and other techniques, has shed light on the mechanisms involved in fundamental biological processes (*e.g.*, backtracking during errors in gene expression by RNA polymerase (Abdelkareem *et al.*, **page 60**); the DNA retention and ejection mechanisms of bacteriophages (Cuervo *et al.*, **page 56**); how an oncogenic hotspot mutant activates Rag GTPases and upregulates mTORC1 (Anandapadamanaban *et al.*, **page 47**); the elucidation of the architecture and molecular mechanism of the adenylyl cyclase–G protein complex (Qi *et al.*, **page 43**); snapshots of the influenza virus transcription-replication machinery (Kouba *et al.*, **page 53**), or iron uptake in cells (Montemiglio *et al.*, **page 59**)).

Several of the above-mentioned studies provide insights into possible avenues for the development of therapeutic strategies to combat disease.

This is also the case for many of the other articles presented here, which focus, variously, on the molecular basis of GPCR pharmacology (Warne *et al.*, **page 41**), the identification of a new class of inhibitors targeting Phosphoinositide-3-kinase γ, a potential target for immune-oncology (Gangadhara *et al.*, **page 46**), the discovery of a neurotoxin that selectively targets mosquitoes that transmit malaria, and which may provide an environmentally friendly approach for tackling malaria (Contreras *et al.*, **page 50**), the development of an approach for the 'de-immunisation' of a drug used in the treatment of multiple sclerosis (Bertrand *et al.*, **page 51**), and the elucidation of the structure of a receptor involved in the formation of neural networks, which could lead to the development of new treatments for cancer (Barak *et al.*, **page 49**).

This chapter also highlights the discovery of the true biological role of the Kiwellin proteins, which are the causatives of human allergy to the kiwi fruit. Here, it is shown that they are actually plant defence proteins against pathogenic fungi, and that they could serve as potential candidates for agricultural biotechnology applications, helping to guarantee food security (Han *et al.*, **page 40**). Also demonstrated here is the mechanism used by cyanobacteria for efficient carbon fixation during photosynthesis (Wang *et al.*, **page 44**), as well as the discovery of an unanticipated asymmetry that provides a mechanism for condensin's ability to extrude DNA loops during mitotic chromosome assembly (Hassler *et al.*, **page 54**). Finally, the crystal structures of the catalytic USP domains are also highlighted. These show that the two enzymes adopt distinct oligomeric states, thus providing a potential route to the development of specific inhibitors for use in the treatment of cancers (Sauer *et al.*, **page 57**).

We hope you enjoy reading the selection of highlights presented here and are looking forward to seeing you all at our beamlines in August, when the EBS adventure can finally begin in earnest for our external user community.

G. LEONARD AND
C. MUELLER-DIECKMANN

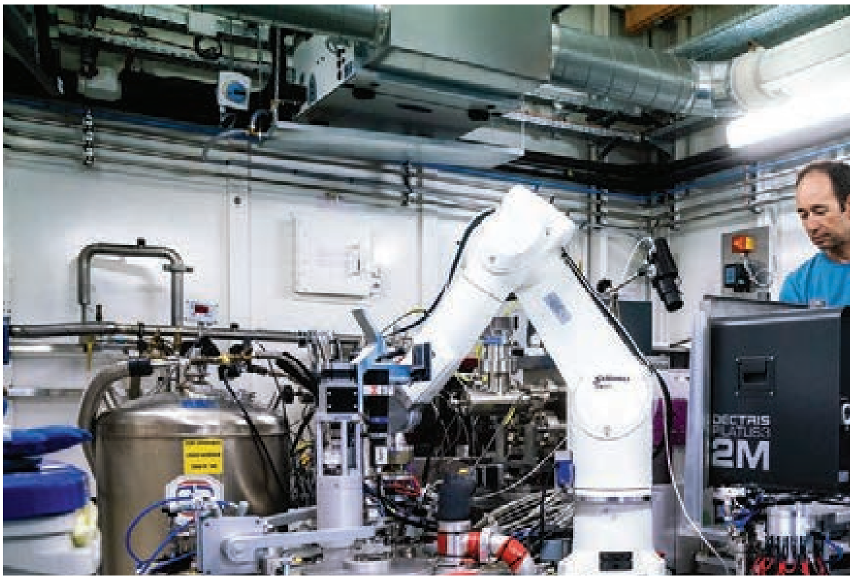

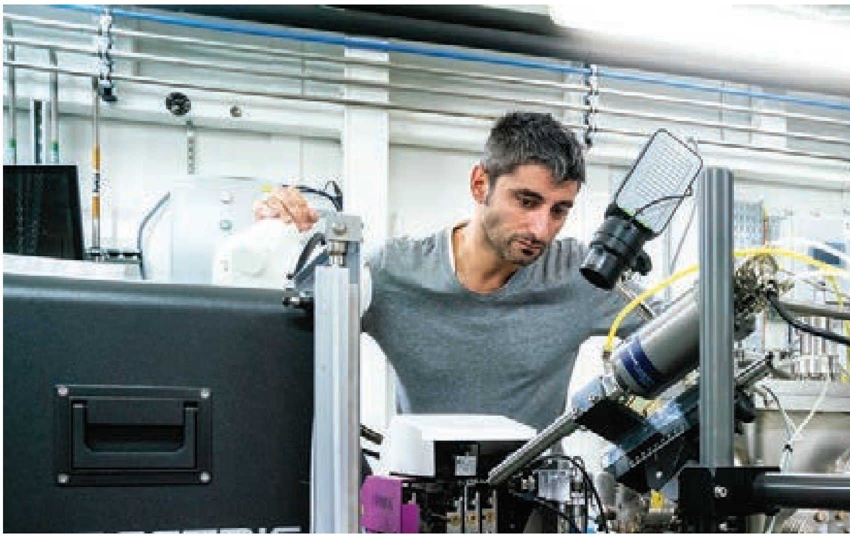

KIWELLIN PROTEINS: FROM HUMAN ALLERGENS TO PLANT DEFENCE

Kiwellin proteins are well-known causatives of human allergy to the kiwi fruit. This study defines their true biological role as plant defence proteins against pathogenic fungi. It further shows that kiwellins are conserved among various agricultural crops and might serve as potential candidates for agricultural biotechnology applications.

Fungal pathogens cause large losses in the five most important crops, with impact growing yearly **[1]**. Among these, smut fungi constitute one of the largest classes of biotrophic pathogens infecting mostly economically important grasses **[2]**. Instead of killing their hosts, biotrophic pathogens establish an intimate relationship with and heavily rely on the viability of their host plants. Studies on *Ustilago maydis* (maize), a well-characterised model organism for biotrophic pathogenic development, have shown that the infection process is guided by effector proteins secreted by the pathogen into the maize plant that modulate the host metabolism and suppress immune reactions **[3]**.

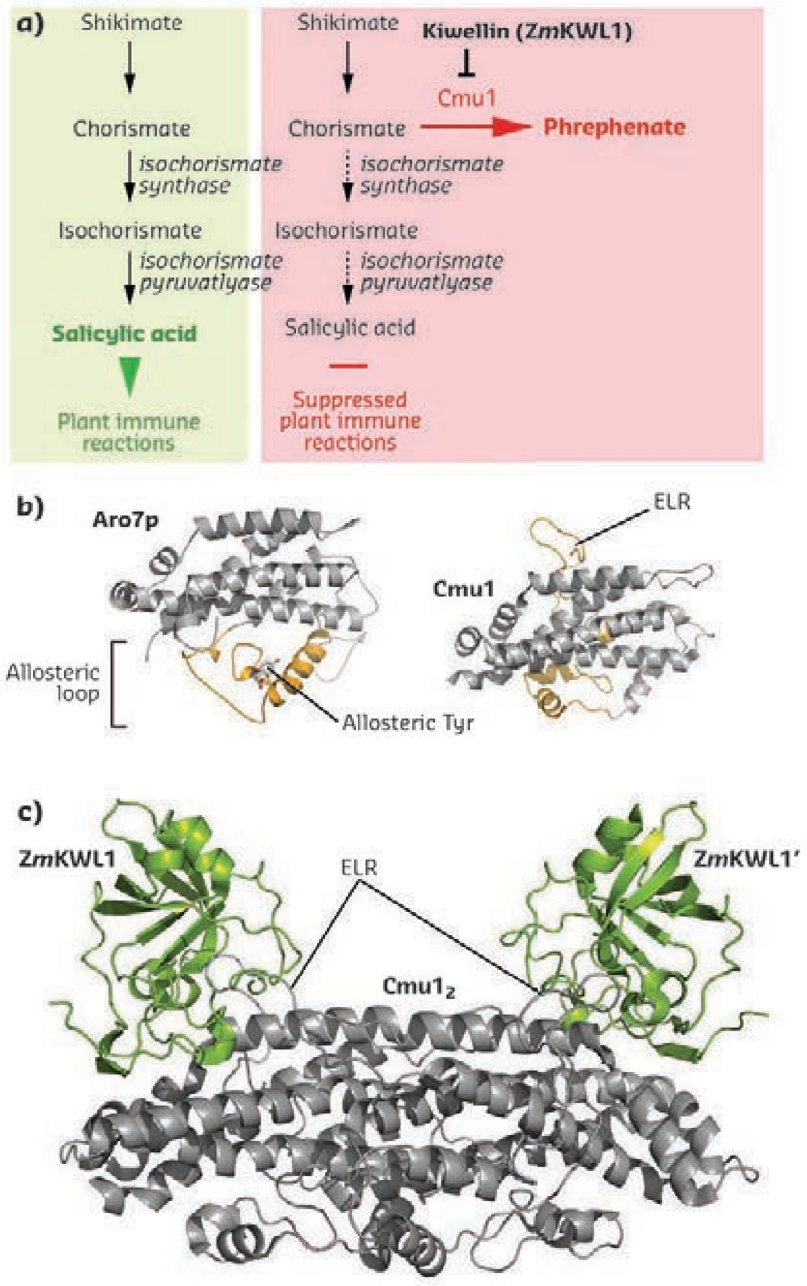

Fig. 31: The fungal effector Cmu1 manipulates the shikimate pathway in maize and is targeted by a kiwellin protein. **a)** The metabolite chorismate serves for biosynthesis of salicylic acid, an important immune signal for plants (green panel). The fungus secretes the virulence effector Cmu1 into the plant. The enzyme converts chorismate to prephenate and prevents production of salicylic acid, thus suppressing the plant immune response (red panel). **b)** Aro7p and Cmu1 share a conserved fold. However, the latter lacks the loop essential for allosteric regulation of Aro7p by the amino acids tryptophan, phenylalanine and tyrosine. **c)** Two molecules of *Zm*KWL1 reside on the ELRs and the active sites of the Cmu1 dimer and block substrate entry.

The secreted chorismate mutase 1 (Cmu1) is a well-studied protein, active in the cytoplasm of the host cell, where it converts chorismate to prephenate **[4]**. This conversion step is part of the shikimate pathway leading to the production of either tyrosine and phenylalanine or tryptophan. In plants, chorismate also serves as a precursor for salicylic acid, a plant hormone important for systemic defence against pathogens (**Figure 31a**). While housekeeping chorismate mutases such as Aro7p are allosterically regulated by either tyrosine/phenylalanine or tryptophan, Cmu1 lacks this allosteric regulation and constantly converts chorismate to prephenate, thereby preventing production of salicylic acid (**Figures 31a** and **31b**) **[4]**. The crystal structure of *U. maydis* Cmu1 was determined at **ID23-1** and clearly shows that the allosteric loop found in other such mutases is replaced by an extensive loop region (ELR) thus preventing allosteric regulation (**Figure 31b**).

The presence of an unregulated effector protein raised the question of whether counteracting strategies have been developed by the plant to minimise the metabolic chaos caused by Cmu1. Interestingly, co-immunoprecipitation in lysates of infected maize leaves analysed by mass spectrometry revealed the presence of a protein binding to Cmu1. It was demonstrated that this secreted maize protein belonging to the kiwellin class binds to and effectively inhibits

Cmu1 activity. The crystal structure of Cmu1 in complex with *Zm*KWL1 was then determined, also at ID23-1, and the molecular mechanism of Cmu1 inhibition by *Zm*KWL1 was thus revealed. Two molecules of *Zm*KWL1 reside on the Cmu1 dimer and directly block substrate access to the active site (**Figure 31c**). The interaction is mediated by several loops on *Zm*KWL1, which protrude from its central β-barrel and interact with the ELR on Cmu1 – a region allowing the effector to distinguish it from housekeeping chorismate mutases.

A more thorough inspection of the kiwellin class revealed a broad conservation among various monocots, dicots and fungi, with 20 kiwellin paralogs present in the maize genome alone. Despite their broad conservation, kiwellins had so far only been recognised as human allergens when isolated directly from kiwi fruit **[5-7]**. Taken together, this demonstrates that kiwellins belong to a broadly distributed class of plant defence proteins and thereby give first insights into the biological function of a human allergen.

PRINCIPAL PUBLICATION AND AUTHORS

A kiwellin disarms the metabolic activity of a secreted fungal virulence factor,
X. Han (a), F. Altegoer (b), W. Steinchen (b), L. Binnebesel (b), J. Schuhmacher (b,f), T. Glatter (c), P. I. Giammarinaro (b), A. Djamei (a,g), S. Rensing (d,e), S. Reissmann (a), R. Kahmann (a) and G. Bange (b), *Nature* **565**(7741), 650-653 (2019); doi: 10.1038/s41586-018-0857-9.

(a) Department of Organismic Interactions, Max Planck Institute for Terrestrial Microbiology, Marburg (Germany)
(b) Philipps-University Marburg, Center for Synthetic Microbiology (SYNMIKRO) and Department of Chemistry, Marburg (Germany)
(c) Facility for Mass Spectrometry and Proteomics, Max Planck Institute for Terrestrial Microbiology, Marburg (Germany)
(d) Faculty of Biology, Philipps-University, Marburg (Germany)
(e) BIOSS Centre for Biological Signalling Studies, University of Freiburg (Germany)
(f) Present address: Max Planck Institute of Molecular Cell Biology and Genetics, Dresden, (Germany)
(g) Present address: Gregor Mendel Institute (GMI), Austrian Academy of Sciences, Vienna Biocenter (Austria)

REFERENCES

[1] M. C. Fisher *et al., Nature* **484**, 186-194 (2012).
[2] W. Zuo *et al., Annu. Rev. Phytopathol.* **57**, 411-430 (2019).
[3] D. Lanver *et al., Nat. Rev. Microbiol.* **15**, 409-421 (2017).
[4] A. Djamei *et al., Nature* **478**, 395-398 (2011).
[5] C. Hamiaux *et al., J. Struct. Biol.* **187**, 276-281 (2014).
[6] M. Tamburrini *et al., Protein J.* **24**, 423-429 (2005).
[7] L. R. Offermann *et al., J. Agric. Food Chem.* **63**, 6567-6576 (2015).

UNDERSTANDING THE MOLECULAR BASIS FOR GPCR PHARMACOLOGY

X-ray crystallography reveals why G protein-coupled receptors (GPCRs) in the active state have higher affinity for agonists as compared to when they are in the inactive state. As GPCRs are exceptionally good targets for drug development, increased understanding of their molecular mechanisms could lead to new, more efficient drugs.

G protein-coupled receptors are integral membrane proteins that form the largest family of receptors in the human body, comprising over 800 different types, and are activated by a wide range of agonists, including hormones, neurotransmitters, ions and even photons of light. Activation of GPCRs is a key step in the process of cells sensing their environment and responding to chemical cues secreted by other cells that could be on the other side of the body. The pivotal role that GPCRs play in intercellular communication makes them ideal drug targets and 34% of US FDA-approved small molecule drugs target GPCRs, *e.g.*, beta blockers, anti-hypertensives and treatments for asthma and migraines.

As part of this focus on drug development, it is essential to understand both how GPCRs function and the molecular basis for their pharmacology. One particularly enigmatic observation was that when G proteins couple to the intracellular side of the GPCR, then the affinity of an agonist increases. This is known as the agonist affinity shift. However, the increase in agonist affinity upon G protein coupling is not always the same for different ligands targeting the same receptor and there is no correlation between ligand efficacy (how efficient a ligand is in activating a receptor) and the agonist affinity shift upon G protein coupling.

In order to determine the molecular basis for the agonist affinity shift upon G protein coupling, the β_1-adrenoceptor (β_1AR) was used as a model GPCR. The structures of the inactive state of β_1AR had previously been determined by X-ray crystallography when bound to four different ligands **[1]**: isoprenaline, dobutamine, salbutamol and cyanopindolol (listed in order of decreasing efficacy). In the current work, X-ray crystallography was carried out on beamlines **ID23-2**, **ID29**, **ID30B**, and **MASSIF-3** to determine the crystal structures of β_1AR bound to the same ligands but with β_1AR moved to an active state through the use of a G protein mimetic (nanobodies Nb80 and Nb6B9). Comparison of the ligand binding pockets showed that, in every case, these had a smaller volume in the active-state structures when compared to the inactive state bound to the same ligand. This led to a decrease in the length of hydrogen bonds and van der Waals distances and, except for salbutamol, to a significant increase in the number of ligand-receptor interactions. A combination of any of these effects would be expected to increase the affinity of the ligand. However, the changes in the ligand-receptor distances were not identical for each ligand (**Figure 32**), explaining the marked differences observed in both the agonist affinity shift and in efficacy. Differences in the structures of the extracellular regions also suggested why some ligands could behave as partial agonists rather than full agonists.

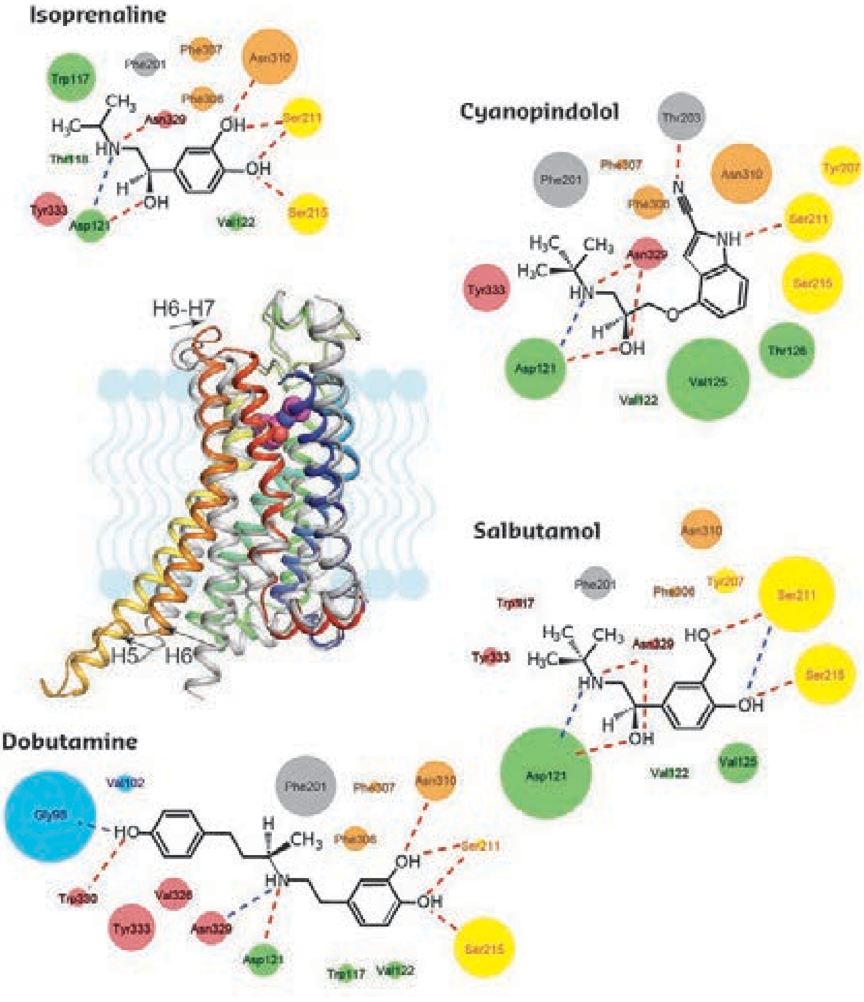

Fig. 32: Structure of an active state of β_1AR. A comparison (centre) of β_1AR in an active state (rainbow coloration) and an inactive state (grey), with the major conformational changes shown (arrows). Structures of the ligands co-crystallised with β_1AR are depicted with the interacting amino acid residues colour-coded according to the regions of the receptor (central panel) and residues in extracellular loop 2 shown in grey. The size of the circles represents the maximum magnitude of decrease in atomic distance between the side chain and ligand when inactive and active state structures are compared.

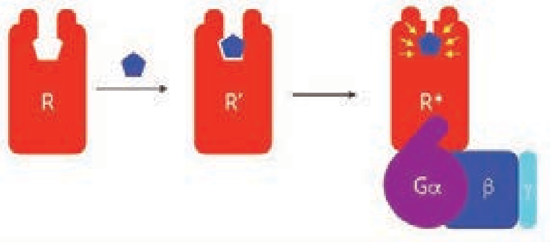

Fig. 33: Cartoon depicting the mechanism of agonist affinity increase in β_1AR upon G protein coupling. The inactive state (R) transitions to an intermediate state (R') upon binding an agonist (blue pentagon), with only minor changes to the structure of the ligand binding pocket. Agonist binding increases the probability of transitions to an active state (R*) with an opened cytoplasmic cleft that allows G protein binding. Upon coupling of a heterotrimeric G protein (Gαβγ) the binding pocket shrinks around the ligand, which increases ligand affinity.

GPCRs are a highly conserved family of proteins with conserved mechanisms of activation, transduction of signals to G proteins **[2]** and a conserved mechanism of activation of the G proteins themselves **[3]**. Thus, other members of the GPCR superfamily are likely to also show a contraction of the binding pocket upon G protein-coupling (**Figure 33**). This could be important in drug discovery, helping to predict how efficient a compound may be in activating intracellular pathways and will improve efficient and effective modelling of the different states of GPCRs for which structures are not available.

PRINCIPAL PUBLICATION AND AUTHORS

Molecular basis for high-affinity agonist binding in GPCRs, T. Warne (a), P. C. Edwards (a), A. S. Doré (b), A. G. Leslie (a) and C. G. Tate (a), *Science* **364**, 775-778 (2019); doi: 10.1126/science.aau5595.

(a) MRC Laboratory of Molecular Biology, Cambridge (UK)
(b) Sosei Heptares, Cambridge (UK)

REFERENCES

[1] T. Warne *et al.*, *Nature* **469**, 241-244 (2011).
[2] A. J. Venkatakrishnan *et al.*, *Nature* **536**, 484-487 (2016).
[3] T. Flock *et al.*, *Nature* **524**, 173-179 (2015).

ELUCIDATING THE ARCHITECTURE AND MOLECULAR MECHANISM OF THE MEMBRANE ADENYLYL CYCLASE-G PROTEIN COMPLEX

Membrane adenylyl cyclases are key components of the cellular signaling machinery. Cryo-electron microscopy (cryo-EM) and single particle analysis were used to determine the first structure of a full-length adenylyl cyclase AC9 bound to its activator, Gαs protein.

One of the major pathways of communication between the cells and their environment is the cyclic adenosine monophosphate (cAMP) pathway **[1]**. This signaling relay consists of several key parts: (i) the G protein-coupled receptors, or GPCRs, (ii) the heterotrimeric G proteins (Gabγ), and (iii) the effector, adenylyl cyclase. The receptors recognise a large variety of 'signals', such as hormones or drugs, and are activated by them. Upon receptor activation, the G protein subunits bind to the activated receptor, dissociate, and the released Gα and Gbγ subunits then transmit the signal to one or more effector proteins. Adenylyl cyclase is the key effector of this signaling cascade, which catalyses the production of a 'second messenger' molecule, cAMP, from the ATP **[2]**. The cAMP molecules in turn regulate a plethora of physiological processes in health and disease via a number of downstream targets, such as protein kinase A or cyclic nucleotide gated ion channels.

Cryo-EM was used to produce a 3D reconstruction of the complex between a full-length membrane adenylyl cyclase AC9 bound to the stimulatory Gαs protein subunit, at a near-atomic resolution of 3.4 Å (**Figure 34**). The structure revealed for the first time the architecture of the full-length adenylyl cyclase, including its membrane-spanning region, the helical domain and the complete catalytic domain that interacts with Gas. Furthermore, this high-resolution structure captured a state of the protein in which the cytosolic C-terminus of AC9 blocked the active site of the enzyme. The biochemical experiments confirmed that this state of AC9 prevents the overproduction of cAMP and may represent an important auto-inhibitory mechanism protecting the cells from excessive cAMP production. Data collected at the cryo-electron microscope **CM01** helped to determine the structure of the truncated form of the Gαs-bound AC9 lacking its C-terminus ($AC9_{1250}$), in the presence of a nucleotide analogue and a small molecule activator, forskolin (**Figure 35**). This 3D reconstruction provided the important supporting evidence for the proposed AC9 auto-regulatory mechanism.

This work provides important insights into the molecular architecture and mechanisms

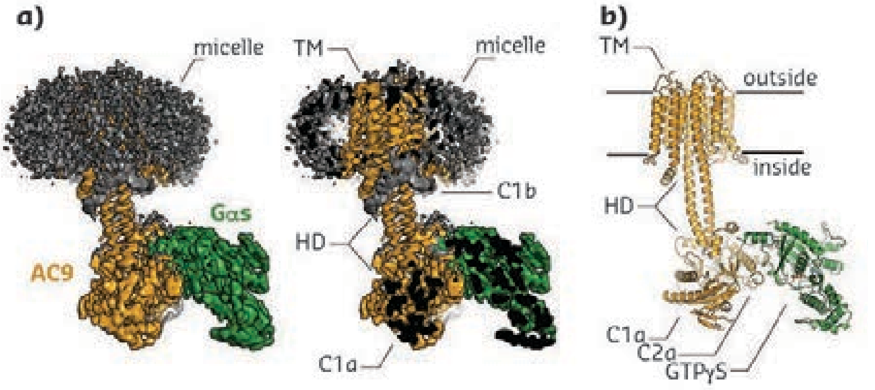

Fig. 34: A cryo-EM density map of the AC9-Gαs complex **(a)** made it possible to build the complete molecular model of the complex **(b)**, revealing its key structural elements: the transmembrane domain bundle (TM), the helical domain (HD), the catalytic domain of AC9 (C2a), and the Gαs protein (Gαs). The density map and model elements corresponding to AC9 and the Gαs proteins are coloured orange and green, respectively. Detergent and unassigned protein density are coloured grey.

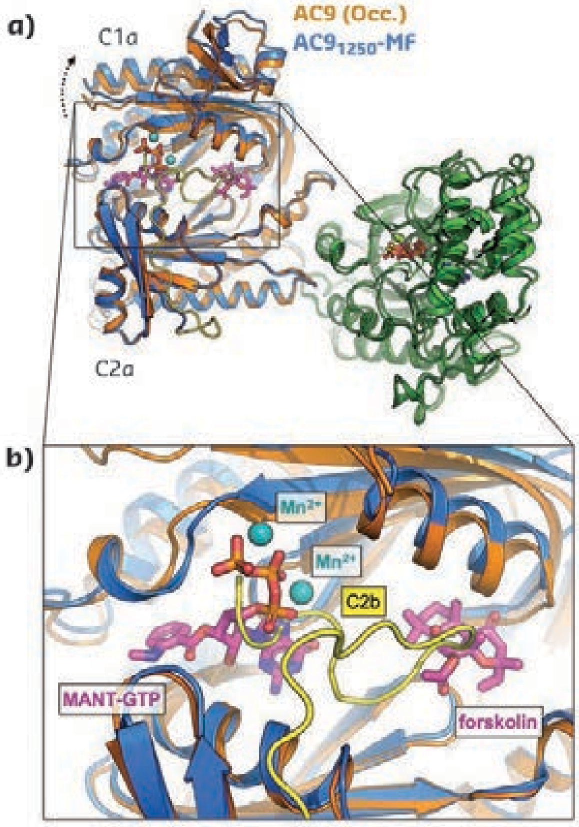

Fig. 35: a-b) The arrangement of the AC9 C1a domain in the occluded state (AC9 (Occ.), orange) and in the nucleotide- and forskolin-bound state ($AC9_{1250}$-MF, blue), based on the corresponding cryo-EM structures. Structural alignment was performed using the C2a domains. The relative C1a domain displacement is indicated by a dotted arrow. The C2b domain is indicated as a cartoon coloured yellow in **(b)**.

of adenylyl cyclases, bringing a deeper understanding of how the primary signals received by the receptors at the cell surface are decoded by the signal transduction machinery. The adenylyl cyclases are highly medically relevant, as cAMP modulation underlies the action of drugs in a number of diseases, including Parkinson's, migraine, asthma, hypertension, etc. The insights into the structure and function of adenylyl cyclases will be crucial for future efforts in development of novel therapies that act on these important membrane enzymes.

PRINCIPAL PUBLICATION AND AUTHORS

The structure of a membrane adenylyl cyclase bound to an activated stimulatory G protein, C. Qi (a,b), S. Sorrentino (c), O. Medalia (c,d) and V. M. Korkhov (a,b), *Science* **364**, 389-394 (2019); doi: 10.1126/science.aav0778.

(a) Institute of Biochemistry, ETH Zurich (Switzerland)
(b) Laboratory of Biomolecular Research, Division of Biology and Chemistry, Paul Scherrer Institute, Villigen (Switzerland)
(c) Institute of Biochemistry, University of Zurich (Switzerland)
(d) Department of Life Sciences and the National Institute for Biotechnology in the Negev, Ben Gurion University of the Negev, Beer-Sheva (Israel)

REFERENCES

[1] W. I. Weis & B. K. Kobilka, *Annu. Rev. Biochem*. **87**, 897-919 (2018).
[2] M. L. Halls & D. M. Cooper, *Pharmacol. Ther*. **172**, 171-180 (2017).

LIQUID–LIQUID PHASE SEPARATION OF RUBISCO DURING CARBOXYSOME BIOGENESIS IN CYANOBACTERIA

Cyanobacteria sequester the enzyme Rubisco into carboxysomes for efficient carbon fixation during photosynthesis. Assembly of these organelles is not well understood. Crystal structures obtained at the ESRF helped in understanding how the adapter protein CcmM concentrates Rubisco into a dynamic, liquid-like network.

Essentially all organic material on earth is the product of photosynthesis, the process that channels the energy from sunlight into the fixation of carbon from atmospheric carbon dioxide (CO_2). Cyanobacteria are reported to be the first organisms on Earth to fix CO_2 via oxygen, producing photosynthesis, and today account for ~10% of worldwide CO_2 fixation. The key enzyme performing carbon fixation is Rubisco (Ribulose-1,5-bisphosphate carboxylase/oxygenase), a ~520 kDa complex of eight large (RbcL) and eight small (RbcS) subunits. Rubisco catalyses the carboxylation of the 5-carbon sugar substrate ribulose-1,5-bisphosphate. However, the enzyme is rather inefficient, with a slow turnover rate and limited selectivity for CO_2 versus O_2. To overcome this problem, cyanobacteria have evolved a CO_2-concentrating mechanism (CCM) by sequestering Rubisco together with the enzyme carbonic anhydrase (CA) into microcompartments called carboxysomes. This serves to generate high levels of CO_2 in the vicinity of Rubisco, thus allowing cyanobacteria to use less selective Rubiscos that are ~10 times faster than the enzymes of land plants. Substantial gains in productivity could be achieved by transplanting functioning carboxysomes into the chloroplasts of crop plants.

Carboxysomes resemble intracellular viruses with a highly symmetric proteinaceous shell, and have been classified into α and β based on the type of Rubisco they encapsulate. During β-carboxysome biogenesis, Rubisco first aggregates, mediated by the protein CcmM, followed by shell formation. There are

Fig. 36: Overlay of the crystal structures of the oxidised SSUL1 module of CcmM from *Synechococcus elongatus* PCC7942 (in magenta) and the small subunit of Rubisco, RbcS (in green).

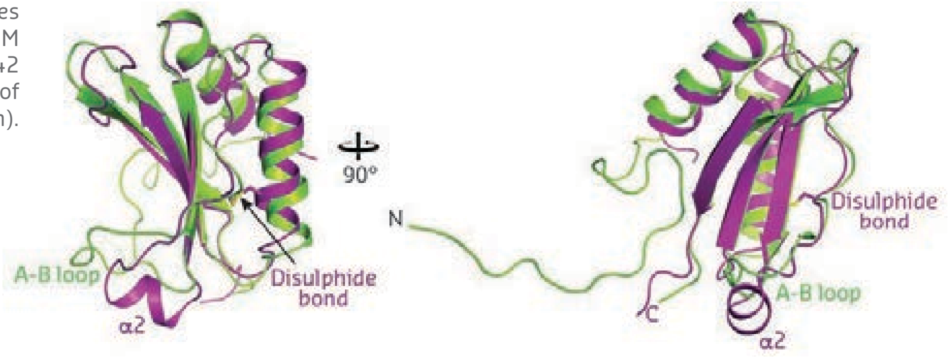

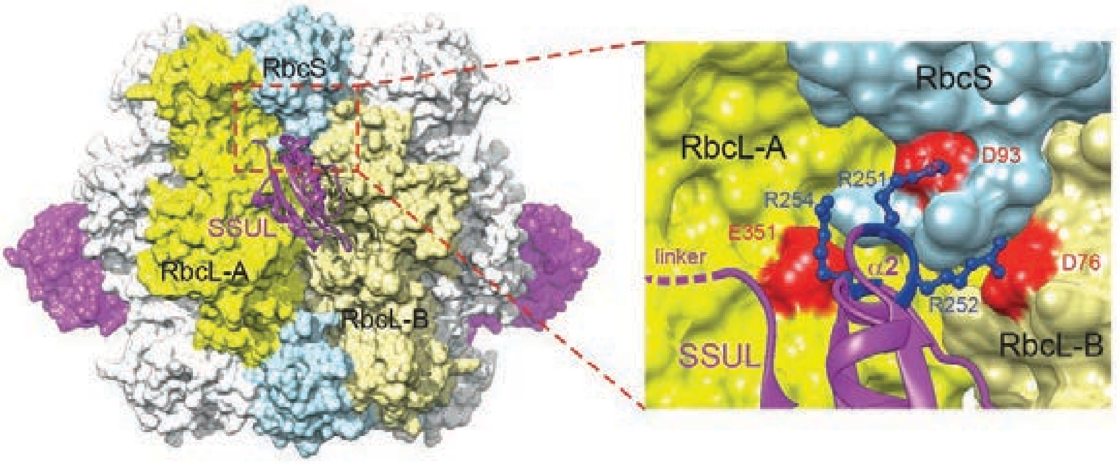

Fig. 37: Model of the Rubisco-SSUL complex showing a hypothetical alternating arrangement of four SSUL modules (magenta) bound. A side view is shown. An enlargement of the boxed region shows the residues in helix α2 of the bound SSUL, which make critical salt-bridges with residues of RbcL-A, RbcS and RbcL-B of Rubisco.

two isoforms of CcmM in the cyanobacterium *Synechococcus elongatus* PCC 7942. The full-length protein (also called M58) contains a CA-like domain, followed by three small subunit-like (SSUL) modules that have 25% sequence identity to RbcS of Rubisco. A smaller isoform, called M35, consists only of the three SSUL modules. It had been speculated that these domains might replace RbcS subunits, thereby linking Rubisco complexes into a 3D network **[1-3]**.

Crystal structures of the SSUL module were solved with X-ray diffraction data collected at beamlines **ID23-2** and **ID30A-1**, and showed that the SSUL backbone indeed resembled Rubisco small subunits (**Figure 36**). A surprising feature was the presence of an intramolecular disulphide bond between conserved cysteine residues, suggesting possible redox regulation. Moreover, the SSUL structure showed a short helical insertion, α2, in place of the A-B loop in RbcS (**Figure 36**). Biochemical binding assays demonstrated that Rubisco aggregation by M35 required the fully-assembled Rubisco and did not occur with assembly intermediates lacking RbcS. Reduced M35 was around five times more efficient in binding than the oxidised protein. This is consistent with Rubisco aggregation occurring in the reducing environment of the cytosol, whereas the interior of the carboxysome is oxidixing. Further analysis by fluorescence recovery after photobleaching (FRAP) showed that M35 induced the phase separation of Rubisco into a liquid-like network, which was more dynamic under oxidising conditions. Prevention of disulphide-bond formation *in vivo* resulted in abnormal carboxysomes, a ~20-fold increase in CO_2 requirement and about a 4-fold slower growth rate of mutant cyanobacteria, supporting the view that redox-regulation in the SSUL module is critical for carboxysome biogenesis and function.

The molecular organisation of the M35-Rubisco network within liquid droplets was analysed by cryo-electron microscopy. The structure of the M35-Rubisco complex at 2.8 Å resolution revealed four pairs of symmetry-equivalent SSUL binding sites at the equator of Rubisco (**Figure 37**). Interestingly, the symmetry-related binding sites overlap so that only a maximum of four SSUL modules can dock. Contrary to the earlier model, the SSUL modules do not displace RbcS but in fact require the presence of RbcS for binding, with critical contacts mediated by the helix α2 of SSUL (**Figure 37**). This mechanism ensures that only Rubisco holoenzyme is packaged into carboxysomes.

Taken together, the findings suggest a model in which Rubisco and CcmM form a liquid-like, phase-separated condensate into which other carboxysome components can exchange. Upon shell formation, preventing entry of reducing agents, the interior of the carboxysome becomes oxidising and renders the Rubisco-CcmM interaction more dynamic. The data show why the CcmM protein is an indispensable component of the carboxysome assembly machinery, providing valuable insights for ongoing attempts to introduce carboxysomes into plant chloroplasts. More efficient carbon fixation would help to meet food demands for an ever-growing human population.

PRINCIPAL PUBLICATION AND AUTHORS

Rubisco condensate formation by CcmM in β-carboxysome biogenesis, H. Wang (a), X. Yan (a), H. Aigner (a), A. Bracher (a), N. D. Nguyen (b), W. Y. Hee (b), B. M. Long (b), G. D. Price (b), F. U. Hartl (a) and M. Hayer-Hartl (a), *Nature* **566**, 131 (2019); doi: 10.1038/s41586-019-0880-5.
(a) Max Planck Institute of Biochemistry, Martinsried (Germany)
(b) The Australian National University, Canberra (Australia)

REFERENCES

[1] G. S. Espie & M. S. Kimber, *Photosynth. Res.* **109**, 7-20 (2011).
[2] B. D. Rae *et al.*, Microbiol. *Mol. Biol. Rev.* **77**, 357-379 (2013).
[3] C. A. Kerfeld & M. R. Melnicki, *Curr. Opin. Plant Biol.* **31**, 66-75 (2016).

STRUCTURAL AND BIOPHYSICAL STUDIES REVEAL A CLASS OF INHIBITORS ACHIEVING SELECTIVITY BY BINDING TO THE ACTIVE STATE OF PI3Kγ

Combining X-ray crystallography and biophysics, a new class of PI3Kγ inhibitors that bind to an active state of PI3Kγ has been identified. These studies have led to identification of the first class of inhibitors that have a mode of action that bears similarity to type II inhibitors in protein kinases.

Phosphoinositide-3-kinase γ (PI3Kγ) belongs to the class I PI3Ks encompassing four isoenzymes (PI3Kα, β, γ and δ). PI3Kγ has been implicated in immune indications and, more recently, as a potential target for immune-oncology **[1]**. As the ATP binding site within the four isoforms is quite homologous, it has been difficult to gain isoform selectivity. Recently, a new class of selective PI3Kγ inhibitors (Isoindolinones) was discovered, exhibiting an unprecedented selectivity over PI3Kα and β **[2]**. Although the inhibitors exhibited great potency for PI3Kγ, it was not possible to obtain complex structures with the catalytic p110γ domain of PI3Kγ. However, some of the potent and highly selective PI3Kγ inhibitors were also active against PI3Kδ, and an X-ray structure was obtained of the complex between the murine version of this isoform and the isoindolinone inhibitor using data collected at beamline **ID23-1** (**Figure 38**). Interestingly, the inhibitor induced a new pocket that has not previously been observed in PI3Ks (**Figure 38**). Key for the induced fit was a cyclopropylethyl moiety of the inhibitor sterically pushing on Asp787. This sterically clashes with the carbonyl oxygen from Phe912 residing on the 'DFG' loop, leading to a 180° flip. This induced fit mechanism has been termed the 'alkyl push' and it was hypothesised that this was responsible for the unprecedented selectivity and that it occurred via a major rearrangement of the activation loop following the DFG loop.

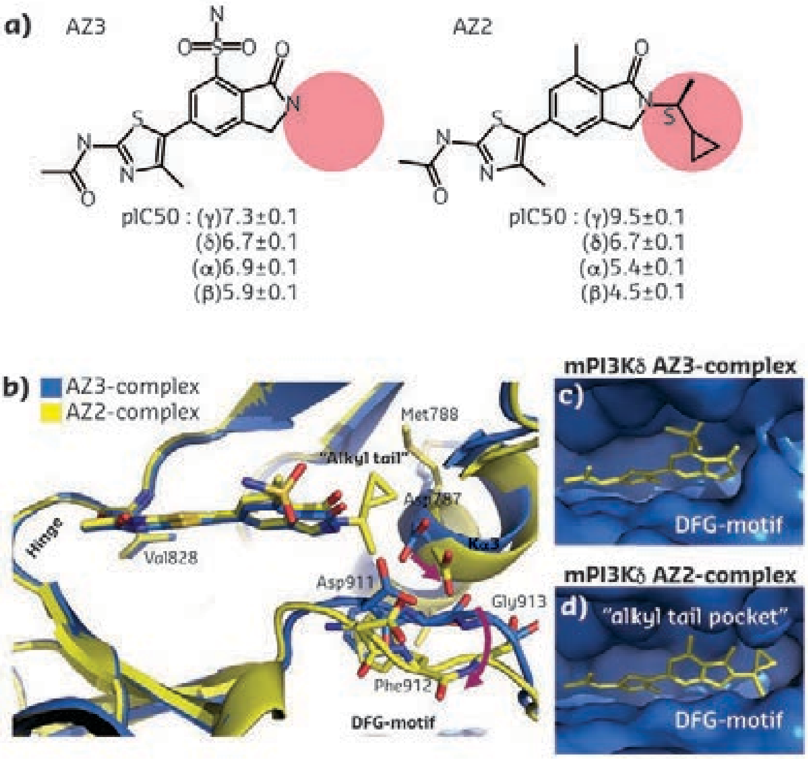

Fig. 38: a) Chemical structure of the two isoindolinone compounds AZ2 and AZ3 with or without the N-cyclopropylethyl tail moiety (red). IC50 for the four PI3K isoforms is also shown. **b)** X-ray crystal structure of mPI3Kδ in complex with AZ3 (blue) and AZ2 (yellow) (PDB code 6GY0 and 6FTN respectively). The *N*-alkyl tail extends deep into the ATP-binding pocket close to both Asp787 and Met788. Movement of Asp787 upon compound binding leads to a conformational change of the 'DFG' motif (residues 911-913). Purple arrows show key conformational changes. **c)** AZ3 (yellow) shown in the active site of mPI3Kδ with surface rendering (blue). **d)** AZ2 tail compound (yellow) shown in active site of mPI3Kδ with surface rendering (blue) showing the induced pocket.

To examine this further, biophysical studies were carried out using both Hydrogen-Deuterium Exchange Mass Spectrometry (HDX-MS) and Surface Plasmon Resonance (SPR) studies of inhibitor–p110γ complexes. Binding kinetics revealed that the binding of these inhibitors occurred via a two-step mechanism, most likely as an induced fit mechanism. HDX-MS revealed that dramatic conformational changes encompassing a large part of the catalytic p110γ subunit occurred when introducing the cycloprolylethyl-alkyl moiety. In particular, regions implicated in activation and catalysis were affected. These included the 'activation loop', the Kα-12 helix and a loop covering the Kα-12 helix that has been termed the 'lock loop'. Regions involved in binding the regulatory subunits were also affected. These changes were only observed in PI3Kγ and also for this class of inhibitors.

From this study, a mechanism is proposed that involves a conformational change of the activation loop that breaks a conformational lock leading to the C-terminal Kα-12 helix becoming unleashed (**Figure 39**). This leads to allosteric changes in regions that are affected upon activation. The conformational changes induced by the inhibitor share similarities to the conformational changes that are observed upon activation of PI3Kγ. This class of inhibitors is the first example of lipid kinase inhibitors that achieve their selectivity by causing a major change via the activation loop, and might constitute a new paradigm for developing inhibitors towards PI3Ks.

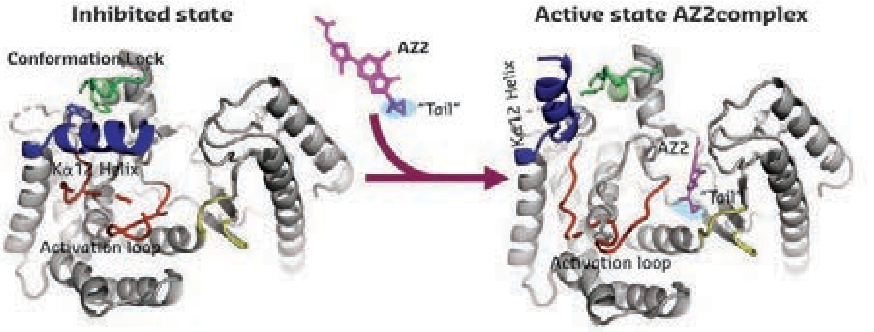

Fig. 39: Proposed mechanism derived from the structural and biophysical studies. The catalytic p110γ domain exists in an inhibited form shown on the left. Upon binding, the cyclopropylethyl alkyl-tail induces large conformational changes in the p110γ domain via conformational change of the activation loop (red), causing the break of a conformational lock (green) leading to the release of the Kα-12 helix (right).

PRINCIPAL PUBLICATION AND AUTHORS

A class of highly selective inhibitors bind to an active state of PI3Kγ, G. Gangadhara (a), G.Dahl (a), T. Bohnacker (b), R. Rae (c), J. Gunnarsson (a), S. Blaho (a), L. Oster (a), H. Lindmark (a), K. Karabelas (c), N. Pemberton (c), C. Tyrchan (c), M. Mogemark (d), M. P. Wymann (b), R. L. Williams (e), M. W. Perry (c), T. Papavoine (c) and J. Petersen (a), *Nature Chem. Biol.* **15,** 348-347 (2019); doi: 10.1038/s41589-018-0215-0.

(a) Discovery Sciences, IMED Biotech Unit, AstraZeneca, Gothenburg (Sweden)
(b) Department of Biomedicine, University of Basel (Switzerland)
(c) Respiratory, Inflammation & Autoimmunity, IMED Biotech Unit, AstraZeneca, Gothenburg (Sweden)
(d) Drug Safety and Metabolism, IMED Biotech Unit, AstraZeneca, Gothenburg (Sweden)
(e) MRC Laboratory of Molecular Biology, Cambridge (UK)

REFERENCES

[1] M. M. Kaneda *et al., Nature* **539**, 437-442 (2016).
[2] N. Pemberton *et al., J. Med. Chem.* **61**, 5435-5441 (2018).

THE STRUCTURE OF MASTER GROWTH REGULATOR mTORC1 BOUND TO HUMAN RAG GTPASES

Nutrient availability and growth factors activate the protein kinase complex mTORC1, which is often upregulated in cancer. Two small GTPases, the Rag GTPases and RHEB, control mTORC1. The structures of active Rag GTPase heterodimers were determined, both on their own and bound to mTORC1. The structures explain how an oncogenic hotspot mutant activates Rag GTPases and upregulates mTORC1.

The mechanistic target of rapamycin complex 1 (mTORC1) is an ancient enzyme complex that integrates signals from nutrient availability, energy, and growth factors to regulate cell growth, proliferation and metabolism. Over-activation of the enzyme complex is associated with many diseases, including cancer, type-2 diabetes and defects in neurodevelopment **[1]**. By integrating growth factor signalling and nutrient availability, proliferation results only when growth is needed and nutrients are plentiful. When nutrients are lacking, mTORC1 is in the cell cytosol in an inactive form, but when nutrients become abundant, it moves quickly to the surface of the lysosomes.

mTORC1 is a 0.93 MDa dimer of a heterotrimer consisting of the mTOR kinase, substrate-binding subunit RAPTOR (regulatory-associated protein of mTOR) and the small WD40 protein mLST8 (mammalian lethal with SEC13 protein 8). The mTORC1 complex is activated by binding to two types of small G-proteins, the Rag GTPases and RHEB, in response to an abundance of amino acids and in the presence of growth factors, respectively.

Unlike other GTPases, Rags are distinctive as they form obligate heterodimers, with RagA or RagB forming a heterodimeric complex with RagC or RagD. The two subunits are very similar to each other and consist of two domains: a GTPase domain that binds a nucleotide such as GTP or GDP, and a C-terminal road-block domain (CRD) that is responsible for forming a tight dimer. The GTPase domains of Rag GTPases, like other small GTPases, have conserved loops that engage the bound nucleotide, and a subset of these loops – the switch regions – change conformation in the GTP and GDP bound states, thereby altering binding to effectors. The GTP-bound RagA or B in a complex with GDP-bound RagC or D forms an 'active' RagA/C that has the greatest affinity for mTORC1. Rag GTPases bind to a membrane-localised heteropentameric complex known as the Ragulator. The Ragulator-bound Rag heterodimers can then interact with mTORC1 causing it to translocate to lysosomes, where mTORC1 is activated upon association with membrane-localised GTP-loaded RHEB. Thus, the Rag and Rheb GTPases are part of a molecular AND gate for mTORC1 activation.

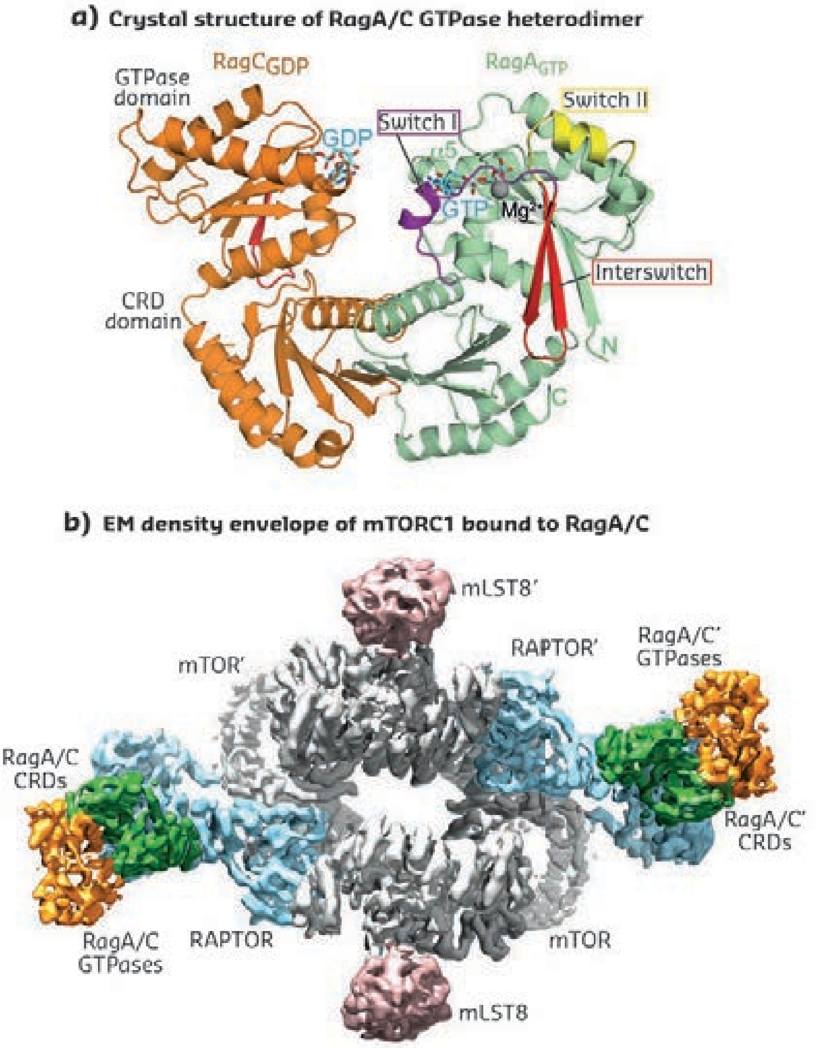

Fig. 40: a) Crystal structure of active RagA/C heterodimer. **b)** Cryo-EM structure of mTORC1-RagA/C complex machinery.

Data collection at beamlines **ID30B** and **ID30-A3** made it possible to determine the high-resolution crystal structure of a RagA/C heterodimer (**Figure 40a**). Using a combination of X-ray crystallography and Hydrogen-Deuterium Exchange Mass Spectrometry, this work shows that the oncogenic mutations in RagC melt structural elements in nucleotide-sensitive regions known as switches so that the RagC GTPase domain changes its contacts with RagA (**Figure 40a**). The mutations permanently fix RagC in its active, GDP-bound form, and thereby result in constitutive mTORC1 signalling that otherwise occurs upon amino acid starvation. A complex of active, oncogenic Rags bound to mTORC1 was reconstituted and its structure obtained by cryo-electron microscopy (**Figure 40b**). The structure shows that the butterfly-shaped Rag dimer clasps the helical-domain of the Raptor subunit of mTORC1 (**Figure 40b**), to fasten mTORC1 to the Ragulator complex on the surface of the lysosomes. By themselves, Rags do not change the conformation of mTORC1. Instead, they simply recruit it to a lysosome so that mTORC1 can interact with membrane-bound Rheb, a small GTPase that allosterically activates mTORC1. Based on this, and on previously published structures of sub-complexes, an organisation of the entire mTORC1/Rags/Ragulator/Rheb complex on the lysosomal membranes is proposed (**Figure 41**).

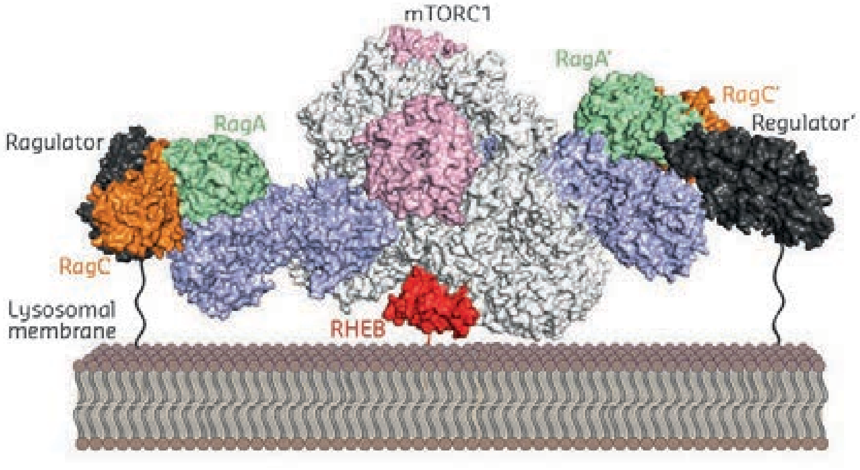

Fig. 41: A model of mTORC1 kinase assembled with machinery (Rags/Ragulator/Rheb) required for its recruitment to, and activation on, lysosomal membranes. The mTOR active sites face away from the membrane toward the cytosol.

PRINCIPAL PUBLICATION AND AUTHORS

Architecture of human Rag GTPase heterodimers and their complex with mTORC1, M. Anandapadamanaban (a), G. R. Masson (a), O. Perisic (a), A. Berndt (a), J. Kaufman (a), C. M. Johnson (a), B. Santhanam (a), K. B. Rogala (b), D. M. Sabatini (b,c,d,e,f) and R. L. Williams (a), *Science* **366**, 203-210 (2019); doi: 10.1126/science.aax3939.

(a) MRC Laboratory of Molecular Biology, Cambridge (UK)
(b) Whitehead Institute for Biomedical Research, Cambridge (USA)
(c) Department of Biology, Massachusetts Institute of Technology, Cambridge (USA)
(d) Howard Hughes Medical Institute, Massachusetts Institute of Technology, Cambridge (USA)
(e) Koch Institute for Integrative Cancer Research, Cambridge (USA)
(f) Broad Institute of MIT and Harvard, Cambridge (USA)

REFERENCES

[1] R. A. Saxton & D. M. Sabatini, *Cell* **168,** 960-976 (2017).

CLEAR VIEW OF NEURONAL RECEPTOR OPENS DOOR FOR NEW CANCER DRUGS

Proper brain function depends on neurons forming accurate circuits in the brain, guided by protein receptors that sense the environment around them. Crystallographic data reveals the molecular mechanism that allows the Robo guidance receptor to react to signals in its environment. Drugs that target Robo could lead to promising treatments for cancer.

During brain development, billions of neuron nerve cells must find accurate pathways in the brain in order to form trillions of neuronal circuits enabling us to enjoy cognitive, sensory and emotional wellbeing. To achieve this with remarkable precision, migrating neurons use special protein receptors that sense the environment around them and guide the way so that they, and their long extensions, stay on the right path. Rare defects in these neuronal guidance proteins can result in severe neurological conditions such as ataxia and epilepsy. This work reports on the discovery of the intricate molecular mechanism that allows a key guidance receptor, Robo, to react to signals in its environment, while avoiding premature activity that can lead to harmful outcomes.

One of the most important protein signaling systems that guide neurons consists of the cell surface receptor Robo and its cognate external guidance cue, Slit, both of which can be identified in virtually all animals with a nervous system. A deficit of either of these proteins results in defects in brain structure and function. For example, their absence compromises the brain's ability to form the correct connection across the *corpus callosum*, the region where neuronal extensions from the two brain hemispheres cross paths to innervate opposite sides of the body, a fundamental attribute of bilateral creatures. Much progress has been made towards understanding Slit-Robo function and the developmental responses that they trigger in the brain and the central nervous system. However, it was still not fully understood how Slit activates Robo and what keeps Robo inactive in the absence of Slit to prevent harmful activation, which has been implicated in kidney diseases and age-related macular degeneration.

Although X-ray diffraction data from Robo crystals had been collected since 2009, it was only recently possible to obtain diffraction data to under 4 Å resolution, using ESRF beamline **ID29** and BESSY II in Germany. Using molecular replacement, the crystal structures of the intact Robo ectodomain (extracellular portion) were determined (**Figure 42**). These indicated how two Robo receptors form active dimers and how their dimerisation interfaces are kept blocked in the absence of Slit. Following crystallographic observations, a new biochemical assay was developed to monitor Robo dimerisation when expressed in cultured cells. In this way, the structural model for Robo's self-control over its oligomeric state was corroborated and it was also shown that the same mechanism exists in other closely related receptors.

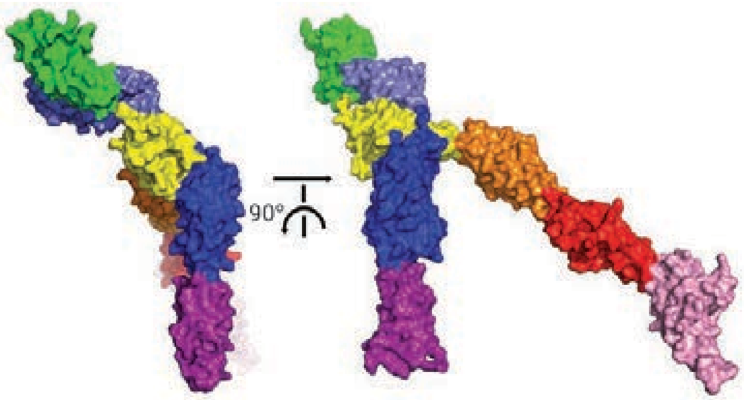

Fig. 42: A surface representation of the crystal structure of the extracellular portion of human Robo2. The yellow region represents the domain where dimerisation takes place. Here, it is blocked by the other domains, meaning dimerisation cannot take place and that Robo2 is inactivated.

Next, the structural model was investigated *in vivo* using the *C. elegans* nematode – a tiny, multi-celled worm that is the only organism to have its complete neuronal wiring diagram known (**Figure 43**). *C. elegans* has only one Robo and one Slit (compared to four Robo genes and three Slits in humans and mice), making it ideal to study. The evidence supported the structural

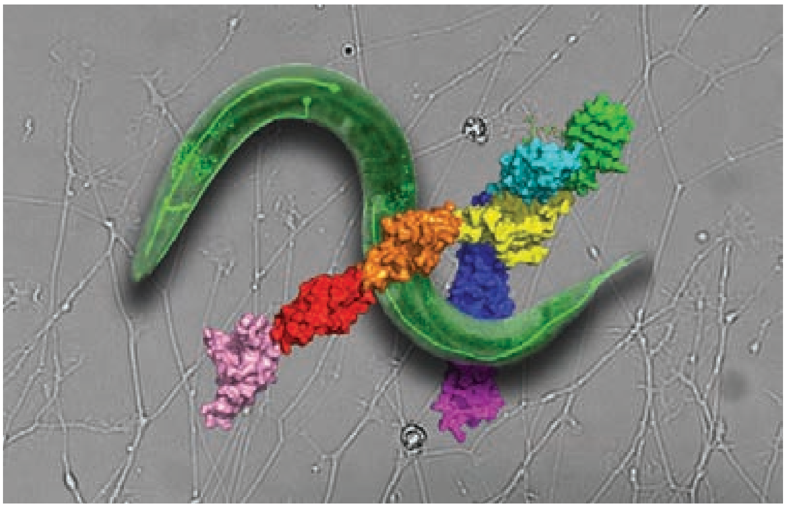

Fig. 43: Crystal structure of human Robo2 receptor depicted here as if entangled with the *C. elegans* nematode axon guidance model that was used to test the structure-based hypotheses *in vivo*. The crystal structure and nematode appear on a background of extending mouse dorsal root ganglion (DRG) axons and growth cones poised for Slit-Robo stimulation and responses.

model that Slit activates Robo through the release of an auto-inhibitory mechanism that keeps Robo inactive in the absence of Slit, and also showed that the same mechanism actually exists in other closely related receptors. Despite an evolutionary distance of about 500 million years between humans and *C. elegans*, the results point toward a similar Robo molecular mechanism.

The involvement of Slit and Robo receptors in cancer is of particular interest to researchers. In cancer, some receptors are 'high-jacked' to drive tumour formation. In personalised cancer therapy, drugs block these rogue receptors, depriving the cancer cells of vital signaling instructions and directing them toward destruction. Targeting Slit and Robo has long been considered a promising therapeutic approach for types of pancreatic, skin and breast cancer. However, and almost certainly due to an insufficient structural and mechanistic understanding of Robo activation and signaling, there are currently no Robo-directed drugs.

These results provide, for the first time, the information necessary to design effective drugs targeting Robo receptors. In particular, the crystal structures revealed molecular sites on the surface of Robo that, when targeted by designed drugs, will make it possible to manipulate Robo activation and inhibition in patients, thus providing new possibilities in the treatment of cancer.

PRINCIPAL PUBLICATION AND AUTHORS

Structural Principles in Robo Activation and Auto-Inhibition, R. Barak (a), G. Yom-Tov (a), J. Guez-Haddad (a), L. Gasri-Plotnitsky (a), R. Maimon (b), M. Cohen-Berkman (a), A. A. McCarthy (c), E. Perlson (b), S. Henis-Korenblit (a), M. N. Isupov (d) and Y. Opatowsky (a), *Cell* **177**(2), 272-285.e16 (2019); doi: 10.1016/j.cell.2019.02.004.

(a) The Mina & Everard Goodman Faculty of Life Sciences, Bar-Ilan University (Israel)
(b) Department of Physiology and Pharmacology, Sackler Faculty of Medicine, Tel Aviv University (Israel)
(c) European Molecular Biology Laboratory, Grenoble (France)
(d) Biosciences, University of Exeter (UK)

STRUCTURE OF A NEW BOTULINUM-LIKE TOXIN SPECIFIC FOR *ANOPHELES* MOSQUITOES, VECTOR OF MALARIA

A new neurotoxin that selectively targets mosquitoes that transmit malaria has been discovered. This could lead to innovative and environmentally friendly approaches to reducing malaria.

Malaria is one of the most common and serious diseases in the world. It is caused by unicellular parasites, which are spread by some mosquitoes. According to the World Health Organization (WHO), about half a million people die of the disease every year, most of them children in Africa. Around 200 million people suffer from malaria.

Botox (Botulinum neurotoxins, or BoNTs) and the toxin causing tetanus belong to the same family of proteins and are among the most toxic substances known **[1]**. Previously, this family of toxins was believed to only target vertebrates such as humans, mice and birds, but now, researchers have found a toxin which targets the group of mosquitoes that are responsible for transmitting malaria.

Fig. 44: Malaria mosquito of the species *Anopheles gambiae*. © Anna-Karin Landin/Stockholm University.

A joint research collaboration between Stockholm and Lund universities in Sweden and the University of California in the USA have discovered a neurotoxin, PMP1, that selectively targets *Anopheles* mosquitoes (**Figure 44**), demonstrating that this family of toxins has a much broader host spectrum than previously believed. PMP1 was isolated from *Paraclostridium bifermentans* strains of bacteria found in two threatened habitats: a mangrove swamp in Malaysia and a forest floor in Brazil. Comparative genomics of several strains of the bacteria presenting, or not, the mosquitocidal activity allowed identification of the neurotoxin. Analysis of the genome showed that the toxin loci was acquired through a megaplasmid. Remarkably, PMP1 targets the nervous system of mosquitoes by proteolytic degradation of intracellular syntaxin, one of the key components of SNARE-mediated exocytosis, resulting in paralysis. The catalytic domain of PMP1 consists in a classical zinc-endopeptidase, similar to other BoNTs **[1]**.

Using diffraction data collected at beamline **ID30B**, the crystal structure of the receptor binding domain of PMP1 was solved, and presented a fold similar to the classic BoNTs with two sub-domains, consisting of a lectin-like region and a β-trefoil fold, which usually presents a conserved carbohydrate-binding site and is responsible for specific cell recognition (**Figure 45**). The structure also revealed unexpected features. For instance, there are many aromatic residues exposed on the surface of the receptor-binding domain of PMP1, which form highly hydrophobic tyrosine-tryptophan patches. In addition, several methionine-tyrosine repeats were observed at the tip of the cell-binding region. Several mutations were performed based on the structure and allowed researchers to determine which hydrophobic clusters were essential for toxicity. The results suggest that several sites are important for receptor binding and interactions with the cellular membrane. The receptors for PMP1 and other BoNT-like toxins remain unknown **[2-3]**. Identifying these receptors will be key in engineering toxin-based molecules with biotechnological potential, as they likely dictate the toxins' species specificity, although other barriers may also exist.

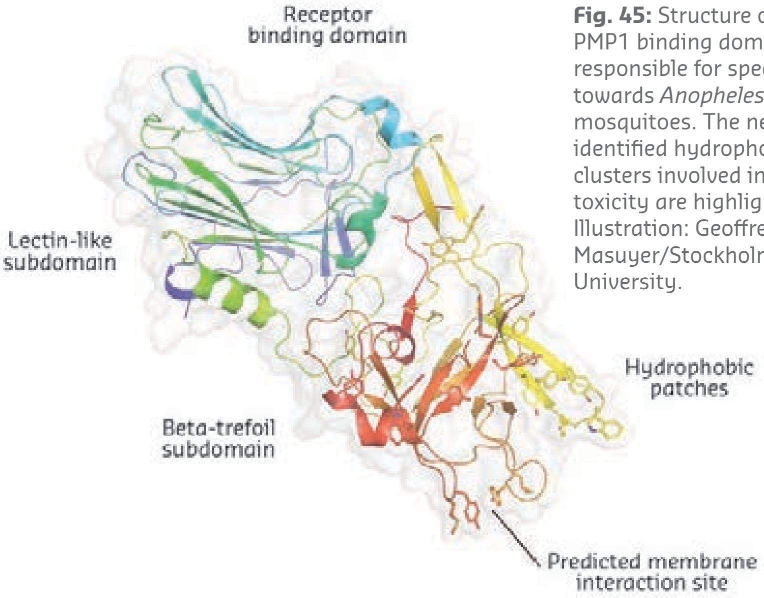

Fig. 45: Structure of the PMP1 binding domain, responsible for specificity towards *Anopheles* mosquitoes. The newly identified hydrophobic clusters involved in toxicity are highlighted. Illustration: Geoffrey Masuyer/Stockholm University.

Today, insecticides and mosquito nets treated with insecticides are the main means of combating the spread of malaria, but new methods of combating malaria mosquitoes must be developed constantly as mosquitoes become resistant to most toxins over time. The discovery of PMP1 could make it possible to reduce the prevalence of malaria in a new and environmentally friendly way – as the toxins are proteins, they do not leave any artificial residues as they decompose. PMP1 may also be developed into biological insecticides designed to target other selected disease vectors or pests.

PRINCIPAL PUBLICATION AND AUTHORS

A neurotoxin that specifically targets *Anopheles* mosquitoes,
E. Contreras (a), G. Masuyer (b), N. Qureshi (a), S. Chawla (a), H. Dhillon (a), H. Lee (c), J. Chen (a), P. Stenmark (b,d) and S. Gill (a),
Nat. Commun. **10**(1), 2869 (2019);
doi: 10.1038/s41467-019-10732-w.
(a) Department of Molecular, Cell and Systems Biology, University of California (USA)
(b) Department of Biochemistry and Biophysics, Stockholm University (Sweden)
(c) Unit of Medical Entomology, Institute for Medical Research, Kuala Lumpur (Malaysia)
(d) Department of Experimental Medical Science, Lund University (Sweden)

REFERENCES

[1] M. Dong *et al., Annu. Rev. Biochem.* **88**, 811-837 (2019).
[2] S. Zhang *et al., Nat. Commun.* **8**, 14130 (2017).
[3] S. Zhang *et al., Cell Host Microbe* **23**(2), 169-176.e6 (2018).

AN APPROACH FOR 'DE-IMMUNISING' ANTIBODY DRUGS

Antibodies were isolated from multiple sclerosis patients who had experienced an allergic reaction after receiving the drug natalizumab. Some of these antibodies interacted so strongly with the drug that its activity was neutralised. This antibody response was triggered by T-cells that recognised a single portion of the drug. A 'de-immunised' version of the drug was engineered to avoid recognition by such T cells.

Monoclonal antibodies have become one of the main therapeutic modalities that are widely used in oncology and the treatment of autoimmune diseases, and, today, there are six antibodies among the 10 top-selling drugs. Antibodies provide an exquisite selectivity and specificity, and are often associated with an acceptable safety profile. However, most antibodies induce an immune reaction in a small number of patients. This reaction can affect treatment efficacy by producing neutralising antibodies and can also affect the overall condition of the patient, ranging from mild effects to severe anaphylactic shock **[1]**. The underlying mechanism leading to the immunogenic reaction is not fully understood. Natalizumab (NZM) is a drug currently used for the treatment of relapsing forms of multiple sclerosis **[2]**. Unfortunately, about 6% of patients cannot benefit from this treatment because they produce anti-drug antibodies (ADA) that neutralise the activity of NZM. Understanding the biological basis of this unwanted immune response is essential for the development of more effective versions of NZM and of therapeutic antibodies in general. In this study, an analysis of the contribution of the B and T cells involved in this process was performed, enabling the design of 'de-immunised' variants of NZM. These ADAs were isolated from patients treated for multiple sclerosis with NZM, who had a hypersensitivity reaction following drug infusion and developed high titers of ADAs.

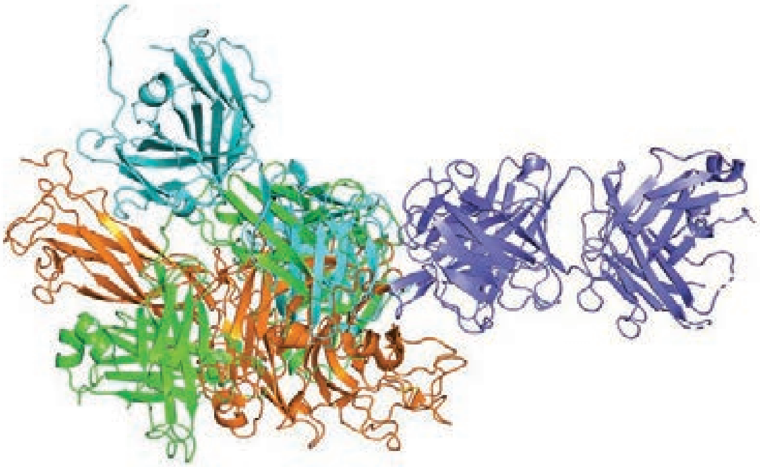

Fig. 46: Ribbon diagram of NAA32 Fab (turquoise), NAA84 Fab (green), α4-integrin (orange) bound to NZM Fab (blue).

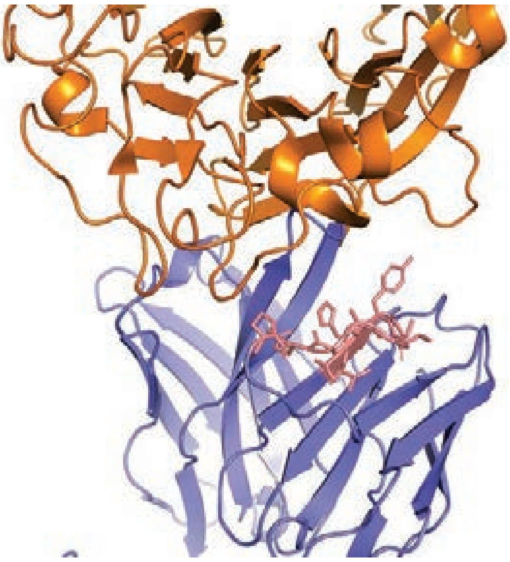

Fig. 47: Ribbon diagram of α4-integrin (orange) bound to NZM Fab (blue). The residue segment from NZM engineered for de-immunisation is shown in pink.

B cells from these patients were screened to isolate monoclonal ADAs binding to NZM. These ADAs exhibited different functional *in-vitro* profiles that could be classified into two categories. The first type includes antibodies that show inhibitory activity with IC_{90} values in the ng.ml^{-1} range and are considered as neutralising antibodies. These antibodies bind strongly to NZM and are characterised by a slow dissociation rate (k_d~10^{-5} s^{-1}). The second type includes antibodies that bind to NZM with fast dissociation rate (k_d~10^{-3} s^{-1}) and display IC_{90} values in the μg.ml^{-1} range. These antibodies do not show inhibitory activity and, therefore, are considered as binding antibodies. Neutralising antibodies are a major concern, as they can affect the efficacy of the drug and consequently the outcome of the treatment.

Epitope mapping of these two antibody classes was performed by swapping hypervariable CDR loops, and it was shown that the difference in IC_{90} was not related to epitope specificity. Subsequently, X-ray crystallography at beamline **ID30A-1** was used to solve the crystal structures of two anti-NZM/NZM Fab complexes: NAA32/NZM and NAA84/NZM. NAA32 is a binding antibody, whereas NAA84 is a neutralising antibody. Both antibodies recognise the same surface area on NZM – α4-integrin – as their target (**Figure 46**). However, they exhibit different binding modes, which are also different from that of α4-integrin when bound to NZM. The difference between binding and neutralising antibodies cannot be accounted for by the epitope with which they interact, but more presumably by the difference in the dissociation rate from NZM. These findings bear some potential clinical implications, as they suggest that binding antibodies are likely to mature into neutralising antibodies following subsequent NZM drug challenges and could present some potential risks for the patients.

The characterisation of T cell clones after *ex-vivo* stimulation, combined with MHC-based proteomics of B cell clones pulsed with NZM, highlighted a single immunodominant T cell epitope located within the light chain of NZM. This unique T cell epitope is likely responsible for the immune reaction observed in patients. Combining this information with structural data, variants of NZM were designed with the objective of removing the immunodominant T cell epitope, while maintaining the ability to bind to α4-integrin (**Figure 47**). A number of NZM variants were generated and were shown to be unable to trigger proliferation of T cell clones specific to the naturally presented immunodominant peptide, while keeping their biological activity. These de-immunised variants of NZM provide attractive avenues for improved therapeutics.

PRINCIPAL PUBLICATION AND AUTHORS

A single T cell epitope drives the neutralizing anti-drug antibody response to natalizumab in multiple sclerosis patients, T. Bertrand (c), S. Pouzieux (c), J. Le Parc (c), P. Ferrari (c), J. Dumas (c), A. Cassotta (a,b), L. Piccoli (a) and V. Mikol (c), *Nat. Med.* **25,** 1402-1407 (2019); doi:10.1038/s41591-019-0568-2.
(a) Institute for Research in Biomedicine, Università della Svizzera italiana, Bellinzona (Switzerland)
(b) Institute of Microbiology, ETH Zurich (Switzerland)
(c) Research Platform, Sanofi R&D, Vitry-sur-Seine (France)

REFERENCES

[1] M. Krishna & S. G. Nadler, *Front. Immunol*. **7**, 21 (2016).
[2] J. Noseworthy & P. Kirkpatrick, *Nat. Rev. Drug. Discov.* **4,** 101 (2005).

SNAPSHOTS OF THE FLU VIRUS TRANSCRIPTION-REPLICATION MACHINE IN ACTION

Influenza viruses cause widespread mild to severe respiratory disease. Despite its prevalence, many details of how the virus replicates in the infected cell are still poorly understood. Using a combination of X-ray crystallography and cryo-electron microscopy (cryo-EM), atomic-resolution structures of the influenza polymerase – key for viral replication – in action were determined for the first time.

When influenza virus infects a host cell, the genomic material of the virus, the viral RNA (vRNA), is transported to the nucleus, where it is first transcribed into viral messenger RNA (mRNA) and is then replicated to produce multiple copies of itself. Influenza polymerase (FluPol) is the key transcription-replication machine responsible for both of these processes and is a promising anti-viral drug target. FluPol employs unique mechanisms to synthesise 5′-capped and 3′-polyadenylated viral mRNA, compatible with the host cell's protein production machinery, tricking it into making viral proteins. The viral proteins in turn package the viral genome copies into progeny virions that are released from the cell to infect new hosts.

At the beginning of transcription, FluPol is initially bound to the vRNA 'promoter' comprising the partially base-paired 3′ and 5′ regions of the template vRNA **[1,2]**. A short, capped primer is 'cap-snatched' from a nascent host polymerase II RNA transcript **[3]** and then directed towards the polymerase active site to hybridise with the 3′ extremity of the template to initiate mRNA synthesis. Attempts to characterise structurally the initial steps of transcription have hitherto been unsuccessful due to the intrinsic flexibility of the 3′ end of the template, the instability of the initiation state and a steric clash in the active site cavity of the primer with the priming loop – a specific feature of the FluPol that is required for vRNA replication **[1,2]**.

A modified 3′ template was employed to stabilise the initial primer-template interaction in order to visualise a transcription initiation-like state by X-ray crystallography using data measured on beamline **ID29** (**Figure 48a**). Subsequent addition of only ATP and GTP leads to product elongation by five nucleotides with concomitant template translocation before the polymerase stalls due to lack of CTP. Trapping this state made it possible to visualise the

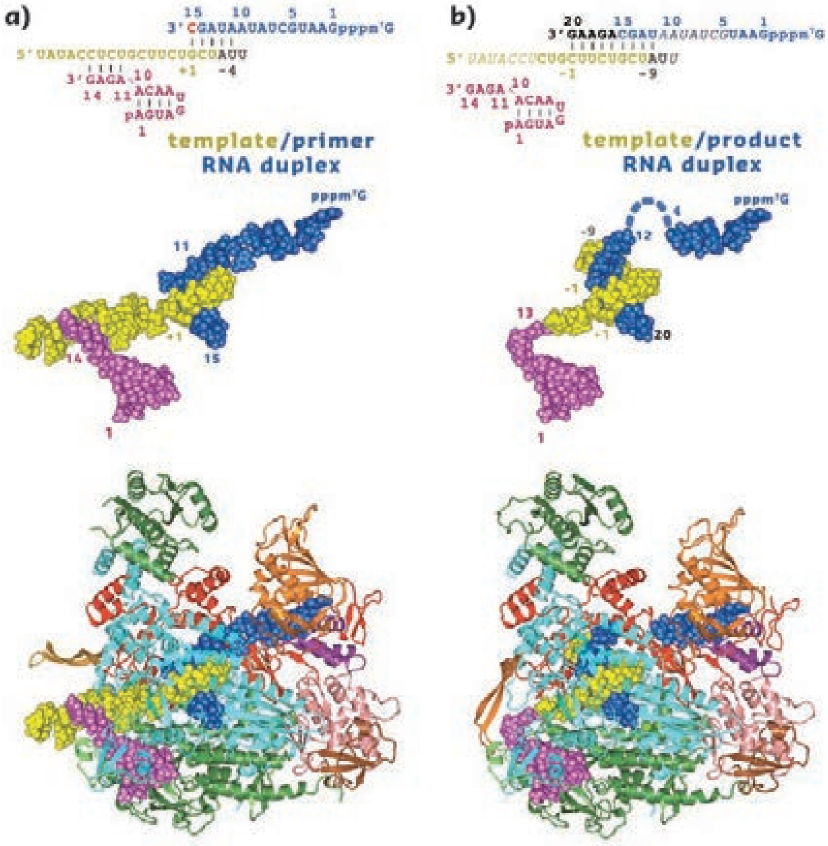

Fig. 48: Structural snapshots of **(a)** mixed initiation and **(b)** elongation state complexes of influenza polymerase. Top: Sequence and secondary structure of nucleic acid moieties in the complex. Template 3′ RNA in yellow, primer RNA in blue, template 5′ in pink. Middle: Structure of the RNA moieties, represented as spheres. Bottom: Ribbon diagrams of the mixed initiation (X-ray) and elongation (cryo-EM) state complexes coloured according to domain structure **[1]**.

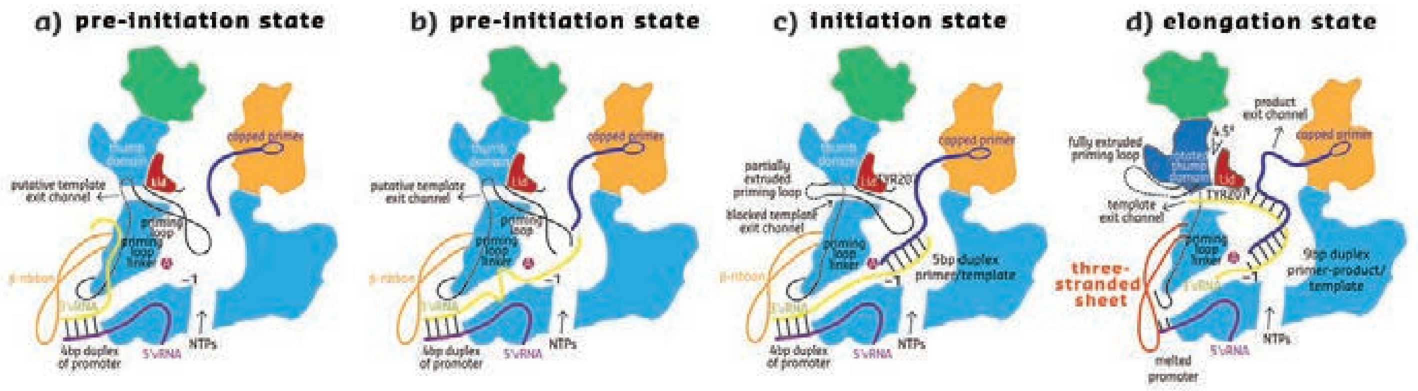

Fig. 49: Schematic of the transitions between the pre-initiation **(a,b)**, initiation **(c)** and elongation **(d)** states for transcribing influenza polymerase.

initiation-to-elongation transition by cryo-electron microscopy on **CM01** (**Figure 48b**).

The results show that the initiation-to-elongation transition involves progressive extrusion of the priming loop coupled to widening of the active site cavity (**Figure 49**). The latter accommodates growth of the product-template duplex to a steady state of nine base pairs. Subsequently, the PB2 helical lid forces strand separation, directing the template and product into separate exit channels. The structures also reveal how the six conserved characteristic structural motifs (A–F) of the catalytic core are responsible, together with two divalent cations, for controlling the nucleotide addition cycle. These motifs interact with the primer, template and incoming nucleotide in both pre- and post-translocation states. The comparison of the two states highlights the role of the flexible, methionine-rich motif B loop (PB1/407-GMMMGMF-413), highly conserved in all influenza viruses, in adapting to the presence of a base at the +1 incoming nucleotide position.

Influenza rapidly mutates, enabling it to outwit the immune system by generating new strains each year that cause seasonal epidemics. It can also jump the species barrier from birds and pigs to humans, resulting in occasional global pandemics. Up to 500,000 people worldwide die from influenza annually with potentially much higher mortality rates when a new pandemic flu strain emerges. Vaccination is not always effective and therefore potent anti-influenza drugs are needed as a complementary treatment option. The advantage of drugs that inhibit the highly conserved FluPol is that resistance mutants are less likely. Knowledge of the different configurations of the polymerase catalytic core will aid optimisation of inhibitors, such as nucleoside analogues, that directly target RNA synthesis. This study thus paves the way for the next generation of anti-flu drugs.

PRINCIPAL PUBLICATION AND AUTHORS

Structural snapshots of actively transcribing influenza polymerase, T. Kouba (a), P. Drncová (a) and S. Cusack (a), *Nat. Struct. Mol. Biol.* **26**(6), 460-470 (2019); doi: 10.1038/s41594-019-0232-z.

(a) European Molecular Biology Laboratory (EMBL), Grenoble (France)

REFERENCES

[1] S. Reich *et al.*, *Nature* **516**, 361-366 (2014).
[2] A. Pflug *et al.*, *Nature* **516**, 355-360 (2014).
[3] M. Lukarska *et al.*, *Nature* **541**, 117-121 (2017).

BREAKING THE SYMMETRY OF THE CONDENSIN ATPASE CYCLE

Five crystal structures of the ATPase catalytic core of the condensin complex and one of its HEAT-repeat subunits result in the first reconstruction of a detailed sequence of events that take place during the condensin reaction cycle. The structures hint at an unanticipated asymmetry that provides the means for condensin's ability to extrude DNA loops during mitotic chromosome assembly.

Upon entry into mitosis, eukaryotic genomes undergo global re-arrangements to form highly ordered rod-shaped chromosomes that can be segregated into daughter cells. The five-subunit condensin complex plays a leading role in the establishment and maintenance of these chromosome structures by extruding large DNA loops during its translocation along the

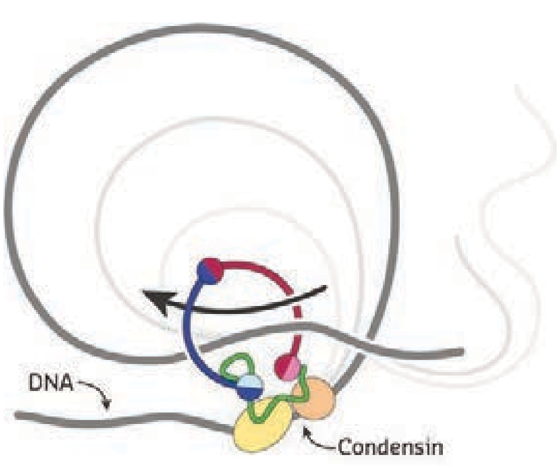

Fig. 50: Model for the processive extrusion of DNA loops by the condensin complex. The complex is thought to encircle DNA within the ring-shaped architecture formed by its Smc2–Smc4 coiled-coil subunits (blue and red) and Cnd2 kleisin subunit (green). HEAT-repeat subunits Cnd1 (yellow) and Cnd3 (orange) bind to Cnd2.

DNA double helix (**Figure 50**). The molecular mechanism behind this DNA motor activity has remained unknown **[1]**.

Condensin contains two structural maintenance of chromosomes (SMC) subunits, which harbour an ATP-binding-cassette (ABC) transporter class of ATPase sites at the end of a ~40-nm-long coiled coil. Each of the two sites sandwiches an ATP molecule between the ABC signature motif of one SMC subunit and the Walker A and B motifs of the other. The SMC subunits, together with a kleisin subunit, create a large tripartite ring architecture (**Figure 51**). The kleisin in turn recruits two additional subunits that are largely composed of alpha-helical HEAT repeats. Condensin shares this basic architecture with other SMC complexes, including cohesin and SMC5/6. All SMC complexes play essential roles during various aspects of chromosome biology, including genome maintenance, chromosome condensation and segregation, DNA recombination and damage repair, and the organisation of chromosomal territories **[2, 3]**.

To gain insight into the condensin catalytic core, different sub-complexes of the ATPase domain of Smc2 or Smc4 bound to the amino or carboxy terminus of the kleisin Cnd2, respectively, were co-expressed and purified. The ATPase head–kleisin sub-complexes from the yeast *Chaetomium thermophilum* were – after extensive engineering and screening – amenable to crystallisation by vapour diffusion. Following several rounds of data collection at beamline **ID29**, two independent crystal structures were determined for the Smc2 head (to 2.0 and 2.6 Å resolution) and one structure was determined for the Smc4 head–Cnd2$_C$ sub-complex (to 3.0 Å resolution). Since Cnd2$_N$ had apparently dissociated from the Smc2 head during crystallisation, its binding interface was instead resolved by nuclear magnetic resonance (NMR). Alignment of both Smc2 head structures to the structure of the Smc4 head or other homologous SMC head domains revealed an unusual rotation in the coiled coils (**Figure 51**). A cascade of structural displacement events linked this rotation to an altered phosphate-binding-loop (P-loop) conformation that was incompatible with ATP binding. This structural singularity explained a newly found asymmetry in the ATP-binding properties of the two SMC head domains: Only Smc4, but not Smc2, was able to bind ATP in biochemical assays.

The ATPase head asymmetry was found to further extend to a highly conserved surface patch on the coiled-coil side of the Smc4 head. *In-vivo* photo-crosslinking revealed that this region of Smc4 binds the condensin HEAT-repeat subunit Cnd1, which had so far been thought to assemble into the condensin complex exclusively through its constitutive interaction with the central regions of the Cnd2 kleisin subunit. Crystal structures of Cnd1–Cnd2$_{central}$ sub-complex alone (solved to 3.3 Å resolution) and when bound to the Smc4 head–Brn1$_C$ sub-complex (solved to 5.8 Å resolution), based on data collected at beamlines **ID30A-1**, **ID30B** and **ID29**, completed the architecture of the condensin core (**Figure 51**). Surprisingly,

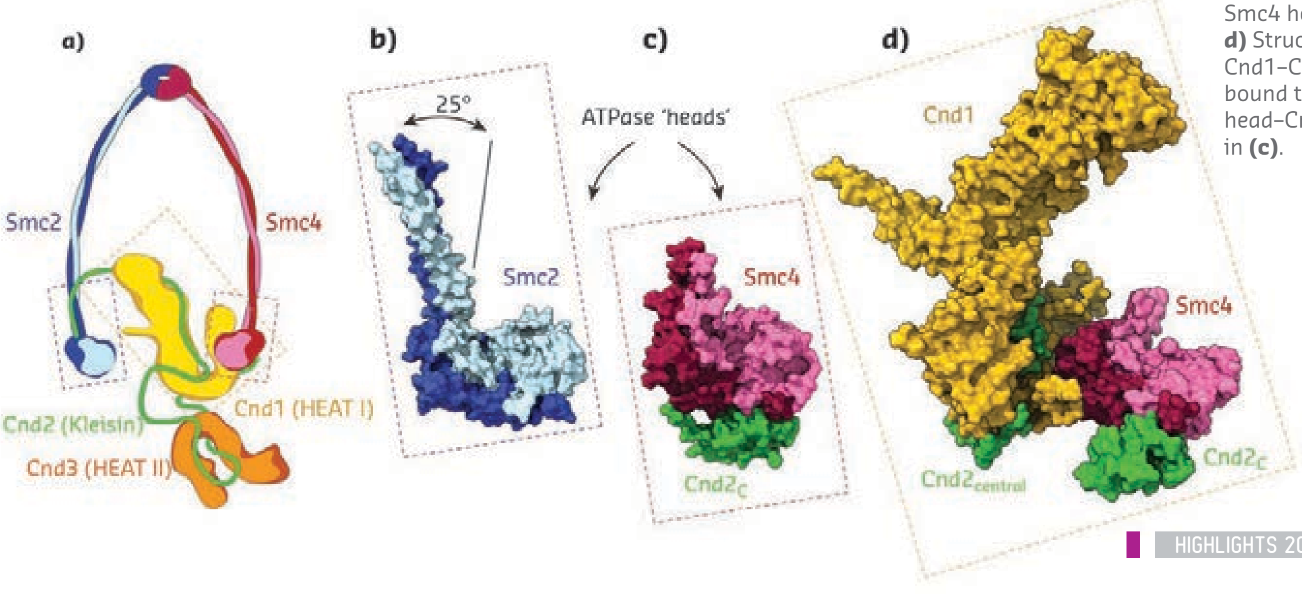

Fig. 51:
a) Positioning of the sub-complexes shown in **(b)**, **(c)** and **(d)** in the condensin architecture.
b) Structure of Smc2 head. **c)** Structure of Smc4 head–Cnd2$_C$.
d) Structure of Cnd1–Cnd2$_{central}$ bound to Smc4 head–Cnd2$_C$ shown in **(c)**.

Cnd1 binding to the Smc4 head domain created a steric clash when the latter engaged with the Smc2 head upon ATP binding. This conundrum was resolved by the finding that ATP binding to the Smc4 active site dissociated Cnd1 from the distant coiled-coil side, in which the so-called glutamine-loop (Q-loop) motif of Smc4 served as an allosteric conformational switch.

Taken together, the structural snapshots of condensin reveal for the first time a series of ATP-dependent conformational changes in an SMC complex at near-atomic resolution that drive an asymmetric ATPase reaction cycle. These findings lay out a mechanistic path towards explaining processive and directional extrusion of large DNA loops, which is now thought to provide the universal principle of organising genomes in all species **[1]**.

PRINCIPAL PUBLICATION AND AUTHORS

Structural Basis of an Asymmetric Condensin ATPase Cycle, M. Hassler (a), I. A. Shaltiel (a), M. Kschonsak (a), B. Simon (b), F. Merkel (a), L. Thärichen (a), H. J. Bailey (a), J. Macošek (b), S. Bravo (a), J. Metz (a), J. Hennig (b) and C. H. Haering (a,b), *Mol. Cell* **74**, 1175-1188 (2019); doi: 10.1016/j.molcell.2019.03.037.
(a) Cell Biology and Biophysics Unit, European Molecular Biology Laboratory (EMBL) Heidelberg (Germany)
(b) Structural and Computational Biology Unit, European Molecular Biology Laboratory (EMBL) Heidelberg (Germany)

REFERENCES

[1] M. Hassler *et al.*, *Curr. Biol.* **28**, 1266-1281 (2018).
[2] M. S. van Ruiten & B. D. Rowland, *Trends Genet.* **34**, 477-487 (2018).
[3] T. Gligoris & J. Löwe, *Trends Cell Biol.* **26**, 680-693 (2016).

UNVEILING THE T7 BACTERIOPHAGE DNA RETENTION AND EJECTION MECHANISMS

X-ray crystallography and single-particle cryo-electron microscopy (cryo-EM) structures of the T7 bacteriophage portal protein and fibre-less tail complex suggest a mechanism for DNA retention and ejection. A closed conformation of the portal could retain the genome before tail assembly, while in mature virions DNA leakage is prevented by the nozzle protein.

Tailed bacteriophages from the *Caudovirales* order share a common mechanism for genome packaging, in which a prohead is assembled before DNA encapsidation, with herpes virus. The key components of the packaging process are the terminase complex, which is the motor providing the energy for DNA translocation, and the portal protein, which is located at a unique pentameric capsid vertex and builds a channel through which the genome passes. After DNA packaging, assembly of the bacteriophage tail occurs at the portal vertex in order to produce the mature viral particle **[1]**. T7 bacteriophage is a member of the *Podoviridae* family, with a short, non-contractile tail formed by four proteins: the portal (gene product 8, gp8), the adaptor (gp11), the nozzle (gp12) and the fibres (gp17) **[2]**.

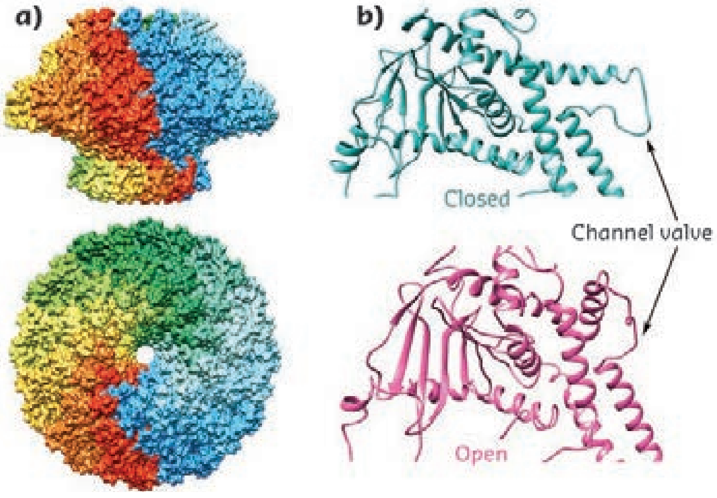

Fig. 52: T7 bacteriophage portal structure. **a)** Ring-shaped dodecameric gp8 particle. **b)** Comparison of the closed and open channel valve conformations.

A number of crystal structures of the T7 bacteriophage portal were solved by combining high-resolution X-ray crystallography and cryo-electron microscopy (cryo-EM). X-ray native data sets were collected at beamlines **ID29** and **ID14-1**. All attempts to determine the phases using heavy-atom methods failed, and the structures were eventually solved by molecular replacement, using a partial structure built into a 5.8-Å-resolution cryo-EM map as an initial search model. The dodecameric crystal structure of the portal obtained at 3.6 Å shows a ring-like assembly with an axial central channel (**Figure 52a**), whose narrowest aperture diameter, 23 Å, as delimited by the tunnel loop, would hardly allow the passage of DNA. The tunnel loop is connected with the 39-residue-long helix α10, oriented in a perpendicular manner with respect to the channel axis. Interestingly, a 4.1-Å-resolution cryo-EM map yielded a second dodecameric atomic structure of the portal. Even though the overall architecture is conserved between the two structures, a conformational change occurs at the α10-tunnel loop channel region. In the cryo-EM structure, the α10 helix is kinked, changing the orientation of its N-terminal region by 90° and increasing the channel diameter of the region to 53 Å. Therefore, this part of the structure may act as a channel valve, able to open and close the central aperture of the portal (**Figure 52b**).

The atomic structure of the 1.5-MDa fibre-less T7 tail complex (gp8-gp11-gp12) was determined at 3.3 Å resolution by cryo-EM. The structure contains two different symmetries, with gp8 and gp11 forming dodecameric rings and gp12 building the six-fold nozzle (**Figure 53a**). The adaptor protein interacts at the distal part of the portal with an extensive network of hydrogen bonds and electrostatic pairings, including those found on an α-helix that embraces the portal clip domain fitting it inside the channel of the adaptor. In the adaptor-nozzle interphase contact surface there is a bipolar distribution of electrostatic charges, with the electronegative distal part of gp11 interacting with the electropositive proximal part of gp12.

In the T7 tail complex, the portal channel valve is found in its open conformation. Therefore, gp8 is not responsible for DNA retention inside the mature viral particles. The gp12 nozzle protein is mainly responsible for securing the DNA in the capsid. With a fold without structural similarity to any bacteriophage tail protein previously reported, each nozzle monomer is organised around a central seven-bladed β-propeller placed with its plane radial-wise with respect to the tail channel. The nozzle contains four closing gates with diameters between 8.6 Å and 23 Å that avoid DNA slipping through the tail channel (**Figure 53b**).

This functional model suggests that the portal channel valve closes upon terminase detachment, temporarily preventing DNA leakage. The portal-adaptor interaction opens the portal channel valve, allowing the DNA to pass along the tail channel. In the mature virus, the gates of the nozzle protein are closed, retaining the DNA in the tail channel until reorganisation of the nozzle, triggered by the tail contact with the host membrane, which opens the gates and allows genome ejection.

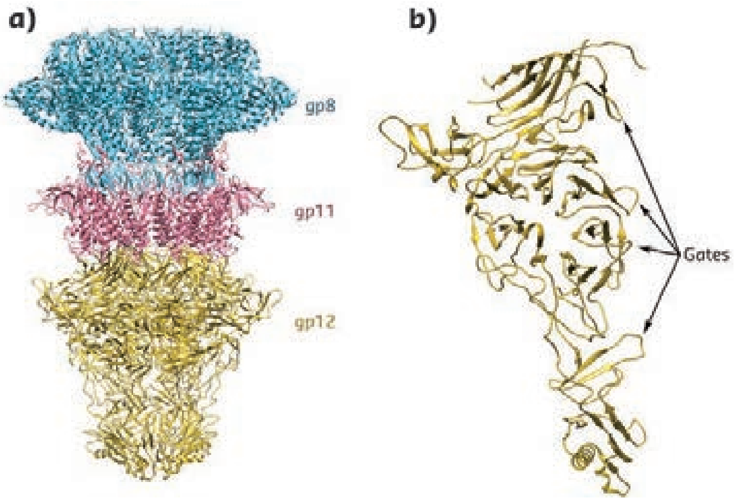

Fig. 53: Fibre-less T7 bacteriophage tail structure. **a)** Gp8-gp11-gp12 structure. **b)** Detail of the nozzle closing gates.

PRINCIPAL PUBLICATION AND AUTHORS

Structures of T7 bacteriophage portal and tail suggest a viral DNA retention and ejection mechanism, A. Cuervo (a), M. Fàbrega-Ferrer (b,c), C. Machón (b,c), J. J. Conesa (a), F. J. Fernández (d), R. Pérez-Luque (b,c), M. Pérez-Ruiz (a), J. Pous (b), M. C. Vega (d), J. L. Carrascosa (a) and M. Coll (b,c), *Nat. Commun.* **10**, 3746 (2019); doi: 10.1038/s41467-019-11705-9.
(a) Centro Nacional de Biotecnología (CNB-CSIC), Madrid (Spain)
(b) Institute for Research in Biomedicine (IRB Barcelona) The Barcelona Institute of Science and Technology, Barcelona (Spain)
(c) Institut de Biologia Molecular de Barcelona (IBMB-CSIC), Barcelona (Spain)
(d) Centro de Investigaciones Biológicas (CIB-CSIC), Madrid (Spain)

REFERENCES

[1] A. Cuervo *et al.*, in *Structure and physics of viruses*, M. G. Mateu (Ed.), Springer, Dordrecht, 361-394 (2013).
[2] A. Cuervo *et al.*, *J. Biol. Chem.* **288**, 26290-26299 (2013).

CONTROL OF DUB ACTIVITY THROUGH OLIGOMERISATION

USP25 and USP28 are two deubiquitylases involved in the progression of certain malignancies. Their high similarity and involvement in essential physiological processes makes high specificity a challenging but necessary task for the development of inhibitors. The crystal structures of their catalytic USP domains were solved and it was found that both enzymes form distinct oligomeric states.

The majority of cellular pathways in eukaryotes are regulated by ubiquitylation, the covalent attachment of ubiquitin (Ub) or ubiquitin chains to either the N-terminus or Lys-ε amino groups of proteins by the enzymatic ubiquitylation cascade (E1 -> E2 -> E3). This modification can be reversed by deubiquitylases (DUBs), isopeptidases that either remove or modify Ub-moieties from target proteins. The fine-tuned interplay of the two antagonistic processes decides the fate of the target protein and ultimately of the cell. The large number and high specificity of both ubiquitylating and deubiquitylating enzymes makes them attractive targets for the pharmacological intervention of pathological conditions.

USP25 and USP28 are two members of the large USP family of DUBs that are involved in the progression of certain types of cancer such as breast (USP25) and colorectal cancer (USP28). Despite their high similarity, both enzymes display distinct substrate specificities and thus fulfill different cellular roles such as the regulation of the innate immune system (USP25) and DNA damage response (USP28). In order to understand the molecular differences and establish a structural basis for the future development of specific DUB-activity-modulating compounds, both human enzymes were characterised (**Figure 54a**). The crystal structure of the catalytic domain of *apo* USP28 (USP28cat) was solved by the single-wavelength anomalous dispersion (SAD) method using diffraction data collected from SeMET derivatised crystals collected at beamline **ID30A-3** (**Figure 54b**). Subsequently, the crystal structures of USP28cat in complex with covalently bound Ub-propargylamide (UbPA) and USP25cat *apo* were solved using native data collected at beamlines **ID29** and **ID23-2** (**Figure 54b**).

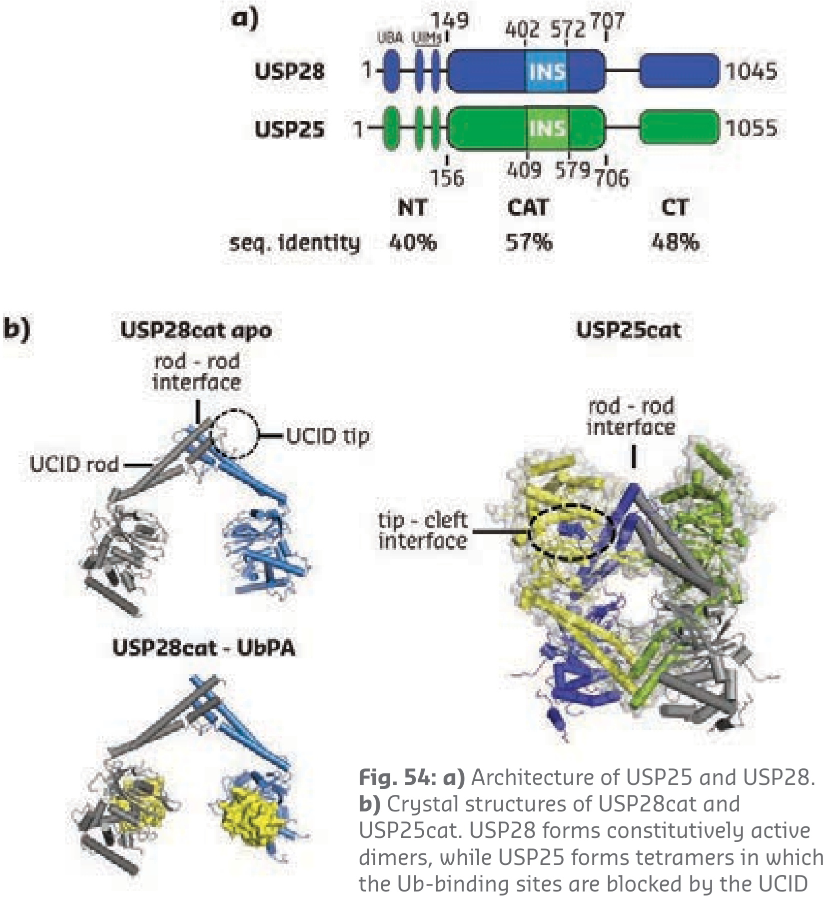

Fig. 54: a) Architecture of USP25 and USP28. **b)** Crystal structures of USP28cat and USP25cat. USP28 forms constitutively active dimers, while USP25 forms tetramers in which the Ub-binding sites are blocked by the UCID tips of the interacting dimer.

USP28cat and USP25cat comprise a four-subdomain architecture, with three subdomains (thumb/palm/finger) being responsible for the formation of the conserved USP domain to provide the S1 binding site for the Ub-substrate and the catalytic centre. The fourth subdomain (UCID) corresponds to a previously described inserted segment of ~20 kDa and consists of two structurally distinct parts: an upper 'tip' devoid of secondary structure and a lower, approximately 7-nm-long coiled-coil 'rod' that extends from the palm subdomain. Dimerisation of USP28 is the result of the symmetric association of two UCID rods through a large (~1850 Å^2) hydrophobic interface located at their upper ends, leading to the formation of a 'cherry couple'-shaped arrangement, in which the domain termini that connect to the N- and C-terminal substrate binding domains point towards the USP domain of the dimer mate.

The USP25cat tetramer is formed by two distinct interfaces. The first interface is highly similar to the USP28 rod–rod interface. The second is formed by the UCID tips that extend perpendicularly from the dimer axis and bind to the USP domains of a second USP25 dimer. Here, the tips are anchored in a cleft between the thumb and the palm within the S1 Ub-binding site, and thus the tetramer of interlinked USP28-like USP25 dimers represents a previously unknown autoinhibited state of the enzyme.

Tumour genome sequencing data permitted the identification of Pro535, which is located in the UCID tip region, as a position essential for the formation of the tetramer. This residue forms a *cis*-peptide bond with His534 (**Figure 55a**), thereby inducing a kink within the tip, which is required for its correct positioning to mediate the dimer–dimer interaction. Mutation of Pro535 (as found in different cancers) or removal of the entire tip region prevented the formation of USP25 tetramers, restored Ub-cleavage activity *in vitro* and led to increased stabilisation of the model substrates tankyrase 1/2 in cells (**Figure 55b**).

The discovery of USP25 autoinhibition and the elucidation of its mechanism by oligomerisation

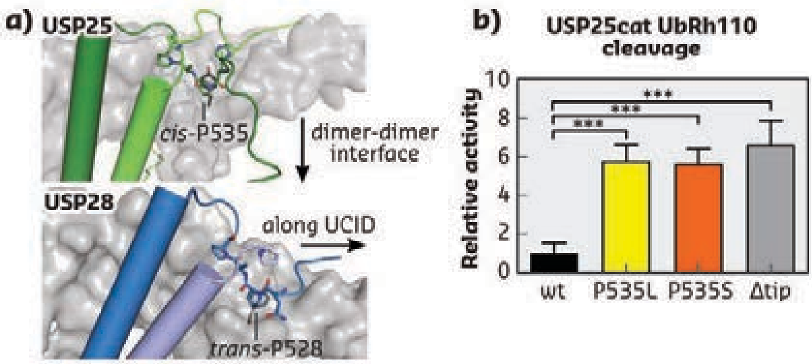

Fig. 55: a) Pro535 in USP25 forms a *cis*-peptide bond with His534, leading to a positioning of the tip C-terminus towards the dimer interface. **b)** Mutation of Pro535 leads to activation of USP25.

could provide a novel lead for the selective modulation of its activity, which has not been achieved so far. In contrast to USP28, which appears to be constitutively active, USP25 may be targeted indirectly by the modulation of a (currently unknown) activator or repressor.

PRINCIPAL PUBLICATION AND AUTHORS

Differential Oligomerization of the Deubiquitinases USP25 and USP28 Regulates Their Activities, F. Sauer (a), T. Klemm (a), R. B. Kollampally (b), I. Tessmer (a), R. K. Nair (a), N. Popov (b), C. Kisker (a), *Mol. Cell.* **74**(3), 421-435.e10. (2019); doi: 10.1016/j.molcel.2019.02.029.
(a) Rudolf-Virchow Center, University of Würzburg (Germany)
(b) Department of Clinical Tumor Biology, University Hospital Tübingen (Germany)

UNVEILING THE LOCK OF THE IRON GATE: CRYO-EM STRUCTURE OF THE HUMAN FERRITIN–TRANSFERRIN RECEPTOR 1 COMPLEX

CD71 is a transmembrane receptor responsible for iron uptake. The structure of CD71 bound to the human iron transporter ferritin revealed that it binds a receptor region that overlaps with the site used by viruses and by the malaria parasite to gain entry into human cells. This explains why evolution cannot mutate this region to block pathogens, since it would also affect physiological iron uptake.

The transferrin receptor 1 (CD71) mediates iron uptake in all vertebrates by importing iron in complex with transferrin (Tf) or ferritin from serum **[1]** through a clathrin-dependent endocytosis mechanism. Ferritin has recently moved to centre stage as a potential nano-carrier for drugs/diagnostics due to its cage-like structure and unique cargo capabilities, coupled with selectivity towards CD71 **[2]**, which is highly expressed in most cancer cell types. CD71 is also a preferred entry point for human pathogenic arenaviruses **[3-7]**, hepatitis C virus **[8]**, feline and canine parvoviruses **[9]**, and for the malaria parasite, *Plasmodium vivax* **[10,11]**. CD71 is a homodimeric transmembrane protein composed of a large ectodomain subdivided in protease-like, helical and apical domains (**Figure 56a**) **[12]**. Tf contacts the helical and the protease-like domains (**Figure 56b**), while the apical domain is the binding epitope of pathogenic proteins (**Figure 56b**). No structural information had previously been reported for the CD71/ferritin complex.

Data collected at the Titan Krios cryo-electron microscope at **CM01** allowed the reconstruction by single-particle analysis of a map of the H-chain ferritin (H-Ft)/CD71 complex at 3.9 Å resolution (**Figure 57a**). H-Ft binds CD71 at the apical domain (**Figure 57b**), a portion that does not overlap with the interacting area of Tf but that largely corresponds to the pathogen epitope. Mutations on H-Ft residues contacting common sites on CD71 strongly affects ferritin-receptor interactions, as observed by surface plasmon resonance (SPR) and cellular ferritin-uptake experiments. The H-Ft/CD71 structure revealed the sites on CD71 recognised by ferritin for physiological access to the cell and accounts for a Tf-independent binding of ferritin to CD71, allowing differential regulation of iron uptake and indicating a physiological role for the CD71 apical domain, unassigned to date. Importantly, pathogens have adapted to unlock cellular barriers by mimicking the physiological interaction of ferritin with the CD71 apical domain **[4]**.

This work provides a sound structural base to elaborate on the possibility of developing alternative, ferritin-like anti-viral or -parasite

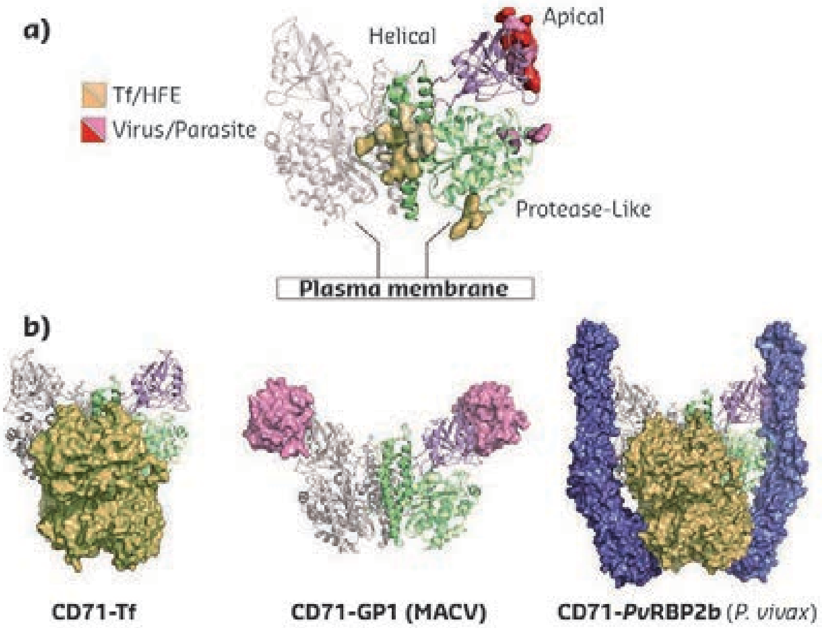

Fig. 56: CD71 receptor: ligand recognition epitopes and binding modes. CD71 homodimer is in ribbon (pdb 3KAS **[7]**): one monomer is in grey, the other is coloured variably to the receptor domains. **a)** CD71 epitopes for Tf/HFE and viruses/parasite are shown in surface representation. **b)** CD71 is shown in complex with Tf (orange surface, pdb 1SUV **[13]**), with the MACV GP1 protein (pink, pdb 3KAS), and with Tf (orange) and *Pv*RBP2b from *P. vivax* (blue, pdb 6D04 **[11]**).

therapeutic ligands targeting 'common contacts' on the CD71 apical domain, and to further develop the engineering of ferritins as nano-carriers.

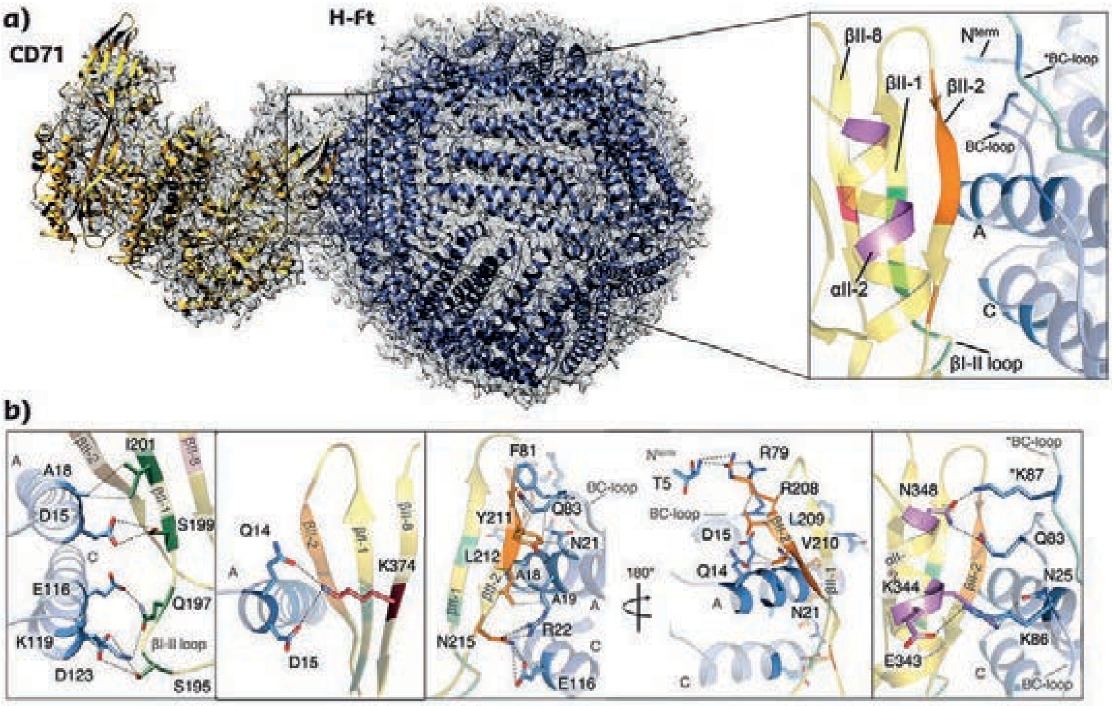

Fig. 57: The human CD71/H-Ft complex. **a)** Atomic model of the complex of CD71 (yellow) and H-Ft (blue) fitted in the cryo-EM map at a global resolution of 3.9 Å (grey mesh). Right, close-up view of the contact region. **b)** CD71-H-Ft interacting regions. Contacting residues (within 5 Å) are shown in stick representation, labeled and coloured according to the scheme used for secondary structure in panel **(a)**. Dashed black lines indicate electrostatic interactions, dotted grey lines represent hydrophobic contacts.

PRINCIPAL PUBLICATION AND AUTHORS

Cryo-EM structure of the human ferritin–transferrin receptor 1 complex,
L. C. Montemiglio (a,b), C. Testi (a,c), P. Ceci (b), E. Falvo (b), M. Pitea (a), C. Savino (b), A. Arcovito (d,e), G. Peruzzi (c), P. Baiocco (a,c), F. Mancia (f), A. Boffi (a), A. des Georges (g,h) and B. Vallone (a,b),
Nat. Commun. **10**(1), 1121 (2019);
doi: 10.1038/s41467-019-09098-w.
Figures adapted from original publication.

(a) Istituto Pasteur-Fondazione Cenci Bolognetti, Dept of Biochemical Sciences A. Rossi Fanelli, University of Rome La Sapienza (Italy)
(b) IBPM, National Research Council, Rome (Italy)
(c) Center for Life Nano Science @ Sapienza, IIT, Rome (Italy)
(d) Istituto di Biochimica e Biochimica Clinica, Università Cattolica del Sacro Cuore, Rome (Italy)
(e) Fondazione Policlinico Universitario Agostino Gemelli-IRCCS, Rome (Italy)
(f) Dept. of Physiology and Cellular Biophysics, CUMC, New York (USA)
(g) ASRC and Programs in Biochemistry and Chemistry at The Graduate Center of the CUNY, New York (USA)
(h) Dept. of Chemistry and Biochemistry, City College of New York (USA)

REFERENCES

[1] L. Li *et al., PNAS* **107**, 3505-3510 (2010).
[2] M. Truffi *et al., Pharmacol. Res.* **107**, 57-65 (2016).
[3] J. Abraham *et al., Nat. Struct. Mol. Biol.* **17**, 438-444 (2010).
[4] A. Demogines *et al., PLOS Biol.* **11**, e1001571 (2013).
[5] S. A. Kerr *et al., J. Virol.* **89**, 11643-11653 (2015).
[6] S. R. Radoshitzky *et al., Nature* **446**, 92-96 (2007).
[7] S. R. Radoshitzky *et al., PLOS One* **6**, e21398 (2011).
[8] D. N. Martin *et al., PNAS* **110**, 10777-10782 (2013).
[9] S. Hafenstein *et al., PNAS* **104**, 6585-6589 (2007).
[10] J. Gruszczyk *et al., Nature* **559**, 135-139 (2018).
[11] J. Gruszczyk *et al., Science* **359**, 48-55 (2018).
[12] C. M. Lawrence *et al., Science* **286**, 779-782 (1999).
[13] Y. Cheng *et al., Cell* **116**, 565-576 (2004).

SNAPSHOTS DURING THE FIRST STEP OF GENE EXPRESSION: HOW DOES RNA POLYMERASE RESUME TRANSCRIPTION AFTER BACKTRACKING?

Errors during DNA transcription can cause RNA polymerase to backtrack and cleave the erroneous part, before resuming transcription. Cryo-electron microscopy (cryo-EM) was used to reconstruct four structures of RNA polymerase in action, representing the entire reaction pathway and providing insight into the catalytic mechanism and dynamics of RNA cleavage and extension.

Genetic information, the blueprint of each organism, is encoded in DNA. Access to and decoding of this information is called gene expression and occurs in two steps: first, DNA is transcribed into RNA by a large, universally conserved, multi-subunit protein enzyme, RNA

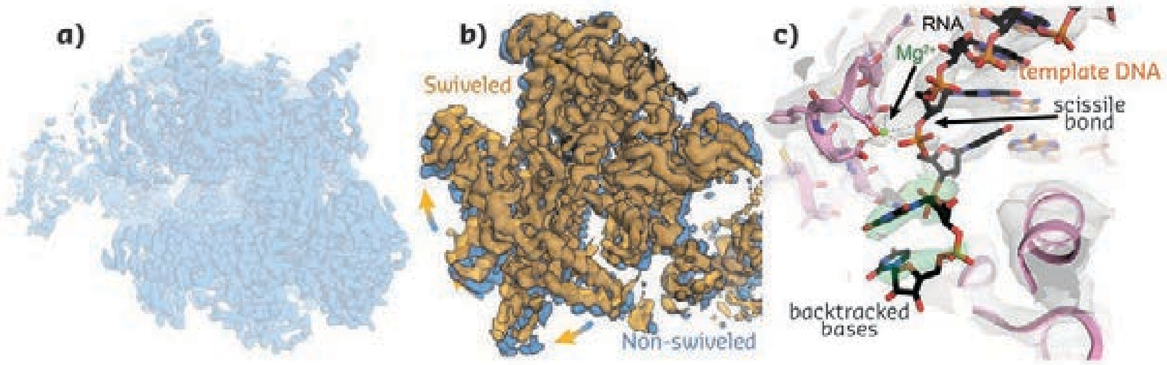

Fig. 58: a) Single-particle cryo-EM reconstruction of a functional, backtracked RNA polymerase elongation complex refined to a nominal resolution of about 3.4 Å.
b) 3D classification allows to refine different RNA polymerase conformations (compare blue *vs.* orange map).
c) In the active site, side chains, ions, and nucleic acid bases are resolved. The backtracked portion of the RNA transcript is visible at a lower contour level (green density).

polymerase. The RNA copy is then translated into protein by another molecular machine, the ribosome. Each species depends on tightly controlled transcription. This ensures access to the appropriate genetic information at the right time to respond to the environment, execute developmental programs, and to maintain homeostasis. Consequently, transcription needs to occur with high fidelity, is highly regulated, and thus affects almost every aspect of Biology. Misregulation, on the other hand, can cause a large variety of diseases with grave consequences.

One way for cells to regulate gene expression is to modulate transcription rates in a process called transcriptional pausing. Pausing, a temporary interruption of transcription elongation, can be achieved in multiple ways. One way is through a process called backtracking, where RNA polymerase stops, reverse translocates along the DNA template, and extrudes the RNA transcript out of the enzyme active site. The very same phenomenon plays another important role for transcriptional proof-reading. In that case, backtracking occurs when RNA polymerase misincorporates a ribonucleoside tri-phosphate substrate into the growing RNA transcript. To continue, the extruded RNA portion is cleaved such that the newly generated, shorter RNA end aligns with the active site and transcription resumes. In case of a misincorporation, this has the added benefit of removing the erroneous part of the transcript. Although this RNA cleavage can be catalysed by the RNA polymerase itself, it is greatly accelerated by protein transcription factors such as bacterial GreA and GreB or eukaryotic TFIIS. The cleavage factors can bind a backtracked RNA polymerase and complement the active site of the enzyme to assist in the RNA cleavage reaction.

Using single-particle cryo-electron microscopy (cryo-EM) it was possible to take snapshots along the entire reaction pathway of backtracking and reactivation using active *Escherichia coli* RNA polymerase complexes (**Figure 58**). High-resolution reconstructions were obtained of (i) a backtracked complex before RNA cleavage; (ii) a backtracked complex bound by the cleavage factor GreB before RNA cleavage; (iii) a complex after RNA cleavage, and (iv) a reactivated complex with a bound ribonucleoside tri-phosphate substrate in the active site.

Two critical datasets were collected on the Titan Krios microscope at beamline **CM01**. The reconstructions obtained made it possible to build atomic models of the RNA polymerase for each of the snapshots and to propose the following model for the mechanisms of RNA cleavage and reactivation: (i) the backtracked RNA induces an active site conformation that is incompatible with further RNA extension and opens a channel to allow cleavage factor access; (ii) binding of GreB further stabilises this inactive state, favours binding of ions involved in the cleavage reaction, and the backtracked RNA substrate itself stabilises GreB; (iii) after the cleavage occurs, GreB can still access the active site but is less ordered, and (iv) binding of a substrate to the active site induces a conformation that is no longer accessible for GreB and thus ensures that cleavage factors do not interfere with regular RNA extension.

Taken together, single particle cryo-EM allows the observation of multiple protein conformations in a single dataset and to trap distinct intermediate states at a resolution comparable to what can be obtained by X-ray crystallography for similar complexes.

PRINCIPAL PUBLICATION AND AUTHORS

Structural Basis of Transcription: RNA Polymerase Backtracking and Its Reactivation, M. Abdelkareem (a,b,c,d), C. Saint-André (a,b,c,d), M. Takacs (a,b,c,d), G. Papai (a,b,c,d), C. Crucifix (a,b,c,d), X. Guo (a,b,c,d,e), J. Ortiz (a,b,c,d,f) and A. Weixlbaumer (a,b,c,d).
Mol. Cell **75**(2), 298-309 (2019); doi: 10.1016/j.molcel.2019.04.029.

(a) Department of Integrated Structural Biology, Institut de Génétique et de Biologie Moléculaire et Cellulaire (IGBMC), Strasbourg (France)
(b) Université de Strasbourg (France)
(c) CNRS UMR7104, Strasbourg (France)
(d) INSERM U1258, Illkirch (France)
(e) Present address: Discovery Sciences, IMED Biotech Unit, AstraZeneca, Gothenburg (Sweden)
(f) Present address: Forschungszentrum Jülich, Ernst Ruska-Centre for Microscopy and Spectroscopy with Electrons, Jülich (Germany)

COMPLEX SYSTEMS AND BIOMEDICAL SCIENCES

During the 2019 shutdown, many engineers and technicians from the Complex Systems and Biomedical Sciences (CBS) group were seconded to the Accelerator and Source division for the assembly of the Extremely Brilliant Source (EBS). Working with new colleagues on a new project was very useful and reinforced team spirit. Otherwise, the key activity was to get the beamlines EBS-ready, preparing for much smaller beams and the higher degree of coherence. Three Eiger 2-4M detectors with CdTe sensors for high-energy radiation were ordered and the first ones arrived at the end of 2019. The data rate from these detectors is challenging, not only for data storage, but also for extracting useful information, in real time, during data acquisition.

The CBS group will recruit more than 10 postdocs at the beginning of 2020, replacing those who left before the 18-month shutdown. The recruitment and training of the new postdocs is a top priority and essential for resuming user operation in August 2020. Finally, a lead scientist for **EBSL1**, the coherence beamline, was appointed. The new beamline will be built on ID18.

The **ID02** beamline made use of the shutdown to improve the experimental setup and sample environments. The most important addition to the beamline is an Eiger 2-4M detector that will be the main SAXS/USAXS detector in the future. This detector will improve the detection capability in SAXS/USAXS from weakly scattering samples, enable extraction of weak signals superimposed on a large background and enhance the data quality in millisecond time-resolved experiments.

The operation of the surface science beamline **ID03** ceased in the autumn of 2018, after 25 years of operation. After the EBS upgrade, ID03 will host the full-field-microscope beamline **EBSL2**. Part of the old surface instrumentation will gradually move to ID10. Despite the shutdown, the ID03 team worked on the implementation of continuous scans for surface science and the upgrade of the BINoculars software with an improved algorithm for error propagation. We would like to thank all previous users and staff for their dedication to ID03.

ID09, the beamline for time-resolved studies, organised two workshops in 2019 to explore the potential for new applications and user communities. The first workshop focused on the complementarity between the FXE beamline at the European XFEL and ID09, including the difference in time resolution and style of experiment (single shot *vs.* multi-shot) at the two facilities. The scientists at the beamlines are now collaborating more closely, developing new methods and sharing software. The second workshop reviewed progress and future prospects in short-pulse science in diffraction, scattering, spectroscopy and imaging.

A new high-speed chopper will be installed in April 2020, making it possible to perform pump-probe experiments at 3 kHz. The coherent femtosecond laser will also be upgraded to 3 kHz. For X-ray emission, the Von Hamos spectrometer will receive 16 new analysers with stronger magnetic mounts. On the theory side, the intensity of a given emission line, stimulated off-resonance by a pink beam, was calculated analytically. It is now possible to predict line intensities and optimise the experimental parameters (concentration, excitation energy, and analyser reflection and detector angle).

The activities on **ID10** were devoted to improving the instrumentation and encouraging the users to take advantage of the new opportunities offered by the EBS. Both end-stations are preparing the infrastructure for the integration of an Eiger 2-4M detector, as on ID02. This detector will fully exploit the increased brilliance at higher energies of the EBS. A workshop dedicated to coherence, and the USTV School on the characterisation of glass structure, were organised to expand the coherence community (X-ray photon correlation spectroscopy, or XPCS, and coherent X-ray diffraction imaging, or CXDI) and to identify new applications such as high-pressure research and dynamics in crowded media. Among the scientific highlights in this chapter, CXDI was used for 3D imaging of coccolithophore skeletons, establishing a link between their morphology and mass (**page 67**).

The activities of the surface science end-station EH1 concentrated on two-dimensional nanomaterials. ID10 is a partner in the European project *Formation of 2D materials on liquid metal catalysts* (LMCat: 2020-FETOPEN), which is funding a reactor for chemical vapour deposition (CVD) of 2D nanomaterials on liquid metals. CVD of graphene was thus characterised on a molten copper surface by X-ray reflectivity and grazing incidence diffraction. In this chapter, a study of a 2D nanomaterial, MXene, is presented on **page 81**. Finally, the beamline is planning new optics for focusing the beam to 3 microns at high energies in both end-stations.

The biomedical beamline **ID17** took advantage of the shutdown to perform a major maintenance campaign. Furthermore, the CT monochromator was refurbished and the pit for the patient positioning system was installed in end-station EH1, in preparation for Microbeam Radiation Therapy (MRT) clinical trials. The scientific highlights in this chapter based on data collected at ID17 comprise a study on the response of radio-resistant melanoma to MRT (**page 71**) and the first direct detection of airway closures in acute respiratory distress syndrome (**page 73**) by phase-contrast CT imaging. While most of the Biomedical Facilities were closed, activity will be ramped up over the coming months and the labs will be fully operational for the restart of user operation.

The search for new partners for the **Partnership for Soft Condensed Matter** laboratory (**PSCM**), which is run jointly by the ILL/ESRF, resulted in the appointment of six partners (four new and two renewals). The partners will contribute to new science and instrumentation for the benefit of ILL/ESRF users in general. Important progress was made in 3D-printed microfluidics, contact-resonance and nanocalorimetry-coupled AFM, cryogenic sample environments and fast nanoscale scanning. New instruments installed in 2019 included an evacuated oven, a spin coater and a refurbished TGA/DTA instrument.

M. WULFF

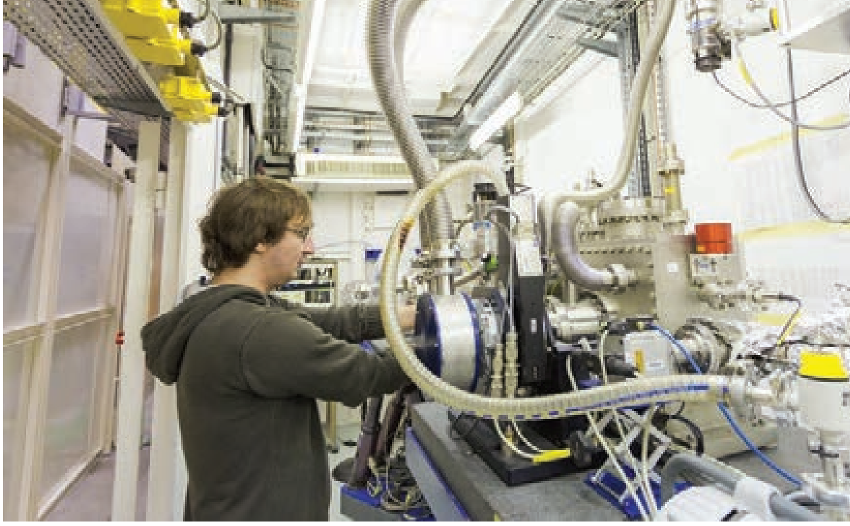

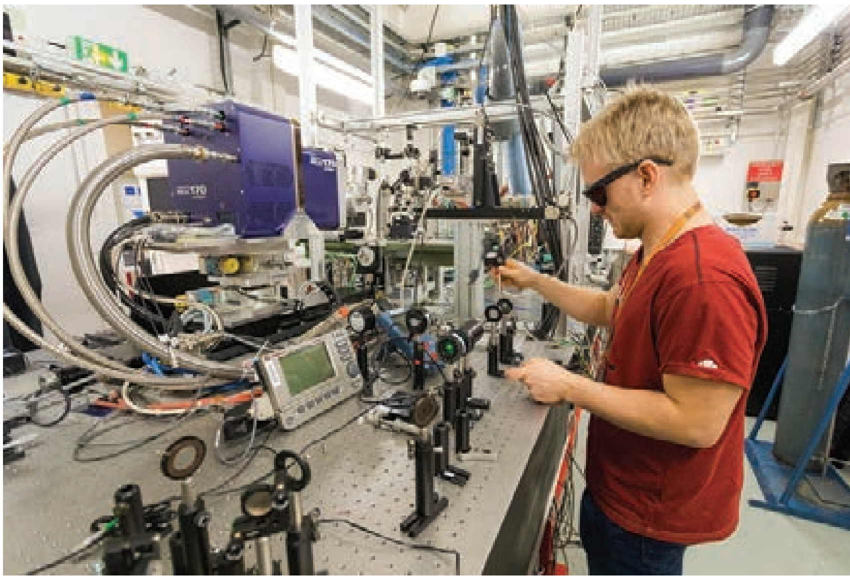

SELF-ORGANISATION OF NANOCRYSTALS INTO SUPERLATTICES

Evaporation-induced assembly of colloidal nanocrystals into highly ordered superstructures is observed in real time using *in-situ* small-angle X-ray scattering. The results show that the superlattice in the swollen state exhibits a hexagonal closed-packed structure, which rearranges into the body-centered cubic structure upon complete solvent evaporation.

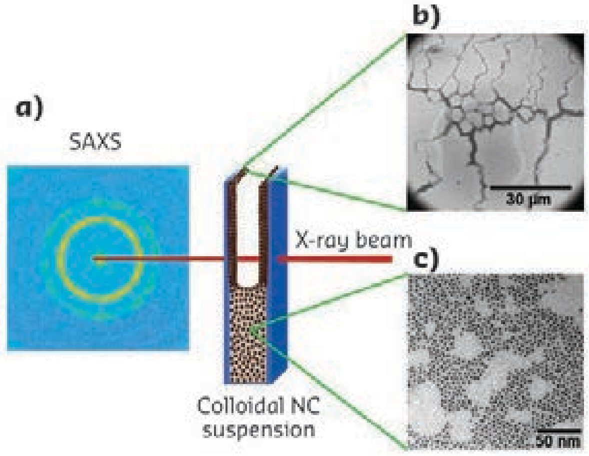

Fig. 59: a) Schematic representation of the sample cell for the *in-situ* SAXS study of the self-assembly of colloidal PbS NCs during controlled solvent evaporation. In the evaporation-induced assembly, NCs self-organise into highly ordered superlattice films along the cell windows. **b)** Scanning electron microscopy (SEM) image of the self-assembled superlattice film. **c)** Transmission electron microscopy (TEM) image of individual NCs.

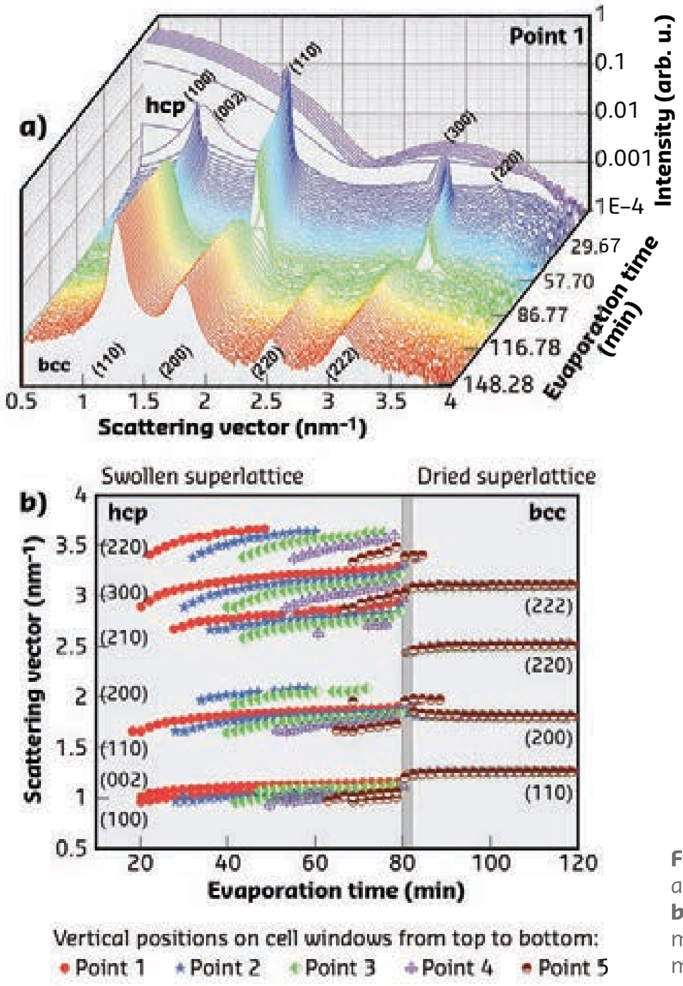

Fig. 60: **a)** Time-resolved SAXS curves during the *in-situ* self-assembly of PbS NCs from a 25 mg/ml suspension in heptane. **b)** Evolution of the positions of Bragg peaks at different measurement points on the cell windows. Grey area indicates the moment of the complete drying of the system.

The ability of colloidal nanocrystals (NCs) to form ordered structures by self-assembly is an attractive way to produce functional devices. However, due to the complex influence of multiple driving forces and interactions between the inorganic hard core, organic soft surface-coating ligands and surrounding solvent molecules, it is difficult to predict and control the obtained superstructure. Consequently, a thorough understanding of a solvent-mediated assembly process is required to produce nanocrystal superlattices with a preferred phase and desired properties **[1]**.

Lead sulfide (PbS) nanocrystals were chosen as a model system to study the assembly process due to the possibility to produce monodisperse particles in a colloidal solution with a precisely controlled size. Moreover, semiconductor PbS NCs exhibit unique electronic properties with tunable bandgap, which makes them attractive for many potential technological applications including solar cells, light-emitting diodes, transistors, photodetectors, etc.

A specially designed sample environment was used **[2]** for *in-situ* small-angle X-ray scattering (SAXS) at **ID02**. **Figure 59** shows how the real-time NC assembly was monitored using SAXS in transmission geometry upon controlled solvent evaporation from a bulk colloidal suspension. Quasi-spherical PbS NCs with 3.9 nm diameter and 8% dispersity were capped with oleic acid ligands and dissolved in a desired organic solvent (heptane or toluene). The oleic acid-stabilised PbS NCs were rather soft, with a ligand length to nanocrystal radius ratio of 1.17, and exhibited a ligand grafting density of ≈ 4.6 molecules/nm^2. The small amount of colloidal suspension (< 25 µl) evaporated within approximately two hours. The evolution of the assembly process was observed at different points of the three-dimensional sample cell, where the superlattice crystallisation occurred along the cell windows upon movement of the evaporation front (**Figure 59**). Using this approach, intermediate superlattice states were recorded with ms time resolution during the transition of the colloidal suspension into ordered superlattices. The assembled superlattices represent films with large domain sizes and thicknesses in the µm range.

During the assembly, the colloidal suspension crystallised into the hexagonal closed-packed (hcp) phase, followed by the rearrangement into the body-centered cubic (bcc) superlattice (**Figure 60a**). Well-resolved Bragg peaks indicate high crystallinity of the obtained superstructures. Using SAXS in transmission geometry, it was possible to scan over different vertical positions on the cell windows and measure the real-time superlattice states. Interestingly, at approximately 80 minutes of elapsed time, the hcp phase at all measurement points rearranged into the bcc superlattice (**Figure 60b**). This indicates that the superlattice structure is different in the solvated atmosphere and in the dried state when the solvent evaporates completely both from the bulk suspension and from the superlattice voids.

Furthermore, a space-filling fraction of soft particles was found in the final bcc superlattice of 71%, which confirms previous observations that soft nanocrystals can fill space more efficiently than hard ones. Additionally, X-ray cross-correlation analysis (XCCA) **[3]** of Bragg reflections was carried out in order to access information on precursor structures in the assembly process, which is not evident from conventional SAXS analysis. Intriguingly, the XCCA results revealed the formation of small amounts of bcc superstructures already in the solvent vapour-saturated hcp superlattice.

To conclude, an *in-situ* SAXS study was performed during the real-time evaporation-induced assembly of colloidal nanocrystals into highly ordered superlattice films. For the first time for the investigated system, the hcp superstructure was observed in the solvent vapour-saturated atmosphere, and rearranged into the bcc phase upon drying. The detailed evolution of the crystal structure with time provides key results for understanding the assembly mechanism and the role of ligand–solvent interactions during the crystallisation process. These findings are important for the manufacturing of functional devices based on NC superlattices with programmable properties.

PRINCIPAL PUBLICATION AND AUTHORS

Monitoring Nanocrystal Self-Assembly in Real Time Using In Situ Small-Angle X-Ray Scattering, I. Lokteva (a, b), M. Koof (a, b), M. Walther (a), G. Grübel (a, b) and F. Lehmkühler (a, b), *Small* **15**, 1900438 (2019); doi: 10.1002/smll.201900438.
(a) Deutsches Elektronen-Synchrotron (DESY) (Germany)
(b) The Hamburg Centre for Ultrafast Imaging (CUI) (Germany)

REFERENCES

[1] M. A. Boles *et al.*, *Chem. Rev.* **116**, 11220-11289 (2016).
[2] I. Lokteva *et al.*, *Rev. Sci. Instrum.* **90**, 036103 (2019).
[3] F. Lehmkühler *et al.*, *J. Appl. Crystallogr.* **47**, 1315-1323 (2014).

USING MICROFOCUSED X-RAY DIFFRACTION TO PROBE 2D GRAPHENE LAYERS

The combination and assembly of 2D layered materials such as graphene opens up a wide range of possibilities for designing new composite materials with novel functionalities. Understanding the structural properties of such materials is key. Here, X-ray diffraction (XRD) is used to investigate micron-sized, single-crystal graphene flakes, including their lithiation *in situ*.

Two-dimensional (2D) layered materials such as graphene are increasingly attracting the attention of researchers, thanks to a variety of interesting properties and functionalities, and especially with respect to their manifold incorporation into novel van der Waals heterostructures – stacked sets of different atomic layers – such as tunnelling transistors, resonant tunnelling diodes and light-emitting diodes **[1]**.

Despite the advent of scalable synthesis methods **[2,3]**, mechanical exfoliation from bulk crystals remains the prime route to manufacturing 2D materials with the highest quality **[4]**.

However, the size of devices produced in this manner is limited, and the characteristic dimensions of atomically thin single-crystalline flakes are on the micrometre scale. Due to the tiny interaction volume, samples of this size are extremely challenging to investigate by X-ray diffraction (XRD). For the case of graphene, only a few XRD investigations have been reported, and these have been restricted to thin-film systems, with atomically thin samples reaching the centimetre scale. This work demonstrates that XRD can be used to investigate individual, micron-sized, single-crystalline bilayer or multilayer graphene flakes, and indeed to study the lithiation of individual single-crystals *in situ*.

Bilayer and multilayer graphene flakes were mechanically exfoliated from bulk graphite and then isolated on Si substrates in order to minimise the substrate XRD contributions. Grazing incidence X-ray diffraction (GIXD) was employed at ANKA synchrotron in Germany to probe the in-plane Bragg peaks, which demonstrated the single-crystalline nature of the flake. Specular X-ray reflectivity (XRR) was then carried out at beamline **ID03**, in order to investigate *in situ* the lithiation of individual graphene single-crystals. A peripheral electrochemical cell was used to induce the intercalation of Li ions between the graphene sheets, as explained in the experimental setup schematic in **Figure 61**. Before and during this process, individual flakes were probed by a microfocused incident X-ray beam with energies of 12 keV (λ = 1.033 Å) for the bilayer and 18.5 keV (λ = 0.670 Å) for the multilayer single crystals, to reveal crystallographic changes induced by the insertion of the Li ions.

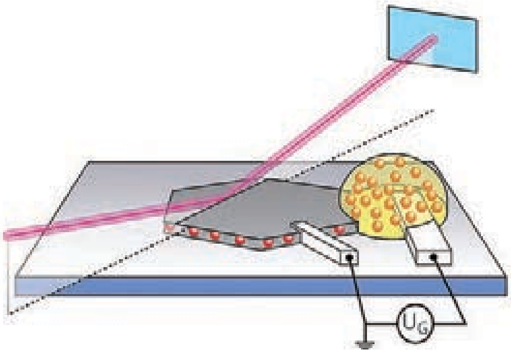

Fig. 61: Schematic experimental configuration for *in-situ* X-ray diffraction investigations on the electrochemical lithiation of exfoliated bilayer graphene flakes. A solidified electrolyte (yellow) serves as a source of Li ions (red spheres) that are forced to intercalate between the graphene sheets (grey) when a gate voltage U_G is applied to a counter electrode with respect to the bilayer. During this process, microfocused X-rays (violet) may be diffracted from the sample to probe structural changes.

Figures 62a and **62c** show the XRR curves before and during lithiation of a bilayer and multilayer graphene flake, respectively. The experimental data were then modelled using Parratt's recursion formalism **[5]**, making it possible to access characteristic crystallographic parameters of the samples, notably the *c*-axis lattice spacing. The interlayer separation *c* was found to increase upon lithiation in bilayer single crystals (**Figure 62*a***) and also – although to a lesser degree – in multilayer single crystals (**Figure 62c**). Valuable information such as the thickness, roughness and density of layers and interfaces at the sample surface was also gained (**Figures 62b** and **62d**).

These experiments demonstrate the feasibility of *in-situ* X-ray diffraction on individual, micron-sized single crystals of bi/multilayered graphene flakes supported on a substrate to directly investigate the structural properties of such ultrathin crystalline layers. Characteristic in-plane Bragg peaks can be observed by GIXD, whereas the *c*-axis lattice spacing can be probed by XRR. These approaches can, in principle, be extended to micron-sized crystalline layers of any other material, including those routinely produced currently by mechanical exfoliation of layered compounds.

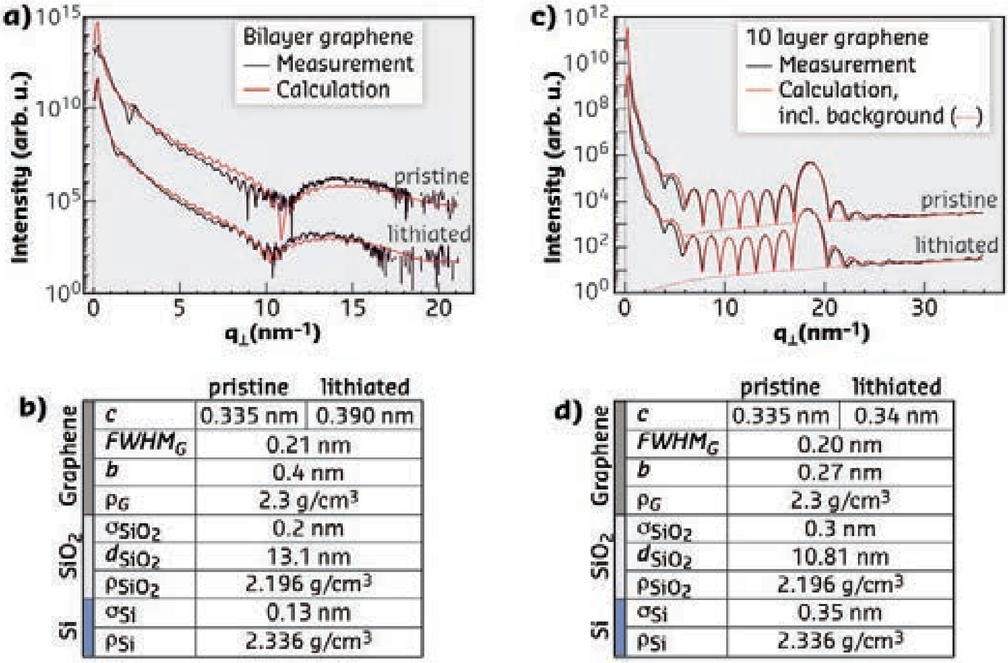

b)

		pristine	lithiated
Graphene	c	0.335 nm	0.390 nm
	$FWHM_G$	0.21 nm	
	b	0.4 nm	
	ρ_G	2.3 g/cm³	
SiO$_2$	σ_{SiO_2}	0.2 nm	
	d_{SiO_2}	13.1 nm	
	ρ_{SiO_2}	2.196 g/cm³	
Si	σ_{Si}	0.13 nm	
	ρ_{Si}	2.336 g/cm³	

d)

		pristine	lithiated
Graphene	c	0.335 nm	0.34 nm
	$FWHM_G$	0.20 nm	
	b	0.27 nm	
	ρ_G	2.3 g/cm³	
SiO$_2$	σ_{SiO_2}	0.3 nm	
	d_{SiO_2}	10.81 nm	
	ρ_{SiO_2}	2.196 g/cm³	
Si	σ_{Si}	0.35 nm	
	ρ_{Si}	2.336 g/cm³	

Fig. 62: Specular X-ray reflectivity (XRR) before (upper curves) and during (lower curves) lithiation of **(a)** a bilayer and **(c)** a multilayer graphene flake. Experimental data (black) in **(a)** and **(c)** are calculated using Parratt's recursion formalism (red) with the parameters given in **(b)** and **(d)** respectively. Parameters are ρ: the density of Si, of SiO$_2$ and of graphitic carbon; σ: the roughness of Si, of SiO$_2$ and of graphene; *d*: the thickness of SiO$_2$; *b*: the separation between the lowest graphene layer and the SiO$_2$ surface, and *c*: the graphene flake's *c*-axis lattice spacing.

PRINCIPAL PUBLICATION AND AUTHORS

Probing Exfoliated Graphene Layers and Their Lithiation with Microfocused X-rays, P. Zielinski (a), M. Kühne (a), D. Kärcher (a), F. Paolucci (a), P. Wochner (a), S. Fecher (a), J. Drnec (b), R. Felici (b) and J.H. Smet (b), *Nano Lett.* **19**(6), 3634-3640 (2019); doi: 10.1021/acs.nanolett.9b00654.
(a) Max Planck Institute for Solid State Research, Stuttgart (Germany)
(b) ESRF

REFERENCES

[1] K. S. Novoselov *et al., Science* **353**, aac9439 (2016).
[2] Z. Lin *et al., 2D Mater.* **3**, 042001 (2016).
[3] K. Kang *et al., Nature* **550**, 229-233 (2017).
[4] K. S. Novoselov *et al., PNAS* **102**, 10451-10453 (2005).
[5] L. G. Parratt, *Phys. Rev.* **95**, 359 (1954).

3D IMAGING OF SINGLE COCCOLITHOPHORE SKELETONS

Coccolithophores are unicellular algae a few micrometres in size that can produce, through a mechanism that is still poorly understood, one of the smallest skeletons in the marine world. For the first time, these skeletons were imaged in three dimensions by tomography, allowing a better understanding of the link between their morphology and certain organelles of the cell.

Around 210 million years ago, at the end of the Triassic period, some unicellular algae belonging to the haptophyte lineage developed the ability to produce biogenic calcium carbonate scales, or 'coccoliths'. Calcification by these 'coccolithophore' microalgae modified the composition of the ocean (and, as a consequence, the atmosphere) by trapping dissolved inorganic carbon (DIC), and also changed the carbonate cycle by forming carbonate-rich deep ocean sediments. Nowadays, coccolithophores are the main extant calcifying organisms and form one of the smallest and lightest exoskeletons in the world – 'coccospheres', composed of 10 to 30 coccoliths.

The complex euhedral 3D morphologies of coccoliths are produced inside the cell in the coccolith vesicle (CV), a dedicated vesicle sandwiched between the nucleus of the cell and the reticular body. Once growth is complete, exocytosis occurs and the newly formed coccolith joins the coccosphere surrounding the cell. Understanding coccolith formation represents a major challenge in the fields of biomineralisation, micropaleontology and environmental science. In this study, single coccolithophore skeletons from the numerically dominant extant family Noëlaerhabdaceae (including the genera *Emiliania*, *Gephyrocapsa* and *Reticulofenestra*) were imaged with a resolution close to 30 nm using three-dimensional coherent X-ray diffraction imaging (CXDI) at beamline **ID10**.

Comparisons between scanning electron microscopy (SEM) and CXDI images validated the accuracy of reconstructions as shown for *G. oceanica* in **Figure 63a**. The significant advantage of CXDI over SEM is to unravel the 3D morphology of the coccosphere. Each coccolith of each skeleton can be segmented as illustrated for *E. huxleyi* in **Figure 63b**. Several extracted coccoliths are shown in **Figure 63c**. Cross sections show that both shields of the coccoliths are out-of-plane inclined by about $\alpha \sim 30 \pm 5°$ along the major axis. These inclinations likely correspond to the curvature of the nuclear membrane to which the coccolith vesicle is apposed during intracellular formation of the coccolith **[1,2]**. The constant value of the inclination of the shield α suggests a positive correlation between the size of the cell nucleus and coccolith size.

A key point is that the mature coccoliths composing the coccosphere exhibit a central area, or 'grid' (shown in yellow in **Figure 63c**) reminiscent of an organic template called the 'organic base plate scale' (OBPS), around which nucleation and growth of the coccolith takes place. By measuring the number of segments *n*, that is to say the number of single calcite crystals composing each coccolith, which are radially distributed around the grid as illustrated in **Figure 63d**, it was found that the longer the peripheral grid perimeter, the higher the number of segments. As the grid perimeter linearly scaled with the number of segments, the average width of the segments at the location of the perimeter was constant and close to w = 115 nm, whatever the species. It was deduced from these analyses that the perimeter of the OBPS controls the nucleation site number with an average site periodicity of around 115 nm. A positive correlation between the mass m of coccoliths and the number of calcite segments n was also observed, obeying to a first approximation the relation:

$$m = 4.73 \times 10^{-5} n^{3.175}$$

with n being the number of calcite segments and m the mass of a coccolith in pg. The results indirectly support the idea that the mass of coccoliths is determined by the size of the OBPS around which crystal nucleation takes place every 115 nm. In addition, the curvature of coccoliths allows inference of a positive correlation between the cell nucleus, the OBPS and coccolith size.

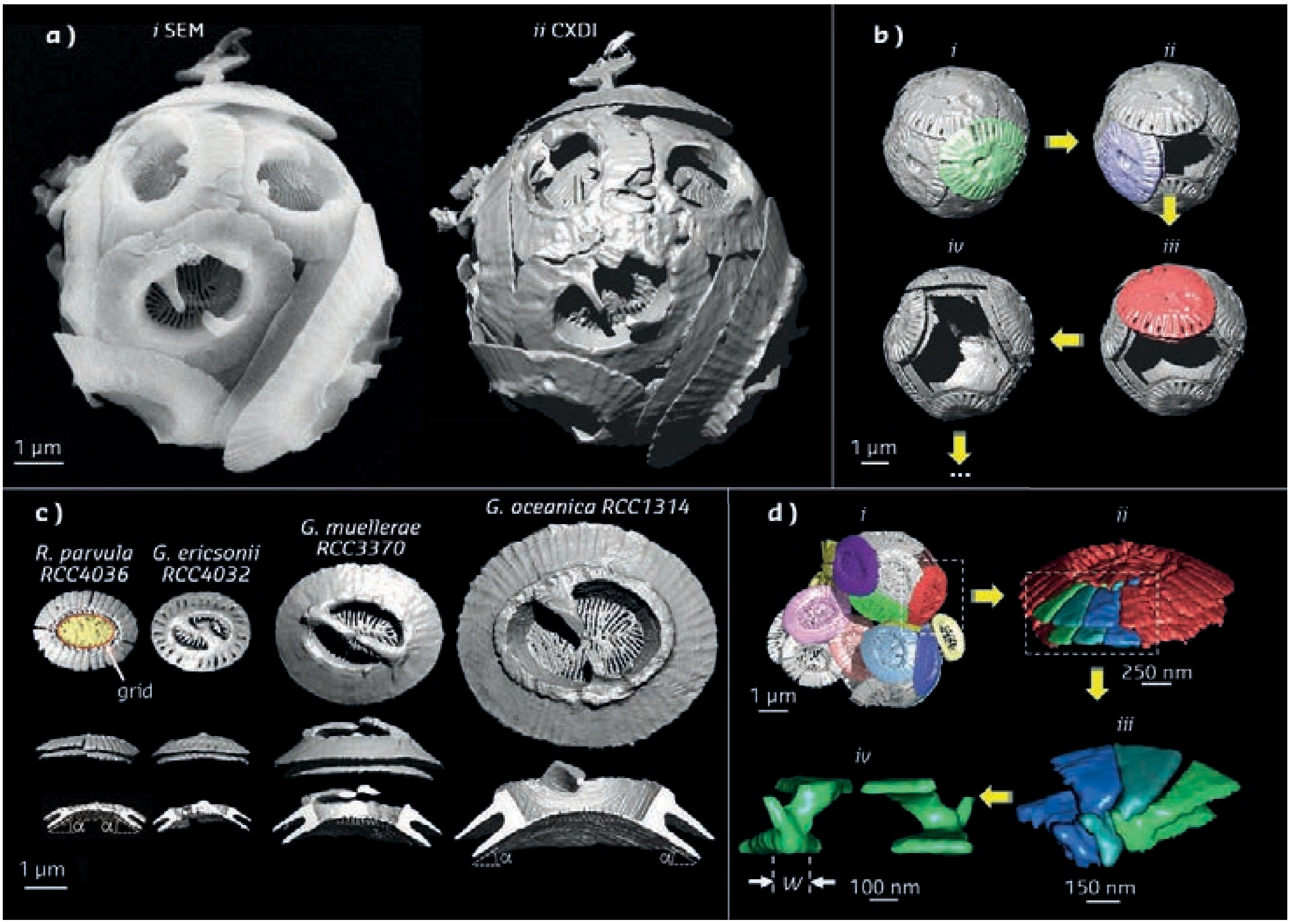

Fig. 63: CXDI of coccospheres. **a)** Comparison between (i) SEM and (ii) CXDI images of *G. oceanica RCC1314*. **b)** Scheme showing the methodology used to extract the coccoliths from the coccosphere: (i) For this species (*E. huxleyi P41*), the whole coccosphere containing 14 coccoliths was segmented into two parts: a first coccolith (in green) and a new coccosphere containing 13 coccoliths. (ii-iv) This procedure was repeated until all coccoliths were extracted. **c)** From top to bottom: distal view, side view along the major axis, and side view along the major axis after sectioning half of the extracted coccoliths for four different species. The grid of *R. parvula* is coloured yellow. **d)** From coccosphere to segments: (i) a coccosphere of *R. parvula*, (ii) an extracted coccolith, (iii) three extracted segments, (iv) side views of one segment.

PRINCIPAL PUBLICATION AND AUTHORS

X-ray nanotomography of coccolithophores reveals that coccolith mass and segment number correlate with grid size, T. Beuvier (a,b), I. Probert (c), L. Beaufort (d), B. Suchéras-Marx (d), Y. Chushkin (b), F. Zontone (b) and A. Gibaud (a), *Nat. Commun.* **10**, 751 (2019); doi: 10.1038/s41467-019-08635-x.

(a) IMMM, Le MANS (France)
(b) ESRF
(c) Université Pierre et Marie Curie, Roscoff (France)
(d) Aix Marseille Univ, CNRS, IRD, INRA, Coll France, CEREGE, Aix-en-Provence (France)

REFERENCES

[1] E. Paasche, *Phycologia* **40**, 503-529 (2001).
[2] X. Yin *et al., J. Phycol.* **54**, 85-104 (2018).

TIME-RESOLVED X-RAY SCATTERING UNVEILS THE KINETICS OF LIGHT-SIGNALLING MECHANISM IN A CYANOBACTERIAL PHYTOCHROME

Structural changes upon light activation in a cyanobacterial phytochrome have been monitored with X-ray scattering. The kinetics of structural changes reveals a complex photoconversion pathway and indicates a time window in which the photoreaction can be characterised (*e.g.*, for optogenetic design) in the photosensory region independently of the nature of the engineered output domain.

Phytochromes are light-sensing proteins that transduce a light signal into a biochemical output to control a number of biological functions in plants, bacteria and fungi **[1]**, with a mechanism that is still unclear. The photosensory activity of phytochromes results from their capacity to undergo a light-induced and reversible switching between two conformers: a red-light-absorbing Pr form and a far-red-light-absorbing Pfr form. These are characterised by distinct 3D structures and spectral properties. Phytochromes are generally soluble and dimeric proteins, with each monomer consisting of multiple domains. The protein consists of an N-terminal photosensory region that comprises three domains, namely a PAS, GAF and PHY domain, and a C-terminal output domain, which is normally a histidine kinase domain.

The light-sensing properties of phytochromes result from the presence of a bilin chromophore, either phytochromobilin in plant phytochromes, phycocyanobilin in cyanobacterial phytochromes or biliverdin in bacterial phytochromes, which is covalently attached to a conserved cysteine residue within the GAF domain. While the initial photoisomerisation of the bilin chromophore has been confirmed by several studies, it was still largely unknown how isomerisation alters the bilin conformation, changes the structure of the bilin binding pocket, and ultimately triggers a rearrangement of the interface between the sensory domain and the adjacent domains, in particular the so-called output domain. It was also unclear if the motions observed in the sensory domain **[2]** were affected by the presence of the output domain in full-length phytochromes.

A combination of steady-state and time-resolved small- and wide-angle X-ray scattering (TR-S/WAXS) approaches at beamline **ID09** has been used to study the conformational changes accompanying photoconversion in the full-length cyanobacterial phytochrome Cph1 from *Synechocystis sp.* PCC6803. The kinetics of structural changes in the full-length protein extends to the seconds timescale and is more complex than that recently reported for a similar phytochrome from *Deinococcus radiodurans* **[3]**. A comparison of data on the full-length protein with data on the photosensory region alone suggests that both localised and global changes on the μs/ms timescale are independent of the presence of the output domain, while those at longer times differ significantly in the presence of the output domain (**Figure 64a**).

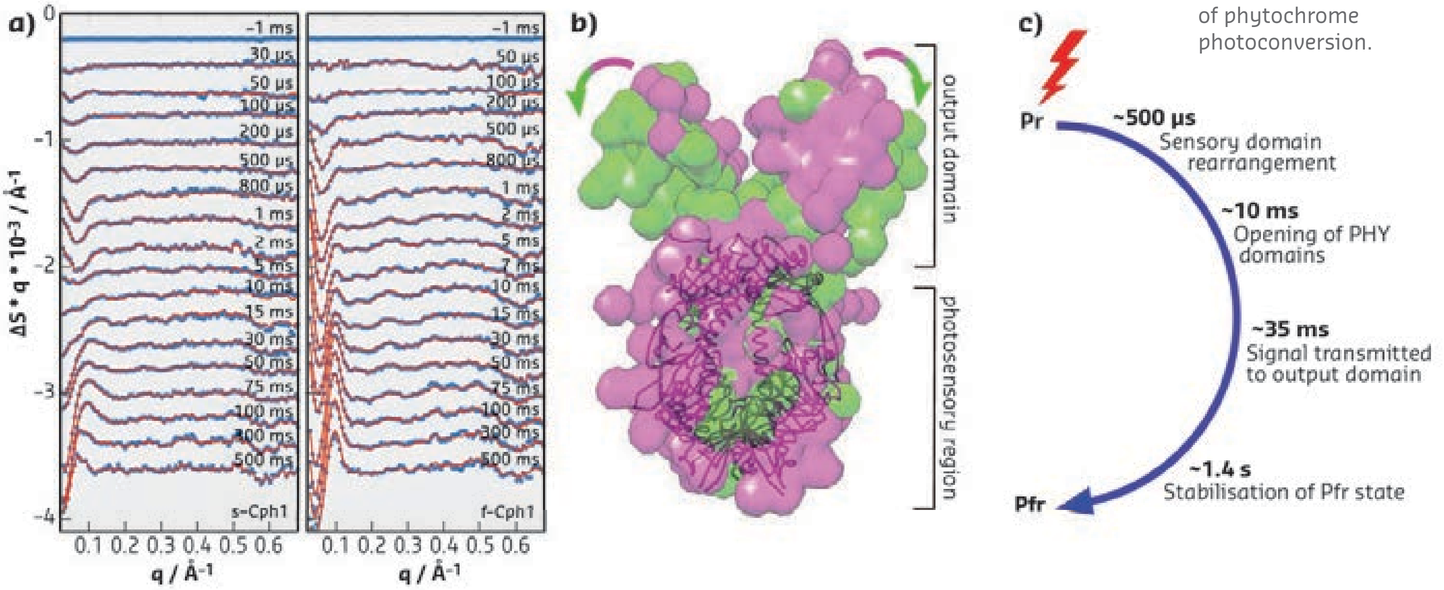

Fig. 64: a) Light-induced TR-S/WAXS patterns for Cph1 sensory region (s-Cph1) and full-length protein (f-Cph1). **b)** *Ab initio* shape reconstructions for full-length Cph1 in Pr (pink) and Pfr (green) state. **c)** Timescales of phytochrome photoconversion.

Low-resolution modelling of small-angle data suggests that the differences in the small-angle scattering reflect a large motion of the output domains (**Figure 64b**), making it possible to propose a complete kinetic model for the structural photoconversion of the full-length cyanobacterial phytochrome (**Figure 64c**).

These results will help in designing optogenetic tools based on phytochromes, where one of the most promising strategies is to replace natural output domains with engineered domains with a desired biological function. Indeed, the separation between the photosensory region dynamics and the output domain on the µs/ms timescale indicates that in this time window the photoreaction can be characterised independently of the nature of the engineered output domain. It is only on slower timescales that the structural changes are propagated to the output domain in a process that is likely to be transmitted through the linker region.

PRINCIPAL PUBLICATION AND AUTHORS

Light-induced structural changes in a full-length cyanobacterial phytochrome probed by time-resolved X-ray scattering, D. J. Heyes (a), S. J. Hardman (a), M. N. Pedersen (b), J. Woodhouse (c), E. De La Mora (a), M. Wulff (b), M. Weik (c), M. Cammarata (d), N. S. Scrutton (a) and G. Schirò (c), *Commun. Biol.* **2**, 1 (2019); doi: 10.1038/s42003-018-0242-0.

(a) Manchester Institute of Biotechnology, University of Manchester (UK)
(b) ESRF
(c) Institut de Biologie Structurale, CNRS, Univ. Grenoble Alpes, Grenoble (France)
(d) Univ. Rennes 1, CNRS, UBL, Institut de Physique de Rennes (IPR) - UMR 6251, Rennes (France)

REFERENCES

[1] F. Nagy & E. Schäfer, *Annu. Rev. Plant Biol.* **53**, 329-355 (2002).
[2] H. Takala *et al.*, *Nature* **509**, 245-248 (2014).
[2] A. Björling *et al.*, *Sci. Adv.* **2**, e1600920 (2016).

PHASE EXPLOSION PHENOMENA IN PULSED LASER ABLATION IN LIQUIDS

Pulsed laser ablation in liquids can be used to produce nanoparticles for a wide range of materials without the use of harmful additives. In the ablation process, however, the size distribution is not well controlled. Time-resolved X-ray scattering reveals how the larger nanoparticles in the size distribution are formed.

In pulsed laser ablation in liquids, a solid target is irradiated by intense short laser pulses that heat the material to thousands of Kelvin, which leads to the emission of nanoparticulate matter **[1]**. While this process is widely used in the synthesis of colloids with unique properties **[2]**, the understanding of how these structures are formed is hampered by the multiscale nature of the phenomena. Heating and melting of the target occur on the pico- and nanosecond time scale and these processes are governed by atomic-scale interactions. The second step, material ejection and vapour formation, takes place on the micrometre to millimetre length scale. Time-resolved X-ray techniques such as imaging **[3]** and scattering are being used to elucidate the formation process. It has been shown that the vapour bubble forms an important compartment for the enrolling reactions, including stabilisation and agglomeration of primary particles **[3]**. In this work, by contrast, earlier steps in ablation, particle solidification and crystallisation are examined.

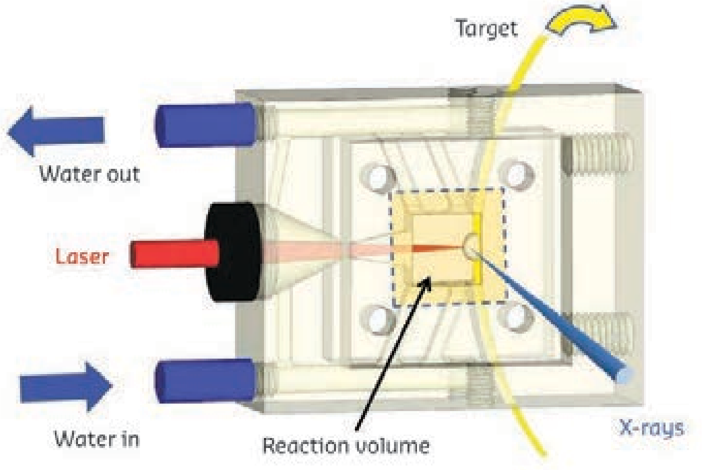

Fig. 65: 3D-printed ablation chamber. The target is confined by polymer foils and it is moved continuously to prevent the laser from melting it.

At beamline **ID09**, small- and wide-angle X-ray scattering (SAXS/WAXS) were used to determine the particle distribution and crystallinity (backed by additional SAXS data from cSAXS at SLS). The diffuse scattering from the surrounding water showed the passage of the explosion shockwave. A miniature chamber was used to refresh the target and liquid continuously during the exposure to the laser and X-ray beam (**Figure 65**). The sample was sufficiently stable to repeat the pump-probe sequence millions of times, which is necessary for capturing extremely weak signals.

The X-ray beam probed the material at a fixed distance above the target (gold and silver ribbons) and probed the ejected particles as a function of laser/X-ray delay. At 0.2 mm above the surface, the expanding water bubble intersected the X-ray beam 6 μs after the excitation with a 1.2 ps laser pulse (see snapshots in **Figure 66**). As the bubble further expanded, the signal dropped. This is followed by a rise upon bubble collapse. This is consistent with the bubble being homogeneously filled with nanoparticles with a particle density inversely proportional to the bubble volume. Importantly, some particles were detected before the bubble arrival. They are crystalline with a large crystallite diametre. This means that the larger particles are not only produced by agglomeration, they are also formed during the initial laser ejection. Indeed, a pioneering simulation has detailed this scenario with laser heating of the target leading to melting, but also sub-surface phase explosion **[4]**. This phase explosion produces atoms, clusters, droplets and a liquid thin film. Rapid rupture and quenching at the liquid–vapour interface leads to large droplets, which quickly crystallise in the high-density water in front of the bubble.

Despite having only a small mass fraction, the large particles can be detrimental for biophotonic applications or catalysis, making monomodal colloid difficult to produce in this way. *In-situ* X-ray measurements with high temporal resolution directly probe the mass distribution and crystallinity of particles formed during laser ablation in liquids, which is essential for understanding the properties of the colloids.

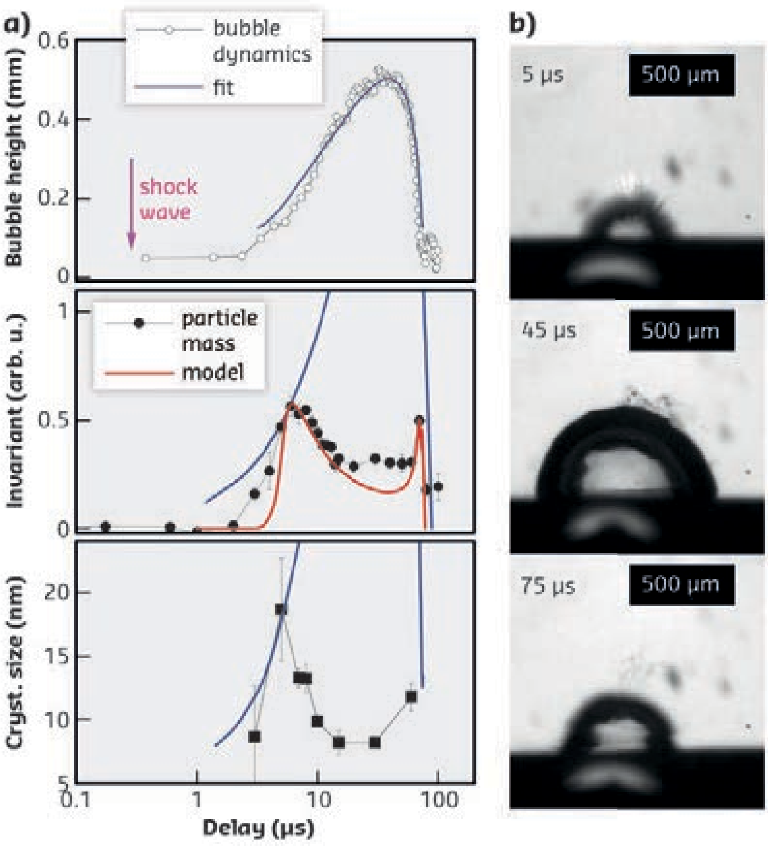

Fig. 66: a) Time-resolved bubble height (top), the particle mass determined from the Porod invariant (middle), and the crystal size distribution from the Scherrer width of the diffraction rings (bottom). The bubble radius is modeled by a parabola (blue line), while the model for particle mass assumes a homogeneously filled bubble at a fixed total particle amount (red line). **b)** Stroboscopic snapshots of the bubble as a function of time.

PRINCIPAL PUBLICATION AND AUTHORS

Early appearance of crystalline nanoparticles in pulsed laser ablation in liquids dynamics, S. Reich (a), A. Letzel (b), A. Menzel (c), N. Kretzschmar (d), B. Gökce (b), S. Barcikowski (b) and A. Plech (a), *Nanoscale* **11**, 6962-6969 (2019); doi: 10.1039/c9nr01203f.
(a) Institute for Photon Science and Synchrotron Radiation, Karlsruhe Institute of Technology (Germany)
(b) Technical Chemistry and CENIDE, University Duisburg-Essen (Germany)
(c) Paul Scherrer Institute, Villigen (Switzerland)
(b) ESRF

REFERENCES

[1] V. Amendola & M. Meneghetti, *Phys. Chem. Chem. Phys.* **15**, 3027-3046 (2013).
[2] D. Zhang *et al.*, *Chem. Rev.* **117**, 3990-4103 (2017).
[3] S. Barcikowski *et al.*, *MRS Bulletin* **44**, 382-391 (2019).
[4] C. Y. Shih *et al.*, *Nanoscale* **10**, 6900-6910 (2018).

RESPONSE OF A RADIO-RESISTANT MELANOMA TO SYNCHROTRON MICROBEAM RADIATION THERAPY (MRT)

With an excellent therapeutic index in a melanoma model, and a high tolerance by normal tissue, MRT, developed at ID17, could be a new therapeutic approach for radio-resistant melanoma. This study demonstrates its potential to disrupt blood vessels, promoting infiltration of the tumour by immune cells, and its induction of senescence.

Synchrotron microbeam radiation-therapy (MRT), a unique method derived from grid radiotherapy and developed at **ID17**, spatially and periodically alternates very high doses (hecto-Gy) by spatial fractionation of the beam into many microbeams. With this technique,

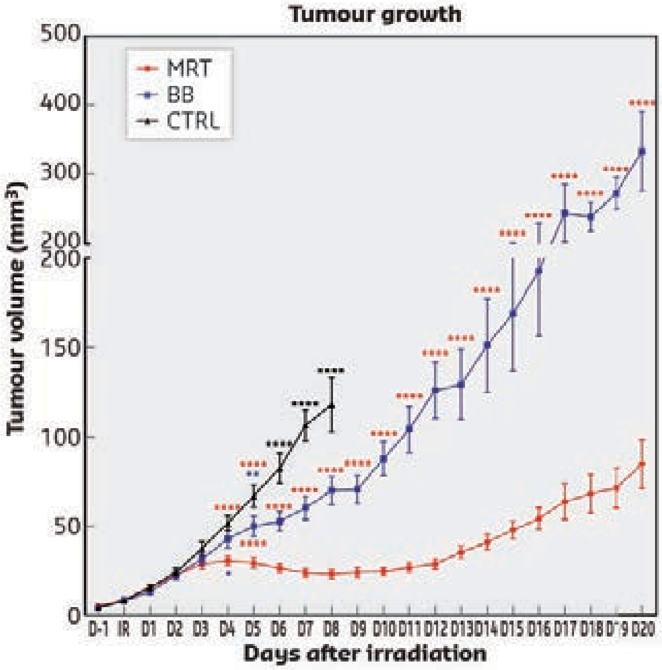

Fig. 67: Effect of irradiations on melanoma regrowth delay. Tumour growth curve after irradiation with MRT (red), BB (blue) or sham-irradiated (black). Red stars: significant difference between MRT and BB or CTRL groups. Blue star: significant difference between BB and CTRL groups. Black stars: significant difference between the CTRL, MRT and BB groups. Mean±SEM; *, $p<0.05$; ****, $p<0.0001$.

the deposition of a high dose within the beam path (peak dose), and lower doses between the microbeams (valley dose), demonstrated high therapeutic efficiency on laboratory animals bearing carcinomas or gliomas **[1]**, while inducing very limited damage to the normal tissue **[2]**. The incidence of melanoma, the most aggressive and particularly treatment-resistant skin cancer, is increasing worldwide. Although melanoma is commonly accepted to be a radio-resistant tumour, radiotherapy can be used as a first-line treatment for inoperable lesions or distant metastases **[3]**. This study sought to evaluate and understand the response of melanoma to MRT.

B16-F10 melanoma locally implanted in mouse ears were irradiated 10 to 11 days after implantation with single synchrotron MRT or broad beam (BB) irradiation. The BB dose (6.2 Gy) was equivalent to the MRT valley dose deposited in tumours (407.6 Gy peak dose and 6.2 Gy valley dose). The tumour follow-up showed significantly better tumour control by MRT with the doubling of the tumour volume time measured as 5.6 days for MRT vs. 3.8 days for BB and 2.1 days for non-treated tumours (**Figure 67**). MRT over BB shows a modification of the intratumoural blood vessel supply (**Figure 68a**). Histological analysis demonstrated a reduction in the number of perfused vessels by 24% at day (D)5 post-irradiation but without modifying the number of or the area occupied by the blood vessels. Moreover, the concentration of VEGF-α decreased after MRT at D9 compared to BB. MRT-irradiated tumours showed a decrease in the cell proliferation index

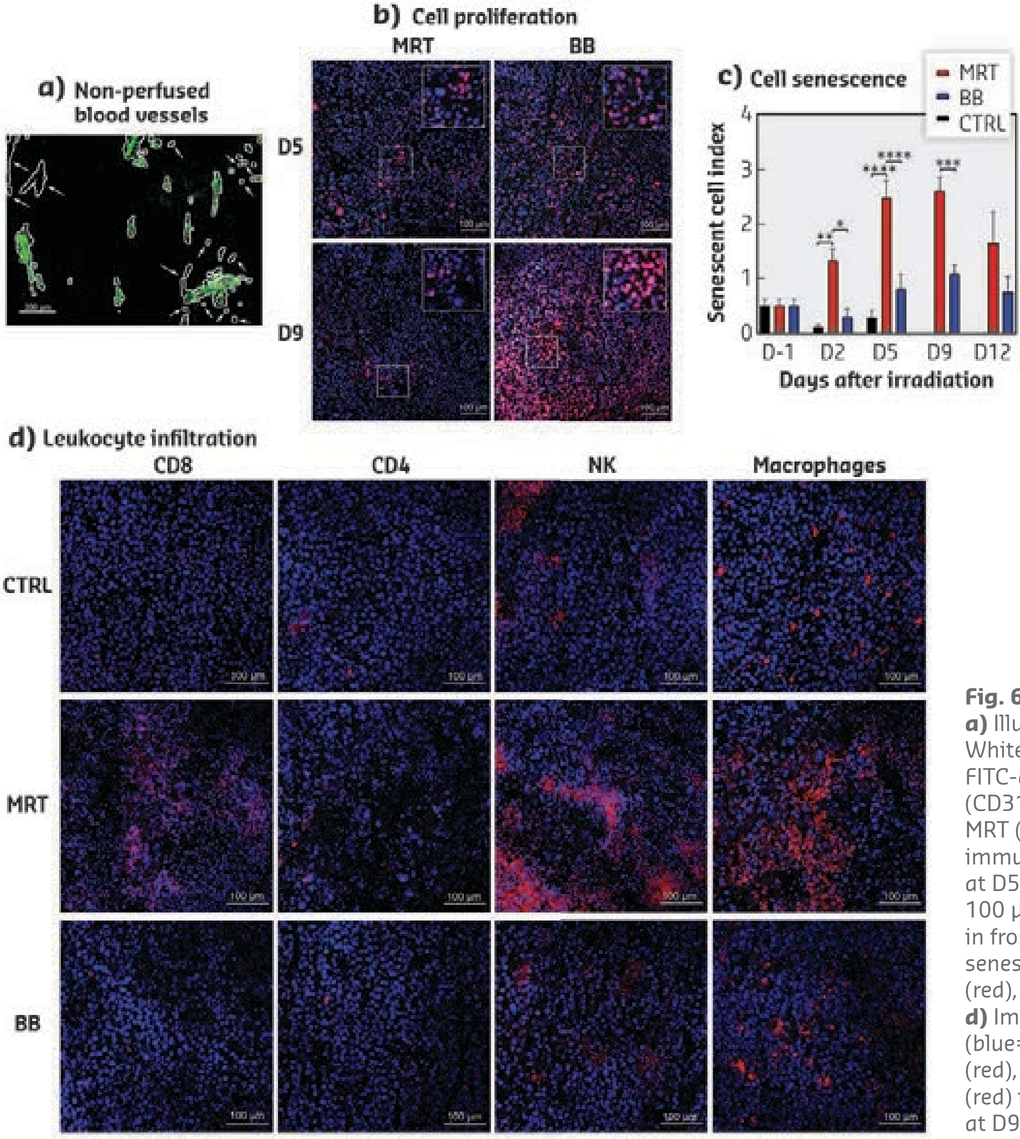

Fig. 68: Effect of MRT on melanoma. **a)** Illustration of perfused blood vessels: White contours: CD31+. Green staining: FITC-albumin+. Arrows: non-perfused vessels (CD31+ and FITC-albumin-). **b)** Images of MRT (left) and BB (right)-irradiated tumours immunostained by KI67 (red) and DAPI (blue) at D5 and D9. Magnification ×20; scale bars 100 μm. Right upper corner squares: zoom in from the indicated areas. **c)** Estimation of senescent cell density per field of view in MRT (red), BB (blue), and control (black) tumours. **d)** Images of immunostained tumour cells (blue=DAPI), CD8 T cells (red), CD4 T cells (red), Natural Killers (red) and macrophages (red) in the control group at D5 (no survivors at D9), and in the MRT and BB groups at D9.

compared to BB with a higher difference (1:4) by D9 (**Figure 68b**). In addition, in MRT-irradiated tumours, the proportion of senescent cells was significantly higher compared to the BB group (**Figure 68c**). Histologic observations have shown an important leukocyte infiltration in the MRT group at D9, attributed mainly to CD8 T cells, Natural Killer cells and macrophages (**Figure 68d**). MRT-irradiated tumours released in their microenvironment a higher amount of cytokines MCP-1 at D5, MIP-1α, MIP-1β, IL12p40 and RANTES at D9 compared to BB-irradiated tumours.

All together, these results suggest that the better tumour control seen after MRT in melanoma is due to: (i) a reduction in the tumour blood supply by vascular disruption and occlusion, leading to (ii) an entrance site for circulating inflammatory and immune cells; (iii) a decrease of the proliferation index, associated with a high tumour senescence, and (iv) a secretion of cytokine, produced by senescent cells, that initiate infiltration of different type of immune cells such as T cells, NK and macrophages, which are involved in the clearance of senescent cells and thus contribute to tumour control.

PRINCIPAL PUBLICATION AND AUTHORS

Synchrotron Microbeam Radiation Therapy as a New Approach for The Treatment of Radioresistant Melanoma: Potential Underlying Mechanisms, M. Potez (a), C. Fernandez-Palomo (a), A. Bouchet (a,b), V. Trappetti (a), M. Donzelli (c,d), Mattia Donzelli (c,d), M. Krisch (c), J. Laissue (a), V. Volarevic (e) and V. Djonov (a), *Int. J. Radiat. Oncol. Biol. Phys.* **105**(5), 1126-1136 (2019); doi: 10.1016/j.ijrobp.2019.08.027.

(a) Institute of Anatomy, University of Bern (Switzerland)
(b) Synchrotron Radiation for Biomedicine, INSERM UA7, Grenoble (France)
(c) ESRF
(d) Joint Department of Physics, The Institute of Cancer Research and the Royal Marsden Hospital, London (UK)
(e) Faculty of Medical Sciences, University of Kragujevac (Serbia)

REFERENCES

[1] L. Eling *et al.*, *Radiother. Oncol.* **139**, 56-61 (2019).
[2] M. Potez *et al.*, *Int. J. Radiat. Oncol. Biol. Phys.* **101**, 680-689 (2018).
[3] A. Mahadevan *et al.*, *Oncology (Williston Park)* **29**, 743-751 (2015).

DIRECT EVIDENCE OF SMALL AIRWAY CLOSURE IN ACUTE RESPIRATORY DISTRESS SYNDROME

Airway closure is thought to play an important role in acute respiratory distress syndrome (ARDS). Airway closure has been imaged for the first time in an ARDS model by synchrotron phase-contrast imaging, providing direct evidence of this phenomenon.

ARDS is an acute inflammatory lung condition associated with high permeability oedema, surfactant dysfunction and widespread collapse of pulmonary alveoli, called atelectasis, which leads to decreased lung compliance and volume **[1]**. Clinicians have long suspected that the collapsibility of small airways is increased in this clinical syndrome, causing atelectasis **[2,3]**. While patients invariably require mechanical ventilation to survive, this life support measure can worsen lung injury due to exaggerated stress and strain applied to the tissue, which is magnified by mechanical inhomogeneity of lung tissue and atelectasis. Efforts to develop ventilation strategies that protect the lung depend on understanding the mechanical behaviour of lung tissue and airways at the microscale. However, traditional computed tomography (CT) studies have not been able to clearly identify airway closure as a cause of atelectasis, due to limited spatial resolution. To better identify the mechanisms involved in airway closure, it is necessary to study individual airways. Here, the same individual small airways

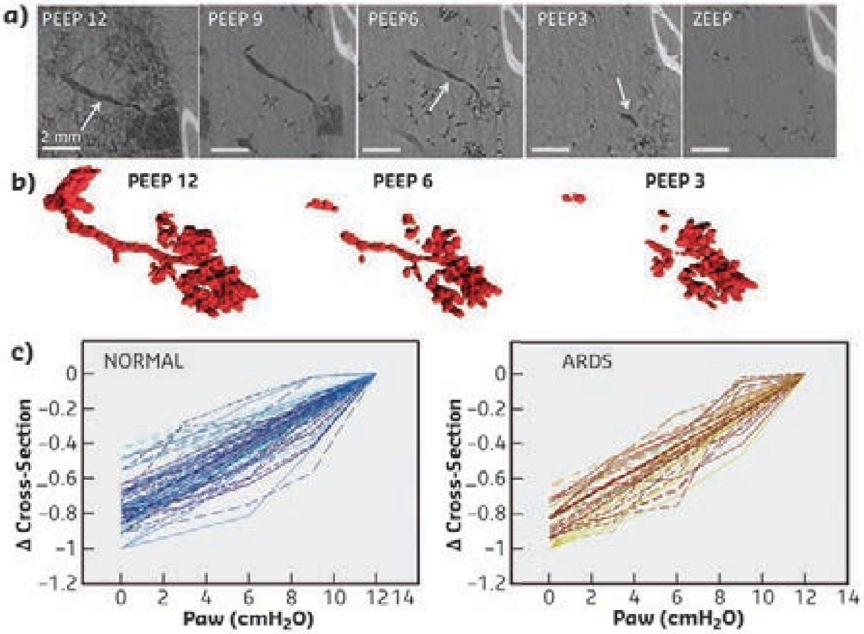

Fig. 69: CT slices **(a)** and 3D rendering of a single terminal airway **(b)** demonstrating closure as airway pressure is reduced. *PEEP*: positive end-expiratory pressure, *ZEEP*: zero end-expiratory pressure. **c)** Relative change in cross-sections of matched individual airways versus airway pressure (*Paw*), in normal (*Left*, n = 48) and ARDS (*Right*, n = 32) lungs. ΔCS: change in airway cross-section.

in intact lungs of anesthetised and mechanically ventilated rabbits with ARDS were studied using high-resolution synchrotron phase-contrast computed tomography at beamline **ID17**.

Propagation-based phase-contrast CT imaging was performed with a 47.5 μm^3 voxel size, at positive end-expiratory pressures (PEEP) of 12, 9, 6, 3 and 0 cmH_2O. The imaging sequence was repeated after lung injury induced by surfactant depletion through whole lung lavage and high-tidal volume mechanical ventilation in anesthetised rabbits. Cross-sections of the same individual airways were measured (**Figure 69**). Airway collapsibility increased in the injured lung with a significantly faster drop in airway cross-section as airway pressure decreased in small airways ranging between 210 – 1690 μm in radius at 12 cmH_2O.

The main mechanism of airway closure in initially patent airways in ARDS was identified as 'compliant collapse' (**Figure 69a**). Theoretical studies suggest that this mechanism involves an instability in the thickness of the fluid lining layer of the airway wall. Where this fluid layer thickens, the compressive forces that are generated cause a buckling of the airway wall that can lead to the collapse of the airway lumen along a certain length. Moreover, the analysis of airway cross-sections vs. length revealed that closure can occur at more than one site, sometimes leading to gas trapping and distension of the lumen (**Figure 70**).

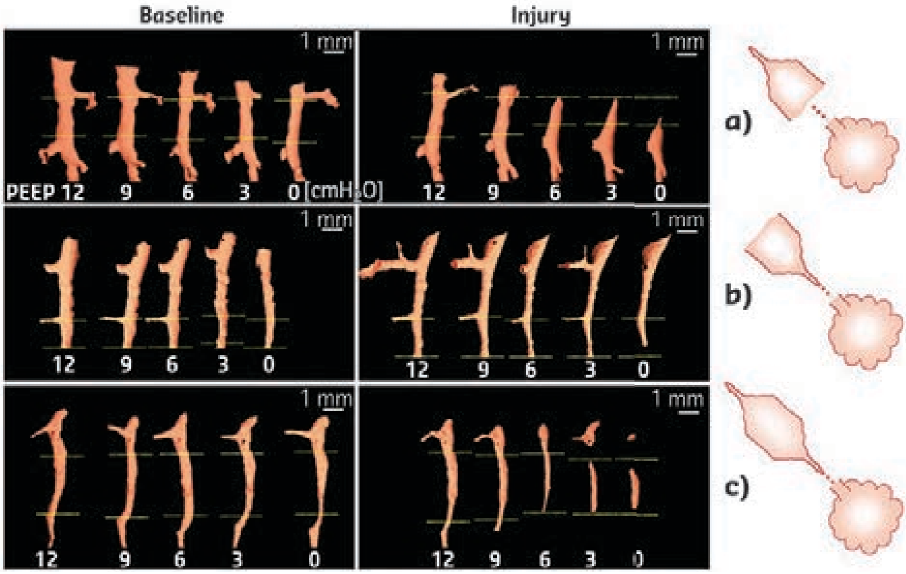

Fig. 70: Examples of matched airways at baseline (*left*) and following lung injury (*right*) demonstrating different locations of airway collapse with respect to the studied segment delineated by the red dotted lines. 3D-rendered airways reoriented for better visibility. Interpretation: **a)** Airway closure occurs upstream to the measured segment. **b)** Closure of the downstream end of the studied segment. **c)** Closure in two locations causing trapping of air within the lumen of the studied segment.

Evidence of compliant collapse of airways in ARDS is indicated by the involvement of fluid layer movements at the microscopic level. This suggests that airway closure and reopening is not merely dependent on critical opening and closing pressures but is also a highly dynamic, time-dependent phenomenon **[4]**. This may have implications for patients with ARDS under mechanical ventilation. Strategies aiming at reducing the time during which respiratory pressure is lowered during the breathing cycle may help prevent airway closure.

This study also underscores the need for further development of fast, high-resolution imaging techniques to dynamically image lung tissue mechanics at the microscale **[5]**, ideally within the time span of a breath. The crucial link between microscopic lung tissue strain, and initiation and maintenance of inflammation, which leads to high mortality levels in ARDS patients, is still to be investigated, and dynamic X-ray tomography with synchrotron sources promises to pave the way.

PRINCIPAL PUBLICATION AND AUTHORS

Individual airway closure characterized In vivo by phase-contrast CT imaging in injured rabbit lung, L. Broche (a,b), P. Pisa (c), L. Porra (d,e), L. Degrugilliers (f), A. Bravin (b), M. Pellegrini (a), J. B. Borges (a), G. Perchiazzi (a), A. Larsson (a), G. Hedenstierna (a) and S. Bayat (g,h). *Crit. Care Med.* **47**, e774-e781 (2019); doi: 10.1097/ccm.0000000000003838.

Further permissions related to the material should be directed to Wolters Kluwer.

(a) Hedenstierna Laboratory, Department of Medical Sciences, Uppsala University (Sweden)
(b) ESRF
(c) University of Picardie Jules Verne Medical Faculty, Amiens (France)
(d) Department of Physics, University of Helsinki (Finland)
(e) Helsinki University Central Hospital Medical Imaging Center (Finland)
(f) Department of Pediatric Intensive Care, Amiens University Hospital (France)
(g) University of Grenoble Alpes & Inserm UA7 STROBE Laboratory (France)
(h) Department of Pulmonology and Physiology, Grenoble University Hospital (France)

REFERENCES

[1] M. A. Matthay & G. A. Zimmerman, *Am. J. Respir. Cell Mol. Biol.* **33**, 319-327 (2005).
[2] G. Hedenstierna & G. S. McCarthy, *Acta Anaesthesiol. Scand.* **24**, 299-304 (1980).
[3] J. E. Baumgardner, *Crit. Care Med.* **47**, 1281-1282 (2019).
[4] L. Broche *et al., Crit. Care Med.* **45**, 687-694 (2017).
[5] L. Fardin *et al., Eur. Respir. J.* **52**, PA851 (2018).

MAY THE FORCE BE WITHIN GEL

Hydrogels with adaptive mechanical properties are excellent materials to capture the dynamic nature of life. This work introduces an interpenetrating network that demonstrates a sharp, intense and reversible stiffening response to a minor change in the environment. Small-angle X-ray scattering (SAXS) experiments were essential to elucidate the mechanism of internal force transfer.

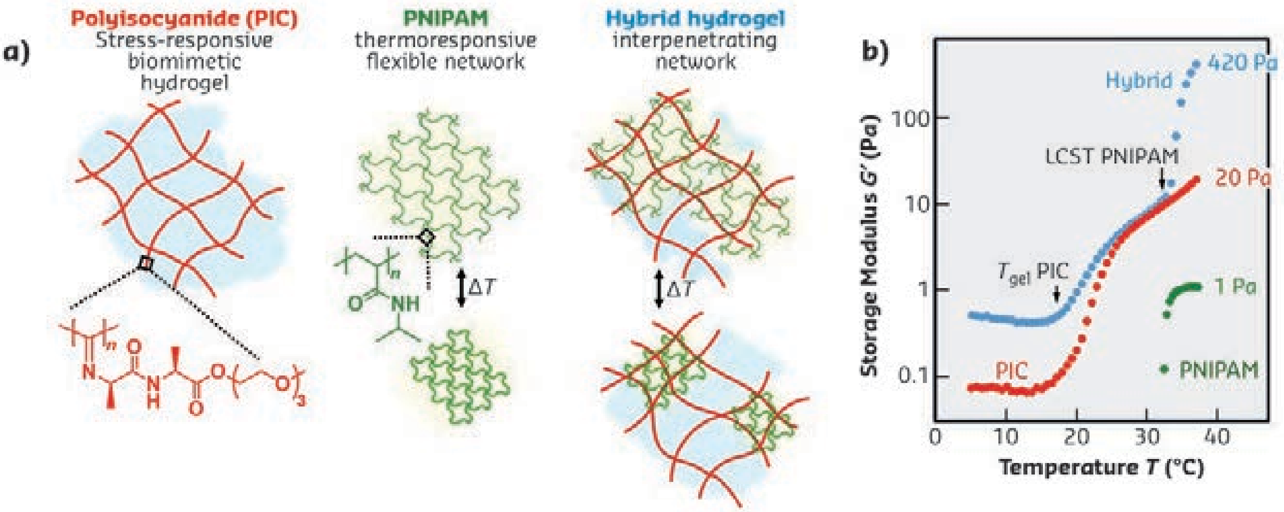

Fig. 71: a) Interpenetrating network composed of PIC (red) and PNIPAM (green). **b)** Heating the hybrid hydrogel stiffens the network at temperatures above the lower critical solution temperature (LCST) of PNIPAM.

Nature uses mechanical cues for a broad variety of cellular processes. While it is acknowledged that the stiffness of the cell's surroundings are crucial for their development **[1]**, the mechanical properties of naturally occurring gels are far from constant; many tissues soften or stiffen due to degradation, disease development or contraction, for instance muscles **[2]**. Although the spectrum of life-like hydrogels with stimuli-responsive properties is expanding **[3]**, capturing these adaptive mechanical properties *in vitro* is still quite challenging. This work reports the development of a synthetic hydrogel based on polyisocyanides (PIC) that uniquely mimics the mechanical properties of biological gels **[4]**. Gel formation is thermally induced through the assembly of polymer chains into bundles (**Figure 71a**) **[5]**. The resulting network is stress-stiffening (*i.e.*, the hydrogel displays a striking increase in the stiffness when stressed).

An interpenetrating network was designed, composed of PIC and the thermoresponsive poly(*N*-isopropylacrylamide) (PNIPAM) (**Figure 71a**). A minute change in the temperature collapses the PNIPAM network (**Figure 71a**), transferring the forces of the collapsing chains onto the PIC network. This internal stress triggers the stress-stiffening response, resulting in a sharp and vast increase of the storage modulus (*G*') of more than 10 times (**Figure 71b**). The stiffening response is completely reversible and controlled by the hydrogel composition. The transition temperature can be tuned as desired. Moreover, quantification of the generated forces shows remarkable similarities with internally stressed networks of actin and myosin motors, the building blocks responsible for the contraction of skeletal muscles.

SAXS experiments at **BM26** made it possible to elucidate the mechanism of force transduction (**Figure 72**). Scattering of the interpenetrating network was dominated by the contribution of the PIC network. Data was collected at temperatures in which the PNIPAM network is swollen ($T = 30$ °C) and collapsed ($T = 40$ °C). The data was then fitted to a composite model that combines the scattering contribution of the PIC bundles (Kholodenko's wormlike chain model) **[6]** and of the network (using the phenomenological correlation length model).

$$I(q) = I_{bundles}(q) + I_{network}(q)$$

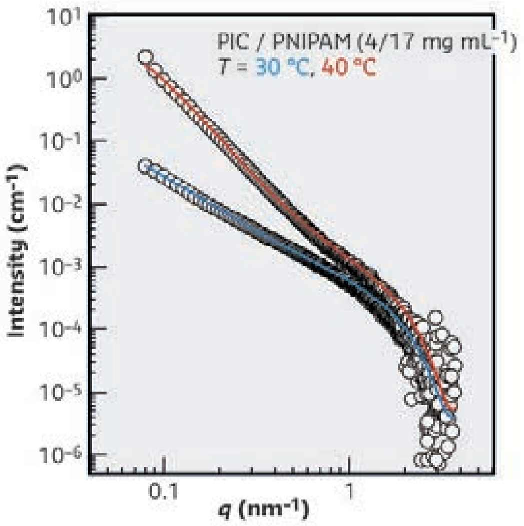

Fig. 72: SAXS profiles of PIC networks at $T = 30$ °C (blue) and $T = 40$ °C (red) with PNIPAM contributions subtracted and best fit using the composite models (lines).

Fitting the curves reveals that the PIC network becomes denser (increase in the Porod exponent *p*) and the average pore size (ξ) decreases with PNIPAM collapse. The results confirm that, indeed, the conformational changes of the PNIPAM network internally stress the PIC network and subsequently induce the large stiffening response.

PRINCIPAL PUBLICATION AND AUTHORS

Cytoskeletal stiffening in synthetic hydrogels, P. de Almeida (a), M. Jaspers (a), S. Vaessen (a), Oya Tagit (b), G. Portale (c), A. E. Rowan (a,d) and P. H. Kouwer (a), *Nat. Commun.* **10**, 609 (2019); doi: 10.1038/s41467-019-08569-4.

(a) Institute for Molecules and Materials, Radboud University, Nijmegen (The Netherlands)
(b) Dept of Tumor Immunology, Radboud UMC, Nijmegen (The Netherlands)
(c) Zernike Institute for Advanced Materials, University of Groningen (The Netherlands)
(d) Australian Institute for Bioengineering and Nanotechnology, University of Queensland (Australia)

ACKNOWLEDGEMENTS

The NWO provided and supported beam time (grants BM26-02773 and BM26-02824). This project has received funding from the EU's Horizon2020 research and innovation program under the Marie Skłodowska-Curie grant agreement No 642687 (BIOGEL) and from the Dutch Ministry of Education, Culture and Science (Gravity program 024.001.035).

REFERENCES

[1] D. E. Discher *et al., Science* **310**, 1139-1143 (2005).
[2] A. M. Hilderbrand *et al., Curr. Opin. Solid State Mater. Sci.* **20**, 212-224 (2016).
[3] M. C. Koetting *et al., Mater. Sci. Eng. R: Rep.* **93**, 1-49 (2015).
[4] P. H. Kouwer *et al., Nature* **493**, 651-655 (2013).
[5] M. Jaspers *et al., Biomacromolecules* **17**, 2642-2649 (2016).
[6] A. L. Kholodenko, *Macromolecules* **26**, 4179-4183 (1993).

STRUCTURAL DYNAMICS OF ASSEMBLING GOLD NANOPARTICLES

The formation mechanism of polymer-coated gold nanoparticles during hydrophobic collapse and clustering was studied *in situ* using time-resolved small-angle X-ray scattering (TR-SAXS). The results provide insights into the interaction energies between particles and their polymer shell dynamics during rapid solvent mixing.

Solvent-induced self-assembly of nanoparticles, driven by hydrophobic interactions in a liquid phase, is a convenient strategy to fabricate complex architectures in a bottom-up fashion. Polystyrene-stabilised gold nanoparticles (Au@PS) of different shapes have been used to build a

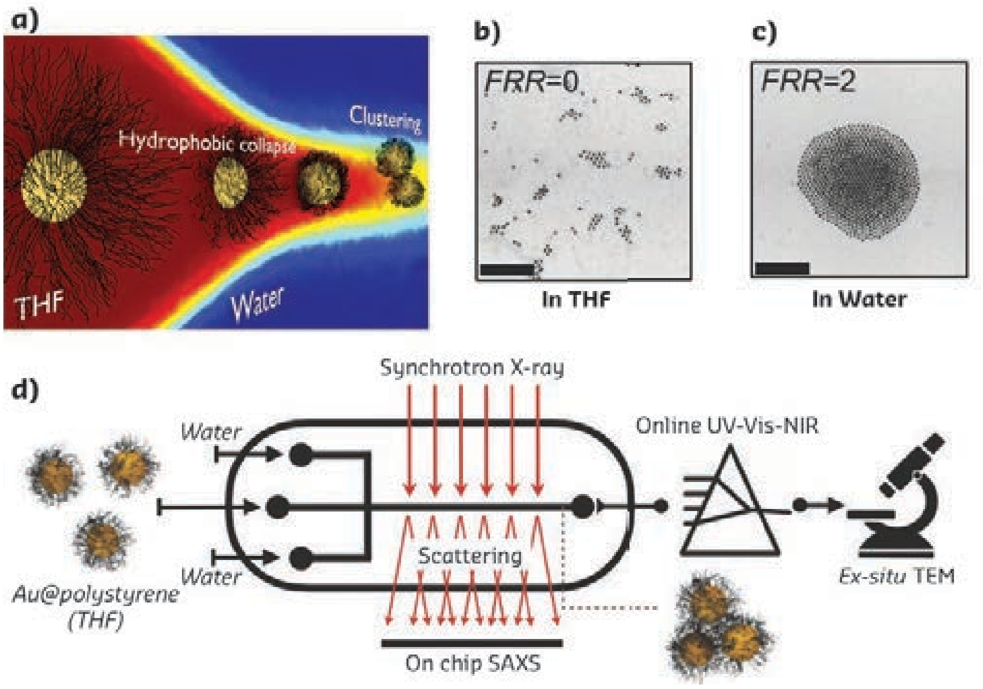

Fig. 73: a) Illustration of polystyrene-coated gold nanoparticles (Au@PS) undergoing a solvent-induced hydrophobic collapse triggered by microfluidic rapid mixing. **b-c)** Transmission electron micrographs of Au@PS (diameter ~25 nm) in **(b)** THF (good solvent) and **(c)** water (poor solvent). Scale bars: 500 nm. **d)** Design of a 3D flow-focusing reactor for studying nanoparticle self-assembly. Au@PS in THF undergo clustering upon mixing with water in a Kapton-based hydrodynamic 3D flow-focusing reactor. Real-time UV−Vis−NIR spectroscopy collects the optical properties of the assemblies at the reactor outlet. On-chip SAXS analysis along the channel (orthogonally to the flow and the lateral focusing directions) allows time-resolved structural changes of the polymer shell and clustering nanoparticles upon mixing to be determined.

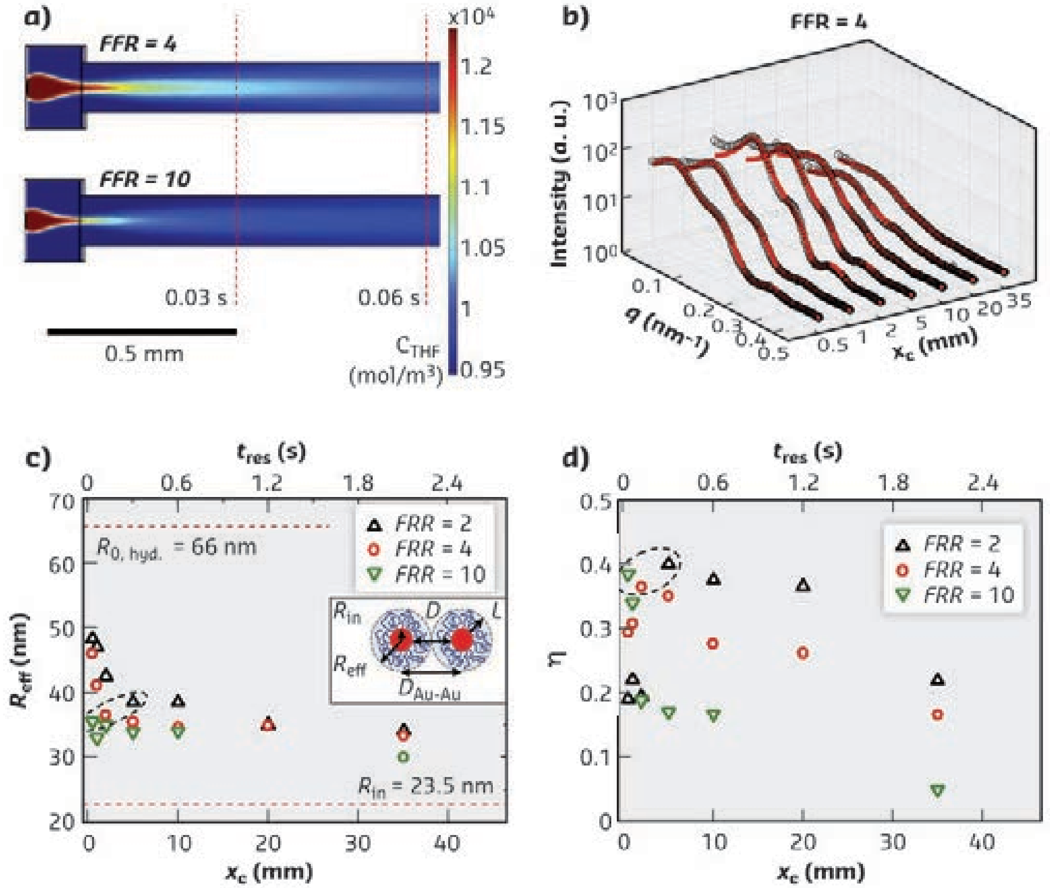

Fig. 74: a) Top view of the longitudinal cross-section of a simulated distribution of THF concentration in the channel. The total flow rate was kept constant (Q_{tot} = 900 µL/h) while the flow rate ratio (FRR) of H_2O:[AuNP]:H_2O was varied between 2 = 1:1:1, 4 = 2:1:2 and 10 = 5:1:5. **b)** Scattering curves of flow-focused Au@PS obtained at various downstream channel positions x_c. The time window corresponds to t_{min} = 4.8 ms ≤ t ≤ t_{max} = 2.8 s. The black circles correspond to the data points while red curves correspond to a fitting model for disordered hard sphere assemblies (Percus-Yevick). **c-d)** Temporal evolution of the effective particle radius R_{eff} **(c)** and the hard sphere volume fraction η **(d)** along the microfluidic channel at FRR = 2, 4, and 10, respectively. Both fit parameters reach an onset (dashed circles), indicating a fast collapse of the polymer shell.

variety of structures including spherical clusters, dynamic chain-like assemblies, vesicles, or low-symmetry dimers. Since the major part of these architectures are kinetic products, their structure and quality depends on the way the non-solvent (water) is added to a dispersion of nanoparticles, which are coated with a radially distributed polymer shell in a good solvent such as dimethylformamide (DMF) or tetrahydrofuran (THF). It has been reported that water addition induces 'hydrophobic collapse', a transition from random coil to compact globule of the grafted polymer, which eventually leads to the formation of regio-specific polymeric patches or compact shells on the surface of the inorganic cores. Although the hydrophobic collapse of grafted polymers is understood at a single molecule level, it remains poorly investigated in colloidal systems during the self-assembly process. Of particular relevance are how fast the polymer shell collapses and how fast the particles agglomerate in reaction to this effect.

To study the dynamics of surface phenomena and self-assembly in response to environmental changes *in situ*, several requirements should be met: ensuring reproducible and controllable solvent mixing (water, THF); knowing the exact concentration of solvents and nanoparticles; and implementing real-time analytics. X-ray compatible microfluidic devices with 3D-hydrodynamic flow-focusing geometries (**Figure 73d**) provide a suitable experimental environment to meet the above requirements **[1,2]**. In this work, the combination of X-ray microbeam scanning and diffusive mixing along the continuous laminar flow was used for the collection of time-resolved SAXS data at beamline **ID02** (**Figure 74b**). This data was complemented by additional techniques to resolve the dynamics of the solvent-induced self-assembly of polystyrene-coated gold nanoparticles. On-chip SAXS analysis of the entire channel of the reactor provides information on the hydrophobic shell collapse, demonstrating that the thiol-terminated polystyrene of 53 kg/mol grafted on gold nanoparticle surfaces experiences relatively fast collapse within the range of 100-500 nm/s. The knowledge of the dynamics of the polymer shell and the amount of water at each point of the channel made it possible to estimate the energy potential of the interacting nanoparticles. It was found that the aggregation process of Au@PS nanoparticles starts once the polymer shells are fully collapsed. These findings support the idea that either kinetically trapped small clusters or larger aggregates can be obtained by the rate of solvent mixing, since the mixing rate determines the interaction potential landscape during solvent-induced gold nanoparticle self-assembly.

PRINCIPAL PUBLICATION AND AUTHORS

Time-Resolved Analysis of the Structural Dynamics of Assembling Gold Nanoparticles, S. Merkens (a,b), M. Vakili (b), A. Sánchez-Iglesias (c), L. Litti (d), Y. Gao (e), P. V. Gwozdz (f), L. Sharpnack (g), R. H. Blick (f), L. M. Liz-Marzán (c,h), M. Grzelczak (h,i) and M. Trebbin (j,b), *ACS Nano* **13**, 6596-6604 (2019); doi: 10.1021/acsnano.9b0057.5

(a) CIC nanoGUNE, Donostia - San Sebastián (Spain)
(b) The Hamburg Centre for Ultrafast Imaging (CUI), University of Hamburg (Germany)
(c) CIC biomaGUNE and CIBER-BBN, Donostia - San Sebastián (Spain)
(d) Dipartimento di Scienze Chimiche, Univerisità degli Studi di Padova (Italy)
(e) Max Planck Institute for the Structure and Dynamics of Matter, Hamburg (Germany)
(f) Center for Hybrid Nanostructures (CHyN), University of Hamburg (Germany)
(g) ESRF
(h) Ikerbasque, Basque Foundation for Science, Bilbao (Spain)
(i) Donostia International Physics Center (DIPC), Donostia - San Sebastián (Spain)
(j) Department of Chemistry, State University of New York at Buffalo (USA)

REFERENCES

[1] S. With *et al.*, *Langmuir* **30**(42), 12494-12502 (2014).
[2] M. Vakili *et al.*, *Langmuir* **35**(32), 10435-10445 (2019).

CATIONIC GOLD NANOPARTICLES INTERACTING WITH LIPID MEMBRANES: A MODEL FOR THE NANO-BIO INTERFACE

The poor understanding of the effects of nanomaterials on biological interfaces is recognised as one of the major challenges limiting nanomedicine. X-ray reflectivity (XRR) and confocal microscopy experiments were combined with computational simulations to unveil the interaction of cationic gold nanoparticles with synthetic lipid bilayers, a mimic of plasma membrane.

Fundamental experimental and theoretical studies simulating the interaction of nanomaterials with biorelevant interfaces represent a valuable approach to improving knowledge in the field and deriving general concepts **[1-3]**. The aim of this study was to merge experimental evidence obtained by XRR, confocal microscopy and fluorescence correlation spectroscopy (FCS) with computer simulations (molecular dynamics, MD) to describe the interaction of cationic gold nanoparticles (AuNPs) with lipid membranes composed of a 1:1 mixture of zwitterionic/anionic phospholipids, both from a structural and dynamical perspective.

Figure 75a shows the confocal microscopy images of the lipid membrane before (upper panel) and after (lower panel) incubation with AuNPs. The effect of AuNPs on the lipid membrane is a decrease in the homogeneity of the label distribution, which is attributable to the formation of areas where the membrane integrity is lost. In order to obtain specific information about the effect of the AuNPs on the structure of the lipid bilayer at a nanometric length scale, XRR was performed at **ID03**. **Figure 75b** shows the XRR curves measured on the supported lipid bilayer before (green curve) and after (purple curve) incubation with AuNPs. Thanks to the sensitivity of the technique to the interfacial features of the membrane, it was possible to measure a decrease in the thickness and increase of roughness of the membrane upon the addition of AuNPs, as highlighted by the scattering length density profile

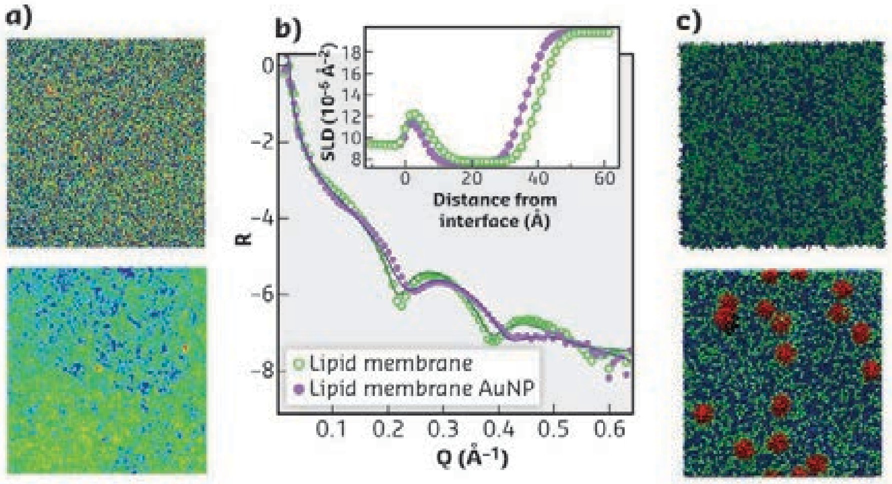

Fig. 75: Structural effects of AuNPs on the lipid membrane. **a)** Confocal microscopy images. **b)** XRR curves. **c)** MD simulations.

Fig. 76: Dynamical effects of AuNPs on the lipid membrane. **a)** FCS curves. **b)** MD trajectories of the AuNP and POPG reported with planar velocity vectors (black arrows). **c)** Lateral section of a AuNP interacting with a 1:1 POPG:POPC bilayer.

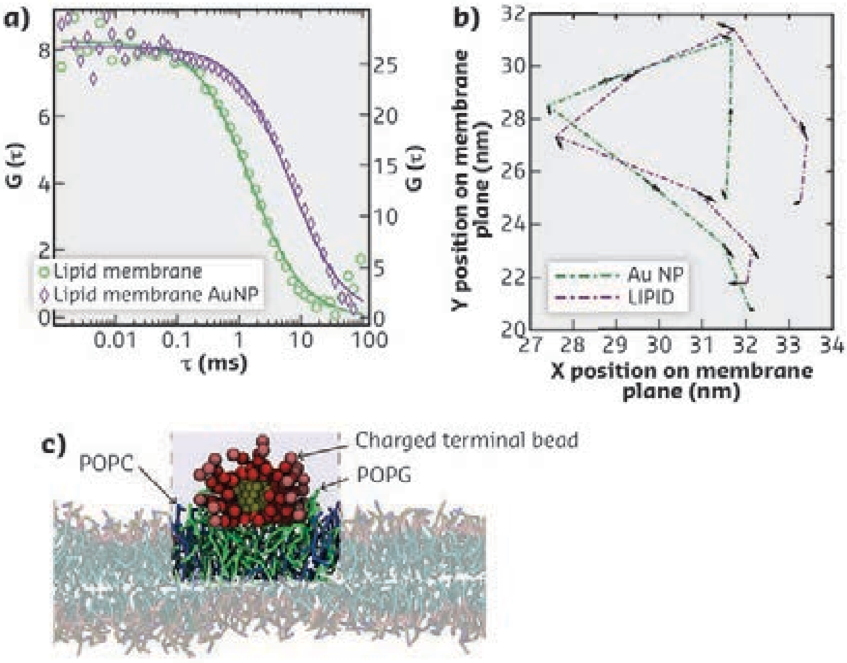

along the surface normal (**Figure 75b**, inset). This result confirms confocal microscopy data and suggests that strong interaction between the AuNPs and the target lipid membrane occurs, leading to lipid extraction from the bilayer and localised membrane disruption phenomena.

MD was used as complementary tool to investigate at the molecular level the structural and dynamic properties of AuNPs at the interface with the lipid bilayer. To this aim, the same experimental composition of lipids was simulated. **Figure 75c** shows the top view of mixed lipid membrane, in particular the distribution of the zwitterionic lipid POPC (blue) and the anionic lipid POPG (green), before (upper panel) and after (lower panel) addition of AuNPs (red). The adhesion of AuNPs to the lipid membrane, which is mainly driven by electrostatic interactions and entropic contributions, leads to a lateral phase separation of the membrane, with formation of negatively charged patched areas enriched with the anionic lipid in correspondence to the AuNP adhesion point. These negatively charged areas of the membrane attract other AuNPs, promoting the formation of clusters on the lipid membrane, ultimately leading to lipid extraction and membrane disruption phenomena experimentally highlighted through XRR and confocal microscopy experiments.

It was also possible to assess the effects of the AuNPs on the fluidity of the lipid membrane, whose variation, in real cell membranes, is important in several biologically relevant phenomena, as cell trafficking. FCS was used to track the diffusion of a lipid fluorescent dye embedded in the lipid membrane (**Figure 76a**). The FCS curves measured in free-standing lipid membranes before (green curve) and after (purple curve) incubation with AuNPs highlight a significant decrease in the diffusion coefficient of the fluorescent lipid upon interaction with AuNPs, consistent with an increased rigidity of the lipid membrane. MD simulations explain the origin of this effect. The trajectories of the AuNPs and of the anionic POPG lipid in correspondence to the AuNP adhesion point (**Figure 76b**) show that the diffusion of the anionic lipids is linked to that of the adhered AuNPs; the presence of this 'slaved' diffusion is consistent with a local increased lateral rigidity of the membrane.

Figure 76c offers a visual aid to understand the mechanics of this phenomenon. The image shows a lateral section of the bilayer upon AuNP adhesion: when the AuNP approaches the membrane, the lipids start to tilt, to maximise the interaction with the AuNP capping agent. The lipid assemblies below the adhered AuNP assume a conical shape to better host the AuNP. Interestingly, the whole conical structure follows the motion of the adhered AuNPs.

The combination of theoretical and experimental studies on the interaction of NPs with biomimetic systems is a valuable approach to derive basic concepts on nano-bio interfaces, which might contribute to improving fundamental knowledge on this topic.

PRINCIPAL PUBLICATION AND AUTHORS

Nanoparticles at Biomimetic Interfaces: Combined Experimental and Simulation Study on Charged Gold Nanoparticles/Lipid Bilayer Interfaces, T. Pfeiffer (a), A. De Nicola (b), C. Montis (c), F. Carlà (d), N. F. van der Vegt (a), D. Berti (c) and G. Milano (b), *J. Phys. Chem. Lett.* **10**, 129-137 (2019); doi: 10.1021/acs.jpclett.8b03399.

(a) Eduard-Zintl-Institut für Anorganische und Physikalische Chemie, Technische Universität Darmstadt (Germany)
(b) Department of Organic Materials Science, Yamagata University (Japan)
(c) Department of Chemistry "Ugo Schiff" and CSGI, University of Florence (Italy)
(d) ESRF

REFERENCES

[1] C. Montis *et al.*, *Nanoscale* **6**, 6452-6457 (2014).
[2] C. Montis *et al.*, *J. Colloid Interface Sci.* **516**, 284-294 (2018).
[3] M. Mendozza *et al.*, *Soft Matter* **15**, 8951-8970 (2019).

IN-SITU X-RAY SCATTERING REVEALS INSIGHTS INTO THE FORMATION OF CdSe NANOPLATELETS

CdSe nanoplatelets are flat nanoparticles with unique light-absorbing and -emitting features but their formation mechanism was still unknown. Using time-resolved small- and wide-angle X-ray scattering (SAXS/WAXS), it is possible to discriminate between the different anisotropic growth schemes and to show that the nanoplatelets grow in a curved fashion.

Colloidal semi-conducting nanoplatelets (NPL) are thin 2D nanoparticles that display outstanding optical properties (**Figure 77a**). The extreme quantum confinement occurring along their thickness, controlled at the atomic level in the nanometre range, yields a monochromatic emission at tunable wavelengths, giant oscillator strength and record low lasing threshold. However, the mechanism by which these NPL form in solution from molecular precursors was unknown. Organometallic precursors of cadmium and selenium were mixed in a solvent and heated to temperatures ranging from 150 to 250°C. Several hypotheses have been proposed in the literature such as a soft templating effect, in which nucleation and growth is circumscribed in the confined space of a surfactant meso-phase. Another possible pathway is the anisotropic assembly of small spherical nanoclusters into NPL, where many small clusters first form in solution and then ripen and restructure to yield crystalline NPL. The last mechanism is anisotropic growth, where initial seeds grow through the addition of monomers in an anisotropic fashion due to a kinetic instability. In order to prove or disprove these different hypotheses, the structure of the solution during the formation of the NPLs needed to be probed *in situ*. This is a difficult task since the formation occurs over a few minutes, at high temperatures and with length scales spanning from atomic distances for the crystalline structure to hundreds of nanometres for the lateral dimensions of the NPL.

The SAXS/WAXS set-up at beamline **ID02** was used for these experiments. A heating method for the synthesis of NPL was devised, consisting of mixing Cd and Se precursors and heating them in octadecene to the desired temperatures. SAXS and WAXS patterns were acquired *in situ* during the nucleation and growth of the NPL. The evolution of the SAXS patterns indicate that as the temperature increases, the precursors first solubilise since the intensity at low q decreases. After a few minutes, the scattered intensity increases, marking the onset of particle formation. When the particles start to form, there is no sign of a molecular template in the SAXS patterns (*e.g.*, as scattering peaks). As the temperature further increases, the SAXS signal changes and a straight line with a q^{-2} slope appears at intermediate wave vectors (**Figure 78a**). This exponent is the signature of 2D objects in solution. Furthermore, this q^{-2} regime extends towards smaller and smaller q with time, showing an increase in the lateral dimensions of the flat objects. In order to find out if the flat shape is due to anisotropic ripening of nuclei or 2D growth from solution, a typical SAXS signal was calculated, showing what would have been observed if CdSe in the NPL was present in solution as small spherical nuclei. It was concluded, from the absence of this signal, that growth occurs through the addition of monomers from solution.

When the temperature was decreased from 200°C to 170°C, the same sequence of events

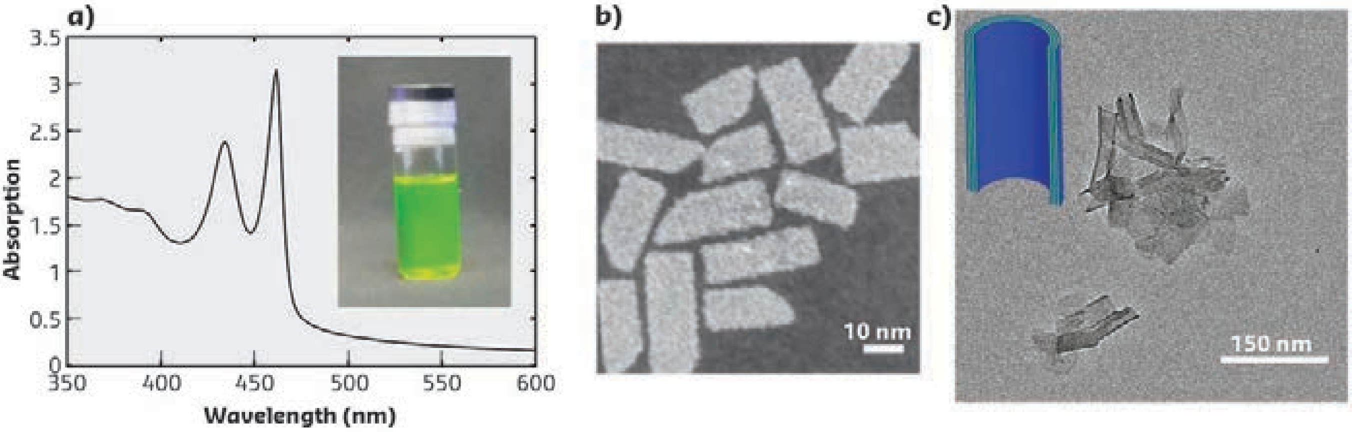

Fig. 77: a) Absorbance spectrum of CdSe nanoplatelets and photograph of the luminescence under UV irradiation. Electron microscopy image of **(b)** flat and **(c)** bent NPL.

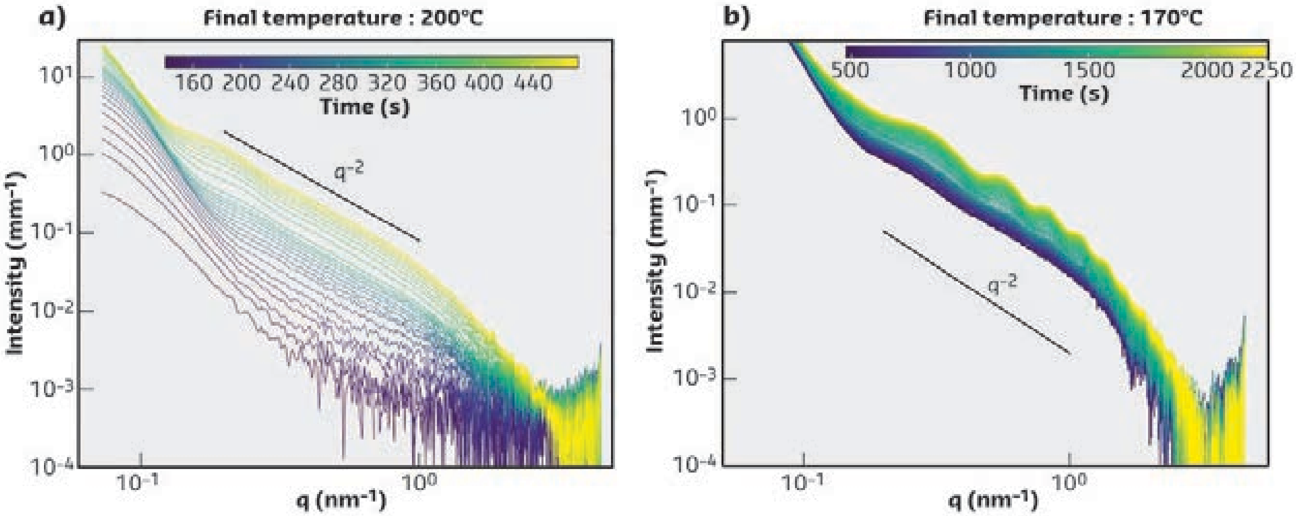

Fig. 78: Time series of SAXS pattern during the NPL nucleation and growth **(a)** for a final temperature of 200°C and **(b)** for a final temperature of 170°C.

occurred: solubilisation of the precursors and onset of 2D growth seen through the extension of a q^{-2} regime. Surprisingly, oscillations in the SAXS intensity appear in a reproducible fashion instead of the straight line observed for higher temperature (**Figure 78b**). These oscillations are due to the bending of the NPL in a scroll-like fashion (**Figure 77c**). Under the effect of the surface stress imposed by the ligands at the nanocrystal–solution interface, the NPL relaxes by adopting a bent configuration. The evolution of the oscillation position with time indicates that the radius of curvature is constant. As the NPL grow and reach a lateral dimension of the same order of magnitude as this curvature radius, the oscillations appear while the NPL could be considered flat for smaller lateral dimensions. These results thus prove that the curvature appears during the growth of the NPL in solution and not after their synthesis.

The formation mechanism of CdSe nanoplatelets was probed by time-resolved *in-situ* SAXS and WAXS. The data show that anisotropic growth occurs through monomer-addition from solution and not from templating or anisotropic ripening. It also shows that they bend in solution during their growth with a constant radius of curvature.

PRINCIPAL PUBLICATION AND AUTHORS

Insights into the Formation Mechanism of CdSe Nanoplatelets Using in Situ X-ray Scattering, N. Castro (a), C. Bouet (b), S. Ithurria (b), N. Lequeux (b), D. Constantin (a), P. Levitz (c), D. Pontoni (d) and B. Abécassis (a,e), *Nano Lett.* **19**(9), 6466-6474 (2019); doi: 10.1021/acs.nanolett.9b02687.

(a) Laboratoire de Physique des Solides, CNRS, Université Paris-Sud, Université Paris-Saclay, Orsay (France)
(b) Laboratoire de Physique et d'Etude des Matériaux, ESPCI-Paris, PSL Research University, Sorbonne Université, CNRS, Paris (France)
(c) Physico-Chimie des Électrolytes et Nanosystèmes Interfaciaux, PHENIX, Sorbonne Université, CNRS, Paris (France)
(d) ESRF
(e) Laboratoire de Chimie, CNRS, École Normale Supérieure de Lyon (France)

FORMATION AND CHARACTERISATION OF MXene MONOLAYER AT THE AIR–LIQUID INTERFACE

The spontaneous assembly of MXene flakes into monolayer film at the air–liquid interface was followed by surface scattering techniques. Interfacial flakes were assembled into a dense monolayer film by layer compression on an acidic sub-phase and then transferred onto solid substrates by the Langmuir-Blodgett approach for further characterisation.

Future generations of nanoelectronic devices will be based on multilayer combinations of two-dimensional nanomaterials (2D NMs), requiring new types of 2D NMs and novel ways of consecutive deposition for building functional devices. 2D NMs such as graphene and molybdenum disulphide have attracted interest because of their outstanding properties and promising prospects for applications. Recently, a new family of 2D NMs called MXenes, with a general formula $M_{n+1}X_nT_x$ (where n=1÷3, M is an early transition metal, X is C and/or N, and T are various terminating groups -OH, =O, -F) was discovered **[1]**. Most MXene compounds exhibit metallic conductivity, hydrophilicity and high flexibility. Due to the unique combination of these properties, MXenes can be utilised successfully in various applications, from manufacturing transparent electrodes or tunable optoelectronic devices to energy storage devices and selective membranes. Unfortunately, current techniques such as spin- and spray-coating typically offer poor morphological control for 2D thin films. Here, for the first time, a MXene monolayer is created on an aqueous surface with a subsequent transfer to a solid substrate by Langmuir-Blodgett (LB) deposition on the inclined support.

The formation and structure of the MXene monolayer at the air–liquid interface was characterised at beamline **ID10** by *in-situ* X-ray reflectivity (XRR), grazing-incidence X-ray fluorescence (GIXRF) and grazing-incidence X-ray diffraction (GIXRD) techniques. To perform studies on liquid surfaces with X-ray scattering, the X-ray beam has to be tilted from the horizontal plane in the desired angular range. ID10 is designed for research on liquid surfaces and interfaces, with a beam steering mechanism (double crystal deflector **[2]**) and a Langmuir trough. Additional off-beam measurements of surface pressure isotherms were performed on a Langmuir trough at the Partnership for Soft Condensed Matter (**PSCM**) laboratory.

The surface structure of MXene suspensions and its evolution in time was studied by XRR recorded in series over a period of 5h after vigorous MXene sol intermixing (**Figure 79a**). A schematic illustration of the reconstructed structures is presented in **Figures 79b-d**. This study revealed that the rather low surface coverage and slow kinetics makes MXene layer assembly at neutral or slightly basic environments poorly applicable for technological tasks, but the process can be boosted by the addition of cationic surfactants (**Figures 79b-c**). The kinetics of surface layer formation on an acidic sub-phase (**Figure 79d**) extracted from XRR data indicates a progressive increase of coverage. The spontaneous assembly of MXene, in this case, is promoted by the amphiphilic nature of MXene layers, coming from the sub-phase and staying at the surface. The formation of dense surface layers on the acidic suspension coincides well with a quick increase of surface tension in time and well-defined compression isotherms of surface layers. The films formed on the acidic suspension were transferred onto inclined solid substrates by LB technique, then characterised by scanning electron microscopy (SEM) and atomic force microscopy (AFM). The formation of the MXene layer at the air–liquid interface is well proved by GIXRF spectroscopy illustrating strong fluorescence of the titanium k-line (**Figures 79e-f**).

Thus the spontaneous assembly of $Ti_3C_2T_x$ MXene layers into monolayer films at the air–water interface is observed both in basic and acidic suspensions. The direct assembly of a 1.5-nm-thick $Ti_3C_2T_x$ monolayer appears at the liquid–air interface at pH~8, while anion coordination of MXene flakes with the formation of a Br_{aq}^- /$Ti_3C_2T_x$/sub-phase interface occurs from the acidic medium. MXene flakes at the interface can be assembled into a dense monolayer film by layer compression with a surface pressure attaining 40 mN/m in the case

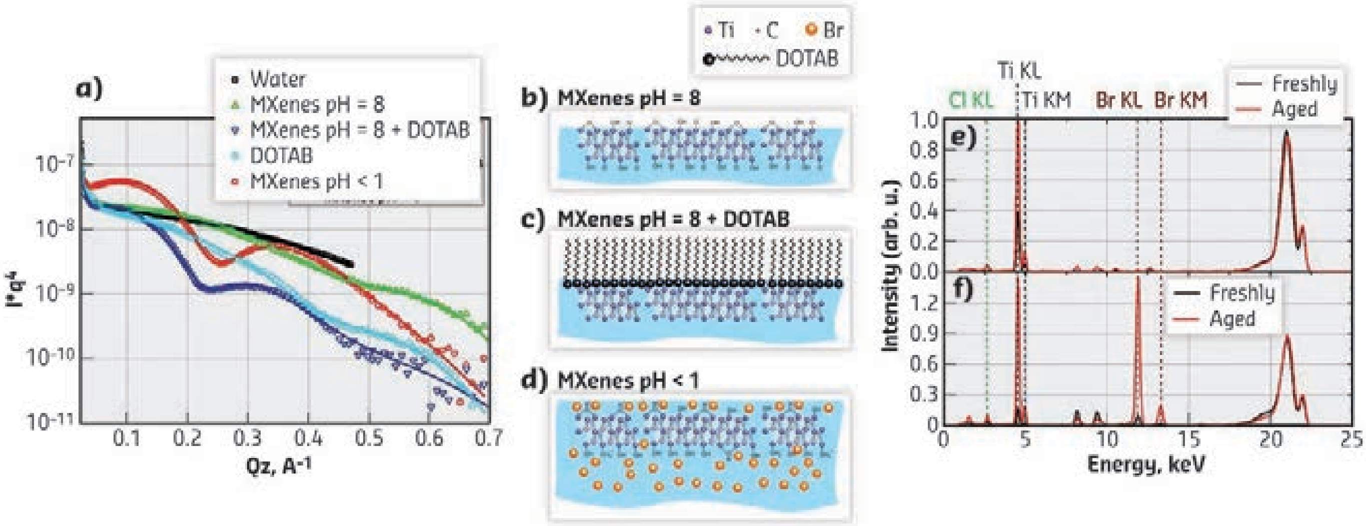

Fig. 79: a) XRR data (symbols) and data fit (lines) and **(b-d)** interface models for liquid–air interfaces of pure water (black), self-assembled film on MXene suspension with pH = 8 aged for 5h (green), the same film after addition of dodecyltrimethylammonium bromide (DOTAB) and 10 mins delay (blue), pure DOTAB film on water (cyan), and self-assembled film on MXene suspension with pH < 1 aged for 5h (red). GIXRF spectra for freshly intermixed and 5h aged self-assembled films on MXene suspensions with pH = 8 **(e)** and pH < 1 **(f)**.

of an acidic sub-phase. Formed layers can be readily transferred onto solid substrates by conventional LB. The presented approach can easily be expanded for all the MXene family. This provides a pathway for the deposition of multilayered structures for automated manufacturing of high-quality MXene films for transparent electrodes or membranes.

PRINCIPAL PUBLICATION AND AUTHORS

Spontaneous MXene monolayer assembly at the liquid-air interface,
D. I. Petukhov (a), A. P. Chumakov (b), A. S. Kan (a), V. A. Lebedev (a), A. A. Eliseev (a), O. Konovalov (b) and A. A. Eliseev (a), *Nanoscale*, **11**, 9980-9986 (2019); doi:10.1039/c9nr00525k.
(a) Lomonosov Moscow State University (Russia)
(b) ESRF

REFERENCES

[1] M. Naguib *et al., Adv. Mater*. **23**, 4248-4253 (2011).
[2] V. Honkimaki *et al., J. Synchrotron Rad*. **13**, 426-431 (2006).

X-RAY NANOPROBE

This year's selection of scientific highlights is a fitting representation of the multidisciplinary nature of the applications and scientific fields covered by the ESRF's X-ray Nanoprobe (XNP) group. XNP beamlines offer a variety of contrast, probing either the elemental composition (via X-ray fluorescence (XRF) regularly used at ID16A, ID16B and ID21), the chemical composition (via X-ray absorption spectroscopy (XAS) at ID16B and ID21), the electron density distribution (via phase-contrast nanotomography at ID16A and ID16B), or the shape of nano-objects (via coherent X-ray diffraction (XRD) at ID01 and ID13) but also physical properties such as lattice strain (via micro- and nano-X-ray diffraction at ID01, ID13 and ID16B).

This portfolio of 2D and 3D imaging techniques is applied to a plethora of materials in a wide variety of scientific domains, from hard nano-objects (*e.g.*, single Pt nanoparticles, used for catalysis (**page 91**)) and thin films (*e.g.*, metal halide perovskite solar cells (**page 86**)), to biological materials (**page 99**) and, notably, biominerals, for example, via the use of a microfluidic device for the *in-situ* study of calcium carbonate precipitation (**page 94**), or the detection of Zn–hydroxyapatite in the early stages of osteogenic differentiation (**page 97**). Furthermore, XNP beamlines are extensively used to study the interactions between synthetic materials and biological systems, including in drug development (for the treatment of breast cancer, **page 100**) or incidental exposure (*e.g.*, to needle debris deposited during tattoo application, **page 95**). The capability to probe simultaneously biological and manufactured systems enables the development of nano-objects that are 'safer by design' (**page 102**).

Imaging experiments aim to characterise materials but also to follow their stability or degradation throughout their lifecycle, for instance, in lithium-ion batteries. The degree of local damage in a composite electrode has been followed as a function of cycling history, both *ex-situ* with ultimate resolution at beamline ID16A (**page 87**), and *in-situ* (*i.e.* during cycles of charge and discharge) with somewhat reduced resolution at beamline ID16B (**page 89**). *In-situ* or *operando* will indeed be an important aspect of the XNP portfolio, post-Extremely Brilliant Source (EBS). With increased flux and improved detection technologies, the duration of standard experiments will dramatically decrease, making it easier to study dynamical systems and fast reactions. Faster acquisition will also be beneficial to the study of static materials such as fragments from historical paintings (**page 92**). Decreased dwell time means that significantly higher throughput is on the horizon, and a larger range of samples (*e.g.*, historical but also model paints, an increased number of replicates of biological samples) can be studied. For X-ray absorption spectroscopy, it means that multi-spectral mapping (µXRF maps at few energies) can be upgraded into hyper-spectral mapping (µXRF maps at hundreds of energies), improving the quality of chemical mapping.

The suite of tools provided by **ID01** will benefit from the increased brilliance of the new source, particularly those exploiting the coherence. Prior to the shutdown period, 35-nm beams were achieved on ID01, and will be available at the start of EBS. In the meantime, ID01 has continued to hone its equipment. Prototypes for water-cooled versions of its high-temperature, gas-compatible, sample environments have been tested at other synchrotron facilities with great success. The integration and calibration of a new remote-controlled retractable light microscope, providing eyes on the sample, will give us a much better handle of the absolute position of the sample at all times, therefore removing one of the major sources of error encountered in most experiments where multiple Bragg reflections were sought.

In 2020, **ID13** will continue adapting and optimising the beamline's capabilities for EBS operation. This includes the implementation of the ESRF data policy with the new BLISS beamline control software. To make best use of the EBS, with assistance from the ESRF X-ray optics group, an upgrade of the monochromator, replacing the existing channel-cut crystal by an optimally polished version produced in collaboration with the University of Osaka, is planned for summer 2020. Based on the increased flux density anticipated in micro-/nano-beam focal spots, together with a significantly increased scanning performance, diffraction experiments combining spatial with temporal resolution will become possible.

At the nano-imaging beamline **ID16A**, correlative microscopy is increasingly used. Online, (cryo) X-ray fluorescence and phase contrast nanotomography are combined both qualitatively and quantitatively. Offline, cryo correlative light microscopy will be available to select optimal samples and to label specific cellular structures. The shutdown has been an active period to prepare the instrument for the EBS. In particular, faster scanning will become possible with a replacement of the rotation, and KB nanofocusing will be improved at 17 keV. Key to the exploitation of EBS is the detector technology. A new multi-element SDD detector for X-ray fluorescence and a large-area image sensor for phase-contrast nanotomography are under implementation.

In-situ and *operando* measurements are an essential part of the research activity addressed by **ID16B**. These are also among the experiments that can benefit the most from the increased flux of EBS. The on-going upgrade of the *in-situ* environments of ID16B will make them better adapted to new experiments that were previously limited by the acquisition time, especially for nanotomography and XAS characterisation. EBS will improve the data quality, detection limits and measurement time on ID16B but will also increase the number of experiments needing cryo-conditions and faster acquisition in order to avoid any potential radiation damage on the samples. The helium and nitrogen cryostats available on ID16B will provide the needed cryo-conditions, whereas the new readout electronics for the XRF detectors will reduce the scan time considerably.

Finally, the refurbishment on **ID21** is progressing. After the replacement of most of the equipment in the optics hutches in 2018, efforts are now concentrated on the design of a new nanoscope (to be implemented in 2021), which will complement the existing microscope (operational at restart). Both of them will work in vacuum conditions, with an optional cryo stage, and will be dedicated to elemental and speciation mapping via XRF and XAS in the 2-11 keV range. With improved optics, mechanics and detectors, the nanoscope should outperform the microscope, notably with a beam size of 100×100 nm^2. The present microscope will be maintained to study large samples (with millimetric or micrometric beam).

M. COTTE

LOCAL STRAIN HETEROGENEITY INFLUENCES THE OPTOELECTRONIC PROPERTIES OF HALIDE PEROVSKITES

Micro- and nano-X-ray diffraction is used to explore how lattice strain in halide perovskite thin films correlates with defect concentrations and non-radiative recombination. The results suggest new pathways to improve perovskite solar cell and light-emitting diode (LED) efficiencies.

Metal halide perovskites are generating enormous excitement for optoelectronic devices including solar cells and LEDs **[1,2]**. However, there are still a number of defects trapping charge carriers, which lead to power losses in devices. This work demonstrates that these defects relate to complicated strain patterns that appear on multiple length scales in perovskite films.

At the micron-scale, scanning micro X-ray diffraction (µXRD) measurements were correlated with PL measurements on the same perovskite film area, revealing that local strain leads to defects such as halide vacancies associated with local non-radiative decay (**Figure 80**). At the nanoscale, scanning nanofocus X-ray diffraction (nXRD) measurements were carried out at beamline **ID13** on a variety of perovskite films **[3]**.

A quiver plot for the <110> orientation is shown in **Figure 81**. Diffraction spots adjacent both in spatial coordinates and in reciprocal space coordinates are considered as belonging to the same cluster, here indicated as 'super-grain'. Two super-grains with the largest covered areas (calculated as the number of pixels within the super-grain times the pixel area) are highlighted in **Figure 81a**. These also exhibit local strain (*q*) variations within their dimensions (**Figures 81b-c**), consistent with variations observed in the µXRD maps. The super-grain sizes for the <110> reflection plotted in **Figure 81d** shows that these largest regions extend well beyond the grain size observed in scanning electron microscopy (SEM) images. This disparity is intensified in the triple cation $MA_{0.15}FA_{0.79}Cs_{0.06}Pb(I_{0.85}Br_{0.15})_3$ samples (**Figure 81d**); this is clearly seen in the overlay of an SEM image and a quiver plot for the <210> reflection in **Figure 81e.**

These results suggest that the critical grain size is actually the longer-range structural super-grains rather than the grains viewed in SEM images. The formation of these large clusters with analogous orientation and facet control may have beneficial properties for carrier transport. The results also suggest that the grain orientation is non-random, with either templated nucleation/growth or fragmentation of larger grains for instance upon drying or annealing. Such a mechanism could be akin to the long-range co-orientation of crystal plates in echinoderms **[4]**.

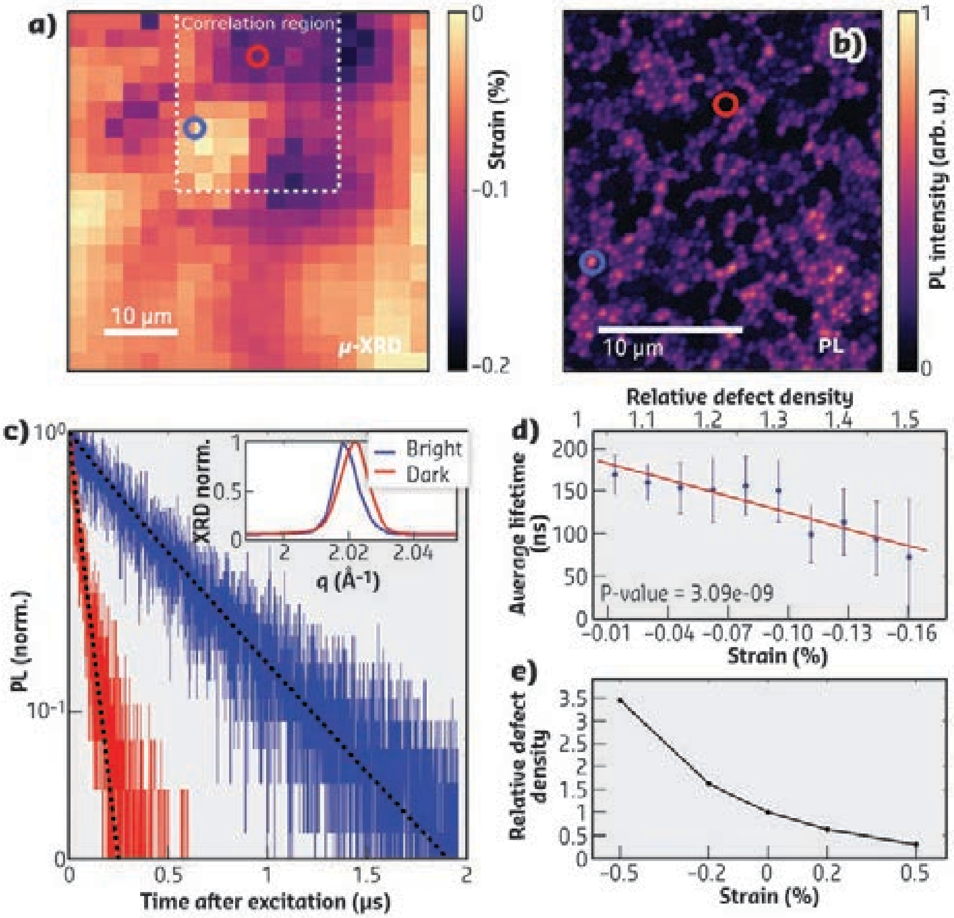

Fig. 80: Correlating the microscale photoluminescence (PL) and local structural properties of $MAPbI_3$ films. **a)** Spatial map of compressive strain variation. The dashed line denotes the correlation region between µXRD and PL. **b)** Confocal PL intensity map of a $MAPbI_3$ perovskite film corresponding to the dashed region in **(a)**. **c)** Time-resolved PL decays of the bright (blue) and dark (red) regions highlighted in **(b)**. Inset: Highlighted <220> peak diffraction pattern for the bright and dark PL regions. **d)** Scatter plots of statistically significant correlations between local PL lifetime and compressive strain (relative defect density; calculated from relationship in **(e)**. **e)** Ratio in concentration of charged iodide vacancies (V_I^+ defects) in <110> strained perovskite crystals to an unstrained crystal.

It is proposed that strain is built into the film during processing, in particular during cooling through the cubic-to-tetragonal phase transition following the standard annealing procedure. The data also demonstrate that improved growth and passivation methods must target strain relief, for example by manipulating the local phase behaviour during growth or post-treatments, which relieve constrained regions.

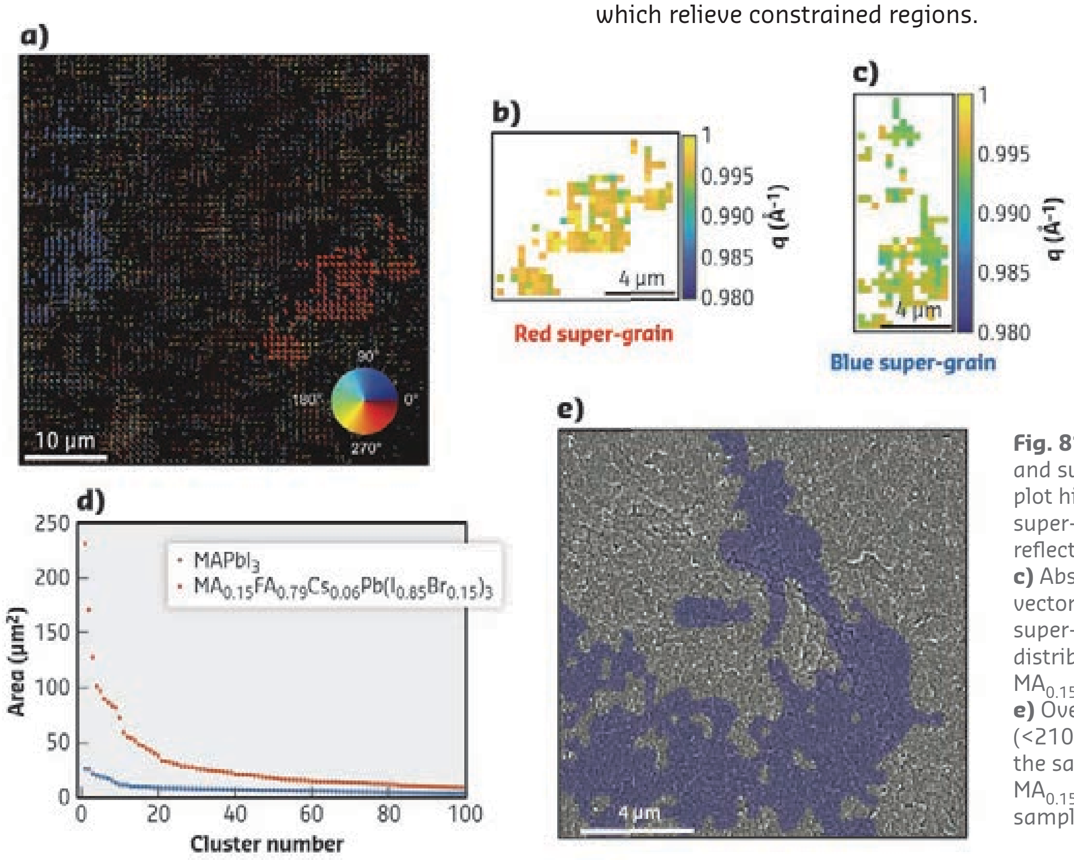

Fig. 81: Scanning nXRD measurements and super-grain analysis. **a)** Quiver plot highlighting the first two largest super-grains showing the <110> reflection in a $MAPbI_3$ sample. **b)** and **c)** Absolute value of the scattering vector q extracted from the two largest super-grains in **(a)**. **d)** Super-grain size distributions for $MAPbI_3$ and $MA_{0.15}FA_{0.79}Cs_{0.06}Pb(I_{0.85}Br_{0.15})_3$. **e)** Overlay between the quiver plot (<210>) and SEM image in the same scan area for a $MA_{0.15}FA_{0.79}Cs_{0.06}Pb(I_{0.85}Br_{0.15})_3$ sample.

PRINCIPAL PUBLICATION AND AUTHORS

Lattice strain causes non-radiative losses in halide perovskites, T. W. Jones (a), A. Osherov (b), M. Alsari (c), M. Sponseller (b), B. C. Duck (a), Y. Jung (d), C. Settens (b), F. Niroui (b), R. Brenes (b), C. V. Stan (e), Y. Li (e,f), M. Abdi-Jalebi (c), N. Tamura (e), J. E. Macdonald (g), M. Burghammer (h), R. H. Friend (c), V. Bulović (b), A. Walsh (d,i), G. J. Wilson (a), S. Lilliu (j) and S. D. Stranks (b,c), *Energy Environ. Sci.* **12**, 596-606 (2019); doi: 10.1039/c8ee02751j. Published by The Royal Society of Chemistry.

(a) CSIRO Energy Centre, Mayfield West (Australia)
(b) Research Laboratory of Electronics, Massachusetts Institute of Technology (USA)
(c) Cavendish Laboratory, University of Cambridge (UK)
(d) Department of Materials Science and Engineering, Yonsei University, Seoul (Korea)
(e) Advanced Light Source, Lawrence Berkeley National Laboratory, California (USA)
(f) Xi'an Jiaotong University, State Key Laboratory for Mechanical Behavior of Materials (China)
(g) School of Physics and Astronomy, Cardiff University (UK)
(h) ESRF
(i) Department of Materials, Imperial College London (UK)
(j) Department of Physics and Astronomy, University of Sheffield (UK)

REFERENCES

[1] H. J. Snaith & S. Lilliu, *Scientific Video Protocols* **1**, 1 (2018).
[2] R. H. Friend *et al., Scientific Video Protocols* **1**, 1 (2019).
[3] S. Lilliu *et al., Adv. Funct. Mater.* **26**, 8221-8230 (2016).
[4] C. E. Killian *et al., J. Am. Chem. Soc.* **131**, 18404-18409 (2009).

QUANTITATIVE FAILURE ANALYSIS OF LITHIUM-ION BATTERIES

A multitude of synchrotron techniques including hard X-ray phase-contrast nanotomography have been used to systematically investigate – with multiscale resolution – the degradation in complex composite lithium-ion battery electrodes under fast-charging conditions. The results could help improve electrode formulation for fast-charging batteries.

The rapidly growing market for consumer electronics and electric vehicles has motivated tremendous ongoing research into rechargeable batteries. An important aspect of battery

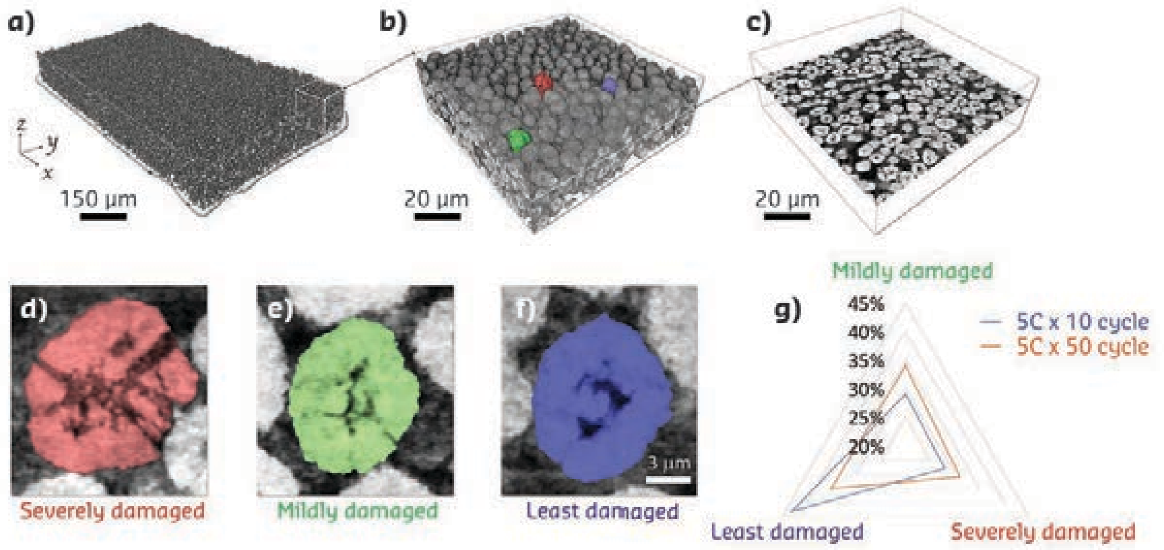

Fig. 82: Multiple-length-scale X-ray tomographic imaging of NMC622 electrode. **a)** Microtomography (650 nm pixel size) data of a piece of NMC electrode. **b)** 3D rendering of the nanotomography data (70 nm pixel size) of an arbitrarily selected region of interest over the electrode, with its central slice in the lateral direction shown in **(c)**. Three of the representative particles are highlighted in red **(d)**, green **(e)**, and blue **(f)**. They are categorised as severely damaged, mildly damaged, and least damaged particles, respectively. The relative population of these three kinds of particles, which changes as a function of the cycling history, is summarised in the radar chart in **(g)**.

research is to identify the fading pathways of battery particles and electrodes at multiple length and time scales under practical operating conditions. These processes are termed 'chemo-mechanical interplay'. The multiscale chemo-mechanical interplay builds up mechanical stress, provokes morphological breakdown, and leads to states of charge heterogeneity in lithium-ion batteries. Synchrotron techniques have been broadly applied to tackle frontier challenges in this field **[1]**.

Quantifying the interplay in complex composite electrodes with multiscale resolution constitutes a challenge in precisely diagnosing the fading mechanism of batteries. By employing the technique of hard X-ray phase contrast nanotomography at beamline **ID16A**, combined with nanoscale hard X-ray spectromicroscopy, soft X-ray absorption spectroscopy (XAS), and transmission electron microscopy (TEM), this study systematically investigated the morphological and chemical degradation in polycrystalline nickel-rich layered nickel-manganese-cobalt oxide (NMC) composite electrodes under fast-charging conditions. The results were used for finite element modeling (FEM) to gain deeper insights into electrode degradation and failure **[2]**.

The degree of local damage in the composite electrode has been visualised and quantified. In particular, hard X-ray phase contrast nanotomography, capable of probing thousands of active particles at once (**Figure 82**), enables an unprecedented statistical analysis of the chemo-mechanical transformation of secondary battery particles under fast charging conditions

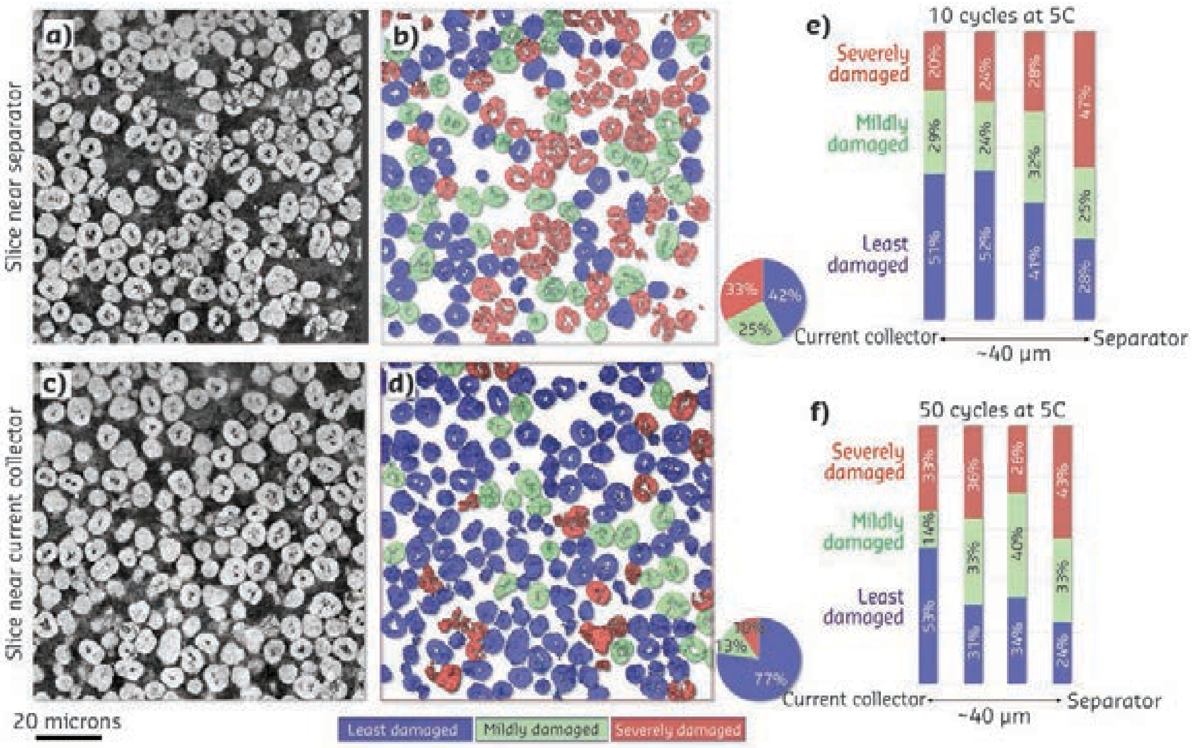

Fig. 83: Comparison of the top (near separator) and the bottom (near collector) layers in the NMC622 electrode that has gone through 10 fast cycles at a rate of 5C. Panels **(a)** and **(b)** (colour-coded) are the same lateral slice over the particle layer that is close to the electrode's top surface (near the separator). Panels **(c)** and **(d)** (colour-coded) are the same lateral slices over the first layer of particles close to the electrode's bottom surface (near the aluminium current collector). The relative particle cracking probabilities over these two slices are quantified in the corresponding pie charts. Fracturing profiles from current collector to separator are shown after 10 and 50 cycles, respectively in panels **(e)** and **(f)**.

(**Figure 82g**). This quantitative visualisation revealed the depth-dependent trend of particle fracturing within the electrode as well as its lateral complexity. The results suggest that the active particles within the electrode contribute to the cell-level chemistry differently in time and position.

Based on the degradation depth profile, it was found that initially more damage takes place near the separator, evolving to a more homogeneous distribution as particles located deeper in the electrode take over the electrochemical activity in later cycles (**Figure 83**). Finally, FEM with shape models recovered from the nanotomography data was also used to gain insights into the electrode level strain distribution and evolution. It was found that the damage heterogeneity prevails at all length scales, which causes unbalanced local electrical and ionic conductivity, and collectively leads to the non-uniform utilisation of active particles spatially and temporally.

The statistical mapping of the chemo-mechanical transformation in the composite electrode offers a diagnostic method for probing and understanding the non-uniform particle utilisation and fading. Thus, it is anticipated that the developed methodology and understanding will pave the way towards improved electrode formulation for fast-charging batteries.

PRINCIPAL PUBLICATION AND AUTHORS

Quantification of Heterogeneous Degradation in Li-Ion Batteries, Y. Yang (a,g), R. Xu (b), K. Zhang (c,d), S.-J. Lee (c), L. Mu (e), P. Liu (b), C. K. Waters (e), S. Spence (e), Z. Xu (e), C. Wei (c), D. J. Kautz (e), Q. Yuan (d), Y. Dong (d), Y.-S. Yu (f), X. Xiao (g), H.-K. Lee (c,h), P. Pianetta (c), P. Cloetens (a), J.-S. Lee (c), K. Zhao (b), F. Lin (e) and Y. Liu (c), *Adv. Energy Mater.* **9**(25), 1900674 (2019); doi: 10.1002/aenm.201900674.

(a) ESRF
(b) School of Mechanical Engineering, Purdue University, West Lafayette (USA)
(c) Stanford Synchrotron Radiation Lightsource, Menlo Park (USA)
(d) Beijing Synchrotron Radiation Facility, Institute of High Energy Physics, Chinese Academy of Science, Beijing (China)
(e) Department of Chemistry, Virginia Tech, Blacksburg, (USA)
(f) Advanced Light Source, Lawrence Berkeley National Laboratory, Berkeley (USA)
(g) National Synchrotron Light Source II, Brookhaven National Laboratory (USA)
(h) Pohang Accelerator Laboratory, Pohang (Republic of Korea)

REFERENCES

[1] F. Lin *et al., Chem. Rev.* **117**(21), 13123-13186 (2017).
[2] R. Xu *et al., J. Mech. Phys. Solids* **129**, 160-183 (2019).

DEGRADATION OF SILICON-BASED ANODES FOR LITHIUM-ION BATTERIES FOLLOWED BY *IN-SITU* X-RAY TOMOGRAPHY

The cracking and interface debonding dynamics of Si-based electrodes for Li-ion batteries have been studied by *in-situ* synchrotron X-ray tomography. This study reveals the positive impact of a 'maturation' procedure on the mechanical properties of the electrodes, resulting in a better cyclability.

Si-based anodes have the potential to replace the usual graphite electrodes in order to increase the energy density of lithium-ion batteries. However, Si-based electrodes suffer from high volume change during lithiation/delithiation cycling, which degrades their structure and shortens the lifetime of the batteries. The degradation includes electrode cracking and delamination, Si particle fracturing and instability of the solid electrolyte interphase (SEI) **[1]**. Significant research efforts are being made to control such expansion effects and to improve the cyclability. Since battery anodes have complex and heterogeneous structures, 3D observation is required to better understand their failure mechanisms and thus subsequently optimise their formulation **[2]**. Therefore, it is pertinent to monitor the morphological changes of the electrode occurring during its operation and at different scales.

The 3D microstructure evolution of two different anodes was studied *in situ* during one discharge/charge cycle by means of X-ray tomography (**Figure 84a**). The standard electrode obtained by routine preparation was scanned at Psiché beamline at Synchrotron Soleil whereas the electrode prepared with a 'maturation' step **[3]** (consisting of storage of the electrode for a few days under a humid atmosphere prior to drying and cell assembly) was imaged at beamline **ID16B**, resulting in an analysed volume of 256 × 256 × 210 μm^3 with an isotropic voxel size of 200 nm.

Subsequently, the dynamics of the expansion and contraction, of the electrode cracking in the bulk (cracks are shown in red in **Figure 84b**) and of the debonding at the interface with the current collector (**Figure 84c**) of these two different electrodes were visualised in 3D and compared quantitatively for volumes of 190 × 190 × 210 µm^3 with high resolution.

From these analyses, it was shown that the 'maturation' treatment limits the macroscopic deformation (expansion/contraction) of the electrode by constraining the displacement of the Si particles. Its most important effect was to decrease the formation of macro-cracks in the composite electrode by a factor of four (**Figure 85**) and reduce its delamination from the current collector by a factor of ten. The intra-connectivity and propagation directions of the cracking pattern was analysed for both electrodes (**Figure 85**). This reveals that a simple 'maturation' procedure can significantly enhance the mechanical properties of the binding phase in the composite electrode. Thereby, the active material network can better adapt to the important volume variations induced by the silicon alloying with lithium through a more ductile and resilient electrode, resulting in a major gain in its cyclability **[3]**.

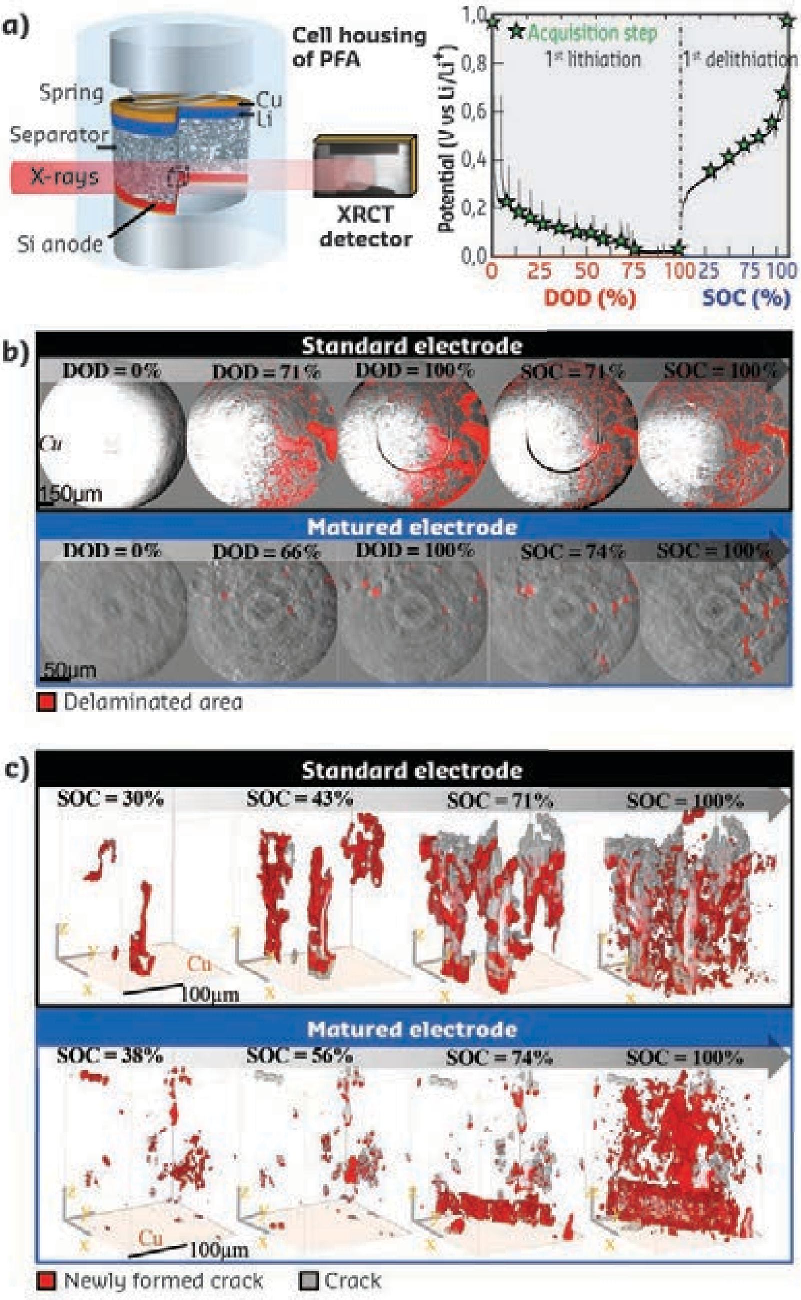

Fig. 84: a) Sketch of the experimental set-up at beamlines ID16B and Pisché and voltage/time electrochemical curve of the cell showing the steps where the electrode was observed (DOD = depth of discharge; SOC = state of charge). **b)** 2D (x,y) slices of the electrode/Cu interface during electrochemical cycling for the standard (pixel size: 650 nm) and matured electrode (pixel size: 200 nm).
c) 3D rendering of the crack volume during delithiation of the standard and matured electrode.

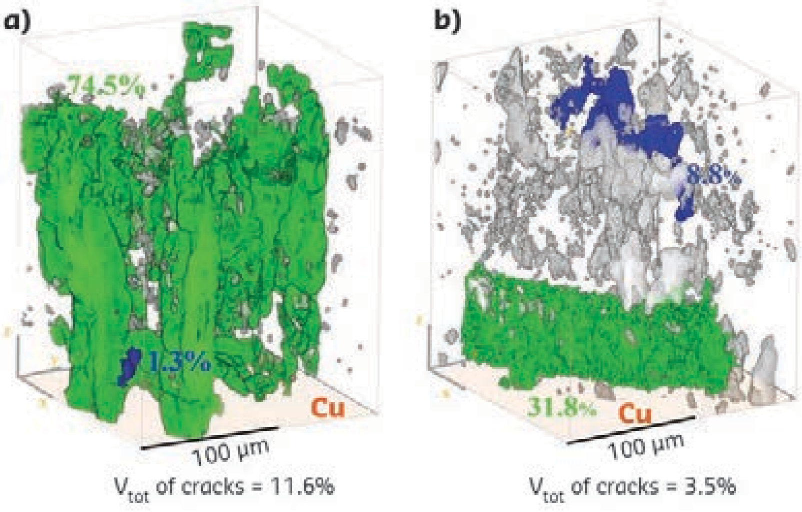

Fig. 85: 3D rendering of the crack volume at the end of the first delithiation. **a)** Standard electrode.
b) Matured electrode. The largest and second largest intra-connected phases are labelled respectively in green and in blue.

PRINCIPAL PUBLICATION AND AUTHORS

Dynamics of the morphological degradation of Si-based anodes for Li-ion batteries characterized by *in-situ* synchrotron X-ray tomography, V. Vanpeene (a,b), J. Villanova (c), A. King (d), B. Lestriez (e), E. Maire (b), L. Roué (a), *Adv. Energy Mater.* **9**, 1803947 (2019); doi: 10.1002/aenm.201803947.

(a) Institut National de la Recherche Scientifique (INRS), Centre Énergie, Matériaux, Télécommunications (EMT), Varennes (Canada)
(b) INSA Lyon, MATEIS, CNRS UMR 5510, Villeurbanne (France)
(c) ESRF
(d) Synchrotron Soleil, Gif-sur-Yvette (France)
(e) Institut des Matériaux Jean Rouxel (IMN), CNRS UMR 6502, Université de Nantes (France)

REFERENCES

[1] M. N. Obrovac, *Current Opinion Electrochem.* **9**, 8-17 (2018).
[2] P. Pietsch & V. Wood, *Annu. Rev. Mater. Res.* **47**, 451-479 (2017).
[3] C. Reale Hernandez *et al.*, *Adv. Energy Mater.* **8**, 1701787 (2017).

CO-INDUCED SHAPE AND STRAIN STATE CHANGES IN A SINGLE Pt NANOPARTICLE – IMPLICATIONS FOR CATALYSIS

Compressive surface strain in Pt nanoparticles is relaxed while switching the gas environment from inert Ar to a mixture of Ar/CO flow. Coherent X-ray diffraction imaging (CXDI) suggests that this lattice relaxation is mainly due to a shape change of the nanoparticles accompanied by a rearrangement of high-index vicinal surfaces.

Oxide-supported nanoparticles play a crucial role as heterogeneous catalysts in various industrial conversion processes **[1]**. A prerequisite for improving catalyst performance and lifetime is to better understand the catalyst deterioration and deactivation in a catalytically relevant gas environment **[2]**. Coherent X-ray diffraction imaging (CXDI) not only permits tracking of the structural details of a single nanoparticle *in situ* but also provides valuable information on the strain state of the nanoparticle in the bulk and on the surface.

The Pt 111 Bragg reflection was used to determine the shape and strain in the bulk and near-surface region of a ~ 160 nm-large Pt nanoparticle epitaxially grown on a strontium titanate substrate. CXDI was employed *in situ* at a temperature of 400 K under continuous gas flow of pure Ar and an Ar/CO mixture. **Figure 86a** is a schematic sketch of the experiment performed at beamline **ID01**. A single Pt nanoparticle was preselected by scanning electron microscopy (SEM) and marked by writing hierarchically arranged markers, using ion- and electron beam-induced deposition of a Pt precursor gas. In this way, the nanoparticle could be relocated by scanning the sample through the X-ray beam (**Figures 86b** and **86c**) using a continuous fast-scan mode. Bragg CXDI enables the retrieval of the shape as well as the strain-distribution in the nanoparticle in three-dimensions **[3]**.

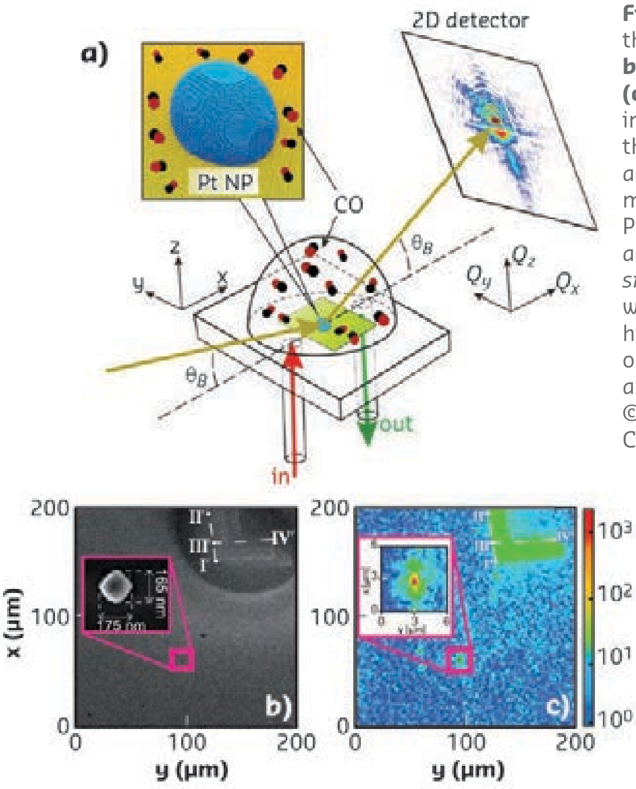

Fig. 86: a) Set-up of the experiment. **b)** Overview SEM and **(c)** X-ray scanning image with one of the hierarchically arranged guiding markers and the Pt nanoparticle analysed using *in-situ* CXDI. Adapted with permission from https://pubs.acs.org/doi/10.1021/acsanm.9b00764. © (2019) American Chemical Society.

From the *in-situ* experiment, it was concluded that under mixed Ar/CO flow at 400 K the expansive strain present in the near-surface region is enhanced as compared to the inert Ar environment (**Figures 87a** and **87b**). This relaxation of the Pt atoms is induced by a shape change of the nanoparticle, indicating that the strain relaxation is not only due to CO atoms adsorbing on the Pt nanoparticle surface, but is rather enhanced by a rearrangement of the present high-index facets, as sketched in **Figures 87c** and **87d**. The region marked in grey corresponds to a stacking fault region from which no CXDI signal is detected on the 111 reflection.

Overall, this experiment provides evidence that the interior strain state of strontium titanate-supported Pt nanoparticles is influenced by the presence of higher-index facets at the nanoparticle surface. The preselection of the Pt nanoparticle overcomes the arbitrariness of previous experiments in searching for a suitable nanoparticle and therefore permits a correlative investigation by complementary lab-based microscopy techniques. As such, it demonstrates that the nanoparticle shape can influence its internal strain state, providing an additional parameter for tailoring strain states, influencing reactivity. Future CXDI experiments will address the shape and the strain state of individual, preselected nanoparticles under dynamical *operando* reaction conditions.

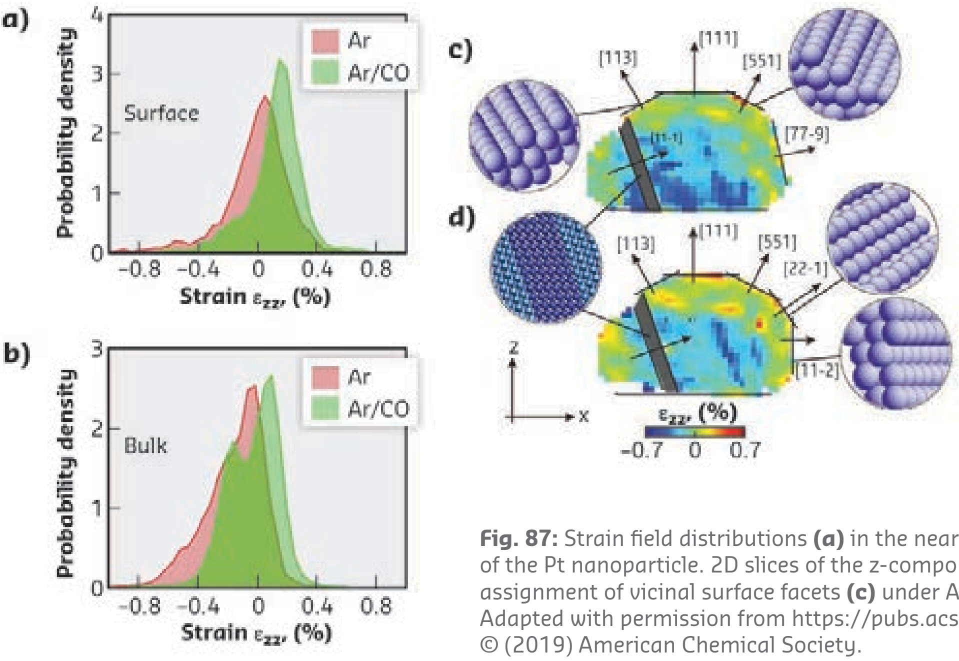

Fig. 87: Strain field distributions **(a)** in the near-surface region and **(b)** inside the bulk of the Pt nanoparticle. 2D slices of the z-component of the strain field with a tentative assignment of vicinal surface facets **(c)** under Ar flow and **(d)** under Ar/CO gas flow. Adapted with permission from https://pubs.acs.org/doi/10.1021/acsanm.9b00764. © (2019) American Chemical Society.

PRINCIPAL PUBLICATION AND AUTHORS

Coherent X-ray imaging of CO-adsorption-induced structural changes in Pt nanoparticles: Implications for catalysis, M. Abuin (a), Y. Y. Kim (a), H. Runge (a,b), S. Kulkarni (a), S. Maier (c), D. Dzhigaev (d), S. Lazarev (a,e), L. Gelisio (a), C. Seitz (a), M. I. Richard (f,g), T. Zhou (f), V. Vonk (a), T. F. Keller (a,b), I. A. Vartanyants (a,h) and A. Stierle (a,b), *ACS Appl. Nano Mater.* **2**, 4818-4824, (2019); doi: 10.1021/acsanm.9b00764. Further permissions related to the material excerpted should be directed to the ACS.

(a) Deutsches Elektronen-Synchrotron (DESY), Hamburg (Germany)
(b) Physics Department, University of Hamburg (Germany)
(c) University of Regensburg (Germany)
(d) Division of Synchrotron Radiation Research, Department of Physics, Lund University (Sweden)
(e) National Research Tomsk Polytechnic University (Russia)
(f) ESRF
(g) Aix-Marseille Université, CNRS, Université de Toulon, Marseille (France)
(h) National Research Nuclear University MEPhI, Moscow (Russia)

REFERENCES

[1] G. Ertl *et al.*, in *Handbook of Heterogeneous Catalysis*, G. Ertl, H. Knözinger, F. Schüth, J. Weitkamp (Eds.), Wiley-VCH, Weinheim, Germany (2008).
[2] H. Lee *et al.*, *Angew. Chem.* **118**, 7988-7992 (2006).
[3] M. A. Pfeifer *et al.*, *Nature* **442**, 63-66 (2006).

REVEALING REMBRANDT'S SECRET RECIPES USING SYNCHROTRON X-RAY DIFFRACTION: THE CASE OF THE IMPASTO TECHNIQUE

Rembrandt (1606–1669) is renowned for his impasto technique: thick paint laid on the canvas to make it stand out from the surface. A combination of high-angular resolution X-ray diffraction (HR-XRD) and micro-X-ray diffraction (μ-XRD) [1] was used to decipher the microstructure and composition of Rembrandt's impasto paint layers.

Rembrandt's renowned impasto technique added a third dimension to his paintings, enhancing their light reflecting properties and achieving extraordinary plays of light and shadow. While experts knew that impasto paint was obtained by combining lead-white pigment (a mixture of the lead carbonates cerussite (C) $PbCO_3$ and hydrocerussite (HC) $Pb_3(CO_3)_2(OH)_2$) with an organic binding medium, the exact formulation used by Rembrandt was still a mystery.

Micrometric fragments of paint were sampled in several of Rembrandt's masterpieces from the collections of the Rijkmuseum, Amsterdam, the Louvre, Paris and the Mauritshuis, The Hague. The first step of the study consisted in HR-XRD bulk analysis, performed at beamline **ID22**. While Rembrandt's non-impasto layers were composed of HC and C, the expected main component of lead white, the obtained diffraction patterns revealed the systematic presence in impasto layers of plumbonacrite (PN) $Pb_5(CO_3)_3O(OH)_2$, an extremely rare lead carbonate phase, undetected until then in paintings predating the twentieth century. Another interesting result was the marginal amount of C in the impasto layers. In addition, very high-quality HR-XRD patterns were collected on one sample by cumulating acquisitions over 4 h. Rietveld refinement of this dataset made it possible to model the crystallite morphologies and sizes at the nanometric scale. It was found that PN crystallites had nanometric dimensions (length in the c axis l_c of about 10 nm), while HC crystals in the same impasto layer were significantly larger (l_c ~ 100 nm) (**Figure 88b**).

The second step of the study was the gathering of μ-XRD phase maps at beamline **ID13**, with the objective of obtaining the distribution of the various lead-based crystalline phases within paint stratigraphies at the micrometric scale. One of the studied samples was exceptional as it presented both an impasto and a non-impasto layer. The unique phase composition of impasto was confirmed again: PN was detected solely in the upper impasto layer, together with HC, while the non-impasto layer was composed of HC and C (**Figure 89**). Furthermore, other μ-XRD maps highlighted the homogeneous distribution within impasto layers of tiny (~ 5 μm) aggregates of PN crystals (**Figure 88a**).

These structural results shed new light on Rembrandt's impasto, as they indicate that the presence of PN is a marker of a specific preparation recipe. PN is only stable in alkaline conditions (pH > 10). The composition of impastos (notably characterised in addition to the presence of PN by a lack of C, stable at pH < 6), as well as their microstructure (homogeneous distribution of nanometric PN crystallites) led to the hypothesis of an *in-situ* formation of the crystalline phase within impasto layers.

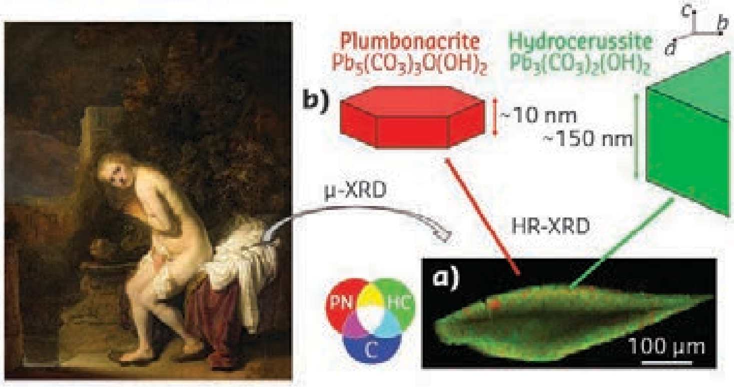

Fig. 88: a) μ-XRD phase map acquired on beamline ID13 from a cross-section of the thickly white drapery of Rembrandt's *Susanna* (1636, Mauritshuis). PN = plumbonacrite, red; HC = hydrocerussite, green; C = cerussite, blue). **b)** Mean dimensions of HC and PN crystallites, produced after Rietveld refinement of HR-XRD data acquired on beamline ID22.

The remaining question was to formulate historically sound hypotheses to account for an alkaline environment in which the crystallisation of PN could be triggered. A possibility is that Rembrandt may have used litharge (lead oxide PbO) in the preparation of his impasto binding medium. The use of PbO by seventeenth-century Dutch golden age painters is indeed attested by several historical sources. The addition of PbO to his oil might have enabled Rembrandt to communicate specific rheological and drying properties to his paint, ideal to build his impasto. Preliminary measurements on model samples containing PbO particles dispersed in a linseed oil medium highlighted how lead carbonates could crystallise in a few months **[2]**.

Fig. 89:
a) Microscope image of a sample collected on Rembrandt's *Bathsheba* (1654, Louvre) showing two white layers: impasto on top of an underlayer. **b)** μ-XRD phase maps acquired on beamline ID13 on a thin section from the same sample.

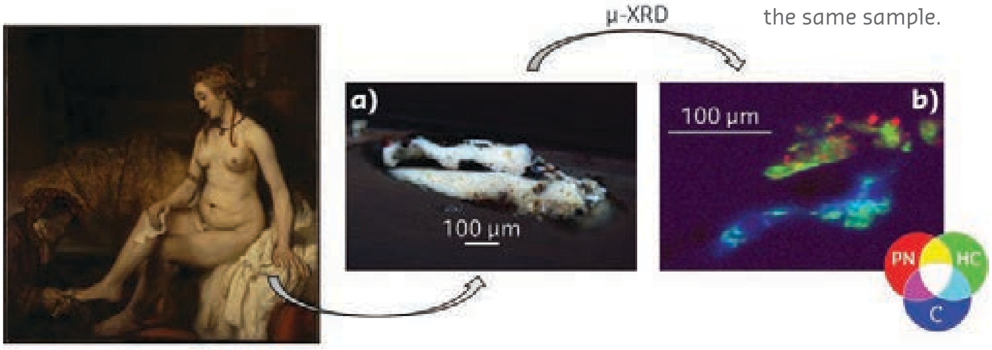

PRINCIPAL PUBLICATION AND AUTHORS

Unraveling the Composition of Rembrandt's Impasto through the Identification of Unusual Plumbonacrite by Multimodal X-ray Diffraction Analysis, V. Gonzalez (a,b), M. Cotte (c,d), G. Wallez (e,f), A. van Loon (b,g), W. de Nolf (c), M. Eveno (f), K. Keune (b,h), P. Noble (b) and J. Dik (a), *Angew. Chem. Int. Ed*. **58**, 1-5 (2019); doi: 10.1002/anie.201813105.
(a) Department of Materials Science and Engineering, Delft University of Technology (The Netherlands)
(b) Rijksmuseum, Science Department, Amsterdam (The Netherlands)
(c) ESRF
(d) Laboratoire d'Archéologie Moléculaire et Structurale (LAMS) Sorbonne Université, CNRS, UMR8220, Paris (France)
(e) Institut de Recherche Chimie Paris, PSL Research University, Chimie ParisTech-CNRS, UMR8247, Paris (France)
(f) Centre de Recherche et de Restauration des Musées de France, Paris (France)
(g) Mauritshuis, Paintings Conservation Department, The Hague (The Netherlands)
(h) Van't Hoff Institute for Molecular Sciences, University of Amsterdam (The Netherlands)

REFERENCES

[1] V. Gonzalez *et al*., *Anal. Chem*. **89**, 13203-13211 (2017).
[2] M. Cotte *et al*., *Stud. Conserv*. **62**, 2-23 (2017).

SYNCHROTRON XRD STUDY OF CALCIUM CARBONATE PRECIPITATION USING A MICROFLUIDIC DEVICE

A versatile and re-usable microfluidic platform that can be employed in many synchrotron X-ray studies of dynamic processes is described. Its use to study crystallisation was demonstrated, where it was employed to obtain quantitative information including induction times and crystallographic parameters, with a sensitivity to crystalline material at ppm levels.

Crystallisation underpins a vast array of processes ranging from the production of functional materials and pharmaceuticals to the formation of biominerals and the prevention of scale. Identification of the mechanisms that govern crystallisation therefore promises the ability to generate crystals with specific structures, morphologies and sizes, to inhibit or promote crystallisation as desired and to determine when and where crystals form. However, this can be extremely challenging as crystallisation is often rapid, and, in bulk solution, is affected by variables including the presence of impurities and the rate of stirring.

Here, a new strategy for studying crystallisation reactions under highly reproducible reaction conditions is reported. A microfluidic device was used to create large numbers of flowing water-in-oil droplets, where each droplet was its own reaction environment. Crystallisation was then studied *in situ* within the droplets using synchrotron powder X-ray diffraction (PXRD). The device employed was constructed as an insert-based device (**Figure 90**) and comprised a polymer insert sealed between two X-ray transparent windows. The crystallising solution was mixed at the inlet junction before forming droplets that flowed along a serpentine channel (diameter 0.3 mm) in the oil carrier phase. The device can be used with different temperatures and solvents and offers residence times of 5-10 minutes.

Fig. 90: Sketch of the construction of the microfluidic device.

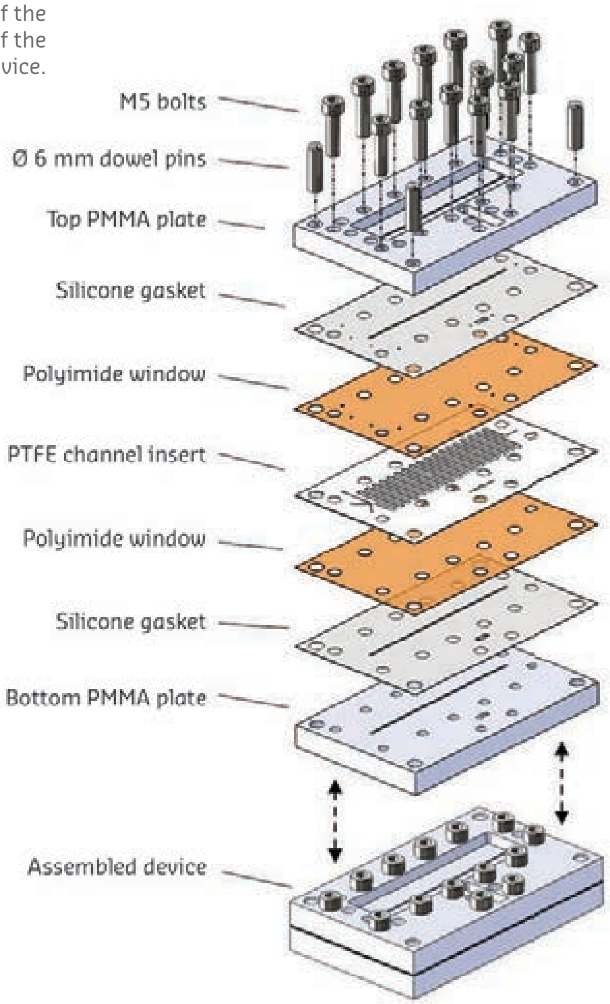

The assembled device was mounted on beamline **ID13** where it could be moved with respect to the X-ray beam. Different positions along the flow channel correspond to specific reaction times and PXRD patterns were acquired from droplets flowing past each position (**Figure 91a**). Excellent time resolution was achieved and the short screening time of individual droplets ensured that the effect of the high-energy X-ray beam on the reaction was minimised. Crucially, the measurements were carried out using a detector frame rate greater than the frequency of passing droplets such that frames taken of the oil phase could be discarded. The remaining frames corresponding to the aqueous droplets were background subtracted, and all of the diffraction data recorded at a specific location were combined into a single diffraction pattern.

This approach was used to identify effective nucleating agents (nucleants) that accelerate the formation of calcium carbonate crystals. While the ability to control nucleation is desirable for numerous applications, effective nucleants are as yet only known for a small number of systems, and many questions remain concerning the mechanisms by which they operate. Non-porous and porous bioactive glasses (BG) (**Figure 91b**), unfunctionalised and carboxylate-functionalised controlled pore glasses (CPG), and the minerals kaolinite, NX illite, amazonite and montmorillonite were investigated as potential nucleants, where these exhibit contrasting surface chemistries and porosities. Droplet microfluidic PXRD was used to determine the induction times – that is the time at which crystals are first detected – and results were compared with nucleant-free conditions and droplets containing calcite nanoparticles; the latter provide ideal nucleants. Induction times varied from ≤ 4.23 sec for experiments with calcite seeds to over 30 minutes (determined by halting flow and incubating droplets on-chip) for control conditions. Notably, the porous BG was almost as effective as the calcite seeds (t_{ind} ≤ 12.15 sec), while NX illite (t_{ind} ≤ 16.00 sec) and the non-porous BG (t_{ind} ≤ 40.77 sec) were also highly active.

Effective nucleants have been proposed to operate via a range of mechanisms including: (i) offering a low crystal/nucleant interfacial energy; (ii) adsorbing ions/molecules from the solution, thus locally increasing supersaturation; (iii) aligning solute molecules; (iv) promoting the formation of different polymorphs and (v) exhibiting surface defects that promote nucleation. BGs are known to promote the formation of hydroxyapatite (calcium phosphate), and mesoporous varieties are effective nucleants for proteins, where the pores appear to promote nucleation.

These experiments showed that both BGs are effective nucleants for calcium carbonate while CPGs with comparable pore sizes are not. Further, after normalising for surface area, the porous and non-porous BGs exhibit comparable activities. The activity of the BG can therefore be attributed to its surface chemistry rather than porosity, where local dissolution of the surface leads to the formation of an amorphous, calcium- and carbonate-rich layer, which facilitates calcite nucleation.

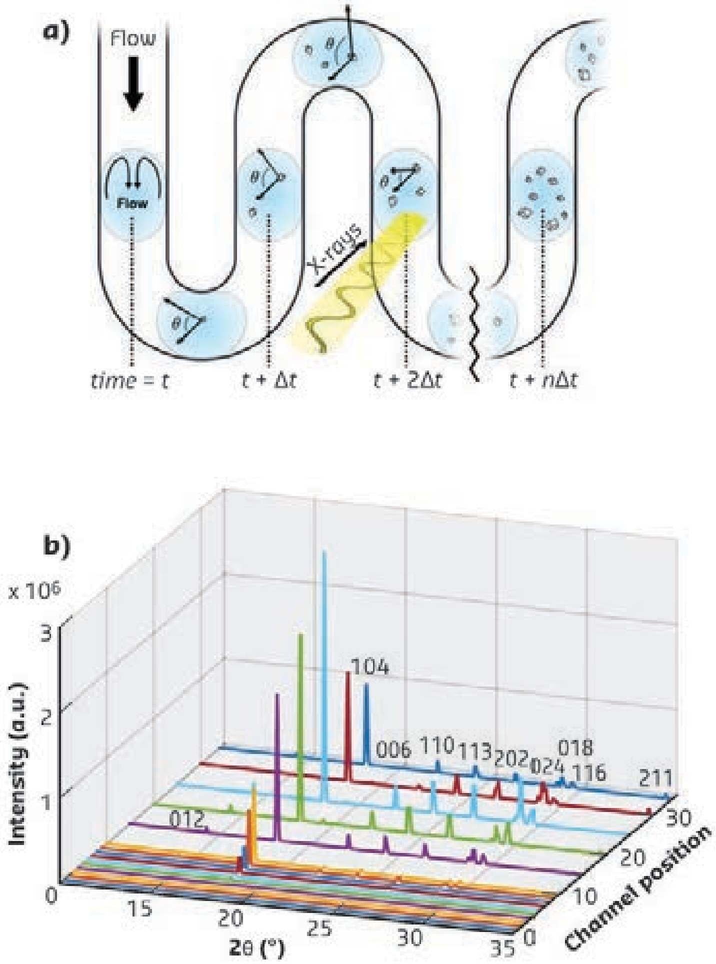

Fig. 91: a) Illustration of the experimental set-up and **(b)** PXRD measurements for experiments with porous bioactive glass. Each channel position corresponds to a specific reaction time.

PRINCIPAL PUBLICATION AND AUTHORS

Droplet Microfluidics XRD Identifies Effective Nucleating Agents for Calcium Carbonate, M. A. Levenstein (a,b), C. Anduix-Canto (b), Y-Y Kim (b), M. A. Holden (b), C. González-Niño (a), D. C. Green (b), S. E. Foster (b), A. Kulak (b), L. Govada (c), N. E. Chayen (c), S. J. Day (d), C. T. Tang (d), B. Weinhausen (e), M. Burghammer (e), N. Kapur (a) and F. C. Meldrum (b), *Adv. Funct. Mater.* **29**(19), 1808172 (2019); doi: 10.1002/adfm.201808172.

(a) School of Mechanical Engineering, University of Leeds (UK)
(b) School of Chemistry, University of Leeds (UK)
(c) Computational and Systems Medicine, Imperial College London (UK)
(d) Diamond Light Source (UK)
(e) ESRF

FOLLOWING NANO- AND MICROPARTICLE DEBRIS OF TATTOO NEEDLES THROUGH THE BODY

Metal particles are released from tattoo needles when the white pigment titanium dioxide is used. The particles are deposited in skin and lymph nodes and contain high amounts of the allergens nickel and chromium, which may be released over time by corrosion.

Pigment-loaded lymph nodes have been observed during medical procedures in tattooed individuals for a long time. In 2017, the first physico-chemical analysis of tattoo pigments in terms of pigment identity and particle size of matching skin and lymph node samples of the same donors was published **[1]**.

In further high-resolution X-ray fluorescence (XRF) studies at beamline **ID16B**, iron particles and high amounts of nickel and chromium (**Figure 92a**) were found in additional skin and lymph node sections – with nickel and chromium particles ranging from 50 nm (resolution limit) to 4 µm. Additional X-ray absorption near

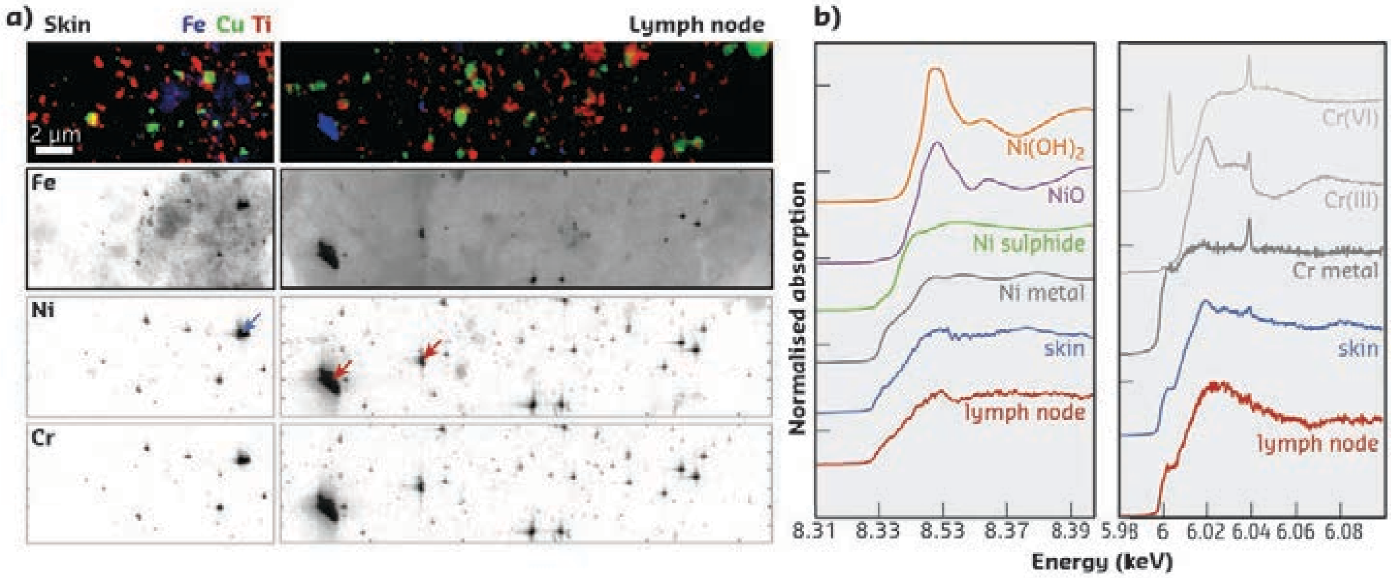

Fig. 92: X-ray fluorescence (XRF) and X-ray absorption near edge structure (XANES) analysis of human samples at ID16B. **a)** Skin and lymph node XRF analysis of one donor. **b)** Nickel and chromium XANES analysis on the indicated particles in (**a**).

edge structure (XANES) analysis revealed that nickel and chromium were mainly present as metals and, to a lesser extent, in oxidised form (**Figure 92b**).

Mixtures of iron, nickel and chromium are commonly used as steel alloy. Therefore, the origin of these particles was investigated. Over 50 ink samples of black, white and red colour were analysed, but none contained similar particles. Hence, contamination from steel vessels during manufacturing of pigments could be excluded.

The same applies for microtome knives, which were used for preparing thin sections of the tissues in the sample preparation process, as they also did not contain nickel. However, all tattoo needles analysed with a table-top XRF instrument (Fischerscope X-ray XDV-SDD) were composed of a steel alloy with up to 9% nickel and 18% chromium.

To get final confirmation of the needles being the origin of nickel and chromium, thawed pig skin was tattooed with inks containing either carbon black or white titanium dioxide pigments. Only the white ink, containing titanium dioxide, led to a major deposition of metal particles in the skin as shown in XRF analysis carried out at **ID21** (**Figure 93a**). Scanning electron microscopy (SEM) images of the needle tips before and after tattooing also revealed the wear of metal from its surface when titanium dioxide was used (**Figure 93b**) – further evidencing that only the dense titanium pigment leads to an abrasion of the metal. This is in accordance with the observation that the metal particles were always located in close proximity to titanium dioxide in human skin and lymph node tissues.

This finding is particularly worrisome because nickel and chromium are the two most common allergens in the European population. Corrosion of these metals over time can release the corresponding allergenic metal ions and thus may play a role in allergy development. Until now, putative nickel allergy in tattoos was always believed to be caused by impurities of iron oxide pigments. These new findings suggest that this metallic debris may be another major source of

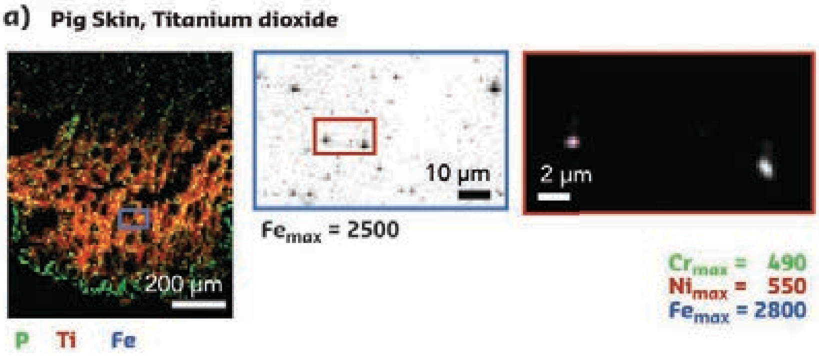

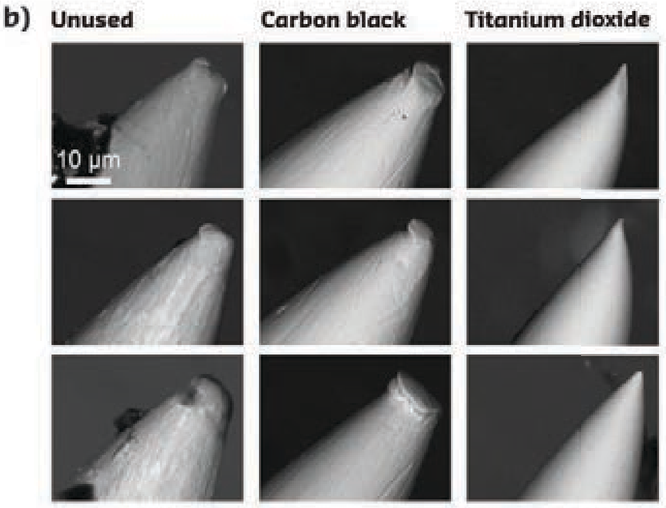

Fig. 93: Tattooed pig skin with carbon black and titanium dioxide white pigments. **a)** XRF mapping at ID21. Tattooing thawed pig skin with titanium dioxide results in deposition of metal particles composed of the iron-nickel-chromium alloy of the tattoo needle. **b)** SEM images of the tattoo needles before and after tattooing reveal prominent wear upon using titanium dioxide.

nickel in tattoos. This hypothesis is underpinned by an observation in a skin biopsy of a nickel-sensitised tattoo-allergy patient in this study: nickel intensities in XRF analysis at ID16B were higher in areas with metal debris and titanium dioxide than in areas with iron oxide pigments.

PRINCIPAL PUBLICATION AND AUTHORS

Distribution of nickel and chromium containing particles from tattoo needle wear in humans and its possible impact on allergic reactions, I. Schreiver (a), B. Hesse (b,c), C. Seim (c,d,e), H. Castillo-Michel (b), L. Anklamm (f), J. Villanova (b), N. Dreiack (a), A. Lagrange (c,g), R. Penning (h), C. De Cuyper (i), R. Tucoulou (b), W. Bäumler (j), M. Cotte (b,k) and A. Luch (a), *Part. Fibre Toxicol.* **16**, 33 (2019); doi: 10.1186/s12989-019-0317-1.

(a) Department of Chemical and Product Safety, German Federal Institute for Risk Assessment, Berlin (Germany)
(b) ESRF
(c) Xploraytion GmbH, Berlin (Germany)
(d) Department of X-ray Spectrometry, Physikalisch-Technische Bundesanstalt, Berlin (Germany)
(e) Institute for Optics and Atomic Physics, Technical University Berlin (Germany)
(f) Helmut Fischer GmbH Institut für Elektronik und Messtechnik, Berlin (Germany)
(g) Institute of Materials Science and Technologies, Technical University Berlin (Germany)
(h) Institute of Forensic Medicine, Ludwig-Maximilians University, Munich (Germany)
(i) Dermatologist, Blankenberge (Belgium)
(j) Department of Dermatology, University of Regensburg (Germany)
(k) Laboratory of Molecular and Structural Archaeology (LAMS), Sorbonne University, Paris (France)

REFERENCES

[1] I. Schreiver *et al., Sci Rep* **7**, 11395 (2017).

HOW BONE IS BORN: OBSERVING ITS ORIGIN INSIDE CELLS

The early stages of biomineralisation have been investigated using phase-contrast X-ray imaging (PCXI) and X-ray fluorescence (XRF) to evaluate the initial mineral depositions in human bone mesenchymal stem cells exposed to an osteogenic cocktail. The results provide a deeper understanding of the intracellular molecular mechanisms governing the initial phases of bone tissue formation.

Biomineralisation is the process by which living systems generate organised mineral crystals. Hydroxyapatite (HA) is a naturally occurring mineral form of calcium apatite with the general formula: $(Ca_{10-x}Y_x)(PO_4)_6(OH)_{2-p}(CO_3)_p$, where Y indicates the typical substituting metals (Zn, Mg, Sr) found in many tissues including bones and cartilage **[1]**. Biomineralisation is a lifelong process, fundamental in bone formation, repair and remodelling. Bone shows a complex structure organised across multiple length scales, from the molecular to the macroscopic level. On the nanometric scale, collagen microfibrils direct the formation of nanosized (HA) platelets oriented parallel to the collagen fibril axis, for interfibrillar mineralisation **[2]**.

Biomineralisation depends upon the complex crosstalk between osteoclasts, osteoblasts and osteocytes. Osteoclasts digest bone matrix while osteoblasts synthesise it and orchestrate its mineralisation. As the precursor of osteoblasts and osteocytes, human bone mesenchymal stem cells (bMSC) were investigated to unveil

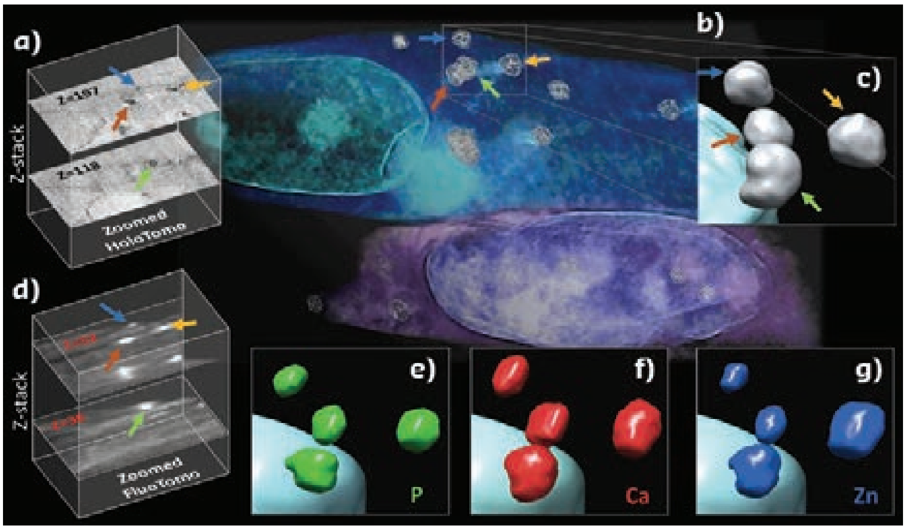

Fig. 94: a) Two slices of the z-stack reconstructed from the phase-contrast tomography. **b)** Volume rendering of the phase-contrast nano-tomography data. The coloured arrows indicate four intracellular depositions. **c)** Zoomed 3D solid nano-rendering of the four granules highlighted in panel **(b)**. **d)** Two slices of the z-stack reconstructed from the X-ray fluorescence tomography. **e,f,g)** Zoomed 3D nano-rendering of P, Ca and Zn intracellular depositions, respectively.

the molecular basis of osteogenesis. Calcium is a crucial mineral for the bone and is present in the extracellular mineralised matrix as an integral component of hydroxyapatite crystals. Very little is known about the progression of the extracellular Ca-phosphate and polyphosphate deposition during osteoblast differentiation. The core knowledge is provided by studies on the advanced phases of biomineralisation, mainly occurring in the extracellular matrix, while studies on the early stages of this process are scarce.

This work reports findings on the early stages of biomineralisation (*i.e.*, the genesis and evolution of the mineral nuclei and their elemental composition during the osteogenic differentiation of human bMSC). Over the last decade, cutting-edge X-ray synchrotron-based microscopy techniques have been improved to overcome the limitations in spatial resolution and in sensitivity, becoming more accessible and common in life science studies. These breakthroughs made it possible to study the biomineralisation in single cells at the intracellular level and in the extracellular matrix where part of this phenomenon takes place. Investigations were conducted on frozen-hydrated samples, keeping the bMSC as close as possible to their natural hydrated state and preserving the structural and chemical information. Combined PCXI and XRF acquisitions (**Figure 94**), carried out at beamline **ID16A**, were pushed to their technical and physical limits in terms of spatial resolution, with pixel sizes down to 15 nm in two and three dimensions. Both the phase-contrast nano-tomography and X-ray fluorescence tomography data were acquired from the same frozen-hydrated cells, enabling a correlative interpretation of the results.

Further combination of different synchrotron microscopy and laboratory X-ray diffraction techniques made it possible to follow the evolution of hydroxyapatite formation in differentiating bMSC during the early stage of biomineralisation. A quantitative assessment of the chemical composition of the mineral depositions, together with the characterisation of their molecular and crystalline structures, is provided. The analysis reveals that biomineralisation starts with hydroxyapatite nucleation *within* the cell, and rapidly evolves toward a hexagonal hydroxyapatite crystal structure very similar to the one present in mature human bone, as detected after just 10 days of osteogenic induction. Zn inclusion in the mineral depositions favours the nucleation of the hydroxyapatite crystal lattice and at 10 days the process of Zn incorporation is almost complete. **Figure 95** shows a proposed model based on these results, with a possible mechanism for the genesis and the evolution of hexagonal hydroxyapatite.

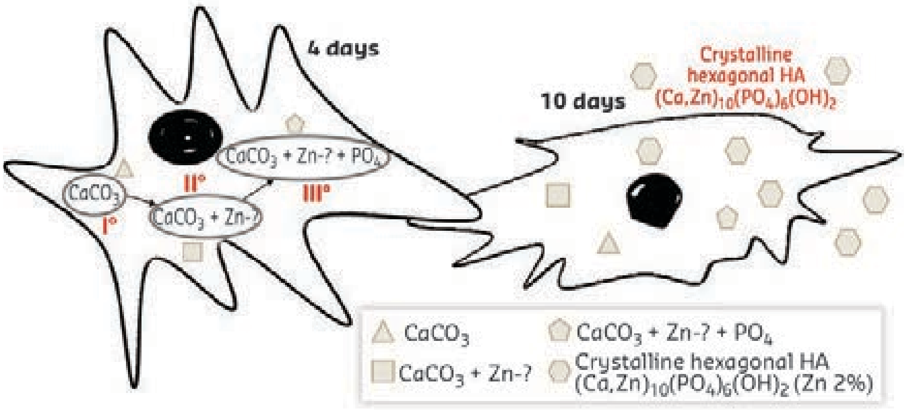

Fig. 95: The graph depicts a model based on the results obtained in this study, hypothesising a mechanism for the genesis and the evolution of the hexagonal hydroxyapatite. The mineral depositions showing a different elemental composition are represented by different polygonal shapes. The roman numerals portray the chronological sequence.

PRINCIPAL PUBLICATION AND AUTHORS

Chemical Fingerprint of Zn–Hydroxyapatite in the Early Stages of Osteogenic Differentiation, A. Procopio (a), E. Malucelli (a), A. Pacureanu (b), C. Cappadone (a), G. Farruggia (a,f), A. Sargenti (a), S. Castiglioni (c), D. Altamura (d), A. Sorrentino (e), C. Giannini (d), E. Pereiro (e), P. Cloetens (b), J. A. Maier (c) and S. Iotti (a,f), *ACS Cent. Sci.* **5**(8), 1449-1460 (2019); doi: 10.1021/acscentsci.9b00509.

(a) Department of Pharmacy and Biotechnology, University of Bologna (Italy)
(b) ESRF
(c) Department of Biomedical and Clinical Sciences L. Sacco, University of Milan (Italy)
(d) Institute of Crystallography, National Research Council, Bari (Italy)
(e) ALBA Synchrotron Light Source, Cerdanyola del Vallès, Barcelona (Spain)
(f) National Institute of Biostructures and Biosystems, Rome (Italy)

REFERENCES

[1] D. M. Roy *et al., Nature* **247**, 220-222 (1974).
[2] F. Nudelman *et al., Nat. Mater.* **9**(12), 1004-1009 (2010).

SUBCELLULAR VISUALISATION OF CELL ARCHITECTURE AND NUTRIENT HOMEOSTASIS IN PLANKTONIC SYMBIOSIS

Photosymbiosis in marine plankton is common in oceans worldwide. High-resolution imaging techniques showed that the structural organisation and nutrient composition of microalgae significantly change following integration into a host, towards a powerful photosynthetic machinery. This improves understanding of the functioning of the ecologically important symbiosis between a host and its intracellular microalgae.

Living in symbiosis with microalgae (photosymbiosis) is a widespread and ecologically important phenomenon in oceanic plankton (**Figure 96**). These planktonic organisms are essential for the global climate since they contribute to the carbon cycle. They are particularly abundant in the world´s open oceans, where nutrients such as P, N and trace metals are poorly available. The ecological success of this cell–cell interaction relies on a mutualistic relationship: the host provides protection and a nutrient-rich microhabitat and in turn, the microalgae provide energy thanks to photosynthesis. However, this paradigm remains largely unexplored. This study combined different nano-imaging approaches to unveil the structural and metabolic strategies of symbiotic cells at the subcellular level, and to answer crucial questions, such as how the host integrates and controls its microalgae.

Live cells were collected in surface waters of the Mediterranean sea and individually isolated through a microscope. Sample preparation protocols were developed in order to conduct multimodal subcellular imaging, using a combination of 3D electron microscopy, nanoscale mass spectrometry, and synchrotron X-ray fluorescence (XRF) imaging. The 3D ultrastructure and nutrient homeostasis were evaluated on microalgae between their free-living (*e.g.*, in culture without the host) and symbiotic (inside a host) stages. Macronutrients such as P and N were visualised with nanoscale secondary ion mass spectrometry (nanoSIMS) while the quantitative mapping of the trace metals Fe, Co and Mn were obtained with XRF on beamlines **ID16B** and **ID21**.

The study revealed that the algal cell inside a host has a larger volume with multiple chloroplasts compared to its free-living stage. There is a ~40-fold increase of the volume of chloroplasts when the algal cell is integrated into a host cell. Physiological measurements showed an increased photosynthetic efficiency of microalgae in symbiosis, corroborating electron microscopy observations. In order to highlight possible metabolic changes induced by symbiosis, the subcellular distribution and composition of nutrients were investigated. NanoSIMS data revealed high content of N in symbiotic microalgae but very low P. This raised the hypothesis of whether low P reflects a host-imposed P limitation for controlling algal growth.

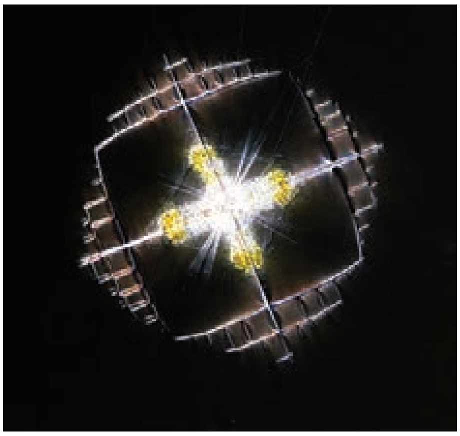

Fig. 96: Light microscopy image showing a host cell with biomineralised skeleton and intracellular microalgae *Phaeocystis*.

Trace metals are essential for photosynthesis, antioxidant protection and other essential biochemical functions of microalgae. These elements are the main drivers of primary productivity in the ocean. XRF imaging showed that Fe concentration in symbiotic microalgae was twice as high (90 ± 23 ppm) as that in free-living microalgae (44 ± 6 ppm) (**Figure 97**). This was mainly due to the presence of large Fe-rich vacuoles in the algal cytosol containing up to 660 ppm Fe. This implies that a significant amount of Fe is delivered to the microalgae by the host in order to sustain their photosynthetic activity. Once sequestered in the microalgae, the homeostasis of this essential yet toxic metal could be regulated through storage vacuoles to minimise oxidative stress. Variability in metal homeostasis was also found for Co. Co was only

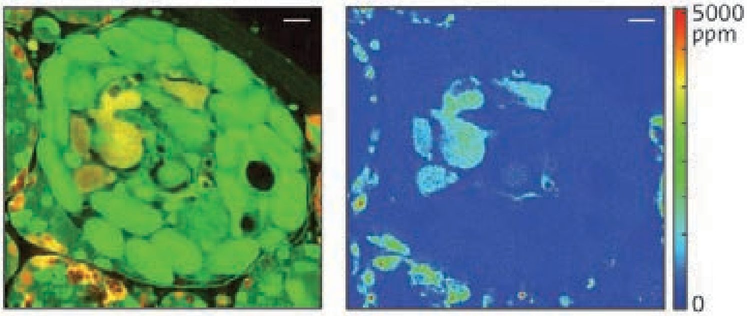

Fig. 97: Subcellular distribution and quantification of the trace metal Fe in symbiotic microalgae by synchrotron X-ray fluorescence imaging on a single cell section.
Left: Os (green) *vs.* Fe (red). Right: Quantitative false-colour representation of Fe concentration. Scale bar = 1 µm.

detected in symbiotic microalgae (25 ± 17 ppm), specifically in the nucleus, some organelles, and the Fe-rich vacuole. Overall, subcellular quantitative mapping of metals showed that the metal homeostasis of microalgae was dramatically altered in symbiosis, implying specific mechanisms by which the host takes up and transfers these key elements to its symbionts.

This study shows that microalgae can radically transform, both morphologically and metabolically, following their integration into a host cell, a process that has not previously been reported in other algal symbioses (*e.g.*, coral reef). This opens new perspectives to further decipher these mechanisms at the molecular level and to better assess the impact of climate change on photosymbiosis in the ocean.

PRINCIPAL PUBLICATION AND AUTHORS

Algal Remodeling in a Ubiquitous Planktonic Photosymbiosis, J. Decelle (a,f), H. Stryhanyuk (a), B. Gallet (b), G. Veronesi (c,i), M. Schmidt (a), S. Balzano (d), S. Marro (e), C. Uwizeye (g), P. H. Jouneau (g), J. Lupette (f), J. Jouhet (f), E. Maréchal (f), Y. Schwab (h), N. L. Schieber (h), R. Tucoulou (i), H. Richnow (a), G. Finazzi (f) and N. Musat (a), *Curr. Biol.* **29**(6), 968-978.e4 (2019); doi: 10.1016/j.cub.2019.01.073.

(a) Helmholtz Centre for Environmental Research - UFZ, Department of Isotope Biogeochemistry, Leipzig (Germany)
(b) Institut de Biologie Structurale (IBS), Université Grenoble Alpes, CNRS, CEA, Grenoble (France)
(c) Laboratoire de Chimie et Biologie des Métaux UMR 5249, Université Grenoble Alpes, CNRS, CEA, Grenoble (France)
(d) NIOZ, Royal Netherlands Institute for Sea Research, Department of Marine Microbiology and Biogeochemistry, and Utrecht University (The Netherlands)
(e) Sorbonne Universités, UPMC Université Paris 06, CNRS, Laboratoire d'Océanographie de Villefranche UMR7093, Observatoire Océanologique, Villefranche-sur-Mer (France)
(f) Cell & Plant Physiology Laboratory, UMR 5168 Université Grenoble Alpes, CNRS, CEA, INRA, Grenoble (France)
(g) Institut Nanosciences et Cryogénie, Université Grenoble Alpes, CEA, Grenoble (France)
(h) Cell Biology and Biophysics Unit, European Molecular Biology Laboratory (EMBL), Heidelberg (Germany)
(i) ESRF

REVEALING THE PATH OF A METALLODRUG IN A BREAST CANCER CELL

Triple-negative breast cancers are known to have poor prognosis and are among the most difficult to treat. Osmocenyl-tamoxifen offers new possibilities to counteract cancer resistance mechanisms. Synchrotron X-ray fluorescence (XRF) nanoimaging offers invaluable capabilities to quantitatively trace the intracellular distribution of metal-based drugs at biologically relevant concentrations in a label-free fashion.

Triple-negative breast cancer (TNBC) represents 10-20% of breast cancers. It is not fuelled by hormones, testing negative for estrogen and progesterone receptors and excess HER2 protein, meaning it does not respond to hormonal therapy and antibody medicines. Although some patients may respond to classic chemotherapy treatment, relapse rates are high and a large number are likely to develop resistance, making this cancer very difficult to treat. Metallocifens, derivatives of the widely used drug tamoxifen, have demonstrated their broad spectrum of efficacy and their potential to significantly overcome drug resistance. To go further, it is critical to understand the path that such organometallic molecules follow to reach cancerous cells and how they manage to kill them.

Cutting-edge synchrotron imaging brought unique insight into the intracellular distribution of osmocenyl-tamoxifen (Oc-OH-Tam), which could be tracked with a resolution down to 35 nm using 2D and 3D cryo-XRF at beamline **ID16A**. The intrinsic presence of an osmium atom in the structure of Oc-OH-Tam allows its direct mapping through the XRF emission spectrum, along with physiological elements such as Zn (**Figure 99a**). The images of chemically fixed MDA-MB-231 cells exposed to 2 μM Oc-OH-Tam for 1h (**Figure 98**), during which no cytotoxicity is observed, demonstrated that osmocenyl-tamoxifen readily reached the targeted intracellular compartments owing to its high lipophilicity. The intracellular distribution of Os remains similar after 24h exposure, with Os areal mass density increasing about 2.3-fold. The extended perinuclear localisation of Os around the nucleus follows a pattern likely consistent with endoplasmic reticulum (ER) and nuclear envelope localisation. Indeed, ER is a well-described organelle organised as an intricate perinuclear network including interconnected membrane structures (tubules, vesicles and cisternae) continuous to the outer nuclear envelope. The additional exposure to the antimitotic agent nocodazole that induces microtubule disruption and a known retraction of the ER back towards the cell centre **[1]** is clearly associated with Os redistribution (**Figure 99a**).

The perinuclear Os localisation follows the distribution of the ER-specific fluorescent probe applied before chemical fixation (**Figure 99b**).

This further supports preferential accumulation of Oc-OH-Tam in the ER. High-energy (17 KeV) 3D XRF nanoimaging of frozen hydrated cells as exemplified in **Figure 99c** supports the above Os distribution and highlights, among an improved preservation of cell volume and distribution of diffusible ions, a very high concentration of Oc-OH-Tam in vesicular structures. As a scenario, the highly lipophilic Oc-OH-Tam targets membrane components that are exchanged among organelles of the endomembrane system. The osmocenyl-tamoxifen is preferentially stored along the ER, where it can be oxidised to release diffusible and highly toxic metabolite quinone methide, leading to the inhibition of the thioredoxin reductase, eventually resulting in cell senescence (**Figure 99d**).

The level of sensitivity and spatial resolution reached by synchrotron cryo-nanoprobes such as ID16A opens exciting possibilities, contributing to a deeper understanding of the time-dependent uptake and behaviour of metallocifens in a cellular environment.

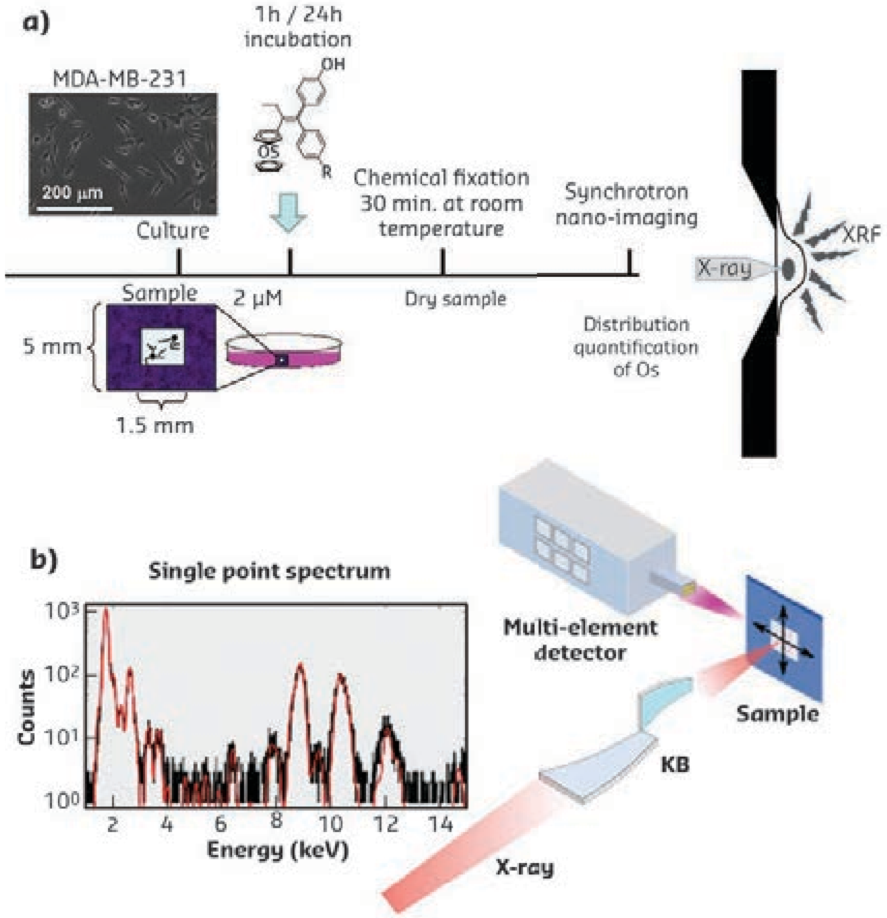

Fig. 98: *a)* MDA-MB-231 cells exposed 1h or 24h to the metallodrug Oc-OH-Tam. Cells are sub-cultured on a silicon nitride window and chemically fixed with 4% paraformaldehyde during 20 mins at room temperature and, after thorough rinsing, left to dry. **b)** XRF nanoanalysis is carried out to produce quantitative elemental images.

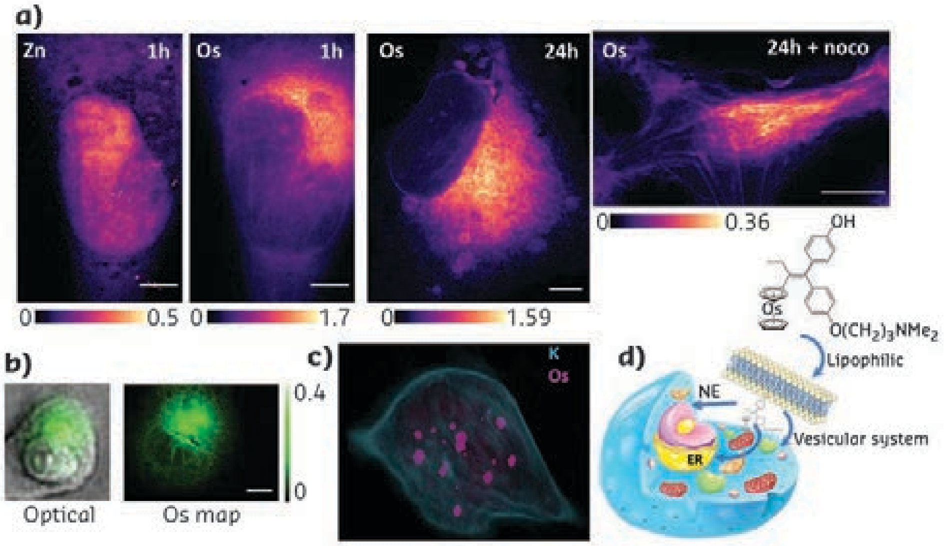

Fig. 99: *a)* XRF maps of Zn and Os of chemically fixed MDA-MB-231 breast cancer cells after 1h and 24h exposure to 2 µM Oc-OH-Tam, or followed by 5h exposure to 5 µM of the microtubule-disrupting drug nocodazole. Images for 1h exposure were raster scanned with 35 x 35 nm^2 step size, while others were obtained at 50 x 50 nm^2, dwell time of 50 ms. **b)** Epifluorescence optical microscopy image of the cell prior to fixation labeled with ER-TrackerQ Blue-White DPX fluorescent dye (green false colour) and its associated Os distribution (projection at normal incidence from the 3D XRF dataset, 100 nm step size and 50 ms dwell time). **c)** 3D rendering of K and Os distributions in a frozen hydrated MDA-MB-231 cell after 1h exposure to 2 µM Oc-OH-Tam (28 projections over 150 deg., 120 nm voxel size, 50 ms dwell time). **d)** Scheme of proposed scenario to explain the anticancer activity of Oc-OH-Tam. Colour calibration bars in µg/cm^2. Scale bar 5 µm.

PRINCIPAL PUBLICATION AND AUTHORS

Intracellular Localization of an Osmocenyl-Tamoxifen Derivative in Breast Cancer Cells Revealed by Synchrotron Radiation X-ray Fluorescence Nanoimaging, F. Fus (a,b), Y. Yang (b), H. Z. Shirley Lee (c), S. Top (c,d), M. C. Carrière (e), A. Bouron (f), A. Pacureanu (b), J. C. da Silva (b), M. Salmain (d), A. Vessières (d), P. Cloetens (b), G. Jaouen (c,d) and S. Bohic (a,b), *Angew. Chem. Int. Ed. Engl.* **58**, 3461 (2019); doi: 10.1002/anie.201812336.

(a) Inserm UA7, Rayonnement Synchrotron pour la Recherche Biomédicale (STROBE) Université Grenoble Alpes (France)
(b) ESRF
(c) 3PSL, Chimie ParisTech, Paris (France)
(d) Sorbonne Université, CNRS, Institut Parisien de Chimie Moléculaire (IPCM), Paris (France)
(e) Université Grenoble Alpes, CEA, CNRS, INAC-SyMMES, CIBEST, Grenoble (France)
(f) Laboratoire de Chimie et Biologie des Métaux, UMR CNRS 5249, Université Grenoble Alpes, CEA, BIG, Grenoble (France)

REFERENCES

[1] M. Terasaki *et al., J. Cell. Biol.* **103**, 1557-1568 (1986).

NANOWIRE INTERNALISATION AND CRUMPLING BY SKIN CELLS OBSERVED BY NANOHOLOTOMOGRAPHY AND SPECTROMICROSCOPY

Silver nanowire (AgNW)-based conductive transparent networks can enable flexible electronics but might expose consumers to nanomaterials. Holotomographic imaging of cells exposed to AgNWs revealed that thinner and flexible AgNWs are mechanically crumpled, reducing toxicity. Products including touchscreens and functionalised paper incorporating thinner AgNWs retain technical performances while being safer.

Future generations of smartphones may incorporate electrically conductive and optically transparent networks of nanowires made of metals such as silver. The high flexibility of such networks is expected to enable the manufacture of exciting new portable consumer devices that include curved or flexible touchscreen displays. Under the European Union's REACH regulations, all new nanomaterials require an assessment of their potential effects on human health and the environment. Silver nanowires (AgNWs) share similar characteristics with asbestos mineral fibres, including a fibrous morphology and high redox reactivity. In the early 20th century, before the health risks of asbestos were understood, this material was widely used for electrical and thermal insulation, construction and many other applications.

Previous studies of AgNWs observed low toxicity in conventional assays that are relevant to inhalation exposure. Because consumer devices could be incorporated into clothing, however, this work evaluated the potential for AgNW toxicity caused by skin exposure. The interactions of AgNWs with dermal cells that have no role in immune response, that is, engulfing and killing bacterial pathogens, was studied. Two types of dermal cell, fibroblasts and keratinocytes, were found to internalise AgNWs added to cell growth media. Uptake by endocytosis led to cellular injury at high doses **[1]**.

Given this finding, it was investigated whether the nanowires could be designed to be safer. It was anticipated that nanowire morphology could be an important factor controlling internalisation but there had been no study elucidating the role of fibre diametre because of the difficulty of controlling this parameter in synthesis. A method was developed to control silver nanowire diametre, and lower-diametre nanowires were shown to be significantly less toxic to human and mouse skin cells and fish gut epithelial cells. Optical microscopy showed that thinner nanowires were just as likely to enter the cells as thicker nanowires. Optical imaging, however, did not have the resolution or chemical sensitivity to reveal the mechanism of this size-dependent toxicity.

Coherent X-ray imaging showed how the nanowires interacted with the cell. Nanoholotomography of frozen cells acquired on beamline **ID16A** provided 3D snapshots showing the location and shape of individual nanowires. X-ray fluorescence and absorption spectroscopy at beamline **ID21** completed the chemical picture. As illustrated in **Figure 100**, the images showed that thinner nanowires were deformed and crumpled inside the cell. Deformed nanowires remained encapsulated by the membrane of the endolysosome

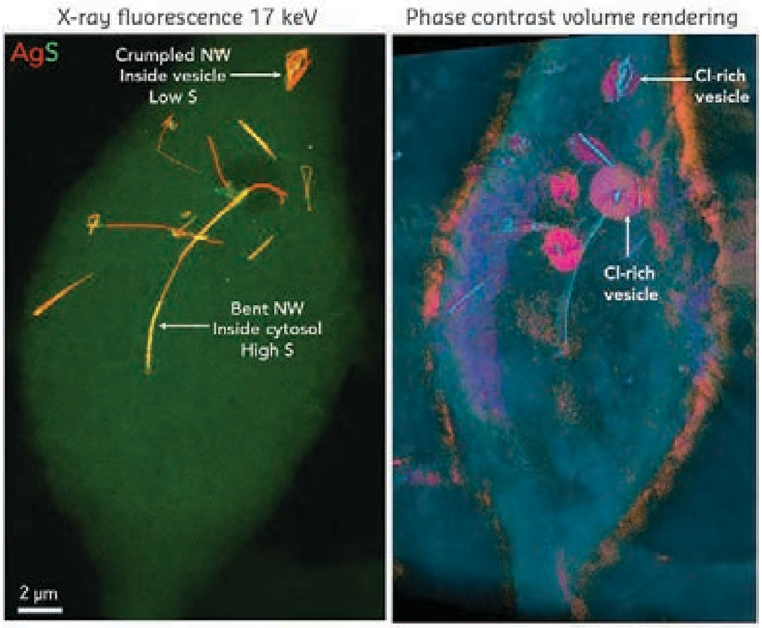

Fig. 100: Two high-resolution X-ray images of silver nanowires (AgNWs) internalised within the same single mouse fibroblast cell. **a)** The elemental map shows bent and crumpled AgNWs by the Ag fluorescence signal (red) that are variably associated with sulphur (green). **b)** 3D holotomography shows all the AgNWs to be associated with Cl-rich vesicles interpreted to be endolysosomes. Non-crumpled AgNWs penetrate from the vesicles into the cytosol.

vesicles. By contrast, thicker nanowires were not significantly bent and actually punctured through the vesicle membrane into the cell interior. A remarkable conclusion of this study is that cell's lipid bilayers can mechanically deform metallic wires. The observations clearly implicate this deformation as being the critical mechanism for reducing toxicity.

The technological performance (electrical conductivity and film transparency) of AgNWs is affected by diametre, but the thinner ones were found to be equally or better suited for transparent conductive networks. This work illustrates an approach to reduce the potential harm from advanced nanotechnologies early in the design stage.

PRINCIPAL PUBLICATION AND AUTHORS

Crumpling of silver nanowires by endolysosomes strongly reduces toxicity, S. G. Lehmann (a), D. Toybou (a,b), A. E. Pradas Del Real (c), D. Arndt (d), A. Tagmount (d), M. Viau (a), M. Safi (a), A. Pacureanu (c), P. Cloetens (c), S. Bohic (c,e), M. Salomé (c), H. Castillo-Michel (c), B. Omaña-Sanz (f,g,h), A. Hofmann (f,g,h), C. Vulpe (d), J. P. Simonato (b), C. Celle (b), L. Charlet (a) and B. Gilbert (i,j)
PNAS **116**(30), 14893-14898 (2019); doi: 10.1073/pnas.1820041116.
(a) Institut des Sciences de la Terre, Université de Grenoble-Alpes, CNRS (France)
(b) Laboratoire d'Innovation pour les Technologies des Energies Nouvelles et les Nanomatériaux, Département des Technologies des Nouveaux Matériaux, Université de Grenoble-Alpes, CEAEA (France)
(c) ESRF
(d) Center for Environmental and Human Toxicology, Department of Physiological Sciences, College of Veterinary Medicine, University of Florida (USA)
(e) Synchrotron Radiation for Biomedicine, Institut National de la Santé et de la Recherche Médicale, Grenoble (France)
(f) Laboratoire d'Océanologie et de Géosciences (LOG), UMR 8187, Université Lille (France)
(g) UMR 8187, CNRS, Lille (France)
(h) UMR 8187, Université Littoral Côte d'Opale, Wimereux (France)
(i) Institut des Sciences de la Terre, Université de Grenoble-Alpes, CNRS (France)
(j) Energy Geoscience Division, Lawrence Berkeley National Laboratory, California (USA)

REFERENCES

[1] S. G. Lehmann *et al*., *Nanomaterials* **8**, 232 (2018)

ELECTRONIC STRUCTURE, MAGNETISM AND DYNAMICS

2019 was an exceptional year that gave us the opportunity to venture beyond the beamlines. We travelled to other synchrotrons and the free electron laser, taught classes at universities and X-ray schools, and finally worked on those data that had been sitting in our drawers. We also improved the instrumentation at the beamlines, upgraded software and hosted several workshops to discuss the new possibilities of the Extremely Brilliant Source (EBS) with the user community.

Theoretical spectroscopy is an important development at the ESRF. In the past year, the graphical user interface for core-level spectroscopy calculations, *Crispy*, was presented during several hands-on tutorials at conferences and thematic schools. *Crispy* has also seen the first external contributions to the source code, highlighting the benefits of releasing the project using a free and open-source licence.

An experimental station dedicated to X-ray magnetic circular dichroism spectroscopy under high magnetic field and low temperatures on **ID12** is gaining much interest from the chemistry community. The 'non-magnetic' ground state of uranium ions in a molecular complex (Pedersen *et al.,* **page 128**) and the magnetic interaction in molecule-based materials mediated by aromatic redox-active ligands (Ma *et al.,* **page 111**) are presented in this chapter of the *ESRF Highlights*. X-ray natural circular dichroism (XNCD) of crystals near absorption edges to visualise chiral domains in non-centrosymmetric crystals is rapidly developing into a sensitive tool to study magnetoelectric properties in multiferroic crystals with micrometre resolution that will be readily achievable with the EBS.

One of the last activities on **ID20** before the EBS shutdown was the installation and commissioning of a new hard-X-ray spectrometer that allows analysis of the polarisation of the scattered photon beam in resonant inelastic X-ray spectroscopic measurements at the Ir L_3-edge. We are eager to exploit the new capabilities of this spectrometer with EBS. Niskanen *et al.* showed that X-ray spectra of liquid water at ambient conditions is compatible with continuous and near-tetrahedral models for its atomic structure (**page 106**). The inherent imaging capabilities of our large-solid-angle spectrometer were used to analyse the carbon speciation in an ancient insect in three dimensions for the first time (Georgiou *et al.,* **page 119**).

The ESRF is moving to new software to run its beamlines. A first stable version of BLISS has been released and **ID26** will be the first EMD beamline to implement the new standard. The beamline further improved its tender-X-ray spectrometer with respect to its energy resolution and the possibility to host various sample environments. Van der Linden *et al.* show on **page 115** how high-resolution spectroscopy combined with theoretical spectroscopy helps to identify the position of a Au atom in a Ag cluster. The activation of the O_2 bond in dicopper complexes is studied using valence-to-core XES by Cutsail *et al.* on **page 107**.

Beamline **ID28** provides complementary measurements with an inelastic X-ray side station and diffuse X-ray scattering. The demand of tandem experiments is expected to grow and extend to the domain of very small samples and thin films. The sample environment portfolio was enlarged by the electric field cells, mainly dedicated to studies of ferroics, and transport measurements *in situ*. Pogna *et al*. used ID28 to characterise the dynamics of very old glassy amber (**page 121**). The role of charge order in cuprates and how it relates to superconductivity is discussed in articles by Kim *et al.* (**page 108**), Miao *et al.* (**page 114**), and Arpaia *et al.* (**page 110**).

ID32 is expected to start user operation again in 2019 with much the same performance as before the EBS shutdown. However, the beamline team has taken the opportunity of the shutdown to start a modest upgrade program. ID32 should be able to offer improved energy-resolution for the RIXS experiments or improved intensity at the previously obtainable energy-resolution. Further improvements on the XMCD and RIXS branches will also be implemented by the end of 2020. The team will also be investigating the possibilities offered by the increased coherent flux in the soft X-ray range.

BM16 has commissioned its large-solid-angle crystal-analyser spectrometer with the aim to record high-energy-resolution X-ray absorption spectra at low absorber concentrations. The article by Sun *et al.* on **page 124** shows the capabilities of the instrument for the study of the electrocatalytic reduction of CO_2 over iron cations inserted into nitrogen-doped carbon.

BM20 has supplemented its ultra-trace EXAFS station with a five-crystal-analyser spectrometer for HERFD-XANES, XES and RIXS, a Pilatus 3x2M detector stage for single-crystal and *operando* powder diffraction, and a six-circle diffractometer for surface-sensitive CT and RAXR, and high-resolution powder XRD. The beamline is now able to offer a portfolio of methods to study actinides and other radionuclides. Dumas *et al.* focus on the chemical behaviour of plutonium, notably the peculiar reduction and incorporation of this element by magnetite (**page 126**).

The EBS shutdown has been an opportunity for **BM28** to undertake major upgrades to the beamline infrastructure as well as to the conditioning and optics elements. Due to the EBS lattice, BM28 will have a new X-ray source – the 0.86 T short-bend magnet has been selected. Coupled with the new storage ring, this choice will significantly increase the capability of XMaS, enabling operation at higher X-ray energies. New beamline optics extend the range to 2.05 – 40 keV and a new suite of 2D detectors will complement the existing pool. Dann *et al.* (**page 118**) measured the L-edges of Pd in nanoparticles at 3.2 keV to study their catalytic activities.

The sample environment unit worked with the radiation protection group on the dismantling of the old storage ring girders. A large robotic arm was installed and programmed allowing all the dismantled parts to be checked for radioactivity. The year was also busy concerning instrumentation for the beamlines. A new He cryostat was assembled and commissioned allowing high-angular-resolution data acquisition and fast 2D imaging for PDF experiments on ID22. EBS requires more precise sample positioning and stability. A review of all the sample environment-related instruments was carried out. The information is available to our user communities through the ESRF web pages and the Way for Light portal.

P. GLATZEL

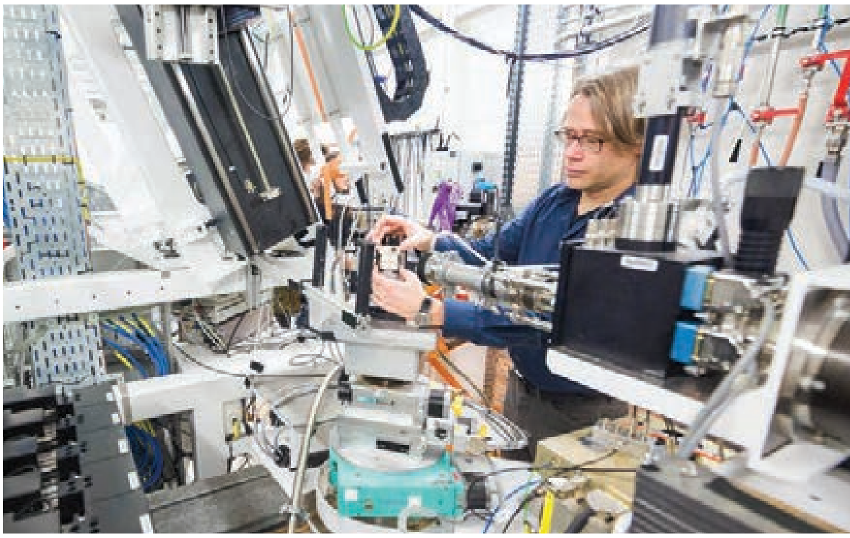

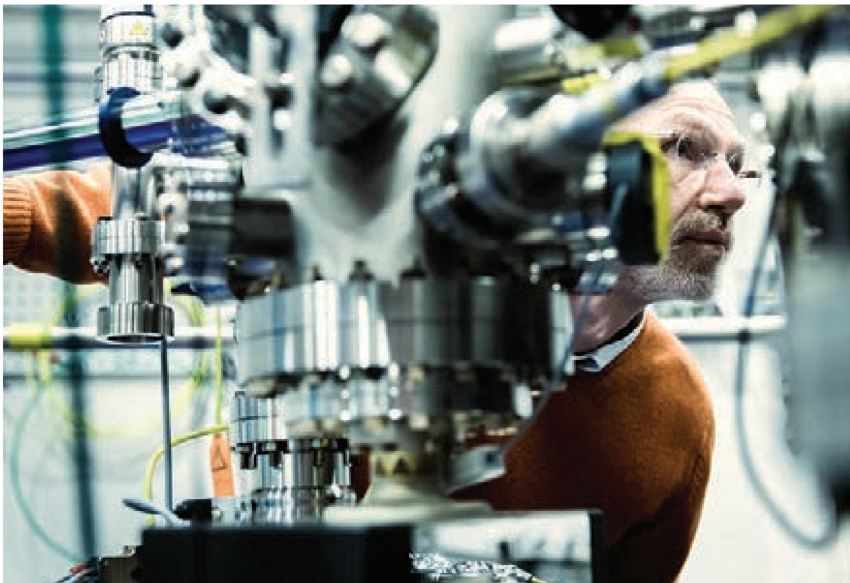

COMPATIBILITY OF QUANTITATIVE X-RAY SPECTROSCOPY WITH CONTINUOUS DISTRIBUTION MODELS OF WATER AT AMBIENT CONDITIONS

A new multi-method study including hard X-ray scattering at beamline ID20 proves that X-ray spectroscopic data of liquid water can be fully and consistently described by continuous-distribution models of near-tetrahedral water at ambient conditions.

Water at ambient conditions is the matrix of life and chemistry. It behaves anomalously in many of its properties with respect to other liquids. Since Wilhelm Conrad Röntgen **[1]**, two distinct separate phases have been argued to coexist in liquid water, competing with a view of a single-phase liquid in a fluctuating hydrogen bond network – the continuous distribution model. Over time, X-ray spectroscopic results have been repeatedly interpreted in support of Röntgen's postulate.

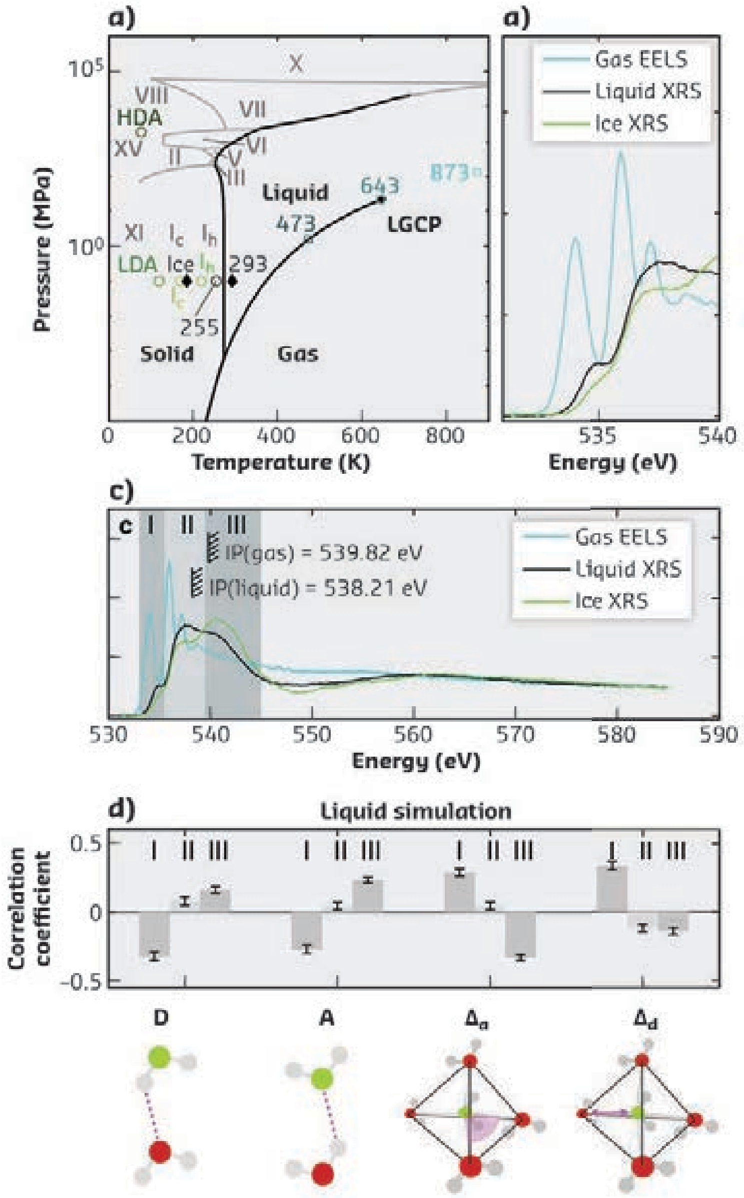

Fig. 101: a) The phase diagram of water with existing core-level excitation spectra. **b), c)** Scans over a long energy range were recorded to calibrate the core-level spectra at the asymptote. The pre-edge region (b, region I) was then used as indicator of the average number of donated hydrogen bonds, motivated by a statistical simulation. **d)** The simulation provides an estimate of structure-to-line-intensity relation, handled by correlation coefficients.

New quantitative X-ray spectroscopic data, collected at the ESRF, Swiss Light Source, and Bessy-II synchrotrons, were all found to be fully and consistently described with continuous distribution models of near-tetrahedral liquid water at ambient conditions. The research revealed also new conceptual insights into the statistical nature of the liquid system and its spectra.

Oxygen K-edge spectra from self-absorption-free X-ray Raman scattering spectroscopy of ambient liquid water and solid ice were taken at the large-solid-angle spectrometer at beamline ID20 (**Figure 101**). In conjunction with electron energy-loss spectroscopy data of the gas phase, the recorded data revealed 1.74 ± 2.1% hydrogen bonds per molecule.

In this multi-method study, high-resolution oxygen K-edge resonant inelastic X-ray scattering spectra of liquid water was subsequently studied. A single dominant mode without substructure was found at the highest resolving power achieved so far of > 10,000. Two distinct modes would be supportive for a heterogeneous or two-phase structure.

Finally, X-ray emission spectra and density functional theory calculations revealed the prominent role of excited state dynamics for the formation of the split $1b_1$ peak in the emission spectrum. The branching ratio of this peak has previously been used as an argument for the two-phase models. However, the new experimental data show the stark photon-energy dependence of the emission lines: truly non-resonant X-ray emission spectra of liquid water show a branching ratio close to that previously observed in ice by using an X-ray tube. In line with previously published results, the researchers found the simulation with dynamics to be needed for the split emission peak. In addition, a statistical analysis revealed that small effects from the structure can still be expected in the X-ray emission spectrum.

This finding supports the overall rationale of computational simulations used widely in chemistry and biosciences, which would have needed revision if the two-phase hypothesis had been proven correct.

PRINCIPAL PUBLICATION AND AUTHORS

Compatibility of quantitative X-ray spectroscopy with continuous distribution models of water at ambient conditions, J. Niskanen (a,b), M. Fondell (b), C. J. Sahle (c), S. Eckert (d,a), R. M. Jay (d,a), K. Gilmore (c), A. Pietzsch (a), M. Dantz (e), X. Lu (e), D. E. McNally (e), T. Schmidt (e), V. Vaz da Cruz (f,a), V. Kimberg (f,g), F. Gel'mukhanov (f,g) and A. Föhlisch (a,d), *PNAS* **116**, 4058-4063 (2019); doi: 10.1073/pnas.1815701116.

(a) Institute for Methods and Instrumentation for Synchrotron Radiation Research, Helmholtz Zentrum Berlin für Materialien und Energie (Germany)
(b) Department of Physics and Astronomy, University of Turku (Finland)
(c) ESRF
(d) Institut für Physik und Astronomie, Universität Potsdam (Germany)
(e) Swiss Light Source, PhotonScience Division, Paul Scherrer Institut (Switzerland)
(f) Theoretical Chemistry and Biology, Royal Institute of Technology, Stockholm (Sweden)
(g) Institute of Nanotechnology, Spectroscopy and Quantum Chemistry, Siberian Federal University (Russia)

REFERENCES

[1] W. C. Röntgen, *Annalen der Physik* **281**(1), 91-97 (1892).

REALISING THE POTENTIAL OF VtC XES TO MEASURE O_2 BOND ACTIVATION

The understanding of the breaking and formation of the dioxygen (O–O) bond is critical to understanding life processes such as respiration and photosynthesis. Here, valence-to-core (VtC) X-ray emission spectroscopy (XES) is used to directly characterise the presence of an O–O bond in dicopper complexes and to measure the degree of O–O bond activation.

Dioxygen is an essential molecule employed in numerous life processes. Nature employs metalloproteins to catalyse the activation of O_2, including copper proteins, such as hemocyanin and tyrosinase. Synthetic biomimetic dicopper complexes are able to coordinate O_2 to stabilise an μ:η^2:η^2-peroxo and interconvert to a bis(μ-oxo) structure (**Figure 102**), where the O-O bond has been further activated and cleaved. These models serve as excellent test cases to explore the capability of valence-to-core (VtC) X-ray emission spectroscopy (XES) to detect the presence of an O-O bond at the two extreme limits of O_2 activation.

VtC XES measures the electronic transitions from the ligand-based valence orbitals refilling the 1s core-hole of a photo-absorber (*i.e.*, Cu 1s hole). Therefore, the VtC XES yields information pertaining to the ligand identity, covalency, and bond strength **[1]**. For instance, the ability of VtC XES to measure the degree of N_2 bond activation in a series of di- and triiron complexes has already been previously demonstrated: the strong triple bond of N_2 results in a large ~12 eV 2s(N) σ/σ^* orbital separation observed by VtC XES, where a diagnostic σ^* transition is observed in the K$\beta_{2,5}$ region of the spectrum **[2]**.

The large emission spectrometer at beamline **ID26** was utilised to measure the Cu VtC XES of these benchmark complexes. Comparing VtC XES spectra of the peroxo and bis(μ-oxo) dicopper complexes shows that the most striking differences are in the K$\beta_{2,5}$ region (**Figure 102**), in particular, a shoulder at the low-energy side

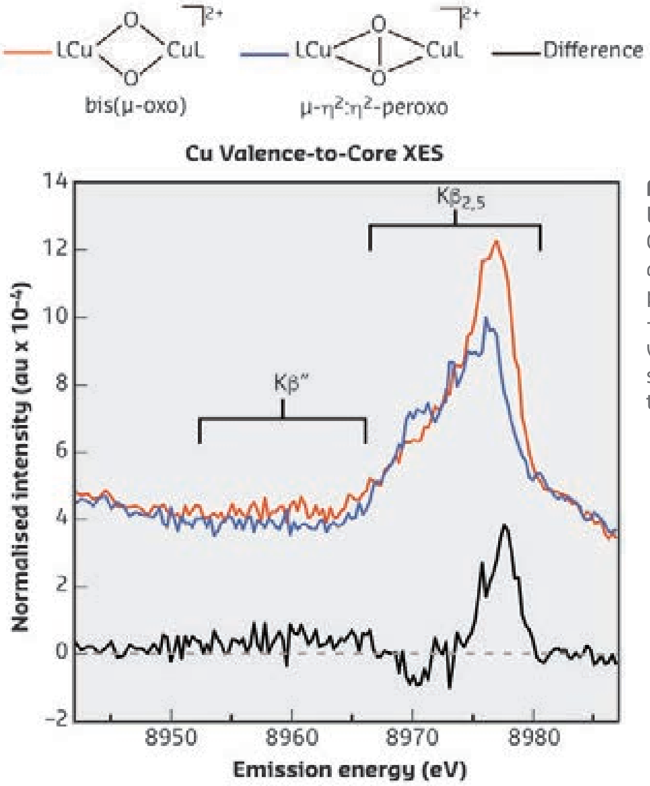

Fig. 102: Experimental Cu VtC XES of a dicopper-peroxo and -oxo complexes with difference spectrum of the two plotted.

of the peak for the peroxo complex. Ground-state density functional theory-calculated VtC XES spectra reproduce each of the observed spectra and allow for the assignment of distinct features (**Figure 103**). Inspection of the molecular orbital corresponding to the transition of the peroxo $K\beta_{2,5}$ low-energy shoulder reveals that this transition arises from the in-plane 2p(O) π_h orbital. While O_2 possesses two degenerate 2p(O) π orbitals, the degeneracy is split in the dicopper-peroxo complex as in-plane 2p(O) π_h is stabilised by favourable overlap with the copper's $d(x^2\text{-}y^2)$ orbitals. Therefore, the in-plane 2p π orbital is of the lowest energy of the 2p(O) orbitals. This transition gains significant intensity as the in-plane 2p(O) π_h orbital has favourable overlap with the Cu 4p orbitals along its plane to make the dipole-allowed transition possible. The other out-of-plane 2p(O) π_v and σ orbitals do not demonstrate favourable geometries to overlap with any Cu 4p orbitals to allow for appreciable VtC XES intensity.

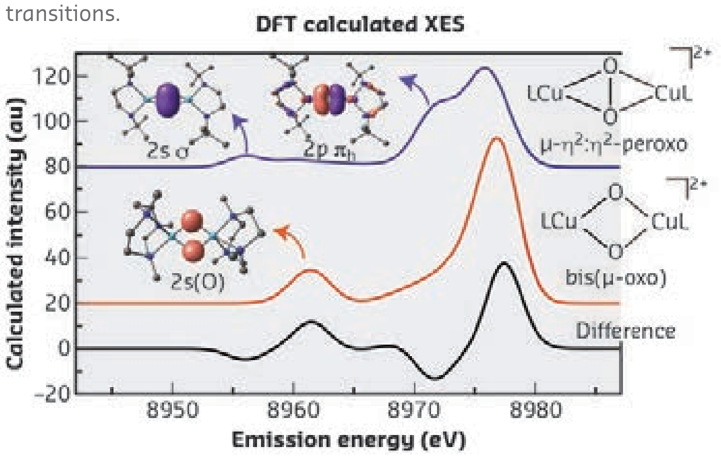

Fig. 103: Ground-state DFT-calculated Cu VtC XES of a dicopper-peroxo and -oxo complexes and select molecular orbitals plotted corresponding to unique transitions.

For the dicopper-peroxo complex studied, the single bond of the coordinated peroxo is much weaker than the triple bond of N_2, and therefore the 2s(O) σ/σ^* orbital separation is smaller, ~ 6.5 eV. As a result, the 2s(O) σ/σ^* VtC features remain completely in the Kβ`` region of the spectrum. While the VtC XES spectrum of the dicopper-peroxo and diiron-N_2 both have diagnostic $K\beta_{2,5}$ features of their small molecule bond's presence, DFT calculations clearly demonstrate that these features arise from distinctly different origins.

These complexes demonstrate the power of VtC XES to directly detect the presence (or absence) of an O-O bond. This proof-of-concept study is clearly of significant interest for numerous potential chemical catalysis and reaction mechanism studies, including future time-resolved studies to observe the process of O-O bond breaking and formation.

PRINCIPAL PUBLICATION AND AUTHORS

Valence-to-Core X-ray Emission Spectroscopy as a Probe of O–O Bond Activation in Cu_2O_2 Complexes, G. E. Cutsail III (a), N. L. Gagnon (b), A. D. Spaeth (b), W. B. Tolman (b,c) and S. DeBeer (a) *Angew. Chem. Int. Ed.* **57**, 9114-9119 (2019); doi: 10.1002/anie.201903749.
(a) Max Planck Institute for Chemical Energy Conversion, Mülheim an der Ruhr (Germany)
(b) University of Minnesota, Minneapolis (USA)
(c) Washington University in St. Louis (USA)

REFERENCES

[1] C. J. Pollock & S. DeBeer, *Acc. Chem. Res.* **48**, 2967-2975 (2015).
[2] C. J. Pollock *et al., J. Am. Chem. Soc.* **135**, 11803-11808 (2013).

UNIAXIAL PRESSURE TUNING OF CHARGE ORDER AND SUPERCONDUCTIVITY IN THE CUPRATES

A combination of large uniaxial compression and inelastic X-ray scattering revealed a new charge-ordered state competing with high-temperature superconductivity in the cuprates. A pronounced softening of an optical phonon mode is associated with the stabilisation of the charge order. This work highlights the perspectives offered by uniaxial stress in the control and study of competing orders in quantum materials.

One of the challenges in understanding high-temperature superconductivity in the cuprates is their remarkably complex phase diagrams. These host a plethora of electronic orders, including superconducting, antiferromagnetic and charge density wave (CDW) orders, all of which are formed within the CuO_2 planes (**Figure 104**). The interplay among these orders and the prevailing electronic ground state can be tuned using parameters such as chemical doping, hydrostatic pressure or high magnetic fields. More importantly, the response of the various phases to these tuning parameters provides valuable insights into their formation mechanism and their interplay with one another.

In this work, large uniaxial stress was used to tune the balance between superconductivity and CDW ordering in $YBa_2Cu_3O_{6.67}$ while monitoring its collective lattice response by means of high-resolution inelastic X-ray scattering (IXS). It was found that large uniaxial compression along the a-axis induces a new three-dimensional (3D) long-range ordered CDW strongly competing with superconductivity. Moreover, the phonon spectra revealed a very strong softening of an optical phonon as the 3D order sets in, suggesting that phonon freezing is responsible for the formation of the 3D CDW.

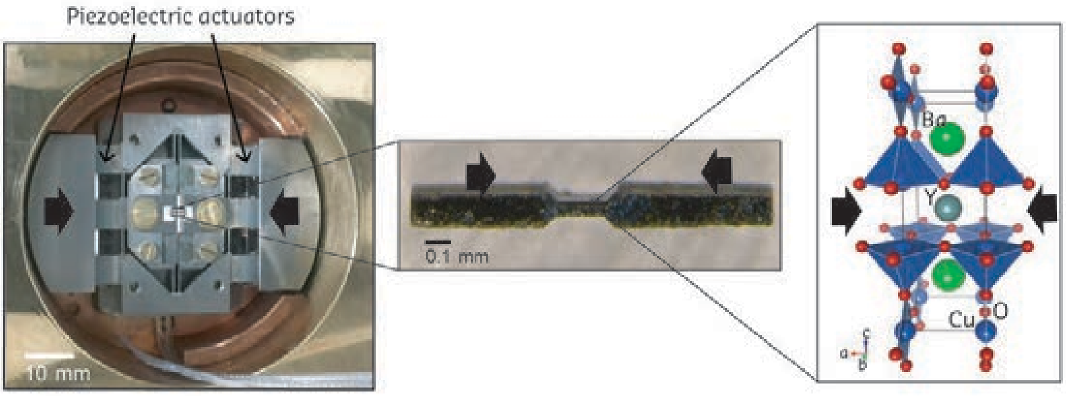

Fig. 104: Photograph of the piezoelectric-based strain apparatus and of the measured sample, and illustration of the crystal structure of $YBa_2Cu_3O_{6+x}$ (the black arrows indicate the direction of uniaxial strain).

The motivation to use uniaxial pressure is based on the anisotropic pressure dependence of the superconducting T_c. While the overall effect of hydrostatic pressure is to increase T_c, it is known that uniaxial compression along the a-axis of $YBa_2Cu_3O_{6.67}$ leads instead to a suppression of T_c **[1]**. $YBa_2Cu_3O_{6.67}$ samples were chosen because at this doping level (p=0.12 holes per planar copper) the charge modulation and its competition with superconductivity are maximised and, at the same time, a-axis compression effectively reduces T_c. In order to achieve large uniaxial compressions, a piezoelectric-based apparatus **[2]** specially modified for temperature-dependent IXS measurements was used. The IXS experiments were carried out at beamline **ID28** on single crystals of $YBa_2Cu_3O_{6.67}$, prepared in the form of a-axis needles and thinned on their central parts by a plasma-focused ion beam (**Figure 104**).

Figure 105 shows the momentum dependence of the elastic X-ray scattering intensity. A broad profile centred around Q_{2D} (L = 6.5) is present at unstrained conditions and arises from the previously reported short-ranged quasi-two-dimensional (2D) CDW order **[3]**. Under uniaxial compression, a sharp maximum appears at Q_{3D} (L = 7) on top of the broad 2D CDW profile, signalling the onset of a long-ranged, 3D CDW order. The 3D CDW appears above the T_c of the unstrained sample and is rapidly and – unlike the 2D CDW – completely suppressed in the superconducting state, testifying to a very strong competition with superconductivity. Moreover, the strain and temperature-dependence of the inelastic part of the IXS spectra suggests that the transition to the ordered state is driven by the complete softening of an optical phonon at Q_{3D} and indicates that the 3D CDW is a thermodynamic ground state competing with high-temperature superconductivity.

The data highlight the potential offered by uniaxial stress to investigate the relationship between superconductivity and charge ordering in the cuprates in detail. More generally, the results illustrate the powerful combination of uniaxial pressure application and X-ray spectroscopic techniques for the study of competing orders in a broad class of materials, and offer a promising prospect for future experiments.

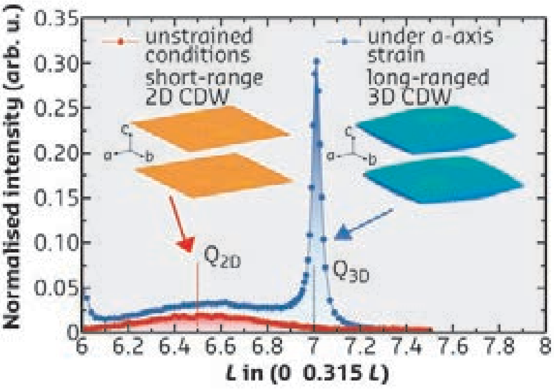

Fig. 105: Strain dependence of the elastic peak intensity along the (0 0.315 *L*) direction. The data recorded under unstrained and under 1% a-axis compressive strain conditions are given in red and blue respectively. The insets show schematic illustrations of the short-ranged 2D and the long-ranged 3D CDW orders.

PRINCIPAL PUBLICATION AND AUTHORS

Uniaxial Pressure Control of Competing Orders in a High Temperature Superconductor, H.-H. Kim (a), S. M. Souliou (b), M. E. Barber (c), E. Lefrançois (a), M. Minola (a), M. Tortora (a), R. Heid (d), N. Nandi (c), R. A. Borzi (c,e), G. Garbarino (b), A. Bosak (b), J. Porras (a), T. Loew (a), M. König (c), P. J. W. Moll (c), A. P. Mackenzie (c,f), B. Keimer (a), C. W. Hicks (c) and M. Le Tacon (d), *Science* **362**, 1040-1044 (2018); doi: 10.1126/science.aat4708.

(a) Max Planck Institute for Solid State Research, Stuttgart (Germany)
(b) ESRF
(c) Max Planck Institute for Chemical Physics of Solids, Dresden (Germany)
(d) Institute for Solid State Physics, Karlsruhe Institute of Technology (Germany)
(e) Instituto de Física de Líquidos y Sistemas Biológicos, La Plata (Argentina)
(f) Scottish Universities Physics Alliance, University of St. Andrews (UK)

REFERENCES

[1] O. Kraut *et al.*, *Physica C* **205**, 139-146 (1993).
[2] C. W. Hicks *et al.*, *Rev. Sci. Instrum.* **85**, 065003 (2014).
[3] G. Ghiringhelli *et al.*, *Science* **337**, 821-825 (2012).

CHARGE DENSITY FLUCTUATIONS IN CUPRATES

The observation of a short-range charge modulation in cuprates by resonant inelastic X-ray scattering indicates that charge instability is inherent in cuprates and can be a crucial factor that influences their properties. This observation can be likened to seeing the bulk of the iceberg of the charge order phenomenon, while charge density waves only represent its tip.

The phase diagram of the high-T_c cuprate superconductors (HTS) is shaped by the spontaneous emergence of various ordered states, tuned by doping and driven by the many competing degrees of freedom, where not only charge and spin are of relevance, but also lattice and orbitals have an active role in building up the ground state. The identification of all these ordered states is a crucial step toward the understanding of high-temperature superconductivity, one of the grand challenges in solid-state physics.

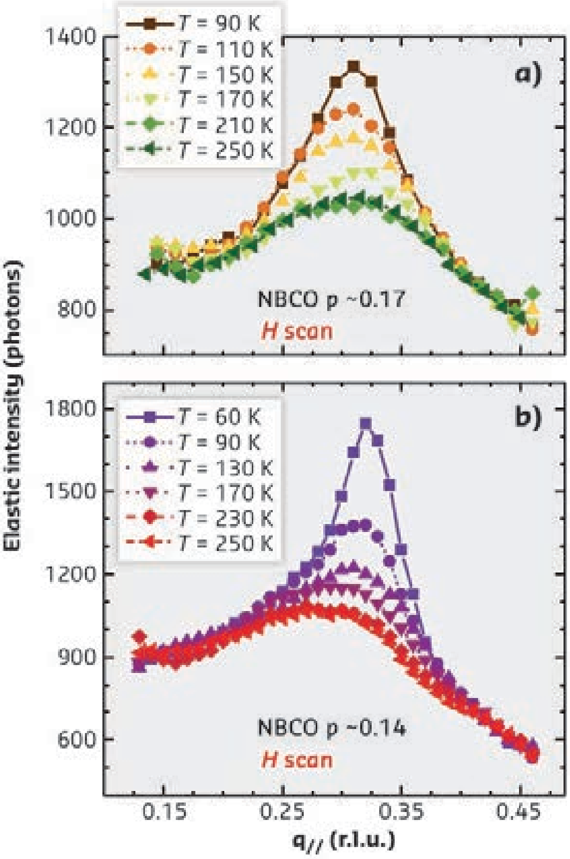

Fig. 106: The intensity was determined by integrating the quasi-elastic region of the Cu L_3 RIXS spectra measured at different $q_{//}$ values along the (H,0) direction. A clear peak is present in the whole temperature range under investigation, in samples from the underdoped up to the slightly overdoped region.

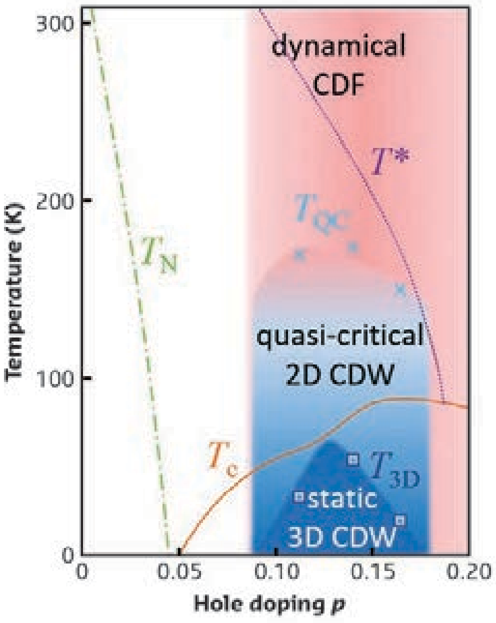

Fig. 107: CDF dominate the phase diagram, coexisting both with the quasi-critical 2D-CDW and with superconductivity. The suggested scenario is of a continuous crossover from the pure 2D dynamical CDF at high T and broad doping range, to a quasi-critical CDW, still 2D, below T_{QC} and for $0.08<p<0.17$, to the static 3D CDW usually hindered by superconductivity.

In strongly correlated systems, the tendency of the valence electrons to segregate into periodically modulated structures can lead to the formation of a peculiar charge order. Although observed in several families of cuprates **[1,2,3]**, it is still unclear to what extent the charge order influences the unusual properties of these systems, since it has been consistently observed – in the shape of incommensurate charge density waves (CDW) – only in underdoped samples (with doping p = 0.08 – 0.16 holes/Cu) and at relatively low temperatures (below 170-200 K). This apparent confinement in a relatively small region of the phase diagram has led to a view of charge order as a mere epiphenomenon of the pseudo-gap opening. This approach has been recently questioned by the observation of long-range CDW in overdoped single layer Bi2201 **[4]**, well outside the pseudo-gap regime.

In this context, the higher sensitivity of the resonant inelastic X-ray scattering (RIXS) instrumentation at **ID32** has been exploited to determine more accurately the temperature dependence of CDW at the Cu L_3 absorption edge, in the same (Y,Nd)BCO family where its first observation was made **[1]**. The results were surprising. Underneath the relatively sharp CDW peak, a broad and almost temperature-independent signal emerged (**Figure 106**). This broad peak is a sort of precursor of the quasi-2D CDW signal, sharing with the latter one the value of the incommensurate wave vector q_c. However, differently to CDW, it is still present both above the pseudo-gap temperature, up to 270 K (maximum temperature compatible with the preservation of the sample chemical integrity under the X-ray beam) and in overdoped samples (p > 0.16 holes/Cu). The broad peak evolves slowly with the temperature: below 150 K, it is superimposed to the quasi 2D CDW peak; below T_c, it is not sensitive to the presence of the superconducting order.

The broad peak was assigned to dynamic charge density fluctuations (CDF). 'Fluctuations', since they have characteristics very close to those of CDW, but an ultra-short correlation length, of the same order as the wave modulation period, and 'dynamic', since the energy of these fluctuations was estimated from high resolution RIXS spectra to be finite, around 10-15 meV at the optimal doping (p = 0.16 holes/Cu). These experimental results look compatible with the picture provided in previous theoretical studies **[5]** of an inherent charge instability in HTS cuprates. Charge density fluctuations can thus be regarded as pervasively present at all T for superconducting cuprates (**Figure 107**) and might therefore have a crucial role in determining the peculiar properties of these compounds both in the normal and in the superconducting state.

PRINCIPAL PUBLICATION AND AUTHORS

Dynamical charge density fluctuations pervading the phase diagram of a Cu-based high-T_c superconductor, R. Arpaia (a,b), S. Caprara (c,d), R. Fumagalli (a), G. De Vecchi (a), Y. Y. Peng (a), E. Andersson (b), D. Betto (e), G. M. De Luca (f,g), N. B. Brookes (e), F. Lombardi (b), M. Salluzzo (g), L. Braicovich (a,e), C. Di Castro (c,d), M. Grilli (c,d) and G. Ghiringhelli (a,h), *Science* **365**, 906-910 (2019); doi: 10.1126/science.aav1315.
(a) Politecnico di Milano (Italy)
(b) Chalmers University of Technology, Göteborg (Sweden)
(c) Università di Roma La Sapienza (Italy)
(d) CNR-ISC, Roma (Italy)
(e) ESRF
(f) Università di Napoli Federico II (Italy)
(g) CNR-SPIN, Napoli (Italy)
(h) CNR-SPIN, Milano (Italy)

REFERENCES

[1] G. Ghiringhelli *et al*., *Science* **337**, 821 (2012).
[2] R. Comin *et al*., *Science* **343**, 390 (2014).
[3] W. Tabis *et al*., *Nat. Commun.* **5**, 5875 (2014).
[4] Y. Y. Peng *et al*., *Nat. Mater.* **17**, 697 (2018).
[5] C. Castellani *et al*., *Phys. Rev. Lett.* **75**, 4650 (1995).

SWITCHING AND CONTROLLING MAGNETIC INTERACTIONS WITH AN AROMATIC REDOX-ACTIVE LIGAND

Controlling the interactions between magnetic centres is a fascinating challenge for scientists, at the basis of any rational design of molecule-based magnets. Supported by a complete set of experimental and theoretical studies on dinuclear complexes, this work aims at a better understanding of the dominant factors governing the strength of the magnetic interactions via an aromatic bridging ligand.

An attractive feature of molecule-based materials is the ability to fine-tune and control their physical properties by a suitable choice of the molecular components. In magnetism, this ability is of great interest as the magnetic properties usually result from cooperative effects between spin carriers. Using a redox-active ligand as a linker between spin carriers is therefore particularly appealing as it is able to favour electronic conductivity, provide multi-switchability and allow a certain tuning and control of the magnetic properties by simple oxidation or reduction processes.

In order to study the influence of both the oxidation state of the bridging ligand and the electronic configuration of the metal centre on the strength of the magnetic interactions, prototype dinuclear complexes based on Co(II) **[1]** or Ni(II) (here) and a redox-active tetrapyridophenazine (tphz) bridging ligand were synthesised and studied (**Figure 108**). Terpyridine (tpy) ligands are also employed to complete the coordination sphere of the metal centre and to prevent the formation of extended coordination polymers. In the light of their electrochemical behaviour in solution, those complexes were chemically reduced to give once- and twice-reduced analogues with similar coordination environments around Co and Ni metal ions. Nevertheless, significant differences are seen when comparing the bond distances within the tphz ligand, suggesting that the two successive reductions are centred on the bridging ligand.

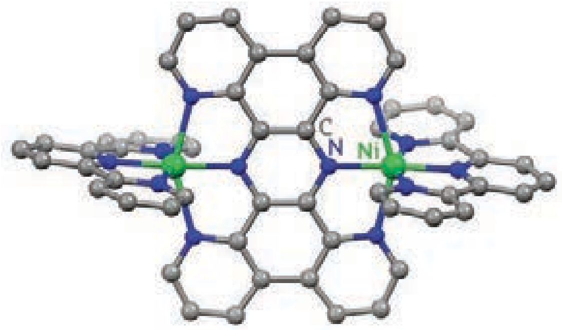

Fig. 108: Crystal structure of the cationic complex $[Ni_2(tphz)(tpy)_2]^{4+}$.

To confirm this hypothesis, the local electronic and magnetic properties of the nickel and cobalt metal ions were studied by X-ray absorption spectroscopy (XAS) and X-ray magnetic circular dichroism (XMCD) at beamline **ID12**. These techniques are particularly relevant for complexes with redox-active ligands, for which the oxidation state of the metal ion can be questioned. The XAS spectrum at the Ni K-edge (**Figure 109**) show very similar maxima for the (i) genuine, (ii) once-reduced and (iii) twice-reduced compounds, as expected for comparable coordination spheres with the same oxidation state. The quasi-identical shape and intensity of the XMCD signals also demonstrate the presence of the same magnetic moment and thus spin-state on the Ni metal ions. These similarities of the XAS and XMCD spectra unambiguously demonstrate that the reductions are centred exclusively on the tphz ligand.

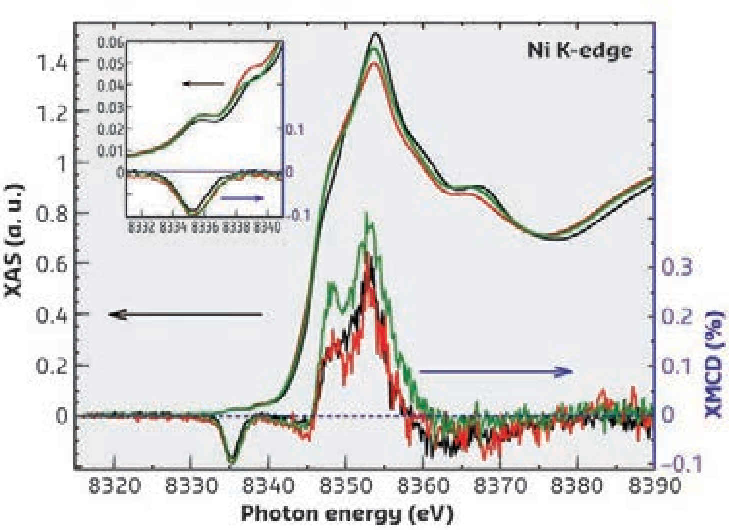

Fig. 109: XAS and XMCD spectra at Ni K-edge for the three Ni(II) complexes. Inset: magnification of the Ni K pre-edge region.

Upon successive reductions of the bridging ligand, the intramolecular magnetic interactions are strongly affected. While the neutral form of tphz mediates a weak antiferromagnetic (AF) exchange between ls-Co(II) (ls: low-spin; $S = 1/2$) or Ni(II) ($S = 1$), the once-reduced radical form, $tphz^{\bullet-}$, stabilises either very strong AF couplings between the $S = 1/2$ organic spin and the two hs-Co(II) (hs: high-spin; $S = 3/2$), or strong ferromagnetic (F) couplings with Ni(II) spins. The resulting high-spin complexes possess a well isolated $S_T = 5/2$ ground state that is, remarkably, the only thermally populated state at ambient temperature for the Co system. Reducing the bridging ligand twice affords weak Ni–Ni interactions, in marked contrast to the Co(II) analogue, for which a surprisingly strong AF coupling was observed, despite the formal diamagnetic state of the $tphz^{2-}$ ligand **[1]**. In this case, the strong magnetic interaction is induced by a large spin delocalisation arising from an efficient orbital mixing of the $tphz^{2-}$ π system and one of the Co(II) singly occupied d orbitals.

Most importantly, this experimental comparative study between Co(II) and Ni(II) analogues, supported by a careful examination of the involved orbitals, provides a clear understanding of the factors that govern the strength and sign of the magnetic exchange through an aromatic bridging ligand. The conclusions of the work, as well as the synthetic approach, should be easily transposed to systems with higher nuclearities and dimensionalities, for which strong magnetic exchanges could be fully exploited to design high-temperature molecule-based magnets.

PRINCIPAL PUBLICATION AND AUTHORS

Using Redox-Active π Bridging Ligand as a Control Switch of Intramolecular Magnetic Interactions, X. Ma (a), E. A. Suturina (b), M. Rouzières (a), M. Platunov (c), F. Wilhelm (c), A. Rogalev (c), R. Clérac (a) and P. Dechambenoit (a), *J. Am. Chem. Soc.* **141**, 19, 7721-7725 (2019); doi: 10.1021/jacs.9b03044.
(a) Univ. Bordeaux, CNRS, Centre de Recherche Paul Pascal, UMR 5031, Pessac (France)
(b) Centre for Sustainable Chemical Technologies, University of Bath (UK)
(c) ESRF

REFERENCES

[1] X. Ma *et al., Angew. Chem. Int. Ed.* **26**, 7841-7845 (2018).

ELECTRONIC STRUCTURE OF OXYHEMOGLOBIN AND ITS MODEL COMPLEX DETERMINED

The electronic structure of the heme oxy-iron centre in oxyhemoglobin and oxymyoglobin has been the subject of debate for decades. This study uses X-ray spectroscopy to settle this longstanding issue in bioinorganic chemistry and provides insight into heme iron-oxygen binding, particularly the differences between oxyhemoglobin and its most studied model compound.

The electronic structure of the active sites in oxyhemoglobin (HbO_2) and oxymyoglobin has been the subject of study and debate for decades. The iron oxygen-binding proteins contain an S=0 $\{FeO_2\}^8$ active site, denoting eight valence electrons delocalised among the Fe 3d (6 e^-) and O_2 π^* (2 e^-) orbitals. Three electronic structure models have been proposed by Pauling (low-spin Fe(II) with singlet O_2), Weiss (low-spin Fe(III) antiferromagnetically-coupled to doublet O_2^-), and McClure, Harcourt, and Goddard (S=1 Fe(II) antiferromagnetically-coupled to triplet O_2, also known as the 'ozone' model). Much computational work has been done, with all three models supported by different calculations. However, there has been a dearth of experimental data to directly probe the electronic structure. In particular, the intense porphyrin $\pi \rightarrow \pi^*$ transitions of the heme make it difficult to probe the highly covalent Fe with traditional spectroscopic methods.

X-ray absorption spectroscopy (XAS) is a site-specific technique that provides a direct probe of the metal centre. L-edge XAS measures the electric dipole-allowed metal $2p \rightarrow 3d$ transitions, where the integrated intensity is proportional to the total amount of metal 3d character in the valence orbitals. Quantitative covalency information can be extracted through modeling of the L-edge XAS spectra using a valence bond configuration interaction (VBCI) multiplet model. This methodology has been applied to iron complexes to extract the differential orbital covalency (DOC), which allows for quantification of ligand σ and π donation and metal π back-bonding, including in heme systems.

One major limitation of iron L-edge XAS is that it occurs in the soft X-ray regime (~710 eV), which requires ultrahigh vacuum and is strongly absorbed by oxygen atoms in water. This limits the measurement of protein or solution samples. To measure the protein samples, hard X-rays (~7100 eV), as used for iron K-edge XAS, are required. However, to obtain 'L-edge like' information with hard X-rays, K-edge XAS is extended to 1s2p resonant inelastic X-ray scattering (RIXS). 1s2p RIXS involves a two-step process, where a hard X-ray incident photon causes a $1s \rightarrow 3d$ transition, followed by $2p \rightarrow 1s$ decay, releasing a photon. The resulting $2p^5 3d^{n+1}$ final state configuration is the same as for L-edge XAS and can be simulated within the VBCI multiplet model to extract the DOC and provide a quantitative bonding description.

This study utilises Fe K-edge XAS and 1s2p RIXS to determine the electronic structure of oxyhemoglobin and its most studied heme $\{FeO_2\}^8$ model compound, $[(pfp)Fe(1\text{-MeIm})(O_2)]$ ($pfpO_2$) (**Figure 110**), which was previously analysed using L-edge XAS. RIXS experiments were performed at beamlines **ID26** at ESRF

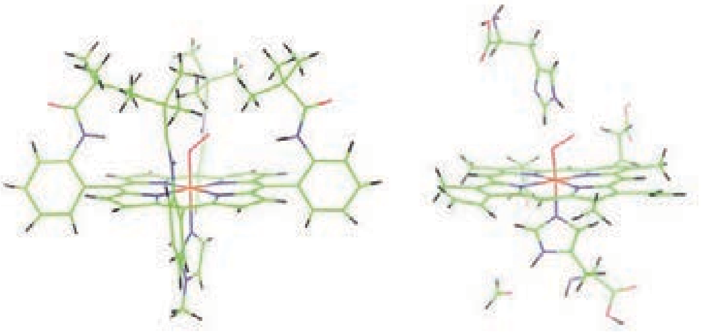

Fig. 110: Structures of $pfpO_2$ (left) and the oxyhemoglobin active site (right). (Fe = orange, C = green, H = black, O = red, N = blue)

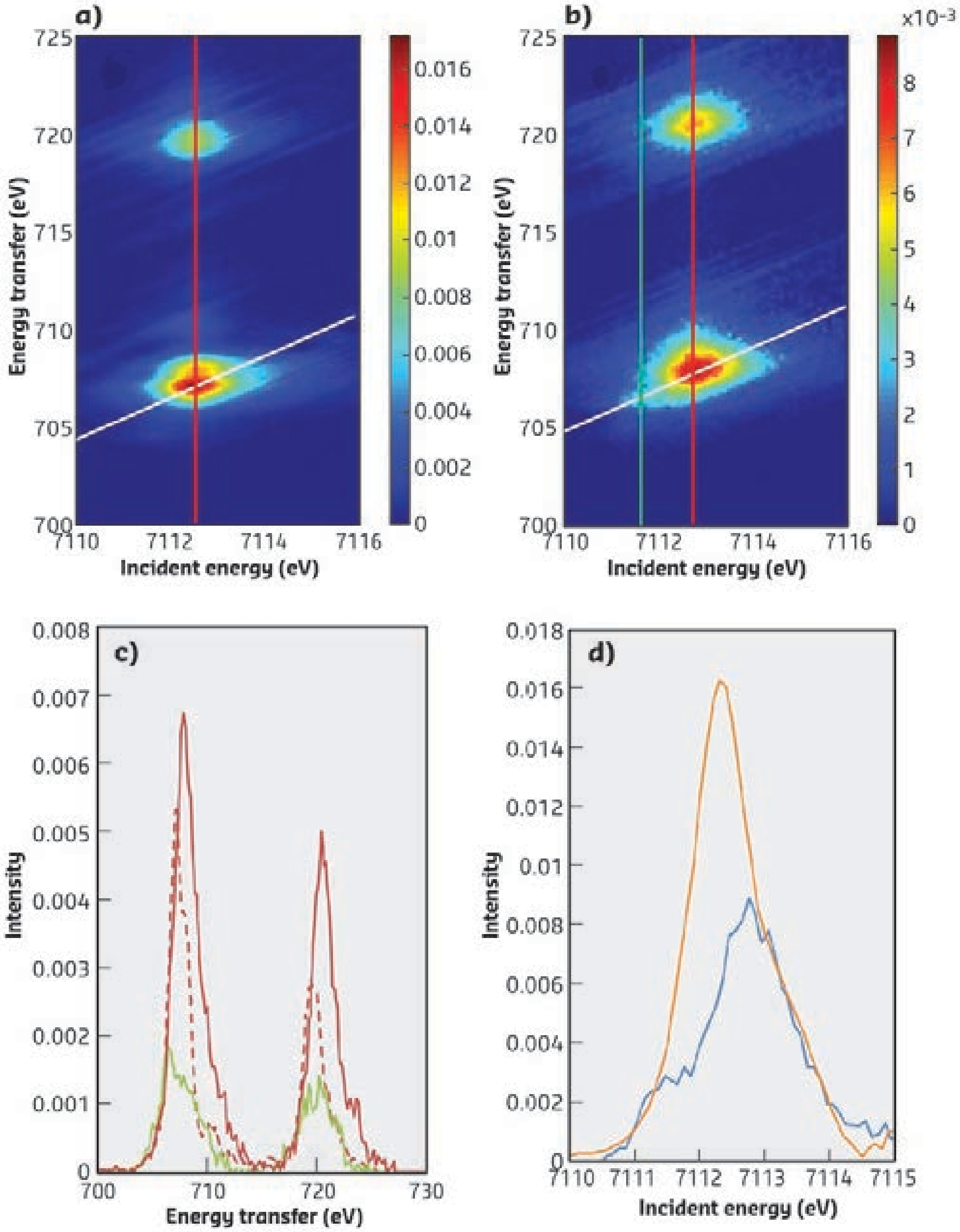

Fig. 111: a) 1s2p RIXS plane of $pfpO_2$. **b)** 1s2p RIXS plane of oxyhemoglobin. **c)** Constant incident energy 'L-edge like' plots for $pfpO_2$ (dashed) and oxyhemoglobin (solid). Red and green plots correspond to respective vertical lines in the RIXS planes. **d)** Constant emission energy plots for $pfpO_2$ (orange) and oxyhemoglobin (blue), corresponding to the white diagonal line in the RIXS planes. Unlike $pfpO_2$, oxyhemoglobin shows two peaks.

and 6-2 at SSRL, USA. The K-edge XAS and RIXS data of pfpO_2 and oxyhemoglobin show stark differences (**Figure 111**). pfpO_2 is similar to Fe(II), while oxyhemoglobin is qualitatively similar to Fe(III), but with significant quantitative differences. DFT calculations show that the difference between pfpO_2 and oxyhemoglobin is due to the combined contributions of a distal histidine H-bond to O_2 and the less hydrophobic environment in the protein, both enhancing back-bonding into the O_2. The VBCI multiplet model used to analyse the RIXS data shows that pfpO_2 is dominantly Fe(II) with 6-8% Fe(III) character, while oxyhemoglobin has a very mixed wave function that has 50-77% Fe(III) character and a partially polarised Fe-O_2 π bond. These RIXS experiments are now being extended to oxygen intermediates in heme enzymes.

PRINCIPAL PUBLICATION AND AUTHORS

Resonant Inelastic X-Ray Scattering Determination of the Electronic Structure of Oxyhemoglobin and Its Model Complex,

J. J. Yan (a), T. Kroll (a,b), M. L. Baker (a), S. A. Wilson (a), R. Decréau (a), M. Lundberg (a,c), D. Sokaras (b), P. Glatzel (d), B. Hedman (b), K. O. Hodgson (a,b) and E. I. Solomon (a,b),

PNAS **116**(8), 2854-2859 (2019); doi: 10.1073/pnas.1815981116.

(a) Department of Chemistry, Stanford University (USA)
(b) Stanford Synchrotron Radiation Lightsource, SLAC National Accelerator Laboratory, Stanford University (USA)
(c) Department of Chemistry - Ångström Laboratory, Uppsala University (Sweden)
(d) ESRF

This work was supported by the National Institutes of Health (GM-40392 to E.I.S.).

FORMATION OF INCOMMENSURATE CHARGE DENSITY WAVES IN CUPRATES

Charge density waves (CDWs) are a ubiquitous phenomenon in underdoped high-T_c cuprate superconductors. In this work, resonant inelastic X-ray scattering (RIXS) is employed to reveal their formation mechanism and their correlation with other electronic and spin orders.

Electronic order in materials arises via spontaneous symmetry breaking and gives rise to collective excitations carrying the order's fingerprint. In the past few years, charge density waves (CDWs) have been established as a ubiquitous phenomenon in underdoped high-T_c cuprate superconductors **[1,2]**. Their formation mechanism and their correlation with other electronic and spin orders, however, remained unresolved, largely due to the absence of direct measurements of inelastic CDW excitations.

Using RIXS at beamline **ID32**, the temperature- and doping-dependent CDW excitations in stripe-ordered $La_{2-x}Ba_xCuO_4$ were uncovered. It was found that the CDW develops in two stages with decreasing temperature. A precursor CDW with quasi-commensurate wave vector emerges first at high-temperature. This doping-independent precursor CDW correlation originates from the CDW phase mode coupled with a phonon excitation and 'seeds' the low-temperature CDW with a strongly doping-dependent wave vector. Observations reveal the precursor CDW and its phase mode as the common thread of underdoped cuprates with important implications for the highly intertwined electronic ground state. These results thus provide a vital new characterisation of the electronic state from which high-temperature superconductivity emerges.

Figure 112 shows the principle of RIXS measurements of CDW correlations in cuprates. A photon energy that resonances with a Cu 2p → 3d core level transition was chosen in order to enhance scattering from valence electrons. The RIXS intensity map (vertical axis: energy loss, horizontal axis: in-plane momentum transfer $\mathbf{Q}_{//}$) is obtained by rotating

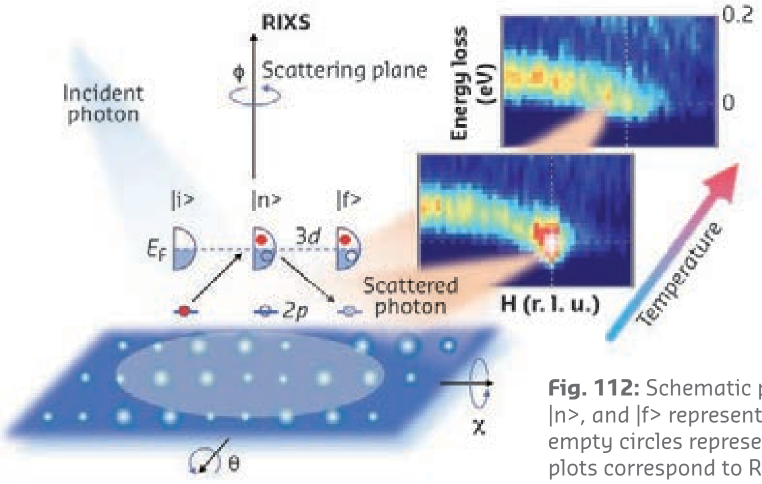

Fig. 112: Schematic plot of the L-edge RIXS process and experimental set-up. |i>, |n>, and |f> represent initial, intermediate, and final states, respectively. Solid and empty circles represent occupied and unoccupied states, respectively. The intensity plots correspond to RIXS spectra of $La_{2-x}Ba_xCuO_4$ (x=0.11) below and above T_{str}.

samples about the θ or χ axes. Using the high energy resolution of the RIXS spectrometer, CDW excitations and their temperature- and doping-dependent evolution were observed. At high temperature, above the stripe-order phase transition temperature T_{str}, the RIXS spectra below 100 meV are dominated by a dispersive charge excitation, whose intensity quickly fades away below $|\mathbf{Q}_{//}| \sim 0.2$ reciprocal lattice units (r.l.u.). This excitation also yields a broad quasi-elastic peak, corresponding to the precursor CDW correlation **[3,4]**. During cooling below T_{str}, a narrower elastic peak emerges on top of the broad dispersive feature corresponding to the low-temperature CDW. These experimental observations are well reproduced by theoretical calculations of a phenomenological model, where the dispersive CDW excitations originate from the CDW phase mode coupled with phonons.

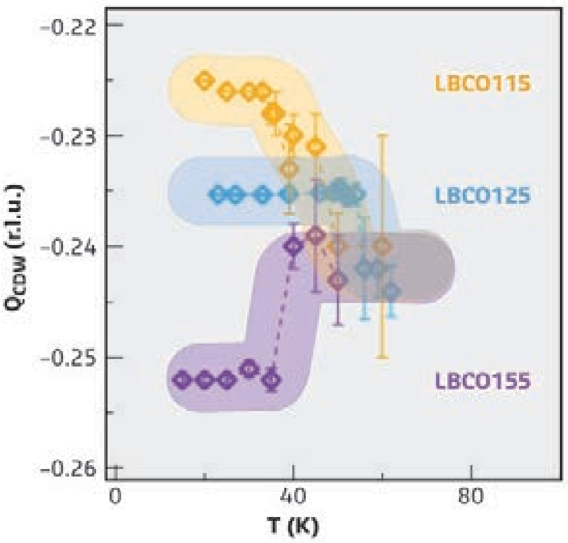

Fig. 113: Temperature-dependent CDW wave vectors. The shaded yellow, blue, and purple curves are guides to the eye for $La_{2-x}Ba_xCuO_4$ with x = 0.115, 0.125 and 0.155, respectively. In the precursor CDW phase, the wave vectors are doping-independent.

Figure 113 shows the experimentally determined CDW wave vectors as a function of doping and temperature. Most remarkably, it is found that while the low-temperature CDW wave vectors are strongly doping-dependent and consistent with the stripe picture, the precursor CDW wave vectors are doping independent and broadly peaked at $\mathbf{Q}_{pCDW} = 0.24$ r.l.u. The extracted correlation length, ξ_{pCDW}, is similar to the real-space CDW period $\lambda_{pCDW} \sim 16$ Å and suggests the existence of locally commensurate correlations without extended phase coherence. These results establish the precursor CDW correlation together with its phase mode as the basic foundation that underpins the emergence of CDW order in the cuprates.

PRINCIPAL PUBLICATION AND AUTHORS

Formation of Incommensurate Charge Density Waves in Cuprates, H. Miao (a), R. Fumagalli (b), M. Rossi (b), J. Lorenzana (c), G. Seibold (d), F. Yakhou-Harris (e), K. Kummer (e), N. B. Brookes (e), G. D. Gu (a), L. Braicovich (b), G. Ghiringhelli (b) and M. P. M. Dean (a), *Phys. Rev. X* **9**, 031042 (2019); doi: 10.1103/PhysRevX.9.031042.
(a) Condensed Matter Physics and Materials Science Department, Brookhaven National Laboratory, New York (USA)
(b) Dipartimento di Fisica, Politecnico di Milano (Italy)
(c) ISC-CNR, Dipartimento di Fisica, Università di Roma La Sapienza (Italy)
(d) Institut für Physik, BTU Cottbus (Germany)
(e) ESRF

REFERENCES

[1] E. Fradkin *et al.*, *Rev. Mod. Phys.* **87**, 457 (2015).
[2] R. Comin *et al.*, *Annu. Rev. Condens. Matter. Phys.* **7**, 369 (2016).
[3] H. Miao *et al.*, *PNAS USA* **114**, 12430 (2017).
[4] H. Miao *et al.*, *Phys. Rev. X* **8**, 011008 (2018).

WHERE IS THE GOLD?

Nanometre-sized silver clusters have unique properties that can be tuned by adding a small amount of gold – on average 1 gold atom per particle. In this study, the position of the gold atom is determined using element-selective X-ray spectroscopy in combination with calculations.

Ligand-protected noble metal clusters are nanoparticles consisting of several hundred atoms or less (around 1 nm). They have unique properties – such as discrete energy levels, luminescence and, potentially, atomic monodispersity – that are not found in larger particles. This makes them interesting for applications such as catalysis, sensing and bio-imaging **[1]**. The properties of these clusters depend on their exact size and composition (*i.e.*, the number and type of metal atoms, the number and type of ligands, and the structure of the cluster). By using two different metals instead of one, a wider range of clusters with different properties can be obtained.

Au and Ag are often used as metals because they have similar electronic properties and similar size, so that Au can easily be introduced into Ag clusters, and vice versa. In this way, bimetallic variants of monometallic ligand-protected clusters such as Ag_{44}, Au_{25} and Au_{38} have been prepared **[1,2]**. In this work, ligand-protected Ag_{29} clusters doped with Au were investigated.

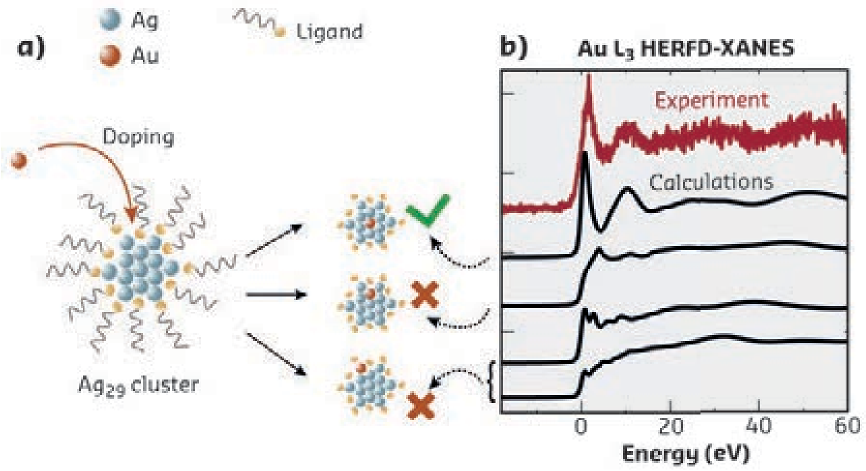

Fig. 114: a) Bimetallic clusters are made by doping Ag_{29} with a small amount of Au. **b)** HERFD-XANES combined with calculations shows the Au atom preferentially occupies the centre of the cluster.

The luminescence quantum yield of the Ag_{29} clusters increased by a factor three when doped with a few percent Au. The clusters were shown to mostly consist of Au_1Ag_{28} species. Ideally, to rationalise changes in cluster properties upon doping with another metal, the exact location of the dopants would be determined. However, this is challenging. The dopant may be randomly distributed in the cluster, effectively giving many different species with the same overall composition. The stabilities of these species may be different so that, depending on analysis technique, only a subpopulation of the clusters is probed.

In this work, the position of Au in Au_1Ag_{28} clusters was determined using Au L_3-edge X-ray absorption spectroscopy (XAS) at beamline **ID26**. Both the extended X-ray absorption fine structure (EXAFS) and X-ray absorption near edge structure (XANES) regions of the spectrum were used. XAS is element-selective and can be used to obtain information about the local geometry of an atom. An advantage of XAS is that the samples do not have to be crystalline but can be disordered solids or liquids. The clusters were prepared in aqueous solution and the sample was used as-synthesised, without any purification or concentration that could affect the stability of the cluster species. Consequently, the sample was dilute, containing around 0.03 mM Au, the element of interest, in addition to 1 mM Ag.

The low Au concentration made it difficult to measure reliable EXAFS, because EXAFS requires high signal-to-noise spectra. Radiation damage was also observed after long measurement times. Nevertheless, Au–Ag bonds were mostly observed with only a small amount of Au-ligand bonding. This indicates a preferential dopant location in the centre of the cluster. The clusters were further studied with XANES with high-energy resolution fluorescence detection (HERFD), which results in a sharpening of the spectral features compared to XAS recorded in transmission mode or using standard fluorescence detection. While XANES is less quantitative than EXAFS, a spectrum could be recorded in 1/50 of the time it took to record EXAFS. It is therefore much less susceptible to radiation damage. The spectrum was compared to first principles calculations with the FDMNES code **[3]** of Au at different positions in the cluster. The analysis showed that the Au atom preferentially occupies the centre of the cluster (**Figure 114**).

In conclusion, HERFD-XANES was combined with quantum chemical calculations, making it possible to determine the dopant location in bimetallic clusters where an EXAFS analysis was not conclusive. The increased spectral resolution and sophisticated theoretical codes provide powerful tools for atomic structural analysis.

PRINCIPAL PUBLICATION AND AUTHORS

Single Au Atom Doping of Silver Nanoclusters, M. van der Linden (a,b), A. J. van Bunningen (c), L. Amidani (b), M. Bransen (d), H. Elnaggar (a), P. Glatzel (b), A. Meijerink (c) and F. M. F. de Groot (a),

ACS Nano **12**, 12751-12760 (2018); doi: 10.1021/acsnano.8b07807.

(a) Inorganic Chemistry and Catalysis, Debye Institute for Nanomaterials Science, Utrecht University (The Netherlands)
(b) ESRF
(c) Condensed Matter and Interfaces, Debye Institute for Nanomaterials Science, Utrecht University (The Netherlands)
(d) Soft Condensed Matter, Debye Institute for Nanomaterials Science, Utrecht University (The Netherlands)

REFERENCES

[1] R. Jin *et al.*, *Chem. Rev.* **116**, 10346-10413 (2016).
[2] H. Yang *et al.*, *Nat. Commun.* **4**, 2422 (2013).
[3] O. Bunau & Y. Joly, *J. Phys. Condens. Matter* **21**, 345501 (2009).

THE ‘COMPLEX’ ROUTE TO SUSTAINABLE CHROME PLATING

Deep eutectic solvent (DES)–water mixtures are emerging as one of the most promising sustainable alternatives to the carcinogenic Cr(VI) electroplating process. This work aims to resolve the poorly understood coordination chemistry and its link with important physicochemical properties for the further optimisation and upscaling of these green electrolytes.

Over the past few decades, concerns about the toxicity and carcinogenicity of Cr(VI) have been increasing. Therefore, governments worldwide are banning the use of this harmful metal ion in various industries. Hence, numerous research centres in academia and industry are looking for viable alternatives to the commonly used Cr(VI)-based electroplating process. A promising candidate is trivalent chromium, which is several orders of magnitude less toxic compared to its hexavalent counterpart. However, several aspects impede the electrodeposition of functional hard chrome coatings from Cr(III) aqueous electrolytes, such as the presence of the kinetically inert $[Cr(H_2O)_6]^{3+}$ complex, its oligomeric products, and the low efficiency due to hydrogen formation. To resolve these issues, ionic liquids and DESs have been proposed as alternative electrolytes. Despite the promising electrochemical properties of these green solvents and their mixtures with water, very little is known about the chemical behaviour of Cr(III) in these liquids and how this is related to the electroplating process. This study therefore focused on the elucidation of the (coordination) chemistry of a deep eutectic solvent based on chromium chloride, choline chloride, and its mixtures with water (xCrCl$_3$•6H$_2$O/yChCl/zH$_2$O).

Previous work compared the coordination chemistry of Cr(III) in various solvents by combining UV/Vis spectroscopy and extended X-ray absorption fine structure (EXAFS) experiments **[1]**. Based on these results, an equation was constructed to predict the coordination chemistry of $[CrCl_x(H_2O)_{6-x}]^{3-x}$ by the wavelength position of one of the UV/Vis absorption bands. In the current work, this equation was used together with UV/Vis and EXAFS experiments (**Figure 115**) to study the coordination chemistry in xCrCl$_3$•6H$_2$O/yChCl/zH$_2$O. It was shown that it is possible to change the complexes from $[Cr(H_2O)_6]^{3+}$ to $[CrCl_{3.5}(H_2O)_{2.5}]^{0.5-}$ (average of the complexes in solution) by varying their composition.

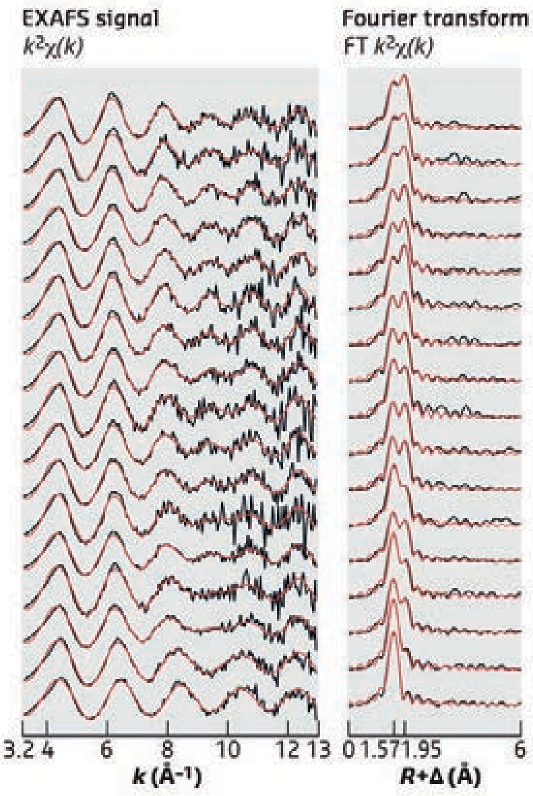

Fig. 115: The EXAFS oscillations and their corresponding Fourier transform spectra clearly show that the relative contributions of the oxygen and chlorine shells depend on the composition of the DES–water mixtures.

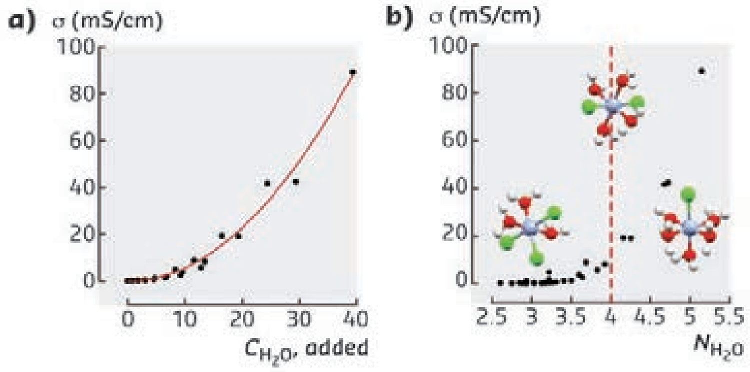

Fig. 116: *a)* The conductivity greatly depends on the amount of added water. **b)** This trend is also correlated with the coordination chemistry and the tendency of water ligands to be incorporated into certain species.

These results were combined with density measurements to provide detailed insight into the concentration profiles of various ions and molecules in these mixtures. Additionally, it was possible to differentiate between the concentrations of ‘total’, ‘coordinated’, and ‘free’ moieties. This yields valuable information about the different species, including how they behave in the new solvents and how they can influence the eventual electroplating. In this respect, the relation of the concentration profiles to other important properties of the electrolytes was studied. From this, the behaviour of the water molecules in the DES–water mixtures could be linked with the conductivity of the liquids (**Figure 116**). For DESs with very little water inside, the dominant species is $[CrCl_3(H_2O)_3]^0$. The low conductivity of these mixtures is due to the combined effect of the low amount of independent charge carriers, low amount of 'free' water and low viscosity. Upon addition of water, the hygroscopic and highly chlorinated complexes will absorb the majority of the water molecules as ligands, and the conductivity will stay low. From the moment that most of the complexes are present as $[CrCl_2(H_2O)_4]^+$, a considerable number of the water molecules will be free to move in the liquid, which results in a lower viscosity and higher ion mobility.

The results of the coordination chemistry and the behaviour of the different moieties in solution were based on EXAFS experiments performed at beamline **BM26** (**Figure 115**). Accurate metal-ligand distances were combined with estimates of the coordination numbers in each complex to support the UV/Vis experiments and to obtain the concentration profiles and links discussed above. These results were also used to construct an analysis tool to monitor concentrations of the 'total', 'coordinating' and 'free' molecules and ions in the DES-water mixtures. This information can be obtained by using three characteristic values of a single UV/Vis spectrum as input for the analysis tool. Consequently, these insights are very valuable for the further optimisation, understanding and monitoring of this innovative and sustainable electroplating process.

PRINCIPAL PUBLICATION AND AUTHORS

Chromium(III) in deep eutectic solvents: towards a sustainable chromium(VI)-free steel plating process, T. Verdonck (a,b), P. Verpoort (b), J. De Strycker (b), A. De Cleene (b), D. Banerjee (c,d), P. Nockemann (e), R. Van Deun (a) and K. Van Hecke (a), *Green Chem.* **21**, 3637-3650 (2019); doi: 10.1039/c9gc00690g.
(a) Ghent University, Ghent (Belgium)
(b) OCAS NV, Zelzate (Belgium)
(c) KU Leuven, Leuven (Belgium)
(d) ESRF
(e) Queen's University Belfast, Belfast (UK)

REFERENCES

[1] T. Verdonck *et al.*, *Dalton Trans.* **48**, 2318-2327 (2019).

IDENTIFICATION AND ROLE OF INTERSTITIAL PALLADIUM NITRIDE STRUCTURES IN THE SELECTIVE OXIDATION OF AMMONIA

This study followed the evolution of palladium nanoparticles during the selective catalytic oxidation of ammonia – an important exhaust after-treatment technology for diesel vehicles. The work was able to identify a previously unreported Pd nitride structure that was present during catalysis and showed how further evolution of the catalyst structure affected its performance.

The harmful nature of NO_x emissions from automotive vehicles is well established and legislation on the quantities of permissible levels of NO_x within exhaust streams is becoming ever tighter. Current de-NO_x technologies utilise NH_3 to reduce NO_x to the environmentally benign N_2 (NH_3-SCR). The current drive to reduce NO_x emissions has led to de-NO_x technologies using greater amounts of NH_3. However, this has led to increased levels of unreacted toxic NH_3 in these exhaust streams. To remediate this issue, a selective NH_3 oxidation step (NH_3-SCO) downstream of the NH_3-SCR process has been introduced; the selectivity must be towards N_2 as over-oxidation will give rise to more unwanted NO_x. Supported Pd nanoparticles have proved highly active for NH_3-SCO, however, there is a strong temperature dependence on the selectivity of the process. This work describes *operando* spectroscopic studies during NH_3-SCO and makes direct correlations between the evolving structures of Pd nanoparticles (NPs) and the selectivity towards different products.

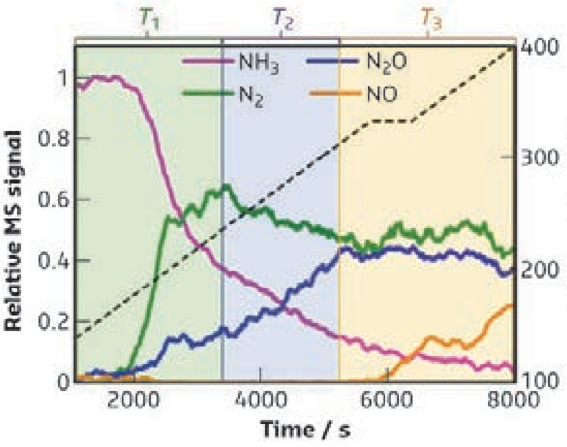

Fig. 117: Catalytic activity of 1.5 wt% Pd/γ-Al_2O_3 for NH_3 oxidation at increasing temperatures. Reactant gas feed: 0.5% NH_3, 2.5% O_2, 97% He.

An initial combined time-resolved Pd K-edge extended X-ray absorption fine structure (EXAFS) and diffuse reflectance infrared Fourier transform (DRIFT) spectroscopy study was performed under NH_3-SCO conditions at SLS, Switzerland (**Figure 117**). Assessing the gas composition as a function of temperature, three distinct phases are observed, and the EXAFS and DRIFTS data lead to the following conclusions: (i) An interstitial Pd species is formed during the low-temperature regime ($100°C \leq T_1 \leq 200°C$), where the main product of NH_3 oxidation is N_2; (ii) Pd NPs with a bulk metallic structure and a surface oxide are formed in the mid-temperature regime ($240°C < T_2 < 300°C$), where an increasing amount of NH_3 is oxidised to N_2O, and (iii) bulk PdO NPs are formed at high temperature ($T_3 > 300°C$), and are linked to the production of NO.

Interstitial Pd hydrides and carbides are often determined through Pd K-edge X-ray absorption near edge structure (XANES) studies, where the maximum of the second XANES peak decreases in intensity and shifts to lower energy. However, in this work, the only two interstitial structure types possible were Pd hydride and Pd nitride. Considering the process conditions (*i.e.*, > 100°C) and the stability of Pd hydrides at these temperatures, it was hypothesised that an interstitial nitride was the most likely structure – something that had not been previously reported. An unambiguous method of differentiating between these two structures was needed. To this end, *operando* NH_3 oxidation studies at the Pd L_3 edge were performed at beamline **BM28**.

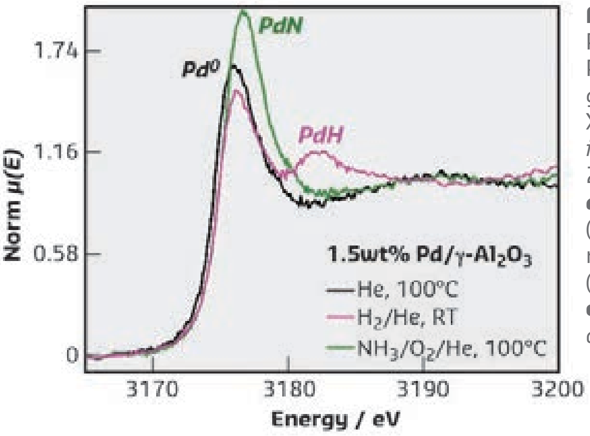

Fig. 118: *In-situ* Pd L_3-edge XANES of Pd/γ-Al_2O_3 in different gas environments. XANES collected after *in-situ* reduction in H_2 at 200°C, then exposure to **a)** inert He at 100°C (black), **b)** 10% H_2 at room temperature (magenta) and **c)** 0.5% NH_3/2.5% O_2/He at 100°C (green).

Pd hydride structures have a clear signature in the post-edge region of the Pd L_3 XANES, which was absent during these investigations. This made it possible to exclude PdH_x as a possible structure type (**Figure 118**).

This study demonstrates the structure–function activity relationships that arise during NH_3 oxidation with supported Pd nanoparticles. Furthermore, it has identified a previously unreported PdN_x structure that forms during catalysis and is responsible for the desired selectivity towards N_2. This is a key finding, not only for NH_3 oxidation, but also in terms of identification of the PdN_x structure, which could have broader applicability to other areas in catalysis.

PRINCIPAL PUBLICATION AND AUTHORS

Structural selectivity of supported Pd nanoparticles for catalytic NH_3 oxidation resolved using combined operando spectroscopy, E. K. Dann (a,b), E. K. Gibson (b,c), R. H. Blackmore (b,d), C. R. Catlow (a,b,e), P. Collier (f), A. Chutia (b,g), T. E. Erden (f), C. Hardacre (b,h), A. Kroner (i), M. Nachtegaal (j), A. Raj (f), S. M. Rogers (a,b), S. F. Taylor (h), P. Thompson (k), G. F. Tierney (b,d), C. D. Zeinalipour-Yazdi (b,l), A. Goguet (b,m) and P. P. Wells (b,d,i),

Nat. Catal. **2**, 157-163 (2019); doi: 10.1038/s41929-018-0213-3.

(a) Department of Chemistry, University College London (UK)
(b) UK Catalysis Hub, Research Complex at Harwell (UK)
(c) School of Chemistry, University of Glasgow (UK)
(d) University of Southampton School of Chemistry (UK)
(e) Cardiff Catalysis Institute, School of Chemistry, Cardiff University (UK)
(f) Johnson Matthey Technology Centre (UK)
(g) College of Science, University of Lincoln (UK)
(h) School of Chemistry, University of Manchester (UK)
(i) Diamond Light Source Ltd., Harwell Science and Innovation Campus (UK)
(j) Paul Scherrer Institute, Villigen (Switzerland)
(k) ESRF
(l) School of Science, University of Greenwich (UK)
(m) School of Chemistry and Chemical Engineering, Queen's University Belfast (UK)

IMAGING THE CARBON IN FOSSILS WITH HARD X-RAYS

Carbon is the essential building block of life on Earth. Its complex speciation drives the functions and properties of all life forms and organic matter. X-ray Raman spectroscopy is combined with tomography to obtain a 3D image of the carbon speciation in a 53-million-year-old ant fossil enclosed in amber.

The methods available for the identification of organic compounds suffer from severe constraints when applied to ancient materials. Invasive 'separative' methods, mostly based on chromatography, allow high-precision identification of ancient molecules in micro-samples but are destructive. Fourier-transform infrared spectroscopy, optical Raman microspectroscopy, and secondary ion mass spectroscopy have limitations due to

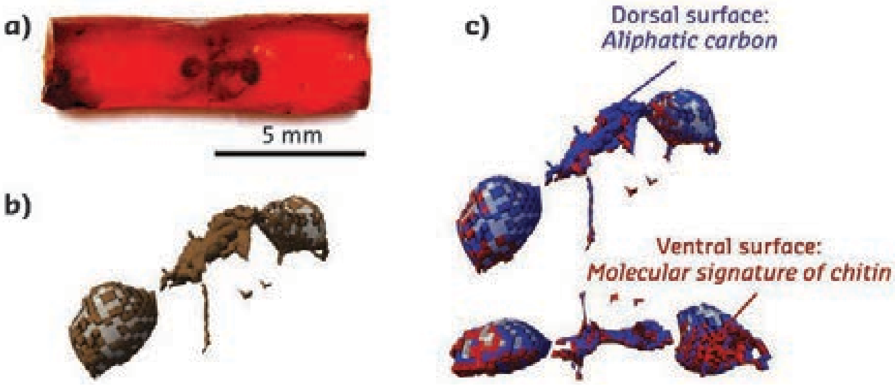

Fig. 119: a) Optical photograph of the specimen. **b)** 3D rendering of the ant cuticle (brown) voxels based on the total signal intensity. **c)** Clustering of the ant cuticle voxels (brown voxels shown in **(b)**) makes it possible to distinguish between two classes of chemical signatures, corresponding to the aliphatic carbon (blue) and chitin (red).

fluorescence background (Raman) and small penetration depths. X-rays have enough energy to eject core electrons from an atom whose binding energies uniquely identify each element.

X-ray absorption near-edge spectroscopy (XANES) probes the energy levels of empty orbitals near an absorption edge, which contain chemical bonding information. XANES is therefore used to quantitatively identify the chemical forms in which a selected element is found in a sample. Carbon has an X-ray absorption edge at 280-320 eV in the soft X-ray regime. The strong absorption and corresponding short penetration depth of X-rays in this energy range impose experimental constraints on the sample and its environment. To overcome this limitation, deeper penetrating hard X-rays can be used with an approach known as X-ray Raman scattering (XRS). In XRS, X-rays are scattered inelastically, giving up a small fraction of their energy (the energy loss) to promote the carbon 1s electron into unoccupied orbitals. XRS spectrometers are able to obtain absorption spectra of low-Z elements, like carbon, using hard X-rays in the 6 to 10 keV range. At these energies, X-rays can pass through up to several millimetres of matter to study the bulk chemical speciation of altered ancient materials. Resulting spectra can be analysed to identify the different carbon-containing chemical groups in the sample from their characteristic absorptions.

3D XRS-based imaging was employed to visualise the chemical composition of a 53-million-year-old ant preserved in amber (**Figure 119a**), using the direct tomography set-up at **ID20**. The collection of successive sections by raster scanning the object made it possible to construct a 3D tomographic volume where the contrast is governed by the inelastic scattering signal (**Figure 119b**). The collected hyperspectral dataset led to direct observation of the fossil morphology (**Figure 120a**). Contrasts observed in the specimen indicate the presence of different chemical compounds. The XRS spectrum $I(\Delta E, X)$ at a given voxel of coordinates, $X = (x,y,z)$, is a linear combination of the spectra of the different compounds present and a background signal from valence electron background and Compton scattering:

$$I(\Delta E, X) = \sum_{n=1}^{N} A_n(X) I_n^{\mathrm{ref,norm}}(\Delta E) + \mathrm{C}_1(X) + \mathrm{C}_2(X)\,\Delta E$$

The fit of each experimental XRS spectrum was performed using a non-linear least-square fitting procedure, where the initial reference spectrum $I^{\mathrm{ref,norm}}(\Delta E)$, was the averaged amber spectrum. As shown on the map of the quadratic error of the fit, the spectral data differ considerably from the amber for a 1-pixel-wide line at the location of the insect's former cuticle (**Figure 120b**).

The arthropod cuticle is a hierarchically structured material composed of an external thin epicuticle layer, rich in lipids and proteins, and the exocuticle and endocuticle composed mainly of chitin-protein complexes. Chitin ($(C_8H_{13}O_5N)_n$), a linear polymer of β-1,4–linked N-acetyl glucosamine, unlike most carbohydrate compounds, is not water soluble and is known to be quite decay resistant. A chitin reference spectrum was therefore added to the fitting model. The results highlight the presence of two distinct chemical fingerprints in the

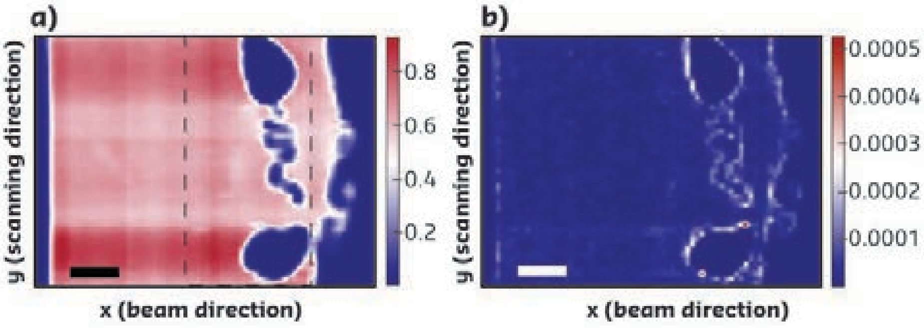

Fig. 120: a) Total intensity virtual cross-sectional image. **b)** Spatial distribution of the quadratic error showing the distinct chemical regions of the sample when performing a fit based on the amber reference.

ant's exoskeleton: the first being a molecular signature typical of polysaccharides such as chitin (ventral surface) – the main structural component of the insect's exoskeleton, and the second aliphatic carbons (dorsal surface), a product of burial diagenetic transformation of the original chemistry of the organism (**Figure 119c**). These findings demonstrate the potential for 3D XRS imaging as a bulk sensitive probe of chemical speciation in a carbonaceous fossil. This approach will help paleontologists to learn about specimens' biochemistry, molecular evolution, and chemical interactions between organisms and their depositional setting.

PRINCIPAL PUBLICATION AND AUTHORS

Carbon speciation in organic fossils using 2D to 3D x-ray Raman multispectral imaging, R. Georgiou (a,b), P. Gueriau (a,c), C. J. Sahle (d), S. Bernard (e), A. Mirone (d), R. Garrouste (f), U. Bergmann (g), J-P. Rueff (b,h) and L. Bertrand (a,b), *Sci. Adv.* **5**(8), eaaw5019 (2019); doi: 10.1126/sciadv.aaw5019.
(a) IPANEMA, CNRS, Ministère de la Culture, Université de Versailles Saint-Quentin-en-Yvelines, Université Paris-Saclay (France)
(b) Synchrotron SOLEIL, Gif-sur-Yvette (France)
(c) Institute of Earth Sciences, University of Lausanne (Switzerland)
(d) ESRF
(e) Muséum National d'Histoire Naturelle, Sorbonne Université, UMR CNRS 7590, IRD, Institut de Minéralogie, de Physique des Matériaux et de Cosmochimie (IMPMC), Paris (France)
(f) Institut de Systématique Evolution Biodiversité (ISYEB), UMR 7205 MNHN/CNRS/Sorbonne Univ./EPHE/Univ. Antilles, Muséum National d'Histoire Naturelle, Paris (France)
(g) Stanford PULSE Institute, SLAC National Accelerator Laboratory, California (USA)
(h) Sorbonne Université, CNRS, Laboratoire de Chimie Physique-Matière et Rayonnement, LCPMR, F-75005 Paris (France)

EVOLUTION OF GLASS ELASTIC PROPERTIES IN 110-MILLION-YEAR AGEING

The way the structure and dynamics of amorphous materials relate to their metastability is one of the current challenges for understanding glass transition. A link between stability and elastic properties of glasses was revealed by applying X-ray methods to a glassy amber dated back to 110 million years ago.

Glasses are in an out-of-equilibrium state, such that their structure continuously evolves to reach energetically favourable, more stable microscopic configurations. Consequently, their physical properties are not uniquely defined but depend on their thermal history. During the last decade, great interest has been focused on investigating the dependence of the vibrational properties of glasses on the ageing dynamics driving their stabilisation. The vibrational properties can give an insight into the shape of the relative minima of the potential energy landscape that the glass explores in the stabilisation **[1]**. Moreover, they are particularly relevant, being responsible for universal thermodynamic anomalies with respect to crystalline solids. These anomalies have been related to a characteristic excess in vibrational density of states (VDOS) over the Debye level, named boson peak.

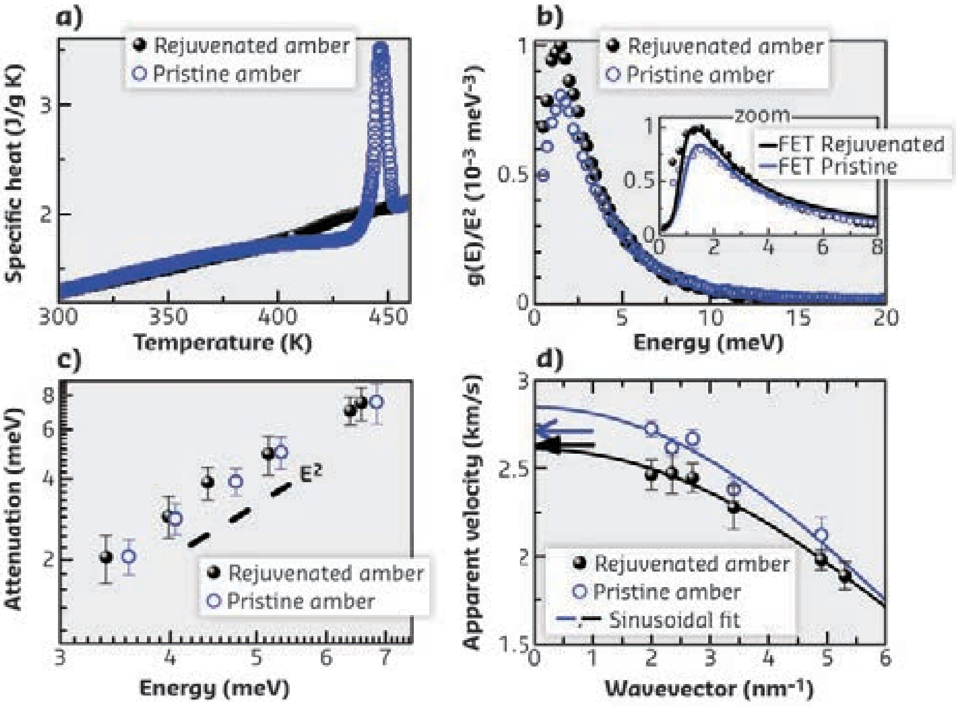

Fig. 121: Comparison of pristine (blue dot and lines) and rejuvenated (black dot and lines) ambers: **(a)** specific heat; **(b)** reduced VDOS g(E)/E² and fit based on FET in the inset; **(c)** acoustic attenuation; **(d)** apparent sound velocity, sinusoidal fits and low frequency limit (arrows) from **[2]**.

From an experimental point of view, one of the major hurdles for addressing ageing effects is the limited stability range accessible on laboratory timescales. Since spontaneous stabilisation is unfeasibly slow, the conventional way of obtaining glasses of different stabilities is by tuning the quenching rate while cooling the liquid. Specifically, slower rates correspond to states with lower potential energy and thus higher stability. However, the stability range covered is limited: upwards by thermal conductivity and annealing technology, and downwards by the occurrence of crystallisation. This study circumvented these limitations by exploiting the unique opportunity offered by a glass that has experienced extreme natural stabilisation: fossil amber extracted from the outcrop of El Soplao, Spain, dated to 110 million years ago.

To compare glasses sharing the same chemical composition but with very different ages, the pristine amber was 'rejuvenated', with an annealing to the supercooled liquid phase to erase its geological thermal history, followed by a cooling at standard rates. The different stability is testified by the endothermic jump in specific heat (**Figure 121a**) and quantified by 9% lower fictive temperature T_f for pristine amber (the lower T_f, the more stable the glass). By applying a combination of X-ray scattering techniques, the structural and vibrational properties of the two ambers were compared in the THz range at characteristic frequencies of the boson peak. Specifically, the reduced VDOS $g(E)/E^2$, was measured by performing inelastic X-ray scattering (IXS) experiments with nuclear resonance analysis at beamline **ID18**, exploiting the high energy resolution and the possibility of integrating the scattered intensity over a large momentum transfer range. The collective excitations contributing to the boson peak were examined measuring phonon dispersion and mode attenuation by momentum-resolved IXS at beamline **ID28**.

Interestingly, it was found that the boson peak, ubiquitously present in standard glasses, persists in pristine amber but appears less pronounced, blue-shifted, and broader (**Figure 121b**) than in the rejuvenated glass. In the hyper-aged amber, the attenuation is slightly reduced (**Figure 121c**), while the acoustic modes are stiffer and exhibit positive dispersion (*i.e.*, excess in apparent velocity (**Figure 121d**) relative to the low frequency limit measured by Brillouin Light Scattering **[2]**, indicating increased relaxation time). Critically, the modifications to the microscopic structure accompanying the changes in the vibrational properties were investigated by wide-angle X-ray diffraction at beamline ID28. Pristine amber appeared homogeneously densified in a way peculiar to natural stabilisation and different from that caused by hydrostatic compression. All the experimental evidence was rationalised within the Fluctuating Elasticity Theory (FET) that accounts for disorder in terms of microscopic random spatial fluctuations of the elastic constants. This makes it possible to establish a quantitative link between glass stability, or equivalently, height on the energy landscape, and the dynamic disorder encoded in the boson peak (**Figure 122**).

In conclusion, these results show that approaching the bottom of the potential energy landscape over an unprecedentedly long spontaneous stabilisation, the elastic matrix of the glass becomes increasingly less disordered (with sharper elastic constant distribution and longer correlation length ε), though the glass retains its characteristic vibrational anomalies.

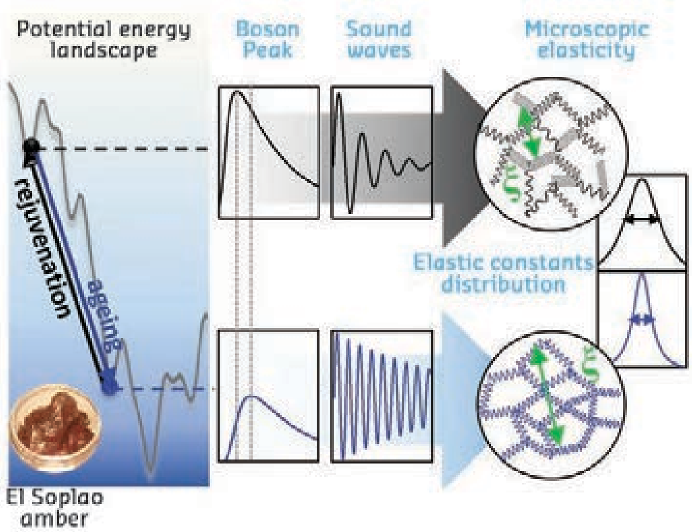

Fig. 122: Sketch of the potential energy landscape (grey line) sampled with pristine (blue dot and lines) and rejuvenated (black dot and lines) ambers and the observed modifications in the vibrational properties.

PRINCIPAL PUBLICATION AND AUTHORS

Tracking the Connection between Disorder and Energy Landscape in Glasses Using Geologically Hyperaged Amber,
E. A. A. Pogna (a), A. I. Chumakov (b), C. Ferrante (c), M. A. Ramos (d) and T. Scopigno (c),
J. Phys. Chem. Lett. ***10***, 427-432 (2019); doi: 10.1021/acs.jpclett.9b00003.

(a) CNR-NANO Pisa (Italy)
(b) ESRF
(c) Università di Roma La Sapienza and IIT-Center for Life Nano Science@Sapienza, Rome (Italy)
(d) Condensed Matter Physics Department (IFIMAC), Universidad Autónoma de Madrid (Spain)

REFERENCES

[1] E. A. A. Pogna *et al., PNAS* **112**, 2331-2336 (2015).
[2] T. Pérez-Castañeda *et al., Phys. Rev. Lett.* **112**, 165901 (2014).

CHEMICAL VARIABILITY IN ARTIFICIAL STONE POWDERS

Artificial stone (AS) is a widespread composite material used for the preparation of countertops and bathroom furniture. Occupational exposure to AS is linked to severe health effects. This study aimed to obtain a chemical, mineralogical and physico-chemical characterisation of the AS powders to gain insight into the possible pathogenetic processes.

AS is a composite material manufactured by assembling powders, and occasionally fragments, of natural stones with a binder. A widespread and appreciated AS employs unsaturated polyester resins as binder, and crystalline silica as stone. Following the use of AS in large-scale production, numerous diseases among AS workers (ASW), often characterised by short latency and high severity, were described **[1]**. Such responses, however, cannot be fully explained by quantitative relationships with exposure. Among the factors mainly affecting the potential toxicity of such systems, the presence of transition metal ions (mainly Fe) and radicals on the AS surface must be taken into account, in addition to possible alterations resulting from mechanical treatments. Experimental studies on AS powders **[2]** pointed out the peculiar interaction between respirable crystalline silica and the resin, providing a film coating over the mineral surfaces during the countertop finishing procedures. An experimental characterisation study was undertaken on industrial AS samples to highlight the chemical and physico-chemical changes that can occur during industrial processing. Raw and processed (under wet and dry polishing) industrial AS was analysed by means of scanning electron microscopy (SEM), powder X-ray diffraction (PXRD), X-ray fluorescence (XRF), X-ray absorption spectroscopy (XAS) at beamline LISA (**BM08**) and continuous wave (cw) and pulsed electron paramagnetic resonance (EPR) spectroscopy.

The main achievements of this characterisation resulted in the description of the mineralogical composition of the powders. The powders are always constituted by crystalline silica, with either quartz (qz) or cristobalite (cb) as major components, and only minor mineralogical phases belonging to the raw formulations. The chemical composition (extremely variable due to the intrinsically heterogeneous nature of the AS materials) does not reveal chemical fingerprints associated to qz- or cb-bearing samples. Conversely, a clear change (verified by means of a detailed statistical analysis, aimed to ascertain natural chemical associations) in the chemical fingerprint discriminates raw from processed samples, and wet from dry processed samples. In agreement with chemical results, extended X-ray absorption fine structure (EXAFS) analyses show that in both wet and dry processing, contamination by metallic Fe (likely provided by working tools) occurs (**Figure 123**).

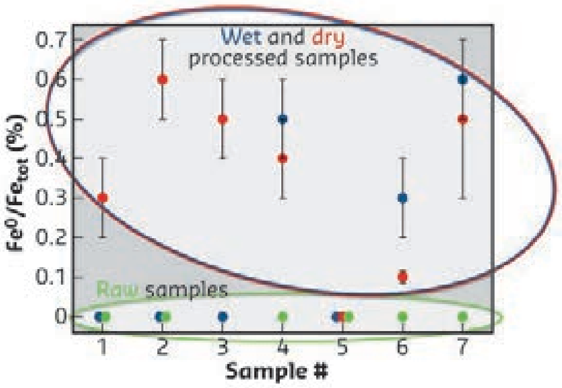

Fig. 123: Ratio between metallic and total Fe content (Fe^0/Fe_{tot}) evaluated from EXAFS data analysis.

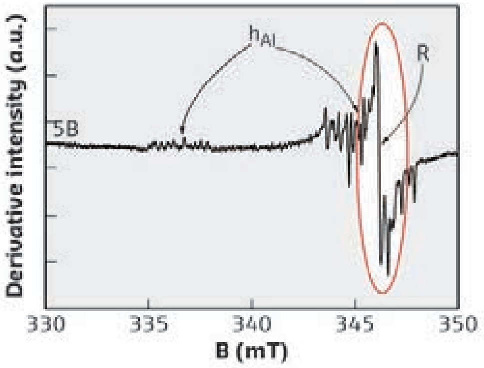

Fig. 124: EPR spectrum of a sample where the additional radical species is highlighted in red.

Moreover, it is found that the modifications induced by mechanical treatments extend to all the detected Fe forms by modifying Fe coordination and/or Fe oxidation state. The cw and pulsed EPR survey of the samples made it possible to assess apparent changes in the radical speciation. Specifically, additional radicals were observed in both the dry- and wet-processed samples (**Figure 124**). No changes associated with the type of processing were found, whereas distinct additional radical species (mainly of the Si• type) were identified in qz- and cb-bearing samples. According to the results, it is noted that: (i) specific chemical contamination of the parent AS occurs depending on the wet or dry processing, and (ii) processing of AS results in detectable changes of the Fe speciation.

The active mechanisms of dust contamination are highly relevant for toxicity studies, since redox and toxic species are involved **[2]**. Moreover, a definite change in radical speciation is operated by AS processing. Indeed, a very peculiar general behaviour of these materials can be inferred, where chemical contamination and irreversible thermo-mechanical processes modify the chemical and physico-chemical features of the parent materials, leading to differentiated types of exposure for AS workers operating the dry or the wet polishing. A last relevant claim deals with the presence of unusually high levels of cristobalite, a contaminant whose toxicity is considered even higher than that of quartz.

PRINCIPAL PUBLICATION AND AUTHORS

Chemical variability of artificial stone powders in relation to their health effects, F. Di Benedetto (a), A. Giaccherini (a), G. Montegrossi (b), L. A. Pardi (c), A. Zoleo (d), F. Capolupo (e), M. Innocenti (e), G. O. Lepore (f), F. d'Acapito (f), F. Capacci (g), C. Poli (g), T. E. Iaia (g), A. Buccianti (a) and M. Romanelli (a), *Sci. Rep.* **9**, 6531 (2019); doi: 10.1038/s41598-019-42238-2.

(a) Dip. Scienze della Terra, Università di Firenze (Italy)
(b) CNR – Ist. Geoscienze e Georisorse, Firenze (Italy)
(c) CNR – Ist. Processi Chimico Fisici (Italy)
(d) Dip. Scienze Chimiche, Università di Padova (Italy)
(e) Dip. Chimica, Università di Firenze (Italy)
(f) ESRF
(g) Dip. Prevenzione, PISLL, Health Agency of Tuscany (Italy)

REFERENCES

[1] R. F. Hoy *et al., Occup. Environ. Med.* **75**, 3-5 (2018).
[2] C. Pavan *et al., Toxicol. Sci.* **153**, 4-17 (2016).

DEFINING THE IRON ACTIVE SITE FOR CO_2 ELECTROREDUCTION IN MESOPOROUS NITROGEN-DOPED CARBON

Electrochemical reduction of CO_2, using water as the proton source, is a sustainable solution for CO_2 abatement. Iron cations inserted into nitrogen-doped carbon have emerged as a promising family of electrocatalysts for this reaction. In this study, several X-ray spectroscopy techniques were applied to unravel the local order of such atomically dispersed iron.

Hydrogenating CO_2 into valuable feedstocks using green hydrogen offers the possibility of directly sequestering this greenhouse gas into highly demanded utility chemicals. Hereby, the electrochemical CO_2 reduction reaction is being increasingly investigated over different electrodes for the production of CO, HCOOH, CH_3OH and others. The possibility to enhance the production of one particular chemical relies on a kinetically controlled reaction which depends itself on the energetics of adsorption of the different reaction intermediates. To this end, emerging atomically dispersed metal catalysts with better-defined structure as active sites, offer a unique opportunity to explore structure–activity relationships driving the selectivity. Herein, a facile approach to prepare mesoporous nitrogen-doped carbons with atomically dispersed iron sites through a metal organic framework-mediated synthesis is reported **[1]**. The current method consists of (i) hydrolysis of tetramethyl orthosilicate (TMOS) in the structure of an iron-containing ZIF-8 material (ZIF-8-Fe), (ii) high-temperature pyrolysis and (iii) SiO_2 template leaching. The SiO_2-assisted approach is vital for inhibiting the formation of iron nanoparticles, preferentially generating atomically dispersed iron sites, and creating high surface area and mesoporosity in the carbon matrix (**Figure 125**).

The material was tested in the electrocatalytic reduction of CO_2 and displayed high CO Faradaic efficiency (>80 %), high CO current density and good stability. Due to the noncrystalline nature of the iron active phase, X-ray absorption and emission spectroscopies (XAS/XES) were applied to unravel the chemical environment

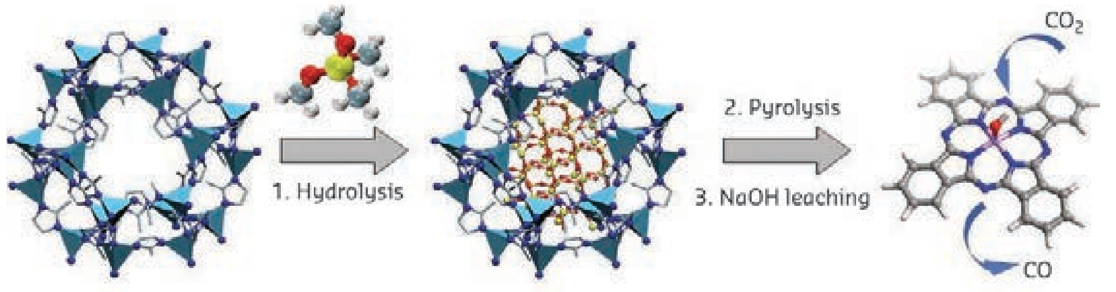

Fig. 125: Schematic illustration of the synthesis of the mesoporous nitrogen-doped carbon with atomically dispersed iron sites.

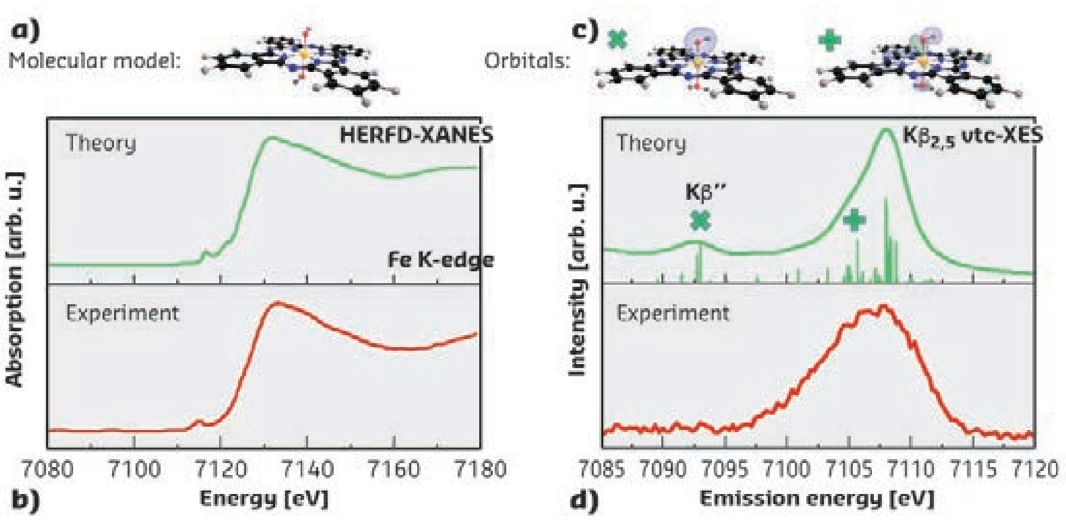

Fig. 126: Comparison of experiments and theory for HERFD-XANES and VTC-Kβ spectroscopies for one molecular model, shown in **(a)**. **b)** HERFD-XANES spectrum of the Fe electrocatalyst compared against FDMNES calculations. **c)** Two selected donor orbitals corresponding to the assigned regions of the Kβ'' and $K\beta_{2,5}$ peaks. **d)** VTC-Kβ spectrum of the Fe electrocatalyst compared against ORCA calculations.

on beamline **BM16**. X-ray absorption near-edge structure (XANES) and extended X-ray absorption fine structure (EXAFS) spectroscopies excluded the square-planar configuration of a simple porphyrinic moiety and confirmed a high dispersion of atomic iron in its trivalent state.

Given the ongoing debate on the structure of iron active sites immobilised on nitrogen-doped graphene and the limits of the above characterisation, valence-to-core (VTC) X-ray emission and high-energy-resolution fluorescence-detected XANES (HERFD-XANES) spectroscopies coupled to density functional theory (DFT) calculations were conducted to further refine a structural model **[2]**. The initial motivation for the XES study was to overcome the limitation of EXAFS concerning the discrimination between oxygen and nitrogen atoms in the first coordination shell by evaluating the energy position of the Kβ" satellite. The experimental VTC-Kβ spectrum of the Fe electrocatalyst is shown in **Figure 126.** Unexpectedly, the VTC-Kβ spectrum presents only a broad peak centred at 7107 eV in the $K\beta_{2,5}$ region with no clear peak in the Kβ'' region. The explanation of the faint Kβ'' intensity involved a conjugated system around the iron centre. With such coordination, the ligands' atomic orbitals contribute significantly through sp^2 hybridisation to the π-system, inevitably decreasing their participation in the σ-framework.

From this idea, seven conjugated models were calculated that were thought to potentially match the experimental VTC-Kβ spectrum (ORCA), together with the HERFD-XANES spectrum (FDMNES). As an illustration, one of the studied models is shown in **Figure 126**, together with its theoretical XANES and XES spectra. The most favourable agreement with theory was observed for models that had in common a porphyrinic environment around iron, completed by the coordination of the water molecules and/or hydroxyl group. The low intensity of the Kβ'' was further explained by this multitude of configurations. Afterwards, the high selectivity to CO observed during the electrocatalytic reduction of CO_2 was explained by additional DFT calculations using the molecular models hinted at by XAS and XES spectroscopies. It was found that the iron cations trapped in such a porphyrinic environment decrease the free energy barriers of *COOH formation and destabilise the adsorption of *H, preventing subsequent hydrogenation steps.

These results demonstrate that HERFD-XANES and VTC-Kβ spectroscopies combined with theory are a powerful tool to explore the coordination environment in these and other atomically dispersed catalysts.

PRINCIPAL PUBLICATION AND AUTHORS

Structure-activity relationships in metal organic framework derived mesoporous nitrogen-doped carbon containing atomically dispersed iron sites for CO2 electrochemical reduction, X. Sun (a), R. Wang (a), S. Ould-Chikh (b), D. Osadchii(a), G. Li(a), A. Aguilar (c), J-L. Hazemann (c), F. Kapteijn(a) and J. Gascon (b), *J. Catal.* **378**, 320-330 (2019); doi: 10.1016/j.jcat.2019.09.013.

(a) Delft University of Technology, Delft (The Netherlands)
(b) King Abdullah University of Science and Technology, Thuwal (Saudi Arabia)
(c) Institut Néel, Grenoble (France)

REFERENCES

[1] L. Oar-Arteta *et al.*, *Mater. Chem. Front.* **1**, 1709-1745, (2017).
[2] Y. Mun *et al., Appl. Catal. B*, **222**, 191-199, (2018).

MAGNETITE INCORPORATES PLUTONIUM THROUGH FORMATION OF PYROCHLORE-LIKE ISLANDS

Underground radioactive waste repositories are characterised by strongly reducing conditions, rendering most radionuclides into their least soluble form. However, under these conditions, plutonium converts into a trivalent aquo-complex, which could leach into groundwater. X-ray absorption spectroscopy is used to show that this risk is not as high as previously assumed, since two competing chemical retention mechanisms are able to retain aqueous plutonium.

Radioactive waste repositories need to retain the most long-lived radionuclides over hundreds of thousands of years. This relies strongly on accurate predictions of chemical processes across such time scales. For instance, waste containers, even when made from the most durable stainless steel, will corrode and hence may no longer present a physical barrier between the radioactive waste and the eventually infiltrating groundwater. The most important corrosion product is magnetite, a Fe(II)/Fe(III)-containing spinel phase of high durability. One of the most radiotoxic elements is plutonium. If plutonium could not only be sorbed at the surface of magnetite, as previously shown **[1]**, but could also be incorporated by this mineral, this would present an even better protection against leaching, especially when the chemistry of the groundwater changes, for instance by the melting glaciers after another ice age.

Previous research has suggested that trivalent lanthanides, which are chemically similar to trivalent plutonium, are structurally incorporated by magnetite, hence it was decided to investigate if this process also takes place for plutonium. Given the expected low plutonium solubility in magnetite, only X-ray absorption fine structure (XAFS) spectroscopy is able to elucidate this at the molecular scale. Therefore, plutonium-doped magnetite samples were investigated at beamline **BM20**, which has all necessary safety features to handle such radiotoxic samples. **Figure 127** shows the obtained spectra of fresh Pu-magnetite coprecipitates (samples Pu-Mag-1300 and Pu-Mag-4400) as well as samples after an Fe(II)-induced recrystallisation procedure (Pu-Mag-1300-rec and Pu-Mag-4400-rec). A comparison of the X-ray absorption near-edge structure (XANES) data (**Figure 127a**) with selected

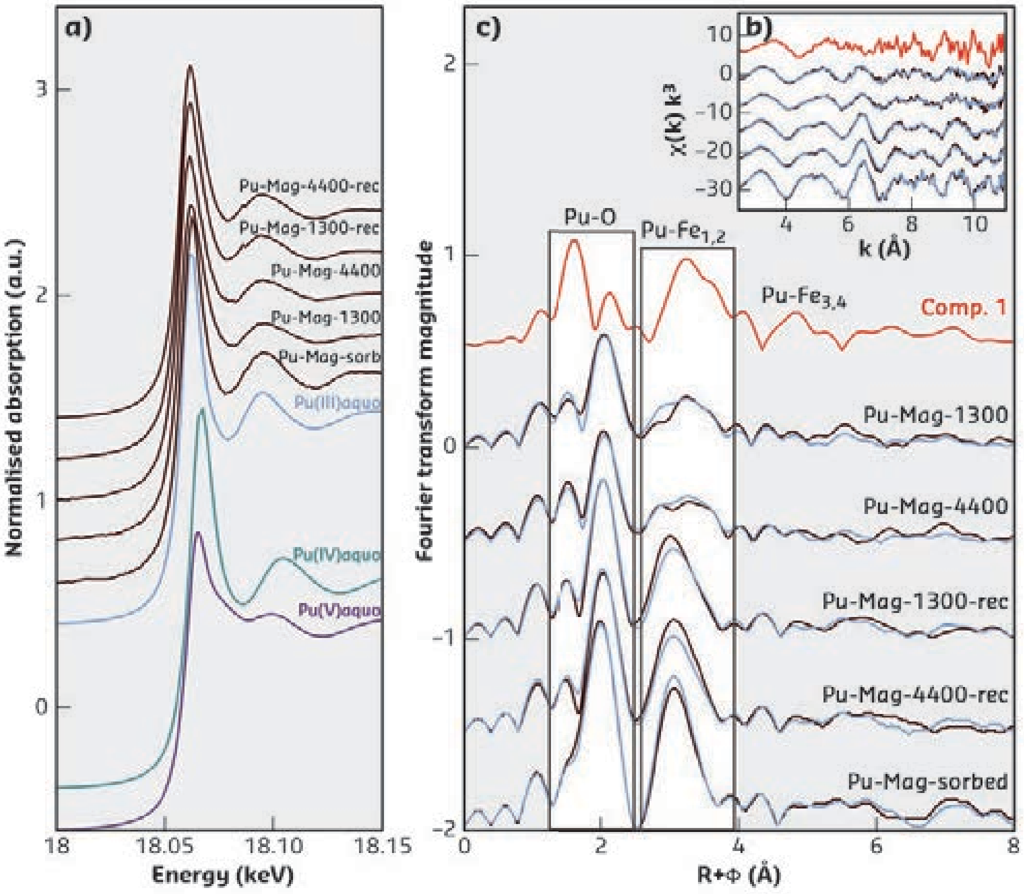

Fig. 127: Pu L_3-edge XAFS spectra of magnetite coprecipitation samples and selected references. **a)** XANES spectra. **b)** k^3-weighted EXAFS spectra. **c)** Corresponding Fourier transform magnitudes. For **(b)** and **(c)**, black lines are experimental data, and blue lines are ITFA-derived reproductions by two components.

references shows that all Pu-magnetites contain plutonium in its trivalent oxidation state. The corresponding EXAFS spectra (**Figure 127b**) reveal that the recrystallised samples contain plutonium prevalently as the tridentate sorption complex previously detected **[1]**. Before the recrystallisation, however, the spectra were impossible to analyse by shell fitting, and a subsequent principal component analysis showed why: these spectra consisted of two different plutonium species in about equal amounts. The spectrum of the first was identical to the sorption complex (Pu-Mag-sorbed); based on this information, the spectrum of the second plutonium species (comp. 1 in **Figure 127c**) could be extracted. Analysis by shell fitting of component 1 showed that plutonium did not simply substitute for iron in magnetite, where it would need an octahedral environment (six nearest oxygen neighbours), but adopted a split eight-fold coordination to oxygen.

This peculiar coordination environment, along with the distances of the nearest Fe atoms, suggested that Pu creates a pyrochlore-like environment in its neighbourhood, out to a radial distance of 3.68 Å, while Pu-Fe distances beyond were commensurate with the longer-range magnetite structure. Pyrochlores are notorious host phases for lanthanides, hence it is not surprising that Pu, with its similar large ionic radius of 1 Å, fitted better in such an environment. Quiet surprising is, however, that pyrochlore did not form as a separate phase, but rather as tiny islands within the already small (5 nm) magnetite nanoparticles.

The adoption of a pyrochlore-like local environment within the magnetite long-range structure is most likely induced by the rapid coprecipitation procedure, a process named kinetic entrapment (**Figure 128**). These small pyrochlore islands are, however, structurally incompatible with the magnetite structure and may present only a metastable thermodynamic state: after the Fe(II)-induced recrystallisation of the Pu-doped samples, the amount of incorporated plutonium decreased to about 30%, while the released plutonium was re-adsorbed at the magnetite surface. Therefore, reactive transport models conducted for the risk assessment of radioactive waste repositories have to take into account retention by the sorption process, while structural incorporation is most likely only a temporary process not very relevant for predicting plutonium migration across geologic timescales.

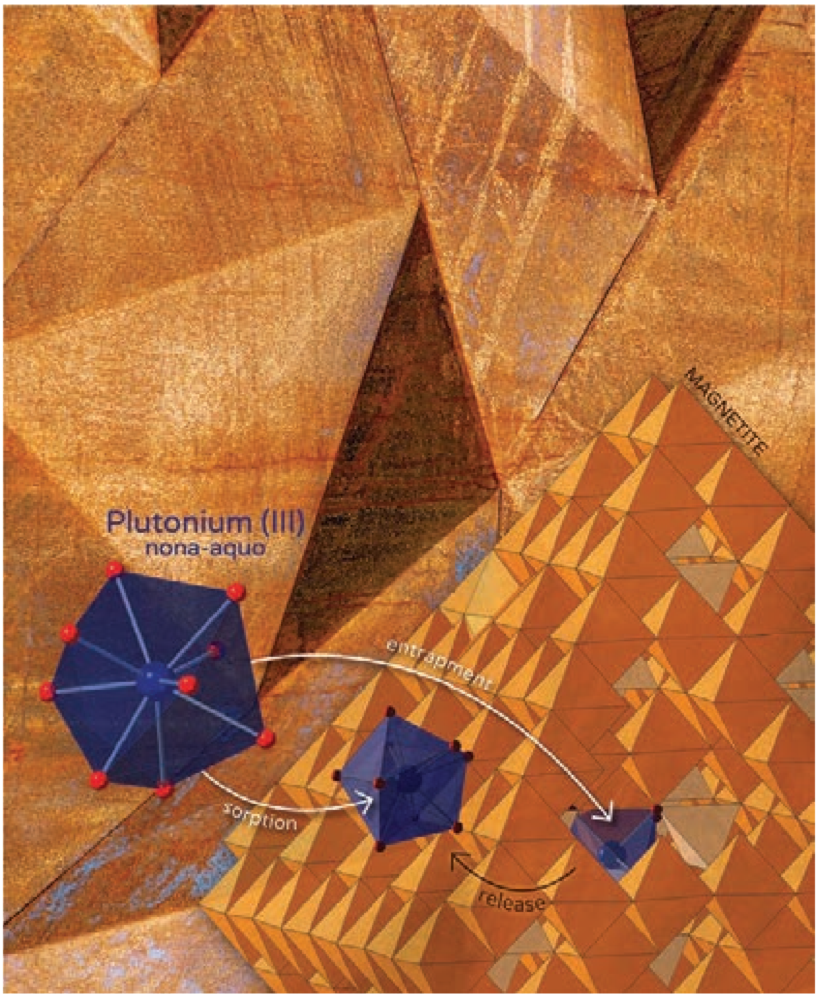

Fig. 128: Plutonium retention mechanisms by magnetite, a steel corrosion product, deciphered: structural incorporation proceeds through formation of pyrochlore-like islands, but recrystallisation of magnetite causes an expulsion of this structural plutonium, which is subsequently re-adsorbed at the most prevalent {111} faces constituting the surface of octahedral magnetite nanoparticles.

PRINCIPAL PUBLICATION AND AUTHORS

Plutonium retention mechanisms by magnetite under anoxic conditions: Entrapment versus sorption, T. Dumas (a,b,c), D. Fellhauer (d,e), D. Schild (d), X. Gaona (d), M. Altmaier (d) and A. C. Scheinost (a,b), *ACS Earth Space Chem.* **3**, 2197-2206 (2019); doi: 10.1021/acsearthspacechem.9b00147.
(a) HZDR Institute for Resource Ecology, Dresden (Germany)
(b) ESRF
(c) CEA Nuclear Energy Division Marcoule, Bagnols sur Cèze (France)
(d) KIT Inst. for Nuclear Waste Disposal, Karlsruhe (Germany)
(e) JRC Karlsruhe, Karlsruhe (Germany)

REFERENCES

[1] R. Kirsch *et al.*, *Environ. Sci. Technol.* **45**, 7267-7274 (2011).

ILLUMINATING THE MAGNETISM OF ACTINIDE-BASED MOLECULES WITH X-RAYS

Molecules and materials incorporating actinide ions possess fascinating magnetic properties, but the understanding of their microscopic origin is masked by the complicated electronic structure of the actinide ions. X-ray spectroscopy experiments have now aided the disentanglement of the spin and orbital contributions to the magnetic moment in a chemically isolated, molecular uranium complex.

The interest in actinide-containing molecules has been reinvigorated by recent key findings of their unique catalytic and magnetic properties **[1]**. The magnetic properties of such complexes are particularly difficult to understand due to the exceedingly complicated electronic structure of actinide ions, resulting from similar-sized and competing effects of the chemical surroundings and relativistic effects intrinsic to such heavy elements. In this work, X-ray magnetic circular dichroism (XMCD) spectroscopy was employed to elucidate the microscopic origin of the magnetism in a uranium-based molecular complex. The elusive $[UF_6]^{2-}$ ion was synthetised as a spatially isolated complex through the employment of large organic counter-ions (**Figure 129**). The large distance between $[UF_6]^{2-}$ ions in the solid, combined with an especially well-defined oxidation state of uranium of +IV in the fluoride-based coordination environment, left this system ideal for a fundamental study of the intrinsic magnetic properties of a uranium(IV) complex in the absence of unwanted magnetic interactions between constituent ions.

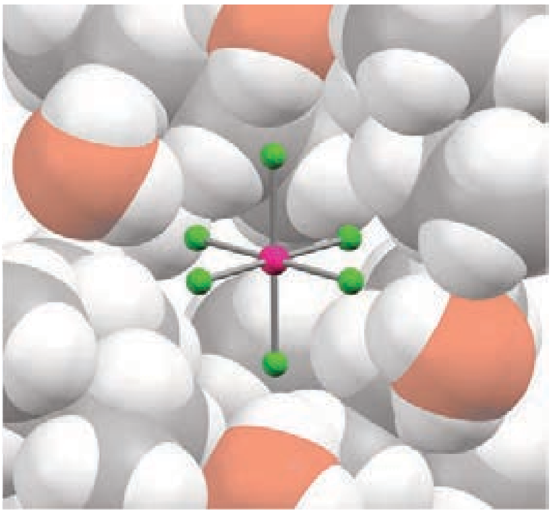

Fig. 129: Chemical structure of the spatially isolated $[UF_6]^{2-}$ complex, showing the magnetically insulating layer generated by the organic counter-ions and co-crystallised water molecules. U: pink; F: green; O: red; H: grey.

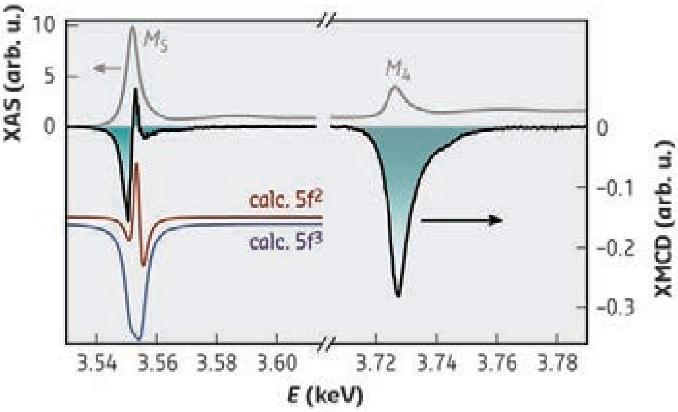

Fig. 130: Experimental XAS (grey lines) and XMCD (black lines) spectra of $[UF_6]^{2-}$ at the $M_{4,5}$ edges obtained in a magnetic field of H = 17 T at 4 K. The theoretical XMCD spectra for both the $5f^2$ (red trace) and $5f^3$ (blue trace) configurations were obtained from multiplet calculations using results extracted from *ab initio* calculations on the experimental structure of $[UF_6]^{2-}$.

The magnetic properties of $[UF_6]^{2-}$ are, at first sight, unexceptional and reflect a non-magnetic ground state. Nonetheless, uranium(IV) possesses two unpaired 5f electrons – a situation that *a priori* would not result in a vanishing magnetic moment. Experiments performed at beamline **ID12** provide unprecedented insight into the magnetic properties of isolated uranium(IV) ions. X-ray absorption spectroscopy (XAS) and XMCD spectra of $[UF_6]^{2-}$ were obtained at the $M_{4,5}$ absorption edges (corresponding mainly to 3d → 5f transitions). At both edges, a clear XMCD signal was observed, which was largely sensitive to the exact number of 5f electrons and the chemical surroundings (**Figure 130**). Combining the quantitative analysis of the XAS and XMCD spectra allows for a deconvolution of the contributions to the magnetic moment of the $[UF_6]^{2-}$ complex; the spin and orbital magnetic moments. Both these moments were found to be sizeable and of similar magnitude (M_{spin} = $-0.41\ \mu_B$ and $M_{orbital}$ = $0.47\ \mu_B$), but opposite in sign. Thus, the $[UF_6]^{2-}$ complex gains its virtually non-magnetic electronic ground state from an almost perfect cancellation of the antiparallel spin and orbital magnetic moments. This peculiar situation parallels that of some transition element systems such as $[OsF_6]^{2-}$ **[2]**, but with the spin and orbital magnetic moments being approximately one order of magnitude larger in the uranium case. Despite the common non-magnetic ground state of U(IV), the observation of individually large spin and orbital magnetic moments should have a decisive impact on the understanding of U(IV)-based materials, especially those displaying complicated magnetic orders **[3]**.

The analysis of the well-resolved experimental XMCD spectra constitutes the first demonstration of the applicability of XMCD spectroscopy to study magnetic properties of actinide-based molecules. These results pave the way for a new approach to acquiring a deeper understanding of the single-ion magnetism of actinide ions in both molecules and solid-state materials.

PRINCIPAL PUBLICATION AND AUTHORS

$[UF_6]^{2-}$: A Molecular Hexafluorido Actinide(IV) Complex with Compensating Spin and Orbital Magnetic Moments,
K. S. Pedersen (a,b), K. R. Meihaus (c), A. Rogalev (d), F. Wilhelm (d), D. Aravena (e), M. Amoza (f), E. Ruiz (f), J. R. Long (g,h), J. Bendix (i) and R. Clérac (a), *Angew. Chem. Int. Ed.* **58**(44), 15650-15654 (2019);
doi: 10.1002/anie.201905056.

(a) Université de Bordeaux, CNRS, Centre de Recherche Paul Pascal, UMR 5031 (France)
(b) Department of Chemistry, Technical University of Denmark (Denmark)
(c) Department of Chemistry, University of California, Berkeley (USA)
(e) ESRF
(f) Departamento de Química de los Materiales Facultad de Química y Biología, Universidad de Santiago de Chile (USACH) (Chile)
(g) Departament de Química Inorgànica i Orgànica and Institut de Química Teòrica i Computacional, Universitat de Barcelona (Spain)
(h) Materials Sciences Division, Lawrence Berkeley National Laboratory, California (USA)
(i) Department of Chemical and Biomolecular Engineering, University of California, Berkeley (USA)
(j) Department of Chemistry, University of Copenhagen (Denmark)

REFERENCES

[1] S. T. Liddle, *Angew. Chem. Int. Ed.* **54**, 8604 (2015).
[2] K. S. Pedersen *et al., Chem. Eur. J.* **23**, 11244 (2017).
[3] V. V. Klepov *et al., J. Am. Chem. Soc.* **141**, 3838 (2019).

STRUCTURE OF MATERIALS

At the time of writing, electrons have been stored for the first time in the new Extremely Brilliant Source (EBS) storage ring. During the shutdown, the Structure of Materials (SOM) beamlines have been preparing for the brighter source. In addition to the increased flux and smaller beam sizes, our users will benefit from the new beamline control system, BLISS, which will allow faster data collection, continuous scans along trajectories, and many other new features.

Following several years of development **[1,2]**, the hard X-ray microscope on **ID06** will accept public users at the restart of user operation. Dark field X-ray microscopy uses full-field illumination of the sample and provides mapping of microstructure and lattice strain in crystalline matter with spatial resolution down to 100 nm. It is analogous to dark-field electron microscopy in that an objective lens magnifies diffracting features of the sample. The use of high-energy X-rays means that these features can be large and deeply embedded. The instrument furthermore allows pre-characterisation of samples at larger length scales using 3D X-ray diffraction or diffraction contrast tomography. A workshop dedicated to the hard X-ray microscope and its evolution into a fully dedicated beamline will be held at the ESRF on April 15 – 17, 2020.

Materials science beamline **ID11** hosts many experimental techniques, from microstructure imaging to the solution and refinement of crystal structures. Some of the first published results from the new nanofocusing end-station have come from chemical crystallography. The detailed atomic structure of a novel cationic Pb dumbbell in $Pb_2Si_5N_8$ was uncovered by Bielec *et al.* (**page 132**) using a tiny microcrystal. The use of high X-ray energies allowed PDF data to be collected up to the Curie temperature for magnetite, Fe_3O_4 (Perversi *et al.*, **page 140**), where the signature of local structure distortions could be quantified. 2019 has been a busy year for ID11 staff with much of the beamline being dismantled due to road works and a large number of maintenance operations. ID11 will have all instrumentation back in place ready to exploit the EBS source and we are looking forward to the delivery of a new CdTe photon-counting pixel detector.

ID15A is optimised for performing high-speed multidimensional studies of working chemical systems under *operando* conditions, very fast time-resolved studies, and high-precision total scattering experiments. The majority of experiments are from the chemical (catalysis, solid-state reactions) and energy (batteries, fuel and solar cells, thermoelectrics and ferroics) fields, with growing applications coming from areas as diverse as geophysics and cultural heritage. Following the EBS upgrade, the methods developed on the beamline, such as five-dimensional X-ray diffraction imaging and high-energy stroboscopic X-ray diffraction and SAXS-WAXS tomography, will be available with unprecedented temporal and/or spatial resolution.

The construction of beamline **BM18** (**EBSL3**: high-throughput, large-field, phase-contrast tomography) is progressing rapidly. The external building and tunnel will be delivered in early 2020. This phase will be followed by the experimental hutch installation. The radiation test of the first optics hutch (OH1) was carried out at the end of 2018 and the radiation test for the experimental hutch is scheduled for September 2020. Therefore, all the optical elements, which are currently being manufactured, can be installed in OH1. Laying out the large marble floor in the experimental hutch and installation of the sample and detector stages will start in September 2020. The commissioning phase will begin in February 2021, with the start of user operation expected in September 2021.

The year of the shutdown was used to shape microtomography beamline **ID19** for the new EBS source: new primary slits are under installation to handle the heat load from the foreseen in-vacuum undulator. After commissioning of the beam enlarger system, it was dismantled and transferred to the optics hutch of BM18. Several mechanical elements of the tri-modal monochromator have been rebuilt to increase their stiffness, resulting in better stability against vibrations. In addition to the selected articles in this chapter of the *ESRF Highlights*, the paper by Kingston *et al.* **[3]** about the first demonstration of ghost tomography with hard X-rays should be noted.

The high-resolution powder diffraction beamline **ID22** will take delivery of a CdTe Eiger 2M detector in June 2020 to replace the scintillation counters behind the analyser crystals. This will lead to improvements in angular resolution, and statistical quality at high angles. The ideas behind this development were tested in 2017 and 2018 **[4]**. The Eiger detector can also be used without analyser crystals, replacing some of the functionality of the Perkin Elmer medical imaging detector that is currently used for fast PDF analysis. A new liquid-helium-cooled cryostat with a large opening window has been delivered by the ESRF sample-environment group and will be put into service during 2020, allowing PDF measurements below 100 K to be carried out more easily.

The reduced team during the shutdown of the high-energy beamline for buried interface structures and materials processing, **ID31**, devoted 2019 to data-processing developments, data analysis and to producing articles for publication. Since the beamline had already been optimised for EBS during its construction, there were no major EBS preparation projects this year. As with all old-lattice low-β beamlines, we expect a 15-fold increase in the incident flux with half the horizontally focused beam size.

A unique new team for topography and microtomography services has been created to coordinate and carry out commercial activities on SOM beamlines. This will help capture opportunities to share resources, and develop automation across several beamlines, in particular for microtomography. Techniques such as white-beam topography, monochromatic rocking curve imaging and depth-resolved sectional topography with automatic sample and film changer allow qualitative and quantitative information to be obtained on defects in single crystals. An advanced sample changer for tomography has been developed, and automatic sample centring using visible light tomography is under development to increase the throughput further. The full service provided by this team, from experiment design to measurement to reporting, gives industry quick and easy access to exceptional tomography and topography measurements, exploiting the high data-quality of ESRF beamlines.

V. HONKIMÄKI

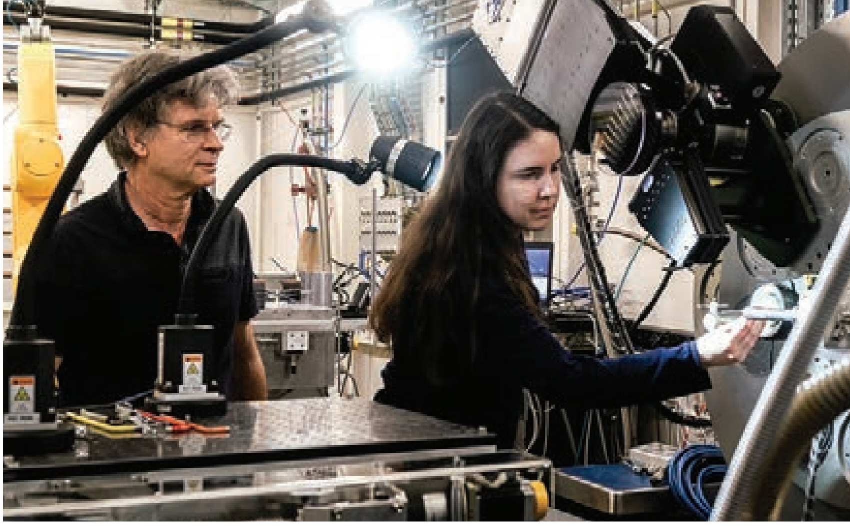

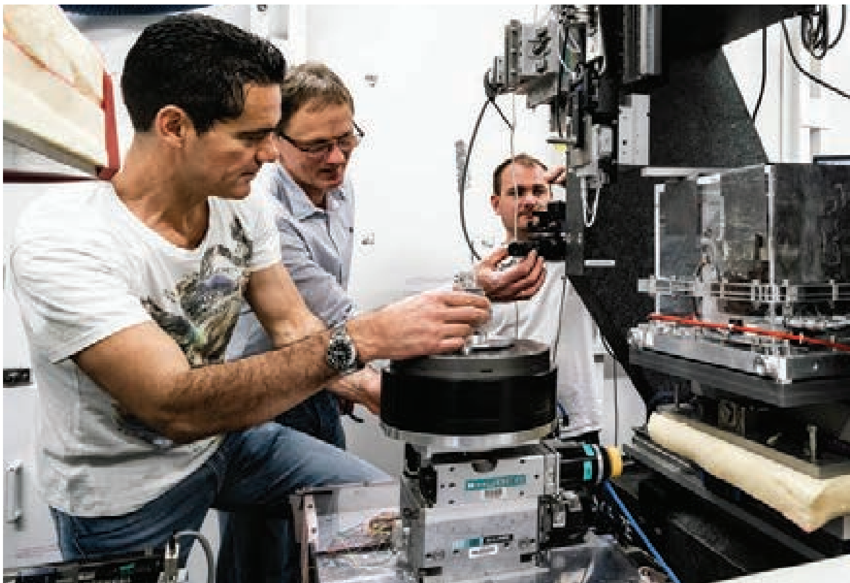

REFERENCES

[1] Kutsal *et al.*, *Mater. Sci. Eng.* **580**, 012007 (2019).
[2] Simons *et al.*, *Nat. Commun.* **6**, 6098 (2016).
[3] Kingston *et al.*, *Optica* **5**, 1516 (2018).
[4] Dejoie *et al.*, *J. Appl. Cryst.* **51**, 1721-1733 (2018).

LEAD-NITROGEN COMPOUNDS: CATIONIC Pb_2 DUMBBELLS IN THE NITRIDOSILICATE $Pb_2Si_5N_8$

As known from the primary explosive lead azide, $Pb(N_3)_2$, Pb-N compounds easily decompose into the elements due to internal redox reactions. Incorporating Pb^{2+} into the pre-built nitridosilicate network $[Si_5N_8]^{4-}$ affords $Pb_2Si_5N_8$, which is stable up to 1000°C and exhibits the first cationic Pb_2 dumbbells.

Nitridosilicates find broad application as luminescent materials in various LED devices when doped with activator ions like Eu^{2+} or Ce^{3+}. In addition to the remarkable rigidity of highly condensed Si–N networks, nitridosilicates intrinsically feature high structural variability. Not only can one N-atom interact with up to four Si-atoms, two SiN_4-tetrahedra may also connect by common edges and not only by common vertices. Hence, a multitude of theoretical structures opens up. Consequently, many different nitridosilicates with various structures and properties have already been discovered **[1]**.

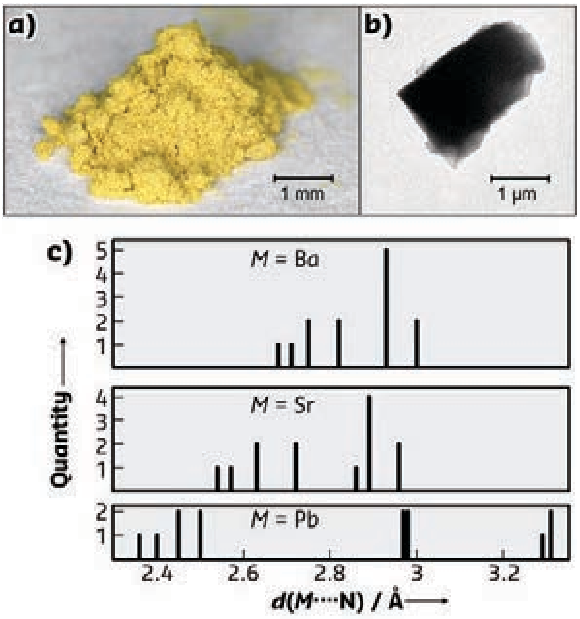

Fig. 131: a) Photograph of a $Pb_2Si_5N_8$ sample. **b)** Bright-field-TEM image of the crystal measured at beamline ID11. **c)** Distribution of distances *M*–N in $M_2Si_5N_8$ (*M*=Sr, Ba, Pb).

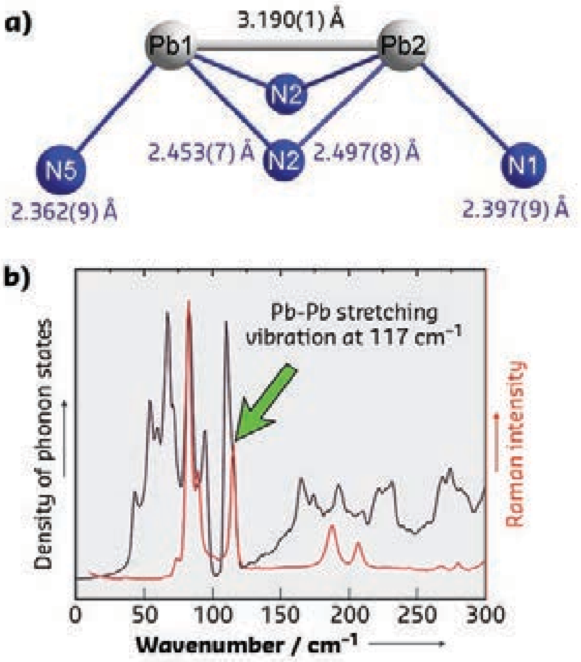

Fig. 132: a) Environment of the Pb_2 dumbbells in $Pb_2Si_5N_8$ and **(b)** comparison between calculated density of phonon states and a Raman spectrum.

As a further challenge, the expansion of elemental variety in *M*–Si–N compounds is a fundamental issue. Due to the comparatively low oxidative force of nitrogen, nitride chemistry in general, and nitridosilicate chemistry in particular, becomes challenging when not working with highly reductive elements such as alkaline, alkaline earth or rare-earth metals. Thus, a novel synthesis strategy for nitridosilicates was recently developed **[2,3]**, given in the following equation (*M*=metal and *Ae*=alkaline earth metal) : $Ae_2Si_5N_8 + MCl_2 \rightarrow M_2Si_5N_8 + AeCl_2$.

This route is particularly advantageous since all covalent bonds within the Si–N network stay untouched in the reaction. Therefore, this approach has been successfully applied (*Ae*=Sr and *M*=Pb) for preparing the first lead-nitridosilicate $Pb_2Si_5N_8$ at 920°C. Due to the enormous stability of the $[Si_5N_8]^{4-}$ network, no internal redox reaction between Pb^{2+} and N^{3-} took place. Moreover, $Pb_2Si_5N_8$ (**Figure 131a**) is stable against air, moisture, concentrated nitric acid, and temperatures up to 1000°C (in N_2).

Because of very small crystallites in $Pb_2Si_5N_8$ samples, which are an intrinsic consequence of the ion exchange approach, the crystal structure could not be sufficiently determined by conventional X-ray diffraction. Thus, a tiny crystal ($1\times3\times3$ µm^3, **Figure 131b**) was identified by transmission electron microscopy (TEM) and X-ray spectroscopy and subsequently analysed at beamline ID11 with microfocused X-rays **[4]**, revealing a fascinating structural and bonding situation.

First, as depicted in **Figure 131c**, the distribution of distances for Pb–N significantly deviates from known compounds $M_2Si_5N_8$ (*M*=Sr, Ba). In contrast to the distances *M*–N (*M*=Sr, Ba), which indicate highly ionic interactions between *M* and N, some Pb–N distances are shorter than Sr–N while others are significantly longer than Ba–N distances, which alludes to significant amounts of covalency. Theoretical investigations of the bonding situation clearly confirmed the high degree of covalency not only for Si–N but also for Pb–N interactions **[5]**.

Second, and even more puzzlingly, the distance between the Pb cations (**Figure 132a**) is much too short when compared with other $M_2Si_5N_8$ compounds. This finding, however, is elucidated from density functional theory (DFT) calculations, which reveal that the above finding is not only due to a reduced effective cationic charge but also to a covalent bonding between the formal Pb^{2+}. Formally, a $(Pb^{2+})_2$ resembles the unstable He_2 in terms of electron count but extreme *sp* mixing on Pb^{2+} as a function of highly covalent Pb–N bonds also allows for Pb–Pb covalent bond formation. Finally, first-principles phonon calculations help to clearly identify the Raman signal at 117 cm^{-1} (**Figure 132b**) as the corresponding Pb–Pb stretching vibration, thereby finally corroborating the cationic Pb_2 dumbbells in the first crystallographically characterised lead nitride.

PRINCIPAL PUBLICATION AND AUTHORS

Cationic Pb_2 Dumbbells Stabilized in the Highly Covalent Lead Nitridosilicate $Pb_2Si_5N_8$, P. Bielec (a), R. Nelson (b), R. P. Stoffel (b), L. Eisenburger (a), D. Günther (c), A.-K. Henß (a), J. P. Wright (d), O. Oeckler (c), R. Dronskowski (b) and W. Schnick (a), *Angew. Chem. Int. Ed.* **58**, 1432-1436 (2019); doi: 10.1002/anie.201812457.
(a) Department of Chemistry, Ludwig-Maximilians-University Munich (Germany)
(b) Institute of Inorganic Chemistry, RWTH Aachen University (Germany)
(c) Institute for Mineralogy, Crystallography and Materials Science, Leipzig University (Germany)
(d) ESRF

REFERENCES

[1] M. Zeuner *et al.*, *Angew. Chem. Int. Ed.* **50**, 7754-7775 (2011).
[2] P. Bielec & W. Schnick, *Angew. Chem. Int. Ed.* **56**, 4810-4813 (2017).
[3] P. Bielec *et al.*, *Angew. Chem. Int. Ed.* **57**, 2409-2412 (2018).
[4] F. Fahrnbauer *et al.*, *Angew. Chem. Int. Ed.* **54**, 10020-10023 (2015).
[5] S. Maintz *et al.*, *J. Comput. Chem.* **37**, 1030-1035 (2016).

OPERANDO IMAGING OF A METHANE-REFORMING CATALYST BED

A complex Ni-Pd/CeO_2-ZrO_2/Al_2O_3 solid catalyst was investigated for the first time with 3D X-ray diffraction computed tomography (XRD-CT) under various operating conditions. This first 5D *operando* tomographic diffraction imaging experiment allowed the evolving solid-state chemistry of a catalyst bed to be tracked and rationalised.

Heterogeneous functional materials and devices, such as catalytic solids, batteries and fuel cells, tend to possess complex structures where the 3D spatial distribution of the various components is rarely uniform. Such materials are known to change with time under operating conditions. Therefore, it is highly desirable to study them *in situ* with spatially resolved techniques to gain an insight into the structure-function relationships **[1]**.

Synchrotron X-ray diffraction computed tomography (XRD-CT) can be used to study complex materials systems in 3D and under real process conditions. This is demonstrated by the investigation described here of a complex multi-component Ni-Pd/CeO_2-ZrO_2/Al_2O_3 solid catalyst under different operating conditions. This catalyst belongs to a family of catalysts used for methane reforming reactions to produce CO and H_2, a mixture also known as 'synthesis gas' and used in gas-to-liquid (GTL) industrial plants to produce synthetic fuels.

As shown in **Figure 133**, XRD-CT is able to discriminate between different crystalline phases present in this multi-component sample and the Rietveld analysis of the obtained diffraction data allows the distribution of these phases to be mapped. These results are derived from a high-resolution XRD-CT dataset of a single catalyst particle collected at **ID15A** (1 μm pixel size; 10 ms per point acquisition time; X-ray energy of 50 keV).

These heterogeneities could also be captured at the reactor level with 3D-XRD-CT, as shown

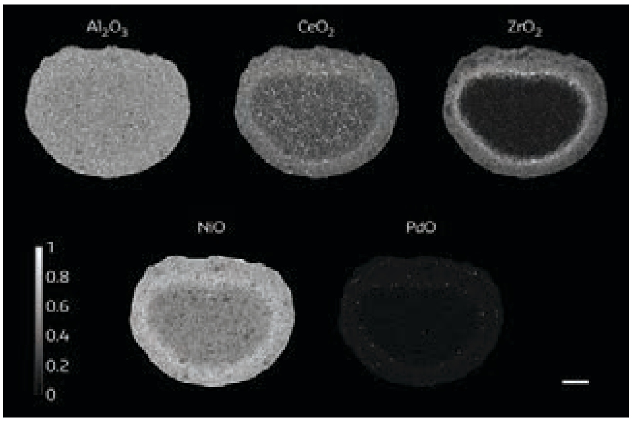

Fig. 133: Phase distribution maps of Al_2O_3, CeO_2, ZrO_2, NiO and PdO. The maps were derived from the Rietveld analysis of the single catalyst particle XRD-CT data. The scale bar corresponds to 0.1 mm.

in **Figure 134**. It should be emphasised that such spatially resolved chemical information cannot be obtained with conventional material characterisation techniques such as X-ray absorption-contrast CT (also known as micro-CT) or bulk XRD. These data were collected at **ID31**, where the behaviour of this catalyst bed was investigated under different operating conditions.

By applying the XRD-CT technique, a non-destructive technique that allows intact reactors to be studied, it was possible to follow the evolving solid-state chemistry in this complex system and relate these changes to the various applied chemical environments. For example, it was shown that the Ni-containing species, the main active catalyst components, can take the form of NiO, $NiAl_2O_4$ or metallic Ni, depending on the operating temperature and gas environment.

These results show that real-time 3D chemical imaging can provide a better understanding of how the catalyst bed behaves under real process conditions and indeed of the complex structure-function relationships. Chemical tomography techniques are set to be further improved with the continuous advancements in synchrotron brightness, detector performance, sample environment (new reactor cells) and data analysis. Such techniques have the potential to provide insight into some of the technical challenges concerning functional materials and device performance in fields such as catalysis, energy storage and transport.

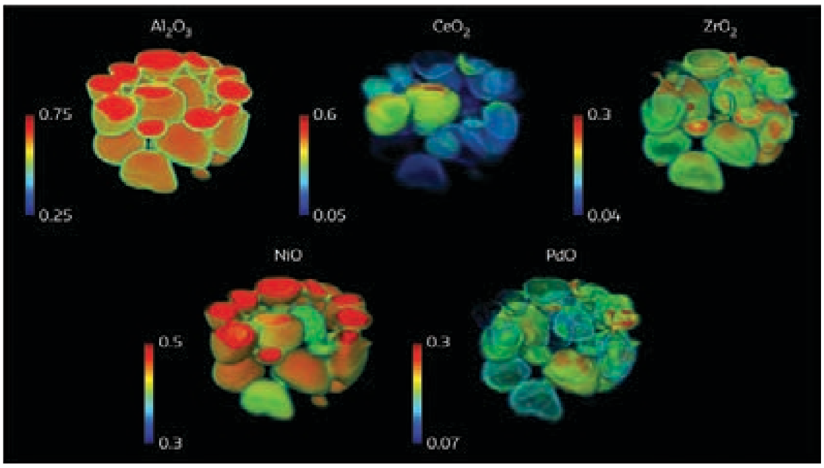

Fig. 134: 3D maps obtained from the Rietveld analysis of the 3D-XRD-CT data collected at room temperature. Volume rendering of the normalised scale factors data volume (phase distribution volumes). The values in the colour bar axes have been chosen to achieve the best possible contrast.

PRINCIPAL PUBLICATION AND AUTHORS

5D tomographic operando diffraction imaging of a catalyst bed,
A. Vamvakeros (a,b,c,d), S. D. Jacques (c), M. Di Michiel (d), D. Matras (b,e), V. Middelkoop (f), I. Z. Ismagilov (g), E. V. Matus (g), V. V. Kuznetsov (g), J. Drnec (d), P. Senecal (a,b) and A. M. Beale (a,b,c),
Nat. Commun. **9**, 4751 (2018);
doi: 10.1038/s41467-018-07046-8.

(a) Department of Chemistry, University College London (UK)
(b) Research Complex at Harwell, Rutherford Appleton Laboratory, Didcot (UK)
(c) Finden, Harwell (UK)
(d) ESRF
(e) School of Materials, University of Manchester (UK)
(f) Flemish Institute for Technological Research, VITO NV, Mol (Belgium)
(g) Boreskov Institute of Catalysis SB RAS, Novosibirsk (Russia)

REFERENCES

[1] A. M. Beale *et al., Coord. Chem. Rev.* **277-278**, 208-223 (2014).

SKULL AND BRAIN DEVELOPMENT OF THE LIVING COELACANTH

The coelacanth *Latimeria* is an iconic and mysterious deep-sea fish closely related to land-dwelling vertebrates the tetrapods. The most unusual thing about this fish is its very tiny brain lying within a hinged braincase. This study illuminates for the first time the development of *Latimeria's* brain and skull.

The coelacanth *Latimeria* has attracted considerable attention ever since a living specimen was captured in 1938. Until then, coelacanths were thought to have been extinct for 70 million years. Coelacanths hold a pivotal position in the vertebrate family tree. They are, together with lungfishes, the only living examples of lobe-finned fishes, and are closely related to tetrapods, the four-legged vertebrates (**Figure 135a**). Therefore, *Latimeria* is critical for our understanding of the origin of tetrapods and the evolution of their closest fish-relatives.

The skull of *Latimeria* is completely split in half by a joint called the 'intracranial joint' (**Figure 135b**). This joint is a very primitive feature that is otherwise found only in many extinct lobe-finned fishes. The rear of the skull

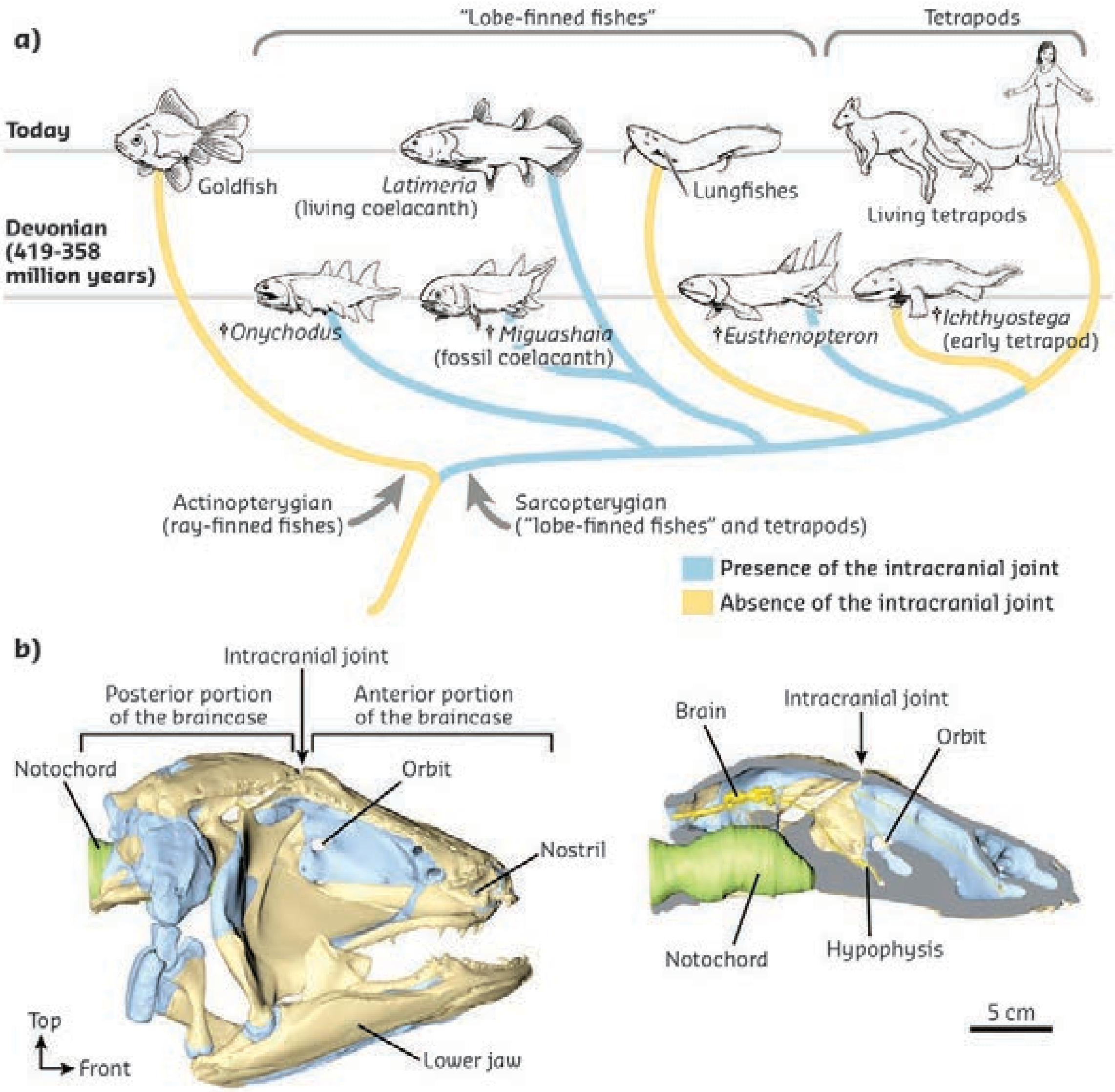

Fig. 135: a) Simplified evolutionary relationships of bony fishes (osteichthyans). **b)** 3D virtual reconstruction of the coelacanth skull in right lateral view. Left: Overall view of the skull. Right: the braincase isolated and virtually cut open along the midline to show the brain (yellow) and the notochord (green). The brain represents about 1% of the volume of the cavity that houses it.

of *Latimeria* and extinct lobe-finned fishes also straddles a surprisingly huge notochord, a tube that spans along the body length in early stages of life and later degenerates in most vertebrates. In contrast with other vertebrates, the brain of *Latimeria* is also extremely small (1%) compared with the cavity that houses it. Although *Latimeria* has been extensively studied for 80 years, most aspects of its development remain virtually unknown. The question of how the skull and brain develop and what it means to vertebrate evolution triggered the study.

Latimeria is ovoviviparous: eggs develop in the oviduct of the female, which then gives birth to live young. Yet, studying the development of this fish was not easy. *Latimeria* cannot be bred in an aquarium, so embryos and fetuses cannot be easily obtained. Moreover, coelacanths cannot be captured in the wild as they are protected. Specimens at different developmental stages were therefore acquired from natural history collections in France (Muséum national d'Histoire naturelle), Germany (Bavarian State Collection of Zoology) and South Africa (South African Institute for Aquatic Biodiversity). These developmental stages are extremely scarce as they came from the rare captures of pregnant females. For a long time, scientists thus could not dissect these precious specimens to study their internal anatomy.

Long-distance phase contrast synchrotron X-ray microtomography (PPC-SRμCT) was performed at beamline **ID19** to digitalise three prenatal stages – including a 5 cm-long fetus, which represents the earliest known developmental stage of *Latimeria*. Very powerful MRI was also carried out at the Brain and Spine Institute in Paris along with conventional X-ray microtomography to image two other specimens. As far as is known, the specimens imaged represent the most complete growth series currently available for this species.

Using the high-resolution scans, it was possible to make detailed 3D models of the skull at each developmental stage (**Figure 136**), demonstrating how the form and the position of different structures of the head change during development. During development, the brain becomes very small with respect to the braincase, and is progressively displaced behind the intracranial joint. The magnitude of the mismatch between the brain and its cavity observed in *Latimeria* is totally unequalled among living vertebrates. The notochord (one of the first structures to form in the embryo) expands considerably to become much bigger than the brain in the adult. This is unique, as the notochord usually degenerates in the early development of most vertebrates. It is thought that the notochord causes the formation of the intracranial joint during the early stages of the development. In addition, the space filled by the notochord likely constrains the size and shape of the brain to some extent. Therefore, it is suggested that the unique development of the notochord has a profound impact on the shaping of the head in coelacanths.

These results illuminate, for the first time, the development of the head of one of our most iconic cousins, and, together with the study of fossil fishes closely related to coelacanths, will contribute to better understanding the evolution of the head.

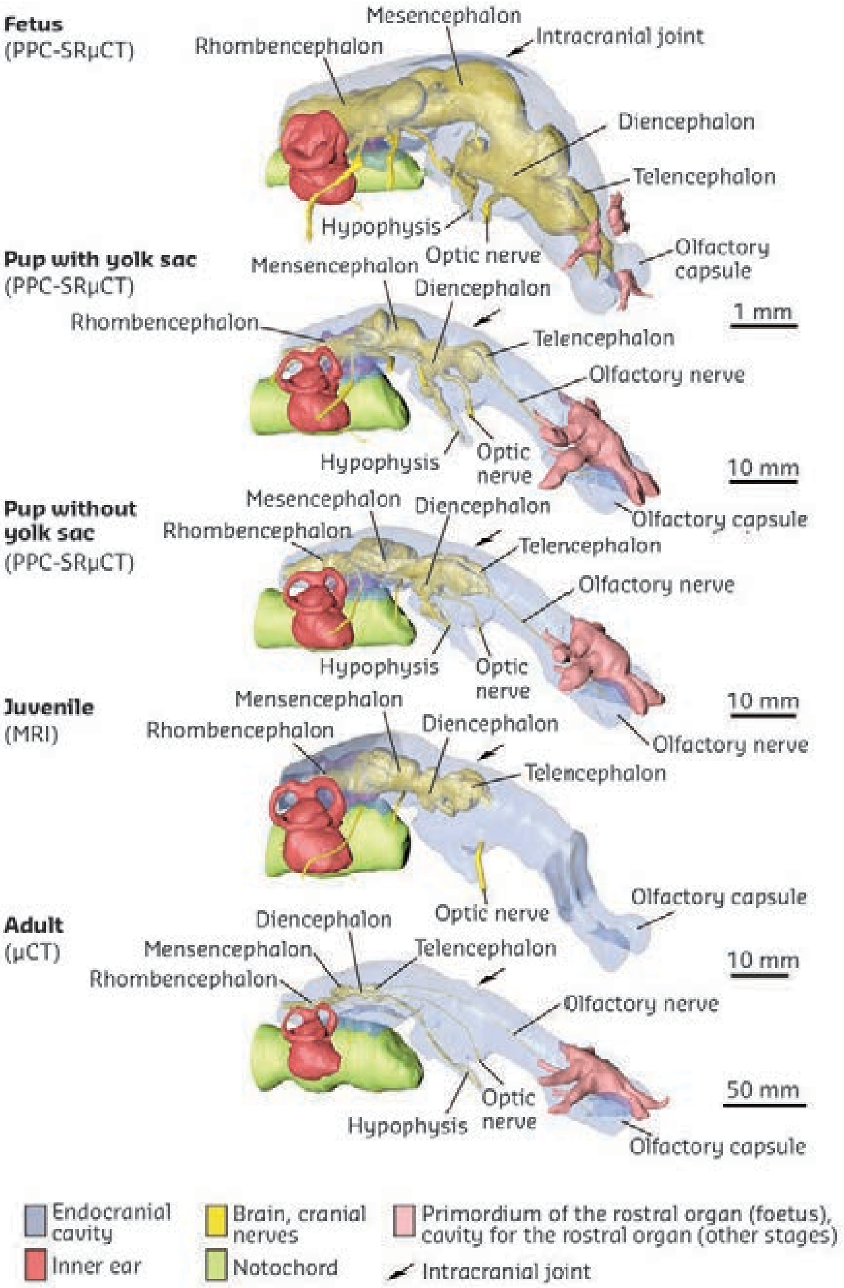

Fig. 136: The brain (yellow) and endocranial cavity (blue) at different developmental stages of *Latimeria*. Note the decrease in the relative size of the brain, and its displacement towards the rear of the braincase during development.

PRINCIPAL PUBLICATION AND AUTHORS

Neurocranial development of the coelacanth and the evolution of the sarcopterygian head, H. Dutel (a,b), M. Galland (c), P. Tafforeau (d), J. A. Long (e), M. J. Fagan (b), P. Janvier (f), A. Herrel (g), M. D. Santin (h), G. Clément (f) and M. Herbin (g), *Nature* **569**, 556-559 (2019); doi: 10.1038/s41586-019-1117-3.
(a) School of Earth Sciences, University of Bristol (UK)
(b) School of Engineering and Computer Science, Medical and Biological Engineering Research Group, University of Hull (UK)
(c) UMR 7206 (MNHN-CNRS-Université Paris Diderot), Éco-Anthropologie et Ethnobiologie, Département Homme et Environnement, Muséum National d'Histoire Naturelle, Paris (France)
(d) ESRF
(e) College of Science and Engineering, Flinders University, Adelaide (Australia)
(f) UMR 7207 (MNHN-CNRS-Sorbonne Université), CR2P Centre de Recherche en Paléontologie-Paris, Département Origines et Évolution, Muséum National d'Histoire Naturelle, Paris (France)
(g) UMR 7179 (MNHN-CNRS) MECADEV, Département Adaptations du Vivant, Muséum National d'Histoire Naturelle, Paris (France)
(h) Inserm U1127, CNRS UMR 7225, Centre for NeuroImaging Research, ICM (Brain & Spine Institute), Sorbonne University, Paris (France)

NEW CRYSTALLINE STRUCTURE OF CALCIUM CARBONATE

For years, only three crystalline polymorphs of calcium carbonate, as well as two hydrated crystal phases, were known to exist at ambient conditions. While investigating the crystallisation of amorphous calcium carbonate, a new hydrated crystalline phase was discovered. It may have important implications in biomineralisation, geology, and even the cement industry.

Calcium carbonate, $CaCO_3$, is one of the most abundant minerals on Earth, comprising nearly 4% of the Earth's crust. It is produced mainly by the sedimentation of skeletal remains of marine organisms accumulated over millions of years in the form of chalk, limestone, or marble (in metamorphic rocks). Calcium carbonate minerals are involved in the global carbon cycle and have been intensively investigated because of their importance for paleoclimate reconstructions, ocean acidification, biomineralisation and some industrial processes utilising the hydration of $CaCO_3$. For more than a century, only three anhydrous crystalline polymorphs of $CaCO_3$ have been documented – rhombohedral calcite, orthorhombic aragonite and hexagonal vaterite – as well as two hydrated crystalline phases, hexagonal monohydrocalcite (MHC) ($CaCO_3$•$1H_2O$) and monoclinic ikaite ($CaCO_3$•$6H_2O$). Hydrated amorphous calcium carbonate (ACC) also exists, and plays a vital role in controlling the formation of $CaCO_3$-biominerals **[1]**.

When investigating the crystallisation pathways of ACC, a hitherto unknown hydrated crystalline calcium carbonate compound, $CaCO_3$•½H_2O, *i.e.*, calcium carbonate hemihydrate (CCHH), was found. Its water content was derived from TGA measurements. CCHH develops from ACC in solution in the presence of Mg^{2+} ions with a Mg/Ca molar ratio of ~5/1, but Mg is not incorporated into the lattice of CCHH in measurable amounts. In a moist environment, CCHH slowly transforms into MHC, but is stable being stored in desiccator. CCHH appears in solution as needle-like crystals with a diameter of ~200 nm and a length of few microns (**Figure 137a**), which in turn are composed of well-aligned nanocrystals with a diameter of ~30 nm (**Figure 137b**). The frequencies of the infrared (IR) and Raman spectral lines of CCHH (**Figures 137c** and **137d**) differ substantially from those known for other calcium carbonate phases, yet the observed frequency bands in CCHH reflect normal vibrational modes of carbonate ions.

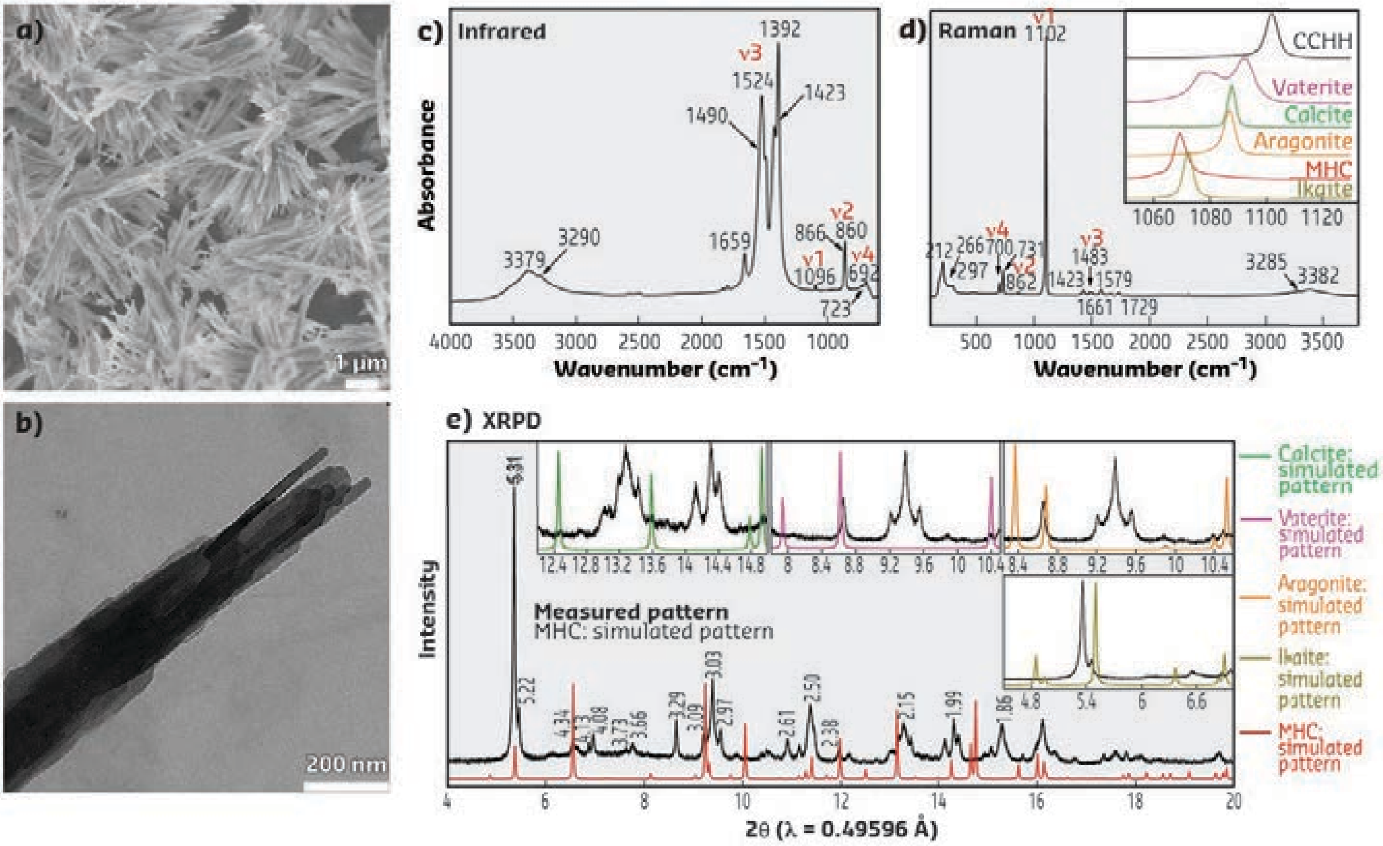

Fig. 137: Characterisation of CCHH by **(a)** SEM, **(b)** TEM, **(c)** IR and **(d)** Raman spectroscopies, and **(e)** synchrotron HRXRPD. The insets in **(d)** and **(e)** show, respectively, a comparison of Raman spectra and HRXRD patterns of CCHH with those of other calcium carbonate phases.

For structural analysis, high-resolution X-ray powder diffraction (HRXRPD) measurements were carried out at beamline ID22. The collected diffraction pattern (**Figure 137e**) did not match any of the known calcium carbonate phases. Similar conclusions were drawn when analysing X-ray absorption near-edge structure (XANES) spectra, taken at the O K-edge and Ca K- and L-edges.

The structural determination of CCHH was perhaps the most difficult task because of complications related to the presence of structural water. CCHH crystals were too small for single-crystal X-ray diffraction and not stable under the electron beam in transmission electron microscopy (TEM). Therefore, automated electron diffraction tomography (ADT) was used to solve the CCHH structure **[2]**, yielding a monoclinic unit cell with space group $P2_1/c$. The structure solution, obtained using the direct method approach, provided the atomic positions of calcium and carbonate ions, as well as the positions of the additional oxygen from water molecules (see **Figure 138**, in which the structures of CCHH and MHC are compared). The simulated HRXRPD pattern fitted the measured synchrotron diffraction pattern well, offering the refined lattice parameters: a = 9.3320 Å, b = 10.4368 Å, c = 6.1624 Å, α = 90°, β = 90.5097°, γ = 90°.

The role of CCHH in nature is not clear yet, but it may likely be involved as an intermediate phase in some biomineralisation processes or in cements. At this stage, the relevant textbooks must include CCHH as a novel crystalline form of calcium carbonate.

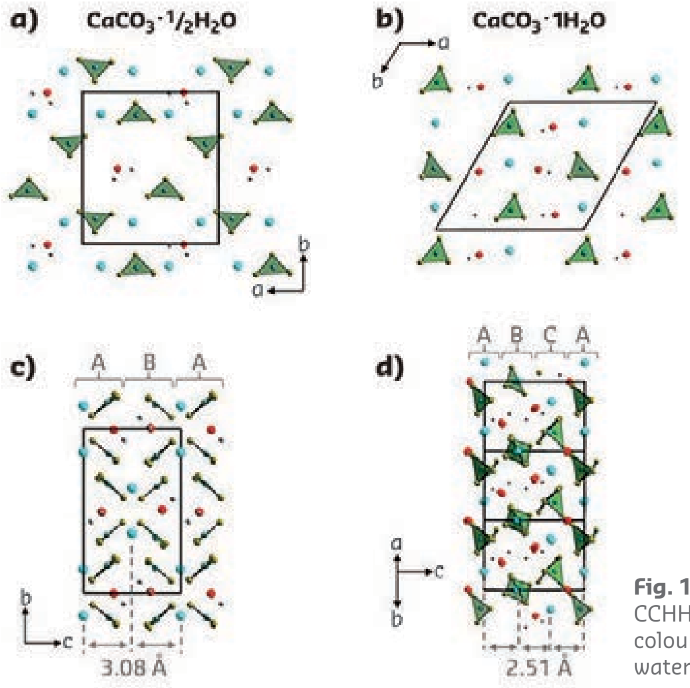

Fig. 138: Comparison of layered motifs in the crystal structures of CCHH **(a)** and **(c)** and MHC **(b)** and **(d)**. Different types of atoms are coloured as follows: Ca - blue; carbonate groups - green; oxygen from water - red; and hydrogen - grey.

PRINCIPAL PUBLICATION AND AUTHORS

A hydrated crystalline calcium carbonate phase: Calcium carbonate hemihydrate, Z. Zou (a), W. Habraken (a), G. Matveeva (b), A. Jensen (a), L. Bertinetti (a), M. Hood (a), C. Sun (c), P. Gilbert (c), I. Polishchuk (d), B. Pokroy (d), J. Mahamid (e,f), Y. Politi (a), S. Weiner (g), P. Werner (h), S. Bette (i), R. Dinnebier (i), U. Kolb (b,j), E. Zolotoyabko (d) and P. Fratzl (a), *Science* **363**, 396-400 (2019); doi: 10.1126/science.aav0210.

(a) Max Planck Institute of Colloids and Interfaces, Potsdam (Germany)
(b) Johannes Gutenberg-Universität, Mainz (Germany)
(c) University of Wisconsin-Madison (USA)
(d) Technion-Israel Institute of Technology, Haifa (Israel)
(e) Max Planck Institute of Biochemistry, Martinsried (Germany)
(f) European Molecular Biology Laboratory, Heidelberg (Germany)
(g) Weizmann Institute of Science, Rehovot (Israel)
(h) Max Planck Institute of Microstructure Physics, Halle (Germany)
(i) Max Planck Institute for Solid State Research, Stuttgart (Germany)
(j) TU Darmstadt (Germany)

REFERENCES

[1] Y. Politi *et al.*, *Science* **306**, 1161-1164 (2004).
[2] U. Kolb *et al.*, *Cryst. Res. Technol.* **46**, 542-554 (2011).

TOWARDS A PERFECT CHEMICAL REACTOR

A perfect chemical reactor would provide separated, pure products and would overcome the chemical equilibrium limitations of reversible reactions. Research involving beamline ID22 shows how such a reactor could be made.

Hydrogen production is an important large-scale chemical process that could underpin any future low-carbon energy economy. It is therefore important to develop new, more efficient approaches. Key to hydrogen production is the water-gas shift (WGS) reaction:

$$H_2O + CO \leftrightharpoons H_2 + CO_2$$

In conventional hydrogen production processes, the WGS reaction is equilibrium-limited and requires two reactors operating at progressively lower temperatures to achieve high conversion

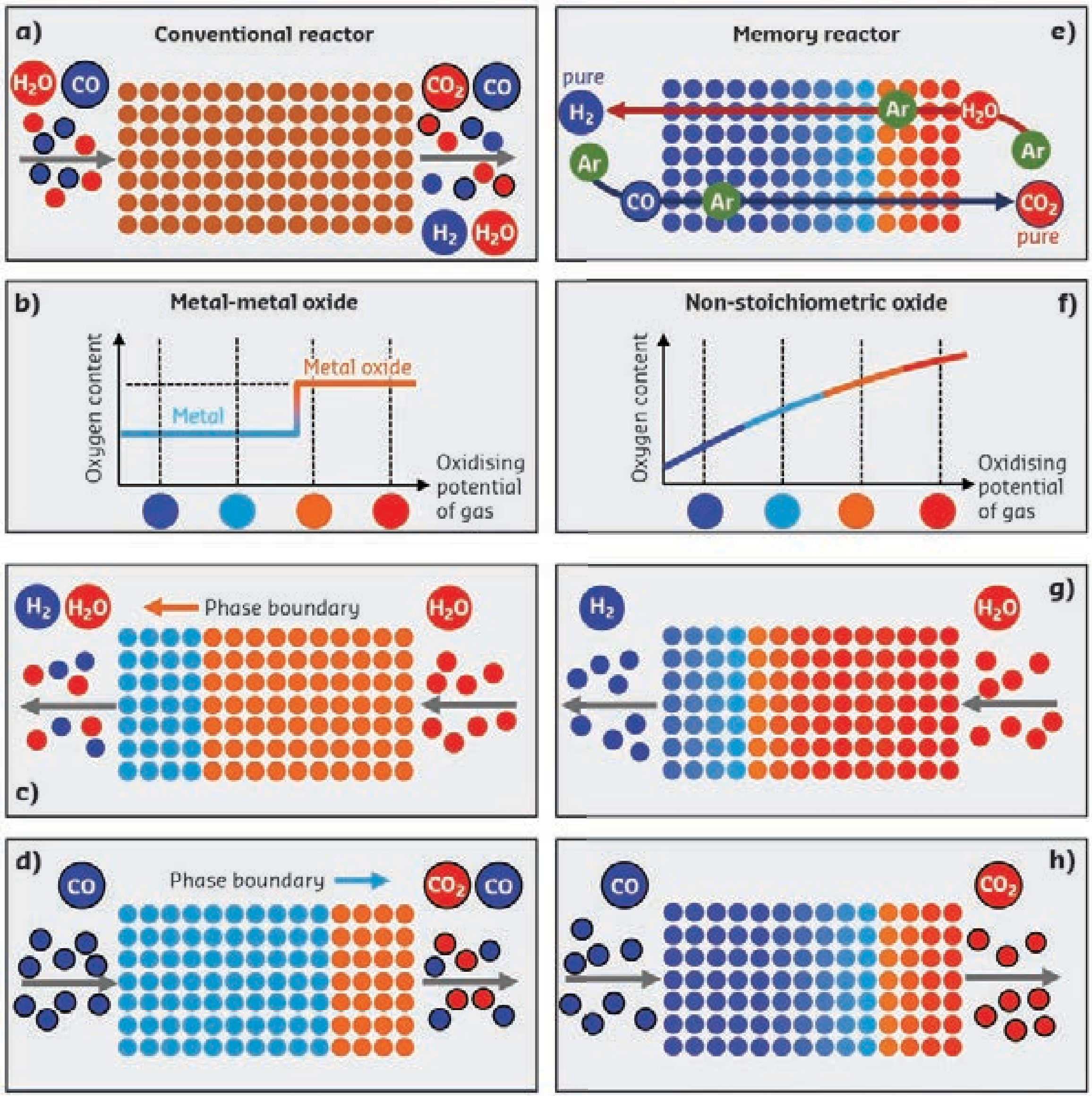

Fig. 139: Thermodynamic reversibility in a WGS reactor. Colour coding: red to blue for oxidising to reducing. **a)** Conventional WGS reactor producing a mixture of reactants and products. **b)** Equilibrium relationship for a metal-metal oxide showing solid-phase oxygen content versus oxygen chemical potential of the gas phase. **c)** The use of metal-metal oxide OCM for H_2 production in a chemical looping cycle where water is fed over the metal. The phase transition is not sufficiently reducing to produce a high mole fraction of H_2. **d)** Reduction of the metal oxide cannot produce a high mole fraction of CO_2. **e)** Mode of operation of the memory reactor. **f)** Equilibrium relationship for a non-stoichiometric oxide showing solid-phase oxygen content versus gas phase oxygen chemical potential. **g)** A H_2O feed is converted almost entirely to H_2 as H_2 exits over the reduced end of the bed before switching the direction of flow **(h)** and converting CO almost entirely to CO_2 as the CO_2 exits over the oxidised end of the bed.

while H_2 and CO_2 must then be separated (**Figure 139a**). This study aims to demonstrate a perfect chemical reactor that can overcome equilibrium limitations and produce pure, separated hydrogen using an approach call chemical looping **[1]**.

To perform the WGS reaction in chemical looping (CL) mode, H_2O (high oxidising potential) is passed over a solid-phase oxygen carrier material (OCM) that accepts oxygen, splits H_2O and produces H_2, as illustrated in **Figure 139c**. In a second step, CO (low oxidising potential) is passed over the OCM, removing the oxygen and simultaneously producing CO_2 (**Figure 139d**). The thermodynamic advantage of this is that the reactants H_2O and CO are not mixed. However, in practice this advantage is not realised because conventional OCMs such as metal-metal oxide systems function by donating and receiving oxygen at one fixed oxygen chemical potential (**Figure 139b**). **Figures 139c** and **139d** show that a conventional metal-metal oxide OCM cannot convert H_2O fully to H_2 or CO to CO_2.

The idea presented here involves using an oxide of variable non-stoichiometry able to donate and receive oxygen over a range of conditions. The oxide used was $La_{0.6}Sr_{0.4}FeO_{3-\delta}$, a perovskite oxide. Because this is non-stoichiometric (see **Figure 139f**), it can exist in many different states of δ and thus better accommodate both half cycles.

If this reactor operates as designed, it should, on cycling, develop an oxidised low-δ end to the reactor (the H_2O-feed end) and a reduced high-δ end to the reactor (the CO feed end). There should be a range of δ values in the bed between these extremes. Beamline **ID22** was used to probe experimentally δ in a working reactor (working at 817°C for the chemistry to function and because the equilibrium constant of the WGS reaction is unity at this temperature). When non-stoichiometric oxides lose oxygen they expand slightly, therefore, an indication of the local value for δ can be obtained from the lattice parameter dependence using X-ray diffraction (XRD). The advantage of using a synchrotron is rapidity: data can be collected much faster than

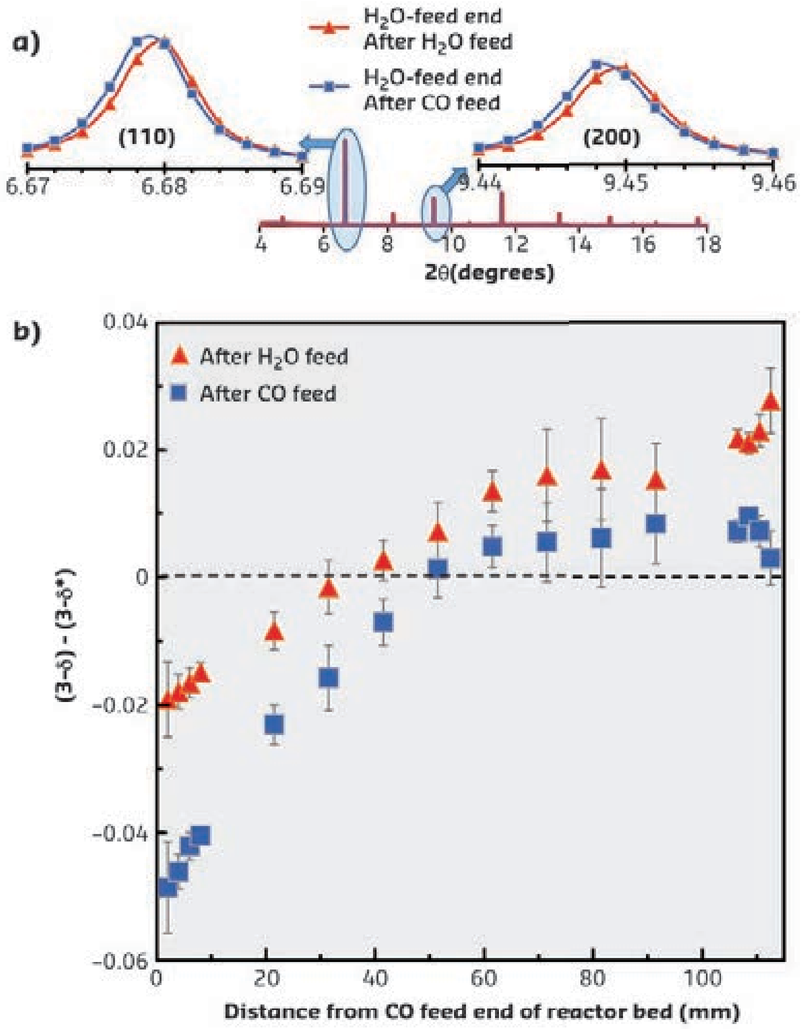

the time constants that govern the reactor (the time between switching from one feed to the other). Very good angular resolution permitted small changes in lattice parameters to be measured, and high-energy X-rays were able to pass through a fully functioning model reactor. **Figure 140** shows an example of the results, demonstrating that oxidising and reducing ends to the bed have been developed.

In summary, the reactor gives much higher conversions than predicted by equilibrium, is 100 times more effective than a conventional approach (using a suitable measure of reactor performance) and produces pure H_2 at one end and pure CO_2 at the other, eliminating the need for complex product separation.

Fig. 140: a) *Operando* XRD scans from the H_2O-feed end of the reactor bed after the CO feed and the H_2O feed showing the lower 2θ peak positions and thus larger cubic lattice parameter after CO feed compared to H_2O feed. **b)** Local oxygen content of the non-stoichiometric solid ($La_{0.6}Sr_{0.4}FeO_{3-\delta}$), 3-δ, relative to the local oxygen content of the reactor bed in the absence of chemical reaction, 3-δ*, versus reactor position immediately after oxidation and reduction.

PRINCIPAL PUBLICATION AND AUTHORS

Overcoming chemical equilibrium limitations using a thermodynamically reversible chemical reactor, I. S. Metcalfe (a), B. Ray (a), C. Dejoie (b), W. Hu (a), C. de Leeuwe (a), C. Dueso (a), F. R. García-García (c), C.-M. Mak (a), E. I. Papaioannou (a), C.R. Thompson (a) and J. S. Evans (d), *Nat. Chem.* **11**, 638-643 (2019); doi: 10.1038/s41557-019-0273-2.

(a) School of Engineering, Newcastle University (UK)
(b) ESRF
(c) School of Engineering, University of Edinburgh (UK)
(d) Department of Chemistry, Durham University (UK)

REFERENCES

[1] A. Thursfield *et al.*, *Energy Environ. Sci.* **5**, 7421-7459 (2012).

LOCAL STRUCTURAL INSTABILITIES IN MAGNETITE INDUCED BY MAGNETISM

This work shows that local structural distortions in the original magnetic mineral magnetite emerge below the magnetic ordering transition at $T_C \approx 850$ K. Fluctuations in Fe–Fe bonding arising from magnetic order are thus identified as the primary electronic instability and are hence the origin of the famous Verwey transition, where long-range-order electronic ordering occurs at $T_V \approx 125$ K.

The nature of the Verwey transition in the spinel magnetite (Fe_3O_4) has been an outstanding problem since it was reported in 1939 **[1]**. The complex superstructure formed below T_V was originally attributed to Fe^{2+}/Fe^{3+} charge ordering but a full determination in 2012 revealed a more complex electronic order of three-atom trimeron groups **[2]**. Trimerons result from coupled Fe^{2+}/Fe^{3+} charge ordering, Fe^{2+} orbital ordering, and weak Fe–Fe bonding effects driven by ferromagnetism within three-Fe atom units, as shown in **Figure 141**.

A variety of measurements such as diffuse X-ray scattering **[3]** have shown that short-range structural correlations persist above the Verwey transition. The present study has followed the thermal evolution of local structure by analysing the interatomic pair distribution function (PDF) derived from total X-ray scattering data, from below the Verwey transition to above the Curie (magnetic ordering) temperature of magnetite. Diffraction data were collected from a polycrystalline sample of highly pure magnetite, with preliminary experiments performed on beamline **ID15B** and full data collected at **ID11**.

The monoclinic superstructure of magnetite below T_V is very complex so the atomic displacements have been modulated by a single 'Verwey shift' parameter f_V to describe the local structure in fits to the PDFs. f_V quantifies an averaged local structural distortion due to electronic fluctuations such that $f_V = 0$ corresponds to the cubic spinel structure without any local fluctuations, and $f_V = 1$ describes the full magnitude of distortions in the monoclinic superstructure. A 'box car' fitting to the PDF at each temperature was performed in three regions corresponding approximately to distances from atoms to their neighbours in the First Unit Cell (distances $r < 9.36$ Å), the Second Unit Cell ($r = 9.30$-16.85 Å) and the Third Unit Cell ($r = 16.80$-24.60 Å) ranges. These correspond to short-, medium-, and long-range orders of the structural fluctuations in magnetite.

The temperature evolutions of the Verwey shift parameter are shown in **Figure 142**. The variations of f_V when fitted to the Second and Third Unit Cell separations are as expected for the first-order Verwey transition, with a fall towards $f_V = 0$ on warming through T_V. However, short-range structural correlations between atoms in the First Unit Cell range show a strikingly different behaviour. f_V falls a little on warming though the Verwey transition but persists to higher temperatures and decreases to zero close to the Curie transition at $T_C \approx 850$ K, with a similar variation to the bulk magnetisation reported for a similar sample **[4]**.

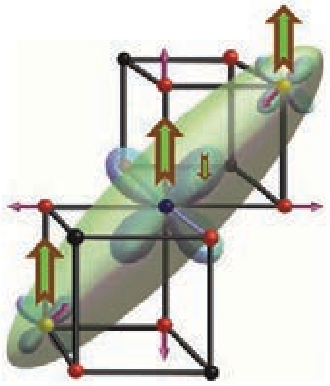

Fig. 141: A trimeron unit spanning Fe^{3+}–Fe^{2+}–Fe^{3+} sites with parallel $S = 5/2$ spins (large brown–green arrows). Charge and orbital order localises the additional, antiparallel spin, electron in one of the t_{2g} orbitals at the central Fe^{2+} site, but weak Fe–Fe bonding interactions spread this onto the two neighbours (green ellipsoid), which distorts local structure as indicated by the purple arrows.

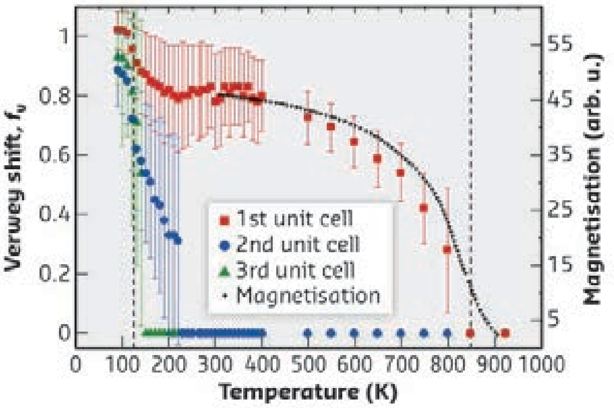

Fig. 142: Thermal variations of the Verwey shift f_V fitted to different interatomic distance ranges. A substantial local distortion in the First Unit Cell range persists up to T_C and scales with reported magnetisation data **[4]**.

This discovery demonstrates that the structural fluctuations responsible for the Verwey transition in magnetite emerge directly with long-range magnetic order below the Curie transition. The weak bonding interactions that shorten Fe–Fe distances in the trimerons require ferromagnetic alignment of the three core $S = 5/2$ spins (**Figure 141**), hence the rapid emergence of structural fluctuations in proportion to magnetisation on cooling below T_C shows that the Fe–Fe bonding interactions are the primary driver of the local distortions. The ratio of energy scales for formation (T_C) and long-range order (T_V) of the electronic distortions, $T_C/T_V \approx 7$ indicates that that the electronic order in magnetite is strongly frustrated.

PRINCIPAL PUBLICATION AND AUTHORS

Co-emergence of magnetic order and structural fluctuations in magnetite, G. Perversi (a), E. Pachoud (a), J. Cumby (a), J. M. Hudspeth (b), J. P. Wright (b), S. A. Kimber (c) and J. P. Attfield (a), *Nat. Commun.* **10**, 2857 (2019); doi: 10.1038/s41467-019-10949-9.

(a) Centre for Science at Extreme Conditions and School of Chemistry, Edinburgh (UK)
(b) ESRF (France)
(c) ICB-Laboratoire Interdisciplinaire Carnot de Bourgogne, Dijon (France)

REFERENCES

[1] E. J. Verwey, *Nature* **144**, 327-328 (1939).
[2] M. S. Senn *et al., Nature* **481**, 173-176 (2012).
[3] A. Bosak *et al., Phys. Rev. X* **4**, 011040 (2014).
[4] V. P. Ponomar *et al., 2017 IEEE 7th International Conference Nanomaterials: Application & Properties (NAP)*, Odessa, 02MFPM03 (2017).

SPATIALLY RESOLVING LITHIATION IN LITHIUM-ION COMPOSITE ELECTRODES

Non-uniform activity in lithium-ion battery electrodes is one of the primary mechanisms that limit electrode performance and lead to degradation during operation. High-resolution, high-speed X-ray diffraction computed tomography (XRD-CT) was used to map the distribution of performance across a next-generation electrode, providing new insight to guide battery design.

Lithium-ion batteries are a critical technology in our society, providing an energy source for applications spanning portable electronics, satellites, and electric vehicles, where the demand for increased energy density is tremendous. Silicon (Si) is a promising alternative negative electrode material for high energy density cells **[1]**, but suffers severe degradation when utilised on its own. Composite electrodes of graphite mixed with Si have been shown to increase energy density while also achieving long cycle lives **[2]**. Si and graphite have different electrochemical properties and respond differently to an applied potential and current. This can lead to imbalances in the state of charge within the electrode where, for example, one material lithiates faster than, and deviates from the electrochemical potential of, the other. Charge imbalance during operation can lead to preferential degradation of one phase. When the cell stops operating, the imbalance of electrochemical potential between the materials can continue to equilibrate for some time.

To understand the dynamic interaction between the two materials during operation, and reconcile the heterogeneous charge distribution spatially throughout the electrode, a fast *operando* method that is sensitive to the crystallographic changes within the electrode materials is needed. In this work, high-energy XRD-CT in concert with high-speed XRD were used at beamline **ID15A** to map the spatial heterogeneities in state of charge within the electrode of a custom cell design (**Figure 143a**), and measure the extent of charge balancing that occurred when operation of the cell was stopped. The cell was imaged under XRD-CT *in situ*, capturing the spatial heterogeneities before and after delithiation of the electrode (**Figure 144**), while *operando* high-speed (100 Hz) XRD recorded the charge-balancing kinetics between the Si and graphite phases following the transition from operation to open circuit (**Figures 143b-c**).

During delithiation, substantial charge balancing occurred when the cell transitioned from operation to open circuit. Depending on the state of charge, the graphite phase would either lithiate or further delithiate during the open circuit relaxation period, indicating

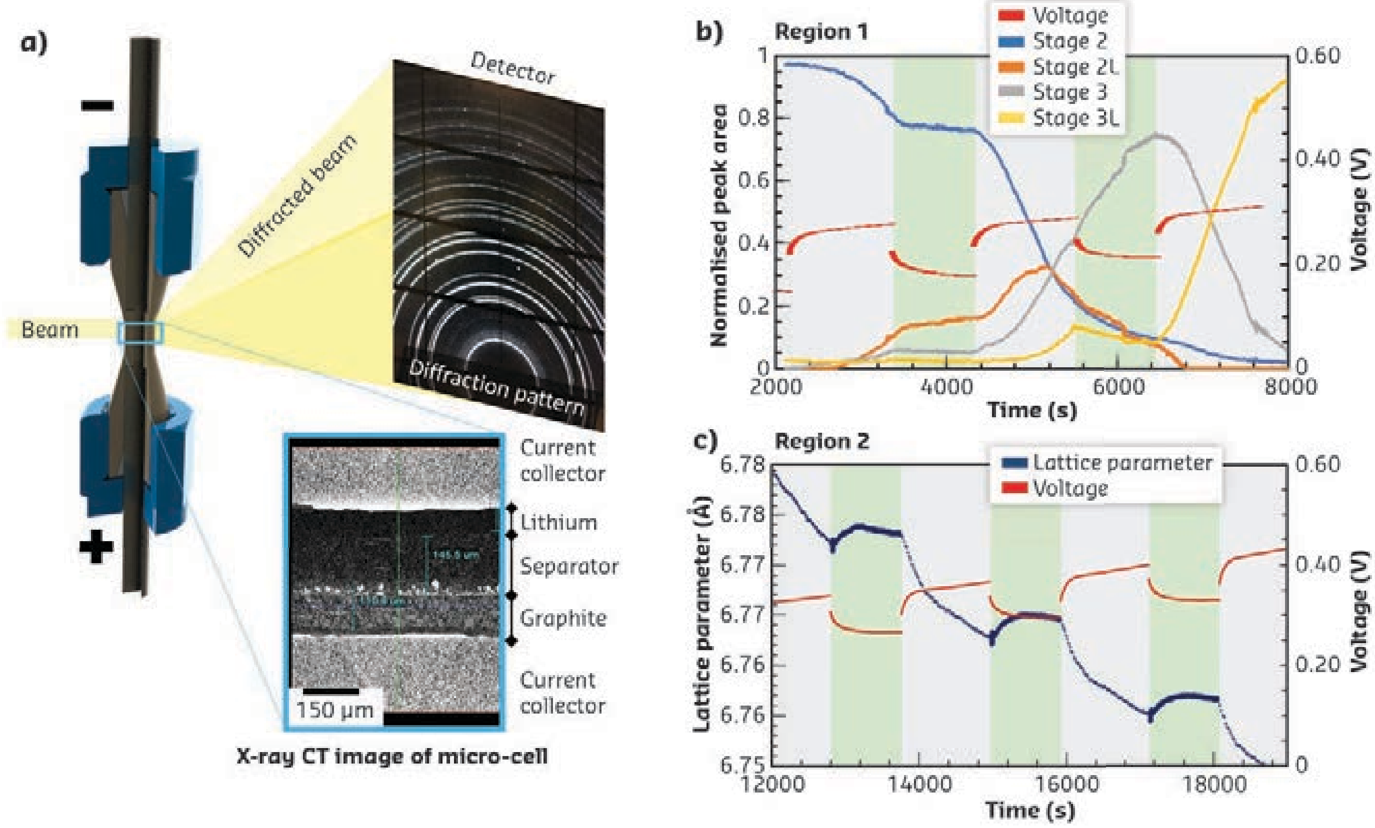

Fig. 143: a) Cross-sectioned illustration of the microcell showing an example of a diffraction profile on the detector and an X-ray CT slice of the internal cell. **b-c)** Examples of times when operation of the cell was stopped, and charge-balancing activity continued. The green bars highlight periods when operation was stopped.

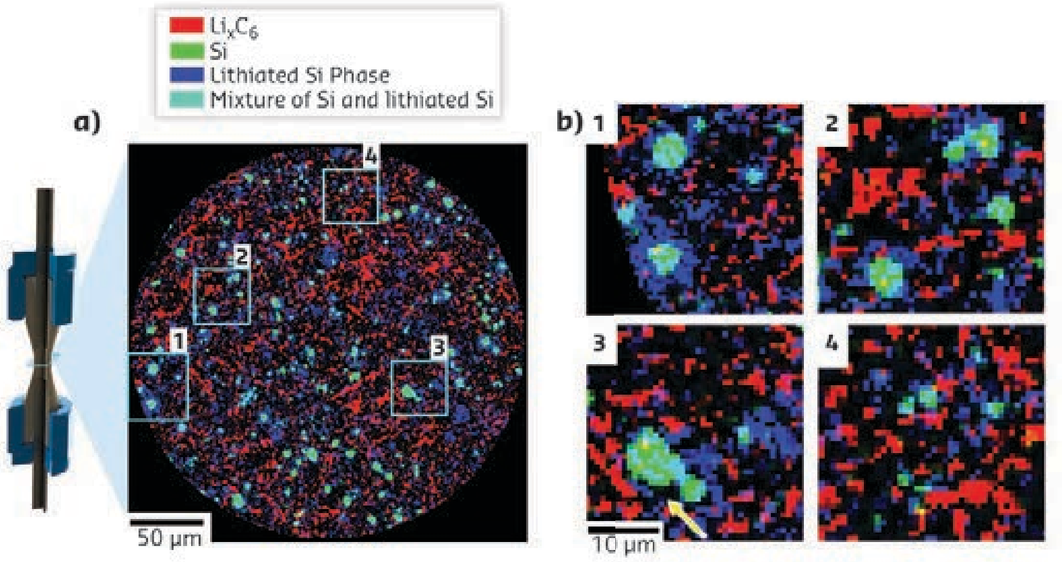

Fig. 144: a) XRD-CT slice taken at the beginning of the charge step showing a phase-distribution map of LiC$_{12}$ (red), crystalline Si (green), and lithium silicides Li$_x$Si (blue). According to additive colour mixing, the colour teal represents a mixture of green (Si) and blue (lithiated Si). **b)** Magnified regions of interest showing large particles of Li$_x$Si phase with crystalline Si cores (1–3) and smaller Li$_x$Si particles (4) interspersed in the graphite matrix. The yellow arrow highlights what looks to be evidence of delamination from the crystalline Si core.

that potential difference between the Si and graphite phase can switch from positive to negative depending on the operating conditions and state of charge. The existence of such charge balancing highlights the importance of allowing relaxation periods for composite electrodes to avoid overcharge of one phase and potentially accelerating degradation. Using XRD-CT to explore the spatial, crystallographic heterogeneities before and after discharge, the different phases of lithiated graphite, lithiated Si and crystalline (pure) Si could be identified and investigated in isolation. It was found that most Si particles under 5 μm in diameter underwent lithiation, whereas larger particles showed a distinct core-shell structure, where the shell was lithiated but the core was not. The presence of pure Si cores showed that there was a severe underutilisation of the cell's capacity.

This demonstration of *in-situ* quantification of intra- and inter-particle crystallographic heterogeneities as well as high-speed *operando* quantification of phase changes opens a plethora of opportunities for furthering understanding of phenomena that lead to limitations and degradation of Li-ion cell performance. Moreover, this demonstrates XRD-CT as a unique tool in the arsenal of battery materials characterisation, providing complementary morphological and crystallographic information and new insight to guide material synthesis, electrode fabrication and battery management system design.

PRINCIPAL PUBLICATION AND AUTHORS

Spatially Resolving Lithiation in Silicon–Graphite Composite Electrodes via in Situ High-Energy X-ray Diffraction Computed Tomography, D. P. Finegan (a), A. Vamvakeros (b,c), L. Cao (a), C. Tan (d,e), T. M. Heenan (d,e), S. R. Daemi (d), S. D. Jacques (c), A. M. Beale (c,f,g), M. Di Michiel (b), K. Smith (a), D. J. Brett (d,e), P. R. Shearing (d,e) and C. Ban (a), *Nano Lett.* **19**, 3811-3820 (2019); doi: 10.1021/acs.nanolett.9b00955.

(a) National Renewable Energy Laboratory, Colorado (USA)
(b) ESRF
(c) Finden Limited, Abingdon (UK)
(d) Electrochemical Innovation Laboratory, Department of Chemical Engineering, University College London (UK)
(e) The Faraday Institution, Quad One, Harwell Science and Innovation Campus, Didcot (UK)
(f) Department of Chemistry, University College London (UK)
(g) Research Complex at Harwell, Harwell Science and Innovation Campus, Didcot (UK)

REFERENCES

[1] X. Su *et al., Adv. Energy Mater.* **4**, 1300882 (2014).
[2] M. Wetjen *et al., J. Electrochem. Soc.* **164**, A2840-A2852 (2017).

THE PATH TO RUPTURE IN ROCKS

In the brittle portion of Earth's crust, rocks are continuously deformed and driven to unstable failure. During the evolution of rock toward catastrophic failure, microfractures nucleate, grow and interact. Laboratory experiments using time-lapse X-ray microtomography enable the dynamics of these processes to be imaged, quantitatively characterised and better understood.

The brittle deformation and failure of rocks, strongly influenced by heterogeneities, controls natural hazards such as rock falls, landslides, earthquakes and volcanic eruptions, and plays an important role in many geotechnical applications. Therefore, it is critical to improve the understanding of brittle deformation prior to macroscopic instability. Destructive methods such the combination of cross-sectioning and microscopy allow only a single snapshot to be obtained. The other commonly used experimental approach, inversion of acoustic emission data, does not directly measure strain, does not detect stable micro processes and has additional difficulties, particularly for heterogeneous and anisotropic materials. To accurately track the microstructural changes in rock samples as they are driven towards failure, a novel experimental technique that combines X-ray microtomography, a triaxial deformation apparatus, Hades **[1]**, and digital volume correlation analysis was developed. This enabled researchers to document the evolution of microfracture opening, closing and shearing, with unprecedented accuracy and resolution.

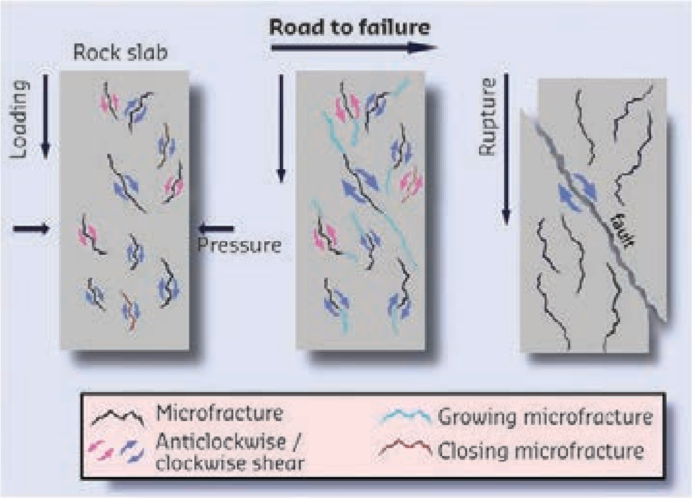

Fig. 145: When loaded under compression, rocks in Earth's crust deform through the formation of microfractures whose sizes and number densities increase as failure is approached. Final catastrophic rupture occurs by a combination of volumetric effects, controlled by growing (dilation) and closing (compaction) microfractures, and clockwise and anticlockwise slip along microfractures.

In the work reported here, the axial stress acting on a cylindrical specimen was increased in small steps with a constant confining pressure and tomograms were acquired after each step. The study demonstrated how the coupling between microfracture growth, opening, coalescence and closing, as well as clockwise and anti-clockwise shear displacement along microfractures, leads to macroscopic brittle failure (**Figure 145**). The data analysis showed that, at the onset of failure, damage was almost entirely connected in three-dimensions, with most of the fracture porosity contained in a single fracture network that spanned the entire volume and evolved into a geometrically complex three-dimensional fault zone.

Analysis of *in-situ* dynamic X-ray tomographic data taken at beamline **ID19** revealed the spatial organisation of microfractures and damage increments characterising the path to catastrophic failure. Failure occurred by the progressive development of damage in the rock volume. The evolution of microfractures was accompanied by the emergence of scaling relationships between microstructural parameters, including total damage volume, incremental damage volume, the largest connected microfracture, and the applied differential stress (the difference between the axial stress and the confining pressure) **[2]**.

As the differential stress increased and failure was approached, the volume of the largest connected microfracture and the incremental damage diverged as powers of the difference between the differential stress at failure and instantaneous differential stress. These characteristic features of brittle failure in crystalline rock under compression are consistent with theoretical

Fig. 146: Stress-strain curve of a crystalline rock sample and digital volume correlation calculations of the locations of large changes in compaction **(a)**, dilation **(b)**, left-lateral shear strain **(c)** and right-lateral shear strain **(d)** when the differential was increased from 47 to 125 MPa (top row) and from 204 to 205 MPa (bottom row).

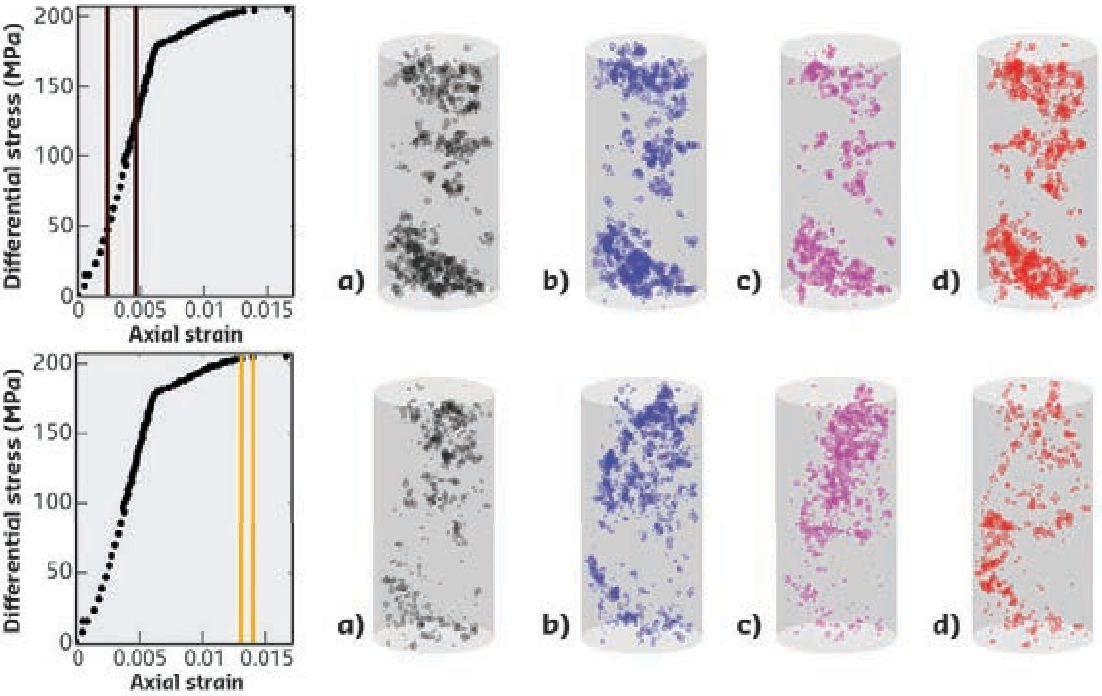

models that consider failure to be like a continuous phase transition, with stress at failure acting as a critical point. Also, the distribution of microfracture volume increments exhibited power-law statistics similar to the Gutenberg-Richter law for earthquakes. Consequently, it is concluded that the strain dissipation in the volume around main faults may participate actively in the preparation process leading to earthquakes.

Figure 146 shows where the incremental changes in compaction, dilation, left-lateral shear strain and right-lateral shear are largest (interpreted as locations of microfracture closing, opening/growth, left-lateral shear displacement and right-lateral shear displacement) for two different differential stress increments. The results indicate that these four modes of microfracture evolution are strongly correlated in both space and time. These correlations, which are yet to be analysed quantitatively, are attributed to coupling between these processes by elasticity and governing failure rheology. The microfractures weaken the rock and damaged zones are more susceptible to additional damage.

PRINCIPAL PUBLICATION AND AUTHORS

Volumetric and shear processes in crystalline rock approaching faulting, F. Renard (a,b), J. McBeck (a), N. Kandula (a), B. Cordonnier (a,c), P. Meakin (d) and Y. Ben Zion (e), *PNAS* **116**, 16234-16239 (2019); doi: 10.1073/pnas.1902994116.
(a) The Njord Centre, University of Oslo (Norway)
(b) ISTerre, University Grenoble Alpes & CNRS, Grenoble (France)
(c) ESRF
(d) Temple University, Philadelphia (USA)
(e) University of Southern California, Los Angeles (USA)

REFERENCES

[1] F. Renard *et al.*, *J. Synchrotron Rad.* **23**, 1013-1034 (2016).
[2] N. Kandula *et al.*, *J. Geophys. Res. Solid Earth* **124** (2019).

UNRAVELLING THE AGEING MECHANISM OF DEFECTIVE ELECTROCATALYSTS BY *OPERANDO* X-RAY STUDIES

The ageing of hollow, bimetallic nanoparticles, a class of highly active and highly defective electrocatalysts for the oxygen reduction reaction, was investigated by a combination of microscopic methods and wide- and small-angle X-ray scattering (WAXS/SAXS), providing *operando* insights into the degradation mechanisms at stake.

One of the greatest challenges faced by proton-exchange membrane fuels cells (PEMFCs) lies in their electrocatalysts: the oxygen reduction reaction, which occurs at the PEMFC cathode, is a sluggish reaction occurring in harsh environmental conditions, including low pH and high temperature. Among the different elements, platinum has always been the most promising, thanks to its near-ideal binding properties toward oxygen intermediates and its noble nature; however, its price and scarcity induce the need to design more complex nanostructures to increase the activity per platinum atom. Such a feat is achievable by either modifying the nanostructures through alloying with rare-earth elements/3d-transition metals or preferential crystallite orientation, which leads to the synthesis of shaped, bimetallic, nanoparticles (octahedral **[1]**, for example), or by increasing the nanostructure structural defectiveness to optimise the coordination number and interatomic distance of specific active sites, which exhibit a greatly enhanced turn-over frequency. A combination of these two approaches can be found in hollow PtNi nanoparticles, which exhibit a six- to tenfold increase in specific activity for the oxygen reduction reaction **[2]** vs. conventional solid Pt nanoparticles, due to the presence of nickel, which contracts the lattice parameter and thus modifies the Pt electronic structure and reactivity, and also to their highly defective structure.

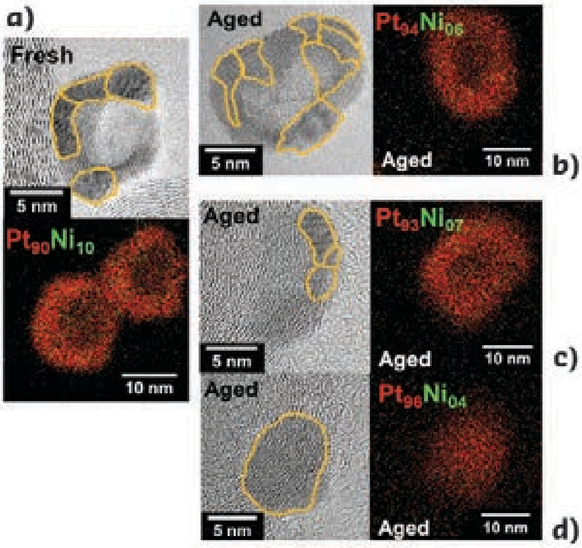

Fig. 147: Scanning transmission electron microscopy and energy dispersive X-ray mapping (STEM/EDX) of the hollow PtNi nanoparticles before **(a)** and after mild **(b)** and hard **(c-d)** ageing.

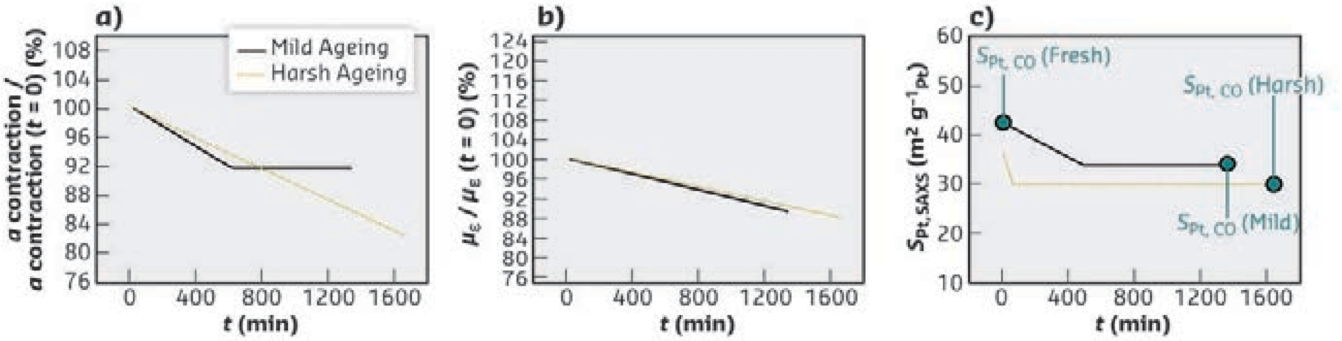

Fig. 148: Evolution of **(a)** lattice parameter contraction, **(b)** the microstrain (measured by WAXS) and **(c)** the specific surface determined from SAXS measurements and compared to the specific surface measured by CO_{ads} stripping.

Studying their morphological and compositional changes in conditions mimicking the proton-exchange membrane fuel cell environment provides information on their overall stability. **Figure 147** and **Figure 148** show hollow nanoparticle evolution, followed by scanning transmission electron microscopy and energy dispersive X-ray mapping (STEM/EDX), and by WAXS and SAXS performed at beamline **ID31**, during two different ageing procedures (5000 cycles between 0.6-1.0 V vs. RHE and 0.6-1.1 V vs. RHE), here defined as mild and harsh, which are representative of the potential range at which the cathode is exposed during a PEMFC operation.

Several critical findings were provided by this combination of *ex-situ* (STEM/EDX) and *operando* (SAXS/WAXS) measurements. The STEM/EDX (see **Figure 147**) showed a decrease of the nickel content during operation, especially under harsher conditions such as cycling up to 1.1 V vs. RHE, and also showed that nanoparticle polycrystallinity is maintained during the mild ageing. This acts as a good indicator of the structural defect stability while cycling up to 1.0 V vs. RHE. In contrast, the harsh ageing led to the formation of a bimodal electrocatalyst – hollow, polycrystalline nanoparticles and plain, monocrystalline nanoparticles, as shown in **Figures 147c** and **147d**. The *operando* SAXS/WAXS (see **Figure 148**) indicates that the relaxation of the lattice parameter is more important during the harsh ageing, while reaching a plateau at around 8% of losses for the mild ageing. It also shows that the microstrain (*i.e.*, the variation of the local strain vs. the average strain) follows identical trends, independently of the ageing harshness. Thirdly, it demonstrates that the variation of the electrocatalyst specific surface and, thus, of the nanoparticle morphology, mainly occurs in the first ageing cycles. For example, after 50 mins, the electrocatalyst specific surface stabilises, hinting toward a morphology stabilisation as well.

Hence, this study provides insights into the processes responsible for the activity losses observed during hollow PtNi nanoparticle operation as an oxygen reduction reaction catalyst. It also suggests a successful methodology for monitoring the structural changes in *operando* conditions of various types of advanced electrocatalysts for PEMFC cathodes: WAXS grants direct insight into the nanostructure modification at the atomic level (microstrain, alloying element), while SAXS unveils the morphological changes at the nanoparticle scale, along with the intermediate structures formed during the ageing process. Together, these methods are complementary and provide a global picture of the structural and chemical changes undergone by bimetallic nanoparticles during ageing.

PRINCIPAL PUBLICATION AND AUTHORS

Disentangling the Degradation Pathways of Highly Defective PtNi/C Nanostructures – An Operando Wide and Small Angle X-Ray Scattering Study, T. Asset (a,b,c), C. J. Gommes (b), J. Drnec (d), P. Bordet (e), R. Chattot (a,d), I. Martens (f,g), J. Nelayah (h), N. Job (b), F. Maillard (a) and L. Dubau (a), *ACS Catal.* **9**, 160-167 (2018); doi: 10.1021/acscatal.8b02665.
(a) Université Grenoble Alpes, CNRS, Grenoble-INP, Université Savoie-Mont-Blanc, LEPMI, Grenoble (France)
(b) University of Liège, Department of Chemical Engineering - Nanomaterials, Catalysis, Electrochemistry, B6a, Liège (Belgium)
(c) Center for Micro-Engineered Materials and Department of Chemical and Biological Engineering, University of New Mexico, Albuquerque (USA)
(d) ESRF
(e) CNRS, Institut Néel, Grenoble (France)
(f) AMPEL, University of British Columbia, Vancouver (Canada)
(g) Department of Chemistry, University of British Columbia, Vancouver (Canada)
(h) Laboratoire Matériaux et Phénomènes Quantiques (MPQ), UMR 7162 CNRS, Université Paris-Diderot, Bâtiment Condorcet, Paris (France)

REFERENCES

[1] C. Cui *et al.*, *Nano Lett.* **12**(11), 5885-5889 (2012).
[2] L. Dubau *et al.*, *ACS Catal.* **5**(9), 5333-5341 (2015).

ATOMIC-SCALE STRUCTURAL CHANGES IN OCTAHEDRAL PtNi NANOPARTICLE CATALYSTS FOR HYDROGEN FUEL CELL CATHODES

Octahedral PtNi nanoparticles are promising catalysts for the oxygen reduction reaction in fuel cell applications. The structural changes associated with Ni leaching during operation have been investigated by *in-situ* wide-angle X-ray scattering (WAXS). Atomic Ni losses, correlating to expansion of the crystal lattice parameters, largely affect the activity.

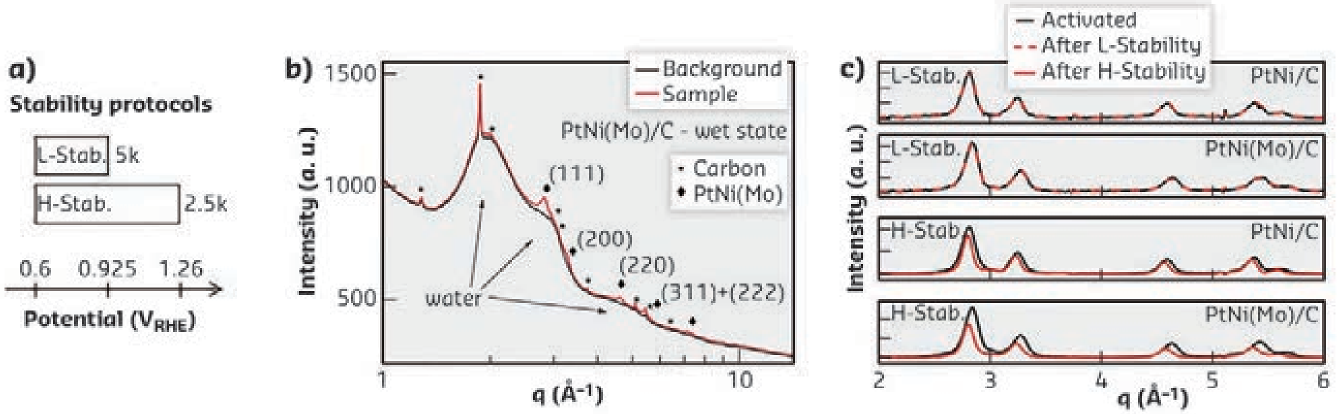

Fig. 149: a) Schematic illustration of the stability test protocols used for *in-situ* WAXS experiments. The potential range and number of cycles are indicated. **b)** *In-situ* WAXS patterns as integrated after collected by the 2D detector of PtNi(Mo)/C (red) and background position (black). **c)** Background subtracted patterns obtained with *in-situ* WAXS for the activated state (black) and after L-stability (red dashed) and H-stability (red solid) protocols.

Fuel cell electric vehicles (FCEVs) are a promising and clean alternative to combustion engine vehicles based on fossil fuels. In FCEVs, the energy stored in the chemical bonds of hydrogen is converted into electricity in proton-exchange membrane fuel cells (PEMFCs). In this process, oxygen from air is reduced to water via the oxygen reduction reaction (ORR). This reaction is particularly challenging and gives rise to significant losses, even with state-of-the-art Pt catalysts. Surface-doped PtNi alloy nanoparticles with octahedral morphology have been shown to possess among the highest Pt-mass-normalised ORR activities in thin film rotating disk electrode (TF-RDE) screening studies **[1]**. However, the translation of performance enhancement in respect to commercial Pt catalysts from TF-RDE to membrane electrode assembly (MEA)-based fuel cells is challenging **[2]**. Furthermore, the structural stability of these catalysts in MEA and the fundamental understanding of the activity enhancement are not completely clear, mainly due to limited *in-situ* characterisation at the atomic and molecular level.

This work combined *in-situ* wide-angle X-ray scattering (WAXS) and *ex-situ* X-ray fluorescence (XRF) spectroscopy to show the correlation between structural transformations involving Ni leaching and the evolution of the ORR activity during accelerated stability tests of octahedral Mo-doped PtNi nanoparticles. The results suggest that the Mo-doping treatment has a positive effect on the elemental composition of the Ni-rich domains and call for a strategy on how to improve the Ni retention to extend the stability of this class of catalysts.

WAXS was performed on beamline **ID31** using an *in-situ* electrochemical transmission set-up, so that structural changes could be investigated under reaction conditions and during operation. Two stability protocols were applied in the WAXS experiments to carbon-supported octahedral PtNi(Mo) and PtNi nanoparticles in a 0.1 M $HClO_4$ electrolyte (**Figure 149a**). The L-stability protocol was designed to simulate lifetime operation (*i.e.*, no exposure to high anodic potentials). In contrast, the H-stability protocol considers higher anodic potentials, which can be reached during start-up/shut-down. Rietveld analysis was performed on the WAXS patterns (**Figures 149b** and **149c**) to determine structural changes (**Figures 150a** and **150b**). The data collected during the L-stability test can be fitted with two face-centred cubic alloy

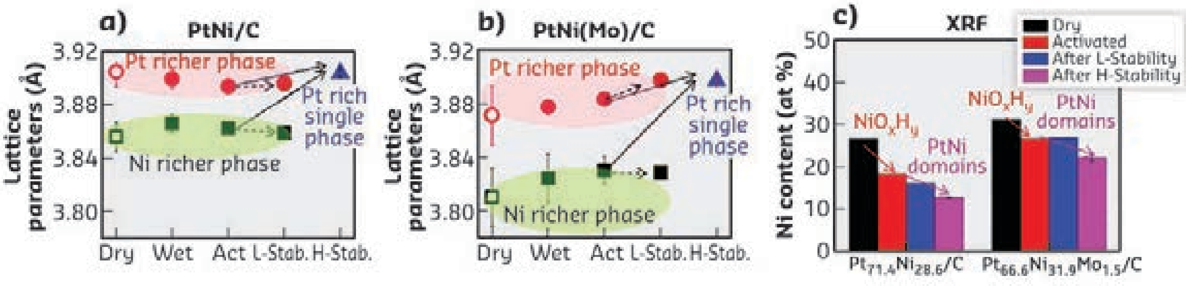

Fig. 150: Lattice parameter *a* calculated with Rietveld refinement for dry, wet, activated, L-stability, and H-stability for **(a)** PtNi/C and **(b)** PtNi(Mo)/C. **c)** Ni at.% composition from XRF measurements of samples in the dry state (black), activated (red), after L-stability (blue), and H-stability (pink).

phases and no significant changes in the lattice parameter *a* are observed. However, a single Pt-rich phase is observed after the H-stability test for both catalysts. These results are in agreement with a structural transformation in which Ni atoms leave the Ni-rich phase. To verify this hypothesis, the Ni atomic content was measured after WAXS experiments by XRF (**Figure 150c**). After the L-stability protocol, either none or only a minor decrease in the fraction of Ni content was observed. This suggests that Ni leaching is slow in these catalysts if the upper potential is controlled below 0.925 V_{RHE}. In contrast, after H-stability, Ni content decreases for both, confirming the hypothesis from the WAXS analysis. Furthermore, higher Ni retention of the Mo-doped catalyst has been associated with its high ORR activity.

This study provides atomic and structural insights into degradation mechanisms of octahedral Pt alloy nanoparticle catalysts for the ORR, defines the optimal operation conditions and highlights the importance of preserving the high Ni content in the PtNi crystalline domains.

PRINCIPAL PUBLICATION AND AUTHORS

Controlling Near-Surface Ni Composition in Octahedral PtNi(Mo) Nanoparticles by Mo Doping for a Highly Active Oxygen Reduction Reaction Catalyst, F. Dionigi (a), C. C. Weber (a), M. Primbs (a), M. Gocyla (b), A. Martinez Bonastre (c), C. Spöri (a), H. Schmies (a), E. Hornberger (a), S. Kühl (a), J. Drnec (d), M. Heggen (b), J. Sharman (c), R. E. Dunin-Borkowski (b) and P. Strasser (a,e), *Nano Lett.* **19**, 6876 (2019);
doi: 10.1021/acs.nanolett.9b02116.
(a) Department of Chemistry, Technical University Berlin (Germany)
(b) Ernst Ruska-Centre for Microscopy and Spectroscopy with Electrons, Forschungszentrum Jülich (Germany)
(c) Johnson Matthey Technology Centre (UK)
(d) ESRF
(e) Ertl Center for Electrochemistry and Catalysis, Gwangju Institute of Science and Technology (South Korea)

REFERENCES

[1] X. Q. Huang *et al., Science* **348**, 1230 (2015).
[2] L. Pan *et al., Curr. Opin. Electrochem.* **18**, 61 (2019).

ORIGIN OF THE ANOMALOUS SURFACE STRUCTURE IN RELAXOR FERROELECTRICS

Surface layers in relaxor ferroelectrics have distinct physical properties from the bulk material, which has caused long-lasting ambiguity in the phase identification and properties of these materials. X-ray diffraction (XRD) has shown the surface structure to be ≈ 20 µm thick and formed due to the relaxation of stress induced by oxygen vacancies.

The susceptibility of relaxor ferroelectrics to distort under an applied electric field or stress has made them ideal for high-performance electro-mechanical transducers, and their high dielectric constants over a broad temperature range mean they find applications in electrical capacitors. While understanding the bulk material structure is central to ferroelectrics research, understanding surface structure and its impact on properties has become imperative with the miniaturisation of electrical components.

The presence of a shoulder peak on the lower-angle side of diffraction patterns obtained from laboratory X-ray diffraction has caused ambiguity in the structural characterisation of lead-based and lead-free ferroelectric ceramics. These shoulders did not correspond to any secondary phases and disappeared when the ceramic was crushed into powder. No prior explanation for the structural origin has been provided, though some theories suggested the shoulder was from polishing effects, random electric fields present in the relaxors resulting from the presence of multiple cations with different valences sharing a sub-lattice position, or the difference in composition between the surface and bulk material.

Using XRD at beamline **ID15A**, the structure of the surface layer was distinctively characterised from the bulk in $(Na_{1/2}Bi_{1/2})TiO_3$-$BaTiO_3$ (NBT-BT) relaxor ferroelectric ceramics. A 10 µm-thick beam was scanned from the surface of the ferroelectric into the bulk, in 5-µm steps. The schematic of the experimental set-up is shown in **Figure 151a**. The shoulders were found to be most intense at the surface, with the ratio of integrated intensities diminishing quickly and stabilising at a depth of approximately 20 µm (**Figure 151b**). This indicates the shoulders are the result of a different structure at the surface.

Angular dispersive diffraction profiles, obtained through radial integration of the diffraction images, showed this surface structure is textured,

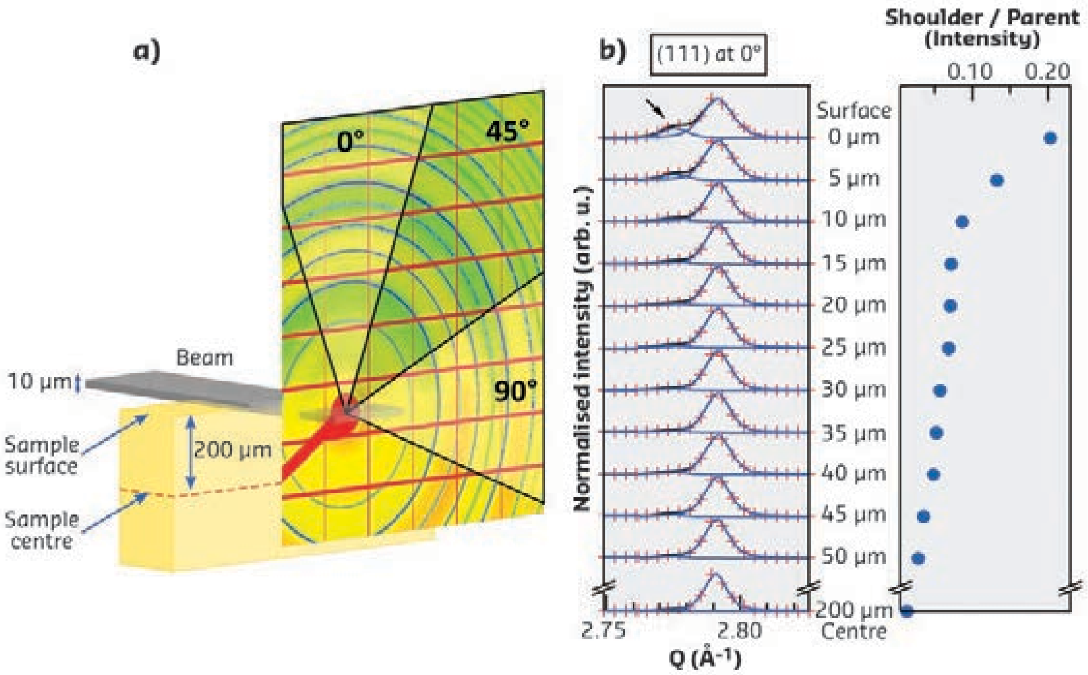

Fig. 151: a) A schematic of the set-up used for scanning diffraction patterns from the surface to the centre of the ceramic using a 10-µm beam height. The angles in the schematic's 2D synchrotron diffraction patterns represent the angles between surface normal and q-vector. The depth profile for (111) peak from the surface to the sample centre is shown in **(b)**. The low-angle shoulder at the surface is indicated with a black arrow. Corresponding ratios of integrated intensities of shoulders to parent peak are also shown, with shoulders significantly reducing in intensity on moving toward the centre of the ceramic.

or preferentially elongated out-of-plane at the surface. The textured nature suggests the presence of different stress conditions at the surface as compared to the bulk material. It is known that the surface exists under a biaxial stress condition (plane stress), with no constraint present normal to the surface. On the other hand, the bulk of the sample is expected to be triaxially constrained under plane strain condition. This is illustrated in **Figure 152b**. At the surface, any strain introduced in the lattice can be relieved by a lattice expansion (or contraction) along the direction of the surface normal (but not in the plane of the surface). In polycrystalline ferroelectrics, since the surface has grains with different orientations intersecting it, a unique distortion and texture exist for all the peaks in the diffraction pattern, resulting in the mixed phase appearance of the diffraction pattern **Figure 152a**.

The presence of this surface structure was demonstrated to be due to the relaxation of stresses imposed by oxygen vacancies. Oxygen vacancies have been known to be a source of internal chemical pressure, altering the lattice parameters in oxide ceramics. Additional experimentation by changing the stoichiometry of NBT-BT found that the intensity of the shoulder, and thus the existence of the surface structure, can be controlled. An extra 2 mol% of bismuth, resulting in fewer oxygen vacancies, eliminated the distorted surface phase, while a decrease in 2 mol% of bismuth, increasing the oxygen vacancy concentration, increased the thickness of the surface phase. The most likely cause of lattice expansion in ceramic oxides can be attributed to the increase in ionic radius of the reducible cation, *e.g.*, Ti^{4+} to Ti^{3+}, for charge compensation of oxygen vacancies.

The results of this study lend important insights not only into answering the long-standing question of the origin of surface structures in relaxor ferroelectrics, but also towards mechanisms to control their formation. This opens potential investigations for functionalising the surface structures, which have caused so much confusion in the structural characterisation of relaxor ferroelectrics in the past.

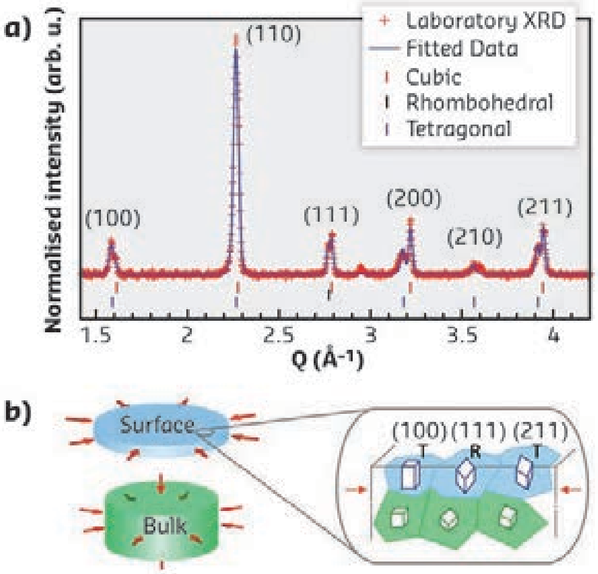

Fig. 152: a) XRD collected with scattering vector, q, perpendicular to the sample surface. Fitted curves showing the parent cubic phase and tetragonal or rhombohedral peaks fitting the low-angle shoulders. **b)** A simplified schematic comparing the stress states in the skin surface and bulk. The right schematic shows that grains with different orientations are present in the skin and expand along the surface normal.

PRINCIPAL PUBLICATION AND AUTHORS

Defect-Driven Structural Distortions at the Surface of Relaxor Ferroelectrics,
S. Kong (a), N. Kumar (a), S. Checchia (b),
C. Cazorla (a) and J. Daniels (a),
Adv. Funct. Mater. **29**(27), 1900344 (2019);
doi: 10.1002/adfm.201900344.
(a) School of Materials Science and Engineering, University of New South Wales, Sydney (Australia)
(b) ESRF

IN-SITU MONITORING OF MECHANOCHEMICAL MILLING DEMONSTRATES FAST ATOMIC AND MOLECULAR EXCHANGE BETWEEN MILLED CRYSTALLITES

Continuous particle comminution and growth enables the bulk of the milled sample to become exposed to the surface and leads to fast atomic and molecular exchanges between milled solids, a process monitored by tandem *in-situ* powder X-ray diffraction (PXRD) and Raman spectroscopy.

With atoms and molecules fixed in near-perfect order in a crystal lattice, diffusion in the solid state is known to be notoriously slow, rendering solids stable and unreactive. This traditional view of the solid state is now becoming outdated, with recent advances in synthesis achieved by mechanochemical milling. Milling reactions exhibit several features that would suggest this slow diffusion is somehow overcome during milling. These features include selectivity **[1]**, strong temperature dependence **[2]**, rapid reactions **[3]** and, more often than not, formation of intermediates. The dynamics of milled solids were probed at beamlines ID15A and ID31 using tandem *in-situ* monitoring of mechanochemical milling by PXRD (a technique pioneered at ID15 **[3]**) and Raman spectroscopy **[4,5]**, together with isotope-labeled solids. Using specific solids containing a deuterium label, fast hydrogen/deuterium (H/D) exchange was observed to take place regardless of whether a chemical reaction was happening or not during milling.

Natural or deuterium-labeled benzoic acid (ba) and 2-pyridone (pyo) were used to study H/D exchange upon cocrystal formation between these two compounds. Both compounds bear one exchangeable hydrogen (deuterium) atom – bonded to either the electronegative oxygen or nitrogen atoms. When these two solids are milled together they form a 1:1 cocrystal (bapyo), where molecules of ba and pyo connect via ring hydrogen bonding into discrete supramolecular assemblies (**Figure 153a**). Regardless of which of the two solids was initially deuterated, the same H/D distribution resulted after 30 minutes milling, indicating a dynamic environment enabling fast redistribution of deuterium atoms, such as could be expected for H/D exchange happening in solution.

It was also shown that H/D exchange is not dependent on new phase formation, as milling of ba and the pharmaceutical paracetamol also led to H/D exchange despite the fact that these two compounds do not form a new phase but remain a physical mixture. Further to H/D exchange, which requires bond breaking, whole molecule exchange was also observed upon milling of ba and ba labelled with a ^{13}C atom, where a heterodimer is formed upon molecular exchange between milled crystallites (**Figure 154**).

These results provide a unique insight into one fundamental aspect of mechanochemical milling: milled particles, despite being in the solid state, exchange atoms and molecules with other milled particles. Moreover, each molecule

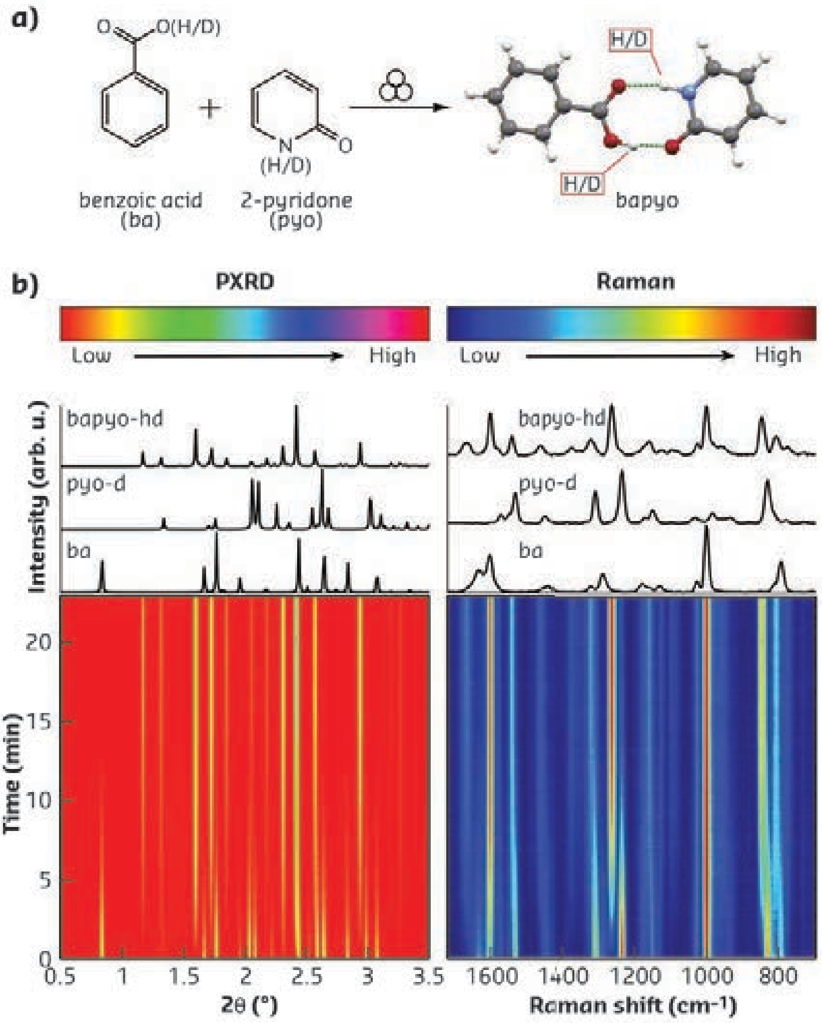

Fig. 153: a) Formation of the bapyo cocrystal between ba and pyo. Exchangeable hydrogens are highlighted. **b)** Tandem *in-situ* monitoring of mechanochemical bapyo formation by PXRD (left) and Raman spectroscopy (right). While PXRD enables the detection of changes in crystalline phases, Raman spectroscopy is also sensitive to H/D exchange, which does not have an influence on diffraction from the bulk crystalline phases. Adapted with permission from S. Lukin *et al., J. Am. Chem. Soc.* **141**, 1212-1216 (2019). Copyright (2019) American Chemical Society.

of the milled particles is exposed to the surface and becomes available for interaction with other particles within around 30 minutes of milling or less. By continuously comminuting particles, milling thus overcomes the inherently slow solid-state diffusion. Next to this fundamental aspect of milling, there is also great potential to use mechanochemistry to deuterate solids efficiently.

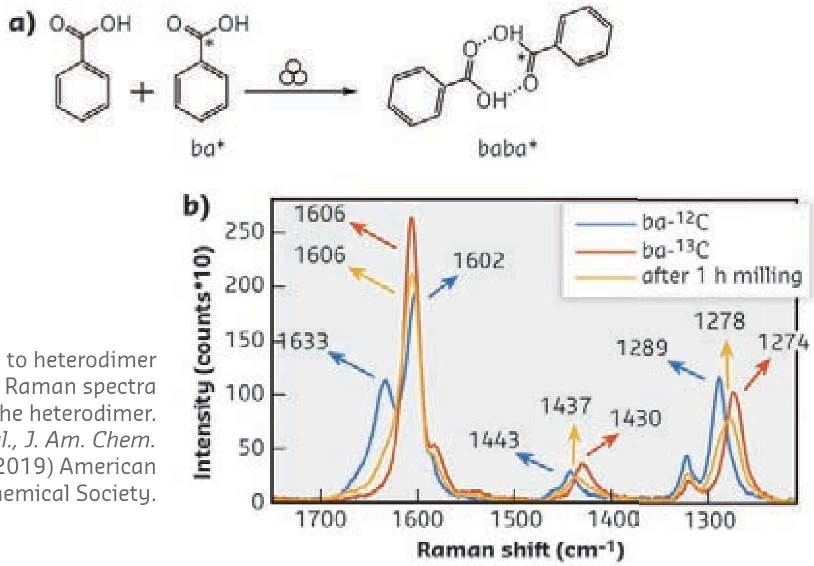

Fig. 154: a) Whole-molecule exchange leading to heterodimer formation between ba and ^{13}C-labelled ba. **b)** Raman spectra of pure acids and their mixture containing the heterodimer. Adapted with permission from S. Lukin *et al., J. Am. Chem. Soc.* **141,** 1212-1216 (2019)**.** Copyright (2019) American Chemical Society.

PRINCIPAL PUBLICATION AND AUTHORS

Isotope Labeling Reveals Fast Atomic and Molecular Exchange in Mechanochemical Milling Reactions, S. Lukin (a), M. Tireli (a), T. Stolar (a), D. Barišić (a), M. V. Blanco (b), M. di Michiel (b), K. Užarević (a) and I. Halasz (a), *J. Am. Chem. Soc.* **141**, 1212-1216 (2019).

(a) Ruđer Bošković Institute, Zagreb (Croatia)
(b) ESRF

REFERENCES

[1] S. Lukin *et al., Cryst. Growth Des.* **18**, 1539-1547 (2016).
[2] J. M. Andersen & J. Mack, *Chem. Sci.* **8**, 5447-5453 (2017).
[3] T. Friščić *et al., Nature Chem.* **5**, 66-73 (2013).
[4] D. Gracin *et al., Angew. Chem. Int. Ed.* **53**, 6193-6197 (2014).
[5] S. Lukin *et al., Chem. Eur. J.* **23**, 13941-13949 (2017).

AFM ELECTRIC FIELD-CONTROL OF TOPOTACTIC TRANSFORMATIONS WITH SUB-MICRON SPATIAL RESOLUTION

X-ray absorption spectroscopy (XAS) with sub-micron spatial resolution has shown that the electric field produced by a voltage-biased atomic force microscopy (AFM) tip can induce the transformation between perovskite $SrFeO_{3-\delta}$ and brownmillerite $SrFeO_{2.5}$ at room temperature. This opens the way for the design of new functional materials through electric field patterning.

Reversible structural transformations between perovskite (PV) $ABO_{3-\delta}$ and brownmillerite (BM) $ABO_{2.5}$ (A = Ca^{2+}, Sr^{2+}; B = $Fe^{4+/3+}$, $Co^{4+/3+}$) oxides can be induced by topotactic oxygen exchange of reducing/oxidising conditions. Combining the large oxide-ion conductivity and a small free-energy difference between the 4+/3+ oxidation states of 3*d* transition metal ions enables these topotactic transformations (TPt) **[1,2]**. However, although TPts have been shown to be a powerful tool to tune the properties of several oxides, the need for either high temperatures or specific electrochemical-cell configurations, along with the lack of spatial control over the position and resolution of the transformation, limits its applications in many technologies requiring spatial sub-micron control **[3]**.

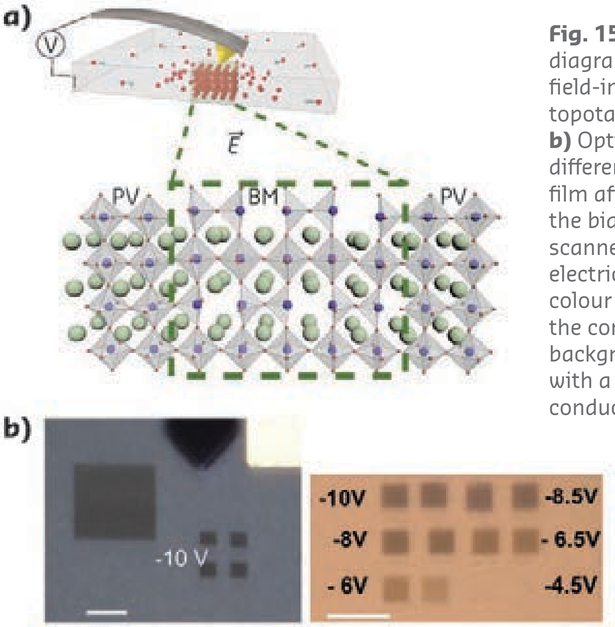

Fig. 155: a) Schematic diagram of AFM electric field-induced local topotactic transformation. **b)** Optical image of different regions of the film after scanning with the biased AFM tip. The scanned areas with the electric field change their colour with respect to the conductive PV film background, consistent with a decrease in electrical conductivity.

This work demonstrates that the electric field produced by a voltage-biased atomic force microscopy (AFM) tip can induce such a transformation between the PV $SrFeO_{3-\delta}$ and BM $SrFeO_{2.5}$ at room temperature (**Figure 155**). Interestingly, after removing the electric field, the structural transformation results in a non-volatile controlling of the local chemical, electrical, optical and magnetic properties (**Figure 155b**). These results open the door for the fabrication of stable ionic-based devices through the electric-field patterning of different crystallographic phases. The TPt was followed through the changes in Fe oxidation state, using XAS with micrometre spatial resolution on **BM25** inside and outside an area scanned with a voltage-biased AFM tip. **Figure 156a** shows an energy shift of the Fe K-edge to lower energies in the scanned region, indicating a lower Fe valence. **Figure 156b** shows the XAS spectra at the Fe $L_{2,3}$-edge. The peak at the low energy side of the L_3-edge (vertical arrow) is characteristic of a lower oxidation state of Fe associated with a reduction in the coordination of the transition-metal ion, from octahedral to tetrahedral. The pre-peak in the O K-edge spectra, shown in **Figure 156c**, hints at the crystal field splitting that produces a double peak at 530 eV and 532 eV, and its strong suppression after electric field scanning is consistent with an increasing population of tetrahedrally coordinated Fe, as the PV transforms into BM.

Different techniques of characterisation (X-ray diffraction, Raman, AFM and spectroscopic experiments) demonstrate that it is possible to achieve a local stable topotactic PV-to-BM transformation in thin films of $SrFeO_{3-\delta}$, by the direct action of an electric field-biased AFM tip. Given the large difference in the electrical conductivity of the PV and BM, as well as their different magnetic configurations, the local control over the TPt reported in this work opens enormous possibilities to study magnetic exchange interactions in a controlled way, fabricate stable resistive memories, or ionic-conducting circuits, with sub-micrometre resolution. Eliminating the use of ionic liquids to achieve the transformation at room temperature also offers important advantages over previously reported methods.

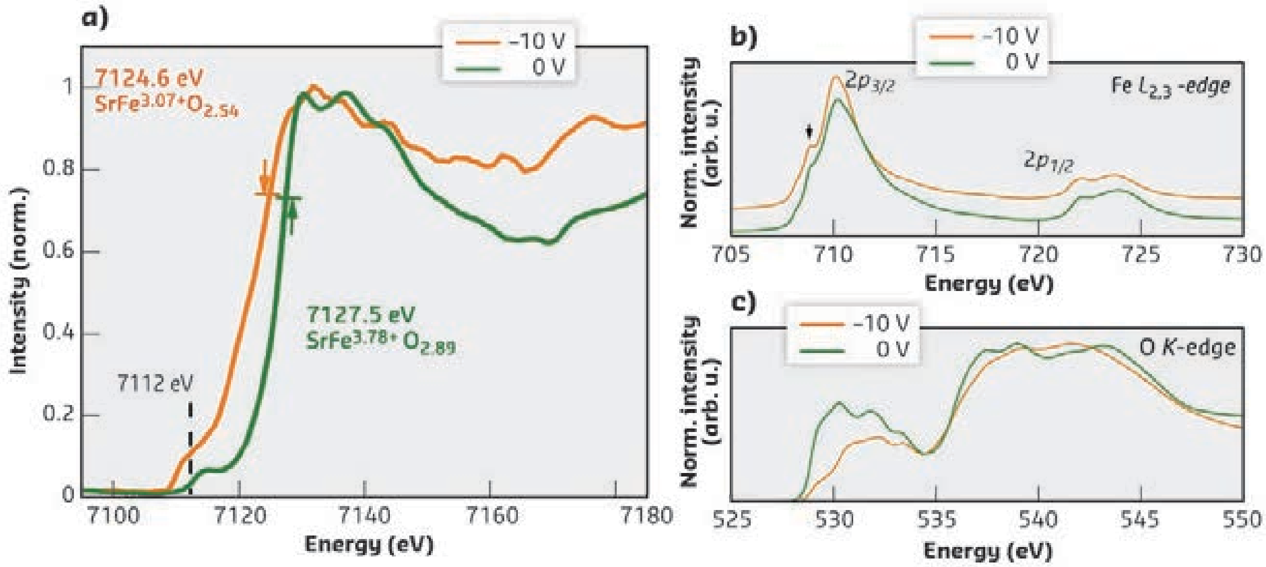

Fig. 156: XAS of local PV to BM transformation evidenced at **(a)** Fe K-edge **(b)** Fe $L_{2,3}$-edge and **(c)** O K-edge. The spectra were taken on an area scanned with the −10 V-biased AFM tip (orange line) and a pristine region of the film (green line). The vertical arrow in **(b)** marks a low energy feature in the $2p_{3/2}$ peak, characteristic of a lower Fe-oxidation state and tetrahedral coordination in this region.

PRINCIPAL PUBLICATION AND AUTHORS

Room Temperature AFM Electric-Field-Induced Topotactic Transformation between Perovskite and Brownmillerite SrFeOx with Sub-Micrometer Spatial Resolution, E. Ferreiro-Vila (a), S. Blanco-Canosa (b), I. Lucas del Pozo (c), H. Babu Vasili (d), C. Magén (c), A. Ibarra (c), J. Rubio-Zuazo (e), G. R. Castro (e), L. Morellón (c) and F. Rivadulla (a), *Adv. Funct. Mater.* 1901984 (2019); doi: 10.1002/adfm.201901984.

(a) Centro de Investigación en Química Biolóxica e Materiais Moleculares (CIQUS), Departamento de Química-Física, Universidade de Santiago de Compostela (Spain)
(b) Donostia International Physics Center (DIPC), San Sebastián (Spain)
(c) Instituto de Nanociencia de Aragón (INA), Universidad de Zaragoza (Spain)
(d) ALBA Synchrotron Light Source, Cerdanyola del Valles, Barcelona (Spain)
(e) ESRF

REFERENCES

[1] N. Lu *et al., Nature* **546**, 124 (2017).
[2] A. Khare *et al., Adv. Mater.* **29**, 1606566 (2017).
[3] B. Cui *et al., Nat. Commun.* **9**, 3055 (2018).

MULTISCALE MULTIPHASE LITHIATION AND DELITHIATION MECHANISMS OF A PROMISING LITHIUM-ION BATTERY CELL ANODE COMPOSITE MATERIAL

Silicon/graphite-based composites are promising high-capacity anode materials for Li-ion batteries. Simultaneous *operando* wide- and small-angle X-ray scattering (WAXS/SAXS) helped unravel the contribution of each anode active component throughout several battery cell charge/discharge cycles. This information is key to understanding and developing new stable and high-capacity materials for future generations of Li-ion battery.

Over the past three decades following the first commercialised cell by Sony in 1990 **[1]**, lithium-ion battery (LiB) technology has evolved from the most promising energy-storage device to the most widely used. Today LiBs are found in a large range of applications such as portable devices, electric vehicles and large stationary energy-storage systems. The continuous success of LiB technology stems from the constant search for higher-performing, lighter, cheaper and safer materials. Concerning the negative electrode, graphite is currently the favoured material due to its high capacity retention, low volume variations upon lithiation (10 %) **[2]**, low cost and low toxicity. However, the LiB energy density is limited by graphite's maximum specific capacity (372 mA.h.g^{-1}). Among the candidates for high specific capacity are the metalloids, such as silicon (3579 mA.h.g^{-1}), but their use is hampered by a high volumetric expansion upon lithiation (297 % for Si) that leads to large internal stress and results in a quick fading of cell capacity.

Nanostructured silicon/graphite-based composite materials are seen as perfect candidates for the next generation of LiB due to their high capacities and cycling stability. In this regard, the a-Si/c-FeSi$_2$/ graphite anode material is very promising due to its low cost, high reversible capacity and good cycling stability **[3]**. After 300 charge/discharge cycles, the cell capacity retention remains above 70 % (**Figure 157a**). However, it was still unclear how this complex material functions and, therefore, how to further improve it. To tackle this issue, *operando* synchrotron experiments were performed to follow both silicon and graphite over several charge/discharge cycles within fresh and aged full LiB cells (**Figure 157**). Using the unique detector set-up on beamline **BM02**, simultaneous WAXS and SAXS experiments (**Figure 157d**) enabled the real-time investigation of both atomic and nanoscale morphological changes within the composite anode. The graphite lithiation/delithiation and the amorphous silicon alloying processes were followed, respectively, by WAXS (*i.e.*, Li$_x$C$_6$ Bragg

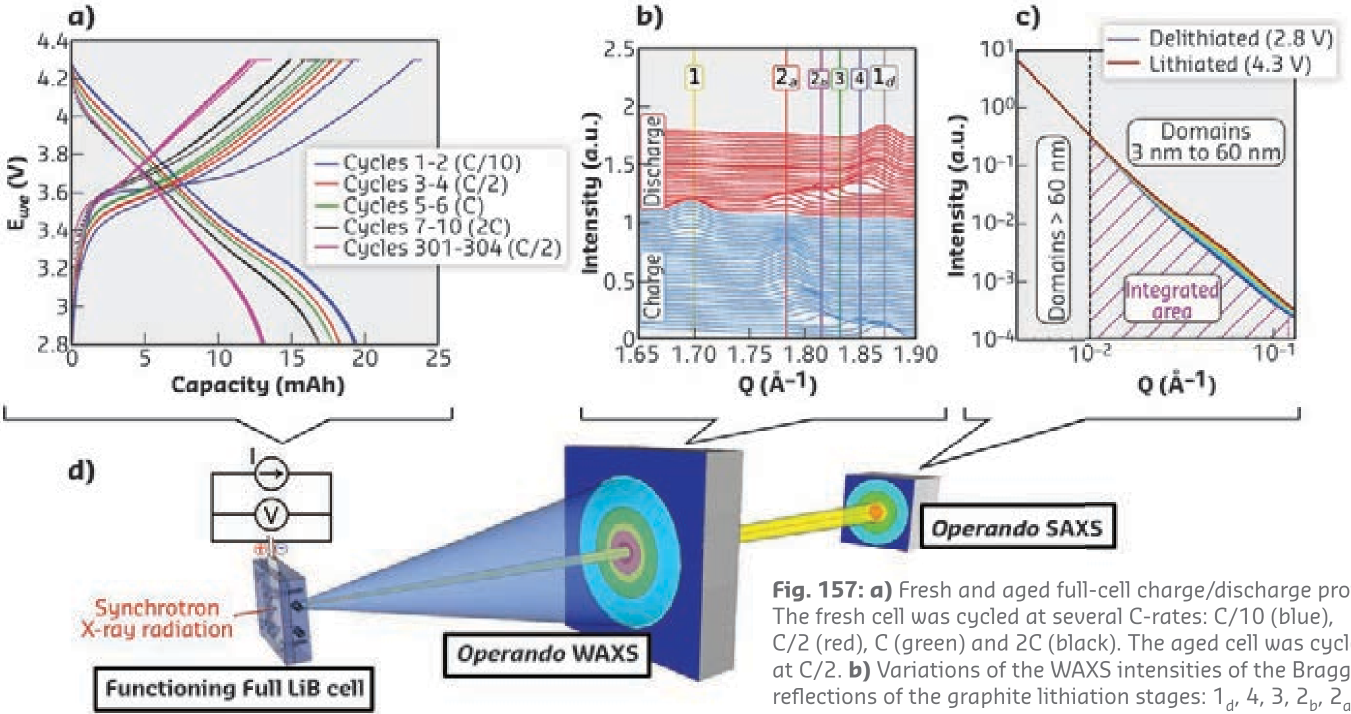

Fig. 157: a) Fresh and aged full-cell charge/discharge profiles. The fresh cell was cycled at several C-rates: C/10 (blue), C/2 (red), C (green) and 2C (black). The aged cell was cycled at C/2. **b)** Variations of the WAXS intensities of the Bragg reflections of the graphite lithiation stages: 1$_d$, 4, 3, 2$_b$, 2$_a$ and 1 during one cell charge/discharge cycle. **c)** SAXS intensity profile variations over the course of one cell charge. **d)** Schematic representation of the set-up at BM02.

reflections) and SAXS (*i.e.*, scattering profile change due to volumetric variations). From the simultaneous, yet independent, acquisition and analysis of WAXS and SAXS data, the respective capacities of both active components could be quantified (**Figure 158a**) at any given cell potential, and a detailed mechanism of the a-Si/c-$FeSi_2$/graphite composite lithiation/delithiation process proposed (**Figure 158b**).

Additionally, both techniques were used to evaluate how the applied current, and thus the C-rate, affects the charge/discharge process. An increase in C-rate disrupts the lithiation mechanism and, consequently, the sequential lithium extraction of silicon and graphite. In contrast, ageing of the cell does not modify the lithiation/delithiation process of the a-Si/c-$FeSi_2$/graphite anode but is responsible for a loss of available lithium and hence a decrease in performance.

Moreover, it was found that the silicon volume does not increase linearly upon lithiation. As the cell reaches a third of its capacity, it is believed that the silicon volumetric expansion is accommodated by the morphology of the composite material. The high cycling stability of this electrode, as compared to pure silicon, could thus be a result of its modified volume variations. These results bring key knowledge on the cyclability of nanostructured silicon-based composite anodes and can help to define the best compromise between the nature and distribution of active components.

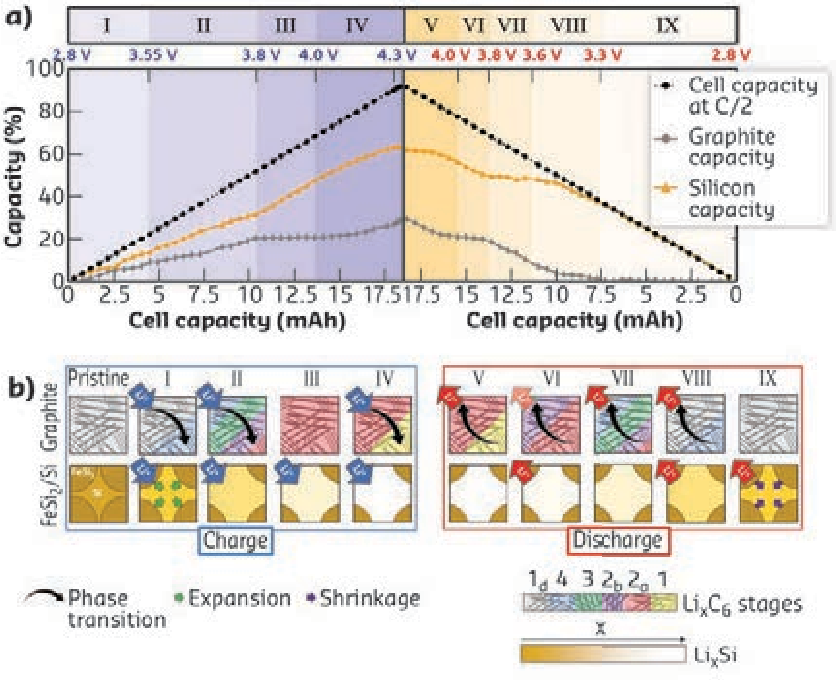

Fig. 158: a) Graphite and silicon contributions to the cell capacity. **b)** Scheme illustrating the proposed (de)lithiation mechanism of the a-Si/c-$FeSi_2$/Gr composite electrode. All results were obtained over the course of a C/2 charge/discharge cycle.

PRINCIPAL PUBLICATION AND AUTHORS

Multiscale Multiphase Lithiation and Delithiation Mechanisms in a Composite Electrode Unraveled by Simultaneous Operando Small-Angle and Wide-Angle X-Ray Scattering, C. L. Berhaut (a), D. Zapata Dominguez (b), P. Kumar (b), P.-H. Jouneau (b), W. Porcher (c), D. Aradilla (a,d), S. Tardif (b), S. Pouget (b) and S. Lyonnard (a), *ACS Nano* **13**, 11538-11551 (2019); doi: 10.1021/acsnano.9b05055.

(a) Université Grenoble Alpes, CEA, CNRS, IRIG, SyMMES, Grenoble (France)
(b) Université Grenoble Alpes, CEA, IRIG, MEM, Grenoble (France)
(c) Université Grenoble Alpes, Liten, Grenoble (France)
(d) University of Goettingen, Institute of Inorganic Chemistry, Goettingen (Germany)

REFERENCES

[1] A. Yoshino, *Angew. Chem. Int. Ed.* **51**, 5798-5800 (2012).
[2] S. Schweidler *et al.*, *J. Phys. Chem. C* **122**, 8829-8835 (2018).
[3] Y. Cao *et al.*, *J. Mater. Chem. A* **7**, 8335-8343 (2019).

OPERANDO XAS/XRD STUDY RELATES THE STRUCTURAL DYNAMICS OF AN In_2O_3 CATALYST WITH ITS ACTIVITY FOR CO_2 HYDROGENATION TO METHANOL

The development of efficient catalysts for the direct hydrogenation of CO_2 to methanol is a key challenge for mitigating increasing emissions of CO_2. Structure-activity relationships were established for a model nanocrystalline In_2O_3 catalyst for CO_2 hydrogenation to methanol, shedding light on the structure of the most active catalyst state and its deactivation pathway.

The direct hydrogenation of CO_2 to methanol is a highly valuable yet underdeveloped reaction **[1]**. Recent studies have shown that In_2O_3-based catalysts feature promising activity and selectivity for this process **[2,3]**. However, an industrial deployment of these emerging

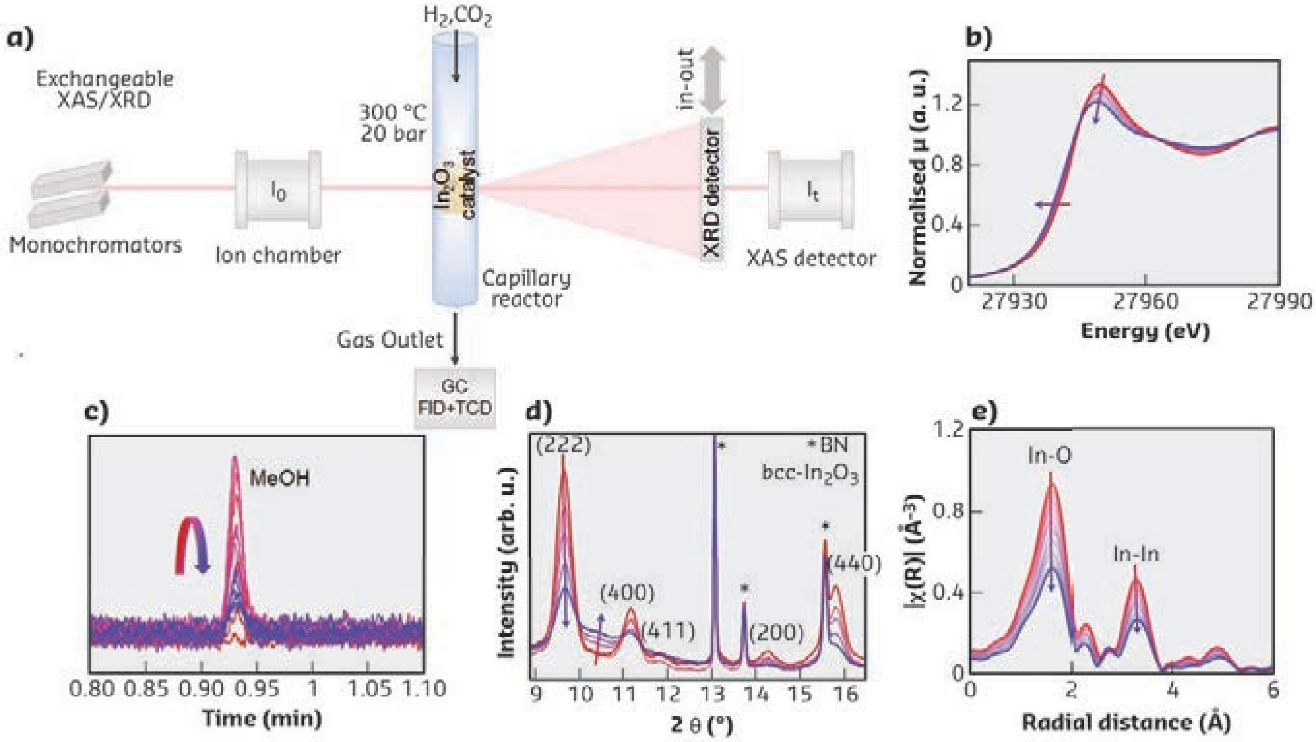

Fig. 159: a) A schematic illustration of the combined *operando* XAS-XRD experiment. **b)** Selected In K-edge XANES spectra. **c)** Chromatographs showing the varying amounts of methanol produced with time on stream (TOS). **d)** XRD profiles over a selected range of Bragg angles (λ = 0.506 Å) with indexed peaks of bcc-In_2O_3 and BN (labelled with *). **e)** The Fourier transform of k^2-weighted EXAFS (not corrected for phase shift) of the In_2O_3 NPs collected during CO_2 hydrogenation. The arrows indicate the direction of changes with TOS. In_2O_3 NPs were mixed with BN for optimal X-ray absorption and to ensure an appropriate gas-particle contact time.

catalysts requires a detailed understanding of their structure at the atomic and nanoscale level at working conditions. Such insight is essential to formulate structure-function relationships to tailor the catalysts' performance through rational design and optimisation. In this work, well-defined In_2O_3 nanoparticles (In_2O_3 NPs) were investigated using a combination of *operando* X-ray absorption spectroscopy (XAS) and powder X-ray diffraction (XRD) techniques coupled with the simultaneous analysis of the effluent gas. These *operando* studies made it possible to correlate the evolution of the oxidation state and the catalyst structure during CO_2 hydrogenation with the rate of methanol production.

Monodisperse In_2O_3 nanoparticles (NPs) with an average diameter of 7 nm were prepared from indium (III) acetylacetonate via a colloidal approach **[4]** and calcined at 400°C. Combined *operando* XAS (In K-edge) and XRD were performed at **BM31** (**Figure 159**) under CO_2 hydrogenation conditions (300°C, 20 bar, H_2:CO_2:N_2=3:1:1) while quantifying the catalytic activity by a compact gas chromatograph (GC). Three distinct catalytic regimes were identified during CO_2 hydrogenation: activation, stable performance and deactivation (**Figure 160a**). The activation stage is associated with the formation of oxygen vacancy sites due to a partial reduction of In_2O_3 (*i.e.*, In_2O_{3-x}). As the reaction proceeds, a reductive amorphisation of In_2O_3 NPs takes place as revealed by combined X-ray absorption near-edge structure (XANES), extended X-ray absorption fine structure (EXAFS) and XRD analyses (**Figure 160**). XANES and the corresponding multivariate curve resolution alternating least squares (MCR-ALS)

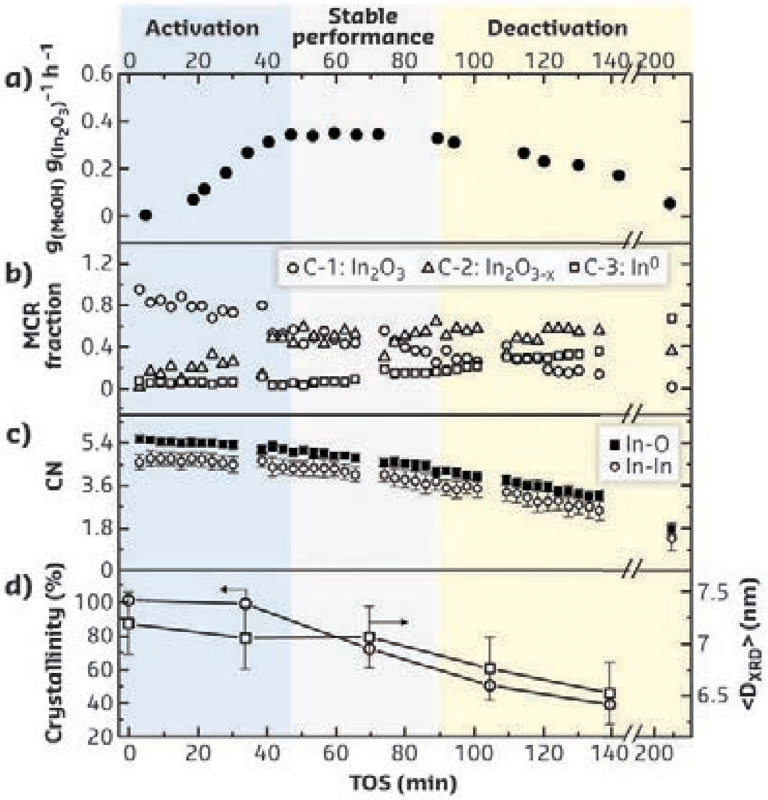

Fig. 160: a) Methanol production rate. **b)** MCR-ALS analysis of the In K-edge XANES data. **c)** In-O and In-In coordination numbers. **d)** Fraction of crystalline bcc-In_2O_3 and crystallite size <D_{xrd}> of the In_2O_3 NPs during the *operando* CO_2 hydrogenation experiment as a function of TOS.

analysis (**Figure 160b**) indicated that the most active catalyst has an average oxidation state between +3 and +2 (corresponding to 50-40% In_2O_3 and 50-60% In_2O_{3-x}). Notably, the onset of the deactivation coincides with the appearance of molten In^0. The amorphisation of In_2O_3 NPs is denoted by the decreasing In-O and In-In coordination numbers (**Figure 160c**) determined by EXAFS, and the decreasing intensity of In_2O_3 peaks with a simultaneous development of a halo in XRD (**Figures 159d** and **160d**). After 210 min, the catalyst lost 86% of its maximal performance, which correlates with a composition of 68% In^0 and 32% In_2O_{3-x}. In^0 could form from catalytically active sites, depleting their density and therefore reducing the yield of methanol. Hence, the over-reduction of In_2O_3 with time on stream (TOS) leads to an amorphous In^0/In_2O_{3-x} material of inferior catalytic activity.

This *operando* study made it possible to establish a correlation between the extent of In_2O_3 reduction, the structure of the material, and the activity for the CO_2 hydrogenation to methanol. These findings represent an important step towards the development of highly active and stable In_2O_3-based catalysts by preventing over-reduction and the associated deactivation with TOS.

PRINCIPAL PUBLICATION AND AUTHORS

The Structural Evolution and Dynamics of an In_2O_3 Catalyst for CO_2 Hydrogenation to Methanol: an *Operando* XAS-XRD and *in situ* TEM Study, A. Tsoukalou (a), P. M. Abdala (a) D. Stoian (b), X. Huang (c), M. G. Willinger (c), A. Fedorov (a) and C. R. Müller (a), *J. Am. Chem. Soc.* **141**, 13497-13505 (2019);

doi: 10.1021/jacs.9b04873.

(a) ETH Zürich, Department of Mechanical and Process Engineering, Zürich (Switzerland)
(b) ESRF
(c) ETH Zürich, Scientific Center for Optical and Electron Microscopy, Zürich (Switzerland)

REFERENCES

[1] A. Goeppert *et al., Chem. Soc. Rev.* **43**, 7995-8048 (2014).
[2] O. Martin *et al., Angew. Chem. Int. Ed.* **55**, 6261-6265 (2016).
[3] J. Ye *et al., ACS Catal.* **3**, 1296-1306 (2013).
[4] W. S. Seo *et al., Adv. Mater.* **15**, 795-797 (2003).

TEXTURE, STRAIN AND PHASE STABILITY OF PHOTOVOLTAIC $CsPb(I_{1-x}Br_x)_3$ THIN FILM

The perovskite materials used for solar cells and light-emitting diodes (black in colour) are generally less stable at room temperature than electronically inactive non-perovskite phases (yellow in colour). *In-situ* grazing-incidence, wide-angle X-ray scattering (GIWAXS) shows how strain and texture in the photovoltaic films can be used to manipulate the stability of the perovskite phase.

Perovskites are promising candidates for photovoltaic cells, having reached an energy harvesting efficiency of 24%, and have recently entered the commercial market. However, applications of these materials are still limited by their instability within real-world devices. The instability arises partly from the polymorphic phenomena. It results, in particular, in useful phases emerging only at conditions that are

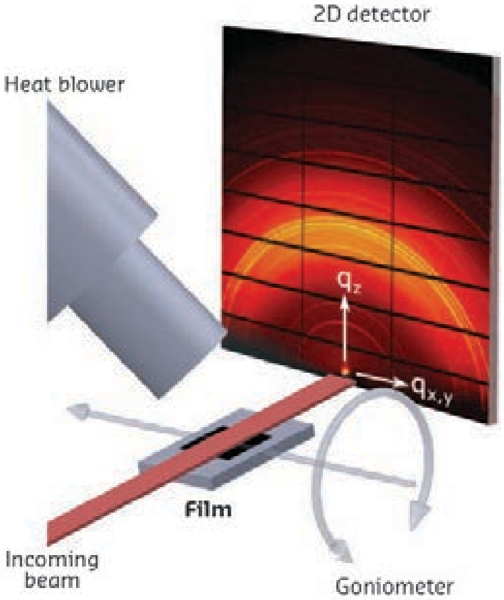

Fig. 161: An illustration of the scattering geometry of synchrotron GIWAXS measurements performed on the $CsPb(I_{1-x}Br_x)_3$ thin films. The incident X-ray beam (λ = 0.95774 Å) scatters from the sample under a grazing angle, projecting ring-shaped diffraction signals onto the detector. The frames were collected during temperature treatments with rate of 0.1-0.4 s^{-1}. The temperature on the sample was controlled with a N_2 gas blower.

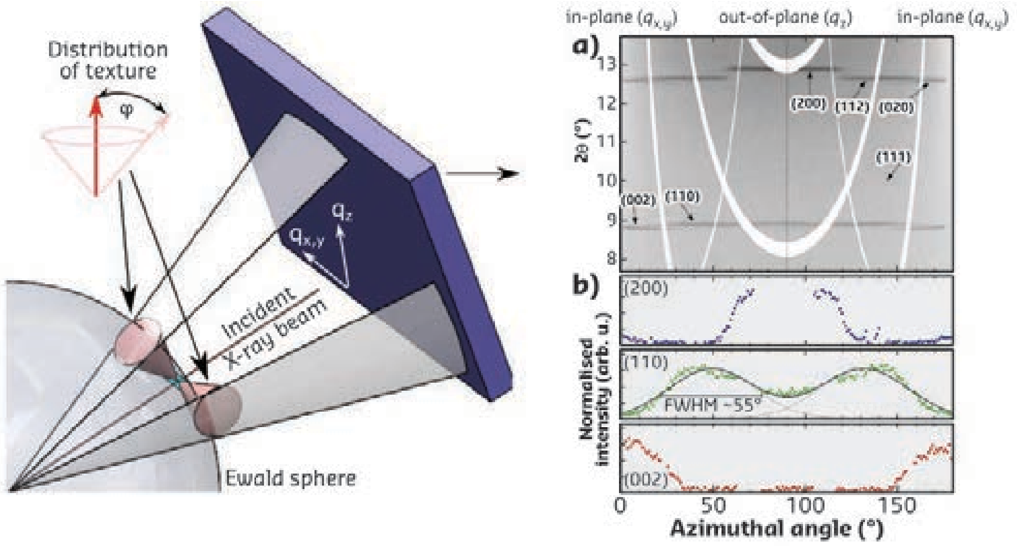

Fig. 162: Left: a schematic illustration of how texture manifests as an anisotropic signal in the GIWAXS data. The two cones depict the relative preferred orientation vectors in and out of the polycrystalline thin film plane. The red vectors trace a texture distribution, defined by the mean-square deviation ϕ. As such, when the Ewald sphere touches the vectors, the diffraction conditions are fulfilled and generate a Bragg intensity. With $\phi > 0$ (zero being a single crystal system), the interception of the cones in the sphere forms diffraction arcs, which are projected onto the detector plane. Right: ***a)*** A 2D intensity image of the thermally quenched strained black $\mathrm{CsPb(I_{1-x}Br_x)_3}$ thin film covering the low angle diffraction rings, as a linear function of the azimuthal angle. **b)** Normalised intensity profiles of the (200), (110) and (002) Bragg lines found in ***(a)***, as a function of the azimuthal angle. A double Gaussian peak fit has been applied to the (110) intensity, showing bi-modal peaks nearing 45° and 135°, with a full-width half maxima of approximately 55°. This width distribution directly reflects the texture distribution parameter ϕ.

impractical for use. For example, at ambient conditions, cesium lead triiodide (and its Br-doped analogue, $\mathrm{CsPb(I_{1-x}Br_x)_3}$) forms a non-perovskite crystal structure that is unsuitable for use in optoelectronic devices such as solar cells. The perovskite phase that would serve for photovoltaic applications forms only at high temperatures. The challenge, then, is to find a way to stabilise the $\mathrm{CsPb(I_{1-x}Br_x)_3}$ perovskite structure at room temperature.

A hint was given by a grazing-incidence wide-angle X-ray scattering (GIWAXS) experiment with a $\mathrm{CsPb(I_{1-x}Br_x)_3}$ thin film at beamline **BM01** (**Figure 161**). The bright synchrotron radiation, the ability to manipulate the X-ray energy (that was set below Pb L-edges), the fast noise-free pixel area detector and the locally developed software for processing and analysis of large volumes of diffraction data made it possible to uncover a new way to manipulate the structural stability of the photovoltaic thin film.

The experiment showed formation of a strong texture in the polycrystalline thin film indicating an anisotropic orientational distribution of $\mathrm{CsPb(I_{1-x}Br_x)_3}$ crystallines (**Figure 162**). Temperature-dependent measurements showed that the difference in thermal expansion coefficients of the film and the substrate induces an anisotropic strain state. The strain stabilises the desired perovskite structure at room temperature, while removing the interface destabilises it back to the useless non-perovskite structure. This result was rationalised with *ab-initio* thermodynamic modeling. Altogether, the experimental and theoretical findings offer a new tool to manipulate the stability of photovoltaic films by carrying out strain engineering based on the difference in thermal expansion between the film and the substrate in highly textured thin films. The further development of this new tool could strongly benefit from *in-situ* synchrotron diffraction experiments with real-world photovoltaic devices.

PRINCIPAL PUBLICATION AND AUTHORS

Thermal unequilibrium of strained black CsPbI3 thin films, J. A. Steele (a), H. Jin (a), I. Dovgaliuk (b), R. F. Berger (c), T. Braeckevelt (d), H. Yuan (a,e), C. Martin (a,f), E. Solano (g), K. Lejaeghere (d), S. M. J. Rogge (d), C. Notebaert (a), W. Vandezande (a), K. P. Janssen (a), B. Goderis (a), E. Debroye (a), Y. Wang (e), Y. Dong (e), D. Ma (e), M. Saidaminov (e), H. Tan (e,h), Z. Lu (e), V. Dyadkin (b), D. Chernyshov (b), V. Van Speybroeck (d), E. H. Sargent (e), J. Hofkens (a) and M. B. Roeffaers (a), *Science* **365**, 679-684 (2019); doi: 10.1126/science.aax3878.
(a) KU Leuven (Belgium)
(b) ESRF
(c) Western Washington University, Bellingham (USA)
(d) Ghent University, Zwijnaarde (Belgium)
(e) University of Toronto, Ontario (Canada)
(f) Universidad de Castilla-La Mancha, Albacete (Spain)
(g) ALBA Synchrotron Light Source, Cerdanyola del Vallès, Barcelona (Spain)
(h) Nanjing University, Jiangsu (China)

DEVELOPING BIOMIMETIC SMALL-DIAMETRE VASCULAR GRAFTS

A hybrid fabrication process was used to generate two-layered vascular grafts. The scaffolds were seeded with cells and tested *in vitro*. The experiments showed that the grafts guided the cells in a physiological tissue-like organisation. Synchrotron sub-micrometre computed tomography (sub-µCT) measurements revealed the porosity of the scaffold area acting as a barrier between the layers.

Mammalian blood vessels are highly adapted tissues that, depending on their specific functions, occur in a variety of sizes and shapes. Generally, they exhibit a hierarchical composition with concentric layers of cells and matrix material. The two most important layers are the *tunica intima*, the layer that is in direct contact with the blood, and the *media* surrounding this *intima*. The *intima* is covered with a monolayer of endothelial cells that prevent agglomeration of blood components and ensure uninterrupted blood flow. The *media* contains collagen fibres and smooth muscle cells that are oriented in a helical manner, assuring the mechanical properties of the vessel. If the vasculature is damaged beyond natural repair, vessels need to be replaced. The gold standard in clinics is to use the patient's own healthy vessels as replacement; however, this is limited to availability, generating a need for synthetic grafts. Replacement of blood vessels with diametres smaller than six millimetres with synthetic grafts is challenging, as they are prone to post-operation occlusion and thrombosis.

To address this need, a novel fabrication technique to make two-layered small-diametre tubular constructs was developed. The grafts were designed so that they can be seeded with cells after fabrication (**Figure 163**). The *intima* was prepared by solution electrospinning (SES), where high voltage is used to generate a jet of material from a polymer solution. On its way to the collector, the jet undergoes instabilities, resulting in random fibre orientations. With SES, mats of thin polymeric fibres can be fabricated from biodegradable polymers like the clinically applicable poly(ε-caprolactone), and tubular constructs can be achieved by using cylindrical collectors. The small fibre diametres result in small pores, proven to prevent undesired cell invasion. This dense mesh presents a good surface for endothelial cell adherence and assures the development of an endothelial monolayer on the inside of the tube.

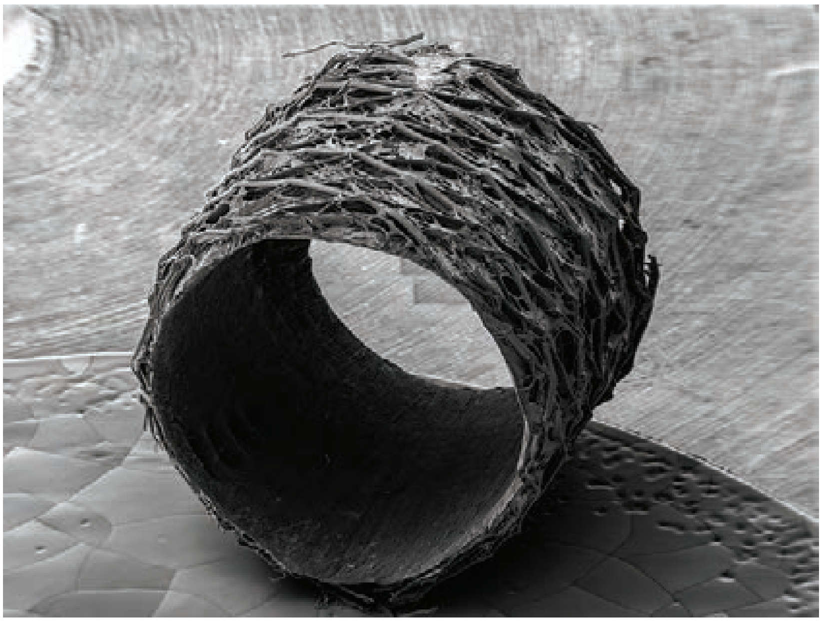

Fig. 163: Electron microscopy image of a section of a cell-seeded scaffold after fixation. The inner diametre of the tube is 3 mm.

The *media* was manufactured using a 3D-printing approach called Melt Electrowriting (MEW). MEW utilises electrohydrodynamic forces but, in contrast to SES, the polymer is processed as melt, changing the viscoelastic properties of the jet. This helps to prevent instabilities during the stretching process. If the collected polymer solidifies and keeps its shape after deposition, MEW can be used in a direct writing approach with precise control over fibre deposition. Compared to conventional filament-based 3D-printing techniques, the fibre diametres in MEW are much lower – measured at 15.2±4.8 µm in this study. The fibres were collected around the SES mats in a helical orientation and the scaffolds were seeded with stromal cells, which can differentiate into smooth muscle cells. The MEW fibres guided cellular orientation similar to native blood vessels, and the layer enabled a faster proliferation and colonisation of the outer part of the scaffold.

Seeding the scaffolds with both cell types was also demonstrated. These co-culture conditions put a special demand on the barrier between the cell types. It needs to enable communication between the cells and, at the same time, assure attachment but prevent mixing of the cell types. The key to overcoming these challenges was choosing the right porosity of the SES layer. To get a clearer idea of the SES layer, composed of fibres with diametres of 1.4±0.2 μm, the scaffolds were analysed using sub-micrometre computed tomography (sub-μCT) at beamline **ID19**, with a voxel size of 0.16 μm. In combination with adapted CT data processing **[1]**, the measurements helped reveal that the porosity of the SES layer was around 80±5%. The resolution of sub-μCT analysis showed that the SES layer had a denser region on the luminal side and a less dense region on the outside, as depicted in **Figure 164**. This finding helped in developing the biomimetic scaffolds and improved its function without disabling the crosstalk between the cell types.

This proof-of-principle study demonstrates how automated processes can help in designing cell-guiding scaffolds, and how advanced analysis of the inner scaffold architecture on a sub-micrometre level reveals details that could not be detected with other methods.

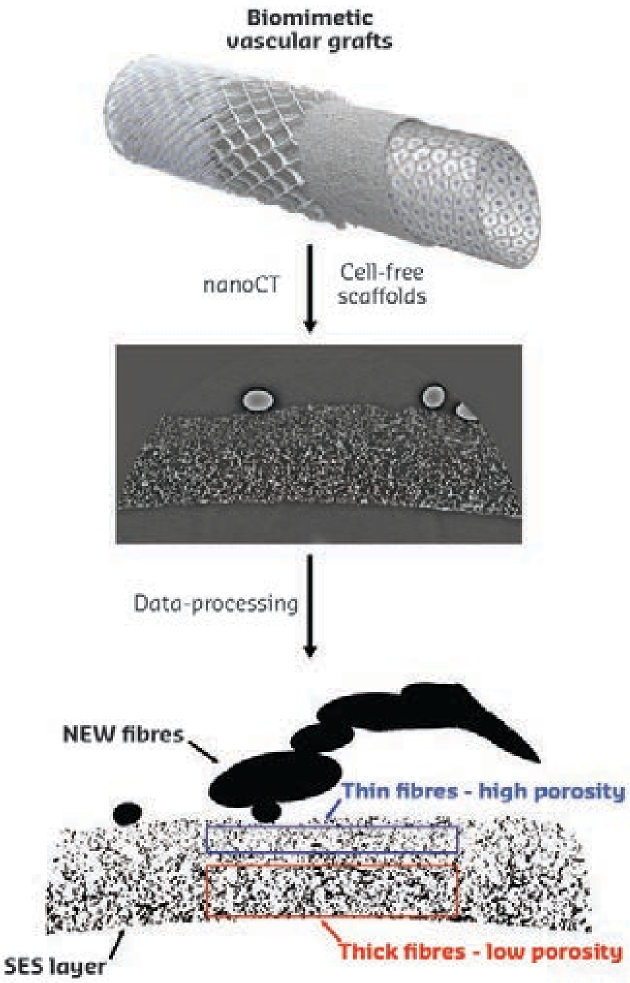

Fig. 164: Porosity determination of vascular grafts.

PRINCIPAL PUBLICATION AND AUTHORS

Heterotypic Scaffold Design Orchestrates Primary Cell Organization and Phenotypes in Cocultured Small Diameter Vascular Grafts, T. Jungst (a), I. Pennings (b), M. Schmitz (a), A. J. Rosenberg (b), D. Gawlitta (b) and J. Groll (a), *Adv. Funct. Mater.* **29**(43), 1905987 (2019); doi: 10.1002/adfm.201905987.
(a) Department for Functional Materials in Medicine and Dentistry, and Bavarian Polymer institute, University of Würzburg (Germany)
(b) Department of Oral and Maxillofacial Surgery & Special Dental Care, UMC Utrecht (Netherlands)

REFERENCES

[1] A. Youssef *et al., Tissue Eng. Part C: Methods* **25**(6), 367-379 (2019).

PEROVSKITE-POLYMER BULK HETEROSTRUCTURES FOR EFFICIENT LIGHT-EMITTING DIODES

Since the demonstration of bright perovskite-based light-emitting diodes (LEDs) [1], much work has gone into improving LED efficiency. By 2018, the external electroluminescence efficiency was improved from ~1% to 12% [2]. This study reports the improvement of the external electroluminescence efficiencies to >20% through the complete elimination of non-radiative decay processes.

In this work, perovskite-polymer (poly-HEMA) bulk heterostructures (PPBH) with photoluminescence quantum yields of up to 96% are demonstrated. Importantly, a record-breaking external electroluminescence efficiency of more than 20% was achieved in LEDs based on perovskite-polymer materials. The emissive heterostructures were prepared from a combination of quasi-2D/3D perovskites and a wide optical gap polymer, poly-HEMA. The absorption profile of the PPBH contains a distinct excitonic peak at ~575 nm, corresponding to quasi-2D perovskite with a formula of $(NMA)_2(FA)_{m-1}Pb_mI_{3m+1}$ with m = 2 (**Figure 165a**). The absorption tail of the PPBH sample extends to ~800 nm, which is attributed

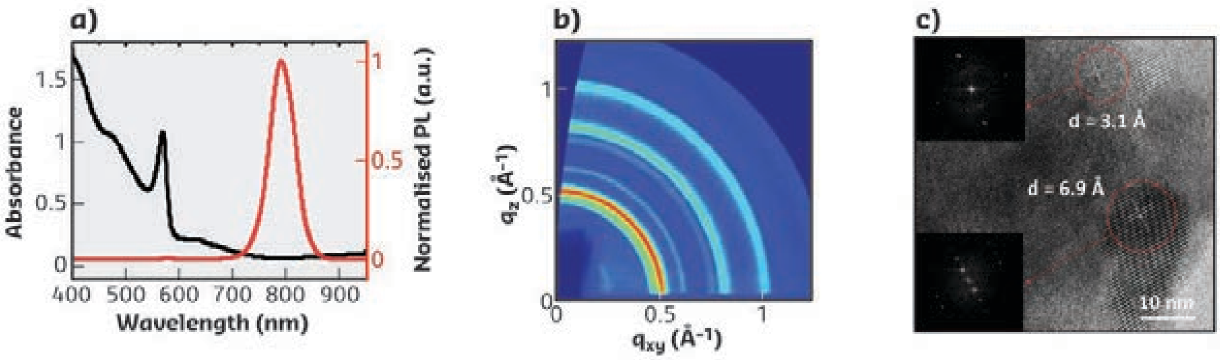

Fig. 165: a) Absorbance (black) and PL (red) spectra of a PPBH film on fused silica. **b)** GIWAXS patterns of a PPBH layer deposited on silicon. **c)** HR-TEM image of a PPBH film. Insets show the fast Fourier transforms of the crystalline regions, exhibiting quasi-2D and 3D structures.

to the quasi-3D phase. The photoluminescence (PL) spectrum of the sample peaks at ~795 nm (~1.56 eV), with a full-width-at-half-maximum (FWHM) of ~55 nm. Grazing-incidence wide-angle X-ray scattering (GIWAXS) measurements carried out at beamline **BM28** indicate that the perovskite crystallites are isotropically oriented in the PPBH film (**Figure 165b**). High-resolution transmission electron microscopy (HR-TEM) results suggest the presence of quasi-2D and 3D crystal structures (**Figure 165c**).

To investigate the electroluminescence (EL) properties of the PPBH, a solution-processed multilayer LED structure was developed: ITO/MZO (magnesium-alloyed zinc oxide)/PEIE/PPBH/TFB-PFO/MoO_x/Au. The peak external quantum efficiency (EQE) of the best devices reached 20.1% (**Figure 166a**), representing a record for perovskite-based LEDs. The angle-dependent EL intensities exhibit a Lambertian profile, allowing accurate estimation of EQEs. The efficiencies of these perovskite-based LEDs are on par with those of the best OLEDs **[3-5]** and quantum-dot (QD) LEDs **[6]**. In addition, a thorough investigation of the light emission process was carried out, using ultrafast transient luminescence and absorption spectroscopy. The ultrafast spectroscopic results reveal that upon excitation, photogenerated excitons at the quasi-2D perovskite component rapidly migrate to low-energy sites within 1 ps. Transient absorption (TA) experiments (**Figure 166b**) confirm that the initial photoexcitation is formed on the quasi-2D perovskite, with a ground-state bleach (GSB) peak at ~575 nm. The peak position is in agreement with the steady-state absorption and transient PL measurements. The GSB feature related to the bi-layer quasi-2D perovskite has an exciton-like character, suggesting the electron-hole pair created in the material is initially bound. As the 575-nm GSB quickly decays, a red-shifting, broad GSB signal rises rapidly and then declines after 10 ps. Coupled with the high photoluminescence yield and negligible luminescence quenching at the interfaces, non-radiative pathways were found to be effectively eliminated.

Furthermore, conventional optical models indicate that the high electroluminescence efficiencies achieved benefit from the reduced effective refractive index, which improves the optical coupling from the emissive layers. The

Fig. 166: a) EQE–current density characteristics of the best PPBH LED (peak EQE = 20.1%) and peak EQE statistics (inset). **b)** Transient absorption (TA) spectra of the sample. The excitation fluence for the TA measurement was 16 μJ cm^{-2}.

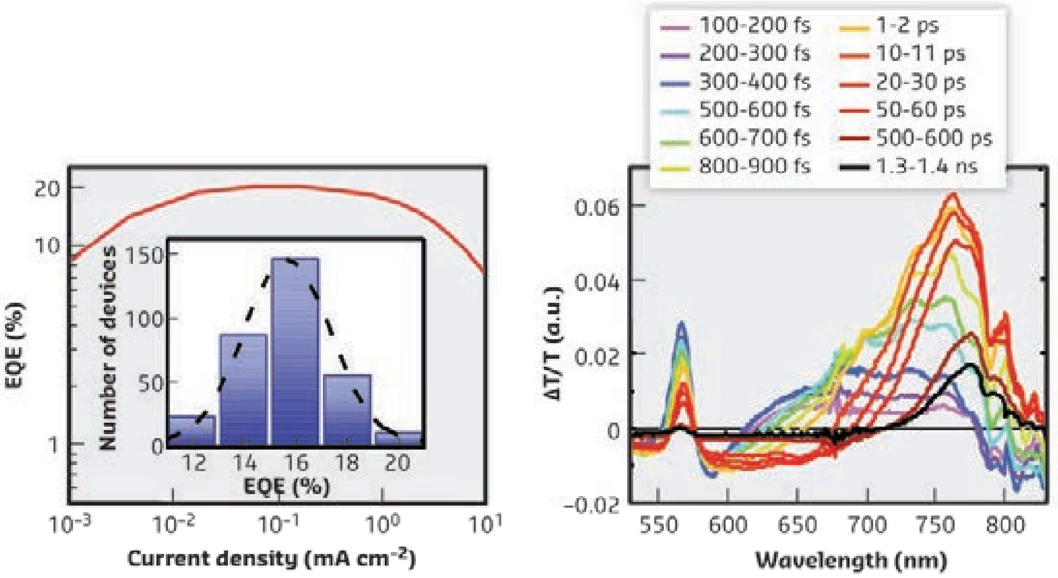

20% external electroluminescence efficiency is further supported by ~100% internal electroluminescence efficiency from modelling. The rapid energy migration, the effective suppression of non-radiative events and the reduced effective refractive index lead to the high efficiency of perovskite-polymer bulk heterostructure LEDs.

PRINCIPAL PUBLICATION AND AUTHORS

High-efficiency perovskite–polymer bulk heterostructure light-emitting diodes, B. Zhao (a), S. Bai (b,c), V. Kim (a), R. Lamboll (a), R. Shivanna (a), F. Auras (a), J. M. Richter (a), L. Yang (a,d), L. Dai (a), M. Alsari (a), X.-J. She (a), L. Liang (e), J. Zhang (a), S. Lilliu (f,g), P. Gao (e), H. J. Snaith (b), J. Wang (h), N. C. Greenham (a), R. H. Friend (a) and D. Di (a), *Nat. Photonics* **12**, 783-789 (2018); doi: 10.1038/s41566-018-0283-4.

(a) Cavendish Laboratory, University of Cambridge (UK)
(b) Department of Physics, University of Oxford (UK)
(c) Department of Physics, Chemistry and Biology (IFM), Linköping University (Sweden)
*(d) Institute of Materials Research and Engineering (IMRE), Agency for Science, Technology and Research (A*STAR) (Singapore)*
(e) Laboratory of Advanced Functional Materials, Xiamen Institute of Rare Earth Materials, Haixi Institute, Chinese Academy of Sciences (China)
(f) Department of Physics and Astronomy, University of Sheffield (UK)
(g) The UAE Centre for Crystallography (United Arab Emirates)
(h) Institute of Advanced Materials (IAM), Nanjing Tech University (China)

REFERENCES

[1] Z.-K. Tan *et al., Nat. Nanotechnol*. **9**, 687-692 (2014).
[2] N. Wang *et al., Nat. Photonics* **10**, 699-704 (2016).
[3] S. Reineke *et al., Nature* **459**, 234-238 (2009).
[4] H. Uoyama *et al., Nature* **492**, 234-238 (2012).
[5] D. Di *et al., Science* **356**, 159-163 (2017).
[6] X. Dai *et al., Nature* **515**, 96-99 (2014).

INDUSTRIAL RESEARCH


HUBER
HUBER

INDUSTRIAL RESEARCH

The ESRF user programme has been paused during 2019 for the installation of the Extremely Brilliant Source (EBS), however, we have been delighted to see several commercial clients using the specialised laboratory facilities available onsite. The articles in this chapter demonstrate once again the value and utility of the ESRF's X-ray beams for industrial research and development, from designing the next generation of fuel cells (**page 166**) and high-performance industrial catalysts (**page 167**) to engineering new materials (**page 168**) and improving image sensors (**page 171**) – not forgetting innovations in the healthcare and pharmaceutical sectors (**page 170**), including investigating new treatments for asthma (**page 169**).

Meanwhile, the Business Development Office (BDO) has been as busy as ever. Work has continued in our manufacture-and-sale of high-performance synchrotron instrumentation, where ESRF technology is demanded by clients around the world. This covers a range of products and manufacturing of specialised equipment, such as detectors, where a transfer of technology to a commercial provider would not be suitable. Our efforts allow ESRF technology to be shared with other light sources.

European grants

The BDO has coordinated the preparation of two European Commission Research and Innovation programme headline grants, succeeding in obtaining Horizon 2020 funding for the ESRF. The first, InnovaXN (www.innovaxn.eu), is a Marie Skłodowska-Curie Action (MSCA) COFUND programme to support 40 PhD students working on projects driven by industrial R&D needs, in collaboration with the ESRF and the ILL. The first set of 20 R&D projects has been selected, with many exploiting both the ESRF's synchrotron X-rays and the ILL's neutron beams. The InnovaXN programme builds on the recommendations of the ESFRI Innovation Working Group Report (March 2016). This report highlights the challenges to overcome for European research infrastructures (RIs) and industry to better work together and calls for the "*training of a new generation of engineers in industry more aware of science and RIs, as well as training of a new generation of researchers, more receptive to industry needs*". InnovaXN is setting out to nurture the next generation of researchers – able to exploit large-scale RIs while being comfortable with the commercial world.

The second, STREAMLINE, is a Horizon2020 programme with a 5M€ budget and aims to ensure the ESRF's sustainability in light of the new scientific and experimental capabilities provided by the ESRF-EBS upgrade. STREAMLINE will make key updates to the facility's scientific strategy, renew its business plan and revisit access modes, creating a new service package for the benefit of both academia and industry. An essential part of STREAMLINE is training and encouraging users to exploit new opportunities, including new experiments and higher throughput (more samples and users, creating more data), which will challenge the existing operational models of the ESRF. A particular target stakeholder group of STREAMLINE is European industry. The project tasks include developing new services for this community, though accessible also to academics, aiming to allow a wider industrial researcher base to take advantage of the powerful synchrotron X-ray beams available at the ESRF.

The BDO team is also active in further grants, including TeesMAT and ENRIITC, both of which obtained funding during 2019. TeesMAT (www.teesmat.eu) is an Open Innovation Test Bed for Electrochemical Energy Storage Materials that has been funded with 9.5M€ via Horizon2020, coordinated by CEA-LITEN. Bringing together 10 academic and 10 industrial partners, TeesMAT will pool techniques in the field of batteries. Within TeesMAT, the ESRF is leading a work package on the development and validation of novel industrially relevant techniques.

ENRIITC is a further Horizon2020 proposal, coordinated by the European Spallation Source (ESS), in which the BDO is a work package leader. The proposal supports development of a pan-European Industrial Liaison and Contact Officer (ILO and ICO) network, largely focused upon facilities on the ESFRI Landmark roadmap, which will act as multipliers to the wider community, enabling all interested parties to participate. The project will begin in January 2020 with 2M€ of funding. ENRIITC will build and consolidate best practices of industrial engagement and pilot activities in training and combined outreach and brokerage towards European industry.

An ongoing project to build an active single-entry point for characterisation needs in the microelectronics industry is part of the IRT NanoElec (www.irtnanoelec.fr), now moving into its second phase of work. An extension of the ESRF's activities (with our partners ILL, CEA-LETI, LPSC, and ST Microelectronics, Schneider Electric and SOITEC) under the Characterisation Programme has been approved until December 2020. During this period, aside from the normal ongoing project actions, the programme partners will define a detailed work programme for the 2021-2025 phase. In particular, this work will set the case for a few priority actions focused around the irradiation hardness of electronic components.

Exporting GIANT globally

As we move closer to the restart of ESRF user operation, with the new opportunities to be afforded by the EBS, the BDO remains very much focused on outreach to industry, at events, with visits and in B2B within our innovation ecosystem, both geographically near to Grenoble but also further afield in the ESRF member countries. Grenoble is a technology hub and the Grenoble Innovation Campus, GIANT, is a central engine, with impact locally, nationally and internationally. Drawing upon this, the ESRF, with our GIANT partners, has been participating in outreach towards industry in sectors most relevant to the activities across the Innovation Campus. Earlier in 2019, GIANT was present at the Electric Vehicle Symposium in Lyon, France, and at the Battery Technology Show in Coventry, UK. The aim was to promote GIANT's capacities, skills and facilities for battery research to an audience that perhaps is not readily aware of (in our case) the application of synchrotron X-rays for battery R&D. Similarly, GIANT attended the strategically important healthcare innovation Biopole annual networking day in Lyon, France, with the ambition to highlight the role of the Innovation Campus, with its international large-scale facilities in biotech and medtech research.

As we continue the build-up towards the restart, the BDO team is already well into our 2020 outreach planning. So look out for us at events across Europe – as GIANT and as the ESRF! We will be more than pleased to visit your company to listen to your R&D challenges and to explain how the ESRF's synchrotron X-rays can help.

E. MITCHELL

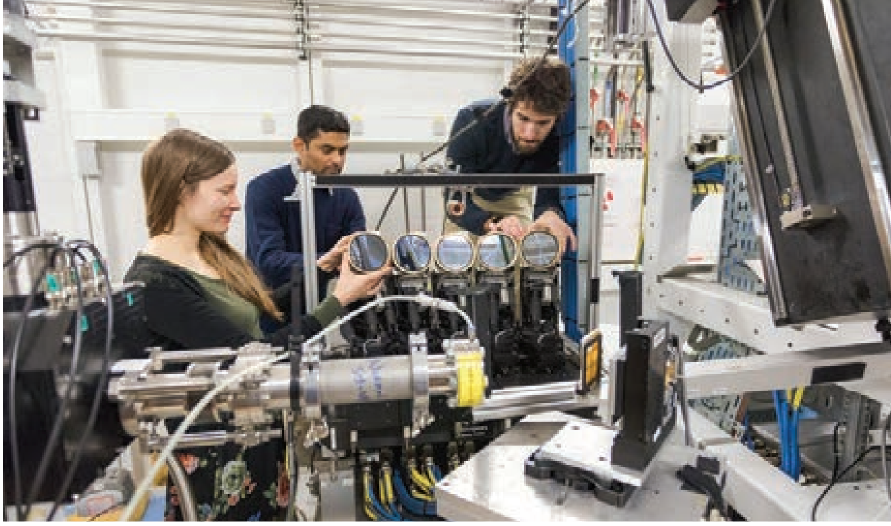

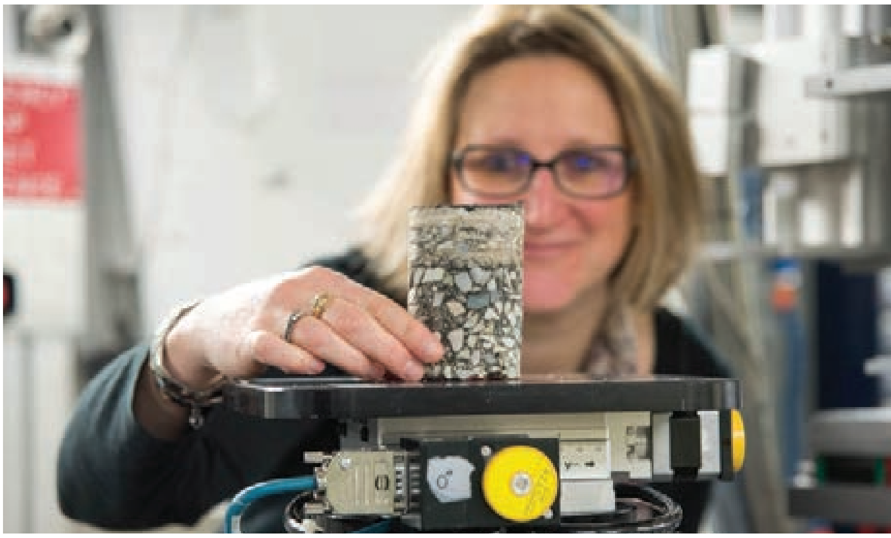

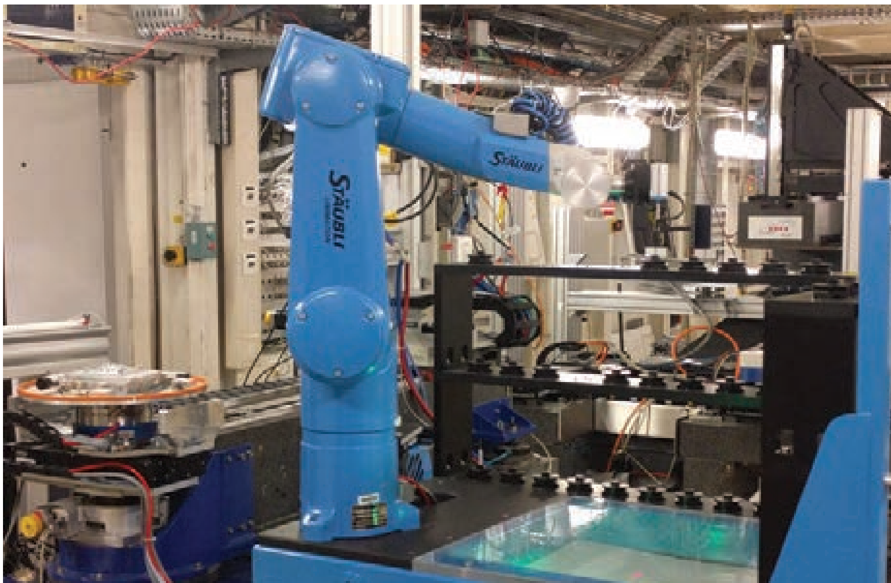

INDUSTRIAL RESEARCH ON THE BEAMLINES

Due to its proprietary nature, much of the commercial research carried out by industry at the ESRF cannot be disclosed. However, sometimes companies authorise the ESRF to discuss their work and they may even publish results or access the ESRF via the public programme. Below are a few examples from 2019.

REAL-TIME CHARACTERISATION OF CERAMIC FUEL CELLS USING XRD-CT

Ceramic fuel cells are considered one of the most promising technologies for sustainable energy generation thanks to their higher efficiency and fuel flexibility that allows for hydrocarbon utilisation such as methane. X-ray diffraction computed tomography (XRD-CT) is used to investigate a new design for the next generation of fuel cells.

Ceramic fuel cells are used in a wide range of applications but the technology still has a long way to go in terms of volumetric power output, long-term stability and cost. A team from Imperial College London has developed a new conceptual fuel cell design to tackle current limitations. By efficiently miniaturising the cell diameter down to the millimetre scale, the design is estimated to produce a volumetric power density exceeding 10 W cm^{-3} – a performance superior to the best planar cells.

Along with University College London and Finden Ltd, UK, the team performed real-time characterisation of the cell on beamline ID15A. XRD-CT was applied for the first time on a complete cell, demonstrating the excellent chemical/structural integrity the new design possessed during thermal cycling (**Figure 167**). Future chemical imaging will benefit from a giant leap forward with the increased photon flux provided by EBS.

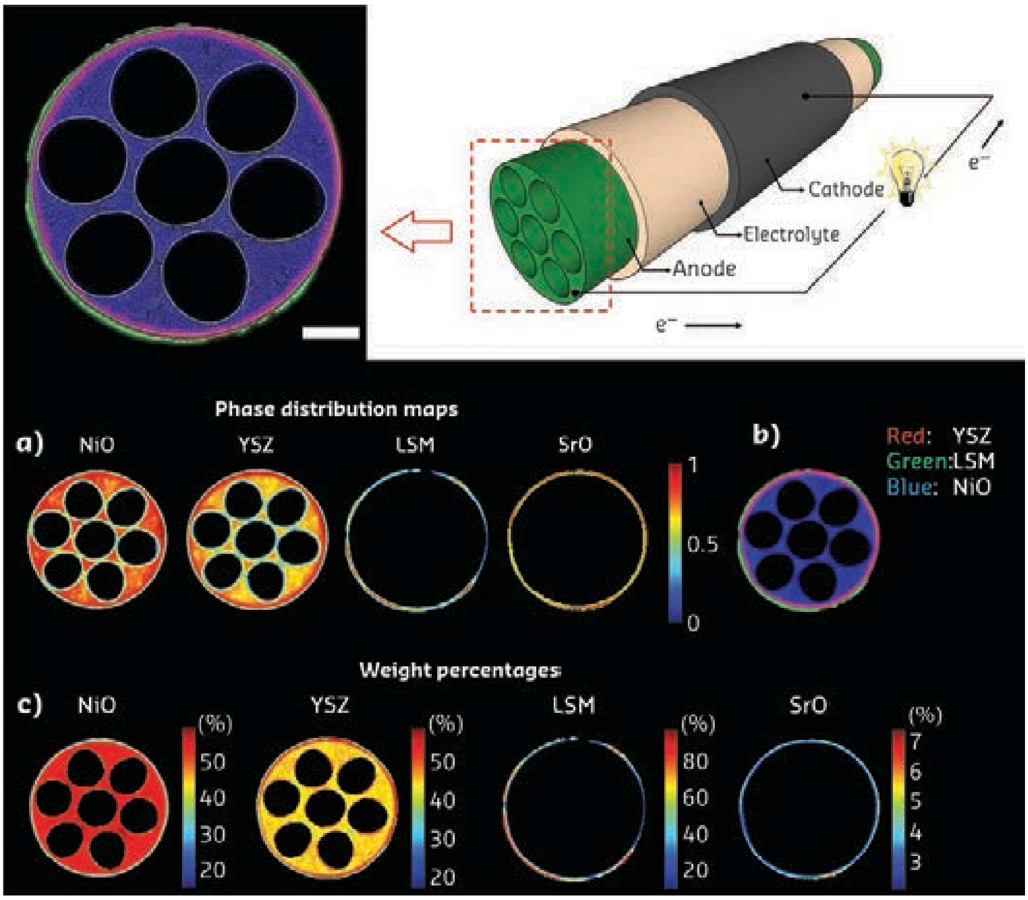

Fig. 167: XRD-CT of the fresh solid oxide fuel cell. **a)** The phase distribution maps of NiO, YSZ, LSM and SrO as derived from the Rietveld analysis of the fresh SOFC XRD-CT datasets (colour bar indicates intensity in arbitrary units). **b)** Red green blue (RGB) Image showing the distribution of YSZ (red), LSM (green) and NiO (blue). **c)** Weight % of all crystalline phases present in the SOFC. Scale bar corresponds to 0.5 mm.

PRINCIPAL PUBLICATION AND AUTHORS

Design of next-generation ceramic fuel cells and real-time characterization with synchrotron X-ray diffraction computed tomography, T. Li *et al.*, *Nat. Commun.* **10**, 1497 (2019); doi: 10.1038/s41467-019-09427-z.

FOLLOWING THE DYNAMIC BEHAVIOUR OF PLATINUM NANOPARTICLES IN HYDROGENATION CATALYSTS UNDER REACTION CONDITIONS

Pt-based heterogeneous catalysts are employed in many industrial processes involving hydrogen, ensuring high selectivity and conversion at relatively mild operating conditions. Being able to follow the dynamic behaviour of the Pt clusters under reaction conditions with synchrotron characterisation techniques is key for designing increasingly potent catalysts.

Pt-based heterogeneous catalysts play a fundamental role in the production of bulk and specialty chemicals and in environmental processes. In reaction conditions, Pt nanoparticles undergo electronic and morphological reconstruction, which in turn affects the type and the fraction of the surface Pt-hydrides – the species involved in catalysis.

Chimet S.p.A., a leading company in the field of recovery of precious metals, and a team of researchers from the University of Torino, ILL and ESRF, investigated an industrial Pt/Al_2O_3 catalyst (**Figure 168a**) during a hydrogenation reaction. The combined diffuse reflectance IR Fourier transform, X-ray absorption and mass spectroscopy (DRIFT/XAS/MS) (**Figures 168b-f**) experiment carried out at beamline **BM23** provided vital, industrially relevant information about the surface Pt-hydride species and the morphology of the Pt clusters.

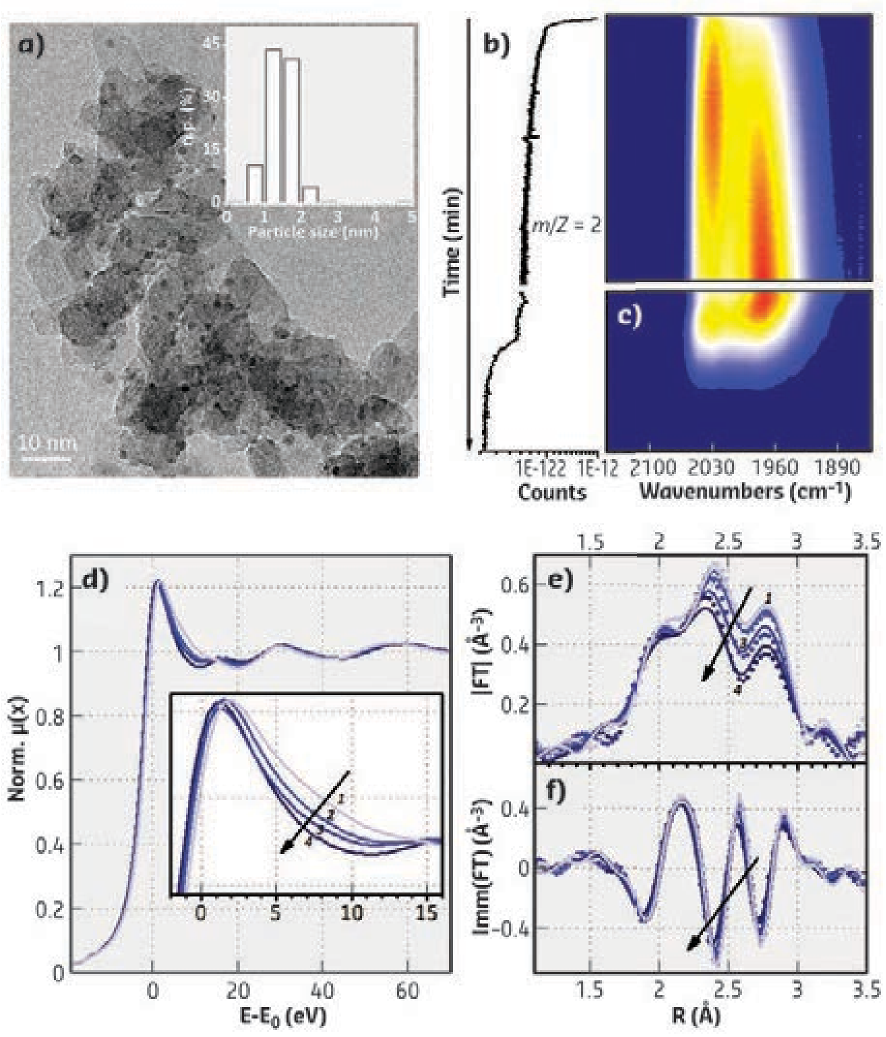

Fig. 168: a) HR-TEM micrograph of the Pt/Al_2O_3 catalyst and corresponding particle size distribution. **b)** Evolution of the signal corresponding to H_2 detected by the mass spectrometer placed at the exit of the reaction cell. **c)** 2D map showing the evolution of the DRIFT spectra as a function of time for the Pt/Al_2O_3 catalyst during dehydrogenation in N_2 flow at 120 °C, for the *operando* DRIFT/XAS/MS experiment. **d-f)** Evolution of the normalised Pt L_3-edge XANES and EXAFS spectra of the Pt/Al_2O_3 catalyst collected simultaneously to the DRIFT spectra in part **(c)**.

PRINCIPAL PUBLICATION AND AUTHORS

Dynamics of Reactive Species and Reactant-Induced Reconstruction of Pt Clusters in Pt/Al_2O_3 Catalysts, M. Carosso *et al., ACS Catal.* **9**(8) 7124-7136 (2019); doi: 10.1021/acscatal.9b02079.

REVEALING SOLUTE-DISLOCATION INTERACTIONS WITHIN EMBEDDED GRAINS DURING RECOVERY ANNEALING

The properties of engineering materials can be improved by optimising the microstructural developments during annealing processes. Dark-field X-ray microscopy (DFXM) was used to investigate the effect of Sn on the recovery annealing of deformed Fe-3%Si alloys, resulting in 3D mapping of orientation and lattice strain within individual grains embedded in bulk samples.

Understanding solute-dislocation interaction is essential for optimising material performance. OCAS (ArcelorMittal), a steel manufacturing company, in collaboration with researchers from France and Denmark, used DFXM at **ID06** to study the effect of Sn solutes in deformed Fe-3%Si alloys during recovery annealing (**Figure 169**).

Figure 169b-c shows the strain and local misorientations in the interior of two embedded grains, within two different samples with and without Sn, as they were mapped during isothermal annealing. The grain with Sn showed ~50% longer relaxation times of the internal stresses during recovery. In accordance with the experimental observations, a kinetic model showed an increase in the dislocation junction strength due to the solute addition, while atomistic modelling demonstrated the solute accumulation around edge dislocations (**Figure 169d**). DFXM provides a direct observation of the evolution of strain fields around dislocation loops, which remain nearly static during recovery due to Sn solute pinning.

These results illustrate the capabilities of DFXM in grain-resolved studies, opening new avenues for the characterisation of highly strained polycrystalline materials.

Fig. 169: ***a)*** DFXM experimental set-up. **b)** Strain evolution of 2D virtual slices of the two grains during annealing. **c)** Local misorientations of virtual slices showing dislocation loops during recovery. **d)** Atomic simulations showing segregation of Sn on dislocations.

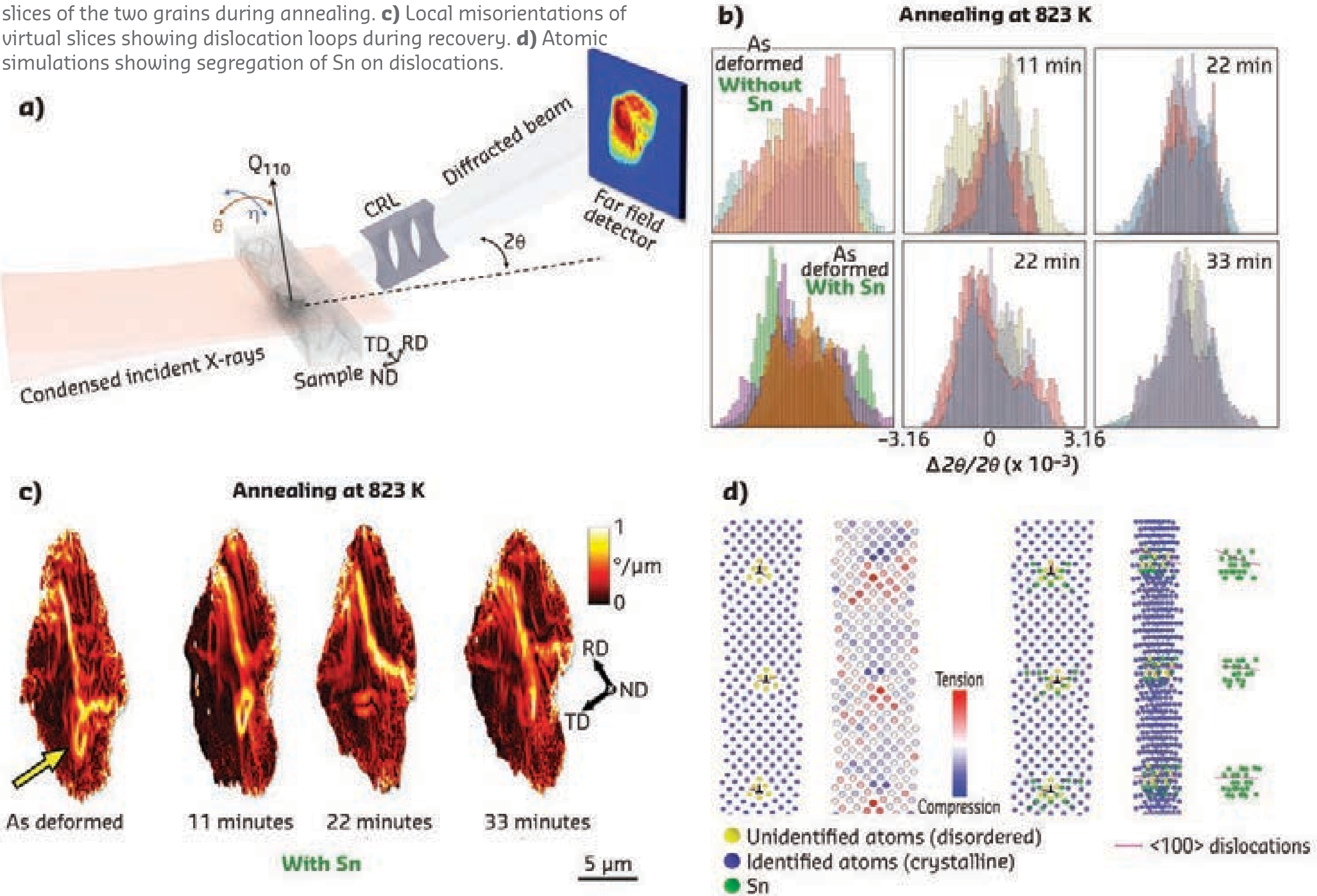

PRINCIPAL PUBLICATION AND AUTHORS

A multi-scale study of the interaction of Sn solutes with dislocations during static recovery in α-Fe, N. Mavrikakis *et al.*, *Acta Mater.* **174**, 92-104 (2019); doi: 10.1016/j.actamat.2019.05.021.

USING MACROMOLECULAR CRYSTALLOGRAPHY TO GUIDE OPTIMISATION OF AN LTC4S INHIBITOR FOR TREATMENT OF ASTHMA

Inhibition of LTC4S, a glutathione transferase central to the production of the cysteine leukotrienes involved in inflammation, bronchoconstriction and pain in asthmatics, could lead to a new and differentiated asthma treatment. Macromolecular crystallography (MX) was used to determine the crystal structure of LTC4S in complex with a candidate inhibitor drug.

Studies show that the cysteine leukotriene cascade remains highly activated in some asthmatics, even those on high-dose inhaled or oral corticosteroids. Hence, inhibition of LTC4S could provide a new treatment for asthma patients with a highly activated cysteine leukotriene cascade. An advanced LTC4S inhibitor, 1, was progressed to preclinical toxicity studies but, due to moderate metabolic stability, transporter interactions, GABA binding and testicular toxicity findings in rats, 1 was not progressed. Further optimisation strongly focused on maintaining high cellular potency while reducing toxicology risks.

As a membrane protein, LTC4S is a challenging target for structure determination. However, a team of researchers from AstraZeneca determined the crystal structure of LTC4S in complex 2, an analog of 1, to 2.35 Å resolution following MX data collection at beamline ID23-1 (**Figure 170**). The structure revealed the binding-mode of 2, enabled structure-based design and guided chemical exploration. Optimising the substitution on the aryl group in the lower part of the pocket, the aliphatic side chain, as well as the ability of the central aryl to form π–π interactions with the enzyme eventually gave AZD9898, which was progressed into clinical studies.

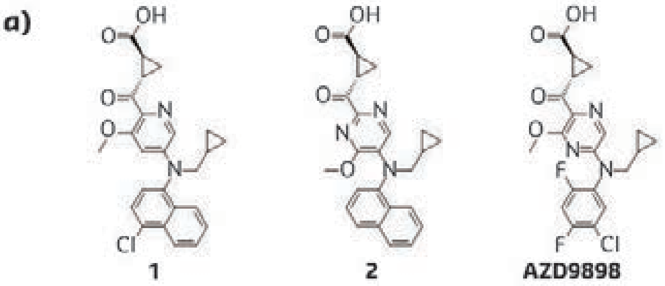

Fig. 170: a) Compounds 1 and 2, and AZD9898. **b)** Compound 2 in complex with LTC4S.

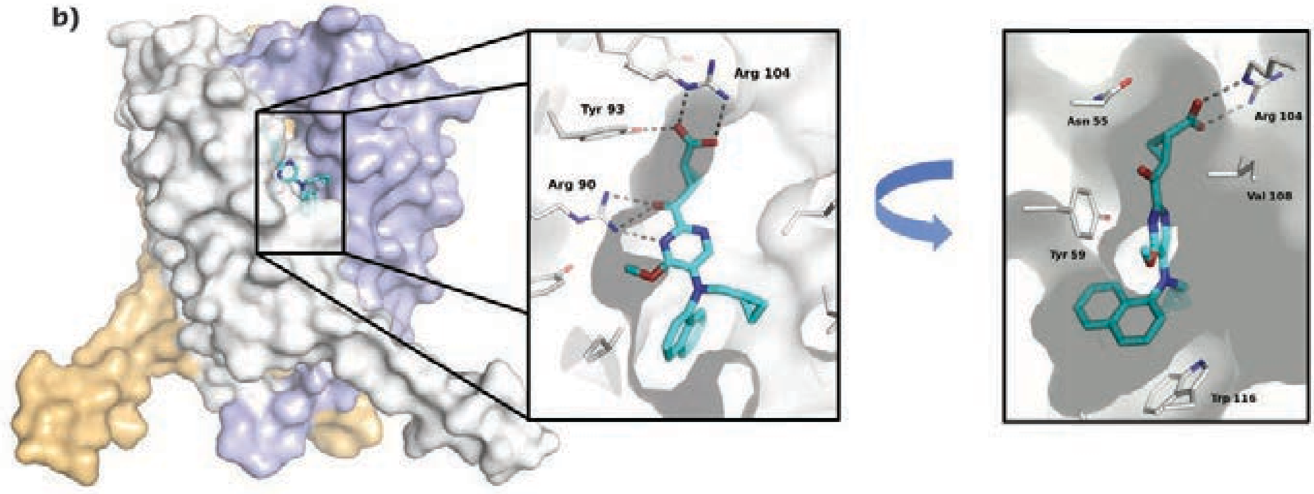

PRINCIPAL PUBLICATION AND AUTHORS

Discovery of the Oral Leukotriene-C4 Synthase Inhibitor (1S,2S)-2-({5-[(5-Chloro-2,4-difluorophenyl)(2-fluoro-2-methylpropyl)amino]-3-methoxypyrazin-2-yl}carbonyl)cyclopropanecarboxylic acid (AZD9898) as a New Treatment for Asthma, M. Munck af Rosenschöld *et al., J. Med. Chem.* **62**(17), 7769-7787 (2019); doi: 10.1021/acs.jmedchem.9b00555.

MAKING THE CRYSTAL STRUCTURE DETERMINATION OF PHARMACEUTICAL SOLIDS MORE STRAIGHTFORWARD

The determination of crystal structures is key for the pharmaceutical industry and, historically, has been provided by single-crystal X-ray diffraction (XRD) data. However, increasing demand to characterise complete series of polymorphs has led to a novel experimental-computational strategy using PXRD to determine the crystal structures of very complex systems.

The determination of crystal structures from powder X-ray diffraction (PXRD) data by using direct-space methods can be significantly limited by the degrees of conformational freedom (DOF). This limit currently lies between 30 and 40 DOF. Consequently, novel approaches are continuously developed to allow an increase in the DOF while keeping computational time realistic.

Scientists from Teva Pharmaceuticals, together with researchers from the Czech Republic, have successfully applied an advanced experimental-computational strategy allowing the crystal structure determination from powder X-ray diffraction (PXRD) data taken at beamline **ID22** of selexipag, a drug for the treatment of pulmonary arterial hypertension (PAH) (**Figure 171**). With 38 DOF, this structure is currently one of the most complex organic molecular structures that has been solved *ab initio* from powder diffraction data.

This should be considered in future as a standard approach for pharmaceutical companies in characterising complex organic molecular structures. The ability to accurately describe all processes that occur in the manufacture and formulation of drugs thus opens a more straightforward way to optimise advanced, highly pharmaceutically active substances.

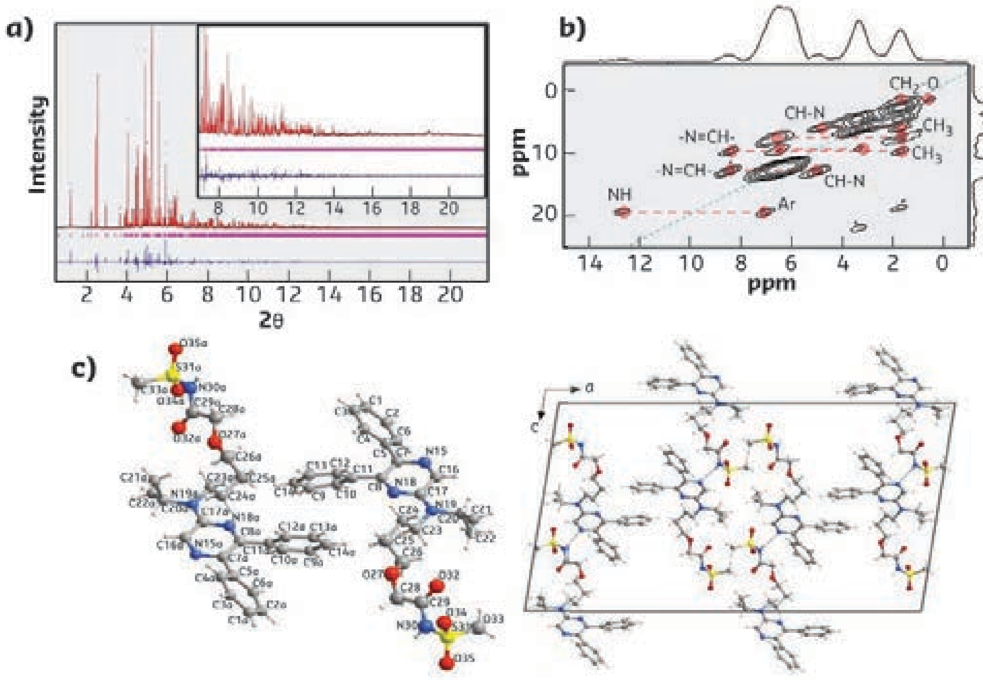

Fig. 171: a) Synchrotron diffraction data. **b)** Solid-state ^1H-^1H MAS NMR correlation spectrum. **c)** Crystal structure of selexipag.

PRINCIPAL PUBLICATION AND AUTHORS

A successful strategy for high degree of freedom crystal structure determination from powder X-ray diffraction data: a case study for selexipag form I with 38 DOF, M. Hušák *et al., Cryst. Growth Des.* 19(8), 4625-4631 (2019); doi: 10.1021/acs.cgd.9b00517.

IMAGING THE DEGRADATION OF INTERCONNECTS IN CMOS IMAGE SENSORS

High-resolution synchrotron tomography has demonstrated a proportionality between electromigration-induced void volume and time-to-failure in interconnects produced for CMOS image sensors. The results could help in designing microelectronics parts that are more reliable.

Researchers from CEA, STMicroelectronics and the Nanoelec Technological Research Institute have carried out an in-depth investigation of the specific reliability of interconnects produced through the hybrid bonding-based semiconductor integration process used in the construction of CMOS image sensors. They needed a non-destructive means to locate and measure voids formed within interconnects. Such voids are evidence of degradation caused by the electromigration effect – the migration of atoms driven by the electric current. The significance of this effect is compounded by the trend of reduction in structure size for more efficient microelectronics and its associated increase in current density.

A test vehicle was fabricated containing 100 linked back-end-of-line (BEoL) interconnects (**Figure 172a**). These interconnects were formed by the direct bonding of two 300 mm patterned wafers, with post-bond anneal applied to strengthen the bonding. The bonded interface, the hybrid bonding metal (HBM), had a dimension of 3.6 microns and each HBM contained 16 hybrid bonding vias (HBVs). The electromigration test involved passing a current through the interconnects until a point of failure was reached, with the failure criterion set to a 10% increase in resistance (this value is indicative for the appearance of voids inactivating some of the HBVs).

Synchrotron-based X-ray phase-contrast nanotomography at beamline ID16A was used to locate the voids formed during electromigration tests and to measure their volume (**Figure 172b**). This technique avoided the complicated sample preparation necessary for other microscopy techniques and provided 3D information, which is preferable to address questions related to voids and porosity in general.

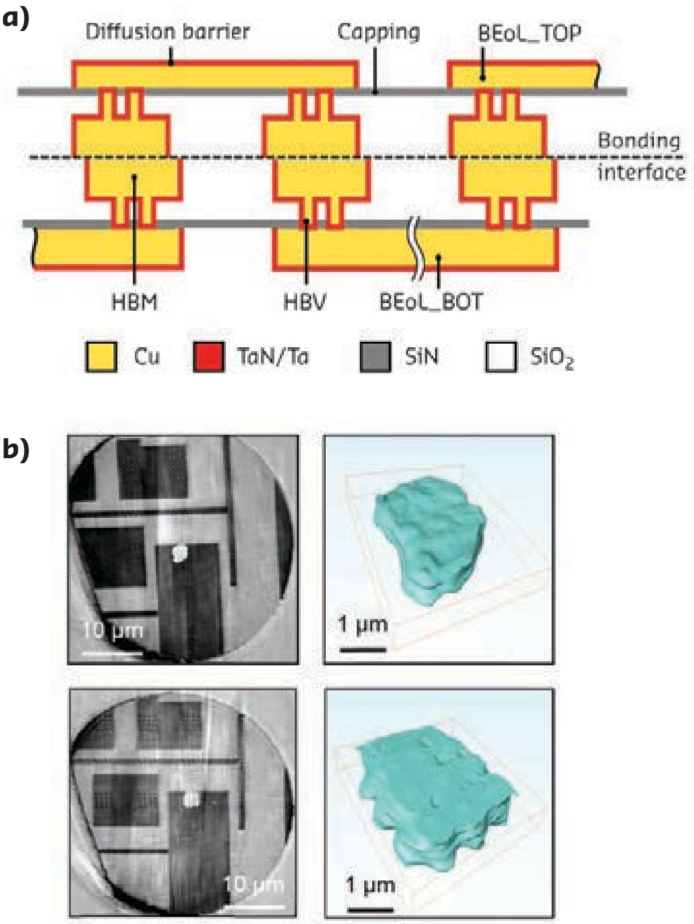

Fig. 172: a) Schematic of the test structure showing its daisy-chain of interconnects. **b)** Illustrative tomography results after an electromigration test (350°C and 20 mA). Above and below, samples with the lowest and highest depleted volumes respectively.

Voids were localised only in the feed line (BEoL_TOP layer) above the via matrix on the anode side confirming that the type of hybrid bonding stack under investigation is immune to electromigration due to its constituent materials. Overall, the experiment demonstrated a linear relationship between electromigration-induced void volumes and time-to-failure in hybrid bonding based test structures.

PRINCIPAL PUBLICATION AND AUTHORS

Correlation Between Electromigration-Related Void Volumes and Time-to-Failure by High Resolution X-Ray Tomography and Modeling, S. Moreau *et al.*, *IEEE Electron Device Letts.* **40**, 11 (2019); doi: 10.1109/LED.2019.2945089.

ENABLING TECHNOLOGIES

ENABLING TECHNOLOGIES

Much of the work of the technical divisions in 2019 focused on the implementation of the Extremely Brilliant Source (EBS). The Technical Infrastructure Division (TID) played a large role in dismantling the third-generation storage ring, preparing the storage ring tunnel for the new machine, managing the intense handling logistics during the entire dismantling and installation phase, installing the vacuum systems, following up the contractors for the cabling and piping installations, and aligning all the components to unprecedented precision. The Instrumentation Services and Development Division (ISDD) continued procurement and development of the optics, detectors, instrumentation and software that will help exploit the new source properties. The successful completion of the dismantling and installation phase demonstrates the extent to which the ESRF is capable of mobilising its teams of experts to accomplish an incredibly complex project within a short time.

With the EBS dismantling and installation phase finished, attention is now turning towards the commissioning of the new accelerator, the restart of all beamlines and, in particular, to the EBS beamline programme. The timely delivery of the infrastructure for the EBS beamlines and refurbishment of many of the other beamlines, followed by the design, procurement and installation of the scientific instrumentation, will be central to the activities of the ISDD and the TID over the coming years. Many of the infrastructure contracts for EBSL3-BM18 and EBSL8-ID29 have already been placed, with the civil works for BM18 well advanced and progressing according to plan and the works for ID29 starting in the Chartreuse Hall. The first article in this chapter outlines the methodology applied for the beamline infrastructure programme, ensuring delivery to specification, on time and within budget (**page 176**), whereas more details on the implementation of the EBS portfolio can be found in the Status of the EBS chapter of the *Highlights* (**page 8**).

The new accelerator complex, the new and refurbished beamlines and new, fast, high-resolution detectors will allow the most advanced experiments to be carried out under ideal experimental conditions. However, this comes at the expense of an exponential increase in the production of data, which need to be annotated, reduced, analysed and archived. The data avalanche is now a common challenge in all large research infrastructures and needs to be addressed urgently to avoid the lack of adequate resources for data management and data analysis decreasing scientific output. The challenge is such that it cannot be addressed in isolation. A collaborative approach, joining forces on a national and European level is required for defining the way forward. We have started putting many of the building blocks into place to implement modern data management and data analysis concepts. This includes the ESRF data policy, the use of innovative technology in the data centre and, foremost, optimised software for data analysis. The PaNOSC project, together with the complementary ExPaNDS project, described in the second article of this chapter (**page 178**), will give a boost to the European Strategy Forum on Research Infrastructures (ESFRI) and national photon and neutron research infrastructures in a coherent approach to data management and data analysis, and will pave the way for much deeper collaboration between the research infrastructures involved. Both projects will also enable interaction with the European Commission to make sure that the voice of our scientific user community is heard and in order for the European Open Science Cloud (EOSC) to develop into something that delivers substantial benefit to our research community. The EOSC intends to allow access to open data, thus also enabling new research by cross-domain use of such data. In this context, the role of research infrastructures is to provide access to open data.

Archiving the data generated by the experiments for future reuse makes sense only if the data is annotated with rich and meaningful metadata. An important component for the metadata capture is an electronic logbook, powerful and flexible enough to capture the activity during and after the experiment. The electronic logbook, described in the third article of this section (**page 179**), is an important part of the implementation of the ESRF data policy and it is part of the implementation road map, which aims to have all ESRF beamlines fully implementing the data policy by the end of 2020.

In addition to the topics presented in the Enabling Technology and Status of the EBS chapters, 2019 has witnessed many important accomplishments and activities in various technological areas, among which we would like to mention specifically:

- The considerable progress in the modelling of the propagation of partially coherent X-rays through imperfect optics (lenses, mirrors, etc.).
- The promising stability improvements achieved in the system performance of the

double-crystal monochromator (DCM) by applying real-time feedback control in scanning mode, and the tendering procedure for two additional complete systems.
- The kick-off for the R&D phase of the XIDER project for the development of a novel 2D detector optimised for high energies and time-resolve experiments, based on a novel concept combining photon counting and charge integration.
- The advances in the high-throughput data acquisition scheme based on the LIMA2 software framework, the RASHPA data transfer architecture and the JUNGFRAU and SMARTPIX detector developments.
- The validation, and purchases of high-performance IT infrastructure components to increase data throughput and data processing capacity.

Last, but not least, we have started to explore and work on the potential of machine learning and artificial intelligence in controls and data analysis. To this aim, a workshop took place on 12 - 14 November 2019, attracting some 160 specialists. The speakers were experts from many labs worldwide and delivered presentations of outstanding quality and depth. The YouTube live transmission of the workshop resulted in more than 2500 connections.

J.-C. BIASCI, R. DIMPER
and C. NEVO

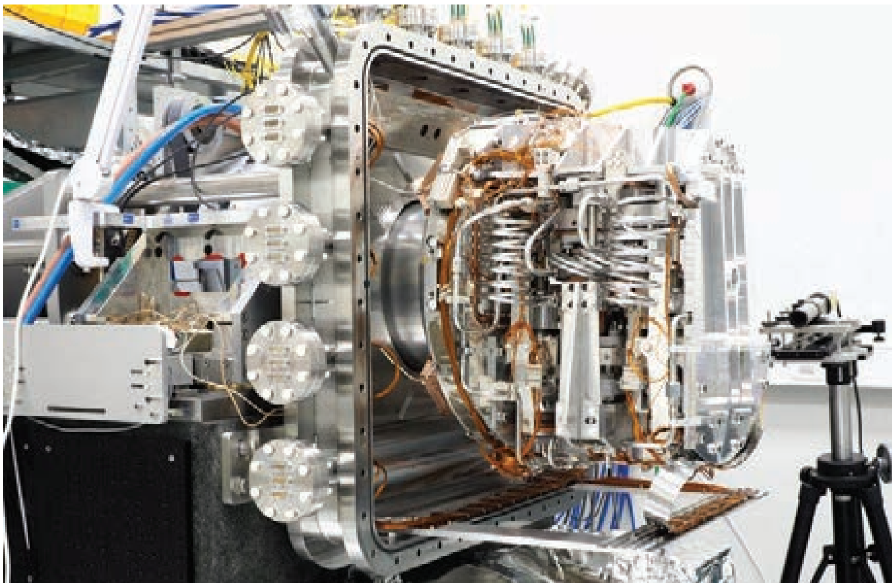

© Robert Baker/ESRF

PROJECT MANAGEMENT OF THE EXTREMELY BRILLIANT SOURCE (EBS) BEAMLINE INFRASTRUCTURE

ESRF beamlines concentrate a large amount of technical infrastructure in a condensed space, giving rise to unique construction challenges. The Technical Infrastructure Division's Buildings & Infrastructure group (TID/BIG) has developed specific project management practices to ensure the efficient implementation of new beamline infrastructure construction projects in the context of EBS.

Four new beamlines will be constructed by the TID/BIG over the period 2020-2022 as part of the EBS upgrade programme, and many others will be rebuilt or refurbished. ESRF beamlines are comprised of one or several optics cabins; an experimental cabin, hosting the sample and detectors; and a control cabin, where the experiment is controlled and data visualised and processed (**Figure 173**).

The optics and experimental cabins are secure areas shielded with lead. Access is strictly controlled via a Personal Safety System (PSS) that automatically stops the beam in case of entry during beamline operation. The cabins also support security systems including an electrical emergency stop system, radioprotection security system, gas content analysis, fire detection system, water leak detection, etc. As well as guaranteeing user safety, the experimental cabin must also provide a technical interface for experiments, ensuring power supply and connections for experimental control systems, data acquisition between external modules, detectors and actuators, cooling systems, gas supply and extraction, etc. These elements are confined in small areas yet optimal conditions should be guaranteed for them to operate correctly, including temperature control, hygrometry, air renewal rate and gas or ozone extraction. The cabins are also equipped with systems to ease maintenance and operation, such as overhead cranes, lifting cranes and false floors to allow access to experimental areas. The ceiling is easily dismountable for handling of experimental equipment. The control cabins are built with dual-skin insulated panels, false ceilings, windows, doors and guard rails, and integrate all the standard facilities for networks, electrical plugs, air conditioning systems, air extraction and fluid distribution.

According to a beamline's requirements, a standard construction typically includes:

- Up to 600 m^2 of lead panels, including walls, floor and ceiling.
- 1500-2200 m of piping for fluid and gas integration, and between 150 and 220 valves.
- 15 000-18 000 m of control cables with 800 to 900 connectors, 4000 m of power cables, 1250 m of cable trays, 250 m of terminal distribution ducts, 60-70 lamps and 250-300 electric plugs.

For the integration of these utilities, the design must take into account several constraints and implementation regulations to optimise installation and provide a simplified distribution of services to users:

- The infrastructure in cabins must be integrated with radioprotection shielding, giving rise to construction, support and access constraints.
- The fluid, electric, gas extraction and air treatment equipment should be installed on a shared mechanical support to optimise the occupied space. Main equipment is installed on support racks independently from the shielded walls.
- These networks should penetrate the cabin through radioprotection chicanes.
- The position and assignment of the electrical network should be carried out according to

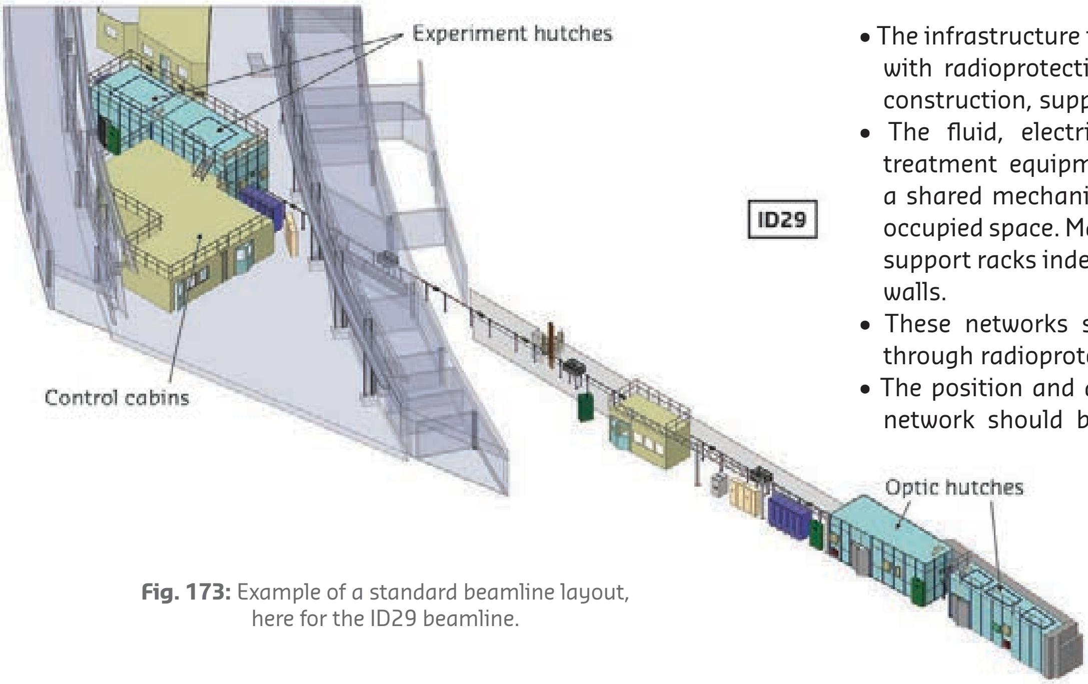

Fig. 173: Example of a standard beamline layout, here for the ID29 beamline.

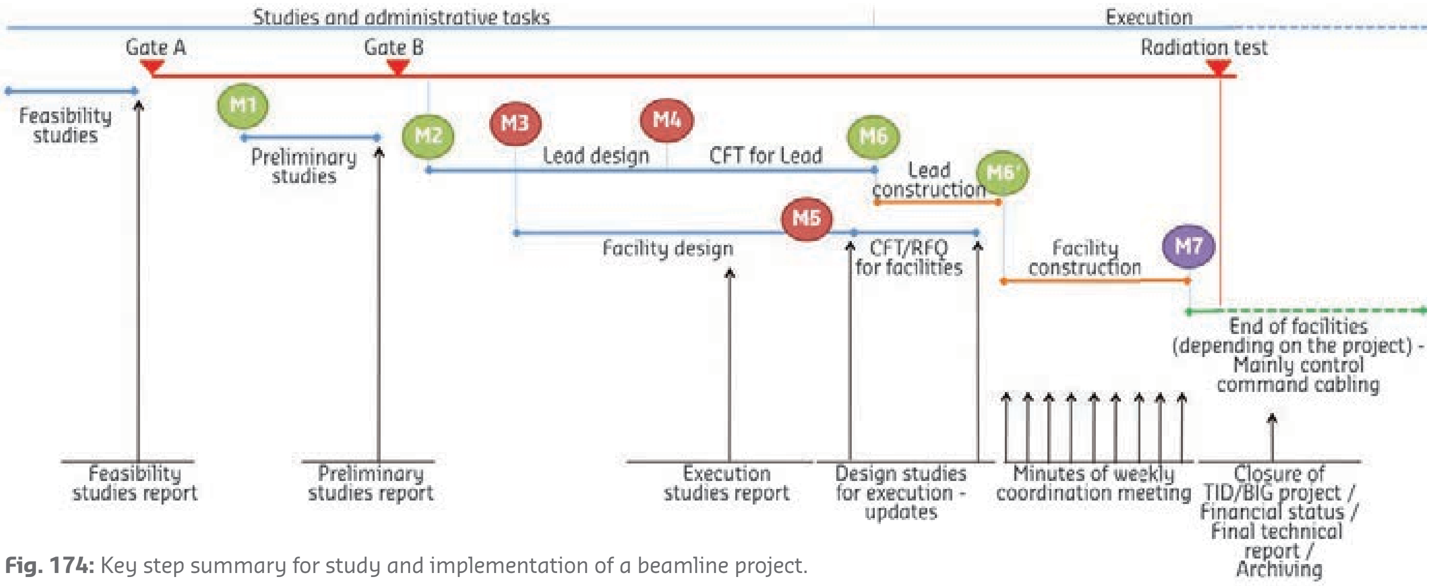

Fig. 174: Key step summary for study and implementation of a beamline project.

installation standards (specific cable trays for power cables, control cables, network cables, and security cables) and should be easily accessible in order to allow modification and future evolution proper to this type of installation.

- The cooling networks must be accessible for an easy installation of subsystems.
- The implementation of these utilities must be in line with French and European standards and regulations.

In order to standardise installation as much as possible and ensure efficient project management, the BIG has developed integration procedures, standard 2D and 3D beamline models and standard technical specifications. A beamline infrastructure project is punctuated by key phases such as the conceptual design phase (CDR) and technical design phase (TDR), and completed with the final step, 'Installation ready for radiation tests'.

The first step focuses on the definition of the user's needs. This starts with a study of radioprotection obligations with the integration of scientific and technical equipment and definition of the layout, followed by a definition of needs for specific infrastructure. From this, the BIG determines the requirements for the construction project, writes the technical specifications, then launches the calls for tender before proceeding to the construction phase. **Figure 174** shows the process of project management according to the steps outlined above and following the standard procedure.

A series of project milestones (**Table 1**) is drawn up and referred to by the project manager and technical designers, allowing them to ensure the timely progression of the project. The coordination tasks are managed and carried out by an ESRF team specialised in construction. This team takes care of technical coordination, interaction management, planning for studies and construction work, and ensures the smooth flow of the project until the commissioning and test phase.

Milestones

Gate A	CDR validation.
M1	Start of pre-study design (first lead, then facilities), first cost estimation (lead and facilities), planning for the construction.
Gate B	TDR validation.
M2	Start of lead design.
M3	Start of the facility design, final requirements, date when the mechanical engineering group (MEG) and beamlines (BL) have fully defined the lead hutch needs to TID.
M4	Launch of call for tender for lead construction.
M5	Launch of calls for tender or requests for quotations for facilities (final requirements for control cabins and facilities, date when MEG, BL and control have fully defined the cabling, fluids, HVAC and LN2 requirements to TID).
M6	Start of lead works.
M6'	Start of facilities works, end of lead works.
M7	All infrastructure ready for radiation tests (RT) / end of works.

Table 1: Milestones for beamline construction projects.

To conclude, specific project management practices ensure a rational and efficient implementation of the ESRF's beamline infrastructure projects. In addition, general coordination enables a global vision so that several projects can be carried out in parallel using the same type of resources. This coordination, undertaken by TID/BIG, is ensured by a regular follow-up of the workload, frequent interaction with the other support services and with the other divisions involved in such projects.

AUTHORS

T. Marchial. Contributors: E. Dodge, F. Favier, Y. Gouez and F. Pegot. *ESRF*.

THE PHOTON AND NEUTRON OPEN SCIENCE CLOUD (PaNOSC) PROJECT

Photon and neutron sources are hitting a data analysis wall with the huge increase in data volumes, new techniques and new user communities. Users are limited by the difficulty in exporting huge data sets and the lack of easy access to data analysis services. For this reason, the ESRF and five other European Strategy Forum on Research Infrastructures (ESFRI) institutes have started the PaNOSC project.

PaNOSC is financed by the EU's science funding framework H2020 (INFRAEOSC-04 programme) as part of the European Open Science Cloud (EOSC) project to make data at ESFRI photon and neutron sources 'FAIR' (*i.e.* Findable, Accessible, Interoperable and Reusable) **[1]** and to share the outcomes with all national photon and neutron sources (**Figure 175**). The PaNOSC partners include ESRF as project coordinator, ILL, EuXFEL, ESS, CERIC-ERIC, ELI-DC and EGI. PaNOSC is also assisted in its missions by GIANT, DESY, CESNET and STFC.

PaNOSC is a 12M€ project aimed at helping all six ESFRI partners to implement modern data management for scientific research data. The PaNOSC partners generate petabytes of scientific data each year – the ESRF alone generated nine petabytes of raw data in 2018. PaNOSC will enable these data to be professionally managed by generating meaningful metadata, minting persistent digital object identifiers, allowing to link publications to the underlying data and eventually to the analysis software, and by making the data available to the wider scientific community via the EOSC. The EOSC is being built by a large collaboration of ESFRI, e-infrastructures, and research infrastructures across Europe. The PaNOSC project is structured into nine work packages (WP):

Fig. 175: PaNOSC objectives.

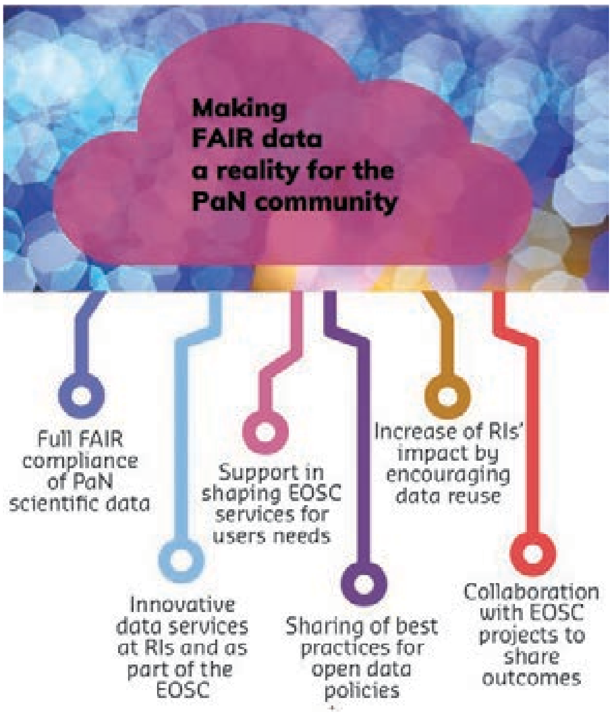

- **WP1 – Management**
The management WP follows up and reports on the financial aspects and deliverables of each WP.

- **WP2 – Data Policy and Stewardship**
Led by the ESRF, WP2 is dedicated to updating its scientific data policy to include the 'FAIR' principles as well as other new data stewardship topics such as GDPR. All six ESFRI partners will adopt or update their data policies accordingly. The second main objective is to prepare a tool for generating and evaluating data management plans.

- **WP3 – Data Catalogues**
Led by ESS, WP3 is dedicated to developing a common tool for searching and finding (to make data more findable) data in the PaNOSC and national photon and neutron data catalogues. An electronic logbook (to make data more reusable) and an enhanced data portal (to make data more accessible) are being developed at the ESRF. The Nexus metadata standard will also be extended (to make data more interoperable).

- **WP4 – Data Analysis Services**
Led by EuXFEL, WP4 will provide local and remote Jupyter notebook services and a remote desktop service. These services will be linked to the data so that users can find their data and run example notebooks on their data. The main developments will be a data analysis portal, improved visualisation for Jupyter and a web-based HDF5 viewer. Each partner institute will provide a production-grade Jupyter service.

- **WP5 – Simulation**
Led by EuXFEL, WP5 will develop and extend existing simulation services for photon (OASYS, SIMEX) and neutrons (McStas).

- **WP6 – Linking to the EOSC**
Led by the ILL, WP6 will make the user authentication authorisation infrastructure (AAI), UmbrellaID, sustainable with the help of partner GÉANT. This WP will link the data and simulation services to EOSC. It will also develop an efficient data download service for raw and reduced data.

- **WP7 – Sustainability**
Led by CERIC-ERIC, WP7 will calculate the costs of implementing 'FAIR' data and the associated data services and develop a sustainability plan for partners.

- **WP8 – Training**
Led by ESS, WP8 will provide an online training platform and develop training material for WPs 2-6. Users will be trained in best practice for 'FAIR' data principles and how to use the data analysis services for different scientific techniques.

- **WP9 – Communication**
Led by CERIC-ERIC, WP9 is in charge of communication of the web site (https://www.panosc.eu) and social media.

The PaNOSC project is a huge opportunity for the ESRFI photon and neutron sources to update and harmonise their data management to be 'FAIR', to develop and provide data analysis and simulation services for scientists, and to provide training. PaNOSC will help build and link to EOSC so that it fits the needs of the scientific communities (**Figure 176**). PaNOSC will share all the outcomes with its sister project – ExPaNDS **[2]**, which is doing the same for national photon and neutron sources in Europe. For more details on PaNOSC, refer to **[3]**.

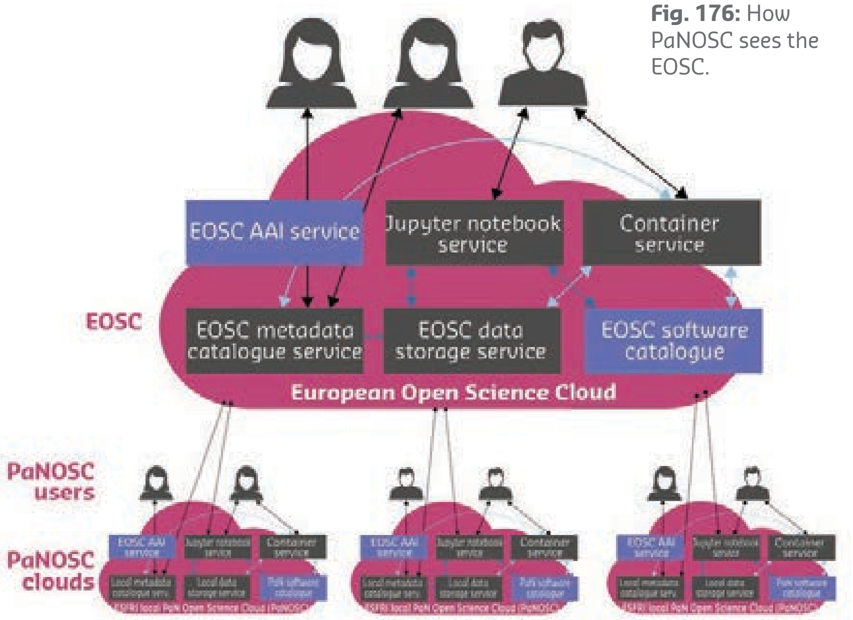

Fig. 176: How PaNOSC sees the EOSC.

AUTHORS

Andy Götz and Rudolf Dimper, on behalf of the PaNOSC partners. *ESRF*.

ACKNOWLEDGEMENTS

Special thanks to ESRF management and ESRF colleagues working on PaNOSC: J. Bodera Sempere, A. de Maria, M. Chaillet, T. Vincent, A. Sole, R. Homs, C. Nemoz, A. Campbell, J. Kieffer, B. Lebayle, E. Eyer and B. Rousselle. Also to M. Bowler, I. Kandiah, A. Gambardella and O. Konovalov, the first scientists to publish and/or help their users publish open data at https://data.esrf.fr.

REFERENCES

[1] M. D. Wilkinson *et al., Sci. Data* **3**, 160018 (2016).
[2] ExpPaNDS project, https://expands.eu/
[3] A. Götz *et al., Proc. of ICALEPCS2019, 7-11 Oct. 2019, New York, USA* (2019).

THE ELECTRONIC LOGBOOK, A TOOL FOR CAPTURING AND PRESERVING ESSENTIAL EXPERIMENTAL METADATA

The ESRF Data Policy was adopted in 2015 and has been in the process of being implemented since then [1]. An essential part of implementing the ESRF Data Policy is a web portal that includes an e-logbook, allowing users to document essential information about their experiments.

The web portal, https://data.esrf.fr, allows users and beamline staff to find, annotate, and download their data (**Figure 177**). The e-logbook is considered part of the metadata of the experiment and is an essential part of making data 'FAIR' (Findable, Accessible, Interoperable, Reusable) **[2]**. Accessing all the datasets obtained during an experiment is one thing, but understanding how these data can be exploited and reused is another. Without additional information, it would be cumbersome for scientists to reuse their data. This is where the e-logbook comes into play.

The main goal of the e-logbook is to enrich the information of a given experiment and especially the decision-making that drives the experiment. By storing all the steps followed during data acquisition in chronological order, it enables users to keep track of the conditions in which

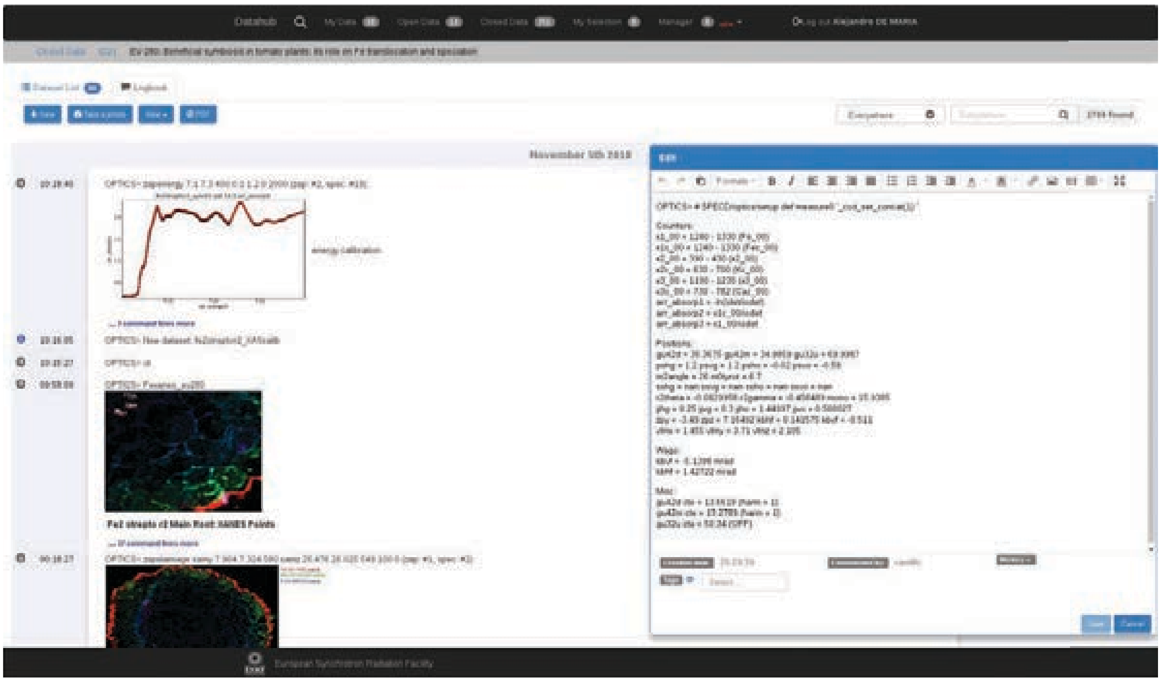

Fig. 177: Screenshot of the electronic logbook. *Image from proposal EV-280, Beneficial symbiosis in tomato plants: its role on Fe translocation and speciation, Dr. Ana Gonzalez Franco, Universidad Autonoma de Chihuahua/ Facultad de Ciencias Agrotecnologicas.*

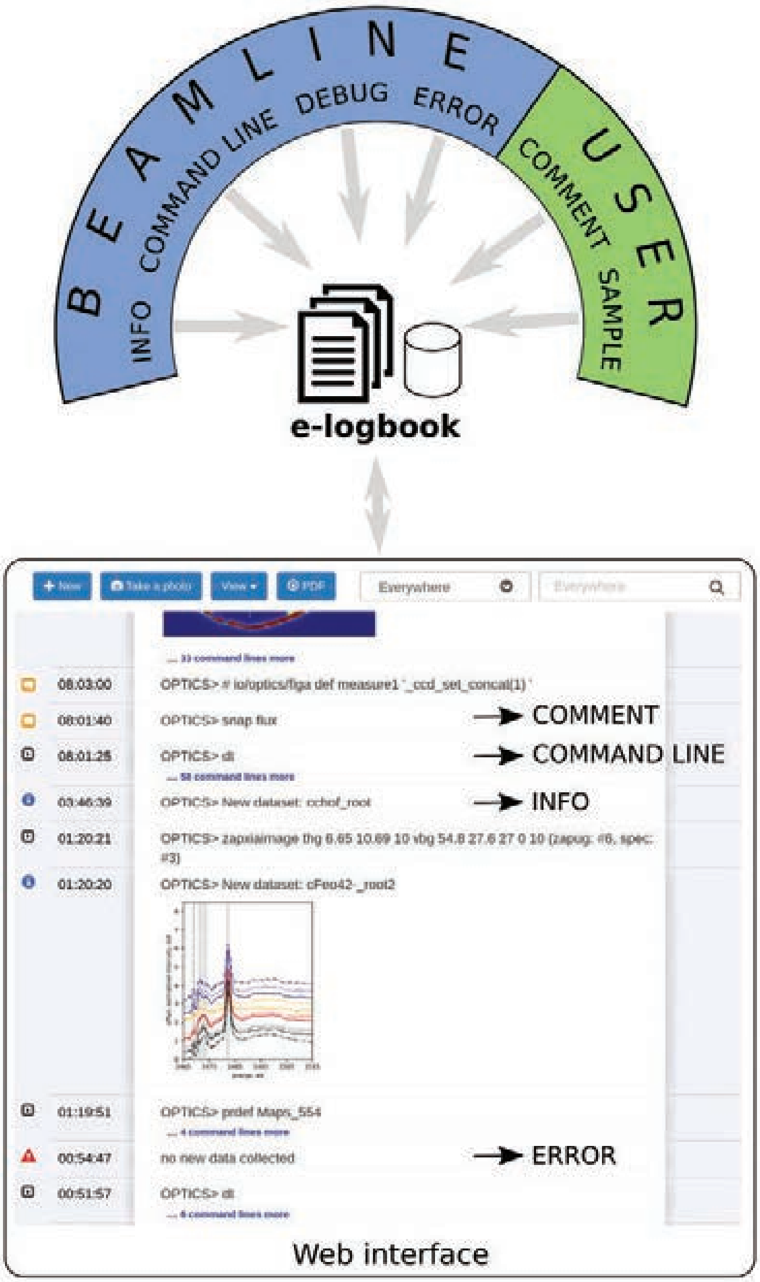

```
08:03:00  OPTICS> # io/optics/figa def measure1 '_ccd_set_concat(1)'
08:01:40  OPTICS> snap flux
08:01:25  OPTICS> dl
          ... 58 command lines more
03:46:39  OPTICS> New dataset: cchof_root
01:20:21  OPTICS> zapxiaimage thg 6.65 10.69 10 vbg 54.8 27.6 27 0 10 (zapug: #6, spec:
          #3)
01:20:20  OPTICS> New dataset: cFeo42-_root2
01:19:51  OPTICS> pdef Maps_554
          ... 4 command lines more
00:54:47  no new data collected
00:51:57  OPTICS> dl
          ... 6 command lines more
```

data and metadata were collected (**Figure 178**). The e-logbook is treated as metadata and is therefore required by the data policy to be archived and stored for as long as possible by the ESRF (raw data are stored for 10 years).

The e-logbook is composed of a series of timestamped logs from different sources: the acquisition side or the user entries, and is accessed via the data portal. During the data acquisition, messages such as errors, motor positions or commands issued by experimental team to the control system console (SPEC or BLISS shell) are sent automatically to the logbook. Beamlines generating images, graphs or tables during the acquisition process can send these to the logbook programmatically. Beamline scientists are able to customise what should be sent to the logbook automatically.

The web-based GUI enables the user to create notes or even comment logs in the e-logbook, thus replacing the beamline paper logbook. The fact that the e-logbook contents are stored centrally and are accessed via the web means it can provide features that are otherwise unavailable with a paper logbook.

A modern rich text editor enables authorised users to populate their e-logbook with rich text,

Fig. 178: The e-logbook stores additional metadata on the experiment. Timestamped logs stored in the e-logbook have two different origins: Either they are sent from the beamline data acquisition side and can correspond to errors, experimentally relevant information, command lines or debugging messages, or they are sent by the experimental team in the form of relevant comments enriching the experimental context or describing the sample, for example.

images and tables or comment existing logs. Each log has its own version modification control system that allows users to know when and by whom the log has been created or modified. While this system allows the experimental team to see who made entries and modifications, a public view does not show the identity of the person who made the entries.

A lot of effort has been invested in making the e-logbook user friendly. It has been developed in collaboration with scientists and improved based on their feedback. As an example, it facilitates insertion of images from any standalone application using a simple Ctrl+C/V keyboard shortcut. A tagging system is available and makes it possible to tag logs for organisation purposes. A log can be tagged with multiple tags: calibration, test, etc. The logbook is accessible from many different kinds of devices (*e.g.*, computers, phones and tablets) because it adapts to different screen sizes and resolution. The logbook supports adding photos from a mobile phone camera.

One big advantage over a paper logbook is the possibility to easily search for keywords, author(s), or timestamps instantaneously. In addition, the export feature enables a PDF document of all or only selected logs to be exported, thus making it possible to share the logbook content as a file.

At the end of the experiment, the corresponding e-logbook remains under embargo and is accessible to the experimental team only. The embargo period can be used to populate, update or enrich the logbook with analysis results that could not be performed during experimental beam time. At the expiration of the embargo period (three years by default), the e-logbook, the data and all the metadata become publicly accessible for peer-review proposals. For proprietary research, the information in the logbook remains confidential.

The e-logbook is an essential part of the data policy implementation at ESRF. The e-logbook software is open source and the source code repository is publicly available **[3]**. It has also been containerised so that it can be tested as a standalone product. It is available on all beamlines that implement the data policy. Development is still ongoing and new features are foreseen, for example, it is envisaged to accept additional logs related to online data analysis. Notably, other photon sources have shown an interest in the e-logbook developed at the ESRF and are planning to test it.

AUTHORS
M. Chaillet, A. De Maria, A. Sole and A. Götz.
ESRF.

REFERENCES
[1] R. Dimper *et al., Synchrotron Radiat. News* **32**(3), 7-12 (2019).
[2] M. D. Wilkinson *et al., Sci. Data* **3**, 160018 (2016).
[3] https://gitlab.esrf.fr/icat/elogbook-standalone

FACTS AND FIGURES

MEMBERS AND ASSOCIATE COUNTRIES

(AS OF JANUARY 2020)

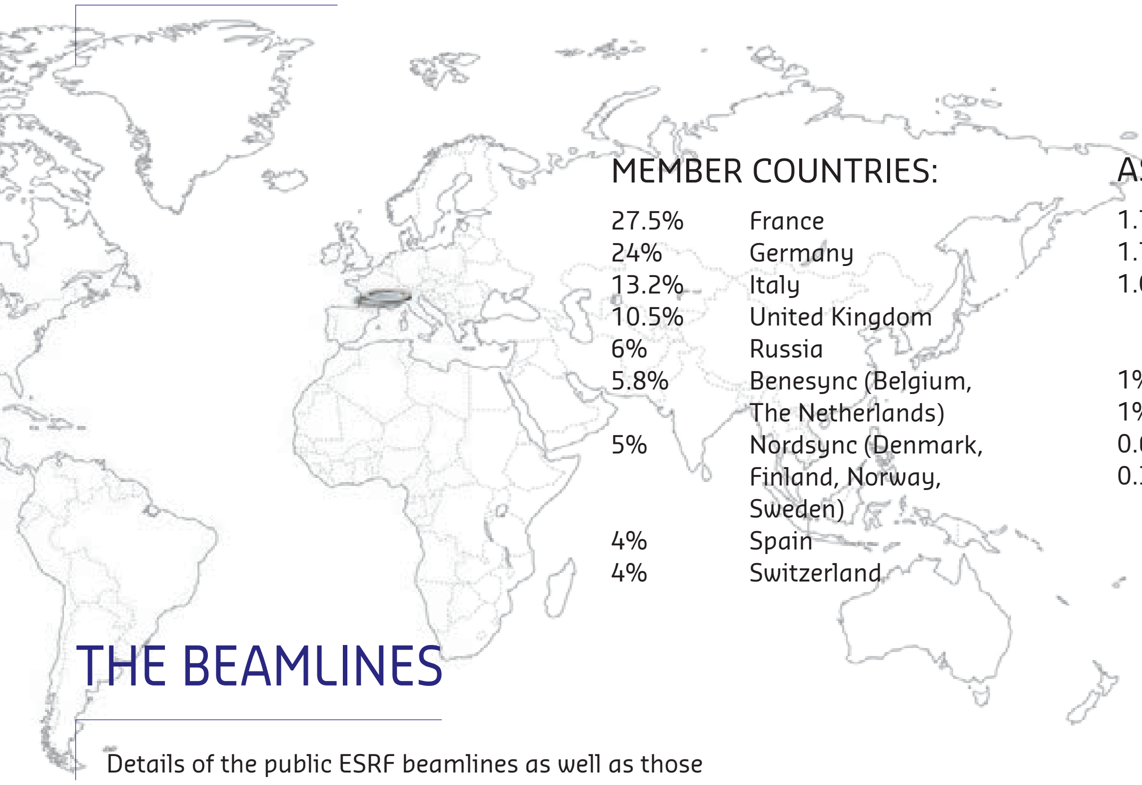

MEMBER COUNTRIES:

27.5%	France
24%	Germany
13.2%	Italy
10.5%	United Kingdom
6%	Russia
5.8%	Benesync (Belgium, The Netherlands)
5%	Nordsync (Denmark, Finland, Norway, Sweden)
4%	Spain
4%	Switzerland

ASSOCIATE COUNTRIES:

1.75%	Israel
1.75%	Austria
1.05%	Centralsync (Czech Republic, Hungary, Slovakia)
1%	Poland
1%	Portugal
0.66%	India
0.3%	South Africa

THE BEAMLINES

Details of the public ESRF beamlines as well as those operated by Collaborating Research Groups (CRG) are given in **Tables 2** and **3**. **Figure 179** shows the location of the beamlines in the experimental halls.

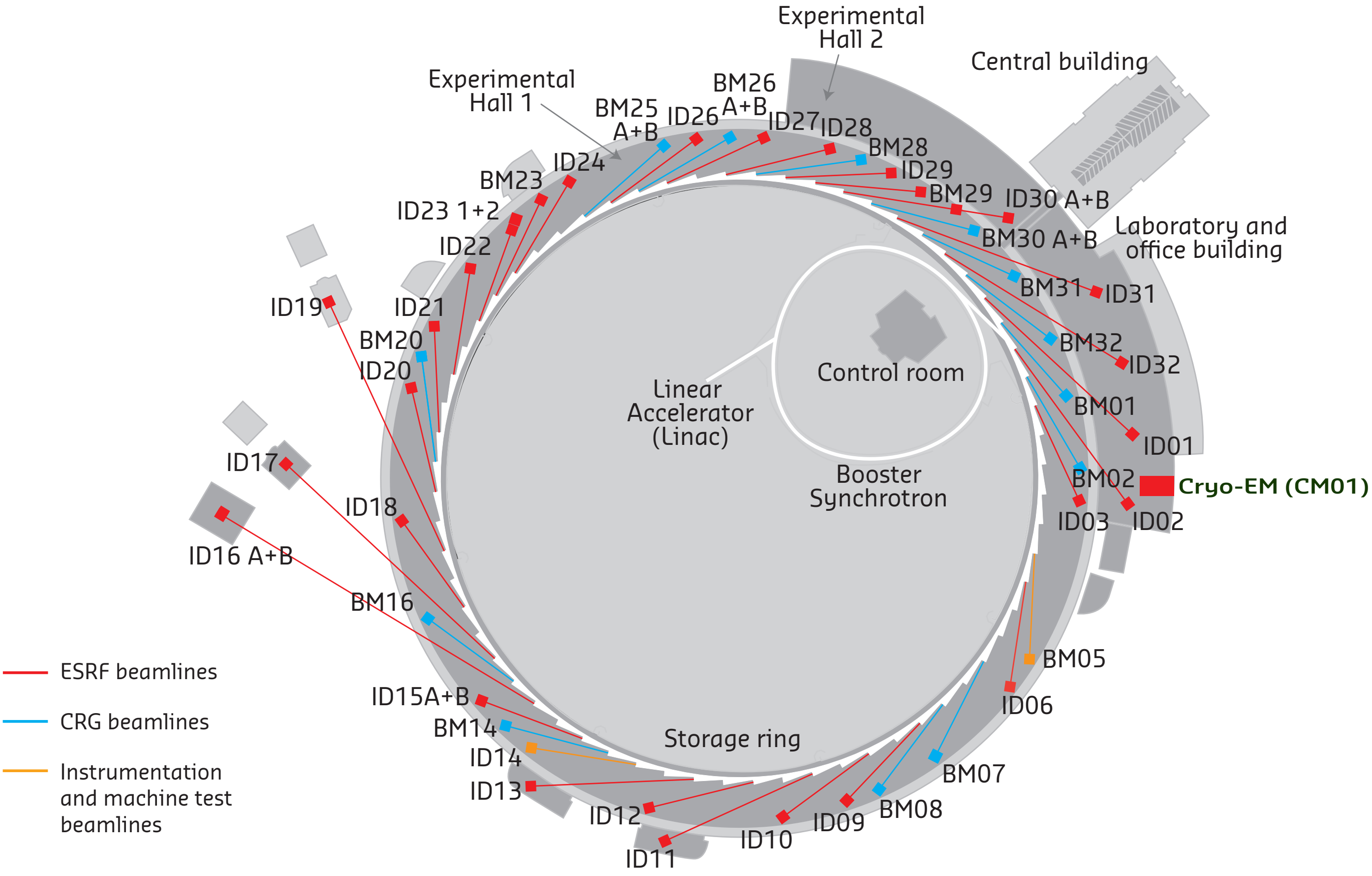

Fig. 179: Experimental hall showing location of the beamlines (public and CRG beamlines).

SOURCE POSITION	NUMBER OF INDEPENDENT END-STATIONS	BEAMLINE NAME	STATUS	
ID01	1	Microdiffraction imaging	Operational	since 12/14
ID02	1	Time-resolved ultra-small-angle X-ray scattering	Operational	since 07/14
ID03	1	Surface diffraction	Operational	since 09/94
ID06	0.4	Large volume press	Operational	since 10/13
ID09	1	Time-resolved structural dynamics	Operational	since 09/94
ID10	1	Soft interfaces and coherent scattering	Operational	since 06/12
ID11	1	Materials science	Operational	since 09/94
ID12	1	Polarisation-dependent X-ray spectroscopy	Operational	since 01/95
ID13	1	Microfocus	Operational	since 09/94
ID15A	0.85	Materials chemistry and engineering	Operational	since 11/16
ID15B	0.75	High-pressure diffraction	Operational	since 11/16
ID16A	1	Nano-imaging	Operational	since 05/14
ID16B	1	Nano-analysis	Operational	since 04/14
ID17	1	Medical	Operational	since 05/97
ID18	1	Nuclear scattering	Operational	since 01/96
ID19	1	Microtomography	Operational	since 06/96
ID20	1	Inelastic X-ray scattering	Operational	since 06/13
ID21	1	X-ray microscopy / IR spectroscopy	Operational	since 12/97
ID22	1	High resolution powder diffraction	Operational	since 05/14
ID23	2	Macromolecular crystallography MAD	Operational	since 06/04
		Macromolecular crystallography microfocus	Operational	since 09/05
ID24	1	Dispersive EXAFS	Operational	since 02/96
ID26	1	X-ray absorption and emission	Operational	since 11/97
ID27	1	High pressure	Operational	since 02/05
ID28	1	X-ray scattering II	Operational	since 12/98
ID29	1	Multiwavelength anomalous diffraction	Operational	since 01/00
ID30A	2	Macromolecular crystallography	Operational	since 07/14
ID30B	1	Macromolecular crystallography	Operational	since 04/15
ID31	1	Interfaces and materials processing	Operational	since 11/15
ID32	1	Soft X-ray spectroscopy	Operational	since 11/14
BM23	1	X-ray absorption spectroscopy	Operational	since 03/11
BM29	1	Bio SAXS	Operational	since 06/12
CM01	1	Cryo-EM	Operational	since 11/17

Table 2: List of the ESRF public beamlines.

SOURCE POSITION	NUMBER OF INDEPENDENT END-STATIONS	BEAMLINE NAME	FIELD OF RESEARCH	STATUS
BM01	1	Swiss-Norwegian BL	X-ray diffraction	Operational since 01/95
BM02	1	D2AM (French)	Materials science	Operational since 09/94
BM08	1	LISA (Italian)	X-ray absorption spectroscopy	Operational since 09/94
BM14	1	DUBBLE (Dutch/Belgian)	EXAFS	Operational since 05/18
BM16	1	FAME-UHD (French)	X-ray absorption spectroscopy	Operational since 02/17
BM20	1	ROBL (German)	Radiochemistry	Operational since 09/98
BM25	2	SPLINE (Spanish)	X-ray absorption and diffraction	Operational since 04/05
BM26	2	DUBBLE (Dutch/Belgian)	Small-angle scattering	Operational since 12/98
			EXAFS	Operational since 06/01
BM28	1	XMaS (British)	Diffraction, scattering and spectroscopy	Operational since 04/98
BM30	2	FIP (French)	Protein crystallography	Operational since 02/99
		FAME (French)	X-ray absorption spectroscopy	Operational since 08/02
BM31	1	SNBL II (Swiss-Norwegian)	X-ray absorption and diffraction	Operational since 09/16
BM32	1	IF (French)	X-ray diffraction and Laue microdiffraction	Operational since 09/94

Table 3: List of the Collaborating Research Group beamlines.

USER OPERATION

2019 was an unusual year for user operation – no X-ray beamlines were operating due to the EBS shutdown and the only user activity was on the cryo-electron microscope for structural biology (identified as 'beamline' CM01), since this facility runs independently of the ESRF accelerator and source. Applications for beamtime on the cryo-electron microscope are submitted on a continuous basis, with no fixed deadline, via the rolling access mechanism. Members of the Beam Time Allocation Panel for the structural biology beamlines reviewed the proposals as they were submitted and experiments were scheduled within two to three months following submission, with a typical duration of nine shifts (three days).

Figure 180 shows the number of applications for beamtime received since 2012. Following the Phase I Upgrade Programme activities, which finished in 2015, record high numbers of proposals were received successively from 2016 to 2018, reaching an all-time high in 2018 despite the shorter operation year (beam availability of 85% compared with a normal year). The 2019 figures for proposals received and allocated correspond mainly to the cryo-electron microscope activities but also include around 20 bio-SAXS and crystallography proposals for the structural biology beamlines. These proposals are also submitted via the rolling access mechanism and were submitted too late to be included in the 2018 figures for requests and allocation (although the experiments themselves were carried out in 2018 and so the beamtime, experiments and user visits are included in the 2018 figures).

The ESRF operation year runs from 1 March to the end of February the following year. The annual number of experimental sessions and user visits since 2012 is also shown in **Figure 180** (the 2019 figures do not include the remaining cryo-electron microscope time to be delivered in January and February 2020). Since 2018, the figure for user visits includes sample dewars sent by users, and paid for by the ESRF in place of a user, for structural biology experiments. Groups using structural biology beamtime may choose to request reimbursement of travel and subsistence for a user or transport costs for a dewar of samples. In 2019, 18 of the 48 experiments carried out so far on the cryo-electron microscope used the latter option, sending a total of 20 reimbursed dewars.

The number of shifts requested, allocated and delivered per year since 2012 is shown in **Figure 181**. The data for delivered shifts in 2019 include experiments up to 31 December 2019, so do not include the cryo-electron microscope time, which will be delivered in the remainder of the 2019 operation year, finishing on 1 March 2020. The average duration of a cryo-electron microscope experimental session in 2019 was nine shifts.

One of the key performance indicators of the ESRF is the number of publications resulting from data taken wholly or partially at the ESRF, or which include ESRF staff as authors, that are accepted in peer-reviewed journals. Yearly publication output from the ESRF has been systematically at a level of over 1800 publications for many years now, as shown in **Figure 182**. At the time of going to press, 1489 publications have already been registered for 2019, giving a total of 33 982 publications accepted in peer-reviewed journals, and this figure will continue to evolve well into next

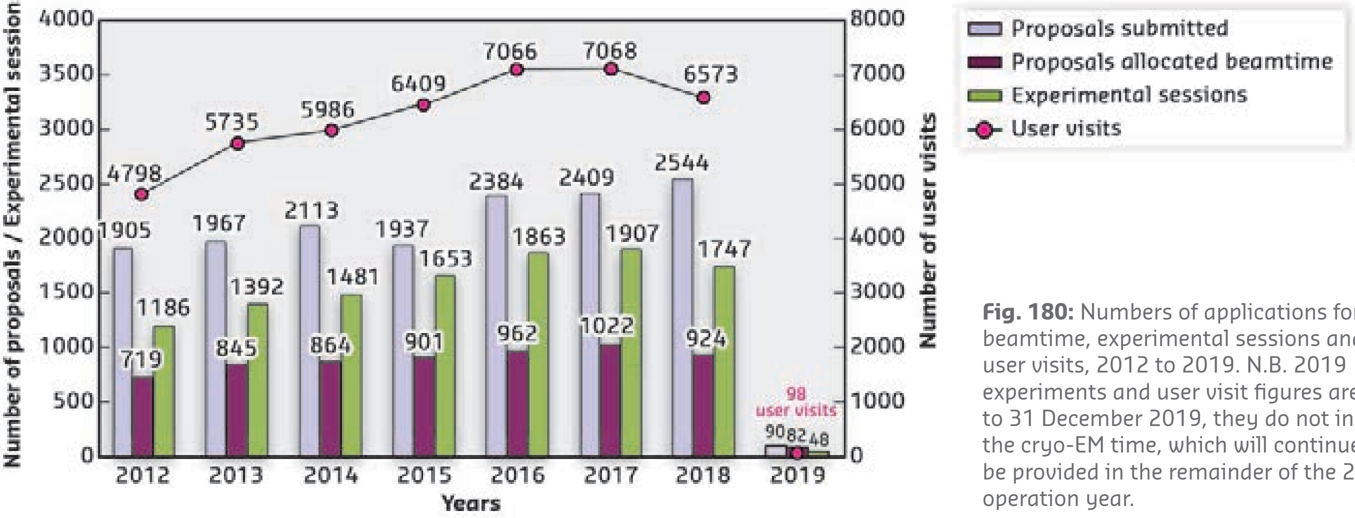

Fig. 180: Numbers of applications for beamtime, experimental sessions and user visits, 2012 to 2019. N.B. 2019 experiments and user visit figures are up to 31 December 2019, they do not include the cryo-EM time, which will continue to be provided in the remainder of the 2019 operation year.

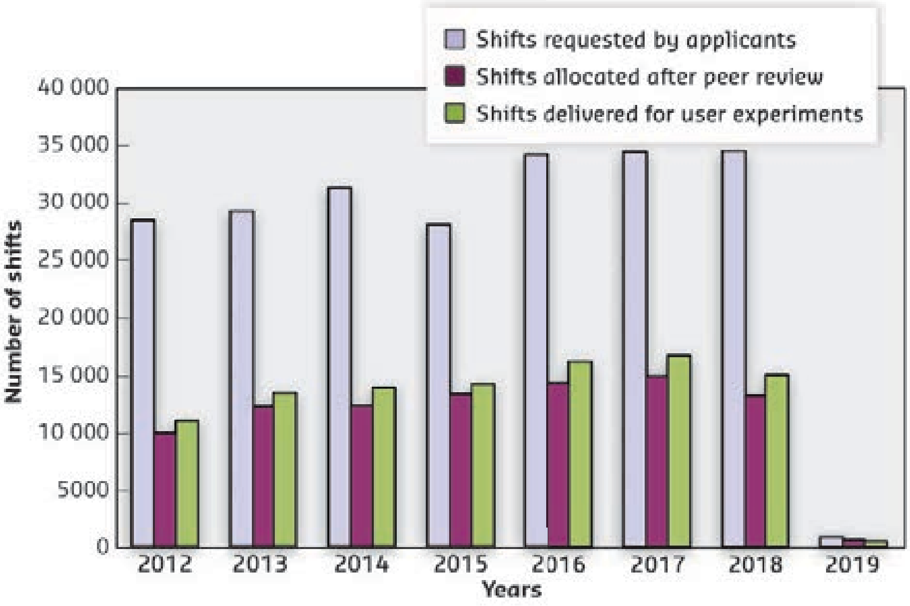

Fig. 181: Amount of beamtime requested, allocated and delivered, 2012 to 2019. N.B. Beamtime delivered for 2019 is up to 31 December. It does not include the cryo-EM time, which will continue to be provided in the remainder of the 2019 operation year.

year. Of these, around 300 every year are published in high impact factor journals (IF > 7). These are excellent figures, showing that the ESRF research output remains one of the highest worldwide.

EBS WORKSHOPS

In 2020, the ESRF will restart with the brand new Extremely Brilliant Source (EBS), and the challenge for our scientific community and staff will be to learn and understand how to fully exploit the properties of this new source to enhance the scientific research carried out at the ESRF. To this end, in 2019 the ESRF organised a series of EBS workshops, covering a multitude of topics and designed to gather together users, staff and other experts to discuss and identify strategies and challenges for performing the best experiments with the new source. These workshops will continue into 2020, and the full list is given in **Table 4**. In 2019, a total of 750 scientists participated in these workshops.

J. MCCARTHY

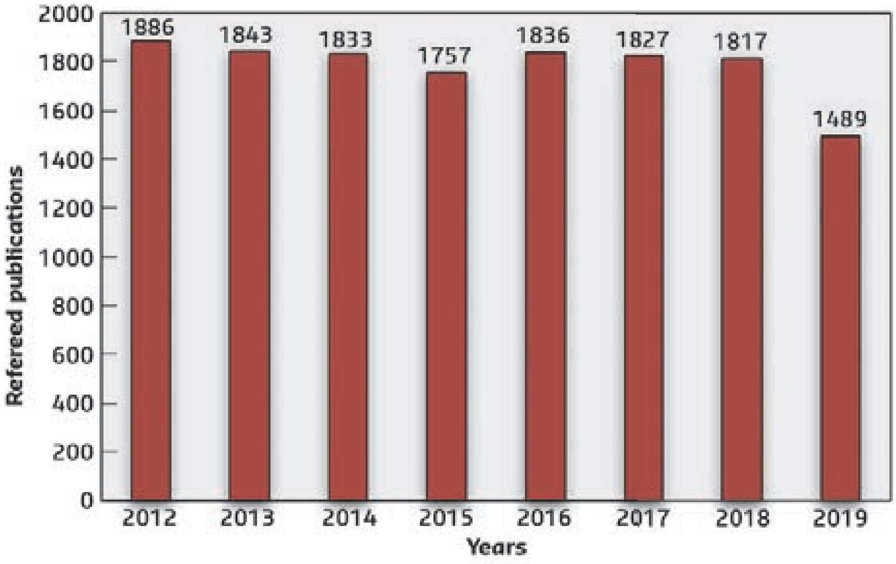

Fig. 182: Numbers of publications appearing in refereed journals reporting on data collected either partially or totally at the ESRF, 2012 to 2019. The number of publications for 2019 is not final at the time of going to press.

EBS Workshop Title	Dates
Time-resolved science at ID09 and its synergy with the EuXFEL programme	4-5 March 2019
Nuclear resonance scattering at the Extremely Brilliant Source	11-12 March 2019
X-ray Raman scattering spectroscopy probing low Z elements using hard X-rays	3-5 April 2019
Hands-on! High-pressure techniques at the ESRF-EBS (school)	17-21 June 2019
Coherence at ESRF-EBS	9-13 September 2019
Emerging synchrotron techniques for characterisation of energy materials and devices	23-25 September 2019
X-ray spectroscopy of magnetic materials	7-9 October 2019
Short-pulse science with the Extremely Brilliant Source	28-29 October 2019
Local electronic structure and coordination probed by X-ray emission spectroscopy	3-5 December 2019
Sample modulation by high photon densities: desired and undesired effects	11-13 December 2019
Cultural and natural heritage at ESRF-EBS	22-24 January 2020
Dark-field X-ray microscopy for EBSL2	15-17 April 2020
Studies of dynamically compressed matter with X-rays (DyCoMaX)	7-9 July 2020

Table 4: EBS Workshops in 2019 and 2020.

ADMINISTRATION AND FINANCE

The budget for 2019 includes additional contributions from Members and Scientific Associates of 11 419 kEUR dedicated to the ESRF-EBS Project. The ESRF-EBS expenditure budget amounts to a total of 29 905 kEUR including 19 521 kEUR of ESRF operating budget.

Expenditure and income 2018

Expenditure		kEuro
Accelerator and Source		
Personnel		7 051,2
Recurrent		2 971,3
Operating costs	*2 777,6*	
Other recurrent costs	*193,7*	
Capital		34 569,0
Accelerator and Source developments	*34 569,0*	
Beamlines, experiments and in-house research		
Personnel		19 696,7
Recurrent		5 583,1
Operating costs	*1 788,0*	
Other Recurrent costs	*3 795,1*	
Capital		6 065,6
Beamline developments	*6 065,6*	
Beamline refurbishment		
Technical and administrative supports		
Personnel		32 585,6
Recurrent		15 267,3
Capital		5 310,2
Unexpended committed funds		
Funds carried forward to 2019		3 683,0
Total		**132 783,0**

Income	kEuro
2018 Members' contributions	91 137,0
Funds carried forward from 2017	907,0
Other income	
Scientific Associates	7 072,9
Sale of beamtime	3 014,9
Scientific collaboration and Special projects	7 054,9
Balance ESRF-EBS	19 913,2
Funds carried forward to 2019	3 683,0
Total	**132 783,0**

Revised expenditure and income budget for 2019

Expenditure		kEuro
Accelerator and Source		
Personnel		6 937
Recurrent		2 072
Operating costs	*1 932*	
Other recurrent costs	*140*	
Capital		19 783
Accelerator and Source developments	*19 783*	
Beamlines, experiments and in-house research		
Personnel		14 819
Recurrent		3 760
Operating costs	*1 612*	
Other Recurrent costs	*2 148*	
Capital		9 921
Beamline developments	*9 921*	
Technical and administrative supports		
Personnel		33 012
Recurrent		10 582
Capital		9 339
Total		**110 225**

Income	kEuro
2019 Members' contributions	96 764
Funds carried forward from 2018	3 683
Other income	
Scientific Associates	7 258
Income from industrial co.activity	600
Scientific collaboration and Special projects	4 024
Balance ESRF-EBS	−2 104
Total	**110 225**

Expenditure 2018 by nature of expenditure	kEuro
PERSONNEL	
ESRF staff	56 916,5
External temporary staff	22,8
Other personnel costs	2 394,2
RECURRENT	
Consumables	9 522,5
Services	11 673,9
Other recurrent costs	2 625,3
CAPITAL	
Buildings, infrastructure	1 105,5
Lab. and Workshops	2 341,1
Accelator and Source incl. IDs and FEs	34 569,0
Beamlines, Experiments	6 065,6
Computing Infrastructure	1 806,3
Other Capital costs	57,3
Unexpended committed funds	
Funds carried forward to 2019	3 683,0
Total	**132 783,0**

Revised budget for 2019 by nature of expenditure	kEuro
PERSONNEL	
ESRF staff	52 300
External temporary staff	20
Other personnel costs	2 448
RECURRENT	
Consumables	5 625
Services	9 669
Other recurrent costs	1 120
CAPITAL	
Buildings, infrastructure	932
Lab. and Workshops	5 330
Accelator and Source incl. IDs and FEs	19 783
Beamlines, Experiments	9 921
Computing Infrastructure	2 977
Other Capital costs	100
Total	**110 225**

2019 manpower *(staff members present on 31/12/2019)*

	Scientists, Engineers, Senior Administrators	Technicians and Administrative Staff	PhD Students	Total
Staff on regular positions				
Accelerator and Source*	36	40	1	77
Beamlines, instruments and experiments*	197	95	11	303
General technical services	35	51		86
Directorate, administration and central services	37	56		93
Sub-total	*305*	*242*	*12*	*559*
Other positions				
Short term contracts	26	12		38
Staff under “contrats de professionnalisation”		21		21
Total	**331**	**275**	**12**	**618**
Scientific collaborators and consultants	*4*			*4*

** Including scientific staff on time limited contracts.*

ORGANISATION CHART OF THE ESRF

(AS OF JANUARY 2020)

Administrative and Finance Committee
Chairperson: J. Pickett

Council
Chairperson:
M. Á. García Aranda
up to 3 delegates per
Contracting Party

Science Advisory Committee
Chairperson: E. Weckert

Machine Advisory Committee
Chairperson: H.-H. Braun

Director General
F. Sette

DG's Services:
- **Head of DG's Office/Secretary of Council: I. Echeverria**
- **Communication Group**
- **Internal Auditor**
- **Safety Group**

ACCELERATOR AND SOURCE

Director: P. Raimondi

Beam dynamics and applications
Power supplies
Insertion devices
Front-ends
Radio frequency and linac
Diagnostics
Operation
Secretariat

ADMINISTRATION

Director: L-J. Sánchez Ortiz

Personnel
Finance
Purchasing

Joint ILL/ESRF
Medical service

EXPERIMENTS

Director: J. Susini

Beamline groups:
- **Complex systems and biomedical sciences**
- **Structural biology**
- **X-ray nanoprobe**

Director: H. Reichert

Beamline groups:
- **Electronic structure, magnetism and dynamics**
- **Matter at extremes**
- **Structure of materials**

Scientific infrastructure
Theory group
User office
CRG liaison office
Business Development Office
Joint ILL/ESRF Library
Secretariat

Beam Time Allocation Panels
C01 (ID01, BM25, BM32) Chairperson: C. Lucas
C02 (ID11, ID15A, ID22, ID31) Chairperson: A. Abakumov
C03 (ID12, ID32) Chairperson: A. Severing
C04 (BM08, BM14, BM16, BM20, BM23, BM30, BM31)
Chairperson: J. Van Bokhoven
C05 (ID06-LVP, ID15B, ID27, BM01)
Chairperson: H. Rosner
C06 (ID17, ID19) Chairperson: R. Cernik
C07 (ID16A, ID16B, ID21) Chairperson: F. Giannici
C08 (ID02, ID13, BM26) Chairperson: A. Petukhov
C09 (ID09, ID10, BM02, BM28) Chairperson: A. Madsen
C10 (Structural Biology Beamlines) Chairperson: M. Degano
C11 (ID20, ID24, ID26) Chairperson: J. Rose
C12 (ID18, ID28) Chairperson: V. Giordano

INSTRUMENTATION SERVICES AND DEVELOPMENT DIVISION

Head: J.-C. Biasci

Advanced analysis and modeling
Detector and electronics
Software
X-ray optics
Mechanical engineering

TECHNICAL INFRASTRUCTURE DIVISION

Head: C. Nevo

Management information systems and web
Systems and communication
Buildings and infrastructure
EX2/CPER project team
Survey and alignment
Vacuum

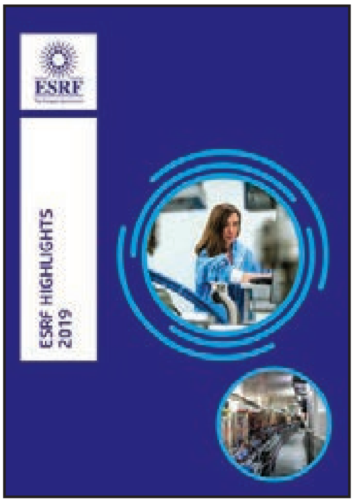

Cover
Cover design by A. Moullec

Photos © S. Candé.

We gratefully acknowledge the help of:

C. Argoud, J.-C. Biasci, A. Bosak, J.F. Bouteille, B. Boulanger, N. Brookes, J. Chavanne, D. Chenevier, A. Chumakov, K. Colvin, M. Cotte, K. Clugnet, E. Dancer, M. Di Michiel, R. Dimper, I. Echeverría, A. Fitch, P. Gaget, S. Gerlier, P. Glatzel, L. Hardy, M. Hahn, V. Honkimäki, J. Jacob, E. Jean-Baptiste, M. Krisch, G. Le Bec, G. Leonard, M. Mezouar, E. Mitchell, A. Moullec, C. Mueller-Dieckmann, J. McCarthy, C. Nevo, J. Pasquaud, P. Raimondi, H. Reichert, M. Retegan, J.L. Revol, S. Rio, B. Roche. A. Rogalev, E. Ryan, C. Sahle, K. Scheidt, F. Sette, J. Susini, N. Theyencheri, Y. Watier, S. White, M. Wulff and all the users and staff who have contributed to this edition of the *Highlights*.

Editor
A. Joly
Layout
Pixel Project
Printing
Imprimerie du Pont de Claix

© ESRF • February 2020

Communication Group
ESRF
CS 40 220
F38043 Grenoble Cedex 9 • France
Tel. +33 (0)4 76 88 20 56
Fax. +33 (0)4 76 88 25 42
http://www.esrf.eu